Astrophysics and Space Science Proceedings 34

Diego F. Torres
Olaf Reimer *Editors*

Cosmic Rays in Star-Forming Environments

Proceedings of the Second Session of the Sant Cugat Forum on Astrophysics

Sant Cugat Forum on Astrophysics

Springer

Astrophysics and Space Science Proceedings
Volume 34

For further volumes:
http://www.springer.com/series/7395

Cosmic Rays in Star-Forming Environments

Proceedings of the Second Session of the Sant Cugat Forum on Astrophysics

Editors

Diego F. Torres
Olaf Reimer

Springer

Sant Cugat Forum on Astrophysics

Editors
Diego F. Torres
ICREA & Institute of Space Sciences
(IEEC-CSIC)
Campus UAB
Fac. de Ciències
Barcelona
Spain

Olaf Reimer
Leopold-Franzens-Universität Innsbruck
Institut für Astro- und Teilchenphysik
Innsbruck
Austria

ISSN 1570-6591
ISBN 978-3-642-35409-0
DOI 10.1007/978-3-642-35410-6
ISSN 1570-6605 (electronic)
ISBN 978-3-642-35410-6 (eBook)
Springer Heidelberg New York Dordrecht London

Library of Congress Control Number: 2013935701

Printed on acid-free paper

Springer is part of Springer Science+Business Media (www.springer.com)

Preface

The Sant Cugat Forum on Astrophysics[1] is a framework designed to host international meetings of scientists directed to analyze violent phenomena in the universe. The forum workshops focus on a specific aspects of astrophysics, are held every 2 years with a typical attendance of up to 100 scientists, and have a duration of 3–4 days. This book gives account of the 2nd forum session: "Workshop on cosmic-ray induced phenomenology in star-forming environments" and was held on April 16–19, 2012.

During the last few years, we witnessed how the newest facilities observing gamma rays of high (>100 MeV) and very high energy (>100 GeV), among them, the GeV-satellites Fermi and AGILE and the ground-based TeV telescopes MAGIC, VERITAS, and H.E.S.S., established interesting facts concerning cosmic-ray-induced phenomenology in stellar environments. Indeed, observations of closer, normal galaxies, like the LMC, have revealed an inner structure that allows comparing with the position, and studying the influence, of star-forming regions directly. The first detections ever of starbursts galaxies in gamma rays were achieved both in GeV and TeV bands, followed by the first population analysis of infrared luminous galaxies. Discussions of the relationship between central AGNs and starbursts as origins of the high-energy emission are starting to be possible, as well as a more detailed analysis of the cosmic ray environment in galaxies other than our own. Also, the relationship between cosmic ray acceleration in shells and their interaction in nearby molecular clouds can at last be studied observationally, with an increasing degree of precision, shedding light on the diffusion properties of cosmic rays in different galactic environments. Additionally to this traditional astroparticle focus for understanding the propagation of the highest energy cosmic rays, molecular abundance ratios could turn out to be a new way to trace the presence of cosmic rays and to infer their fluxes, given that observed abundance enhancements could be due to ionization by X-rays and/or interactions of low-energy CRs with gas and dust. Finally, the fluorescent Fe Kα line at 6.4 keV is also

[1] http://www.ice.csic.es/research/forum

detected from molecular clouds in the galactic center region and can be accounted for in terms of the impact of low-energy CRs with neutral gas in the clouds. These are the topics of this book.

In a sense, this workshop built up on a very interesting meeting held at the Lorenz Center in Leiden, earlier in 2011: "Cosmic Ray Interactions: Bridging High and Low Energy Astrophysics," and was organized by S. Markoff, J. Martín Pintado, J. Vink, F. Yusef-Zadeh, and one of us (D. F. Torres). It was clear in that meeting that the topic deserved further discussion, as well as a reference book. We hope that this volume could help filling this gap.

We would like to warmly thank the Scientific Organizing Committee (SOC), who have helped us shape the content and direction of the workshop. The SOC was formed by:

Wlodek Bednarek (Lodz University, Poland)
Giuseppe Bono (U. Rome, Italy)
Margarita Hernanz (IEEC-CSIC, Spain)
Jürgen Knödlseder (CESR, France)
Yoel Rephaeli (Tel Aviv and UC San Diego)
Olaf Reimer (U. Innsbruck, Austria)
Todd Thompson (U. Ohio, USA)
Diego F. Torres (ICREA & IEEC-CSIC, Spain)
Rens Waters (SRON, Netherlands)

Similarly, the local support team (LOC) has helped us along the way in every organizational issue. The LOC was formed by:

Anna Bertolin (IEEC)
Marco Padovani (IEEC)
LLuis Campins (Museu Monastir, Sant Cugat)
Ana Castells (Casa de la Cultura, Sant Cugat)
Marta de Castro (Oficina de Turismo, Sant Cugat)
Valenti Feixas i Sibila (Sant Cugat City Hall, Spain)
Daniela Hadasch (IEEC-CSIC)
Pilar Montes (IEEC)
Nanda Rea (IEEC-CSIC)
Jonatan Martin Rodriguez (IEEC-CSIC)

We would also like to thank our sponsors, the Institut d'Estudis Espacials de Catalunya (IEEC), the Institute for Space Sciences (ICE-CSIC), the Ministery of Economy of Spain (MINECO), and especially, the City Hall of Sant Cugat, whose continued involvement is a driving force behind the forum project. Among the many with whom we have interacted from the Sant Cugat City Hall, we especially acknowledge the Major, Excma. Sra. Mercè Conesa i Pages; the Regidora

d'Educació, Universitat i Família de l'Ajuntament de Sant Cugat, Sra. Esther Salat; and the former Director of Cultural Affairs, Valentí Feixas i Sibila.

Sant Cugat
September 2012

Diego F. Torres
Olaf Reimer

Contents

Contributors

Rebeca Aladro Department of Physics and Astronomy, UCL, London, UK

Antxon Alberdi Instituto de Astrofísica de Andalucía (IAA-CSIC), Glorieta de la Astronomía s/n, Granada, Spain

Yago Ascasibar Universidad Autónoma de Madrid, Madrid, Spain

Manda Banerji Institute of Astronomy, University of Cambridge, Cambridge, UK

Estelle Bayet Sub-Department of Astrophysics, University of Oxford, Oxford, UK

J.K. Becker Fakultät für Physik & Astronomie, Ruhr-Universität Bochum, Bochum, Germany

J. Becker Tjus Ruhr-Universität Bochum, Fakultät für Physik & Astronomie, Bochum, Germany

W. Bednarek Department of Astrophysics, The University of Lodz, Lodz, Poland

Thomas A. Bell Centro de Astrobiologa, CSIC–INTA, Madrid, Spain

J.H. Black Department of Earth and Space Sciences, Onsala Space Observatory, Chalmers University of Technology, Onsala, Sweden

G. Bono Dipartimento di Fisica, Universita' di Roma Tor Vergata, Roma, Italy

INAF– Osservatorio Astronomico di Roma, Monte Porzio Catone, Italy

Science visitor, European Souther Observatory, Garching bei München, Germany

Dieter Breitschwerdt Zentrum für Astronomie und Astrophysik, TU Berlin, Berlin, Germany

Damiano Caprioli Princeton University, Princeton, NJ, USA

Emiliano Carmona Max-Planck-Institut für Physik, München, Germany

Centro de Investigaciones Energéticas, Medioambientales y Tecnológicas (CIEMAT), Madrid, Spain

S. Casanova Unit for Space Physics, North-West University, Potchefstroom, South Africa

G. Chaparro Molano Kapteyn Astronomical Institute, Groningen, The Netherlands

Roland Crocker Max-Planck-Institut für Kernphysik, Heidelberg, Germany

Miguel de Avillez Department of Mathematics, University of Évora, Évora, Portugal

A. Decourchelle Service d'Astrophysique (SAp)/IRFU/DSM/CEA Saclay, Gif-sur-Yvette Cedex, France

Laboratoire AIM, CEA-IRFU/CNRS/Univ Paris Diderot, CEA Saclay, Gif sur Yvette, France

Eduardo de la Fuente Dpto. de Física, CUCEI, Universidad de Guadalajara (U de G), Guadalajara, Jalisco, México

Ángeles I. Díaz Universidad Autónoma de Madrid, Madrid, Spain

Ernst Dorfi Institut für Astronomie, Universität Wien, Wien, Austria

Wing Fai-Thi UJF-Grenoble 1/CNRS-INSU, Institut de Plantologie et d'Astrophysique (IPAG) UMR 5274, Grenoble, France

Yasuo Fukui Department of Physics, Nagoya University, Nagoya, Japan

Stefano Gabici AstroParticule et Cosmologie, Université Paris Diderot, CNRS/IN2P3, CEA/IRFU, Observatoire de Paris, Sorbonne Paris Cité, Paris Cedex 13, France

Daniele Galli INAF – Osservatorio Astrofisico di Arcetri, Firenze, Italy

José Luis García–Luna for the HAWC Collaboration Dpto. de Física, CUCEI, Universidad de Guadalajara (U de G), Guadalajara, Jalisco, México

Guillermo García–Torales Dpto. de Electrónica, CUCEI, U de G, Guadalajara, Jalisco, México

K. Genovali Dipartimento di Fisica, Universita' di Roma Tor Vergata, Roma, Italy

Andrea Goldwurm Service d'Astrophysique (SAp), IRFU/DSM/CEA-Saclay, Gif-sur-Yvette Cedex, France

Unité mixte de recherche Astroparticule et Cosmologie, Paris, France

Rebecca Gozzini Deutsches Elektronen-Synchrotron (DESY), Zeuthen, Germany

Michał Hanasz Centre for Astronomy, Faculty of Physics, Astronomy and Informatics, Nicolaus Copernicus University, Grudziadzka 5, 87-100 Toruń, Poland

Thomas W. Hartquist School of Physics and Astronomy, University of Leeds, Leeds, UK

Rubén Herrero-Illana Instituto de Astrofísica de Andalucía (IAA-CSIC), Glorieta de la Astronomía s/n, Granada, Spain

Nick Indriolo Johns Hopkins University, Baltimore, MD, USA

L. Inno Dipartimento di Fisica, Universita' di Roma Tor Vergata, Roma, Italy

Fabian Jankowski on behalf of the MAGIC Collaboration Deutsches Elektronen-Synchrotron (DESY), Zeuthen, Germany

I. Kamp Kapteyn Astronomical Institute, Groningen, The Netherlands

Jürgen Knödlseder IRAP, Toulouse Cedex 4, France

Kacper Kowalik Centre for Astronomy, Faculty of Physics, Astronomy and Informatics, Nicolaus Copernicus University, Grudziadzka 5, 87-100 Toruń, Poland

Julian Krause Max-Planck-Institut für Physik, München, Germany

Brian C. Lacki Jansky Fellow of the National Radio Astronomy Observatory, Institute for Advanced Study, Astronomy, Princeton, NJ, USA

E.P. Lagioia Dipartimento di Fisica, Universita' di Roma Tor Vergata, Roma, Italy

U. Lisenfeld Department of Física Teórica y del Cosmos, Universidad Granada, Granada, Spain

M. Mandelartz Fakultät für Physik & Astronomie, Ruhr-Universität Bochum, Bochum, Germany

N. Matsunaga Department of Astronomy, School of Science, The University of Tokyo, Tokyo, Japan

G. Maurin Laboratoire d'Annecy le Vieux de Physique des Particules, Univ de Savoie, CNRS, Annecy-le-Vieux Cedex, France

Thierry Montmerle Institut d'Asttrophysique de Paris, Paris, France

Mark R. Morris Department of Physics and Astronomy, University of California, Los Angeles, CA, USA

Alberto Noriega-Crespo IPAC, California Institute of Technology, Pasadena, CA, USA

Aura C. Obreja Universidad Autónoma de Madrid, Madrid, Spain

Tomas Oceguera–Becerra CUCEA, U de G, Zapopan, Guadalajara, Jalisco, México

J. Pabich Department of Astrophysics, The University of Lodz, Lodz, Poland

Marco Padovani Laboratoire de Radioastronomie Millimétrique, UMR 8112 du CNRS, École Normale Supérieure et Observatoire de Paris, Paris cedex 05, France

Padelis P. Papadopoulos Max Planck Institute for Radioastronomy, Bonn, Germany

Miguel Ángel Pérez-Torres Instituto de Astrofísica de Andalucía (IAA-CSIC), Glorieta de la Astronomía s/n, Granada, Spain

Massimo Persic INAF/Osservatorio Astronomico di Trieste and INFN-Trieste, Trieste, Italy

Gabriele Ponti Max-Planck-Institut für extraterrestrische Physik, Garching bei München, Germany

Ignasi Reichardt IFAE, Bellaterra, Spain

Yoel Rephaeli School of Physics and Astronomy, Tel Aviv University, Tel Aviv, Israel

Center for Astrophysics and Space Sciences, University of California, San Diego, La Jolla, CA, USA

Denise Riquelme Instituto de Radioastronomía Milimétrica, Granada, Spain

S. Schöneberg Ruhr-Universität Bochum, Fakultät für Physik & Astronomie, Bochum, Germany

F. Schuppan Ruhr-Universität Bochum, Fakultät für Physik & Astronomie, Bochum, Germany

Fakultät für Physik & Astronomie, Ruhr-Universität Bochum, Bochum, Germany

Meng Su Institute for Theory and Computation, Harvard-Smithsonian Center for Astrophysics, Cambridge, MA, USA

V. Tatischeff Centre de Spectrométrie Nucléaire et de Spectrométrie de Masse, IN2P3/CNRS and Univ Paris-Sud, Orsay Campus, France

Regis Terrier Unité mixte de recherche Astroparticule et Cosmologie, Paris, France

Todd A. Thompson Department of Astronomy and Center for Cosmology & Astro-Particle Physics, The Ohio State University, Columbus, OH, USA

Serena Viti Department of Physics and Astronomy, University College London, London, UK

H.-J. Völk Max-Planck-Institut für Kernphysik, Heidelberg, Germany

David A. Williams Department of Physics and Astronomy, University College London, London, UK

Dominik Wóltański Centre for Astronomy, Faculty of Physics, Astronomy and Informatics, Nicolaus Copernicus University, Grudziadzka 5, 87-100 Torún, Poland

F. Yusef-Zadeh Department of Physics and Astronomy, Northwestern University, Evanston, IL, USA

Prologue: γ-Rays from Star-Forming Regions, a Historical Perspective

Thierry Montmerle

Abstract At last, we are in a position to scrutinize the acceleration, diffusion and propagation processes of cosmic rays in the vicinity of supernova shocks, the interaction of both high-energy (GeV-TeV) and low-energy (100 MeV and below) cosmic rays with molecular clouds, generating high-energy gamma-rays and ionization processes respectively. This prologue provides a historical introduction to the studies of the interaction of cosmic-rays and star-forming regions.

Contrary to what people might think today, γ-ray astronomy already has a long history – "long" meaning here over 50 years. Indeed, in a pioneering paper, P. Morrison [15] established the theoretical basis of γ-ray astronomy as we know it today. In particular, he pointed out π^0 decay as a potentially important mechanism of interaction between high-energy particles ("cosmic rays") and matter in space. Other studies along the same lines followed (e.g., [2, 7, 19]), but somewhat later, as experiments began to investigate the sky at γ-ray energies.

At that time, the detection of very high-energy (VHE) cosmic rays by the air shower technique, pioneered by L. Leprince-Ringuet, was well known, but the experimental set-ups could detect only nuclei. Apart from the fact that lower energy cosmic rays had to be studied from balloons to overcome atmospheric attenuation (think of Victor Hess and his electrometer in 1912!), a long-term goal was *to find the location of "cosmic-ray sources"*, using the fact that VHE cosmic rays are almost insensitive to deviations by the weak galactic magnetic fields.

It took more progress on the theory of the development of air showers to establish criteria to detect γ-rays and distinguish them from nuclei ([12], et sq.). As a result, based on the experience gained with cosmic-rays, Čerenkov telescopes (this time in the real sense of detecting photons coming from a given direction in the sky) were

T. Montmerle (✉)
Institut d'Asttrophysique de Paris, Paris, France
e-mail: montmerle@iap.fr

D.F. Torres and O. Reimer (eds.), *Cosmic Rays in Star-Forming Environments*,
Astrophysics and Space Science Proceedings 34, DOI 10.1007/978-3-642-35410-6_1,

built in the early 1960s by several groups, including on Mt Whipple in Arizona (T. Weekes et al.), and near Simferopol in Crimea (A.A. Stepanian et al.).

The first goal was of course to try and find "point sources" of γ-rays in the sky. At this time, quasars ("quasi-stellar objects") has just been discovered ([17]: 3C273), with their unusual optical spectra and high redshifts, so the high-galactic latitude part of the sky became the prime target, even though of course the whole sky (i.e., visible from a given observatory), including parts of the galactic plane, was scanned.

However, this first era of observational γ-ray astronomy brought only upper limits, and since there were no a priori quantitative expectation that quasars should be γ-ray emitters, the field looked like a dead end to many astronomers.

The breakthrough came with the discovery of pulsars (1967, published in 1968: [11]). With their pulsating radio emission and power-law spectra, they were an entirely new class of astronomical objects. Extrapolating to high energies resulted in a "prediction" of γ-ray emission up to the TeV range ([9], et sq.), and boosted the morale of γ-ray astronomers! The fact that the emission was periodic allowed to enhance the S/N ratio, and therefore the probability of detection, by selecting events in phase with the radio emission. And the discovery of the pulsed γ-ray emission of the Crab pulsar NP0532 was indeed soon to follow [10], and could be considered as marking the real birth of γ-ray astronomy.

Since celestial sources were found to exist at TeV energies, it was of course tempting to detect them at lower energies – but from GeV energies down to the UV domain photons are absorbed by the Earth's atmosphere without giving rise to detectable secondary particles as TeV photons do. So the techniques to be used had to be entirely different from ground-based Čerenkov telescopes. While coming also from accelerator physics, like proportional counters for X-rays or spark chambers for GeV γ-rays, these techniques had, in addition, to be adapted to be able to fly on balloons, rockets, or even better, go to space aboard satellites.

Keeping in mind the milestone date of 1967 for the discovery of pulsars, the reactivity of the community was astounding. In the framework of NASA's "Small Astronomical Satellites", part of the Explorer program, the first X-ray satellite, SAS-1 (aka Explorer 42, which became famous under the name of "Uhuru") was launched in December 1970 – to last until 1973 – and the first γ-ray "observatory", operating in the 10 MeV–1 GeV range, SAS-2 (aka Explorer 48), was launched in 1972 – unfortunately forced to silence because of an electrical breakdown after only 6 months of operation.[1]

However short-lived, SAS-2 was able to provide the first γ-ray map of part of the sky, revealing two of the most luminous pulsars and their γ-ray pulsations, the Crab and Vela, and, most importantly for our purpose in the present chapter, *diffuse γ-ray emission from the galactic plane* (see Fig. 1, [6]). After this unfortunate failure, the

[1] Strictly speaking, the first celestial γ-rays were detected in the >70 MeV range by the OSO-3 satellite, which was a solar observatory. The main result was the detection of an excess in the galactic center direction [4].

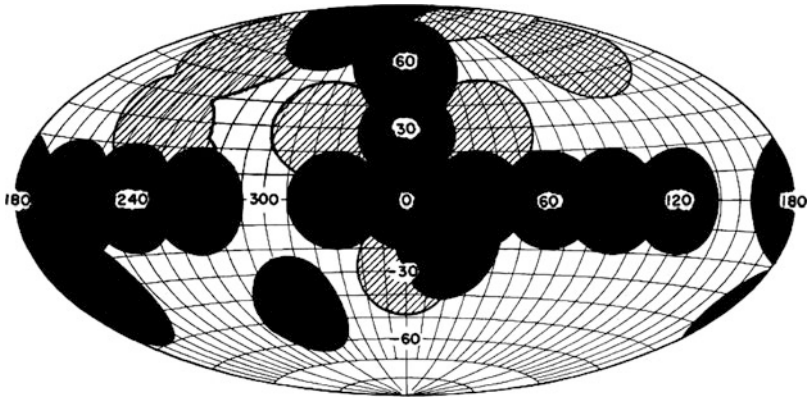

Fig. 1 The areas observed by the SAS-2 satellite in its 8-month lifetime. The Crab and Vela pulsars were detected, as well as evidence for galactic diffuse emission. Only upper limits could be obtained in the other regions (Fichtel et al. [6])

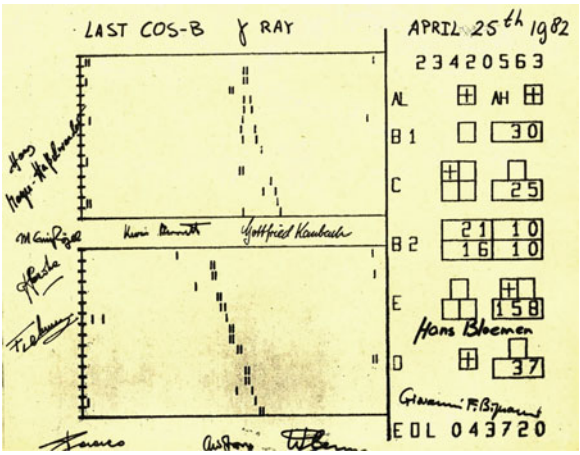

Fig. 2 The last γ-ray observed by COS-B's spark chamber. The inverted "V" is a signature of the creation of a secondary electron-positron pair as the incoming γ-ray is absorbed by the spark chamber plates. The two views are orthogonal, and allow to reconstruct the photon arrival direction with a typical resolution of $\sim 1^\circ$ HWHM above 300 MeV. The image is signed by the main actors of the COS-B saga (Source: ESA)

leadership of γ-ray astronomy shifted across the Atlantic with the launch by ESA of the COS-B satellite in 1975. COS-B, which lasted until 1982 (see the "last photon" signature in Fig. 2), made the γ-ray all-sky a reality, with its point sources, both galactic and extragalactic, and the first detailed mapping of the galactic plane.

In other words, γ-ray astronomy really came of age in the COS-B era. Interestingly, major ingredients in our understanding of galactic γ-ray emission features fell into place during this era, almost simultaneously but independently: (i) the detection of the CO molecule, as a tracer of molecular hydrogen, at mm wavelengths, in other words the discovery of molecular clouds ([18], et sq.); (ii) the positioning of HII regions as tracers of the spiral structure of the galaxy [8]; (iii) the realization of the so-called "sequential star formation" in molecular clouds [5]; (iv) a breakthrough in

the theory of cosmic-ray acceleration by shock waves [1], now known and developed as the "diffusive shock acceleration" theory. Very exciting times indeed!

This converging set of ingredients led to two major consequences on the interpretation of the galactic γ-ray emission, as seen by COS-B:

(i) The excellent correlation on the sky, both in longitude and in latitude (within $\pm 5°$), with the CO distribution, immediately suggested that the π^o-decay mechanism was dominant (albeit mixed with other processes like inverse Compton in some places), and that the galactic cosmic-ray flux ("GCR": above $\sim$1 GeV, i.e., essentially insensitive to the solar modulation) had to be fairly uniform across the galaxy (e.g., [16]). Furthermore, by using distances derived from the galactic velocity curve for CO and HII regions, and masses for molecular clouds derived from a nominal CO/H_2 ratio, it was possible to feed into the γ-ray data a model for the galactic spiral arms, and then deduce the arm-interarm GCR contrast, which turned out to be not more than a factor 2–3. In turn, this supported the idea that cosmic ray nuclei diffuse very efficiently from their sources out in the galactic disk. Good news for understanding cosmic-ray propagation – but bad news to find GCR sources!

(ii) However, even the γ-ray longitude profile displayed localized "hot spots" that could not be explained by a simple CO-γ-ray correlation. Within the COS-B angular resolution ($\sim 1°$ HWHM), these hot spots could be called "sources". Some of them were identified with pulsars, confirming the SAS-2 results, like the Vela pulsar.[2] Several others were unidentified, but it became quickly clear that several of them were in fact well correlated spatially with giant HII regions, excited by stellar "OB associations", or, in modern parlance, massive star forming regions. But an additional, essential feature characterized most (not all) of them: *they were also harboring supernova remnants*. For that reason, these γ-ray sources were dubbed "SNOBs" by Montmerle ([13]; see also [3]). These sources accounted for about half (5/11) of the unidentified COS-B sources, and conversely up to 3/4 of the $\sim$30 SNOB list had hints of γ-ray emission. Given the poor COS-B angular resolution, these identifications were only tentative - albeit convincing-; in particular, there was always the possibility that an unseen pulsar could be the real γ-ray source.

Still, given the context at the time, it was easy to elaborate a semi-quantitative SNOB scenario, in three parts. First, the shock wave would sweep the solar-mass members of the OB association, which would, with their giant flares like on the Sun (which would be detected later in X-rays by the *Einstein* satellite, Montmerle et al. [14]), inject low-energy ($\sim$MeV) particles necessary to trigger the acceleration process.[3] Second, the accelerated particles would irradiate both the HII region and

[2]The two other strong sources detected, the Crab pulsar and the mysterious *Geminga*, now identified with the neutron star nearest to the Sun, do not lie in the galactic plane.

[3]This assumption was based on the correlation between the GCR composition with the First Ionization Potential (FIP) in the solar corona. Since then, it has been found that the GCR

the parent molecular cloud (which contains most of the mass). Third, γ-ray emission would take place via the π^o-decay mechanism, just as for the whole galaxy.

The major implication was that, given the γ-ray flux detected from the SNOBs, the *in situ* accelerated cosmic-rays (above $\sim$1 GeV) would have a flux over one order of magnitude larger than the average galactic flux! In other words, *SNOBs were localized sources of cosmic-rays*. They were too few (probably not more than a few tens at the scale of the whole galactic disk) to be the sources of all GCR, but clearly they had the potential to offer a close-up view of cosmic-ray acceleration processes and their interaction with interstellar matter – already seen on a galactic scale.

The next γ-ray satellite, the *Compton Gamma-Ray Observatory*, or *CGRO*, was launched in 1991, i.e., almost a decade after COS-B ended its mission, and was brought down voluntarily 9 years later. From the point of view of the association of GeV γ-ray sources with SNOB-like sources, it is fair to say that there was not much progress, because galactic γ-ray sources were swamped by hundreds of extragalactic ones (at least, lying at high galactic latitudes), and the spatial resolution of its spark-chamber experiment, *EGRET*, was not so much better than that of COS-B ($\sim$0.5° HWHM at high energies). At least, it was still insufficient to resolve SNOB-like sources, and in fact this essentially is still the case today with *Fermi*.

The real breakthrough came from *HESS*. Although operating at a much higher energy range than the γ-ray satellites, its sensitivity, and above all, its angular resolution, were the decisive factors that contributed to the "revival" of SNOB-like γ-ray sources. Indeed, the typical resolved massive star-forming regions are located at distances 2–3 kpc from the Sun. And at this distance, the $\sim$0.1° resolution of *HESS* allows to image molecular clouds! Early results of *HESS*, and similar Čerenkov telescopes that followed (MAGIC, VERITAS...) confirmed, beyond doubt, that massive star forming regions hosting a supernova remnant indeed make a well-defined, if not dominant, class of TeV γ-ray sources, many of which have GeV counterparts seen by *Fermi*.

So now, we are at last in a position to scrutinize the acceleration, diffusion and propagation processes of cosmic rays in the vicinity of supernova shocks, the interaction of both high-energy (GeV-TeV) and low-energy ($\sim$100 MeV and below) cosmic rays with molecular clouds, generating high-energy γ-rays and ionization processes respectively. It is clear that such studies go far beyond the "simple" study of these sources, and will have a broader impact on our understanding of high-energy processes at work in the Milky Way at large.

This is all that the present book is about. For the first time, a whole volume gives a fresh, but comprehensive view of this growing topic, written by the best experts. It should be a precious reference source, not only for aficionados that have contributed to the field for 40 years or more, but for all the newcomers (presumably young!). I wish it a great success.

---

composition is better correlated with that of interstellar grains, so this part of the SNOB scenario doesn't hold anymore – but the "injection problem" for the diffusive acceleration mechanism remains.

References

1. Bell, A.R. 1978, MNRAS, 182, 443
2. Cavallo, G., Gould, R.J. 1971, Nuovo Cimento, 2B, 77
3. Cesarsky, C.J., Montmerle, T. 1983, Sp. Sci. Rev., 36, 173
4. Clark, G.W., Garmire, G.P., Kraushaar, W.L. 1968, ApJ, 153, L203
5. Elmegreen, B.G., Lada, C.J. 1977, ApJ, 214, 725
6. Fichtel, C.E., et al. 1975, ApJ, 198, 163
7. Garmire, G., Kraushaar, W.L. 1965, Sp. Sci. Rev., 4, 123
8. Georgelin, Y.M., Georgelin, Y.P. 1976, A&A, 49, 57
9. Goldreich, P., Julian, W.H. 1969, ApJ, 157, 859
10. Grindlay, J.E. 1972, ApJ, 174, L9
11. Hewish, A., et al. 1968, Nature, 217, 709
12. Hayakawa, S., Yamamoto, Y. 1963, Prog. Theor. Phys., 30, 71
13. Montmerle, T. 1979, ApJ, 231, 95
14. Montmerle, T., et al. 1983, ApJ, 269, 182
15. Morrison, P. 1958, Nuovo Cimento, 1, 858
16. Paul, J.A., et al. 1978, A&A, 63, L31
17. Schmidt, M. 1963, Nature, 197, 1040
18. Scoville, N.Z., Solomon, P.M. 1975, ApJ, 187, L67
19. Stecker, F. 1973, ApJ, 185, 499

Cosmic Rays in the Interstellar Medium

Serena Viti, Estelle Bayet, Thomas W. Hartquist, Thomas A. Bell, David A. Williams, and Manda Banerji

Abstract In this article we will highlight the importance of cosmic rays for the chemistry of the interstellar medium (ISM) in our own Milky Way as well as in external galaxies. We will review the methodologies employed to determine the cosmic ray ionization rates in the ISM, how cosmic rays rates can influence the determination of the mass of a galaxy and, finally, how cosmic rays affect star formation and its rate.

S. Viti (✉) · D.A. Williams
Department of Physics and Astronomy, University College London, Gower St., London, WC1E 6BT, UK
e-mail: sv@star.ucl.ac.uk; daw@star.ucl.ac.uk

E. Bayet
Sub-Department of Astrophysics, University of Oxford, Denys Wilkinson Building, Keble Road, Oxford, OX1 3RH, UK
e-mail: Estelle.Bayet@astro.ox.ac.uk

T.W. Hartquist
School of Physics and Astronomy, University of Leeds, Leeds, LS2 9JT, UK
e-mail: twh@ast.leeds.ac.uk

T.A. Bell
Centro de Astrobiologa, CSIC–INTA, 28850, Madrid, Spain
e-mail: tab@cab.inta-csic.es

M. Banerji
Institute of Astronomy, University of Cambridge, Madingley Road, Cambridge, CB3 0HA, UK

Department of Physics and Astronomy, University College London, Gower St., London, WC1E 6BT, UK
e-mail: mbanerji@ast.cam.ac.uk

D.F. Torres and O. Reimer (eds.), *Cosmic Rays in Star-Forming Environments*, Astrophysics and Space Science Proceedings 34, DOI 10.1007/978-3-642-35410-6_2,

1 The Chemistry of Cosmic Rays

Cosmic rays are superthermal particles, which are mostly ionized hydrogen and helium. In the interstellar medium (ISM) they initiate and drive most of the interstellar chemistry by colliding with and ionising atoms and molecules. During ionization they transfer energy to the ejected electrons and by doing so they heat the gas. Moreover, secondary photons generated by cosmic rays are a source of photodissociation and ionization in a UV shielded gas. Hence cosmic rays also help to maintain the ionization fraction deep within molecular clouds.

While the energies of cosmic rays range from MeV to ultrarelativistic values, the rays that most ionize the ISM are those with energies $\leq$1 GeV. Unfortunately below $\sim$2 GeV the observed flux from Earth has to be corrected by the effects of the solar wind and such corrections, and hence the cosmic ray ionization rate, can be rather uncertain [33]. We will describe later different ways one can determine such rate but first it is worth summarizing the general chemical effects of cosmic rays on the molecular and atomic content of the ISM.

Low energy cosmic rays are capable of ionizing all atoms and molecules, including the most abundant ones. In Table 1 we list the important reactions involving cosmic rays for the most abundant elements.

In particular, it is the creation of the H^+, He^+ and H_2^+ ions that then drive much of the chemistry in the ISM. This is because many ion-molecule reactions, unlike neutral-neutral exchanges, are rapid and occur at almost every collision, even at low temperatures ($\sim$10 K), typical of cold molecular clouds. For example, with molecular hydrogen being the most abundant molecule in dark clouds, the ion H_2^+ will always encounter an H_2 molecule and form a new species, H_3^+ which in turn will react with oxygen or carbon monoxide. On the other hand, the ion He^+ is very destructive in that it easily dissociates molecules via charge transfer.

In summary, cosmic rays are key in initiating oxygen and carbon chemistries and ultimately more complex chemistry. The rate of ionization induced by cosmic rays is therefore a parameter of fundamental importance.

1.1 Determining the Cosmic Ray Ionization Rate in the ISM

The most direct way to determine the cosmic ray ionization rate within our own Galaxy is from direct measurements on Earth. However, as mentioned in the previous section, below $\sim$2 GeV the observed flux must be corrected for the effects of the solar wind but the uncertainties from these corrections can be as high as a factor of 3 at 1 GeV and much higher for energies less than 0.3 Gev [13]. There are alternative ways to measure this rate, in our own as well as in external galaxies, essentially from studies of the products of ion-neutral chemistry inside the molecular clouds. Different species have been used in recent years but generally one can assume that every cosmic ray ionization of H_2 will eventually produce a molecule of H_3^+ and so the abundance of this ion is often used as a tracer of the

Table 1 Chemical reactions involving cosmic rays

$H + cr \rightarrow H^+ + e^- + cr$
$He + cr \rightarrow He^+ + e^- + cr$
$H_2 + cr \rightarrow H_2^+ + e^- + cr$
$C + cr \rightarrow C^+ + e^- + cr$
$O + cr \rightarrow O^+ + e^- + cr$
$CO + cr \rightarrow CO^+ + e^- + cr$

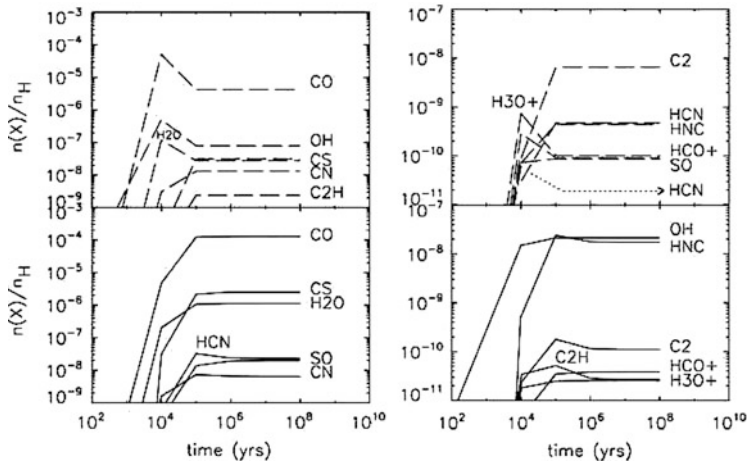

Fig. 1 Taken from Bayet et al. ([5], Fig. 4): the influence of cosmic ray ionization rate variations on selected molecular abundances are plotted for a model where $\zeta = 100\,\zeta_o$ (*top panels*) and a model where $\zeta = \zeta_o$ (*bottom panels*)

cosmic ray ionization rate, referred also as ζ. This however is only possible in a steady-state scenario where one can 'fit' the required cosmic ray ionization rate to the observed (or derived from OH observations) abundance of H_3^+ in steady state [11, 16], essentially by treating ζ as a free parameter. The inferred values of ζ are of the order of $10^{-17}\,s^{-1}$, which is now routinely called the 'standard' ISM cosmic ray ionization rate, or ζ_o. However, more recent observational studies of H_3^+ towards several lines of sight in the Galactic Plane have in fact derived higher values for ζ, of the order of $10^{-16}\,s^{-1}$, averaged over all the lines of sight [18].

A step further has been taken by e.g. Meijerink et al. [23] and Bayet et al. [7] where the authors look at the variations of the whole chemistry as the cosmic ray ionization rate is varied. Figure 1 shows an example taken from Bayet et al. [7]: here ζ is varied from the $5 \times 10^{-17}\,s^{-1}$ to two orders of magnitude above this value and some molecular species, such as OCS, SO_2 and H_2CS stand out as being the most sensitive species to variation in the cosmic ray ionization rate. In principle, therefore, assuming all other physical properties are known, once could derive ζ in a sample of molecular clouds by observing these species.

2 The Chemistry in Cosmic Ray Dominated Regions

The fact that we can now identify molecular species sensitive to variations in cosmic rays leads to the possibility of using astrochemistry as a tool for the characterization of regions where the cosmic ray ionization rate is higher than in our own galaxy. For example, the high spatial density of massive star formation in mergers and starburst galaxies (e.g. [1, 2, 30]) creates regions of extremely high cosmic ray energy density, up to about 10,000 times that in the Milky Way Galaxy. Papadopoulos [26] has proposed that these large energy densities alter the heating rates and ionization fractions in dense gas ($n(H_2) \geq 10^4\,cm^{-3}$) in the UV-shielded cores that contain much of the molecular gas in these galaxies, so that these cosmic ray dominated regions (CRDRs) have different initial conditions for star formation. These conditions affect the subsequent evolution of the gas and may even lead to a top-heavy initial mass function and bimodal star formation [26, 27].

2.1 Theoretical Considerations

Can we determine useful molecular tracers of CRDRs? Bayet et al. [7] showed that it is necessary to make a complete and self-consistent thermal/chemical model of dense gas subjected to very high fluxes of cosmic rays in order to do so. They compute the variation of the chemistry as the ionization rate is increased for a large network of 131 species connected in 1,700 reactions in a self-consistent thermal/chemical and time-dependent one-dimensional model. The chemistry is computed using the UCL_PDR code [9] and ζ is varied from Milky Way values up to about one million times larger.

The UCL_PDR code is a time dependent photon dominated regions (PDR) model which self-consistently computes the thermal balance by taking into consideration all the relevant cooling and heating mechanisms [9]. Of particular importance for CRDRs is the inclusion of minor coolants such as the CO isotopologues, CS, H_2O and OH [7].

Figure 2 (reproducing Fig. 1 from Bayet et al. [7]) shows the gas temperature as a function of cosmic ray ionization rate for three different A_V: regardless of the visual extinction the temperature of course rises as ζ is increased. More interestingly, we find that the temperature at 20 mag is in fact higher than at 8 mag, due to the fact that lines of two of the main coolants, atomic carbon and carbon monoxide become optically thick and so the gas is not efficiently cooled. The most important implication is that, while at standard values of ζ the chemistry reaches equilibrium once photons stop dominating (i.e. at large enough visual extinctions), at very high cosmic ray ionization rates equilibrium may never be reached.

The chemistry of course gets affected by these high temperatures: Figs. 3 and 4 show the fractional abundances of several atomic and molecular species as a function of ζ for $A_V = 3$ and 20 mag. In general we find that a fairly rich chemistry can be maintained up to a critical value of ζ of $10^{-12}\,s^{-1}$. The driver of the decline

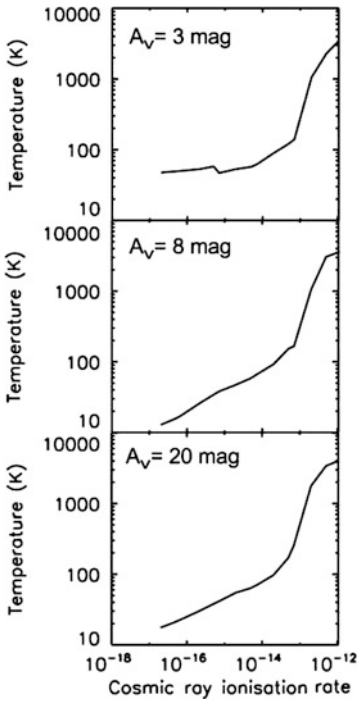

Fig. 2 Taken from Bayet et al. ([7], Fig. 1): gas temperature in K as a function of ζ for three different visual extinctions

in molecular abundances is H_2 which starts declining at $\zeta \sim 10^{-14}\,s^{-1}$. The resultant atomic hydrogen is very destructive. This together with the fact that the suppression of molecular hydrogen coincides with an abrupt increase in gas temperature assures fast dissociation for all molecules. Nevertheless we see that different species decline at different paces and times. While the chemistries at $A_V = 3$ and 20 mag are fairly similar, we note that at large depths higher molecular abundances are reached; in particular CS seems to be higher by a factor of 10^4 at 20 mag compared to its abundance at 3 mag.

While sulfur bearing species are confirmed as good sensitive tracers of ζ, regardless of visual extinctions ions *increase* with ζ. Interestingly HCO^+, often used as a tracer of high cosmic ray ionizations regions, is not useful above $\zeta = 10^{-13}\,s^{-1}$.

2.2 What Do Observations Tell Us?

The Bayet et al. [7] work, as well as others such as that presented in Meijerink et al. [24], give us some interesting and general conclusions on the temperatures achieved in these environments (e.g. much more elevated than in our own Milky Way up to values of 3,000 K or even higher) and on the chemistry, where it is found that even at ζ as high as $10^{-12}\,s^{-1}$ some, albeit few, molecular tracers exist (e.g. OH and OH^+) as well as, of course, atomic ones (C and C^+). However comparisons

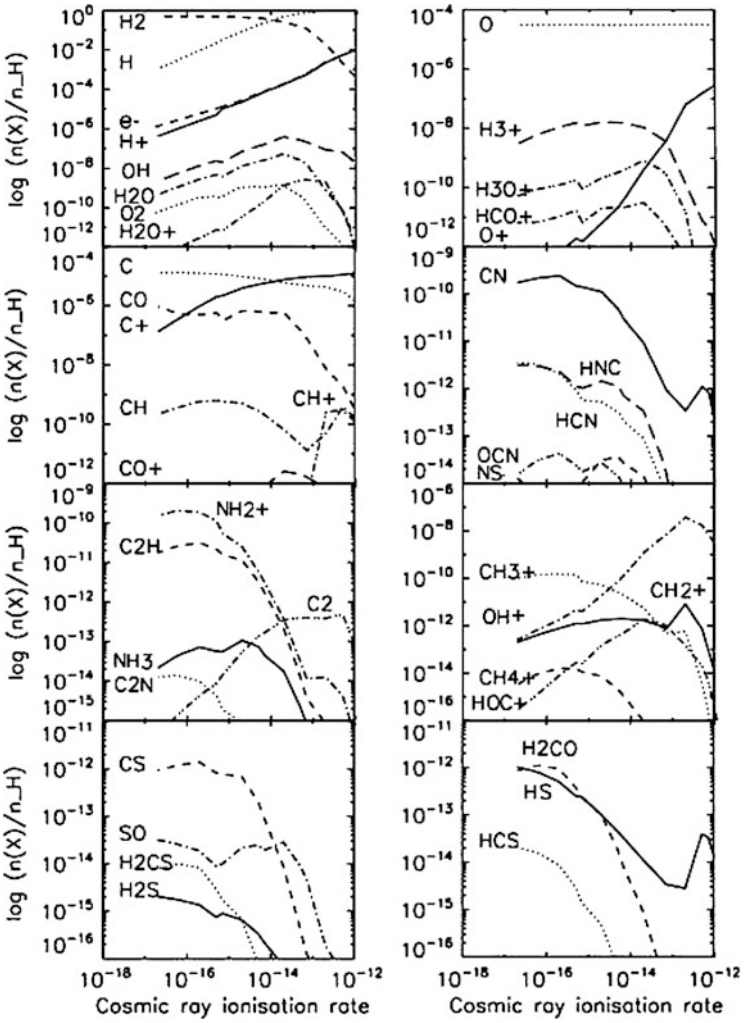

Fig. 3 Taken from Bayet et al. ([7], Fig. 2): fractional abundances of selected species as a function of ζ for a low metallicity environment (1/10 of solar) for $A_V = 3$ mag

with observations are needed in order to validate the relevance of these theoretical predictions for extragalactic studies.

It is convenient to compare theoretical predictions of chemistry in CRDRs with observations of starburst galaxies, since they have high cosmic ray energy density and possibly higher heating rates and higher ionization fractions. The best example is M82, an irregular starburst galaxy which is the most studied of all nearby galaxies. The high cosmic ray ionization rate has been postulated by e.g. the high C/C+ and C/CO ratios (e.g. [29]). Originating in the nucleus, the starburst activity within M82 is currently seen to be propagating into the molecular rings, disrupting the

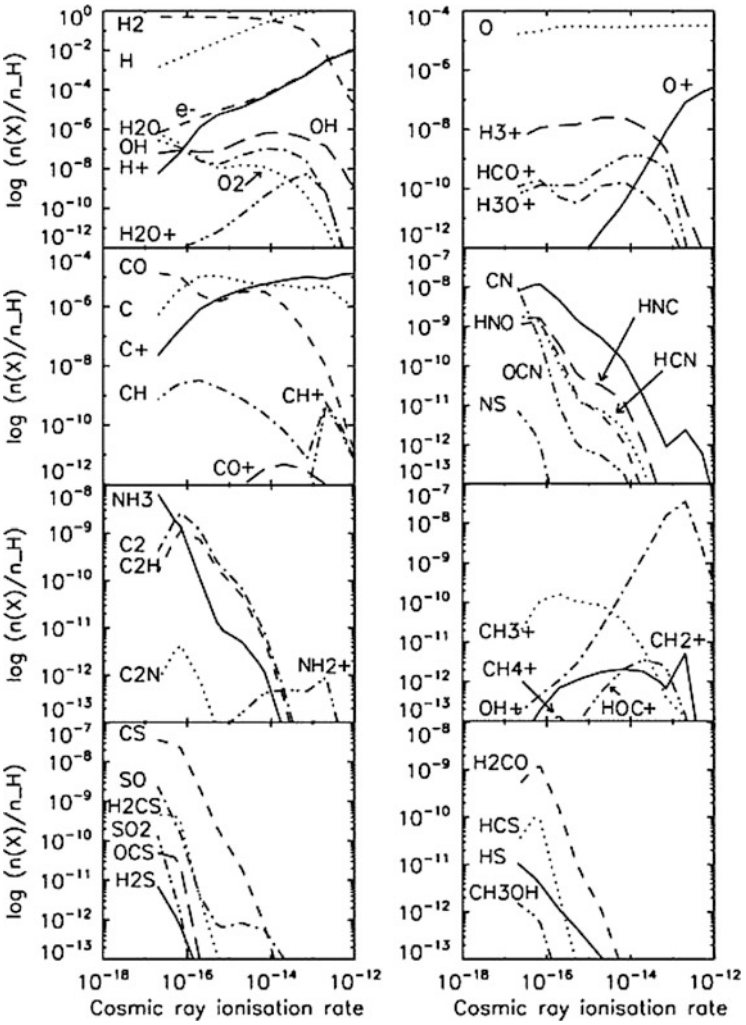

Fig. 4 Taken from Bayet et al. ([7], Fig. 4): fractional abundances of selected species as a function of ζ for a low metallicity environment (1/10 of solar) for $A_V = 20$ mag

surrounding ISM and causing the interstellar clouds to fragment. van der Tak et al. [31] detected the ion H_3O^+ in M82 and found a fractional abundance of 2–10×10^{-9} which they could only match with a high ζ PDR, i.e. an evolved starburst. In fact, the Bayet et al. [7] models indicate that one can obtain high abundance of this ion at low (i.e. in a PDR) as well as high (i.e. dense star forming gas) extinction as long as $\zeta \sim 10^{-13}\,s^{-1}$ and the metallicity is solar. At high extinction, which could represent the nuclear part of the galaxy, the abundance of H_3O^+ is higher, providing possibly a better match for the observations.

Ultra Luminous Infrared Galaxies (ULIRG) are also interesting objects where molecular ions are abundant: a high resolution SPIRE FTS spectrum of MrK 231 reveals the presence of ions such as OH^+, CH^+ and H_2O^+ [32]. While abundances are not derived, van der Werf et al. [32] explained the high abundances of these ions by invoking X-rays and describing the emission as coming from X-ray dominated regions (XDRs); however Bayet et al. [7] shows that the type of model that is also able to produce high fractional abundances ($\geq 10^{-10}$) of these three ions is one representing an environment with low metallicity (0.1 solar), high cosmic ray ionization rates ($\geq 10^{-16}\,s^{-1}$) and low visual extinction. Hence, as Papadopoulos [26] also points out, determining the origin of molecular emission from ULIRGs such as Mrk 231 is not trivial when both sources of energy (CR and X-rays) are present.

2.2.1 The Perseus Cluster

One of the most interesting clusters of galaxies where cosmic ray ionization rates may be much higher than in our own Galaxy is NGC1275, the Perseus cluster. In particular, this cluster contains filaments about 100 pc thick that are thought to originate from interactions between hot intercluster medium and relativistic plasma associated with AGN (e.g. [21]). Ferland et al. [14, 15] modelled optical and IR emission arising from gas heated by dissipation and cosmic rays and found that the best models required heating rates several orders of magnitudes higher than in our own galaxy. Bayet et al. [6] explored the chemistry of molecular regions subject to heating rates per volume and cosmic ray ionisation rates per particle in ranges suitable for the NGC 1275 filaments. They identify detectable molecular species that may provide a diagnostic of the dissipation heating as well as the cosmic ray ionization rate. Figure 5 (Fig. 3 from Bayet et al. [6]) compares the chemistry, density and temperature for a low and a high cosmic ray ionization regime, both with an additional heating source. They find that, unfortunately, it is not easy to distinguish between additional heating sources and enhanced cosmic ray ionization rates by looking at the chemistry. However, the molecular species HCO^+, C_2H and CN are certainly good tracers of heating in these filaments and their abundance ratios may provide a way of disentangling the effects of a high cosmic ray ionization rate from that of an additional heating source.

Therefore, the same authors followed up these predictions with an observational campaign of the Perseus central region and filaments [8]. They detected for the first time emission lines of CN(2-1), HCO^+(3-2) and C_2H(3-2) in two positions: directly at the central galaxy, NGC1275, and also at a position about 2″ to the east where associated filamentary structure has been shown to have strong CO emission. In the central region, there is a clear detection in CN and HCO^+ and a weak detection of the C_2H transition; in the filamentary structure weak detections of CN and HCO^+ were found. Crude estimates of the column densities and fractional abundances were compared with the Bayet et al. [6] models and it was found that the models in which heating is caused mainly by cosmic rays can account for the molecular observations. However, the cosmic ray heating rate needs to be at least two orders of magnitude larger than that in the Milky Way.

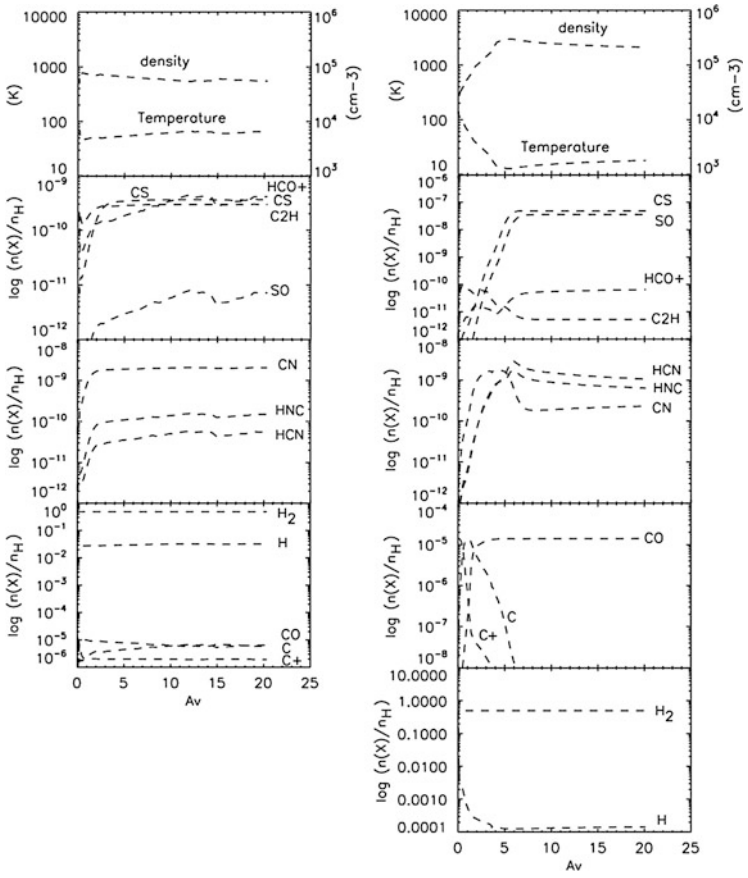

Fig. 5 Taken from Bayet et al. ([6], Fig. 3): temperature, density and selected fractional abundances as a function of visual extinctions for $\zeta = \times 10^{-15}\,\mathrm{s}^{-1}$ (*Left*) and $\zeta = \times 10^{-17}\,\mathrm{s}^{-1}$ (*Right*); both models also have an additional source of heating included

3 Cosmic Rays and the X Factor

Another indirect effect of high cosmic ray ionization rates is on the CO-to-H_2 conversion factor, often used to determine the mass of galaxies since, unlike molecular hydrogen, CO is readily observable. This factor is usually expressed by the equation:

$$X = \frac{N(H_2)}{\int T_A(CO)\mathrm{d}v} \tag{1}$$

in units of $[\mathrm{cm}^{-2}(\mathrm{K\ km\ s}^{-1})^{-1}]$ and where $N(H_2)$ is the column density of H_2 and $T_A(CO)$ is the antenna temperature of the CO(1-0) line (see e.g. reviews by Maloney [22], Combes [12], and Young [34]). Bell et al. [9] explored the sensitivity

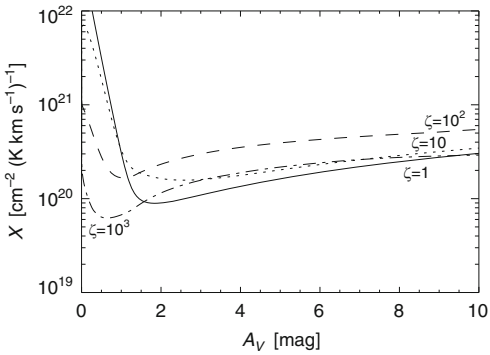

Fig. 6 The X factor as a function of A_V for various ζ (Adapted from Fig. 5 of Bell et al. [9])

of this factor for a range of conditions including variations in the cosmic ray ionization rate. Figure 6 shows the influence of varying ζ on the X factor. The characteristic depth profile of the X factor has three main features: near the outer edge of the cloud, where the H/H_2 transition occurs and H_2 is present without CO, X is large. As we move towards higher depths, all hydrogen is in molecular form, CO self-shielding becomes sufficiently strong to prevent photodissociation, and this allows its abundance and emission strength to rise sharply. This causes X to drop, reaching a minimum value in the region where CO emission is strongest. As the CO line becomes optically thick with increasing depth, local emission gradually declines and X begins to rise slowly again. It is indeed this minimum of the depth profile that determines X because it corresponds to the peak emission of the CO line. From Fig. 6, one sees that as the ionization rate increases from the standard value, CO is initially destroyed more effectively (through reactions with He^+) and its abundance drops, causing an upward shift in the X profile. However, the corresponding increase in the cosmic ray heating rate causes a rise in gas temperature, becoming the dominant heating mechanism. This promotes CO formation and emission, and counters, in part, the increased destruction rate. The X profile minima become lower and nearer the cloud surface. Thus, a slight rise in ionization rate shifts the X profile minimum upwards, whilst a further increase in ionization rate leads to the X minimum dropping and moving towards the cloud surface. So, in summary, X increases as ζ increases up to 100 times the standard value, but then decreases as ζ approaches 10^{-14} s^{-1}; the profile is raised due to the dissociation of CO; the subsequent lower and sharper minimum is due to the increased OH formation and dissociation of H_2.

3.1 The X Factor in Starburst Galaxies

The X factor as defined in Eq. 1 for CO(1-0) may also be defined for other transitions in CO as well as for transitions in atomic and molecular species other than

Table 2 Values for the CO-to-H_2 and C-to-H_2 conversion factors for starburst galaxies. Values of X_{CO} and X_{CI} are given in units of 10^{20} cm^{-2} (K km s^{-1})$^{-1}$

Galaxy	J = 1 → 0	J = 2 → 1	J = 3 → 2	J = 4 → 3	J = 6 → 5	J = 9 → 8	[CI] 609 μm
NGC6946	0.2	0.1	0.1	0.2	0.6	2.3	0.4
M82	1.5	1.7	2.9	9.5	79.4	203.7	1.3

CO [25,28]. Bell et al. [10] computed suitable CO-to-H_2 (for several transitions) and C-to-H_2 conversion factors for several galaxy types, including regular and irregular starbursts. They chose NGC6946 as a prototype regular starburst, while M82 as a prototype irregular starburst, as examples of their applications. In order to derive appropriate physical parameters for these galaxies, they compared emission line intensity ratios predicted by their PDR models to those observed. The best-fitting models were determined by performing a χ^2 fit for several atomic and molecular ratios:

1. OI(63) μm/CII
2. OI(145) μm/OI(63) μm
3. CII/CI(609) μm
4. CII μm/CO(3-2)
5. CI(609) μm/CO(3-2)
6. CO(3-2)/CO(1-0)

Table 2 summarizes their results for NGC6946 and M82.

Interestingly Bell et al. [10] found that the best χ^2 fit for both types of starburst galaxies was reached for standard cosmic ray ionization rates, apparently in contrast with the results from Bayet et al. [7]. However, Bell et al. [10] point out that for M82 the models with cosmic ray ionization rates of 10 and 100 times higher produce χ^2 values which are only 3 and 2 higher than that for the best fit model, respectively. Moreover the line ratios considered in Bell et al. [10] are not necessarily sensitive to the conditions in CRDR environments: for example the [CII] and [OI] lines trace only the PDR surfaces, not the dark regions where cosmic rays would be most important.

4 Cosmic Rays and Their Influence on the Low Mass Star Formation Rate

Estimates of the evolution of the space density of the massive star-formation rate are routinely made [17, 19, 20], and, although very uncertain, at least they provide some constraints for the high end of the Initial Mass Function (IMF). On the other hand, there is very little information on the formation of extragalactic low mass stars, which may influence galaxy formation and evolution by shaping the IMF and its slope.

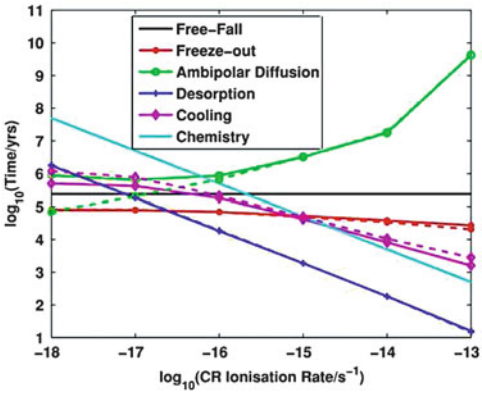

Fig. 7 Taken from Banerji et al. ([3], Fig. 1): Timescales for different processes as a function of ζ

Low-mass star formation (at least in the Milky Way) is controlled by several critical timescales associated with processes such as gravitational collapse and thermal and magnetic support, cooling, ionization and hence chemistry, which itself is moderated by cosmic ray and photon fluxes, and metallicity. While in our own Galaxy these timescales are such that they favour formation of low mass stars, the physical properties in external galaxies may depart significantly from the Milky Way values. Banerji et al. [3] computed how these relevant timescales may vary when physical conditions are modified from Milky Way values and used the results to determine the regions of parameter space in which low-mass star formation is unlikely to occur. Banerji et al. [3] computed these timescales for a large range of physical conditions ($n_H = 10^2 - 10^6\,cm^{-3}$; metallicity $= (10^4 - 3) \times$ solar; ζ: 10^{-18}–$10^{-13}\,s^{-1}$; FUV: $(1–10^4) \times FUV_{MilkyWay}$) in order to represent a wide range of galaxy types. We show in Fig. 7 (taken from [3]) how the different timescales vary with cosmic ray ionization rate.

As one can see from Fig. 7, as ζ increases, the cooling time falls and when ζ has increased to $10^{-16}\,s^{-1}$ it drops below the free fall time. As a consequence more cores should be able to collapse because the chemistry is also quick, again due to the high cosmic ray ionization rate. The freeze out time is longer than desorption time, hence molecules remain in the gas for longer periods and cool the gas, again in favour of high rates of star formation. However ambipolar diffusion, the process by which, due to low ionization, the field lines decouple from the neutral matter allowing therefore the material to drift in response to the gravitational potential, will be very slow as ions do indeed increase; this implies that star formation may not be viable in clouds that are magnetically subcritical under these conditions and, hence, depending on the magnetic field, collapse may be halted, possibly resulting in a high-mass-biased stellar IMF.

Chemistry may produce tracers of top-heavy stellar IMF. This is explored in Banerji et al. [4]; the authors find that while the rotational distribution of CO should be similar between galaxies with top-heavy IMFs and those with unbiased IMFs, the high-J to peak CO ratio differs according to their metallicity and can therefore

be used to roughly infer the metallicity of a galaxy provided we know whether it is active or quiescent. The metallicity strongly influences the shape of the IMF. They also find that CS may be a good tracer of metallicity while HCN, HNC, and CN are found to be relatively insensitive to the IMF shape at the large visual magnitudes typically associated with extragalactic sources.

5 Conclusions

Cosmic rays initiate and very quickly affect the chemistry of the interstellar medium (ISM). It is therefore crucial to accurately determine the cosmic ray ionization rate, ζ, in the ISM. Clearly, the rate may vary among galaxy types. In our own Galaxy it is believed to be $\sim 10^{-17}\,\mathrm{s}^{-1}$ although studies of the diffuse medium may indicate a somewhat higher value. In active galaxies, such as starburst or AGNs, ζ is certainly larger than $10^{-17}\,\mathrm{s}^{-1}$. High ζ will increase the average kinetic temperature of the gas (to possibly over 3,000 K for $\zeta = 10^{-12}\,\mathrm{s}^{-1}$). We find that chemistry can indeed still trace the cosmic ray ionization rate, up to $\zeta = 10^{-12}\,\mathrm{s}^{-1}$. However interpreting atomic and molecular observations of starburst galaxies in order to trace the cosmic ray ionization rate is not trivial, as ζ is likely to spatially vary. Another important consequence of variations in the cosmic ray ionization rates is its non linear influence on the X factor and one must take care when estimating molecular masses from CO if ζ is not known. Finally, because the cosmic ray ionization rate influences the star formation rate, there may be important consequences for the Initial Mass Function at high redshift.

References

1. Acciari, V. A., Aliu, E., Arlen, T., et al. 2009, Nature, 62, 770
2. Acero, F., Aharonian, F., Akhperjanian, A. G., et al. 2009, Science, 326, 1080
3. Banerji, M., Viti, S., Williams, D. A., Rawlings, J. M. C., 2009a, ApJ, 692, 283
4. Banerji, M., Viti, S., Williams, D. A., 2009b, ApJ, 703, 2249
5. Bayet, E., Viti, S., Williams, D. A., Rawlings, J. M. C., Bell, T. A., 2009, ApJ, 696, 1466
6. Bayet, E., Hartquist, T. W., Viti, S., Williams, D. A., Bell, T. A., 2010, A&A, 521, A16
7. Bayet, E., Williams, D. A., Hartquist, T. W., Viti, S., 2011a, MNRAS, 414, 1583
8. Bayet, E., Viti, S., Hartquist, T. W., Williams, D. A., 2011b, MNRAS, 417, 627
9. Bell, T. A., Roueff, E., Viti, S., Williams, D. A., 2006, MNRAS, 371, 1865
10. Bell, T. A., Viti, S., Williams, D. A., 2007, MNRAS, 378, 983
11. Black, J. H., Dalgarno, A., 1977, ApJS, 34, 405
12. Combes, F., 1991, ARA&A, 29, 195
13. Draine, B. T., 2011, "Physics of the Interstellar and Intergalactic Medium", Princeton Series in Astrophysics.
14. Ferland, G. J., Fabian, A. C., Hatch, N. A., Johnstone, R. M., Porter, R. L., van Hoof, P. A. M., Williams, R. J. R., 2008, MNRAS, 386, 72
15. Ferland, G. J., Fabian, A. C., Hatch, N. A., Johnstone, R. M., Porter, R. L., van Hoof, P. A. M., Williams, R. J. R., 2009, MNRAS, 392, 1475

16. Hartquist, T. W., Black, J. H., Dalgarno, A., 1978, MNRAS, 185, 643
17. Hopkins, A. M., & Beacom, J. F., 2006, ApJ, 651, 142
18. Indriolo, N., Geballe, T. R., Takeshi, O., McCall, B. J., 2007, ApJ, 671, 1736
19. Lilly, S. J., Le Fevre, O., Hammer, F., Crampton, D., 1996, ApJ, 460, 1
20. Madau, P., Ferguson, H. C., Dickinson, M. E., Giavalisco, M., Steidel, C. C., Fruchter, A., 1996, MNRAS, 283, 1388
21. McNamara, B. R., O'Connell, R. W., Sarazin, C. L., 1996, AJ, 112, 91
22. Maloney, P., 1990, ApJ, 348, 9
23. Meijerink, R., Spaans, M., Israel, F. P., 2006, ApJ, 650, 103
24. Meijerink, R., Spaans, M., Loenen, A. F., van der Werf, P. P., 2011, A&A, 525, 119
25. Papadopoulos, P. P., Thi, W.-F., Viti, S., 2004, MNRAS, 351, 147
26. Papadopoulos, P. P., 2010, ApJ, 720, 226
27. Papadopoulos, P. P., Thi, W-F., Miniati, F., Viti, S., 2011, MNRAS, 414, 1705
28. Sakamoto K., Okumura S. K., Ishizuki S., Scoville N. Z., 1999, ApJS, 124, 403
29. Schilke, P., Carlstrom, J. E., Keene, J., Phillips, T. G., 1993, apJ, 417, 67
30. Suchkov, A., Allen, R. J., Heckman, T. M., 1993, ApJ, 413, 542
31. van der Tak, F. F. S., Aalto, S., Meijerink, R., 2008, A&A, 477, 5
32. van der Werf, P. P., Isaak, K. G., Meijerink, R., et al., 2010, A&A, 518, 42
33. Webber, W. R., Yushak, S. M., 1983, ApJ, 275, 391
34. Young, J. S., Scoville, N. Z., 1991, ARAA, 29, 581

The Influence of Cosmic Rays in the Circumnuclear Molecular Gas of NGC 1068

Rebeca Aladro, Serena Viti, Estelle Bayet, and Denise Riquelme

Abstract We surveyed the circumnuclear disk of the Seyfert galaxy NGC 1068 between the frequencies 86.2 and 115.6 GHz, and identified 17 different molecules. Using a time and depth dependent chemical model we reproduced the observational results, and show that the column densities of most of the species are better reproduced if the cold gas is heavily pervaded by a high cosmic ray ionization rate of about 1,000 times that of the Milky Way. We discuss how molecules in the NGC 1068 nucleus may be influenced by this external radiation, as well as by UV radiation fields.

1 Introduction

The NGC 1068 proximity (D = 14.4 Mpc, [6]) and luminosity ($L_{\rm IR} = 3 \times 10^{11} L_{\odot}$, [20]) make this galaxy the best studied object in the local universe hosting an active galactic nucleus (AGN). Besides, NGC 1068 shows an extremely rich molecular complexity, as shown by many studies conducted in the millimeter (mm) and sub-mm ranges (e.g. [7, 12, 17]). Molecular emission is one of the best tools to study the physical properties of the interstellar medium in galaxy nuclei, and in particular in

R. Aladro (✉) · S. Viti
Department of Physics and Astronomy, UCL, Gower Street, London, WC1E 6BT, UK
e-mail: r.aladro@ucl.ac.uk; sv@star.ucl.ac.uk

E. Bayet
Sub-Department of Astrophysics, University of Oxford, Denys Wilkinson Building, Keble Road, Oxford, OX1 3RH, UK
e-mail: Estelle.Bayet@astro.ox.ac.uk

D. Riquelme
Instituto de Radioastronomía Milimétrica, Avda. Divina Pastora, 7, Local 20, E-18012 Granada, Spain
e-mail: riquelme@iram.es

D.F. Torres and O. Reimer (eds.), *Cosmic Rays in Star-Forming Environments*, Astrophysics and Space Science Proceedings 34, DOI 10.1007/978-3-642-35410-6_3,

AGN where the gas is heavily obscured by large amounts of dust that absorb the emitted radiation in other wavelengths. NGC 1068 has a circumnuclear disk (CND) with a thickness of 10 pc [18], where the gas seems to be heavily pervaded by X-ray radiation originated in the nuclear accretion disk, forming a giant X-ray dominated region (XDR) which leaves particular imprints in the chemical composition of the ISM, such as enhanced SiO and CN abundances [9, 21]. Previous studies done toward galaxy nuclei have already shown the connection between the intensity of some molecular species and the dominant physical processes, such as UV fields and large-scale shocks (e.g. [1, 15]). Here, to understand the role of X-rays in AGN galaxies, we conducted an unbiased molecular line survey towards the CND of NGC 1068, and modelled its molecular emission considering different combinations of far UV (FUV) radiation fields and cosmic ray ionization rates.

2 Observations, Data Reduction and Analysis

We observed the CND of NGC 1068 ($\alpha_{2,000} = 02{:}42{:}40.9$, $\delta_{2,000} = -00{:}00{:}46.0$) with the IRAM 30-m telescope[1] (Pico Veleta Observatory, Spain) between October 2009 and July 2010. Using the band E0 of the EMIR receiver and the WILMA autocorrelator, we covered the frequencies between 86.2 and 115.6 GHz, for which the telescope beam size ranged from $21''$ to $29''$, and the channel width spacing was 7–9 km s^{-1}. The data were calibrated using the standard dual method. The observations were done wobbling the secondary mirror with a switching frequency of 0.5 Hz and a beam throw of $220''$ in azimuth. We checked the pointing accuracy every hour towards nearby bright continuum sources. The pointing corrections were always better than $4''$. The focus was also checked at the beginning of each run and during sunsets.

The observed spectra were converted from antenna temperatures (T_A^*) to main beam temperatures (T_{MB}) using the relation $T_{MB} = (F_{eff}/B_{eff})\, T_A^*$, where F_{eff} is the forward efficiency of the telescope, whose values were between 0.94 and 0.95, and B_{eff} is the main beam efficiency, ranging from 0.77 to 0.81. Linear baselines were subtracted in all cases. The rms achieved is $\leq$2 mK across the whole survey. The data were also corrected by beam dilution effects as $T_B = [(\theta_s^2 + \theta_b^2) / \theta_s^2]\, T_{MB}$, where T_B is the source averaged brightness temperature, θ_s is the source size and θ_b is the beam size. Based on NGC 1068 interferometric observations of ^{12}CO, HCN and ^{13}CO (e.g. [11, 18]) we have assumed an average source size of $4''$ for all the species detected in this survey. focused in the CND of NGC 1068 (e.g. [5, 12, 13]).

Gaussian profiles were fitted to all the detected lines. The reduction of the spectra and Gaussian profile fitting were done using the CLASS [2] and MASSA[3] software

[1] IRAM is supported by INSU/CNRS (France), MPG (Germany) and IGN (Spain).

[2] CLASS http://www.iram.fr/IRAMFR/GILDAS

[3] MASSA http://damir.iem.csic.es/mediawiki-1.12.0/index.php/MASSA_User's_Manual

packages. Figures showing the spectra, the resulting parameters from the Gaussian fittings, and details about each detected molecule are shown in [2].

Assuming local thermodynamic equilibrium (LTE) and optically thin emission for all the detected species, we made Boltzmann diagrams to estimate the column densities of the molecules. Despite the gas in galaxy nuclei is not always under these conditions, Boltzmann diagrams give good approximations to the densities, and are usually used in this type of studies (e.g. [1,15]), where a large amount of species are observed and the physical properties of each one are not well known. In fact, some species such as CO and HCN, are certainly affected by optically thickness in the CND of NGC 1068. The derived values of the column densities for each species, as well as the impact of opacity effects in our calculations, are shown in [2].

3 Modelling of the Data

To model the observations we used the time and depth dependent chemical model UCL_CHEM [22,23], which was run in two separate phases. During Phase I, we first simulated the formation of a dark cloud by collapsing an atomic diffuse gas from a density of $100\,cm^{-3}$ to a final density of $10^5\,cm^{-3}$. During the collapse atoms and molecules freeze onto the dust grains forming icy mantles. Both gas and surface chemistries are self-consistently computed. Once the gas is in equilibrium again, UCL_CHEM compiles in Phase II the chemical evolution of the gas and the dust after a burst of star formation has occurred, so, while the temperature during the first phase of the modelling was kept to 10 K, during the second phase it is increased to 100–350 K and the icy mantles are evaporated. The chemical evolution of the gas is then followed for 10^7 years. In both phases of the UCL_CHEM model the chemical network is based on more than 2,345 chemical reactions involving 205 species of which 51 are surface species. The gas phase reactions were adopted from the UMIST data base [14, 16, 24]. The surface reactions included in this model are assumed to be mainly hydrogenation reactions, allowing chemical saturation where this is possible.

To sample the likely co-existing conditions that molecules are experiencing in the nucleus of NGC 1068, we run four models (named a, b, c, and d), which allowed us to investigate the response of the chemistry to the changes in FUV radiation fields and cosmic-rays ionization rate, ζ (which can be used to simulate XDR-like environments). The values of these two parameters are listed in Table 1. On the other hand, in order to reproduce the physical conditions of the CND of NGC 1068, we used a final density of $n_H = 10^5\,cm^{-2}$ and a metallicity value of $Z = 1.056\,Z_\odot$, based on previous studies of the galaxy (e.g. [12, 19, 25]). The initial elemental abundances (C/H, O/H, N/H, S/H, He/H, Mg/H and Si/H) used in our study are those corresponding to extragalactic environments as described in [3]. Other parameters not mentioned (e.g. grain size) have been kept to their standard (Milky Way) values.

Using the results of the models, we calculated the column densities of the 17 species detected in our survey at a representative time of 10^5 year (but note that

Table 1 Parameters that characterise our different UCL_CHEM models

Parameter	Model a	Model b	Model c	Model d
Temperature (Phase II)[a]	200/100 K	300/100 K	250/300 K	350/300 K
Visual extinction	2 & 10 mag	2 & 10 mag	2 & 10 mag	2 & 10 mag
External UV radiation intensity	1 Habing[b]	1,000 Habing	1 Habing	1,000 Habing
Cosmic-ray ionization rate (ζ)	1.3×10^{-17} s^{-1}	1.3×10^{-17} s^{-1}	1.3×10^{-15} s^{-1}	1.3×10^{-15} s^{-1}

[a] First value corresponds to $A_v = 2$ mag and second to $A_v = 10$ mag
[b] 1 Habing corresponds to 1.6×10^{-3} erg cm^{-2} s^{-1} when integrated between 91.2 and 240 nm [10]

chemistry has not necessarily reached steady state by then), using the formula:

$$N_{mol} = X_{mol} \times A_V \times 1.6 \times 10^{21} \quad (1)$$

where X_{mol} is the fractional abundance of the molecule, A_{V} is the visual extinction, and 1.6×10^{21} is the column density of hydrogen at a visual extinction of one magnitude. Note that the formulation above simply gives an 'on the spot' approximation of the column density. We set $N_{\mathrm{mol}} = 10^{12}\,\mathrm{cm}^{-2}$ as the minimum theoretical column density to consider a species detectable. Below this value we do not take into account the results of the models.

3.1 Influence of Cosmic Rays and UV Fields on Molecules

Our modelling results show that most molecular species are sensitive to the presence of external fields. We checked the variations of their column densities as a function of UV and CRs strengths (i.e. for the four different models). A summary of the findings is shown in Table 2. While the column density of HOC^+ is enhanced by the presence of UV radiation, many other species are easily dissociated by UV fields in the external layers of the molecular clouds (such as CO, HCN, or NS). On the contrary, we found that methanol (CH_3OH) is clearly destroyed by cosmic rays, while the production of several other species is favoured by the presence of CR photons in the ISM of NGC 1068 (e.g. SiO, CN, or N_2H^+). Finally, only C_2H shows similar column densities (within one order of magnitude of variation) for all the models.

Our results agree well with those of [3], who also used the UCL_CHEM model to find suitable molecular tracers of hot cores under different physical conditions. In general, the trends of chemical abundances with respect to ζ variations found by Bayet et al. [3] are similar to what is shown in our Table 2, with few exceptions, CS being the most contrasted species between both works. For this species [3] predicted a decrease of its abundance with increased ζ, while our models predict a slight increase. This may be explained by the different physical parameters used

Table 2 Molecular trends with UV fields and cosmic rays in the CND of NGC 1068

Easily dissociated by UV fields	CO, CS, HCN, CH_3OH, SO, HCO, SO, NS, HNC, SO_2, N_2H^+, SiO, CH_3CN, H_2CS, H_2CO, HC_3N, CH_3CCH
Enhanced by UV fields	HOC^+,
Easily dissociated by cosmic rays	CH_3OH, HC_3N
Enhanced by cosmic rays	CN, HCN, HCO^+, HNC, SO, NS, N_2H^+, SiO, SO_2, HOC^+
Insensitive	C_2H

in both works (other ζ strength, initial and final densities, visual extinction and final temperatures).

On the other hand, the comparison of our models with those of [4], where the PDR chemistry is explored in a variety of extragalactic environments, leads to big discrepancies regarding the response of the molecular abundances as a function of ζ and FUV radiation fields. For example, Bayet et al. [4] deduced that CN and HCO^+ are not affected by the variations of ζ, while our results predict enhancements of those species. Also, Bayet et al. [4] found that CO, HNC, HCN and H_2CO are not influenced by changes of the FUV radiation field, whereas our results indicate that the abundances of these molecules are reduced by at least one order of magnitude when the FUV field increases. These disagreements are mainly due to the fact that [4] used the UCL_PDR model where, unlike the UCL_CHEM code used here, the depletion of atoms and molecules onto grains, and the subsequent surface chemistry, is not included. In other words, our present modelling assumes that even the gas affected by UV photons has undergone sufficient processing involving gas-grain interactions.

3.2 Comparison with the Observations

By considering a multi-component model we succeed in reproducing the observed column densities (shown in [2]) of almost all the detected molecules in our survey within one order of magnitude, HOC^+ being the only exception. We consider this a good match, as the resolution of the IRAM-30 m telescope is not high enough to disentangle the origin of each species, and the column densities derived have relevant uncertainties due to the assumption of LTE conditions. In general, the observations are better reproduced by the models which consider a high cosmic ray ionization rate, but low FUV radiation (Model c), and high values of both parameters (Model d).

However, as expected, the scenario depicted by the models reflects clear differences in the origin and timescales of the species, as well as highlighting some degeneracies; nevertheless sometimes the same degeneracies can highlight the

prevalence of a particular energetic process. For example CO, ubiquitously tracing gas at a wide range of densities, is well matched by all the models, yet models with high and low radiation field, as long as the cosmic ray ionization rate is high, match the observations better. On the other hand, methanol is much better matched by a model where both radiation field and cosmic ray ionization rates are low: we interpret this 'mismatch' in physical conditions between CO and CH_3OH as an indication that the two species, on average, arise from different gas; methanol clearly seems to arise from regions where the cosmic ray ionization rate is close to standard, probably not representative of the average cosmic ray ionization rate of NGC 1068s. This rate is in fact well known to be variable within our own galaxy [8], and it may well vary in NGC1068 too. On the other hand, the HCO^+ observed abundance is only matched if the cosmic ray ionization rate is high (i.e. Models c and d), independently of the FUV field strength.

Unlike for cosmic rays, there are very few species that help us determining the average UV field(s) strength in NGC1068; of particular interest we have HCO, which seems to get closer to the observed value only in models where the UV field is low, while there is no molecule that *needs* a high radiation field in order to match the observations. While this does not exclude a high radiation field for this galaxy, especially near the nucleus, it seems unlikely that a rich chemistry comprising of species such as HCO would survive is the average radiation field were to by much higher than the canonical interstellar one.

Finally it is interesting to note that our models show different recycling cycles among molecules. This behaviour seems to be related to the nature of the species rather than a dependence on the radiation field and cosmic rays strength. For example, the observations of some species, such as CH_3OH and NS, are better matched at early times ($\sim 10^3$ year), since their abundances quickly drop afterwards by at least three orders of magnitude. Similarly, the column densities of some important undetected species (e.g. CH_3CCH) drop dramatically below the detectable levels at later times (i.e. $\sim 10^5$ year). On the other hand, CO, HCO^+ and HOC^+ always maintain constant values.

4 Summary

We used the IRAM-30 m telescope to carry out a spectral line survey (from 86.2 to 115.6 GHz) towards the nucleus of the AGN galaxy NGC 1068. We ran chemical models to determine the influence of strong UV fields and cosmic rays on the molecular abundances. We used a high rate of cosmic ray ionization rate to qualitatively simulate a XDR-like environment. Our models indicate that high rates of cosmic rays are present in the nucleus of NGC 1068, albeit a combination of high rates of cosmic rays and UV fiels may also explain the observed abundances in the galaxy. The chemical models applied to NGC 1068 predict that while UV radiation easily dissociate a large number of molecules (e.g. HCN, CO and NS), cosmic rays enhance the abundances of a good number of others, such as CN, SiO, and N_2H^+.

References

1. Aladro, R., Martín, S., Martín-Pintado, J., et al. 2011, A&A 535, A84
2. Aladro, R., Viti, S., Bayet, E., et al. 2012, submitted to A&A.
3. Bayet, E., Viti, S., Williams, D. A., et al. 2008, ApJ 676, 978
4. Bayet, E., Viti, S., Williams, D. A., et al. 2009, ApJ 696, 1466
5. Bayet, E., Aladro, R., Martín, S., et al. 2009, ApJ 707, 126
6. Bland-Hawthorn, J., Gallimore, J. F., Tacconi, L. J., et al.& Cecil, G. N. 1997, Astrophys. & Space Sci. 248, 9
7. Costagliola, F., Aalto, S., Rodriguez, M. I., et al. 2011, A&A 528, A30
8. Dalgarno, A. 2006, Proc. of the Natl. Acad. of Sci. 103, 12269
9. García-Burillo, S., Usero, A., Fuente, A., et al. 2010, A&A 519, A2
10. Habing, H. J. 1968, Bull. Astron. Inst. Neth. 19, 421
11. Helfer, T. T., & Blitz, L. 1995, ApJ 450, 90
12. Kamenetzky, J., Glenn, J., Maloney, P. R., et al. 2011, ApJ 731, 83
13. Krips, M., Neri, R., García-Burillo, S., et al. 2008, ApJ 677, 262
14. Le Teuff, Y. H., Millar, T. J., & Markwick, A. J. 2000, Astron. & Astrophys. Ser., 146, 157
15. Martín, S., Mauersberger, R., Martín-Pintado, J., Henkel, C., & García-Burillo, S. 2006, Astrophys. J. Supl. Ser. 164, 450
16. Millar, T. J., MacDonald, G. H., & Gibb, A. G. 1997, A&A 325, 1163
17. Nakajima, T., Takano, S., Kohno, K., et al. 2011, ApJ Lett. 728, L38
18. Schinnerer, E., Eckart, A., Tacconi, L. J., et al. 2000, ApJ 533, 850
19. Tacconi, L. J., Genzel, R., Blietz, M., et al. 1994, ApJ Lett. 426, L77
20. Telesco, C. M., & Harper, D. A. 1980, ApJ 235, 392
21. Usero, A., García-Burillo, S., Fuente, A., et al. 2004, A&A 419, 897
22. Viti, S., & Williams, D. A. 1999, MNRAS 305, 755
23. Viti, S., Collings, M. P., Dever, J. W., et al. 2004, Mon. Not. R. Astron. Soc. 354, 1141
24. Woodall, J., Agúndez, M., Markwick-Kemper, A. J., et al. 2007, A&A 466, 1197
25. Zaritsky, D., Kennicutt, R. C., Jr., & Huchra, J. P. 1994, ApJ 420, 87

Star Formation in the Milky Way: The Infrared View

Alberto Noriega-Crespo

Abstract I present a brief review of the some of the most recent and active topics of star formation process in the Milky Way using mid and far infrared observations, and motivated by the research being carried out by our science group using the data gathered by the Spitzer and Herschel space telescopes. These topics include bringing together the scaling relationships found in extragalactic systems with that of the local nearby molecular clouds, the synthetic modeling of the Milky Way and estimates of its star formation rate.

1 Introduction

In December 2007 we, Kartik Seth and I, organized a meeting in Pasadena called "The Evolving ISM in the Milky Way and Nearby Galaxies" [26]; it was the fourth conference under the auspices of the Spitzer Science Center. The main goal of that meeting was to bring together two communities using the same tools, methodology and looking essentially at the same issues, with the only differences being on the spatial scales and samples of astrophysical objects that they were studying. Two of the leading participants were Dr. Neal Evans and Dr. Robert Kennicutt, both Principal Investigators of two very successful Spitzer Legacy Surveys, "c2d" ('Core to Disks') and "SINGS" ('The Spitzer Infrared Nearby Galaxies Survey'), respectively. Both interested on the star formation process, one locally (Evans) and one on nearby galaxies (Kennicutt). Therefore, it was not a surprise that the same day I gave this presentation at Sant Cugat in the workshop on *Cosmic-ray induced phenonmenology in star-forming environments*, that Kennicutt and Evans submitted

A. Noriega-Crespo (✉)
IPAC, California Institute of Technology, Pasadena, CA 91106, USA
e-mail: alberto@ipac.caltech.edu

D.F. Torres and O. Reimer (eds.), *Cosmic Rays in Star-Forming Environments*,
Astrophysics and Space Science Proceedings 34, DOI 10.1007/978-3-642-35410-6_4,

to astroph (arXiv:1204.3552) a review on "Star Formation in the Milky Way and Nearby Galaxies" to appear in the Annual Reviews of Astronomy and Astrophysics during the Fall of 2012 [14]. And although their review is certainly more ambitious and complete than this summary, I was quite pleased to see that we identified some of the same main issues and progress on the subject.

Understanding the star formation process locally or in extragalactic systems is a very active research area, and where infrared observations have played a major role in bringing together a wholistic view. Measuring the star formation rate (SFR) of the Milky Way (MW) or other galaxies is like "taking their pulse" [7], since the transformation of molecular gas into stars, plus the energetics and evolution of the massive stars, sets some of the main characteristics of what we can observe, e.g. the interstellar medium chemical composition, the overall gas mass and the bolometric flux densities at different wavelengths. From the point of view of the Cosmic Ray community, the interest on star formation and what has been learned at infrared wavelengths is quite clear, since massive stars, their fast evolution and transformation into supernovae, is one of the main sources of cosmic ray acceleration.

This contribution will follow a similar path as that of the original oral presentation, starting with the star formation rate estimates from nearby clouds (Sect. 1), connecting these estimates with those obtained from the extrapolation of the SFR extragalactic indicators (Sect. 2), using then the concept of a high density molecular gas threshold to connect local and extragalactic measurements (Sect. 3), follow by the analysis of synthetic modeling of the SFR in the Milky Way (Sect. 4) and finally looking at what the latest far-infrared measurements of the Galactic Plane from Herschel are telling us on the SFR (Sect. 5).

Stars need to form from gas, and although this may seem too obvious today, it was Schmidt [27] nearly 50 years ago who suggested it, by looking at the distribution of the Population I stars in the Milky Way, that stars form from HI gas and that the rate of star formation (SFR) was proportional to the square of the volumetric gas density, i.e. $SFR \propto \rho^2$. Stars actually form in molecular clouds, where H_2 is the dominant specie, and this is quite relevant because there is not in our Galaxy or other extragalactic systems a one-to-one correlation between the spatial distribution of HI and that of H_2, in other words Schimdt did not get it quite right. Nevertheless, this prescription, allowed him to study fundamental properties of the Galaxy, like its luminosity function, the spatial distribution of stars and its chemical evolution [27]. Another key characteristic of the star formation process, it that the process itself seems to be different for low mass stars (0.1–8 $M_\odot$) and high mass stars ($\geq 8M_\odot$). And although there is a consensus on the main phases of the accretion process that leads to the formation low mass stars, this is not the case for high mass protostellar objects (see e.g. [1]).

2 From Local to Global Star Formation Rates and Efficiencies

A handful of studies have been published by the Galactic astronomers on the star formation rates (SFR) and efficiencies over the past 3 years that have tried to connect what is measured in the local molecular clouds with the results and relationships obtained by the extragalactic groups. The extragalactic scaling relations are of course based on the Scmidtt-Kennicutt "law" that describes the star formation rate (per unit area) as a function of the gas mass of the system (gas surface density). Indeed, it is our understanding of what 'kind' of gas mass is truly involved in the star formation process, that has evolved since the time that Schmidt postulated a relation between the SFR as a power of the volumetric gas density of the neutral Hydrogen (HI) (see e.g. [12]).

The star formation process in nearby clouds, within 500 pc or so from the Solar neighborhood, can be studied in great detail. Not only one can count the exact number of young stars that are formed in each cloud, but also one can determine their evolutionary stage, and therefore to have a complete picture of the process. One of the well known disadvantages of using the 'local' clouds, is that except for Orion, all of them are tracing the low mass star of $\sim 0.5 M_{\odot}$ over a time scale of $\sim 2.1 \times 10^6$ year [16]. Massive star formation does take place in the Milky Way, but the larger distances to these star forming regions, at least of couple of kiloparsecs away, skews our view of the star formation process towards the highest mass young stellar objects (see Sect. 4, Fig. 7), and therefore, our view still is incomplete.

One of the leading groups studying the star formation process taking place nearby is that of the Spitzer Legacy from Cores to Disk (c2d) [10]. This group not only have used the infrared detectors on board the Spitzer Space Telescope, but has supported their data with both optical, near-IR and sub-millimetric observations. The c2d group has analyzed the properties of 5 cold clouds (Cha II, Lupus, Perseus, Serpens and Ophiuchus; see Fig. 1) and found current star formation rates efficiencies ranging from 3 to 6 %, with a accumulated rate of the five clouds of $2.6 \times 10^{-4}\, M_{\odot}\, \mathrm{year}^{-1}$. Even in this small sample of clouds, the variation in efficiency strongly suggests that the SF process changes from cloud to cloud. Furthermore, they found a star formation rate per unit area (or specific SFR) at least ten times larger than that predicted by extrapolating the extragalactic Schmidt-Kennicutt relation to their low mass range (see Fig. 2), and they have interpreted this discrepancy as due to the fact that at large scales, like those in extragalactic systems, one includes both high and low density gas in the mass estimates (or gas surface density). This last conclusion was partially motivated by a previous study by Wu, Evans et al. [29], where a high gas density tracer, HCN $J = 1 - 0$ (88.63 GHz), was used to measure the high density gas, rather than the standard CO $J = 1 - 0$, to estimate the gas mass of Galactic dense cores, nearby spiral galaxies and farther away starburst galaxies. By using a high density gas tracer, they found a tight correlation over 7 and 8 orders of magnitude, between the IR luminosity, a direct tracer of the star formation activity, and the dense material, i.e. a Schmidt-Kennicutt

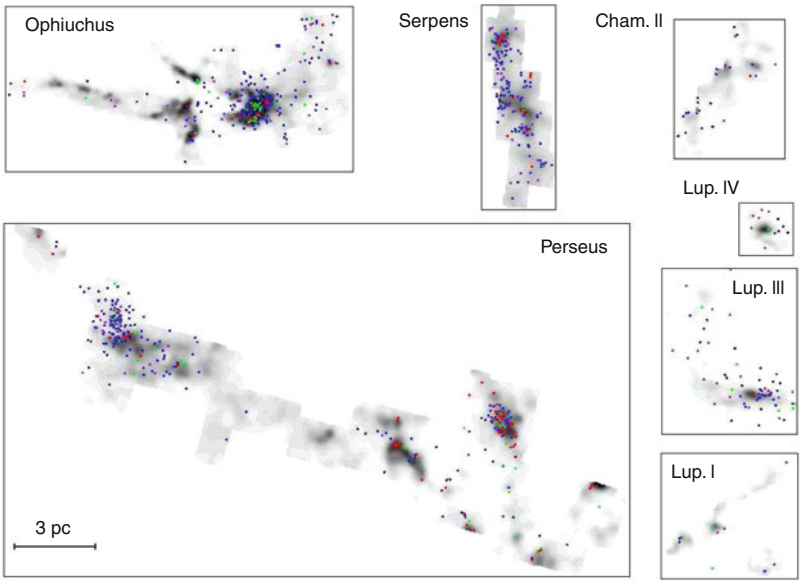

Fig. 1 The seven nearby star forming molecular clouds observed by the c2d team to determine their star formation rate (from Evans et al. [10]), defined by the extend of their extinction (*grayscale*) maps from $A_V = 1$ to 25 mag. The colored points correspond to the different classes of low mass young stellar objects, I (*red*), II (*blue*) and III (*purple*), within them

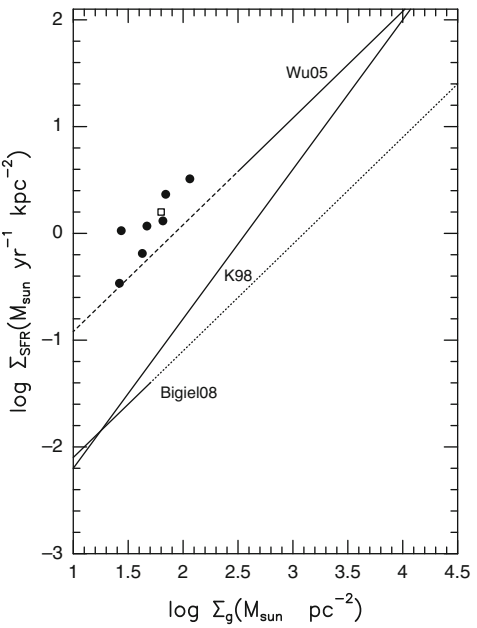

Fig. 2 The specific star formation rate as a function of specific gas density for the c2d local star forming clouds. The *open square* is the average of the seven clouds (*filled circles*). The *different lines* show the SFR relationships derived by Kennicutt [13], Bigiel et al. [2], using CO as the dense gas tracer, and Wu et al. [29], using HCN for tracing the dense gas (From Evans et al. [10])

type of relationship that connected the local SF activity in the MW with that of extragalactic systems, both normal and highly active.

3 A High Density Molecular Gas Threshold for Star Formation

The Spitzer Legacy surveys were meant to provide a wealth of high quality IR data that could be used by a wider community to explore topics beyond those that were originally intended by the project. In the true spirit of taking advantage of the Legacy data, Lada, Lombardi, and Alves [16] added the c2d clouds to their sample of star forming regions for extinction studies in the near infrared (NIR). NIR extinction has been successfully used to study the total mass of nearby clouds, as well as their structure. Some of the clouds in the extinction studies are relatively massive, e.g. the Pipe and California nebulae, but with very little star formation. The sample of extinction studied clouds doubled (11 clouds) that of the c2d group, and included some of the clouds forming massive stars like Orion A and B. The extinction method also allows a normalization of all the clouds to a given extinction threshold, and this idea is quite powerful since brings the studied molecular clouds on the same mass scale (see Fig. 3). Lada, Lomabardi, and Alves [16] found that when comparing the star formation inventories for these clouds with their extinction masses at a given threshold in the NIR K band (at $\sim$2.2 μm) of $A_K = 0.8$ mag, there was a linear relationship between their SFR and the $M_{0.8}$ mass of the clouds, of the form $SFR(M_\odot\ year^{-1}) = 4.6 \pm 2.6 \times 1^{-8} M_{0.8}$ (see Fig. 4).

This $A_K = 0.8$ mag threshold corresponds to a gas surface density of $\Sigma = 116\,M_\odot\,pc^{-2}$, and can be interpreted as a volumetric gas density threshold in molecular Hydrogen of $n(H_2) = 10^4\,cm^{-3}$. A similar threshold was determined by the c2d group [11] using the local clouds, with $\Sigma = 129 \pm 14 M_\odot\,pc^{-2}$, where the Galatic SFR versus the gas mass of the parent cloud becomes linear and not very different than that of the extragalactic indicators (see Fig. 5). The nice physical interpretation of these results is that star formation takes place in the densest regions, above a given threshold, and when this is taking into account the SFR corresponds to that specific mass of dense gas. Indeed, Lada, Lombardi & Alves suggested that if this is the case, then one should be able to place in the same relationship, SFR vs dense mass, Galactic Cores and extragalactic objects, and they explored this possibility in another study [17].

Figure 6 shows the SFR vs. cloud molecular mass for the local galactic clouds (circles), normal galaxies (pentagons), luminous (squares) and ultraluminous (inverted triangles) active star formation red galaxies (LIRGS & ULIRGS) plus high redshift BzK galaxies (triangles). The open symbols are for measurements of the gas mass based on CO observations ("mean" molecular masses), while the solid symbols are those based on a dense gas tracer (e.g. HCN) or extinction. The broken parallel lines correspond to constant fractions of the dense gas ($n(H_2) \geq 10^4\,cm^{-3}$)

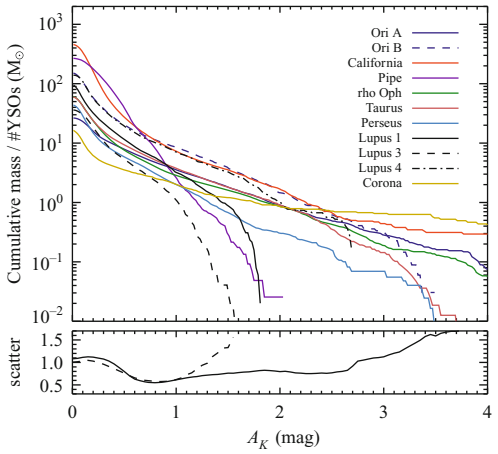

Fig. 3 The cumulative mass profile of the clouds in Lada. et al. [16] sample normalized to their corresponding number of YSOs as a function of infrared extinction. The 11 clouds reach a minimum at nearly the same magnitude $A_K = 0.8 - 0.9$ mag, suggesting that there is a threshold in extinction at which the mass contained is the one most directly involved in the star formation of the cloud

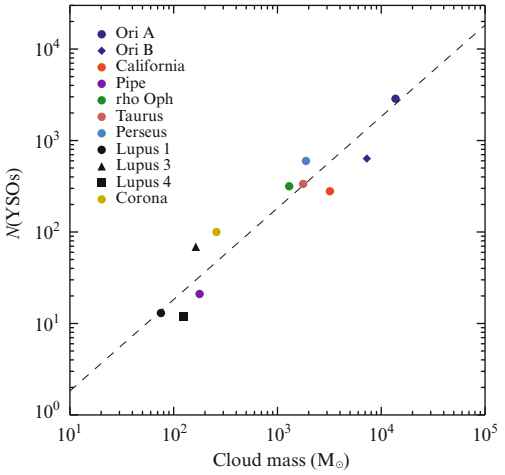

Fig. 4 The number of YSOs as a function of the mass of the cloud set by the $A_K = 0.8$ mag threshold (from Lada, Lombardi, and Alves [16]), i.e. the mass of the dense gas directly involved with the star formation process

and their slopes are those found by Lada, Lombardi, and Alves [16]. If one takes into account that the CO mass measurements reflect an average on relatively large spatial scales in extragalactic systems (∼1 kpc), and corrects for this effect, such that the true mass involved in the star formation process (that of the dense gas) is included in the SFR-dense gas mass diagram, then local galactic molecular clouds and extragalactic system share the same relationship. According to Lada et al. [17], "there is a fundamental empirical scaling relation that directly connects the local star forming process with that operating globally within galaxies."

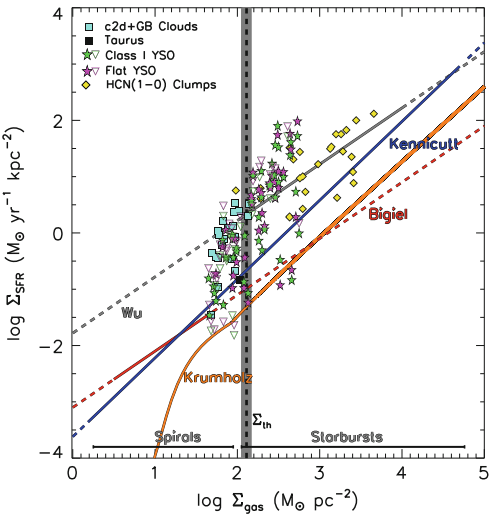

Fig. 5 The local Galactic star forming clouds do behave linearly in the specific star formation rate versus specific gas cloud density diagram, above a certain threshold (Σ_{th}), and not very different than the relationships found for the extragalactic indicators (See [11] for details)

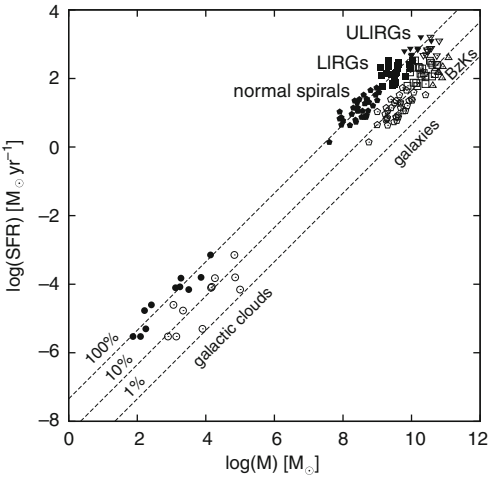

Fig. 6 The SFR-molecular cloud mass diagram according to Lada et al. [17]. Open symbols correspond to "mean" molecular gas masses, while the solid ones to those obtained for a dense gas either using extinction or HCN measurements (see text)

4 Synthetic Modeling of the Milky Way

When studying extragalactic systems, either nearby or at a high redshift, a common technique to interpret the observations is to compare them with synthetic models of a galaxy. In a model one can modify the Initial Mass Function and rate of star formation, plus add more information like a stellar spectra library to follow the spectral evolution of a system (see e.g. [4, 5]). Recently this technique has been applied by Robitaille and Whitney [24] to estimate the star formation rate

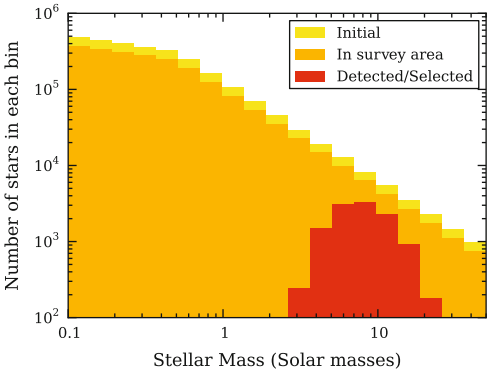

Fig. 7 The mass distribution function of the synthetic YSOs for a given synthesis model. The *yellow* and *orange* histograms show the initial and surveyed distributions, respectively; while the *red* only those YSOs detected/selected by GLIMPSE and MIPSGAL surveys [24]

of the Milky Way, based on a comparison with the mid-IR data obtained by GLIMPSE plus MIPSGAL [6, 8], and as an extension to the thorough modeling carried out by Robitaille et al. [22] of the spectral energy distribution (SED) of protostellar objects. For the Milky Way, Robitaille and Whitney looked at the 3D distribution of star formation within the disk in such way to take into account not only their YSO theoretical SED models, but also including the limitations in sensitivity by the IRAC instrument as well as the effects of dust extinction. Although the technique is quite powerful, it does depend on the assumptions of the model. The prescription of Robitaille and Whitney [24] goes as follows: distribute the YSOs in random positions, use random age and mass given by the Kroupa [15] Initial Mass function (within 0.1–50 $M_\odot$), control the upper and lower stellar age, include a reasonable spatial distribution of dust, use the synthetic SEDs to estimate the intrinsic magnitudes and IRAC colors, select only those YSOs that fall within the survey area and fulfill the criteria of color and brightness defined by Robitaille et al. [23]; and finally, adjust the SFR to match the observations. In practice, only sources that are younger than 2 Myr are used to really match the observations.

Figures 7 and 8 show the results for one of these models, the mass distribution function of the synthetic YSOs and their corresponding spatial distribution in the Milky Way, respectively. The red histogram of the mass distribution (Fig. 7) corresponds to what is actually observed, and this "represents to less than 0.5 % of all the YSOs in the Galaxy" [24], i.e. the SFR is obtained from a very small fraction of objects. Also these YSOs are systematically more massive with a median value of 10–15 $M_\odot$, but within a 3–20 $M_\odot$ range. The spatial distribution (Fig. 8) is color coded according to extinction along the line-of-sight from us, and shows that most of the sources that are counted [23] are within 10–15 kpc from us.

After several "realizations" of the synthetic models, and taking into account that the contamination by AGB stars in the GLIMPSE & MIPSGAL sample ranges from 30 to 50 %, the SFR in the Galaxy is estimated to be between 0.68 to 1.45 $M_\odot$ year^{-1} [24].

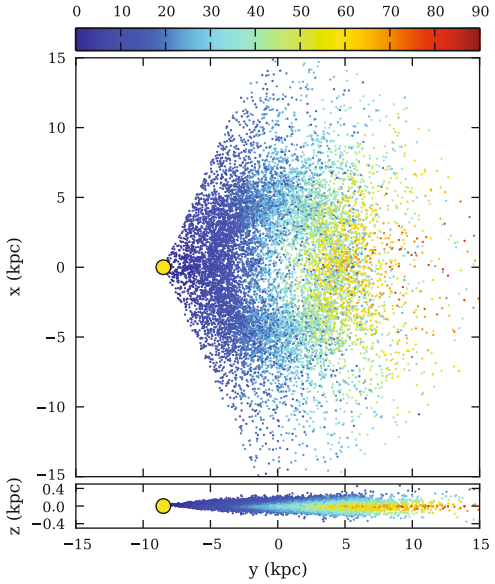

Fig. 8 The synthetic 3-dimensional spatial distribution of the YSOs as detected by GLIMPSE & MIPSGAL. The points are color-coded according to the extinction values along-the-line of sight from us (See Robitaille and Whitney [24] for details)

5 Far Infrared Star Formation Rate Estimate

The star formation rate estimated using mid-IR observations, like that using the synthetic models, does not take into account deeply embedded protostellar objects which are detected at wavelengths longer than 24 μm, and this should not be a problem for the far-IR observations. Recently Veneziani et al. [28] have used data from the Herschel Space telescope of the HiGAL Key Project [20] to estimate the rate of star formation in the Milky Way. The HiGAL KP surveyed the inner Galaxy ($l = \pm 60°, b = \pm 1°$) using the PACS and SPIRE instruments in parallel mode, covering five wavelengths: 70,160, 250, 350 and 500 μm. At 70 μm the angular resolution is 6″, while at 500 μm is ∼36″, and therefore, one of the biggest challenges of this type of survey is to correctly bandmerge the flux densities of the compact sources between short and longer wavelengths [21]. This is an issue because it is quite possible that many massive protostars deeply embedded are surrounded by low mass protostars when forming, and the long wavelength observations cannot resolve the multiple components (see e.g. [19]) (Fig. 9).

Veneziani et al. used the data from the so called Science Demonstration Phase (SDP), taken at two latitudes, $l = 30°$ and $l = 59°$, where the conditions of star formation are quite different. The $l = 30°$ region is very active, including the well known W43 complex in its 2° field-of-view, while the $l = 59°$ field looks into the Vulpecula region, tangent to a spiral arm [3]. For both of these fields there are very good estimates of the distances [25], so mass envelope and bolometric luminosities for the compact protostellar sources can be measured and be placed in the L_{BOL} vs M_{ENV} diagram (see e.g. [9, 19]). This diagram allowed Veneziani et al. to follow

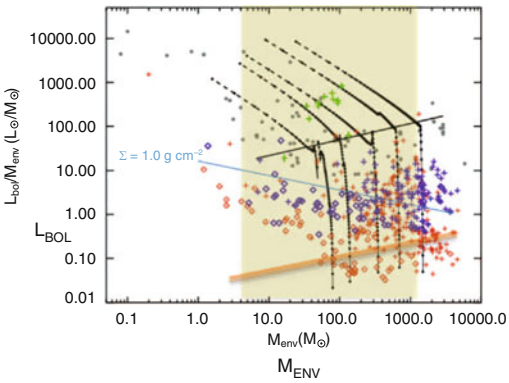

Fig. 9 YSOs found in the $l = 30°$ SDP field place in the massive star formation bolometric luminosity (L_{BOL}) vs. mass envelope (M_{ENV}) diagram (after Molinari et al. [19] and Elia et al. [9]). The shaded region marks the range of envelope masses considered by Veneziani et al. [28] in their SFR estimate

the protostellar objects through their evolutionary tracks to their final zero age main sequence mass and count how many young stars per unit mass per unit time were found in the SDP fields. Preliminary results for the $l = 30°$ field found 690 sources, with ∼323 being likely to be protostars, within a range of mass envelope of 80–2,000 $M_\odot$ and a median mass of 540 $M_\odot$. These objects have a median evolutionary time of $\sim 2.5 \times 10^5$ year and a median final main sequence mass of ∼15 $M_\odot$. Using Lada et al. [16] relationship for the star formation rate using the median mass and evolutionary time, one gets SFR $= N_{YSOs}\, M_{final}/t_{evol}$ or $\frac{323 \times 15}{2.5 \times 10^5} = 0.02\, M_\odot$/year. This rate is approximately 20 times that of Orion A and B [16], perhaps too high to be representative of the entire Milky Way. This rate suggests that the simple method of counting protostellar objects is more complicated when dealing with high mass protostars, and that the number of YSOs identified plus their median final mass and lifetime under the "accretion" formation scenario can be a bit uncertain.

Given the relatively high luminosity at 70 μm of the $l = 30°$ SDP field, and the fact that the selected YSOs were those found in the densest regions, Veneziani et al. considered a second approach to estimate the SFR, by using an extrapolation of the FIR extragalactic indicator developed by Li et al. [18]. The Li et al. 70 μm SFR indicator is based on a sample of 40 SINGs galaxies and uses 'sub-galactic' regions with sizes between 0.05 and 2 kpc, and in this sense closer to the scales that are sampled in the Milky Way. The indicator is calibrated for a range of 70 μm luminosities of $5 \times 10^{40} \leq L(70) \leq 5 \times 10^{43}$ erg s^{-1} and given by, SFR($M_\odot$ year^{-1}) $= L(70)/1.067 \times 10^{43}$ erg s^{-1}. For the 70 μm luminosity of the $l = 30°$ field, this corresponds to a SFR of $3.8 \pm 0.7 \times 10^{-4}\, M_\odot$ year^{-1}.

If one assumes that HiGal $l = 30°$ tile is representative of the entire Milky Way, then is possible to have a rough estimate of the SFR rate in the Galaxy, by weighting the volume of each tile with respect to that of the Milky Way (see [28]). Approximating the Galaxy as a simple disk with a scale heigh of 100 pc and a mean radius of 15 kpc, the total mean star formation rate is $2.1 \pm 0.4\, M_\odot$ year^{-1}, i.e. within the range obtained by the synthetic modeling of the Milky Way.

Acknowledgements The bulk of this contribution was written during two visits to Paris, I thank Francois Boulanger and Ken Ganga for providing me with a working environment to complete it. I also thank the Organizing Committee for their kind invitation.

References

1. Beuther, H., Churchwell, E., McKee, C. F., & Tan, J. C. 2007: The Formation of Massive Stars. Protostars and Planets V, B. Reipurth, D. Jewitt, and K. Keil (eds.), University of Arizona Press, Tucson, 165
2. Bigiel, F., Leroy, A., Walter, F. Brinks, E. et al. 2008: The Star Formation Law in Nearby Galaxies on Sub-Kpc Scales. AJ, 136, 2846
3. Billot, N., Noriega-Crespo, A., Carey, S., Guieu, S. et al. 2010: Young Stellar Objects and Triggered Star Formation in the Vulpecula OB Association. ApJ, 712, 797
4. Bruzual, A.G. & Charlot, S. 1993: Spectral evolution of stellar populations using isochrone synthesis. ApJ, 405, 538
5. Bruzual, G. & Charlot, S. 2003: Stellar population synthesis of 2003. MNRAS, 344, 1000
6. Carey, S. J., Noriega-Crespo, A., Mizuno, D. R., Shenoy, S. et al. 2009: MIPSGAL: A Survey of the Inner Galactic Plane at 24 and 70μm. PASP, 121, 76
7. Chomiuk, L. & Povich, M. S. 2011: Toward a Unification of Star Formation Rate Determinations in the Milky Way and Other Galaxies. AJ, 142, 197
8. Churchwell, E., Babler, B. L., Meade, M. M., Whitney, B. A. et al. 2009: The Spitzer/GLIMPSE Surveys: A New View of the Milky Way. PASP, 121, 213
9. Elia, D., Schisano, E., Molinari, S., Robitaiile, T. et al. 2010: A Herschel study of YSO evolutionary stage and formation timelines in two fields of the Hi-GAL survey. A&A, 518, 97
10. Evans, N. J. II, Dunham, M. M., Jorgensen, J. K., Enoch, M. L. et al. 2009: The Spitzer c2d Legacy: Star-Formation Rates and Efficiencies; Evolution and Lifetimes. ApJS 181, 321
11. Heiderman, A., Evans, N. J., Allen, L.E., Huard, T. & Heyer, M. 2010: The Star Formation Rate and Gas Surface Density Relation in the Milky Way: Implications for Extragalactic Studies. ApJ, 723, 1019
12. Kennicutt, R. C. Jr. 1998a: Star Formation in Galaxies along the Hubble Sequence. ARA&A, 36, 189
13. Kennicutt, R. C., Jr. 1998b: The Global Schmidt Law in Star-forming Galaxies. ApJ, 498, 541
14. Kennicutt, R. C., Jr & Evans, N. J., II 2012: Star Formation in the Milky Way and Nearby Galaxies. ARA&A, 50, 513 (arXiv1204.3552)
15. Kroupa, P. 2001: On the variation of the initial mass function. MNRAS, 322, 231
16. Lada, C.J., Lombardi, M. & Alves, J.F. 2010: On the Star Formation Rates in Molecular Clouds. ApJ, 724, 687
17. Lada, C. J., Forbrich, J., Lombardi, M. & Alves, J. F. 2012: Star Formation Rates in Molecular Clouds and the Nature of the Extragalactic Scaling Relations. ApJ, 745, 190
18. Li, Y., Calzetti, D., Kennicutt, R. C., Hong, S. et al. 2010: Spitzer 70μm Emission as a Star Formation Rate Indicator for Sub-Galactic Regions. ApJ, 725, 677
19. Molinari, S., Pezzuto, S., Cesaroni, R., Brand, J. et al. 2008: The evolution of the spectral distribution in massive young stellar objects. A&A, 481, 345
20. Molinari, S., Swinyard, B., Bally, J., Barlow, M. et al. 2010: Clouds, filaments and protostars: The Hesrchel Hi-GAL Milky Way. A&A, 518, 100
21. Molinari, S., Schisano, E., Fautini, F., Pestalozzi, M. et al. 2011: Source extraction and photometry for far-infrared and sub-millimeter continuum in the presence of complex backgrounds. A&A, 518, 100
22. Robitaille, T.P., Whitney, B. A., Indebetouw, R. & Wood, K. 2006: Interpreting Spectral Energy Distributions from Young Stellar Objects. I. A Grid of 200, 100 YSO Model SEDs. ApJS, 167, 256

23. Robitaille, T.P., Meade, M. R., Babler, B. L., Whitney, B. A. et al. 2008: Intrinsically Red Sources Observed by Spitzer in the Galactic Midplane. AJ, 136, 2413
24. Robitaille, T. P. & Whitney, B. A. 2010: The Present-Day Star Formation Rate of the Milky Way Determined from Spitzer-Detected Young Stellar Objects. ApJ, 710, 11
25. Russeil, D., Pestalozzi, M., Mottram, J. C., Bontemps, S. et al. 2011: Giving physical significance to the Hi-GAL data: determining the distance of cold dusty cores in the Milky Way. A&A, 526, 151
26. Sheth, K., Noriega-Crespo, A., Ingalls, J. & Paladini, R. 2009: Preface: The Evolving ISM in the Milky Way and Nearby Galaxies. "The Fourth Spitzer Science Center Conference, Proceedings of the conference held December 2–5, 2007 at the Hilton Hotel, Pasadena, CA, Eds.: K. Sheth, A. Noriega-Crespo, J. Ingalls, and R. Paladini, Published online at http://ssc.spitzer.caltech.edu/mtgs/ismevol/"
27. Schmidt, M. 1959: The Rate of Star Formation. ApJ, 129, 243
28. Veneziani, M., Elia, D., Noriega-Crespo, A., Paladini, R. et al. 2013: An analysis of the star formation with Herschel in the Hi-GAL Survey. I. The Science Demonstration Phase Fields. A&A, 549, 130
29. Wu, J., Evans, N. J., Gao, Y., Solomon, P. M. et al. 2005: Connecting Dense Gas Tracers of Star Formation in our Galaxy to high-z Star Formation. ApJ, 635, 173

The Initial Conditions of Star Formation: Cosmic Rays as the Fundamental Regulators

Padelis P. Papadopoulos and Wing-Fai Thi

Abstract Cosmic rays (CRs) control the thermal, ionization and chemical state of the dense H_2 gas regions that otherwise remain shielded from far-UV and optical stellar radiation propagating through the dusty ISM of galaxies. It is in such CR-dominated regions (CRDRs) rather than Photon-dominated regions (PDRs) of H_2 clouds where the star formation initial conditions are set, making CRs the ultimate star-formation feedback factor in galaxies, able to operate even in their most deeply dust-enshrouded environments. CR-controlled star formation initial conditions naturally set the stage for a near-invariant stellar Initial Mass Function (IMF) in galaxies as long as their average CR energy density U_{CR} permeating their molecular ISM remains within a factor of $\sim$10 of its Galactic value. Nevertheless, in the extreme environments of the compact starbursts found in merging galaxies, where $U_{CR} \sim (\text{few}) \times 10^3\, U_{CR,Gal}$, CRs dramatically alter the initial conditions of star formation. In the resulting extreme CRDRs H_2 cloud fragmentation will produce far fewer low mass ($<8\, M_\odot$) stars, yielding a top-heavy stellar IMF. This will be a generic feature of CR-controlled star-formation initial conditions, lending a physical base for a bimodal IMF during galaxy formation, with a top-heavy one for compact merger-induced starbursts, and an ordinary IMF preserved for star formation in isolated gas-rich disks. In this scheme the integrated galactic IMFs (IGIMF) are expected to be strong functions of the star formation history of galaxies. Finally the large, CR-induced, ionization fractions expected for (far-UV)-shielded H_2 gas in the CRDRs of compact starbursts will lengthen the ambipolar diffusion

P.P. Papadopoulos (✉)
Max Planck Institute for Radioastronomy, Auf dem Huegel 69, D-5312, Bonn, Germany
e-mail: padelis@mpifr-bonn.mpg.de

W.-F. Thi
UJF-Grenoble 1/CNRS-INSU, Institut de Plantologie et d'Astrophysique (IPAG) UMR 5274, 38041, Grenoble, France
e-mail: wing-fai.thi@obs.ujf-grenoble.fr

D.F. Torres and O. Reimer (eds.), *Cosmic Rays in Star-Forming Environments*, Astrophysics and Space Science Proceedings 34, DOI 10.1007/978-3-642-35410-6_5,

(AD) timescales so much as to render the alternative AD-regulated rather (Jeans mass)-driven star formation scenario as utterly unrealistic for the ISM in such galaxies.

1 Cosmic Rays Versus Far-UV and Optical Photons

Much of the interstellar medium (ISM) in galaxies resides in the so-called Photon-dominated regions (PDRs) where stellar far-UV photons ($6\,\mathrm{eV} < h\nu < 13.6\,\mathrm{eV}$) determine the thermal, ionization and chemical state of atomic (HI) and molecular (H_2) hydrogen gas [1] (see also Fig. 1). For HI these phases are the Warm Neutral Medium (WNM, with $T_{kin} \sim 10^4\,K$ and $n \sim (0.1\text{–}1)\,cm^{-3}$) and the Cold Neutral Medium (CNM, with $T_{kin} \sim (80\text{–}200)\,K$ and $n \sim (10\text{–}100)\,cm^{-3}$) [2]. For the molecular PDRs in H_2 clouds on the other hand: $n \sim (10^2\text{–}10^6)\,cm^{-3}$ and $T_{kin} \sim (30\text{–}100)\,K$. Such PDRs start from the surface of molecular clouds (MCs) with a layered distribution (Fig. 2) of atomic and ionized species on the outside (HI, C^+, C, O), and continue deep inwards where molecules such as CO dominate [3, 4], marking the location of such clouds via their mm/submm rotational line emission. The thermal, ionization, and chemical state of all these phases is determined by the far-UV photons whose influence, especially on the ISM chemistry, can extend very deep inside the low-density MCs ($n(H_2) \sim (100\text{–}500)\,cm^{-3}$) typical in the Galaxy. The dust in PDRs is heated via absorption of the ambient far-UV and optical radiation and cools via continuum thermal IR/submm emission while the gas is heated via electrons ejected by the photoelectric effect on the concomitant dust grains and polycyclic aromatic hydrocarbons (PAHs). Despite the gas receiving $\sim 10^2\text{–}10^3$ *less* heating per unit volume than the dust, in PDRs it is always $T_{kin} > T_{dust}$. This is because of the much less efficient cooling of the gas via spectral lines while dust cools via continuum radiation across a wide range of wavelengths (typically peaking at IR/submm wavelengths). Turbulent heating of the gas in MCs will further reinforce the $T_{kin} > T_{dust}$ inequality, since it does not involve the dust reservoir.

For MCs in the typical ISM conditions of spiral disks where $\langle A_v \rangle \sim 3\text{–}7$ (in units of optical extinction), there can only be very little H_2 gas residing in their dense (far-UV)/optical-shielded regions. Its mass fraction per MC is $\sim(1\text{–}5)\,\%$, a census found from surveys of CO $J = 1 - 0$ (total H_2 mass indicator) and rotational transitions of dense gas tracer molecules such as the HCN (mostly $J = 1 - 0$), and using the HCN/CO line ratio to determine $f_{dense} = M(n \geq 10^4\,cm^{-3})/M_{tot}(H_2)$ [5, 6]. Here is important to note that the more complex heavy rotor molecules such as HCN will necessarily trace the dense but also (mainly) the (far-UV)-shielded mass of MCs since, unlike H_2 and its tracer molecule CO, they have much lower dissociation potentials ($\sim$5 eV for HCN versus $\sim$13 eV for H_2, and $\sim$10 eV for CO).

Simple approximate estimates of the mass fraction contained in the PDRs of (far-UV)-irradiated MCs can be found by computing the mass of outer atomic HI layer marking the HI $\rightarrow$ H_2 transition, itself comparable to the mass of the warm PDR H_2 gas layer extending further inwards. Thus the PDR-residing gas column density

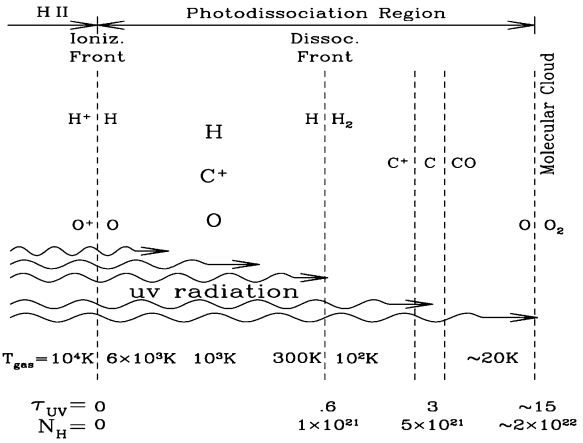

Fig. 1 The structure of a typical PDR/CRDR. Atomic and ionized species reside on the (far-UV)-illuminated outer parts (*left*) while neutral atoms (O) and molecules such as CO dominate deeper inside, the domain of CRDRs and CR-controlled thermal and chemical gas states

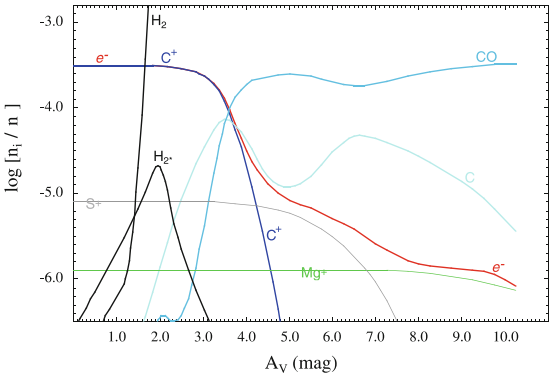

Fig. 2 The PDR → CRDR transition zone as marked by the rapidly decreasing C^+ and e^- abundances deep inside a (far-UV)-illuminated molecular cloud (radiation field incoming from the *left*). Note the dramatic fall of the electron abundance beyond $A_v \sim 4$

(HI and H_2) will be $\sim 2 \times N_{tr}(HI)$. The latter can be computed for a given radiation field G_o (in Habing units), metallicity Z (Z = 1 being solar), average gas density n, and an H_2 formation rate R_f. In units of optical extinction this transition layer is [9]:

$$A_v^{(tr)} = 1.086 \xi_{FUV}^{-1} \ln\left[1 + \frac{G_o k_o}{n R_f} \Phi\right] \tag{1}$$

where $k_o = 4 \times 10^{-11}\ s^{-1}$ is the H_2 dissociation rate (for $G_o = 1$), $R_f \sim 3 \times 10^{-17}$ $cm^{-3}\ s^{-1}$ its formation rate on grains (for typical CNM HI), and $\Phi = 6.6 \times 10^{-6} \sqrt{\pi}$ $Z^{1/2} \xi_{FUV}$ is the H_2 self-shielding function integrated over the HI/H_2 transition layer, with $\xi_{FUV} = \sigma_{FUV}/\sigma_V \sim 2$–3 being the dust cross section ratio for far-UV and optical light. Using existing formalism [9] the PDR-related gas mass fraction per MC then is:

$$f_{PDR} \sim 2 \times \left[1 - \left(1 - \frac{4 A_v^{(tr)}}{3 \langle A_v \rangle}\right)^3\right], \tag{2}$$

assuming spherical and uniform MCs that do not cross-shield and hence each receives the full (far-UV)/optical radiation field, assumptions that make the computed f_{PDR} a maximum. The average optical extinction $\langle A_v \rangle$ per MC is of course finite and a function of the ambient ISM conditions, mainly the gas pressure (dominated by supersonic non-thermal rather than thermal velocity fields). Expressing an empirical Galactic (average MC density)-(size) relation: $n \propto (2R)^{-1}$, along with its expected normalization in terms of cloud boundary pressure P_e [9] in terms of average optical extinction yields:

$$\langle A_v \rangle \sim 0.22\, Z\, \frac{n_o}{100\,\mathrm{cm}^{-3}} \left(\frac{P_e/k_B}{10^4 \mathrm{cm}^{-3}\mathrm{K}} \right)^{1/2}, \tag{3}$$

where $n_o \sim 1{,}500\,\mathrm{cm}^{-3}$. For average MC densities of $\sim 100\,\mathrm{cm}^{-3}$, Solar metalicities, $\xi_{FUV} = 2$, and $G_o = 5$–10 (for typical star-forming gas) Eq. 1 yields $A_v^{(tr)} \sim 0.50$–0.75, while for typical interstellar pressures in galactic disks $P_e/k_B \sim (1\text{–}2) \times 10^4\,\mathrm{K\,cm}^{-3}$ it would be $\langle A_v \rangle \sim 3.3$–$4.7$. The latter is the A_v range over which the abundance of C^+ plummets, giving rise to C and CO while the free electron abundance is much reduced (see Fig. 2).

For the finite MCs this outer HI/(warm H_2) PDR gas still contains $f_{PDR} \sim 0.74$–1 of their mass (from Eq. 2), i.e. *most of the HI and H_2 gas in typical star-forming ISM environments resides in PDRs.* Later we will see that this will not be so in the high-pressure ISM of Ultra Luminous Infrared galaxies (ULIRGs), merger systems with very IR-luminous ($L_{IR} \geq 10^{12}\,L_\odot$) compact starbursts (Sect. 4).

2 The Physical Conditions of the Gas: PDRs Versus CRDRs

The wide range of physical conditions of the HI and H_2 gas in PDRs (Sect. 1) is the direct result of: (a) the widely varying strengths of the dust-absorbed far-UV and optical radiation (and thus of the gas photoelectric heating per H, and dust heating) within the PDRs, and (b) the large range of densities (and thus of the cooling power per H) that are expected in the supersonically turbulent MCs [7]. Dissipation of the supersonic turbulence via shocks [8] will further contribute to the wide range of temperatures observed in the PDR-residing gas of MCs. Moreover their average electron abundance $x(e) = n_e/[2n(H_2)]$ changes by $\sim$2–3 orders of magnitude, starting from a maximum of $\sim 3 \times 10^{-4}$ (that corresponds to a fully ionized carbon).

The dense gas cores ($n \sim (10^5\text{–}10^6)\,\mathrm{cm}^{-3}$) in Galactic CRDRs on the other hand span a much narrower range of temperatures and ionization states, with $\langle T_{kin} \rangle \sim 10\,\mathrm{K}$ (and $\sim$30 % dispersion), and $x(e) \sim (\mathrm{few}) \times 10^{-8}$ (varying by less than a factor of $\sim$5). These CRDR conditions, widely observed in the Galaxy [10, 11], are a result of a nearly complete lack of far-UV and optical photons in such regions (thus no photoelectric gas heating or strong dust heating), nearly complete dissipation of supersonic gas motions [12], and the onset of strong gas-dust thermal

coupling setting $T_{kin} \sim T_{dust}$. This simply means that cold dust grains inside CRDRs, warmed only by the feeble IR radiation able to leak inside them, can now act as powerful 'thermostats' of the H_2 gas. The latter is now heated almost exclusively by primary and secondary ionizations induced by low-energy CRs ($10\,\mathrm{MeV} \leq E_{CR} \leq 100\,\mathrm{MeV}$) [13] which, unlike far-UV and optical photons, penetrate deep inside such regions, and thus *fully regulate their thermal, ionization and chemical states.*

The aforementioned CR-controlled dense H_2 gas states in ordinary star-forming environments is expected also on broad theoretical grounds, namely: (a) high density gas regions will be typically nested well inside less dense gas structures of supersonic MCs [14], and thus will always 'see' a much-attenuated stellar radiation field, (b) high-density gas is also strongly cooling gas (since (line-cooling)$\propto [n(H_2)]^2$), and (c) turbulent energy injected on the largest gas structures with low average densities $\sim(10\text{–}10^3)\,\mathrm{cm}^{-3}$ will have fully dissipated in the high density gas of CRDRs. It is actually these three reasons, along with the strong thermal coupling of the gas in CRDRs to a necessarily cold dust (for lack of far-UV/optical photons) reservoir, that *make it very difficult for large masses of warm and dense H_2 gas to exist in ordinary star-forming galaxies.* Finally, as already mentioned in Sect. 1, only few% of the total H_2 gas mass resides at such high densities anyway, as expected also from MC simulations [7] under conditions found in ordinary star-forming spiral disks.

2.1 Computing T_{kin} and x(e) in CRDRs: A Simpler Method

In CRDRs the $T_{kin}^{(min)}$ and $x_{min}(e)$ minimum values expected for H_2 gas in galaxies are set. However determining them involves solving the coupled equations of thermal, chemical and ionization balance in such regions since CRs heat the gas but also affect the abundance of various molecular and atomic coolants. We can nevertheless make some simplifying assumptions that will keep the physics involved transparent while demonstrating the range of $T_{kin}^{(min)}$ and $x_{min}(e)$. Following standard methods [15] $T_{kin}^{(min)}$ in CRDRs can be computed by solving the equation of thermal balance:

$$\Gamma_{CR} = \Lambda_{line} + \Lambda_{g-d}, \tag{4}$$

where $\Gamma_{CR} \propto \zeta_{CR} n(H_2)$ is the CR heating with $\zeta_{CR} \propto U_{CR}$ being the CR ionization rate, and U_{CR} the average CR energy density. For $T_{kin} \leq 50\,\mathrm{K}$ (which encompasses what is expected for CRDRs of ordinary star-forming galaxies), the line cooling term Λ_{line} is dominated by CO lines. However for the much more extreme CRDRs expected in ULIRGs, higher temperatures are possible and thus cooling from the atomic fine structure lines O I (at $63\,\mu\mathrm{m}$) and C^+ (at $158\,\mu\mathrm{m}$) can become important. The C^+ abundance in CRDRs is not necessarily negligible as it is no longer controlled by a stellar far-UV radiation field (as in PDRs), but by ISM-CR

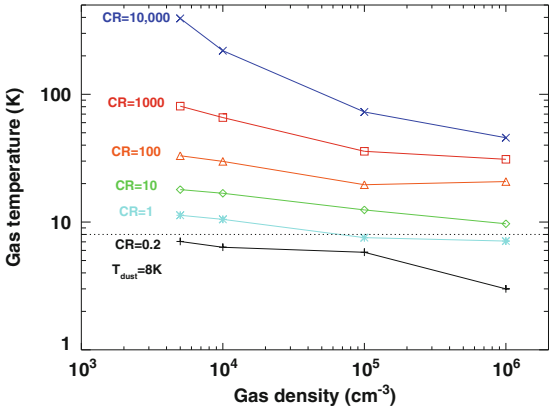

Fig. 3 The equilibrium temperature of (far-UV)-shielded regions in CRDRs computed from Eq. 5. The CR energy densities range from those expected in ordinary star-forming environments Galaxy [$U_{CR} = (0.2-10) \times U_{CR,Gal}$] to those expected in the extreme CRDRs of ULIRGs [$U_{CR} = (10^2–10^4) \times U_{CR,Gal}$]. A dust temperature of $T_{dust} = 8\,K$, and a Galactic CR ionization rate of $\zeta_{CR} = 5 \times 10^{-17}\,s^{-1}$ have been assumed

interactions inducing internal UV radiation which destroys CO and produces C^+, a clear demonstration of the coupled thermal and chemical states of the gas in CRDRs. Finally the term Λ_{g-d} denotes the all-important (in CRDRs) cooling of the gas via the gas-dust coupling which depends on the gas and dust temperatures. Thus the thermal balance equation becomes

$$\Lambda_{CO}(T_{kin}) + \Lambda_{g-d}(T_{kin}, T_{dust}) + \Lambda_{OI\,63}(T_{kin}) + \Lambda_{C^+}(T_{kin}) = \Gamma_{CR}, \qquad (5)$$

(see the Appendix for the detailed expressions used). We have not considered turbulent gas heating since we want to compute the minimum CR-controlled gas temperatures and since supersonic turbulence (and thus shock-heating) has typically dissipated in the dense pre-stellar gas regions inside CRDRs.

In order to solve the gas thermal balance equation in principle we also must solve for T_{dust} in CRDRs. For the purposes of computing $T_{kin}^{(min)}$ we set $T_{dust} = 8\,K$, which is typical for CR-dominated cores in the Galaxy. Any stronger IR radiation field leaking inside such cores (as expected in starbursts) or remnant turbulent gas heating can only raise the gas temperatures computed here. In Fig. 3 the $T_{kin}^{(min)}$ values show that CR-heated dense gas ($>10^4\,cm^{-3}$) remains cold ($\sim$(10–15) K) for U_{CR} within $\sim(0.2-10)\times U_{CR,Gal}$, rising decisively only when $U_{CR} \sim$ (few) $\times 10^3\,U_{CR,Gal}$ where the thermal balance equation yields $T_{kin}^{(min)} \sim$ (40–100) K.

Solving for the coupled chemical and thermal states of dense gas in CRDRs does not change much of the aforementioned picture while it makes clear another important aspect that of CR-controlled thermal states of the gas, namely that high CR energy densities *will induce a strong gas-dust thermal decoupling*, with $T_{kin}^{(min)}$ remaining significantly higher than T_{dust}, even at high gas densities (Fig. 4).

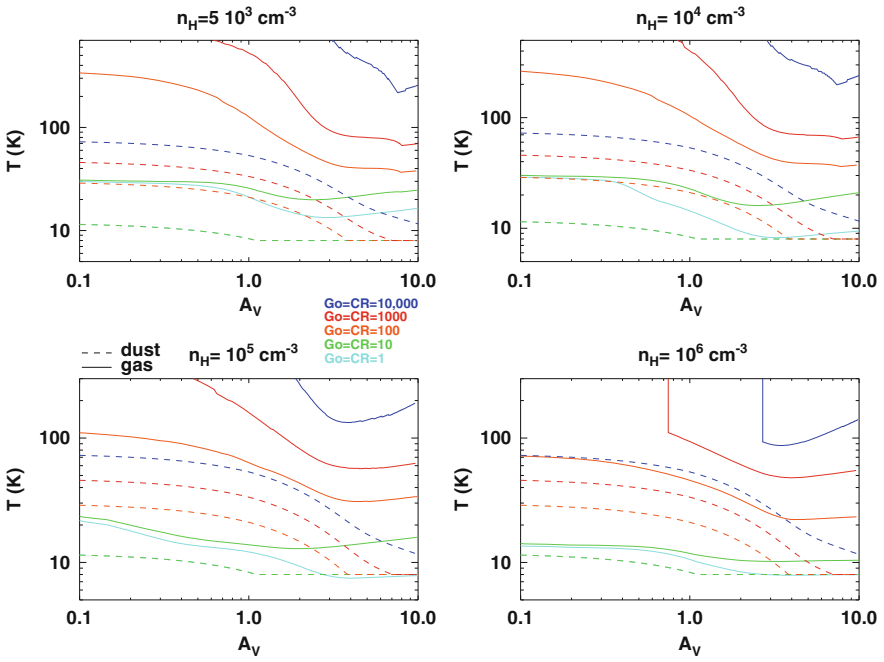

Fig. 4 The gas and dust temperature profiles (*solid* and *dotted lines* of similar color) versus optical extinction inside a molecular cloud. These were computed by solving the coupled thermal and chemical balance equations [19], while also assuming a far-UV radiation field (incident on the $A_v = 0$ surface of plane clouds) that scales in an identical fashion as the average CR energy density pervading the H_2 cloud. Their common scaling runs as (1, 10, 10^2, 10^3, 10^4) × Galactic. Unlike in Fig. 3 the dust is significantly warmed by the stronger (far-UV)/optical radiation fields absorbed by the outer cloud layers and the re-radiated dust IR emission that penetrates deeper into the cloud

This happens even as the dust temperatures deep inside H_2 clouds rise because of an incident radiation that is now set to scale identically to the average CR energy density (both assumed proportional to the average star-formation rate density $\dot{\rho}_{sfr}$). This CR-induced thermal decoupling persists deep inside the cloud (A_v = 5–10) even at the highest gas densities explored here where gas-dust thermal interaction will be the strongest. It must also be noted that for a given average $\dot{\rho}_{sfr}$ in a galaxy, the resulting gas-dust temperature inequality will likely be even larger since cross-shielding between H_2 clouds as well as dusty WNM and CNM HI gas interdispersed between such clouds will reduce the average radiation field incident on them, but not the deeply penetrating CRs. Thus while $U_{CR} \propto \dot{\rho}_{sfr}$, the scaling of average G_o with $\dot{\rho}_{sfr}$ will be weaker than linear (unlike what was assumed in Fig. 4 for simplicity).

From Fig. 4 it can also be discerned that even for strongly boosted far-UV radiation fields, gas temperatures are solely CR-controlled and remain almost invariant with A_v beyond $A_V \sim 5$. This characteristic of CRDRs is of great importance when it comes to the initial conditions of star formation, and the near-invariant mass scale of the stellar IMF found in the Galaxy and ordinary star-forming galaxies.

An order of magnitude estimate of the CR-regulated equilibrium ionization fraction of (far-UV)-shielded gas can also be found without resorting to solving the full chemistry network involved. Following an analytical approach [20] yields

$$x(e) = 2 \times 10^{-7} r_{gd}^{-1} \left(\frac{n_{ch}}{2n(H_2)} \right)^{1/2} \left[\left(1 + \frac{n_{ch}}{8n(H_2)} \right)^{1/2} + \left(\frac{n_{ch}}{8n(H_2)} \right)^{1/2} \right] \quad (6)$$

where $n_{ch} \sim 500 \left(r_{gd}^2 \, \zeta_{-17} \right) \, cm^{-3}$ is a characteristic density encapsulating the effects of cosmic ray ionization and ambient metallicity on the ionization balance (r_{gd} is the normalized gas/dust ratio $r_{gd} = [(G/D)/100]$ with G/D(gas-to-dust mass) = 100 for Solar metallicities. The main assumptions underlying the validity of Eq. 6 are three, namely: (a) all the gas is H_2 and all the carbon is locked in CO (so C^+ does not dominate the ionization), (b) all negative charge is carried by the free electrons and molecular ions are destroyed mostly by recombination with these free electrons, and (c) the metal abundance is small with respect to the heavy molecule abundance.

For the Galaxy ($\zeta_{CR,Gal} = 5 \times 10^{-17} \, s^{-1}$) it is $n_{ch} = 2.5 \times 10^3 \, cm^{-3}$, and for a typical dense core of $n(H_2) = 10^5 \, cm^{-3}$ it would be $x(e)_{Gal} \sim 2.4 \times 10^{-8}$. A boost of ζ_{CR} by a factor of 10 yields $x(e) = 8.4 \times 10^{-8}$, retaining the low ionization fraction necessary for an ambipolar-diffusion regulated star-formation to proceed in such cores [20].

3 CRDRs and the Star formation Initial Conditions in Galaxies

CRDRs are the ISM regions where the initial conditions of star-formation are set. Thus their thermal and/or ionization state is expected to play a critical role on the emergence of the stellar IMF and its mass scale. This remains the case for both main star formation scenaria proposed, namely: (a) star formation driven by gravitational collapse of high overdensity peaks in supersonically turbulent H_2 clouds, and (b) regulated by ambipolar-diffusion (AD) in dense cores whose low x(e) allows the magnetic field lines to slip away making them supercritical (i.e. $M_{core}/M_\Phi > 1$ where $M_\Phi = 0.12\Phi/G^{1/2}$, and Φ is the magnetic field flux threading the cores, [21]) and able to collapse towards star formation. The only difference will be which CRDR gas property: the Jeans mass or x(e), is important in determining the stellar IMF.

It is worth emphasizing that star formation initial conditions set in CRDRs naturally explain the first mystery regarding the stellar IMF, namely its near-universality in ordinary ISM environments. Indeed the large range of thermal, turbulent, and ionization states present for the H_2 gas phase in the Milky Way, makes the emergence of a near-universal stellar IMF an unlikely outcome even for the Galaxy if such states were all used as star formation initial conditions. The gas in

CRDRs on the other hand, lying beyond the reach of varying far-UV radiation fields and turbulence-induced shock heating, with a near-isothermal state at $T_{kin} \sim T_{dust}$, near-thermal motions, and the lowest possible x(e) values, is a natural choice of well-protected initial conditions of star formation that can then lead to a near-invariant stellar IMF mass scale. Similar arguments have been made in the past [22], but only recently it was demonstrated just how robust the cold thermal state of CRDRs remains irrespective of the average conditions prevailing at the outer boundaries of the MCs that contain them [23]. Finally, as long as the average CR energy density pervading CRDRs remains within a factor of ∼10 of its Galactic value, neither the temperature nor the ionization fraction within CRDRs changes substantially. This state of affairs is however dramatically altered in the compact, merger-induced starbursts found in ULIRGs.

4 CRDRs in Compact Starbursts: New Initial Conditions for Star Formation

Some of the most spectacular star formation events in the local and the distant Universe are found in strong galaxy mergers. In such systems tidal torques funnel the bulk of the molecular gas of their gas-rich disk progenitors into regions not much larger than the Galactic Center [24]. There they settle into small ($2r \leq (100–300)\,pc$) and very turbulent H_2 gas disks, fueling extreme star-forming events [24, 25]. The H_2 gas in ULIRGs, with one-dimensional Mach numbers of $M_{ULIRGs} \sim (5–30) \times M_{spirals}$, is expected to have larger mass fractions at densities of $>10^4\,cm^{-3}$ [8], and this is indeed observed [5, 6].

However most of the large dense H_2 masses found in ULIRGs cannot reside in PDRs, a result of the high (turbulent) pressures ($P_e/k_B \sim 10^7\,K\,cm^{-3}$) and high gas densities in these galaxies. Indeed, from Eq. 3 (and a Solar metallicity) such high gas pressures yield $\langle A_v \rangle \sim 100$, while for the high *average* gas densities of $\geq 10^4\,cm^{-3}$ typical for ULIRGs [26], it is $A_v^{(tr)} \leq 2$ (Eq. 1) even for far-UV radiation fields as strong as $G_\circ = 10^4$. Thus any warm gas mass fraction residing in PDRs will be $\leq 15\,\%$ (Eq. 2). In summary, while much larger dense gas mass fractions are expected and indeed observed in ULIRGs than in isolated star-forming gas-rich spirals, *most of their dense gas mass will not reside in PDRs*. Nevertheless recent observational results indicate large amounts of warm *and* dense gas in some ULIRGs, with average gas temperatures much larger than those deduced for the concomitant dust [27, 28]. Since a massive warm and dense H_2 phase cannot be in PDRs, far-UV/optical photons are inadequate energy suppliers of its observed state in ULIRGs. Only high CR energy densities (and/or strong turbulent heating) is capable of volumetrically heating the H_2 gas (unlike far-UV photons in PDRs) while also maintaining a significant $T_{kin} > T_{dust}$ inequality.

CR energy densities of $U_{CR} \sim [(few) \times 10^2–10^4] \times U_{CR,Gal}$ are expected in the compact starbursts found in ULIRGs [29] and, as indicated by Fig. 4, such high U_{CR} can easily maintain high gas temperatures while the concomitant dust remains

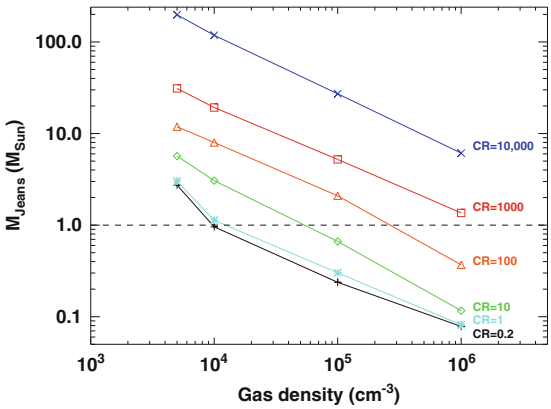

Fig. 5 The Jeans mass estimated from Eq. 7 and the gas temperatures inside CRDRs, which were determined by solving the fully coupled thermal and chemical balance equations. The temperatures shown are averages of the $A_v = 5$–10 part of the H_2 clouds where CR become dominant regulators of the gas thermal and chemical states (Fig. 4)

much cooler. Such conditions have been inferred in the past for the Galactic Center [30] as well as for the center of NGC 253 [31, 32]. However in the case of ULIRGs these conditions prevail over galaxy-size H_2 gas reservoirs that are ∼2–3 orders of magnitude more massive. Thus temperatures of $T_{kin} \sim (50–100)\,K$ are the new *minimum* values possible for gas in ULIRGs, and represent dramatically different initial conditions for star formation in their ISM environments.

The thermal state of dense gas in CRDRs is thus no longer a near-invariant but strongly altered by the high CR energy backgrounds expected in ULIRGs. In the so-called gravoturbulent H_2 cloud fragmentation scenario [33] this large temperature boost across a wide density range (Fig. 3) is expected to surpress low mass star formation. This is because the Jeans mass of the CR-heated gas in CRDRs,

$$M^{(c)}_{Jeans} = \left(\frac{k_B T_k}{G\mu m_{H_2}}\right)^{3/2} \rho_c^{-1/2} = 0.9 \left(\frac{T_k}{10K}\right)^{3/2} \left[\frac{n_c(H_2)}{10^4 cm^{-3}}\right]^{-1/2} M_\odot,$$

changes from $M^{(c)}_{Jeans} \sim 0.3\,M_\odot$ for $n_c(H_2) = 10^5\,cm^{-3}$, and $T_k = 10\,K$ (typical for the Galaxy) to $M^{(c)}_{Jeans}, \sim (3–10)\,M_\odot$ for the same density and $T_k = (50–110)\,K$ expected to be the new minimum in the extreme CRDRs of ULIRGs. It is worth pointing out that an $M^{(c)}_{Jeans} \sim 0.3\,M_\odot$ nicely matches the characteristics mass of the stellar IMF (the so-called IMF 'knee'). Its observed near invariance under a wide range of ISM conditions (e.g. radiation fields) has been demonstrated theoretically [23], leaving CR energy densities *as the sole star-formation feedback mechanism that can decisively alter the initial conditions of star formation in galaxies.* This mechanism, driven by the massive stars (whose strong winds and explosive deaths provide the CR acceleration), will operate unhindered in the dusty ISM environments of extreme merger/starbursts (unlike photons), and it can reach where supersonic turbulence cannot, the small, dense and (far-UV)-shielded cores deep inside H_2 clouds.

In Fig. 5 the Jeans masses are shown for a density range encompassing that of typical star-forming H_2 clouds, demonstrating that for $U_{CR}/U_{CR,Gal} \geq 10^3$, M_{jeans}

increases by a factor of ∼10 across the entire density range. This will invariably lead to higher characteristic mass $M_{ch}^{(*)}$ for newly formed stars, and thus a top-heavy stellar IMF [22, 23]. For an $M_{ch}^{(*)} \sim M_{Jeans}(n_c)$ at the typical density of Galactic CRDR dense gas cores ($n_c \sim$ (few) $\times 10^5\,cm^{-3}$) Fig. 5 also shows that variations of $U_{CR}/U_{CR,Gal} \sim 0.2$–10 would leave $M_{ch}^{(*)} \sim (0.3–0.5)\,M_\odot$ and still compatible with a standard stellar IMF. This is important since a larger sensitivity of $M_{ch}^{(*)}$ on U_{CR} would have been incompatible with its observed near-invariance in ordinary star-forming environments (where variations of the star-formation rate density $\dot{\rho}_{sfr}$, and thus of U_{CR}, by factors of ∼5–10 are not extraordinary).

It must be noted that the choice of the particular (n, T_k) phase whose M_{Jeans} sets $M_{ch}^{(*)}$ is not without ambiguities even if some concensus has been established on the decisive role of $M_{Jeans}(\mathbf{r}, t)$ in driving the outcome of the gravoturbulent process at each spatial and temporal point $(\mathbf{r}, t)$. Arguments have been made both for $M_{ch}^{(*)} \propto \langle M_{Jeans} \rangle$ at the *onset* of a gravoturbulently driven MC fragmentation process [33], and for $M_{ch}^{(*)} \sim M_{Jeans}(n_c, T_k)$ at some characteristic gas density n_c. For gravoturbulent-regulated star-formation n_c is the density where efficient gas-dust thermal coupling of (far-UV)/optically-shielded gas lowers its temperature to the minimum value possible, i.e. that of $\sim T_{dust}$, rendering such gas regions nearly isothermal. For the Galaxy this occurs at $n_c \sim 10^5\,cm^{-3}$, which is also similar to the density of regions where the transition from supersonically turbulent to near thermal gas motions occurs [10, 22].

For CRDRs with high average U_{CR} like those expected in compact starbursts, Fig. 4 makes obvious that gas-dust coupling is no longer adequate to lower T_{kin} to that of the concomitant dust for densities as high as $10^6\,cm^{-3}$. Thus a characteristic gas density can no longer be defined by the onset of thermal equilibrium between gas and dust in CRDRs, at least within the range of densities where appreciable amounts of mass can be found in ordinary MCs. This leaves the choice of $M_{ch}^{(*)} = M_{Jeans}(n_c, T_k)$ open, and thus it is worth examining the possible direction its value would take in extreme CRDRs. In the CR-innudated H_2 clouds inside compact starbursts n_c can now be set only as the typical density of regions where supersonic turbulence has fully dissipated and near-thermal motions dominate. The average density of such transition regions can be determined from two well-known scaling relations found for H_2 clouds: $\sigma_V(r) = \sigma_\circ (r/pc)^h$ (linewidth-size) and $\langle n \rangle = n_\circ (r/pc)^{-1}$ (density-size) after setting $\sigma_V(min) = (3k_B T_k/\mu m_{H_2})^{1/2}$ as the minimum linewidth possible, and solving for the corresponding mean density,

$$\langle n_c \rangle = n_\circ \left(\frac{\mu m_{H_2} \sigma_\circ^2}{3 k_B T_k} \right)^{1/2h} \sim 11 n_\circ \left(\frac{\sigma_\circ}{km\,s^{-1}} \right)^2 \left(\frac{T_k}{10K} \right)^{-1}. \quad (7)$$

For h = 1/2 (expected for pressurized H_2 virialized clouds [34]), $\sigma_\circ = 1.2\,km\,s^{-1}$ and $n_\circ =$ (few) $\times 10^3\,cm^{-3}$ (from observations), it is $\langle n_c \rangle \sim$ (few) $\times 10^4\,cm^{-3}$. For the CR-boosted $T_{kin}(min)$ of extreme CRDRs $T_k(min) \sim (50–100)\,K$: $\langle n_c \rangle \sim$ few $\times 10^3\,cm^{-3}$. Thus the (turbulent gas) → (thermal core) transition in extreme

CRDRs will occur at lower densities *as well as* higher (CR-boosted) T_{kin} values than in ordinary Galactic ones. This will then shift a $M_{ch}^{(*)} \sim M_{Jeans}(n_c, T_k)$ both vertically (higher T_{kin}), as well as to the left (lower $n(H_2)$) of Fig. 5, yielding even higher $M_{ch}^{(*)}$ values than those resulting from only a vertical shift of M_{Jeans} because of CR-boosted gas temperatures. Thus irrespective of the H_2 cloud fragmentation details, and as long as the Jeans mass plays a decisive role in it, *a much larger characteristic mass* $M_{ch}^{(*)}$ *is expected for stars forming in the CRDRs of extreme starbursts.*

4.1 Ambipolar-Diffusion Regulated Star Formation

The CR-induced boost of the ionization fraction x(e) inside the CRDRs of extreme starbursts dramatically alters the star-formation initial conditions relevant for the ambipolar-diffusion (AD) regulated star formation scenario. Indeed, the much larger ionization fractions that can now be achieved deep inside H_2 clouds can in principle: (a) keep the magnetic field lines strongly "threaded" into molecular gas at much higher densities, and (b) as a result render much of its mass incapable of star-formation, at least in the simple (AD)-regulated star formation scenario. This stems from the now much longer ambipolar diffusion timescales: $\tau_{AD} \sim 1.6 \times 10^{14}$x(e) years needed for a CR-ionized core with density $n(H_2)$ to lose magnetic flux and collapse [20]. Indeed, after inserting x(e) (from Eq. 6) it is:

$$\tau_{AD} = 3.2 \times 10^7 r_{gd} \left(\frac{n_{ch}}{2n(H_2)}\right)^{1/2} \left[\left(1 + \frac{n_{ch}}{8n(H_2)}\right)^{1/2} + \left(\frac{n_{ch}}{8n(H_2)}\right)^{1/2}\right] \text{years}. \tag{8}$$

In Fig. 6 τ_{AD} is shown as a function of the CR ionization rate ζ_{CR} (assumed $\propto U_{CR}$) for three typical densities of cloud cores inside CRDRs. It is obvious that the much higher ζ_{CR} values expected in the CRDRs of (U)LIRGs will make the corresponding τ_{AD} timescales much longer than those expected in the Galaxy. Moreover τ_{AD} in (U)LIRGs will be longer than their so-called gas consumption timescales $\tau_{cons} = M(H_2)/SFR$, which are observationally determined using $M(H_2)$ (usually obtained via CO $J = 1 - 0$) and the star formation rate (SFR) (usually obtained from L_{IR}).

For any theory of star formation τ_{cons} represents a natural *maximum* for any theoretically deduced characteristic star-formation timescale $\tau_{*,ch}$ since star-formation feedback (via SNR-induced shocks, O, B star far-UV radiation) will only lengthen any such $\tau_{*,ch}$ by destroying the H_2 clouds fueling star formation (which then have to reform to be SF-capable again). From Fig. 6 it is obvious that for (U)LIRGs it will always be $\tau_{AD} > \tau_{cons}$, thus rendering AD-regulated star formation as unrealistic. For the average ISM conditions in such vigorously star-forming galaxies a process such as reconnection diffusion [35] can still provide magnetic field diffusion fast enough as to keep $\tau_{*,ch} < \tau_{cons}$ [36].

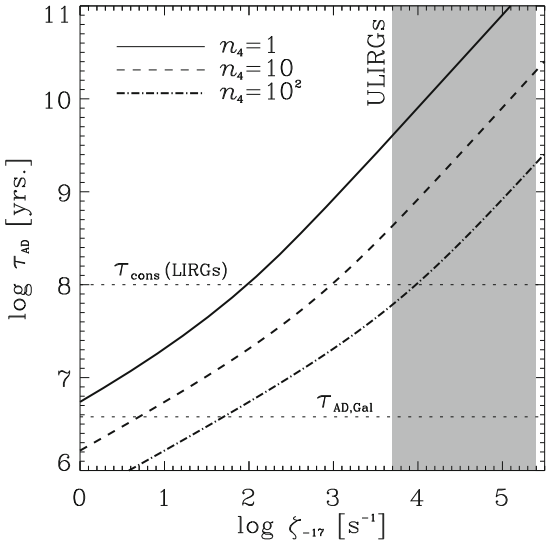

Fig. 6 The ambipolar diffusion (AD) timescale as a function of the CR ionization rate $\zeta_{-17} = \zeta_{CR}/(10^{-17}s^{-1})$ (assumed $\propto U_{CR}$), for $n = [10^4, 10^5, 10^6]\,cm^{-3}$ ($n_4 = n(H_2)/(10^4\,cm^{-3})$). For comparison the AD timescale for ISM conditions typical in the Galaxy is also shown as a *horizontal line* at the *bottom*. The H_2 gas consumption timescale $\tau_{cons} \sim M(H_2)/SFR$ for a typical (U)LIRG is also marked by the *higher horizontal line*. The *shaded area* marks the region where such galaxies are expected to be in terms of the ζ_{CR} in their CRDRs, where clearly $\tau_{AD} > \tau_{cons}$

In summary, in the AD-diffusion regulated star-formation scenario, as in the gravoturbulent one, *the large CR energy densities in the CRDRs of compact starbursts will dramatically alter the initial conditions for star formation.* The effects on the emergent stellar IMF are however less clear to discern than for gravoturbulently-regulated star formation, especially if fast reconnection diffusion plays a role in removing magnetic field support from dense H_2 gas with orders of magnitude larger ionization fractions than in ordinary star-forming galaxies.

4.2 CR-Induced Effects on the Equation of State of the H_2 Gas

Another effect of the large CR energy densities in the CRDRs of compact starbursts is *the erasing of the so-called inflection point of the effective equation of state (EOS) of the H_2 gas.* The latter, parametrized as a polytrope $P = K\rho^{\gamma}$, is used in many numerical simulations of self-gravitating turbulent gas. These found its polytropic index γ, and more specifically the so-called EOS inflection point (i.e. the characteristic density n_c where $\gamma < 1$ for $n < n_c$ flips to $\gamma \geq 1$ for $n \geq n_c$), playing a crucial role in determining the functional shape and mass scale of the resulting mass spectrum of the collapsed dense gas cores (and thus the stellar IMF) [37, 38]. For ordinary ISM conditions this inflection point occurs within CRDRs at

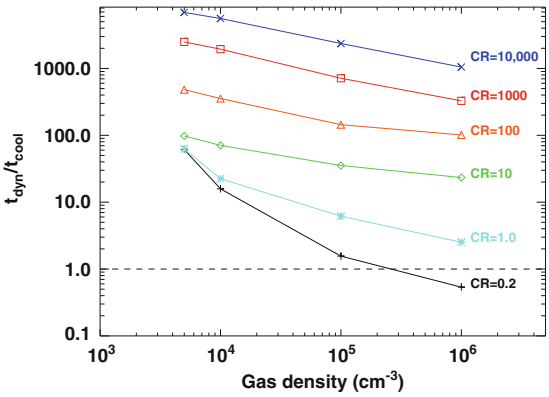

Fig. 7 The ratio of dynamical/cooling timescales for H_2 gas in CRDRs, for CR energy densities expected in star-formation-quiescent up to starburst galaxies (scaled to the average Galactic value)

$n_c \sim 10^5\,cm^{-3}$ [22, 38] because of the onset of strong thermal gas-dust coupling in the (far-UV)/optically-shielded gas regions, which makes them nearly isothermal and sets a characteristic IMF mass scale of $M_*^{(ch)} \sim M_{jeans}(n_c)$.

In the CRDRs of compact starbursts the H_2 gas and the dust remain thermally decoupled with $T_{kin} > T_{dust}$ for densities as high as $n \sim 10^6\,cm^{-3}$ (Fig. 4), erasing the EOS inflection point. This maintains strong H_2 gas cooling ($\propto n^2$) at much higher densities ($\geq n_c$), rendering local cooling timescales (τ_{cool}) much shorter than the dynamical ones (τ_{dyn}). This allows thermodynamics to always stay a step ahead of self-gravity in decreasing the local Jeans mass (as densities climb and temperatures drop) faster than the gravitationally-driven evolution of the cloud fragments it to mass fragments of $\sim M_{jeans}(\mathbf{r}, t)$. A comparison of these two important timescales as a function of the CR energy densities is shown in Fig. 7, from where it becomes obvious that an inflection point where $\tau_{dyn}/\tau_{cool} \sim 1$ is not even approached once $U_{CR}/U_{CR,Gal} \geq 10$, even for densities as high as $\sim 10^6\,cm^{-3}$. Clearly *any future numerical simulations of molecular clouds in extreme CRDRs must take this into account, or abandon the use of an EOS for the gas altogether.*

5 A CR-Controlled Stellar IMF: Some Consequences

A top-heavy stellar IMF can be the result a higher characteristic mass $M_{ch}^{(*)}$ for the young stars (the so-called IMF 'knee', which is $\sim$(0.3–0.5) $M_\odot$ for the Galaxy) or a shallower power law than its Salpeter value of $\alpha \sim 2.35$ (for an IMF functional form of $dN(M_*)/dM_* \propto M_*^{-\alpha}$ and stellar masses between 1 and 100 $M_\odot$). In a gravoturbulent scenario the exact shape and mass scale of the emergent stellar IMF under the very different star formation initial conditions in extreme CRDRs of ULIRGs can only be determined with new H_2 cloud simulations that make use of these new conditions. In the past simulations using so-called starburst ISM conditions have been done, recovering large $M_{ch}^{(*)}$ in such environments [39].

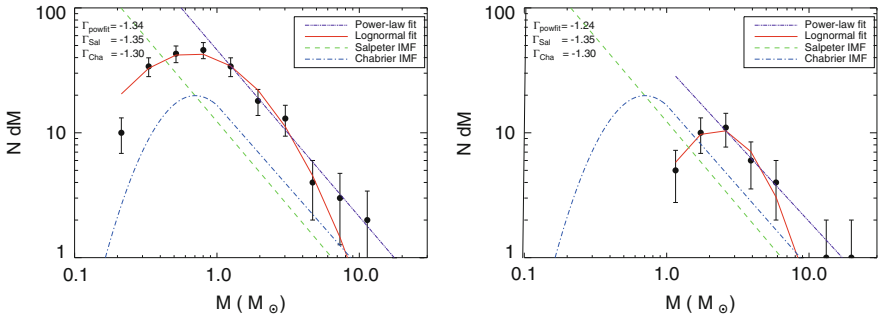

Fig. 8 The stellar initial mass functions (IMFs) from numerical simulations of turbulent H_2 clouds, for $U_{CR} = U_{CR,Gal}$ (*left*), $100 \times U_{CR,Gal}$ (*right*) [40]. For comparison purposes, a Salpeter-type (*green dashed*) and Chabrier-type (*blue dot-dashed*) IMF fits to the emergent mass spectrum are also shown along with a linear fit and a lognormal fit (*purple* and *red lines*). The power-law slopes above the turn-over mass $M_{ch}^{(*)}$ are given in the *upper left corner*

Unfortunately such simulations used conditions typical of PDRs rather than CRDRs, an approach that would have then produced a varying IMF even in the Milky Way given the large range of gas properties in its PDRs. It was only recently that the effects of large CR energy densities on H_2 cloud fragmentation and the stellar IMF have been explored [40] and found $M_{ch}^{(*)}$ boosted to $\sim$(2–3) $M_\odot$ (Fig. 8).

The dependance of the thermal and ionization state of the gas in CRDRs on the average U_{CR} permeating the ISM of a galaxy naturally links the SF initial conditions and the resulting IMF to the average SFR density $\dot{\rho}_{sfr}$, provided $U_{CR} \propto \dot{\rho}_{sfr}$ (with the details of CR transport/escape mechanisms in quiescent SF disks and starbursts setting the proportionality factor). CR-controlled star formation initial conditions then naturally yield a bimodal stellar IMF in galaxies, with high values of $\dot{\rho}_{sfr}$ determining the branching point, namely:

(merger-driven star formation) $\rightarrow$ (high $\dot{\rho}_{sfr}$) $\rightarrow$ (high U_{CR}) $\rightarrow$ (top heavy IMF),
(isolated gas-rich disk star formation) $\rightarrow$ (low $\dot{\rho}_{sfr}$) $\rightarrow$ (low U_{CR}) $\rightarrow$ (Galactic IMF).

Such an IMF bimodality, with a top-heavy IMF in merger/starbursts versus a regular IMF in isolated gas-rich disks has been postulated for some time in hierarchical galaxy formation models seeking to explain their relative populations across cosmic time in ΛCDM cosmologies [41]. *CR-controlled star formation initial conditions in galaxies can now set this on a firm physical basis for the first time.* It must be noted that a top-heavy IMF in high-$\dot{\rho}_{sfr}$ systems such as compact starbursts in mergers, will also have serious implications on the SFRs deduced from their observed IR luminosities as such IMFs will have several times higher energy outputs per stellar mass than the ordinary one. Then the tremendeous SFRs deduced for merger/starbursts, especially at high redshifts ($\sim 10^3\ M_\odot\ year^{-1}$), may actually be $\sim$(3–5) times lower.

Finally an $\dot{\rho}_{sfr}$-dependant IMF as the outcome of CR-controlled star formation initial conditions in galaxies will also naturally yield integrated galactic IMFs

(IGIMFs) that depend on the star formation history (SFH) of galaxies. This is simply because $\dot{\rho}_{sfr}$ can change significantly during the evolutionary track of a galaxy, especially during its early gas-rich epoch, even in the absence of mergers. Such a SFH-dependance of the IGIMFs has been considered as the cause behind the well-known mass-metallicity relation of galaxies [42].

6 Future Outlook

The unique signatures imparted on the thermal and chemical state of the H_2 gas in extreme CRDRs have now been studied extensively [29, 43, 44], and most of them will be easily accessible in the new era of ALMA whose commissioning is now ongoing at Llano de Chajnantor on the Atacama Desert Plateau. Numerical studies of H_2 clouds without the use of an EOS for the gas, that take also into account the strongly anchored magnetic fields on dense gas with large ionization fractions are now becoming possible. High-energy γ-ray observations now started directly probing the average CR energy densities of other galaxies [45, 46]. Thus we are looking at a decade where the properties of CRDRs, their effect on the stellar IMF of galaxies, and their role in galaxy formation can be decisively explored with powerful theoretical and observational tools. Finally these explorations will critically benefit from studies of the stellar IMF and its dependence on ambient conditions in galaxies that are now converging to much sharper picture [47].

Acknowledgements Padelis P. Papadopoulos would like to warmly thank the organizers of the conference in Sant Cugat for an exciting week where much was learned and new vistas for both high energy and the so-called low energy Astrophysics came into view. This project was also funded by the John Latsis Public Benefit Foundation. The sole responsibility for the content lies with its authors.

Appendix

The CR heating rate used in this work is given by

$$\Gamma_{\rm CR} = 1.95 \times 10^{-28} {\rm n_H} \left(\frac{\zeta_{\rm CR}}{1.3 \times 10^{-17}\,{\rm s^{-1}}} \right) {\rm ergs\ \ cm^{-3}\,s^{-1}} \tag{9}$$

where $\zeta_{\rm CR} \propto {\rm U_{CR}}$ being the Cosmic Ray ionization rate (in $\rm s^{-1}$), with an adopted Galactic value of $\zeta_{\rm CR,Gal} = \times 10^{-17} {\rm s^{-1}}$ (corresponding to ${\rm U_{CR}} = {\rm U_{CR,Gal}}$), and ${\rm n_H} = 2{\rm n(H_2)}$ for fully molecular gas. For an optically thin OI line (and thus maximal cooling) $\Lambda_{\rm OI63} = \chi_{\rm O} {\rm n_H C_{lu} E_{ul}}$, which becomes

$$\Lambda_{\rm OI63} = 3.14 \times 10^{-14} \chi_{\rm O} {\rm n_H C_{ul}} \left(\frac{\rm g_u}{\rm g_l} \right) \exp\left(-227.72/{\rm T_{kin}}\right) {\rm ergs} \tag{10}$$

where $g_u = 3$ and $g_l = 5$, and $\chi_O = [O/H]$ being the abundance of oxygen not locked onto CO ($\chi_O \sim 4.89 \times 10^{-4}$). The collisional de-excitation coefficient is given by [16]

$$C_{ul} = n_H 10^{0.32 \log T_{kin} - 10.52} = 3.02 \times 10^{-11} n_H T_{kin}^{0.32} \, cm^{-3} \, s^{-1}, \tag{11}$$

Thus finally Eq. 11 becomes,

$$\Lambda_{OI63} = 2.78 \times 10^{-28} n_H^2 T_{kin}^{0.32} \exp(-227.72/T_{kin}) \, ergs \;\; cm^{-3} \, s^{-1}. \tag{12}$$

For densities of $n_H < 10^5 \, cm^{-3}$ and strong CR fluxes, a small fraction of carbon remains in the form of C^+, acting as a coolant with

$$\Lambda_{C+} = 1.975 \times 10^{-23} n_H^2 \chi_{C+} \exp(-92.2/T_{kin}) \, ergs \;\; cm^{-3} \, s^{-1}, \tag{13}$$

computed in a similar fashion as the OI(63 μm) line cooling, and for a fully transparent medium. Gas-grain accommodation cooling the gas depending on their temperature difference can be expressed as [17]:

$$\Lambda_{g-d} = 4.0 \times 10^{-12} \alpha n_H n_d \sigma_g \sqrt{T_{kin}} \, (T_{kin} - T_{dust}) \tag{14}$$

where n_g is the number density of dust grains and σ_g is the grain cross-section (cm^{-2}). If the gas-to-dust ratio is 100, the dust mass density is $\rho_d = 3.5 \, g \, cm^{-3}$, and a dust radius of $a = 0.1 \, \mu m$ then

$$n_d = 2.2 \times 10^{-2} \times \mu_H n_H / (4/3 \pi \rho_d a^3) = 7.88 \times 10^{-12} n_H. \tag{15}$$

The gas-grain accommodation factor α is given by [18]:

$$\alpha = 0.35 \exp\left(-\sqrt{\frac{T_{dust} + T_{kin}}{500}} \right), \tag{16}$$

which we set to the maximum value $\alpha = 0.35$ (i.e. maximum gas cooling from gas-dust interaction). Thus the cooling term due to the gas-dust interaction (Eq. 15) becomes

$$\Lambda_{g-d} = 3.47 \times 10^{-33} n_H^2 \sqrt{T_{kin}} \, (T_{kin} - T_{dust}) \, ergs \;\; cm^{-3} \, s^{-1}. \tag{17}$$

Finally detailed PDR code models allow us to parametrize the cooling due to the CO rotational transitions as

$$\Lambda_{CO} = 4.4 \times 10^{-24} \left(\frac{n_H}{10^4 \, cm^{-3}} \right)^{3/2} \left(\frac{T_{kin}}{10 \, K} \right)^2 \left(\frac{\chi_{CO}}{\chi_{[C]}} \right) \, ergs \;\; cm^{-3} \, s^{-1}, \tag{18}$$

where we set $\chi_{CO}/\chi_{[C]} = (0.97, 0.98, 0.99, 1.0)$ for densities of 5×10^3, 10^4, 10^5, $10^6\,cm^{-3}$ respectively (with $\chi_{CO}/\chi_{[C]} = 1$ corresponding to all carbon locked onto CO).

References

1. Hollenbach D. J., & Tielens A. G. G. M. Reviews of Modern Physics Vol. 17, No1, January 1999
2. Wolfire M. G., McKee C. F., Hollenbach D., Tielens, A. G. G. M. 2003, Astrophysical Journal, 587, 278
3. Tielens A. G. G. M. & Hollenbach D. J. 1985a Astrophysical Journal, 291, 722
4. Tielens A. G. G. M. & Hollenbach D. J. 1985b Astrophysical Journal, 291, 747
5. Gao Yu, & Solomon P. M. 2004, Astrophysical Journal Supplement, 152, 63
6. Solomon P. M., Downes D., & Radford S. J. E 1992, Astrophysical Journal Letters 387, 55
7. Padoan P., & Nordlund A. 2002, Astrophysical Journal, 576, 870
8. Pan L., & Padoan P. 2009, Astrophysical Journal, 692, 594
9. Pelupessy F. I., Papadopoulos P. P., & van der Werf P. P. 2006, Astrophsyical Journal, 645, 1024
10. Bergin, E. A. & Tafalla, M. 2007, Annual Reviews of Astronomy & Astrophysics, 45, 339
11. Pineda, J. L. & Bensch, F. 2007, Astronomy & Astrophysics, 470, 615
12. Pineda, J. E., Goodman, A. A, Arce, H. E. et al. 2010, Astrophysical Journal Letters, 712, L116
13. Goldsmith, P. F., & Langer, W. D. 1978, Astrophysical Journal, 222, 881
14. Ossenkopf, V. 2002, Astronomy & Astrophysics, 391. 295
15. Goldsmith, P. F. 2001, Astrophysical Journal, 557, 736
16. Liseau, R. et al. 1999, Astronomy & Astrophysics 1999, 344, 342
17. Burke, J. R., & Hollenbach, D. J. 1983, Astrophysical Journal, 265, 223
18. Groenewegen, M. A. T. 1994, Astronomy & Astrophysics, 290, 531
19. Papadopoulos, P. P., Thi. W.-F., Miniati, F., & Viti S. 2011, Monthly Notices of the Royal Astronomical Society, 414, 1705
20. McKee, C. F. 1989, Astrophysical Journal, 1989, Astrophysical Journal, 345, 342
21. Mouschovias, T. Ch., & Spitzer L. Jr, 1976, Astrophsyical Journal, 210, 326
22. Larson, R. B. 2005, Monthly Notices of the Royal Astronomical Society, 359, 211
23. Elmegreen B. G., Klessen R. S., & Wilson C. D. 2008, Astrophysical Journal, 681, 365
24. Sakamoto, K. et al. 2008, Astrophysical Journal, 684, 957
25. Downes D., & Solomon P. M. 1998, Astrophysical Journal, 507, 615
26. Greve T. R., Papadopoulos P. P., Gao Y., & Radford S. J. E. 2009, Astrophysical Journal, 692, 1432
27. Papadopoulos P. P., van der Werf P. P., Xilouris E. M., Isaak K. G., Gao Y., & Muehle S. 2012, Monthly Notices of the Royal Astronomical Society, (in press, arXiv:1109.4176)
28. Rangwala N. et al. 2012, Astrophysical Journal, 743, 94
29. Papadopoulos P. P., 2010, Astrophysical Journal, 720, 226
30. Yusef-Zadeh F., Wardle M., Roy S. 2007, Astrophysical Journal Letters 665, L123
31. Bradford C. M., Nikola T., & Stacey G. J. 2003, Astrophysical Journal 586, 891
32. Hailey-Dunsheath S., Nikola T., Stacey G. J. et al. 2008, Astrophysical Journal Letters, 689, L109
33. Klessen R. S. 2004, Astrophysics and Space Science, 292, Issue 1, p. 215
34. Elmegreen B. G. 1989, Astrophysical Journal, 338, 178
35. Lazarian A. 2011, Nonlin. Processes Geophys. (in press, arXiv:1111.0694)
36. Lazarian A. Esquivel A., & Crutcher R. 2012, Astrophysical Journal (arXiv:1206.4698)
37. Li Y., Klessen R. S., & McLow M.-M. 2003, Astrophysical Journal, 592, 975

38. Jappsen A.-K., Klessen R. S., Larson R. B., Li Y., McLow M.-M. 2005, Astronomy & Astrophysics, 435 611
39. Klessen R. S., Spaans M. & Jappsen A.-K. 2007, Montly Notices of the Royal Astronomical Society, 374, L29
40. Hocuk S., & Spaans M. 2011, Astronomy & Astrophysics, 536, 41
41. Baugh C. M. et al. 2005, Monthly Notices of the Royal Astronomical Society, 356, 1191
42. Koeppen J., Weidner C., & Kroupa P. 2007, Monthly Notices of the Royal Astronomical Society, 375, 673
43. Meijerink R., Spaans M., Loenen A. F., & van der Werf P. P. 2011, Astronomy & Astrophysics, 525, 119
44. Bayet E., Williams D. A., Hartquist T. W., & Viti S. 2011, Monthly Notices of the Royal Astronomical Society, 414, 1583
45. Acciari V. A. et al. 2009, Nature, 462, 770
46. Acero F. et al. 2009, Science, 326, 1080
47. Kroupa P. et al. 2012, in *Stellar Systems and Galactic Structure*, Vol. V. (in press, arXiv:1112.3340)

Cosmic-Ray Propagation in Molecular Clouds

Marco Padovani and Daniele Galli

Abstract Cosmic rays constitute the main ionising and heating agent in dense, starless, molecular cloud cores. We reexamine the physical quantities necessary to determine the cosmic-ray ionisation rate (especially the cosmic-ray spectrum at $E < 1\,\mathrm{GeV}$ and the ionisation cross sections), and calculate the ionisation rate as a function of the column density of molecular hydrogen. Available data support the existence of a low-energy component (below $\sim$100 MeV) of cosmic-ray electrons or protons responsible for the ionisation of diffuse and dense clouds. We also compute the attenuation of the cosmic-ray flux rate in a cloud core taking into account magnetic focusing and magnetic mirroring, following the propagation of cosmic rays along flux tubes enclosing different amount of mass and mass-to-flux ratios. We find that mirroring always dominates over focusing, implying a reduction of the cosmic-ray ionisation rate by a factor of 3 to 4 depending on the position inside the core and the magnetisation of the core.

1 Introduction

Although the origin of the cosmic radiation and the mechanisms of acceleration are not well established, this corpuscular radiation has a central role in the high-energy processes of our galaxy. For instance, cosmic rays (CRs) approximately constitute one third of the energy density of the interstellar medium and, on a galactic scale, they form a relativistic gas whose pressure is comparable with that of

M. Padovani (✉)
Laboratoire de Radioastronomie Millimétrique, UMR 8112 du CNRS, École Normale Supérieure et Observatoire de Paris, 24 rue Lhomond, 75231 Paris cedex 05, France
e-mail: padovani@lra.ens.fr

D. Galli
INAF – Osservatorio Astrofisico di Arcetri, Largo E. Fermi 5, 50125 Firenze, Italy
e-mail: galli@arcetri.astro.it

D.F. Torres and O. Reimer (eds.), *Cosmic Rays in Star-Forming Environments*, Astrophysics and Space Science Proceedings 34, DOI 10.1007/978-3-642-35410-6_6,

the galactic magnetic field. CR electrons are a source of bremßtrahlung, synchrotron emission and inverse Compton scattering, revealing the large-scale configuration and the intensity of the galactic magnetic field. CR nuclei are the unique sample of interstellar matter which is measurable out of the solar system, including all the elements, from hydrogen to actinides. The abundances of elements and isotopes of CR nuclei bring information not only with respect to their origin, but, through the radioactive species, show the required time for their acceleration and the history of their propagation in the interstellar magnetic field.

Low-energy CRs are the dominant source of ionisation for molecular cloud cores and they represent an important source of heating because the energy of primary and secondary electrons produced by the ionisation process is in large part converted into heat by inelastic collisions with ISM atoms and molecules. In addition, the observed diffuse gamma-ray emission from the galactic plane is believed to be the result of the decay of neutral pions produced during inelastic collisions of high-energy (>1 GeV) CRs with the ISM [18].

In general, the CR ionisation rate in the interstellar gas depends on the relative amount of H, H_2, and He [13]. The first theoretical determination of the CR ionisation rate was performed for clouds made only by atomic hydrogen by Hayakawa et al. [27]. They assumed a proton specific intensity (hereafter, for simplicity, *spectrum*) proportional to the proton energy E_p for $0.1\,\mathrm{MeV} < E_\mathrm{p} < 10\,\mathrm{MeV}$ and computed $\zeta^\mathrm{H} \approx 4 \times 10^{-16}\,\mathrm{s}^{-1}$. Spitzer and Tomasko [52] determined a value (actually a lower limit) of $\zeta^\mathrm{H} \gtrsim 6.8\times10^{-18}\,\mathrm{s}^{-1}$ for H I clouds, assuming a CR proton spectrum declining below $E_\mathrm{p} \approx 50\,\mathrm{MeV}$, and an upper limit of $\zeta^\mathrm{H} \lesssim 1.2\times10^{-15}\,\mathrm{s}^{-1}$, taking into account an additional flux of $\sim$2 MeV protons produced by supernova explosions. To obtain the CR ionisation rate of molecular hydrogen, ζ^{H_2}, a useful approximation is $1.5\zeta^{\mathrm{H}_2} \approx 2.3\zeta^\mathrm{H}$ [23], giving $\zeta^{\mathrm{H}_2} \approx 10^{-17}\,\mathrm{s}^{-1}$, in agreement with the lower limit on ζ^H of Spitzer and Tomasko [52]. This value of ζ^{H_2} is often referred to the "standard" CR ionisation rate in molecular clouds.

A major problem in determining the CR ionisation rate is that low-energy CRs are prevented from entering the heliosphere by the solar wind and the interplanetary magnetic field. In fact, the outer part of the solar atmosphere, namely the solar corona, is in continuous expansion, producing a plasma flux towards the interplanetary medium: the solar wind. The solar magnetic field is frozen with the plasma and radially dragged outwards, and this field strongly affects the extrasolar CR particles. In particular, less energetic particles are swept away from the solar system and for this reason, the extrasolar CR density we observe from the Earth is lower than the density of the local interstellar medium and the observed spectra are *modulated*, that is altered with respect to their original shapes. In practice, this means that Earth-based measurements of CR fluxes give no information on the interstellar spectrum of protons and heavy nuclei for energies below $\sim$1 GeV/nucleon. Solar modulation also suppresses the flux of low-energy CR electrons, that already shows considerable fluctuations at energies of 10–100 GeV [4]. Since the cross section for ionisation of molecular hydrogen by collisions with protons and electrons has a maximum at $\sim$10 keV and $\sim$50 eV, respectively (see Sect. 2), it is clear that a knowledge of CR spectrum at low energies is an important limiting factor for

any accurate calculation of the ionisation rate in the ISM. A direct measurement of the shape of the CR spectrum at these energies will be possible only when spacecrafts such as *Pioneer* and *Voyager* are well beyond the heliopause, the outermost boundary for solar modulation effects, believed to lie at 100–150 AU from the Sun.

Over the past three decades, several values of ζ^{H} ranging from a few $10^{-17}\,\mathrm{s}^{-1}$ to a few $10^{-16}\,\mathrm{s}^{-1}$ have been obtained in diffuse interstellar clouds from measurements of the abundances of various chemical species, in particular OH [1, 2, 25] and HD [17, 59]. However, the derived rates are sensitive to several model assumptions, e.g. the value of specific chemical reaction rates and the intensity of the UV background. In dense molecular clouds, determining the CR ionisation rate is made even more uncertain by the sensitivity of molecular abundances to the level of depletion of the various species and the role of small and large grains in the chemical network. The values of $\zeta^{\mathrm{H_2}}$ derived by Caselli et al. [5] through $\mathrm{DCO^+}$ and $\mathrm{HCO^+}$ abundance ratios span a range of about two orders of magnitudes from $\sim 10^{-17}\,\mathrm{s}^{-1}$ to $\sim 10^{-15}\,\mathrm{s}^{-1}$, with a scatter that may in part reflect intrinsic variations of the CR flux from core to core. Finally, values of $\zeta^{\mathrm{H_2}}$ of a few times $10^{-17}\,\mathrm{s}^{-1}$ have been obtained in clouds of higher column density ($N(\mathrm{H_2}) \sim 10^{23}$–$10^{24}\,\mathrm{cm}^{-2}$) like the envelopes surrounding massive protostellar sources [16, 57].

The discovery of significant abundances of $\mathrm{H_3^+}$ in diffuse clouds [37], confirmed by follow-up detections [20, 32, 38], has led to values of $\zeta^{\mathrm{H_2}}$ larger by about one order of magnitude than both the "standard" rate and previous estimates based on the abundance of OH and HD in dense clouds. Given the relative simplicity of the chemistry of $\mathrm{H_3^+}$, it is now believed that diffuse clouds are characterised by CR ionisation rates $\zeta^{\mathrm{H_2}} \approx 2 \times 10^{-16}\,\mathrm{s}^{-1}$ or larger. This value has been confirmed by Neufeld et al. [40] who found $\zeta^{\mathrm{H_2}} = 0.6-2.4\times 10^{-16}\,\mathrm{s}^{-1}$ probing the CR ionisation rate in clouds of low $\mathrm{H_2}$ fraction from observations of $\mathrm{OH^+}$ and $\mathrm{H_2O^+}$.

2 CR Reactions with $\mathrm{H_2}$ and He

CR particles (electrons, protons, and heavy nuclei) impact with atoms and molecules of the ISM producing ions and electrons. Table 1 lists the main CR ionisation reactions involving $\mathrm{H_2}$ and He.

In molecular clouds, a large majority of CR–$\mathrm{H_2}$ impacts leads to the formation of $\mathrm{H_2^+}$ via the *ionisation* reaction

$$k_{\mathrm{CR}} + \mathrm{H_2} \rightarrow k_{\mathrm{CR}} + \mathrm{H_2^+} + e, \tag{1}$$

where k_{CR} is a cosmic-ray particle of species k and energy E_k, with cross section $\sigma_k^{\mathrm{ion.}}$. Here we consider CR electrons ($k = e$), protons ($k = p$), and heavy nuclei of charge Ze ($k = Z$, with $Z \geq 2$). Low-energy CR protons, in addition, may react with ambient $\mathrm{H_2}$ by *electron capture* reactions,

Table 1 CR reactions in molecular clouds

$p_{\rm CR} + {\rm H_2} \rightarrow p_{\rm CR} + {\rm H_2^+} + e$	$\sigma_p^{\rm ion.}$
$p_{\rm CR} + {\rm H_2} \rightarrow {\rm H} + {\rm H_2^+}$	$\sigma_p^{\rm e.\ c.}$
$p_{\rm CR} + {\rm H_2} \rightarrow p_{\rm CR} + {\rm H} + {\rm H^+} + e$	$\sigma_p^{\rm diss.\ ion.}$
$p_{\rm CR} + {\rm H_2} \rightarrow p_{\rm CR} + 2{\rm H^+} + 2e$	$\sigma_p^{\rm doub.\ ion.}$
$e_{\rm CR} + {\rm H_2} \rightarrow e_{\rm CR} + {\rm H_2^+} + e$	$\sigma_e^{\rm ion.}$
$e_{\rm CR} + {\rm H_2} \rightarrow e_{\rm CR} + {\rm H} + {\rm H^+} + e$	$\sigma_e^{\rm diss.\ ion.}$
$e_{\rm CR} + {\rm H_2} \rightarrow e_{\rm CR} + 2{\rm H^+} + 2e$	$\sigma_e^{\rm doub.\ ion.}$
$p_{\rm CR} + {\rm He} \rightarrow p_{\rm CR} + {\rm He^+} + e$	$\sigma_p^{\rm ion.}$
$p_{\rm CR} + {\rm He} \rightarrow {\rm H} + {\rm He^+}$	$\sigma_p^{\rm e.\ c.}$
$e_{\rm CR} + {\rm He} \rightarrow e_{\rm CR} + {\rm He^+} + e$	$\sigma_e^{\rm ion.}$

$$p_{\rm CR} + {\rm H_2} \rightarrow {\rm H} + {\rm H_2^+}, \tag{2}$$

with cross section $\sigma_p^{\rm e.\ c.}$. For an isotropic distribution of CR particles, the production rate of $\rm H_2^+$ (per $\rm H_2$ molecule) is then

$$\zeta^{\rm H_2} = 4\pi \sum_k \int_{I({\rm H_2})}^{E_{\rm max}} j_k(E_k)[1 + \phi_k(E_k)]\sigma_k^{\rm ion.}(E_k)\,{\rm d}E_k$$
$$+4\pi \int_0^{E_{\rm max}} j_p(E)\sigma_p^{\rm e.\ c.}(E_p)\,{\rm d}E_p, \tag{3}$$

where $j_k(E_k)$ is the number of CR particles of species k per unit area, time, solid angle and per energy interval (hereafter, we will refer to $j_k(E_k)$ simply as the spectrum of particle k), $I(\rm H_2) = 15.603\,eV$ is the ionisation potential of $\rm H_2$, and $E_{\rm max} = 10\,{\rm GeV}$ is the maximum energy considered.

The quantity $\phi_k(E_k)$ is a correction factor accounting for the ionisation of $\rm H_2$ by secondary electrons. In fact, secondary electrons are sufficiently energetic to induce further ionisations of $\rm H_2$ molecules, and their relatively short range justifies a local treatment of their ionising effects. The number of secondary ionisation produced per primary ionisation of $\rm H_2$ by a particle k is determined by

$$\phi_k(E_k) \equiv \frac{1}{\sigma_k^{\rm ion.}(E_k)} \int_{I({\rm H_2})}^{E'_{\rm max}} P(E_k, E'_e)\sigma_e^{\rm ion.}(E'_e)\,{\rm d}E'_e, \tag{4}$$

where $P(E_k, E'_e)$ is the probability that a secondary electron of energy E'_e is ejected in a primary ionisation by a particle of energy E_k. The spectrum of secondary electrons declines rapidly with E'_e from the maximum at $E'_e = 0$ [8, 21]. The function $\phi_e(E_e)$ giving the number of secondary ionisations after a single ionisation by an electron of energy E_e has been computed by Glassgold and Langer [21] for energies of the incident electron up to 10 keV. Above a few 100 eV, ϕ_e increases logarithmically with E_e. For secondary electrons produced by impact of particles k, we adopt the scaling $\phi_k(E_k) \approx \phi_e(E_e = m_e E_k/m_k)$ valid in the Bethe-Born

approximation. Calculations by Cravens and Dalgarno [12] confirm this scaling for protons in the range 1–100 MeV.

Additional ionisation reactions that produce electrons are the *dissociative ionisation* of H_2 and the *double ionisation* of H_2. These two processes contribute to the total CR production rate of electrons per H_2 molecule,

$$\begin{aligned}\zeta^e = 4\pi \sum_k \int_{I(\mathrm{H_2})}^{E_{\max}} j_k(E_k)[1+\phi_k(E_k)]\sigma_k^{\mathrm{ion.}}(E_k)\,\mathrm{d}E_k \\ +4\pi \sum_k \int_{E^{\mathrm{diss.\ ion.}}}^{E_{\max}} j_k(E)[1+\phi_k(E_k)]\sigma_k^{\mathrm{diss.\ ion.}}(E_k)\,\mathrm{d}E_k \\ +8\pi \sum_k \int_{E^{\mathrm{doub.\ ion.}}}^{E_{\max}} j_k(E_k)[1+\phi_k(E_k)]\sigma_k^{\mathrm{doub.\ ion.}}(E_k)\,\mathrm{d}E_k\ , \end{aligned} \tag{5}$$

where $E^{\mathrm{diss.\ ion.}} = 18.1\,\mathrm{eV}$ and $E^{\mathrm{doub.\ ion.}} = 51\,\mathrm{eV}$. The cross sections of these processes are smaller by at least one order of magnitude than the corresponding ionisation cross section, and the relative contribution of dissociative ionisation and double ionisation to the total electron production rate is expected to be small [42].

Similarly, the CR production rate of He^+ (per He atom) is

$$\begin{aligned}\zeta^{\mathrm{He}} = 4\pi \sum_k \int_{I(\mathrm{He})}^{E_{\max}} j_k(E_k)[1+\phi_k(E_k)]\sigma_k^{\mathrm{ion.}}(E_k)\,\mathrm{d}E_k \\ +4\pi \int_0^{E_{\max}} j_p(E)\sigma_p^{\mathrm{e.\ c.}}(E_p)\,\mathrm{d}E_p\ , \end{aligned} \tag{6}$$

where $I(\mathrm{He}) = 24.587\,\mathrm{eV}$ is the ionisation potential of He, $\sigma_k^{\mathrm{ion.}}$ is the ionisation cross sections of He for impact by particles k, and $\sigma_p^{\mathrm{e.\ c.}}$ is the electron capture cross section.

Figure 1 shows that ionisation cross sections peak at about 10 and 0.1 keV for protons and electrons colliding with H_2, respectively, and at about 30 and 0.1 keV for protons and electrons colliding with He, respectively. This means that, to compute reliable CR ionisation rates, the CR spectrum needs to be extrapolated down to $\sim$ keV energies where the ionisation cross sections have their maximum.

3 Local Interstellar Spectra

It is generally assumed that the local interstellar (LIS) spectrum, namely the CR spectrum in the solar neighbourhood, characterises the energy distribution of CR everywhere in the galactic disc, as long as the ISM properties do not depart from the uniform conditions assumed in the propagation model.

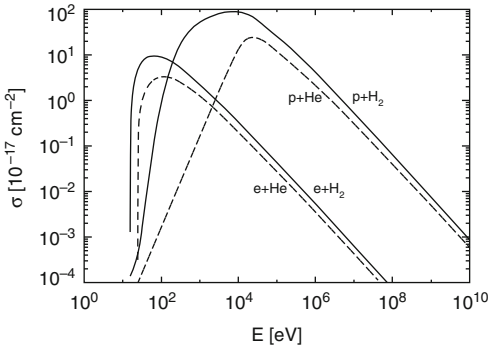

Fig. 1 Ionisation cross sections for proton and electron impact on H_2 (*solid lines*) and on He (*dashed lines*)

It is very uncertain, however, whether the LIS spectrum is really representative of the whole galactic disc, especially because the Solar System resides in a low-density ($n \approx 10^{-3}\,\mathrm{cm}^{-3}$) region. We assume a uniform distribution (in space and time) of CR sources characterised by a given "source spectrum". CR propagation models can generate steady-state LIS spectra resulting from a number of processes affecting the CR transport in the galactic disc (see Sect. 4), which, in turn, can be used as input for solar modulation calculations to reproduce the CR spectrum and the relative abundances of CR particles measured at the Earth. The LIS spectra obtained in this way are clearly not uniquely defined, and a considerable range of LIS spectral shapes can be shown to be consistent with the measured CR flux with appropriate choices of parameters of the transport model (see e.g. Mewaldt et al. [36], especially their Fig. 1).

We consider for both protons and electrons a "minimum" and "maximum" LIS spectrum compatible with the available observational constraints, and we compute the resulting ionisation rates with the objective of comparing them with existing data for diffuse and dense clouds. We extrapolate the LIS spectra for the CR proton and electron components to lower energies with power-laws to reach the peak of the ionisation cross section. The two determinations of the proton LIS spectrum (left panel of Fig. 2) that we considered are given by Webber [61] ("minimum", hereafter W98) and Moskalenko et al. [39] ("maximum", hereafter M02). W98 estimated the LIS proton spectrum down to ∼10 MeV, starting from an injection spectrum parameterised as a power-law in rigidity, propagated according to the model of Webber [60] and accounting for solar modulation following Potgieter [46]. M02 reproduces the observed spectrum of protons, antiprotons, alpha nuclei, the B/C ratio, and the diffuse γ-ray background. The two electron LIS spectra adopted (right panel of Fig. 2) both derive by Strong et al. [53]: the former ("minimum", hereafter C00) is mostly derived from radio observations. It reproduces the spectrum of electrons, protons, and alpha nuclei above ∼10 GeV, but fails to account for the γ-ray background for photons with energies below ∼30 GeV and above ∼1 GeV. The latter ("maximum", hereafter E00) reproduces the γ observations at photon energies below ∼30 GeV by a combination of bremßtrahlung and inverse Compton emission, assuming a steepening of the electron spectrum below ∼200 MeV to compensate for

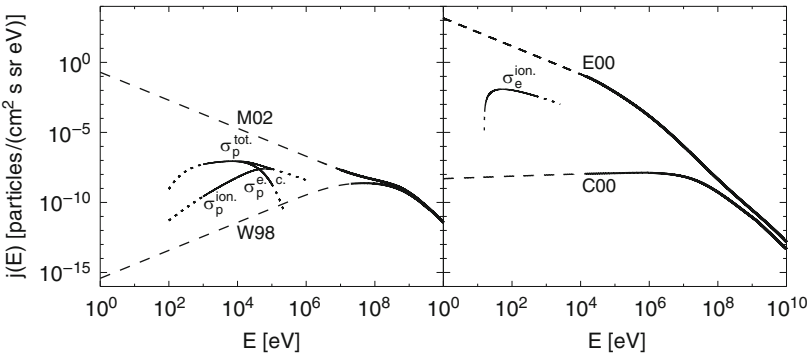

Fig. 2 *Left panel:* proton LIS spectra of M02 and W98 (*solid curves*). The *dashed curves* represent our power-law extrapolations of the spectra. For comparison, the cross sections for ionisation of H_2 by proton impact, electron capture, and total ionisation are also shown. *Right panel:* electron LIS spectra of E00 and C00 (*solid curves*). The *dashed curves* represent our extrapolations of the spectra. For comparison, the cross section for ionisation of H_2 by electron impact is also shown. All the cross sections are in arbitrary units

Table 2 CR ionisation rates $\zeta_k^{H_2}$ and ζ_k^{He}, electron production rate ζ_k^e, energy densities $\mathcal{E}_k$, and exponent of the power-law extrapolation of the spectrum at low energies for CR protons[a] (p) and electrons (e)

k	ref.	$\zeta_k^{H_2}$ [s^{-1}]	ζ_k^{He} [s^{-1}]	ζ_k^e [s^{-1}]	$\mathcal{E}_k$ [eV cm^{-3}]	β
p	W98	2.08×10^{-17}	1.33×10^{-17}	2.50×10^{-17}	0.953	0.95
p	M02	1.48×10^{-14}	2.16×10^{-15}	3.49×10^{-15}	1.23	−1
e	C00	1.62×10^{-19}	1.05×10^{-19}	1.94×10^{-19}	0.0167	0.08
e	E00	6.53×10^{-12}	2.46×10^{-12}	7.45×10^{-12}	0.571	−1

[a] The proton ionisation rates include the contribution of heavy nuclei

the growth of ionisation losses. Our extrapolations at low energies are power-law in energy, $j(E) \propto E^\beta$. The values of β are shown in Table 2.

The values of $\zeta_k^{H_2}$, ζ_k^e and ζ_k^{He} per H_2 molecule and He atom, respectively, obtained from numerical integration of Eqs. (3), (5) and (6), with the $j_k(E_k)$ taken to be the adopted LIS spectra, are listed in Table 2. We have assumed a mixture of H_2 and He where the ratio of He to H nuclei is 0.1 and all hydrogen is in molecular form, such that the gas consists of about 83 % H_2 and 17 % He. We checked that our extrapolations at low energies were compatible with energy constraints. To this purpose, we computed the energy density of each CR component, defined as

$$\mathcal{E}_k = 4\pi \int_0^\infty \frac{j_k(E_k) E_k}{v_k(E_k)} \, \mathrm{d}E_k \tag{7}$$

where $j_k(E_k)$ is the particle's LIS spectrum and $v_k(E_k) = c(E_k^2/m_k^2c^4 + 2E_k/m_kc^2)^{1/2}/(1 + E_k/m_kc^2)$ is the velocity of particle k with kinetic energy E_k. We compute the total energy density of CR as $\sum_k \mathcal{E}_k \approx (1 + \xi)\mathcal{E}_p$, where $\xi = 0.41$ is the correction factor for the abundance of He and heavy nuclei. We found that the total CR energy density varies from a minimum of $0.97\,\mathrm{eV\,cm^{-3}}$ (W98 plus C00) and a maximum of $1.80\,\mathrm{eV\,cm^{-3}}$ (M02 plus E00), corresponding to an equipartition magnetic field of 6.2 and 8.5 μG, respectively. These equipartition values are compatible with the "standard" value of the magnetic field of 6.0 ± 1.8 μG in the cold neutral medium of the Galaxy [28].

4 Energy Losses of CRs in the ISM

The penetration of primary CR and secondary particles in interstellar clouds was studied by Takayanagi [54] and in more detail by Umebayashi and Nakano [56]. The quantity which describes the "degradation spectrum" of the CR component k resulting from the energy loss of the incident particles is called *energy loss function*, defined by

$$L_k(E_k) = -\frac{1}{n(\mathrm{H_2})}\left(\frac{\mathrm{d}E_k}{\mathrm{d}\ell}\right), \tag{8}$$

where $n(\mathrm{H_2})$ is the density of the medium in which the particles propagate and ℓ is the path length. Since we consider only energy losses in collisions with $\mathrm{H_2}$, our results are applicable only to clouds in which hydrogen is mostly in molecular form. Some energy loss processes are common to CR protons and electrons, like Coulomb interactions, inelastic collisions and ionisation; others are peculiar to protons (elastic collisions, pion production and spallation), others to electrons (bremßtrahlung, synchrotron emission and inverse Compton scattering). These processes are briefly reviewed in the following subsections.

4.1 Energy Loss of Protons Colliding with H_2

To determine the energy loss function of protons we have used the results collected by Phelps [44] for energies in the range from 10^{-1} to 10^4 eV. For higher energies, between 1 keV and 10 GeV, we have used data from the NIST Database[1] for atomic hydrogen multiplied by a factor of 2 to obtain the corresponding values for collisions with molecular hydrogen. NIST data do not include pion production at energies higher than about 0.5 GeV, that we computed following Schlickeiser [49].

[1] http://physics.nist.gov/PhysRefData/Star/Text

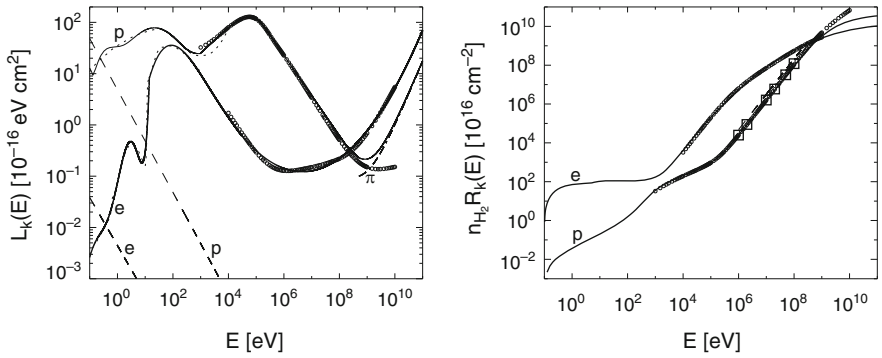

Fig. 3 *Left panel:* energy loss functions $L_e(E_e)$ and $L_p(E_p)$ for electrons and protons, respectively, colliding with H_2 (*solid curves*), compared with NIST data (*circles*); *dashed curves* show Coulomb losses for a fractional electron abundance $n_e/n(H_2) = 10^{-7}$; *dash-dotted curve* labelled with π represents the energy loss by pion production computed following Schlickeiser [49]; *dotted curves* show the results by Phelps [44] and Dalgarno et al. [13] for p–H_2 and e–H_2, respectively. *Right panel:* range $R_e(E_e)$ and $R_p(E_p)$ for electrons and protons colliding with H_2 (*solid curves*), respectively, compared with NIST data (*circles*) and the results of Cravens and Dalgarno [12], *squares*; the *dashed curve* shows the fit by Takayanagi [54]

The resulting energy loss function is shown in the left panel of Fig. 3. The broad peak in $L_p(E_p)$ at $E_p \approx 10\,\text{eV}$ is due to elastic collisions and to the excitation of rotational and vibrational levels, the peak at $E_p \approx 100\,\text{keV}$ to ionisation, and the rapid increase at energies above $\sim$1 GeV is due to pion production. For the low ionisation levels characteristic of molecular clouds, the energy loss for Coulomb interactions of CRs with ambient electrons can be neglected at energies above $\sim$1 eV (dashed line in the left panel of Fig. 3), since $L_p(E_p) \propto n_e E_p^{-0.5}$, where n_e is the electron density of the traversed matter [49].

4.2 Energy Loss of Electrons Colliding with H_2

To determine the electron energy loss function we have adopted the results of Dalgarno et al. [13] for $10^{-2}\,\text{eV} \le E_e \le 1\,\text{keV}$ and those of Cravens, Victor, and Dalgarno [11] for $1\,\text{eV} \le E_e \le 10\,\text{keV}$. For higher energies, $10\,\text{keV} \le E_e \le 10\,\text{GeV}$, we have adopted the loss function for electron-H collisions from the NIST Database multiplied by a factor of 2. The resulting energy loss function is also shown in the left panel of Fig. 3. The first peak in $L_e(E_e)$ is due to the excitation of vibrational levels, the second to the excitation of the electronic levels and ionisation, while at higher energies the energy loss function is dominated by bremßtrahlung. As in the case of CR protons, we can neglect the contribution of Coulomb interactions for electrons at energies above $\sim$1 eV, since $L_e(E_e) \propto n_e^{0.97} E_p^{-0.44}$ [51].

5 Propagation of a Cosmic Ray in a Molecular Cloud

We assume a plane-parallel geometry and we follow the propagation of CR particles inside a molecular cloud with the so-called *continuous-slowing-down approximation* (hereafter CSDA) which is also referred as the *continuous energy loss regime* or *thick target approximation* when the propagation is dominated by these losses [47, 48]. It is useful to introduce the column density of molecular hydrogen $N(\mathrm{H}_2)$,

$$N(\mathrm{H}_2) = \int n(\mathrm{H}_2)\,\mathrm{d}\ell\,, \tag{9}$$

and to rewrite the energy loss function (Eq. 8) as

$$L_k(E_k) = -\frac{\mathrm{d}E_k}{\mathrm{d}N(\mathrm{H}_2)}\,. \tag{10}$$

Let us then define $j_k(E_k, N)$ as the spectrum of CR particles of species k at depth $N(\mathrm{H}_2)$, with $j_k(E_k, 0)$ representing the LIS spectrum incident on the cloud's surface, defined by a column density $N(\mathrm{H}_2) = 0$. To compute $j_k(E_k, N)$ we must consider all the processes that degrade the energy of the incident CR particles. Assuming that the direction of propagation does not change significantly inside the cloud, it follows from Eq. (10) that particles of initial energy $E_{k,0}$ reach energy $E_k < E_{k,0}$ as a consequence of energy losses after propagating across a column density $N(\mathrm{H}_2)$ given by

$$N(\mathrm{H}_2) = -\int_{E_{k,0}}^{E_k} \frac{\mathrm{d}E_k}{L_k(E_k)} = n(\mathrm{H}_2)[R_k(E_{k,0}) - R_k(E_k)]\,, \tag{11}$$

where $R_k(E_k)$ is the *range*, defined as

$$R_k(E_k) = \int_{E_k}^{0} \mathrm{d}\ell = \int_0^{E_k} \frac{\mathrm{d}E_k}{-(\mathrm{d}E_k/\mathrm{d}\ell)} = \frac{1}{n(\mathrm{H}_2)} \int_0^{E_k} \frac{\mathrm{d}E_k}{L_k(E_k)}\,. \tag{12}$$

In the right panel of Fig. 3 we show the quantity $n(\mathrm{H}_2)R_k(E_k)$ for $k = p, e$, obtained with a numerical integration of Eq. (12), compared with data from the NIST Database at energies from 1 keV to 10 GeV for protons and from 10 keV to 1 GeV for electrons. For protons we also show the fit adopted by Takayanagi [54] in a limited range of energies and the results of Cravens and Dalgarno [12]. As one can see, except for energies higher than ∼100 MeV, where the NIST data do not include energy losses by pion production, there is a complete agreement between our results and the NIST data.

Conservation of the number of CR particles of each species implies

$$j_k(E_k, N)\,\mathrm{d}E_k = j(E_{k,0}, 0)\,\mathrm{d}E_{k,0}\,, \tag{13}$$

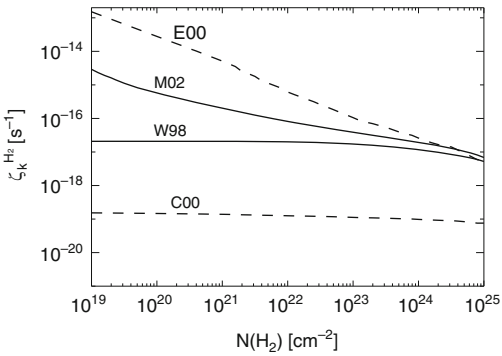

Fig. 4 CR ionisation rate $\zeta_k^{H_2}$ as a function of the column density $N(H_2)$. *Solid curves*, contribution of CR protons (spectra W98 and M02); *dashed curves*, contribution of CR electrons (spectra C00 and E00)

where, for a given value of $N(H_2)$, the infinitesimal variation $dE_{k,0}$ of the particle's initial energy corresponds to an infinitesimal variation dE_k of its energy at a depth $N(H_2)$ given by

$$\frac{dE_k}{L_k(E_k)} = \frac{dE_{k,0}}{L_k(E_{k,0})} \tag{14}$$

We ignore here that electron capture reactions of CR protons with H_2 and He do not conserve the number of CR protons and also the $\alpha + \alpha$ fusion reactions that produce ^{6}Li and ^{7}Li because of the small cross sections [35]. Thus, the relation between the incident spectrum $j_k(E_{k,0}, 0)$ and the spectrum $j_k(E_k, N)$ at depth $N(H_2)$ in the CSDA is

$$j_k(E_k, N) = j_k(E_{k,0}, 0)\frac{dE_k}{dE_{k,0}} = j_k(E_{k,0}, 0)\frac{L_k(E_{k,0})}{L_k(E_k)} \,. \tag{15}$$

We are now able to calculate the CR ionisation rate inside a molecular cloud as a function of the column density, with the attenuated spectra given by Eq. (15). We compute the CR ionisation rate for $N(H_2)$ between 10^{19} and 10^{25} cm^{-2}, and we show the results for the four incident LIS spectra in Fig. 4. Since we assume an isotropic CR distribution (see Sect. 2), the ionisation rate calculated for a given $N(H_2)$ corresponds to the ionisation rate at the centre of a spherical cloud with "radius" $N(H_2)$.

As a result of the detailed treatment of CR propagation, the decrease of the ionisation rate with increasing penetration in the cloud at column densities in the range $\sim 10^{20}$–10^{25} cm^{-2} is characterised by a power-law behaviour, rather than exponential attenuation, and can be approximated as

$$\zeta_k^{H_2} \approx \zeta_{0,k}\left[\frac{N(H_2)}{10^{20}\ \mathrm{cm}^{-2}}\right]^{-a} . \tag{16}$$

We have fitted this expression to the numerical results shown in Fig. 4. The coefficients $\zeta_{0,k}$ and a are given in Table 3. The exponential attenuation of the

Table 3 Fitting coefficients for Eq. (16) for CR protons (p, also including heavy nuclei) and electrons (e)

k	Spectrum	$\zeta_{0,k}$ [s^{-1}]	a
p	W98	2.0×10^{-17}	0.021
p	M02	6.8×10^{-16}	0.423
e	C00	1.4×10^{-19}	0.040
e	E00	2.6×10^{-14}	0.805

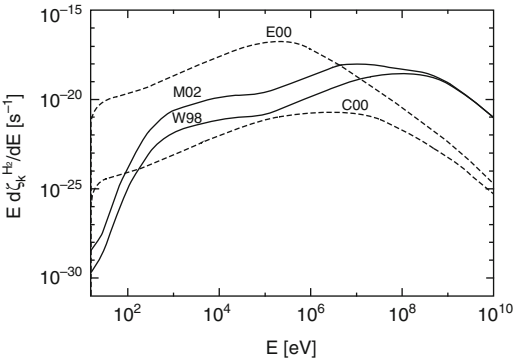

Fig. 5 Differential contribution to the ionisation rate $E\mathrm{d}\zeta_k^{H_2}/\mathrm{d}E$ per logarithmic interval of kinetic energy, for the four spectra considered at a depth $N(H_2) = 10^{22}\,\mathrm{cm}^{-2}$ (*solid curves*, protons; *dashed curves*, electrons)

CR ionisation rate sets in for column densities larger than $\sim 10^{25}\,\mathrm{cm}^{-2}$, where $\zeta_k^{H_2}$ depends essentially on the flux of CR particles in the high-energy tail of the incident spectrum (above $\sim$0.1–1 GeV), and directly measurable on the Earth.

It is important to stress that a large contribution to the ionisation of H_2 comes from low-energy protons and electrons constantly produced (in our steady-state model) by the slowing-down of more energetic particles loosing energy by interaction with the ambient H_2. In Fig. 5 we show the differential contribution of CR protons and electrons to the ionisation rate at a depth of $N(H_2) = 10^{22}\,\mathrm{cm}^{-2}$, corresponding to the typical column density of a dense cloud. For protons and heavy nuclei, the bulk of the ionisation is provided by CR in the range 1 MeV–1 GeV and by a "shoulder" in the range 1–100 keV produced by slowed-down protons while, for electrons, the largest contribution to the ionisation is distributed over energies in the range 10 keV–10 MeV. This low-energy tail is produced during the propagation of CR protons and electrons in the cloud even when the incident spectrum is devoid of low-energy particles. Thus, the ionisation rate at any depth in a cloud cannot be calculated by simply removing from the incident spectrum particles with energies corresponding to ranges below the assumed depth.

6 Comparison with Observations

To obtain the total CR ionisation rate in molecular clouds, we sum the ionisation rates of protons (corrected for heavy nuclei) and electrons. With two possible spectra for each component, we obtain four possible profiles of ζ^{H_2}. These are

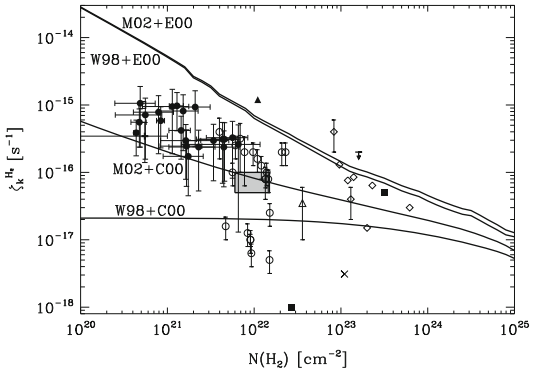

Fig. 6 Total CR ionisation rate ζ^{H_2} as a function of $N(H_2)$ according to our models (*solid curves*). Observational data: *filled circles*, diffuse clouds [32]; *empty square*, diffuse cloud W49N [40]; *empty circles*, dense cores [5]; *empty triangle*, prestellar core B68 [34]; *filled squares*, T Tauri discs TW Hya and DM Tau [6]; *filled triangle*, SNR W51C [7]; *diamonds*, protostellar envelopes [14, 16, 29, 57, 58]; *cross*, massive star-forming region DR21(OH) [29]. The *filled box* indicates the range of column densities and CR ionisation rates compatible with the data analysed by Williams et al. [61]

shown in Fig. 6 as a function of $N(H_2)$, compared with a compilation of empirical determinations of ζ^{H_2} in diffuse and dense environments.

The comparison between model results and observational data shown in Fig. 6 should be taken as indicative and interpreted in a statistical sense, as also suggested by the large spread of values of ζ^{H_2} at each value of $N(H_2)$. First, the *observational* $N(H_2)$ is the entire column density through the cloud, whereas the *model* $N(H_2)$ is the column traversed by CRs incident over the cloud's surface. The exact relation between the quantities depend on factors like the cloud geometry and orientation with respect to the line-of-sight, and the variation of CR ionisation rate with depth within the cloud. In addition, for the cloud cores of Caselli et al. [5] we adopted the H_2 column density estimated by Butner et al. [3] from measurements of $C^{18}O$ multiplied by a factor of 2, to account for depletion of CO onto grains [5]. Second, many of the sight-lines where ζ^{H_2} has been determined in diffuse clouds may have multiple cloud components, which would reduce the column density of a single cloud. It is probably safe to conclude that the *observational* column density is an *upper limit* to the column density traversed by CRs incident on each cloud, and therefore the data shown in Fig. 6 should probably be shifted to the left by a factor of 2 or so. At any rate, from the comparison with observational data, shown in Fig. 6, we can draw the following conclusions:

1. Although the gas column density of the object is by no means the only parameter controlling the CR ionisation rate, the data suggest a decreasing trend of ζ^{H_2} with increasing $N(H_2)$, compatible with our models M02+C00, W98+E00, W98+C00. However, the measured values of ζ^{H_2} are very uncertain, especially in dense environments. Part of the large spread in the sample of cloud cores may be due to a poor understanding of the chemistry.

2. The highest values of ζ^{H_2}, measured in diffuse clouds sight lines, could be explained if CR electrons are characterised by a rising spectrum with decreasing energy. The E00 spectrum represents an extreme example of this kind, and it results in values of ζ^{H_2} somewhat in excess of the diffuse clouds observations. The same spectrum accounts simultaneously for the CR ionisation rates measured in most protostellar envelopes of much higher column density. Conversely, a spectrum of protons and heavy nuclei rising with decreasing energy, like the M02 spectrum, can provide alone a reasonable lower limit for the CR ionisation rate measured in diffuse clouds.
3. Without a significant low-energy (below $\sim$100 MeV) component of electrons and/or protons and heavy nuclei, it is impossible to reproduce the large majority of observations. The combination of the C00 spectrum for electrons with the W98 spectrum for protons and heavy nuclei clearly fails over the entire range of column densities.

7 Effects of Magnetic Field on CR Propagation

The high values of ζ^{H_2} in the diffuse interstellar gas can be reconciled with the lower values measured in cloud cores and massive protostellar envelopes by invoking various mechanisms of CR screening in molecular clouds due to either self-generated Alfvén waves in the plasma [26, 41, 50] or to focusing and magnetic mirror effects [9, 10, 43]. Besides, a few molecular cloud cores and one dense envelope (Fig. 6) are characterised by $\zeta^{H_2} \leq 10^{-17}\,\mathrm{s}^{-1}$ and probably can only be explained by invoking the CR suppression mechanisms. Mirroring and focusing are due to the non-uniformity of the large-scale (mean) component of the field, whereas diffusion is associated to magnetic field fluctuations on the scale of the Larmor radius of CR particles. The relative importance of these processes in the ISM depends on a number of variables not always well determined (geometry and strength of the magnetic field, nature and characteristics of turbulence, etc.), and is unclear whether they can significantly reduce (or enhance) the CR ionisation of molecular cloud cores. In addition, the damping of small-scale magnetic fluctuations (e.g. Alfvén waves) that affect the propagation of CRs is strongly dependent on the ionisation fraction of the medium, which, in turn, is mostly determined by the CRs themselves.

CRs perform an helicoidal motion around the magnetic field lines. For a uniform magnetic field $B = 10\,\mu\mathrm{G}$, the Larmor radii, r_L of ionising CRs (CR protons and heavy nuclei with $E \lesssim 1$ GeV/nucleon and CR electrons with $E \lesssim 10$ MeV, see Padovani et al. [42]) are less than $\sim 10^{-7}$ and $\sim 10^{-9}$ pc for protons and electrons, respectively, many orders of magnitude smaller than the typical size of Bok globules, dense cores, and giant molecular clouds [43], see Fig. 7. In the absence of small-scale perturbations in the field, we can therefore assume that low-energy CRs propagate closely following the magnetic field lines.

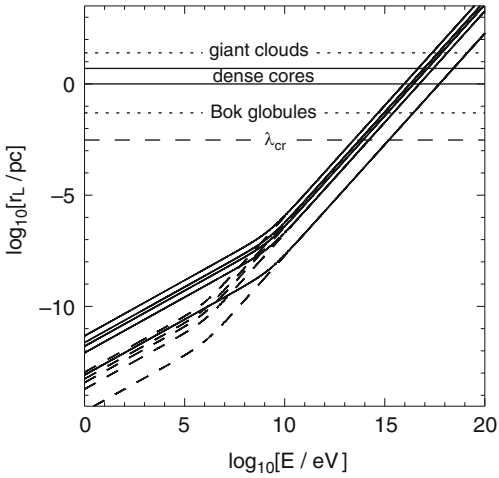

Fig. 7 Larmor radius as a function of the cosmic-ray energy for $\alpha = 1, 10, 20, 30,$ and 90. *Solid* and *dashed lines* represent cosmic-ray protons and electrons, respectively

Perturbations in the forms of magnetohydrodynamic (MHD) waves with wavelength of the order of the Larmor radius of the particle can efficiently scatter CRs. The waves can be part of an MHD turbulent cascade, or can be self-generated by the CRs themselves [30]. However, in a mostly neutral ISM, turbulent MHD cascades are quenched at scales of roughly the collision mean free path of ions with neutrals, if the ion-neutral collision rate exceeds the energy injection rate. Alfvén waves are efficiently damped by collision with neutrals below a critical wavelength $\lambda_{\rm cr}$ [31] and, for typical molecular cloud conditions, $\lambda_{\rm cr} \approx 3\times10^{-3}$ pc [45]. Thus, for typical values of the cloud's parameters, only CR particles with energy larger than a few TeV, and Larmor radii $r_{\rm L} \geq \lambda_{\rm cr}$ find MHD waves to resonate with. These particles however do not contribute significantly to the ionisation of the cloud.

We expect that CRs in the energy range between 100 MeV/nucleon and 1 GeV/nucleon, that provide the bulk of the ionisation in a cloud core, stream freely through the core without self-generating MHD waves. We ignore therefore the presence of self-generated waves in cloud cores in the following, but we believe that this problem deserves further scrutiny.

8 Magnetic Focusing and Mirroring

Theoretical models predict that collapsing cloud cores must overcome the support provided by their magnetic field in order to form stars. In the process, the competition between gravity pulling inward and magnetic pressure pushing outward is expected to produce a warped, *hourglass* pattern of the magnetic field. Recently, this scenario has received support from observations [22, 55] showing a magnetic field geometry consistent with the formation of solar-type stars, in which ordered large-scale magnetic fields control the evolution and collapse of molecular cloud

cores [24]. We therefore adopt the hourglass geometry as the basis of our analysis of CR penetration into a cloud core.

The effects of magnetic mirroring and focusing in a hourglass geometry can be simply described following e.g. Desch et al. [15]. A charged particle travelling in a magnetised medium conserves its kinetic energy γmc^2 and its magnetic moment $\mu = \gamma m v^2 \sin^2\alpha/2B$. It follows that CRs propagating from the intercloud medium (ICM) to the cloud's interior must increase $v_\perp^2$ to conserve μ and decrease $v_\parallel$ to conserve $|\mathbf{v}|^2$. Thus, the pitch angle of the particle must increase from the value $\alpha_{\rm ICM}$ to a value α as

$$\frac{\sin^2\alpha}{\sin^2\alpha_{\rm ICM}} = \frac{B}{B_{\rm ICM}} \equiv \chi\,, \tag{17}$$

where $\chi > 1$. Therefore, a CR starting in the ICM with a pitch angle $\sin\alpha_{\rm ICM} > 1/\chi^{1/2}$ cannot penetrate a region with magnetic field $B > \chi B_{\rm ICM}$, and will be bounced out (*magnetic mirroring*). Conversely, the CR flux $j(E)$ in the cloud is increased by the opening out of the field lines by a factor proportional to the density of magnetic field lines per unit area (*magnetic focusing*),

$$j(E) = \chi j_{\rm ICM}(E)\,. \tag{18}$$

The effects of focusing and mirroring depend only on the magnetic field strength, and are the same for CR protons, electrons, and heavy nuclei.

9 CR Ionisation Rate in Presence of a Magnetic Field

In order to study the effects of the magnetic field on the propagation of CRs in molecular cores, we adopt the models of Li and Shu [33] (see also [19]), for magnetostatic, scale-free, self-gravitating clouds supported by axially-symmetric hourglass-like magnetic fields. For simplicity, we consider models with an isothermal equation of state. These models are characterised by a value of the non-dimensional mass-to-flux ratio λ defined by

$$\lambda = 2\pi G^{1/2}\frac{M(\Phi)}{\Phi}\,, \tag{19}$$

where G is the gravitational constant, Φ the magnetic flux, and $M(\Phi)$ the mass contained in the flux tube Φ. For our reference model we choose $\lambda = 2.66$, assuming a sound speed $c_{\rm s} = 0.2\,{\rm km\,s^{-1}}$ and an intercloud magnetic field $B_{\rm ICM} = 3\,\mu{\rm G}$. We focus on a flux tube enclosing a mass $M(\Phi) = 1\,{\rm M}_\odot$, a typical value for a low-mass core. The following equations are written as a function of the polar angle θ: a CR is outside the core for $\theta = 0$ and reaches the midplane when $\theta = \pi/2$.

Following the assumptions in Sect. 8, CRs starting with pitch angles $\alpha_{\rm ICM}$ smaller than a critical value $\alpha_{\rm cr}$ are able to reach the cloud's midplane. When $\alpha_{\rm ICM} > \alpha_{\rm cr}$ then CRs will be pushed back by magnetic mirroring before reaching the midplane

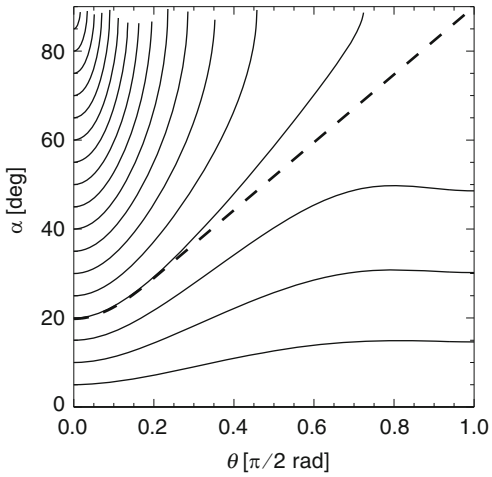

Fig. 8 Variation of the CR pitch angle as a function of the polar angle for values of $\alpha_{\rm ICM}$ between 0° and 90° in steps of 5°. The *dashed line* represents the critical pitch angle $\alpha_{\rm cr} = 20.5°$

at a position $\theta_{\rm max}(\alpha_{\rm ICM}) < \pi/2$. Inverting this relation, one finds the value of the maximum allowed pitch angle $\alpha_{\rm ICM,max}(\theta)$ for a CR to reach a given position θ. Figure 8 shows the variation of the pitch angle computed from Eq. (17) assuming the magnetic field profile of the reference 1 $M_\odot$ flux tube.

The contribution to the CR ionisation rate of H_2 for CRs entering the core is

$$\zeta^{\rm H_2}(\theta) = 2\pi\ \chi(\theta) \int_0^\infty {\rm d}E \int_0^{\alpha_{\rm ICM,max}(\theta)} j\left[E, N(\theta, \alpha_{\rm ICM})\right] \times [1 + \phi(E)]\ \sigma^{\rm ion}(E)\ \sin\alpha_{\rm ICM}\ {\rm d}\alpha_{\rm ICM}\,, \tag{20}$$

where $N(\theta, \alpha_{\rm ICM})$ is the column density of H_2 into the core (with $N = 0$ at $\theta = 0$), $\phi(E)$ is given by Eq. (4), $\sigma^{\rm ion}(E)$ is the ionisation cross section of H_2 (see Sect. 2), and the column density passed through by a CR propagating along a magnetic field line is

$$N(\theta, \alpha_{\rm ICM}) = \frac{1}{\mu\, m_{\rm H}} \int \rho\, \frac{{\rm d}\ell}{\cos\alpha}, \tag{21}$$

where $\mu = 2.8$ is the molecular weight, ${\rm d}\ell = [{\rm d}r^2 + (r{\rm d}\theta)^2]^{1/2}$ is the element of magnetic field line, and the factor $1/\cos\alpha$ accounts for the increase of the actual path length of a CR performing a helicoidal trajectory around a magnetic field with respect to the displacement along the field line. Figure 9 shows the column density passed through by the CR before reaching the mirror point. As a first approximation one can assume that CRs coming from the ICM and travelling towards the cloud's midplane experience a similar increase in column density, independently on the initial pitch angle $\alpha_{\rm ICM}$, the latter mainly determining the value of the column density at which the CRs are pushed out by magnetic mirroring. For this reason, we assume for all CRs the column density profile corresponding to $\alpha_{\rm ICM} = 0$, but truncated at increasingly larger values depending on the initial pitch angle $\alpha_{\rm ICM}$,

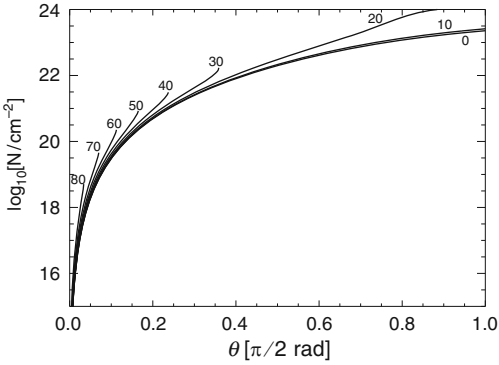

Fig. 9 Column density passed through before reaching the mirror point by CRs propagating along a field line of the reference flux tube enclosing 1 $M_\odot$, as function of the polar angle θ for different values of the initial pitch angle $\alpha_{\rm ICM}$ (labels in degrees)

$$N(\theta, \alpha_{\rm ICM}) \approx N(\theta, 0) \quad \text{if} \quad 0 < \theta < \theta_{\rm max}(\alpha_{\rm ICM})\,. \tag{22}$$

Adopting the CSDA (see Sect. 5), the total CR ionisation rate, see details in Padovani and Galli [43], is then given by two contributions due to CRs entering the core from the upper side (subscript +) and the lower side (subscript −) of the core

$$\zeta^{\rm H_2}(\theta) = \zeta_+^{\rm H_2}(\theta) + \zeta_-^{\rm H_2}(\theta)\,, \tag{23}$$

with

$$\begin{aligned} \zeta_+^{\rm H_2}(\theta) &= \varphi_+(\theta)\, \zeta_0^{\rm H_2}[N_0(\theta)] \\ \zeta_-^{\rm H_2}(\theta) &= \varphi_-(\theta)\, \zeta_0^{\rm H_2}[2N_0(\pi/2) - N_0(\theta)]\,. \end{aligned} \tag{24}$$

$\varphi_+(\theta)$ and $\varphi_-(\theta)$ are factors accounting for magnetic effects

$$\begin{aligned} \varphi_+(\theta) &= \frac{\chi(\theta)}{2}[1 - \cos\alpha_{\rm ICM,max}(\theta)] \\ \varphi_-(\theta) &= \frac{\chi(\theta)}{2}(1 - \cos\alpha_{\rm cr}) \end{aligned} \tag{25}$$

and $\zeta_0^{\rm H_2}[N_0(\theta)]$ is the CR ionisation rate in the non-magnetic case, see Eqs. (3), (6), and (5).

Mirroring and focusing have opposite effects of comparable magnitude on the ionisation rate, both becoming more and more important approaching the core's midplane where the field is stronger. However, as shown in the left panel of Fig. 10, magnetic mirroring always reduces the CR ionisation rate more than magnetic focusing can increase it, the total effect being a net reduction of $\zeta^{\rm H_2}$ by a factor between 2 and 3. Notice that the maximum effect of the magnetic field on $\zeta^{\rm H_2}$ is obtained at an intermediate position corresponding to column densities of 10^{21}–$10^{22}\,{\rm cm}^{-2}$ where the reduction factor $\mathcal{R} = \zeta^{\rm H_2}/\zeta_0^{\rm H_2}$ is about 0.3 (see right panel of

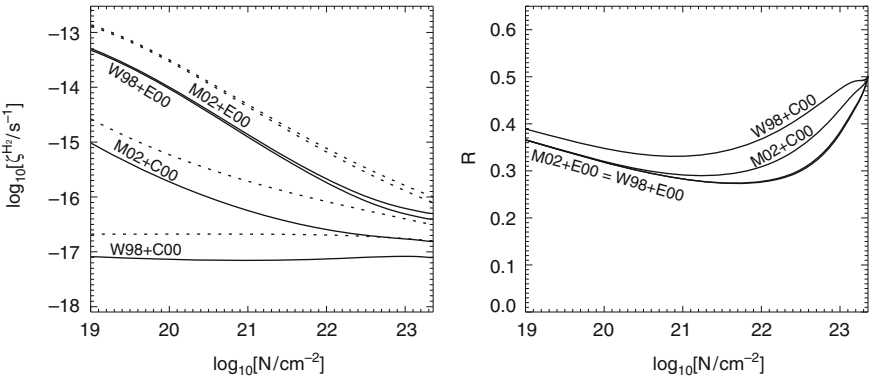

Fig. 10 *Left panel*: comparison between the CR ionisation rate with and without the effects of magnetic field (*solid* and *dotted lines*, respectively) as function of the column density. *Right panel*: ratio between the ionisation rates in the magnetic and non-magnetic case. The curves are labelled as in Fig. 6

Table 4 Values of the parameters described in the text as function of the mass, $M(\Phi)$, contained within flux tube Φ

$M(\Phi)$ ($M_\odot$)	r_{eq} (pc)	$N_0(\pi/2)$ (10^{23} cm^{-2})	α_{cr}	$\chi(\pi/2)$	$\mathcal{R}(\pi/2)$
0.5	0.018	4.54	14.8°	15.347	0.508
1	0.036	2.27	20.5°	8.174	0.516
5	0.180	0.45	39.9°	2.435	0.566
10	0.360	0.23	49.7°	1.717	0.608
50	1.802	0.05	69.3°	1.143	0.739
100	3.604	0.02	75.0°	1.072	0.794

Fig. 10), while the value at the core's midplane is independent on the assumed CR spectrum, a result also obtained by Desch et al. [15].

We explored the parameter space, investigating the variation of the relevant quantities of the problem as a function of the enclosed mass for our reference core. Flux tubes enclosing smaller masses intersect the midplane at smaller equatorial radii (r_{eq}) and are characterised by larger values of the magnetic field and density. As a consequence, focusing becomes more important, since χ increases, but also mirroring becomes more severe, since α_{cr} decreases. The net effect is a stronger reduction of ζ^{H_2} in the innermost regions of the core as compared to the envelope (see Table 4). As the field strength increases approaching the central singularity of the model, $\chi \to \infty$ and the reduction factor of the CR ionisation rate in the core's midplane approaches the asymptotic value $\mathcal{R}(\pi/2) = 1/2$. Conversely, for flux tubes enclosing larger masses, the field strength approaches the ICM value, and the density decreases to zero. Therefore both focusing and mirroring become weaker, and α_{cr} approaches 90°, as shown by Table 4. As expected, for increasing values of $M(\Phi)$, ζ^{H_2} approaches the value of the non-magnetic case, because the magnetic field strength decreases away from the centre of the core, approaching the ICM value.

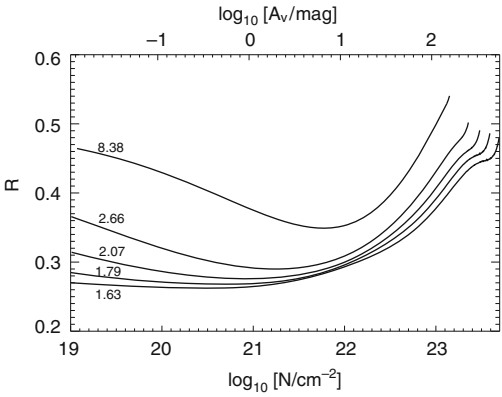

Fig. 11 Reduction factor $\mathcal{R}$ between the CR ionisation rates in the magnetic and non-magnetic case for the case of M02+C00 spectrum (see Fig. 6 for the label). The curves are computed for a flux tube containing 1 $M_\odot$ and for different values of $\lambda = 8.38, 2.66, 2.07, 1.79, 1.63$. The upper scale shows the extinction through the cloud obtained from $A_V/\mathrm{mag} = N/10^{21}\ \mathrm{cm}^{-2}$

For cores with strong magnetic support (lower values of λ), the equatorial squeezing of the field lines is stronger, and the lines reach more internal regions of the core where the density is higher. As a consequence, $\alpha_{\rm cr}$ decreases, the mirroring effect becomes stronger, and a smaller fraction of CRs can penetrate the cloud. In Fig. 11 we show the reduction factor $\mathcal{R}$ as a function of column density for decreasing values of λ. For simplicity, we have considered only the combination of the proton spectrum M02 and the electron spectrum C00 (the results obtained with the other spectra are similar). As the Figure shows, the reduction of $\zeta^{\rm H_2}$ is larger in cores with larger magnetic support, due to the increase in the field strength and concentration of field lines. The reduction is a factor $\sim$4 for the outer regions of cores with $\lambda = 1.63$, the lowest value of mass-to-flux ratio considered in our models.

For $\lambda \to 1$, the density distribution becomes more and more flattened, the core assumes the shape of a thin disc, and the column density from the ICM to the core's midplane becomes larger. For these magnetically dominated disc-like configurations, the reduction of the CR ionisation rate approaches the asymptotic value 1/2.

10 Conclusions

The comparison between our models and the observational data available for diffuse clouds, dense cores and massive protostellar envelopes indicates that good agreement between theory and observations can be obtained for the CR ionisation rate of the ISM by including CR electrons with an energy spectrum increasing towards low energies, as also suggested by Webber [61]. Despite the observational uncertainties due to the uncertainty in the CR spectrum at energies below $\sim$1 GeV and the uncertainties in the empirically determined values of $\zeta^{\rm H_2}$ in diffuse and dense molecular clouds, several important conclusions clearly emerge from our study:

1. Values of ζ^{H_2} measured in diffuse clouds are greater on average by an order of magnitude than those ones measured in dense molecular clouds. If confirmed, these data imply the presence of a CR proton and/or CR electron spectrum which increases at low energies.
2. Values of ζ^{H_2} measured in dense molecular clouds span a range of about two orders of magnitude and are subject to considerable uncertainty. It is difficult to establish how much of the observed spread is due to variations in the CR ionisation rate. It is likely that in dense clouds the effects of magnetic fields on the propagation of CR particles cannot be neglected. In addition, it might be necessary to take into account the density distribution inside each cloud.
3. The values of ζ^{H_2} measured in massive protostellar envelopes are somewhat higher than the predictions of our models at the corresponding column densities. This seems to suggest the presence of further ionisation sources in these objects, as, for example, X-ray emission from the young stellar objects.
4. ζ^{H_2} in a magnetised core is always reduced with respect to its non-magnetic value, by a factor depending on the core's mass-to-flux ratio (λ) and the amount of mass contained in the flux tube considered. The reduction is less severe for flux tubes enclosing larger masses and for larger values of λ. Thus, the values of ζ^{H_2} derived for dense cores and globules [5, 34, 62] probably underestimate the "external" (i.e. intercloud) CR ionisation rate by a factor of $\sim$3 to 4, thus alleviating the discrepancy with measurements of ζ^{H_2} in diffuse clouds.

References

1. Black, J. H. & Dalgarno, A. 1977, ApJS, 34, 405
2. Black, J. H., Hartquist, T. W. & Dalgarno, A. 1978, ApJ, 224, 448
3. Butner, H. M., Lada, E. A., Loren, R. B. 1995, ApJ, 448, 207
4. Casadei, D. & Bindi, V. 2004, ApJ, 612, 262
5. Caselli, P., Walmsley, C. M., Terzieva, R., et al. 1998, ApJ, 499, 234
6. Ceccarelli, C., Dominik, C., Lefloch, B., et al. 2004, ApJ, 607, L51
7. Ceccarelli, C., Hily-Blant, P., Montmerle, T., et al. 2011, ApJL, 740, L4
8. Cecchi-Pestellini, C. & Aiello, S. 1992, MNRAS, 258, 125
9. Cesarski, C. J. & Völk, H. J. 1978, A&A, 70, 367
10. Chandran, B. D. G. 2000, ApJ, 529, 513
11. Cravens, T. E., Victor & G. A., Dalgarno, A. 1975, Plan. Space Sci., 23, 1059
12. Cravens, T. E. & Dalgarno, A. 1978, ApJ, 219, 750
13. Dalgarno, A., Yan, M. & Liu, W. 1999, ApJS, 125, 237
14. de Boisanger, C., Helmich, F. P. & van Dishoeck, E. F. 1996, ApJ, 463, 181
15. Desch, S. J., Connolly, H. C., Jr. & Srinivasan, G. 2004, ApJ, 602, 528
16. Doty, S. D., van Dishoeck, E. F., van der Tak, F. F. S., et al. 2002, A&A, 389, 446
17. Federman, S. R., Weber, J. & Lambert, D. L. 1996, ApJ, 463, 181
18. Gabici, S., Aharonian, F. A. & Blasi, P. 2007, Ap&SS, 309, 365
19. Galli, D., Lizano, S., Li, Z.-Y., et al. 1999, ApJ, 521, 630
20. Geballe, T. R., McCall, B. J., Hinkle, K. H., et al. 1999, ApJ, 510, 251
21. Glassgold, A. E. & Langer, W. D. 1973, ApJ, 186, 859
22. Girart, J. M., Rao, R. & Marrone, D. P. 2006, Science, 5788, 812

23. Glassgold, A. E. & Langer, W. D. 1974, ApJ, 193, 73
24. Gonçalves, J., Galli, D. & Girart, J. M. 2008, A&A, 490, L39
25. Hartquist, T. W., Black, J. H. & Dalgarno, A. 1978, MNRAS, 185, 643
26. Hartquist, T. W., Doyle, H. T. & Dalgarno, A. 1978, A&A, 68, 65
27. Hayakawa, S., Nishimura, S. & Takayanagi, T. 1961, PASJ, 13, 184
28. Heiles, C. & Troland, T. H. 2005, ApJ, 624, 773 C
29. Hezareh, T., Houde, M., McCoey, C., et al. 2008, ApJ, 684, 1221
30. Kulsrud, R. M. 2005, Plasma physics for astrophysics, Princeton University Press
31. Kulsrud, R. & Pearce, W. P. 1969, ApJ, 156, 445
32. Indriolo, N. & McCall, B. J. 2012, ApJ, 745, 91
33. Li, Z.-Y. & Shu, F. H. 1996, ApJ, 472, 211
34. Maret, S. & Bergin, E. A. 2007, ApJ, 664, 956
35. Meneguzzi, M., Adouze, J. & Reeves, H. 1971, A&A, 15, 377
36. Mewaldt, R. A., Wiedenbeck, M. E., Scott, L. M., et al. 2004, Physics of the Outer Heliosphere, AIP Conference Proceedings, vol. 719, p. 127
37. McCall, B. J., Geballe, T. R., Hinke, K. H., et al. 1998, Science, 279, 1910
38. McCall, B. J., Huneycutt, A. J., Saykally, R. J., et al. 2003, Nature, 422, 500
39. Moskalenko, I. V., Strong, A. W., Ormes, J. F. et al. 2002, ApJ, 565, 280
40. Neufeld, D. A., Sonnentrucker, P., Phillips, T. G., et al. 2010, A&A, 518, L108
41. Padoan, P. & Scalo, 2005, ApJ, 624, L97
42. Padovani, M., Galli, D. & Glassgold, A. E. 2009, A&A, 501, 619
43. Padovani, M. & Galli, D. 2011, A&A, 503, A109
44. Phelps, A. V. 1990, J. Phys. Chem. Ref. Data, 19, 3
45. Pinto, C., Galli, D. & Bacciotti, F. 2008, A&A, 484, 1
46. Potgieter, M. S. 1995, Adv. Space Res., 16 (9), 191
47. Ramaty, R., & Lingenfelter, R. E. 1975, Solar Gamma-, X-, and EUV Radiation, 68, 363
48. Ramaty, R., Kozlovsky, B., & Lingenfelter, R. E. 1996, ApJ, 456, 525
49. Schlickeiser, R. 2002, in Cosmic Ray Astrophysics, (Springer: Berlin)
50. Skilling, J. & Strong, A. W. 1976, A&A, 53, 253
51. Swartz, W. E., Nisbet, J. S. & Green, A. E. S. 1971, J. Geophys. Res., 76, 8425
52. Spitzer, L. & Tomasko, M. G. 1968, ApJ, 152, 971
53. Strong, A. W., Moskalenko, I. V. & Reimer, O. 2000, ApJ, 537, 763
54. Takayanagi, M. 1973, PASJ, 25, 327
55. Tang, Y.-W., Ho, P. T. P., Koch, P. M., et al. 2009, ApJ, 700, 251
56. Umebayashi, T. & Nakano, T. 1981, PASJ, 33, 617
57. van der Tak, F. F. S. & van Dishoeck, E. F. 2000, A&A, 358, L79
58. van der Tak, F. F. S. & van Dishoeck, E. F. & Evans, N. J., II et al. 2000, ApJ, 537, 283
59. van Dishoeck, E. F. & Black, J. H. 1986, ApJS, 62, 109
60. Webber, W. R. 1987, A&A, 179, 277
61. Webber, W. R. 1998, ApJ, 506, 329
62. Williams, J. P., Bergin, E. A., Caselli, P. et al. 1998, ApJ, 503, 689

Distribution of Cosmic-Ray Ionization Rates in the Galactic Diffuse Interstellar Medium as Inferred from Observations of H_3^+, OH^+, and H_2O^+

Nick Indriolo

Abstract Cosmic rays play a vital role in initiating the chemistry that occurs in molecular clouds. The ionization of H and H_2 begins a network of ion-molecule reactions responsible for generating many of the diatomic and small polyatomic molecules observed in the ISM. A few such species—OH^+, H_2O^+, and H_3^+ in particular—are formed and destroyed by rather simple processes, making them powerful probes of the cosmic-ray ionization rate. At present, we have performed observations searching for H_3^+ absorption in over 50 sight lines, and for OH^+ and H_2O^+ absorption in an additional 8 sight lines. Using these observations, we have inferred the distribution of cosmic-ray ionization rates in the diffuse ISM throughout the Galaxy. Some of the highest ionization rates are about 25 times larger than the lowest upper limits, suggesting variations in the underlying low-energy cosmic-ray flux across the Galaxy. We posit that such variations are caused by the distance between an observed cloud and the nearest site of particle acceleration, a conjecture supported by the high ionization rates found in close proximity to supernova remnants.

1 Introduction

In the diffuse, molecular interstellar medium (ISM), chemistry is driven by fast ion-molecule reactions [5, 15]. The reaction network begins with ionization of H and H_2 by cosmic rays, such that the ionization rates of these species (denoted ζ_H and ζ_2 for H and H_2, respectively) are important parameters for chemical modeling. There have been many estimates of the cosmic-ray ionization rate—both from observations of molecules (e.g., [4]) and from measurements of the local interstellar

N. Indriolo (✉)
Johns Hopkins University, Baltimore, MD 21218, USA
e-mail: indriolo@pha.jhu.edu

D.F. Torres and O. Reimer (eds.), *Cosmic Rays in Star-Forming Environments*, Astrophysics and Space Science Proceedings 34, DOI 10.1007/978-3-642-35410-6_7,

proton spectrum (e.g., [16])—with values ranging from a few times $10^{-18}\,s^{-1}$ up to a few times $10^{-14}\,s^{-1}$. Most recently, we used a survey of H_3^+ in 50 diffuse cloud sight lines to determine the distribution function of cosmic-ray ionization rates in the Galactic ISM [7]. In that study, we found a mean ionization rate of $\zeta_2 = 3.5\times10^{-16}\,s^{-1}$, with 68.3 % (Gaussian 1σ equivalent) of ionization rates in the range $0.5\times10^{-16}\,s^{-1} < \zeta_2 < 8.8\times10^{-16}\,s^{-1}$. Herein we review the primary results from Indriolo and McCall [7], as well as the methods used in obtaining those results, and update our analysis to include recent estimates of the cosmic-ray ionization rate of atomic hydrogen from observations of OH^+ and H_2O^+.

1.1 Hydrogen Chemistry

In the ISM the formation of H_3^+ begins with the ionization of H_2 by cosmic rays

$$H_2 + CR \rightarrow H_2^+ + e^- + CR', \tag{1}$$

a process quickly followed by a reaction of H_2^+ with H_2,

$$H_2^+ + H_2 \rightarrow H_3^+ + H. \tag{2}$$

Reaction (2) is many orders of magnitude faster than reaction (1), such that cosmic-ray ionization of H_2 is the rate-limiting step, and can be taken as the formation rate of H_3^+. In diffuse molecular clouds H_3^+ is predominantly destroyed by dissociative recombination with electrons

$$H_3^+ + e^- \rightarrow H_2 + H \text{ or } H + H + H, \tag{3}$$

and although proton transfer to O and CO do occur, they have a negligible effect on the destruction rate of H_3^+ in such environments (see Fig. 14 of [7]).

1.2 Oxygen Chemistry

The formation of oxygen bearing ions in the diffuse ISM begins with the ionization of atomic hydrogen by cosmic rays

$$H + CR \rightarrow H^+ + e^- + CR'. \tag{4}$$

This is followed by the endothermic charge transfer to oxygen to form O^+,

$$H^+ + O \rightarrow O^+ + H, \tag{5}$$

and hydrogen abstraction from H_2,

$$O^+ + H_2 \rightarrow OH^+ + H. \tag{6}$$

OH^+ is either destroyed by further hydrogen abstraction to form H_2O^+,

$$OH^+ + H_2 \rightarrow H_2O^+ + H, \tag{7}$$

or by dissociative recombination with electrons.

$$OH^+ + e^- \rightarrow \text{products}. \tag{8}$$

The same is true for H_2O^+,

$$H_2O^+ + H_2 \rightarrow H_3O^+ + H, \tag{9}$$

$$H_2O^+ + e^- \rightarrow \text{products}, \tag{10}$$

but H_3O^+ is only destroyed by dissociative recombination with electrons.

$$H_3O^+ + e^- \rightarrow \text{products}. \tag{11}$$

1.3 Steady-State Relations

In order to relate the abundances of various species, we assume that chemistry is in steady-state (i.e., the formation rate of each species is equal to its destruction rate). Given the short expected lifetimes of the ions under consideration, about 100–1,000 years, with respect to the estimated lifetime of diffuse clouds, $\sim 10^6$ years, the steady-state approximation is reasonable. Taking reactions (1) and (3) to govern the H_3^+ abundance, steady state is given by

$$\zeta_2 n(H_2) = k(H_3^+|e^-) n(H_3^+) n(e), \tag{12}$$

where $n(X)$ is the number density of species X, and $k(X|Y)$ is the rate coefficient for the reaction between species X and Y. Making substitutions as in Indriolo and McCall [7] we arrive at

$$\zeta_2 = k(H_3^+|e^-) x_e n_H \frac{N(H_3^+)}{N(H_2)}, \tag{13}$$

where $N(X)$ is the column density of species X, $n_H \equiv n(H) + 2n(H_2)$ is the number density of hydrogen nuclei, and $x_e \equiv n(e)/n_H$ is the fractional abundance of

electrons with respect to hydrogen. Equation (13) is used in determining the cosmic-ray ionization rate of H_2 from observations of H_3^+.

Assuming the H_2O^+ abundance is controlled by reactions (7), (9), and (10) results in the OH^+/H_2O^+ abundance ratio relation given in Gerin et al. [2], which can be re-arranged to produce

$$f_{H_2} = \frac{2x_e k(H_2O^+|e^-)/k(OH^+|H_2)}{N(OH^+)/N(H_2O^+) - k(H_{2O}{}^+|H_2)/k(OH^+|H_2)}, \tag{14}$$

where $f_{H_2} \equiv 2n(H_2)/n_H$ is the molecular hydrogen fraction.

Taking reactions (4), (7), and (8) to control the OH^+ abundance, steady state is given by

$$\epsilon\zeta_H n(H) = n(OH^+)[n(H_2)k(OH^+|H_2) + n(e)k(OH^+|e^-)]. \tag{15}$$

Here, the destruction of OH^+ is thought to be complete, but not all H^+ will eventually lead to OH^+. To account for processes competing with reactions (5) and (6)—i.e., that prevent H^+ from forming OH^+—we introduce an efficiency factor, ϵ, to the left hand side of Eq. (15), as in Neufeld et al. [11]. This parameter gives the fraction of H^+ formed by cosmic-ray ionization of H that produces OH^+. Solving for the product $\epsilon\zeta_H$ and making substitutions results in

$$\epsilon\zeta_H = \frac{N(OH^+)}{N(H)} n_H \left[\frac{f_{H_2}}{2} k(OH^+|H_2) + x_e k(OH^+|e^-)\right], \tag{16}$$

which allows us to find ζ_H after making assumptions about ϵ.

In Eqs. (13), (14), and (16), we adopt the rate coefficients used by the 2006 version of the UMIST Database for Astrochemistry ([17], database available online at: www.udfa.net). $N(H)$ is determined from 21 cm observations of H I, and $N(H_2)$ from direct observations of H_2 in the UV, or from observations of CH and the empirical relation $N(CH)/N(H_2) = 3.5^{+2.1}_{-1.4} \times 10^{-8}$ found by Sheffer et al. [13]. The electron fraction, x_e, is either determined from observations of C^+ or set equal to the average value of $x(C^+) = 1.5 \times 10^{-4}$ [14], assuming nearly all electrons are the result of singly photoionized carbon. The hydrogen number density, n_H, is difficult to determine, and unless an estimate is available in the literature for a particular sight line, we adopt a rough average value of 200 cm^{-3} for the molecular interior of a diffuse cloud. Assuming pressure balance, this translates to $n_H \sim 70\,cm^{-3}$ in the warmer, primarily atomic outskirts of such a cloud (H_3^+ is thought to reside in the molecular interior of clouds, while OH^+ and H_2O^+ are in the atomic outer layers). Recent modeling efforts [6] and observations [9] suggest a low value for the efficiency factor, and herein we adopt $\epsilon \sim 0.1$. To directly compare ζ_2 and ζ_H, we convert values determined from H_3^+ and from OH^+ and H_2O^+ to the primary

cosmic-ray ionization rate, ζ_p. This is the ionization rate of atomic hydrogen due to cosmic rays alone (i.e., not accounting for ionization by secondary electrons), and is related to the total ionization rates of H and H_2 by $\zeta_H = 1.5\zeta_p$ and $\zeta_2 = 2.3\zeta_p$, respectively [3].

2 Summary of Observations

We have performed observations searching for H_3^+, OH^+, and H_2O^+ in absorption in order to determine the column densities of these species and calculate ionization rates from Eqs. (13), (14), and (16). Observations of H_3^+ targeted ro-vibrational transitions near 3.7 μm in 50 diffuse cloud sight lines, and were made using a variety of ground based telescopes with high resolution IR spectrographs (e.g., CRIRES at VLT). A list of the targeted sight lines along with H_3^+ column densities and inferred cosmic-ray ionization rates (or upper limits on these parameters) is presented in Indriolo and McCall [7]. Observations searching for OH^+ and H_2O^+ absorption were made using HIFI aboard *Herschel* as part of the PRISMAS (PRobing InterStellar Molecules with Absorption line Studies) key programme, and targeted rotational transitions near 971 and 1,115 GHz, respectively. The PRISMAS programme observed eight sight lines in total, and preliminary results for the oxygen chemistry in two of those, W 31C and W 49N, have been reported in Gerin et al. [2] and Neufeld et al. [11].

3 Distribution of Ionization Rates

In Indriolo and McCall [7] we reported the distribution of cosmic-ray ionization rates in the diffuse ISM as determined from observations of H_3^+ (see Fig. 16 therein). With observations of OH^+ and H_2O^+ toward the eight PRISMAS sight lines, we have now also determined the ionization rate in several clouds where the necessary supplementary data such as $N(H)$ are available. The full analysis of these data (i.e., $N(OH^+)$, $N(H_2O^+)$, ζ_H, etc.) will be presented in a future manuscript. For the time being, we have simply combined the ionization rates inferred from OH^+ and H_2O^+ with those reported in Indriolo and McCall [7] to update the overall distribution of cosmic-ray ionization rates. The results are shown in Fig. 1, where the solid black curve is $\zeta_p f(\zeta_p)$, i.e., the probability density function of ionization rates scaled by the ionization rate. See the Fig. 1 caption for a complete description of what is shown.

In Fig. 1 we see that the addition of 9 ionization rates to the previous sample of 52[1] does not significantly alter the distribution of ionization rates. Both the peak

[1]Two of the fifty sight lines observed have two distinguishable velocity components in H_3^+

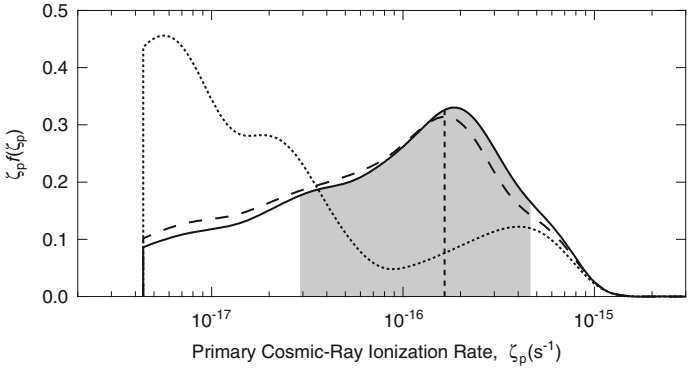

Fig. 1 Shown here is $\zeta_p f(\zeta_p)$—the product of the probability density function of cosmic-ray ionization rates, $f(\zeta_p)$, and the ionization rate, ζ_p—as a function of the ionization rate. The definition of $f(\zeta_p)$ is such that the probability of the cosmic-ray ionization rate being in any particular range is given by $P(a \leq \zeta_p \leq b) = \int_a^b f(\zeta_p) d\zeta_p$. Scaling $f(\zeta_p)$ by ζ_p makes it easy to see "by eye" what portion of $f(\zeta_p)$ carries the largest probability given the logarithmic x-axis. The solid curve combines ionization rates and upper limits from the 50 sight lines observed in H_3^+ by Indriolo and McCall [7] with preliminary ionization rates inferred for 9 cloud components observed in OH^+ and H_2O^+ as part of the PRISMAS key programme. The mean value of $\zeta_p = 1.65 \times 10^{-16}\,s^{-1}$ is marked by the vertical dotted line, and the shaded region that extends from 0.29×10^{-16} to $4.6 \times 10^{-16}\,s^{-1}$ shows the minimum range of ionization rates (in log space) that contains 68.3 % (Gaussian 1σ equivalent) of the area under $f(\zeta_p)$. The dashed curve is found using only the ionization rates inferred from H_3^+ in Indriolo and McCall [7], and is identical to the distribution in that paper, except in terms of ζ_p instead of ζ_2. The dotted curve is for four sight lines (o Sco, HD 147889, ρ Oph D, and χ Oph) in the Ophiuchus-Scorpius region where H_3^+ is not detected, and some of the lowest upper limits on the cosmic-ray ionization rate are found. The sharp cutoff on the low end of the distribution is a "floor" value ($\zeta_p = (1.0/2.3) \times 10^{-17}\,s^{-1}$), above which the ionization rate in diffuse clouds is expected to remain due to the continuous diffusion of energetic particles throughout the Galactic disk

of $\zeta_p f(\zeta_p)$ and the mean ionization rate shift to slightly higher values as most of the ionization rates inferred from OH^+ and H_2O^+ are relatively close to $\zeta_p \sim 2 \times 10^{-16}\,s^{-1}$. It is surprising that the adopted value of $\epsilon = 0.1$ results in ionization rates so consistent with the mean value found in Indriolo and McCall [7], but because of the uncertainty in ϵ these results must be viewed as highly preliminary.

Also of interest is the vastly different shape of $\zeta_p f(\zeta_p)$ as determined from four sight lines in the Ophiuchus-Scorpius region. H_3^+ has not been detected in any of these sight lines, and 3σ upper limits on the ionization rates toward o Sco and HD 147889 are $\zeta_p < 1.44 \times 10^{-17}\,s^{-1}$ and $\zeta_p < 4.70 \times 10^{-17}\,s^{-1}$, respectively—some of the lowest values in our entire sample. In fact, the largest value inferred for ζ_p—toward HD 183143—is more than 30 times larger than the upper limit toward o Sco. This suggests that the ionization rate varies significantly between sight lines, and that the distribution of ionization rates may vary between specific regions of the sky.

4 Discussion

The wide distribution of ionization rates shown in Fig. 1 and the potential variation between different regions of the Galaxy require some underlying physical explanation. We posit that such variations are caused by the distance between an observed cloud and the nearest site of particle acceleration for the following reasons. The cross section for ionization of H and H_2 by cosmic rays increases as the particle energy decreases, such that particles with energies of a few MeV are the most efficient at ionization (see, e.g., [12]). This also means that low-energy particles lose their energy to ionization faster than high energy particles and cannot travel very far from their acceleration sites. For example, a 20 MeV proton can traverse a column of about $6 \times 10^{22}\,\mathrm{cm}^{-2}$, over 60 times more material than a 2 MeV proton, which can traverse a column of about $9 \times 10^{20}\,\mathrm{cm}^{-2}$ [1]. Particles with even higher energies ($E > 1\,\mathrm{GeV}$) are thought to diffuse throughout the Galactic disk, creating a relatively uniform underlying cosmic-ray spectrum that sets the floor value assumed above [16]. Given this picture, the cosmic-ray ionization rate at any arbitrary position in the Galaxy is determined by the sum of the underlying interstellar particle spectrum and contributions to the particle flux from any nearby sites of particle acceleration.

In the above scenario, molecular material in close proximity to a supernova remnant—likely candidates for particle acceleration—should show higher ionization rates than in the average diffuse ISM. To test this theory, we made observations searching for H_3^+ in six sight lines near the supernova remnant IC 443 [8]. H_3^+ was detected in two sight lines—ALS 8828 and HD 254577—and inferred ionization rates were $\zeta_p = 7.0^{+3.5}_{-5.2} \times 10^{-16}\,\mathrm{s}^{-1}$ and $\zeta_p = 11^{+5.7}_{-8.3} \times 10^{-16}\,\mathrm{s}^{-1}$, the two largest values found in the Galactic disk from H_3^+ observations to date. Upper limits inferred for the other four sight lines are consistent with ionization rates found in the diffuse ISM. Recent observations of IC 443 in ^{12}CO $J = 1-0$ suggest that only the two sight lines with H_3^+ detections probe gas that is interacting with the supernova remnant, while the other four likely probe foreground material [10]. As such, these results confirm the picture where the cosmic-ray ionization rate is controlled by proximity to a site of particle acceleration.

5 Summary

We have combined cosmic-ray ionization rates inferred from a preliminary analysis of 9 cloud components observed in OH^+ and H_2O^+ with those inferred in 50 sight lines from observations of H_3^+ reported in Indriolo and McCall [7]. The result is an updated distribution function for the primary cosmic-ray ionization rate that has a mean value of $\zeta_p = 1.65 \times 10^{-16}\,\mathrm{s}^{-1}$ and a 1σ range of $0.29 \times 10^{-16}\,\mathrm{s}^{-1} < \zeta_p < 4.6 \times 10^{-16}\,\mathrm{s}^{-1}$. The wide range of ionization rates is indicative of variations in the flux of low-energy cosmic-rays, something likely controlled by the distance between

an observed cloud and the nearest site of particle acceleration. Observations of H_3^+ in molecular material that is interacting with the supernova remnant IC 443 give the highest ionization rates found in the Galactic disk to date, thus supporting this scenario.

Acknowledgements I would like to thank David Neufeld for performing a significant portion of the OH^+ and H_2O^+ data processing, Maryvonne Gerin for encouraging my involvement in the PRISMAS key programme for Herschel, and Ben McCall for support during graduate school when the bulk of the H_3^+ analysis was done.

References

1. Cravens, T. E., & Dalgarno, A. 1978, ApJ, 219, 750
2. Gerin, M., de Luca, M., Black, J., et al. 2010, A&A, 518, L110
3. Glassgold, A. E., & Langer, W. D. 1974, ApJ, 193, 73
4. Hartquist, T. W., Doyle, H. T., & Dalgarno, A. 1978, A&A, 68, 65
5. Herbst, E. & Klemperer, W. 1973, ApJ, 185, 505
6. Hollenbach, D., Kaufman, M. J., Neufeld, D. A., Wolfire, M., & Goicoechea, J. R. 2012, ApJ, 754, 105
7. Indriolo, N., & McCall, B. J. 2012, ApJ, 745, 91
8. Indriolo, N., Blake, G. A., Goto, M., et al. 2010, ApJ, 724, 1357
9. Indriolo, N., Neufeld, D. A., Gerin, M., et al. 2012, ApJ, 758, 83
10. Lee, J.-J., Koo, B.-C., Snell, R. L., et al. 2012, ApJ, 749, 34 (arXiv:1202.4789v1)
11. Neufeld, D. A., Goicoechea, J. R., Sonnentrucker, P., et al. 2010, A&A, 521, L10
12. Padovani, M., Galli, D., & Glassgold, A. E. 2009, A&A, 501, 619
13. Sheffer, Y., Rogers, M., Federman, S. R., et al. 2008, ApJ, 687, 1075
14. Sofia, U. J., Lauroesch, J. T., Meyer, D. M., & Cartledge, S. I. B. 2004, ApJ, 605, 272
15. Watson, W. D. 1973, ApJ, 183, L17
16. Webber, W. R. 1998, ApJ, 506, 329
17. Woodall, J., Agúndez, M., Markwick-Kemper, A. J., & Millar, T. J. 2007, A&A, 466, 1197

Consequences of Starbursts for the Interstellar and Intergalactic Medium

Dieter Breitschwerdt, Miguel de Avillez, and Ernst Dorfi

Abstract Star formation in general, and starbursts in particular, drive the evolution of galaxies. To understand the process of galactic matter cycle quantitatively, it is absolutely necessary to follow the evolution of the components of the interstellar medium, such as gas, magnetic fields, cosmic rays in detail over sufficiently long time scales. Due to the non-linearity of the interactions between the various components, and the turbulent nature of the plasma, high resolution numerical simulations offer the best strategy to further our understanding. The results of our numerical studies can be summarized as follows: (i) Supernova explosions are the most important energy input sources in the ISM and lead to a high level of turbulence in the plasma, coupling structures on all scales, (ii) more than half of the disk mass resides in classically thermally unstable temperature regimes, (iii) turbulent mixing is the dominant energy transport process over a wide range of scales, (iv) proportionality between magnetic field and density is generally weak, except for the densest regions, (v) magnetic fields, even if they are parallel to the galactic disk, cannot prevent outflow into the halo, (vi) the ionization structure of the plasma depends on its thermal history, and is in general not in collisional ionization equilibrium, (vii) the cooling function varies in space and time, (viii) X-rays can be emitted even at plasma temperatures of the order of 10^4 K due to delayed recombination, both in the disk and the halo, (ix) cosmic rays can help

D. Breitschwerdt (✉)
Zentrum für Astronomie und Astrophysik, TU Berlin, Hardenbergstr. 36,
D-10623 Berlin, Germany
e-mail: breitschwerdt@astro.physik.tu-berlin.de

M. de Avillez
Department of Mathematics, University of Évora, R. Romao Ramalho 59, 7000 Évora, Portugal
e-mail: mavillez@lca.galaxy.uevora.pt

E. Dorfi
Institut für Astronomie, Universität Wien, Türkenschanzstr. 17, A-1180 Wien, Austria
e-mail: ernst.dorfi@univie.ac.at

D.F. Torres and O. Reimer (eds.), *Cosmic Rays in Star-Forming Environments*,
Astrophysics and Space Science Proceedings 34, DOI 10.1007/978-3-642-35410-6_8,

driving a galactic wind, (x) cosmic rays can be accelerated to high energies beyond 10^{15} eV (the "knee") in long lived shocks propagating into the galactic halo, because of time-dependent star formation.

1 Introduction

The rôle of galactic winds (GWs) in the context of galaxy formation and the state and evolution of the interstellar (ISM) and intergalactic medium (IGM) can hardly be overestimated. It has become clear during the last decades, that GWs are an accompanying phenomenon through episodes of star formation in galaxies. The star formation rate (SFR) per unit area, $\dot{\Sigma}_*$, correlates with the surface density of the gas, expressed by the so-called Schmidt-Kennicut law [42, 61], $\dot{\Sigma}_* = k\left[\Sigma_g/(M_\odot \mathrm{pc}^{-2})\right]^n$, where $k = (2.5 \pm 0.7) \times 10^{-4}\, M_\odot\, \mathrm{year}^{-1}\, \mathrm{kpc}^{-2}$, and $n = 1.5 \pm 0.15$, respectively. This relation can be understood heuristically, if we assume that the characteristic time scale for star formation is the free fall time, $\tau_{\mathrm{ff}} = \sqrt{3\pi/(32G\rho)}$, in which gas with a certain surface density Σ_g is converted into stars with an efficiency ϵ, i.e. $\dot{\Sigma}_* = \epsilon\Sigma_g/\tau_{\mathrm{ff}} = \epsilon\sqrt{32G/(3\pi H_g)}\,\Sigma_g^{3/2} = k\Sigma_g^{3/2}$, with H_g being the scale height of the molecular gas. Assuming $H_g = 50\,\mathrm{pc}$, for the vertical scale height of molecular clouds in the Galaxy, and comparing the above relation to the Schmidt-Kennicutt law, we infer $\epsilon \approx 0.043$ for the conversion factor of molecular gas into stars. It is this low efficiency, which renders star formation a continuous process over gigayears in spiral galaxies. But what is the reason for keeping a galaxy sizzling rather than bursting into stars?

If the gas in the galactic disk gets compressed, the Jeans mass drops and the SFR increases, leading eventually to an increase of the ISM pressure, which leads to a higher density in surrounding clouds and an ever increasing SFR. The feedback loop is closed by the generation of an outflow of gas into the halo, due to supernova (SN) explosions of massive stars, and thus to a reduction of ISM pressure and a self-regulation of the SFR. Thus outflows, which comprise galactic fountains and winds, are a key element in the evolution of star forming galactic disks. The question, whether a galactic fountain or wind will ensue, depends on the SFR, and hence on the possibility to build up pressure in the disk, which scales with the depth of the potential well. Thus more massive galaxies will form more stars, but have also a higher potential well for the gas to overcome and become unbound (if we define a GW to be a gravitationally unbound outflow). In fact, in order to drive a GW, only a locally enhanced SFR is needed, which can be triggered by SN shocks, and more generally by gravitational interaction with neighbouring galaxies. Under these circumstances, also small galaxies with a shallow potential can develop high SFRs, eventually resulting in a starburst, and drive a massive GW, like e.g. M 82.

Recently, it has been emphasized, that GWs are key players through their feedback during cosmological evolution. Analysing the luminosity functions of galaxy samples and their spatial distribution out to large redshifts, the cosmic star formation rate density, i.e. the SFR per unit co-moving volume of the Universe,

has been determined and found to have been largest and roughly constant between redshifts 2–5 [52, 55], implying massive galactic mass losses by SN driven GWs in the early Universe. GWs have also been hypothesized to be the cause of the so-called baryon deficit [63]. An inventory of the baryon fractions [31], ranging from primordial nucleosynthesis, the cosmic microwave background power spectrum, and the Lyman alpha forest to the hot intracluster medium, thus covering a redshift range from $z \sim 10^9$ to $z = 0$, has revealed a deficit of 10–20 % not accounted for by the so-called warm hot intergalactic medium (WHIM), which is assumed to trace the large scale structure in the cosmic web (see [12]). Models of galaxy formation, including our Milky Way, predict an initial gas fraction of 10–20 % within the virial radius, although only about half of it is found (e.g. 6 % in the case of the Milky Way, see [43]). Even taking into account a fraction of MACHOs in the halos, which probably does not exceed 30 %, the deficit cannot be explained except by galactic outflows.

Crude recipes for describing GWs exist in abundance, but a profound analysis, proceeding from dissipative baryon physics in a turbulent multiphase medium, and including other important ISM components like magnetic fields and cosmic rays, is still needed. We will outline the basic physics of the ISM, how the medium is structured by turbulence, and how outflows naturally occur within the framework of a model including feedback.

The structure of this paper is as follows: Sect. 2 describes the basic physics of the ISM and how to model it in star forming galaxies, and Sect. 3 stresses the importance of the non-equilibrium ionization (NEI) structure of the disk and halo plasmas. In Sect. 4 the rôle of starbursts and cosmic rays, including magnetohydrodynamical (MHD) waves, in driving GWs, is discussed. Section 5 shows how GWs offer an elegant possibility to post-accelerate Galactic cosmic rays from the so-called knee at 10^{15} eV up to the ankle at 10^{18} eV. In Sect. 6 we give an outlook on the effect of winds in the intergalactic medium, and Sect. 7 closes with our summary and conclusions.

2 The Interstellar Medium in Star Forming Regions

2.1 Turbulence

The ISM in star forming galaxies is a highly turbulent and compressible medium, as has been already stated more than 60 years ago by von Weizsäcker [66]. Turbulence needs to be sustained by a constant input of energy due to its dissipative nature. It is fortuitous that in the inertial range, i.e. $\eta \ll l \ll l_0$, where η is the dissipation scale and l_0 the integral scale where energy is fed in, no physical length scale enters the problem, so that turbulence is self-similar and can be described by scaling laws. In the inertial range, there exists a constant transfer of kinetic energy to smaller scales in a cascade as a result of a dynamical instability, driven by inertial forces. Hence large turbulence elements (eddies) break up into smaller ones on an ever decreasing

time scale, $\tau \sim l/u \sim l^{2/3}$ (for incompressible flow and constant energy input rate $\varepsilon = \rho u^2/\tau \sim \rho u^3/l \rightarrow u \sim l^{1/3}$, with τ being the turnover time of an eddy, and u the velocity fluctuation on scale l). The Reynolds number $Re = ul/\nu$ is a measure of the inertial over the viscous forces, characterized by the kinematic viscosity ν, and decreases with length scale as $Re \sim l^{4/3}$ until viscous forces take over. This occurs when $Re \sim 1$, i.e. at a microscale $\eta \sim (\nu^3/\varepsilon)^{1/4} = Re^{-3/4}\, l$, at which strong dissipation sets in. Thus the microscale is independent of the Reynolds number of the flow, which, in case of the ISM, can be as large as $Re \sim 10^5 - 10^7$ [25], and η can therefore be a fraction of $1.8 \times 10^{-4} - 6 \times 10^{-6}$ of the outer scale at which turbulence is injected. Physically, viscosity can be associated with the transfer of transverse momentum between molecules, and is therefore small for gases, because of the small collision rate (but increasing with temperature), whereas it can be large in liquids due to intermolecular forces. However, magnetic fields are ubiquitous in the ISM, and as a result of flux freezing due to high conductivity, they can couple fluid elements over large distances, thus enhancing viscosity substantially.

In his scaling model, Kolmogorov [44] assumed that on small scales turbulence is (i) statistically isotropic, and (ii) determined by dissipation (see above). Hence the spectral energy density $E(k)$ at some wave number k, representing the contribution to the energy density of all Fourier modes between k and $k + dk$, depends only on k and the energy dissipation rate ε, $E(k) = f(k, \varepsilon)$, and can be obtained by simple dimensional analysis: $E(k) = C\varepsilon^{2/3}k^{-5/3}$, with C being a universal constant. While such a simple scaling law gives surprisingly good results, e.g. the velocity dispersion in molecular clouds was found to be $\sigma \sim l^{0.38}$ [50], as compared to $u \sim l^{0.33}$, with the small difference being presumably due to compressibility, which leads to dissipation by shocks on larger scales than the microscale and hence to a steepening of the spectrum, turbulence is much more complex. In contrast to a chaotic system, like e.g. the three-body problem, turbulence has a large number of degrees of freedom, and exhibits special properties like intermittency, i.e. random turbulent bursts of vorticity. It has therefore been pointed out already by Landau and Lifshitz [49], that C may not be universal, i.e. the same for all kinds of turbulent energy injection, because ε is rather a local than a global quantity, so that its averaging over larger scales may be different for flows varying in space and time. The departure from Kolmogorov turbulence can best be studied by considering higher order structure functions, defined by $\langle(\Delta\mathbf{u}(r))^p\rangle = \langle[\mathbf{u}(\mathbf{x}+\mathbf{r}) - \mathbf{u}(\mathbf{x})]^p\rangle$, with $\langle\ldots\rangle$ denoting ensemble averages; since turbulence is considered statistically isotropic, velocity *increments* depend only on r and not on direction. For example, the second order structure function is a measure of the kinetic energy contained in an eddy of size r. Scale invariance implies for $r \rightarrow \lambda r$ that $\Delta\mathbf{u}(\lambda r) \sim \lambda^q \Delta\mathbf{u}(r)$, with some similarity exponent q, and thus for Kolmogorov's law we obtain for the structure function of order p, $\langle(\Delta\mathbf{u}(r))^p\rangle = C_p\varepsilon^{p/3}\, r^{p/3}$. While for lower orders p, the Kolmogorov model gives a satisfactory description, the deviation for higher orders can be substantial, and numerical studies are needed.

Solutions of the Navier-Stokes equations for high Reynolds numbers are unstable with respect to small perturbations in the initial and boundary conditions. The origin

of turbulence lies in the advection term $\mathbf{u}\nabla\mathbf{u}$ in the Navier-Stokes equation, which is non-linear in $\mathbf{u}$, and hence leads to strong coupling of different modes k. For simplicity, let us look at an incompressible Newtonian fluid, in which the shear stress is proportional to the velocity gradient perpendicular to the direction of shear. Thus $\tau_{ij} = \nu\rho S_{ij}$, where $S_{ij} = 1/2(\partial u_i/\partial x_j + \partial u_j/\partial x_i)$ is the strain rate tensor, which is composed of the shear velocity components, and which relates to the energy dissipation rate by $\varepsilon = 2\nu S_{ij} S_{ij}$. The Navier-Stokes equations then read:

$$\frac{\partial \mathbf{u}}{\partial t} + (\mathbf{u}\nabla)\mathbf{u} = -\nabla\left(\frac{P}{\rho}\right) + \nu\nabla^2\mathbf{u}, \,. \tag{1}$$

The rate of rotation of a fluid element is proportional to the vorticity, defined by $\boldsymbol{\omega} = \nabla \times \mathbf{u}$. If we take the curl of Eq. (1), it can be written as an equation describing the evolution of vorticity:

$$\frac{\partial \boldsymbol{\omega}}{\partial t} = \nabla \times [\mathbf{u} \times \boldsymbol{\omega}] + \nu\Delta\boldsymbol{\omega} \,. \tag{2}$$

Using the vector identity $\nabla \times [\mathbf{u} \times \boldsymbol{\omega}] = (\boldsymbol{\omega} \cdot \nabla)\mathbf{u} - (\mathbf{u} \cdot \nabla)\boldsymbol{\omega}$, Eq. (2) can be cast into the form:

$$\frac{D\boldsymbol{\omega}}{Dt} \equiv \frac{\partial \boldsymbol{\omega}}{\partial t} + (\mathbf{u} \cdot \nabla)\boldsymbol{\omega} = (\boldsymbol{\omega} \cdot \nabla)\mathbf{u} + \nu\Delta\boldsymbol{\omega} \,. \tag{3}$$

This equation can be interpreted as follows: the change of vorticity with space and time is given by the change of the moment of inertia and is increased by the stretching of a fluid element (first term on the right hand side) and by the viscous torque due to shear stresses (second term). Thus vorticity can be generated by shear flows, typically in boundary layers, where circulation is not conserved.

In the ISM there is ample evidence for shear flows, in particular in star forming regions. The expansion of HII regions, stellar winds, supernova remnants (SNRs), and superbubbles (SBs) due to correlated explosions in space and time, generate both vorticity due to shear in the surrounding medium and also by breaking up of bubbles due to ambient density gradients. We can therefore picture the ISM as a fluid filled with vortex tubes, which are stretched out, thereby increasing their volume filling factor. Consider a droplet of ink immersed in a turbulent fluid. First individual streaks of ink can be seen, combed and thinning out by increasing vorticity and distributing the ink in space (turbulent mixing), while molecular diffusion, driven by small scale gradients, accomplishes the rest. Thus chemically enriched material injected by SN explosions will be efficiently mixed into the ISM, with an effective turbulent viscosity $\nu_T = Re\,\nu \sim \delta u\, l$ (where δu is the fluctuating velocity component and l the eddy correlation length), which can be orders of magnitude higher than molecular viscosity. The energy, which is stored in turbulence, and dissipated continuously, is drawn from the mean flow. The flow velocity $\mathbf{u} = \overline{\mathbf{u}} + \delta\mathbf{u}$ can be decomposed into a mean flow component $\overline{\mathbf{u}}$ and a fluctuating component $\delta\mathbf{u}$. Thus ensemble averaging of the Navier-Stokes equations yields terms of the form $\tau_{ij} = \rho\overline{\delta u_i \delta u_j}$, which denote the components of

the Reynolds stress tensor, where δu_i and δu_j are the respective fluctuating velocity components. The diagonal part of the stress tensor can be interpreted as turbulent pressure, while the off-diagonal elements are proportional to the turbulent viscosity. In order to calculate the elements, higher order correlations have to be considered, which leads to a typical closure problem, well known in kinetic gas theory.

The vast space between stars is not filled by gas and dust only, but also permeated by magnetic fields and penetrated by high energy particles, the cosmic rays (CRs). Owing to the high conductivity in the ISM, gas and magnetic fields are tightly coupled, with flux freezing being a good description on all scales, except the smallest, where resistivity may become large in current sheets, leading to magnetic reconnection, and hence to a change in topology of the field. It is therefore not surprising that magnetic fields change the nature of turbulence by their pressure and tension forces. The momentum equation of the fluid is supplemented by magnetic stresses with components $T_{ij}^M = B^2/(8\pi)\delta_{ij} - B_i B_j/(4\pi)$, which adds to the total stress tensor

$$T_{ij} = -\left(p + \frac{B^2}{8\pi}\right)\delta_{ij} - \left(\rho u_i u_j - \frac{B_i B_j}{4\pi}\right) + \mu\left(\partial_i u_j + \partial_j u_i - \frac{2}{3}\delta_{ij}\nabla\cdot\mathbf{u}\right) \quad (4)$$

$$= -P\delta_{ij} + R_{ij} + \sigma_{ij}\,, \quad (5)$$

which can be thought of being the sum of total pressure, P, as well as Reynolds plus Maxwell stresses (R_{ij}) and viscous (σ_{ij}) stresses in the fluid. Here B_i, δ_{ij}, $\mu = \nu\rho$ are the magnetic field components, the Kronecker delta (components of the unit tensor) and the dynamic viscosity, respectively. In the magnetohydrodynamical (MHD) limit, electric fields are generated by large scale motions, and magnetic fields vary according to $\partial B/\partial t - \nabla\times(\mathbf{u}\times\mathbf{B}) = \eta\nabla^2\mathbf{B}$, with the magnetic diffusivity $\eta = c^2/(4\pi\sigma)$, and σ being the conductivity of the plasma. Magnetic differs from hydrodynamic turbulence by the fact that the mean field is important, since it introduces an anisotropy into the medium. In addition magnetosonic and Alvén waves can propagate in the plasma, which can interact non-linearly. It can be shown that in case of incompressible MHD, the equations can be written in simple form using Elsässer [26] variables $\mathbf{z}^{\pm} := \mathbf{u}\pm\mathbf{b}$, splitting up the magnetic field $\mathbf{B} = \mathbf{B_0}+\mathbf{b}$ into a regular ($\mathbf{B_0}$) and a fluctuating component, $\mathbf{b} = \pm\sqrt{4\pi\rho}\,\mathbf{v_A}$, with $\mathbf{v_A}$ being the Alfvén speed of magnetic transverse field perturbations. Neglecting viscosity and resistivity, it can be shown that there are no self-coupling, but only cross-coupling, terms in $\mathbf{z}^{\pm}$, and $\mathbf{z}^{-} = f_1(\mathbf{r}-\mathbf{v_A}t)$, describing waves travelling in the direction of the mean field $\mathbf{B_0}$, and $\mathbf{z}^{+} = f_2(\mathbf{r}+\mathbf{v_A}t)$ opposite to $\mathbf{B_0}$. Thus interaction occurs only between wave packets (or eddies) propagating in opposite directions. If this happens many times in an uncorrelated fashion before the energy is transferred to smaller scales, the resulting energy spectrum becomes $E(k) \propto k^{-3/2}$ [38, 46]. This does, however, not take into account the anisotropy of the turbulent eddies itself, and it also implies that turbulence becomes weaker with decreasing scales. The interaction time is of the order of the crossing time between two distorted eddies passing each other, and indirectly turns out to be of the order of the eddy turnover time.

Assuming that the energy cascade is scale invariant, the energy spectrum becomes $E(k) \propto k_{\perp}^{-5/3}$ [32], corresponding, not surprisingly, to Kolmogorov scaling, since the interaction time is roughly the eddy turnover time scale; $k_{\perp}$ denotes the wave mode perpendicular to the mean magnetic field. The anisotropy of the fluctuations is given by the relation $k_{\parallel} \propto k_{\perp}^{2/3}$. However, the anisotropic spectrum depends on the large scale magnetic field strength, in the sense that for decreasing scales the dynamical alignment of eddies with the field becomes stronger and hence more anisotropic locally, so that in essence $E(k) \propto k_{\perp}^{-(5+\alpha)/(3+\alpha)}$ and $k_{\parallel} \propto k_{\perp}^{2/(3+\alpha)}$ [6], where $0 \leq \alpha \leq 1$. The underlying assumption here is that the interaction of counterpropagating fluctuations is reduced by a factor $(\delta v_{\lambda}/v_A)^{\alpha}$, with δv_{λ} and $v_A = B_0/(4\pi\rho)$ being the velocity fluctuation in the eddy at the transverse scale λ and the Alfvén speed, respectively.

Turbulence at much smaller scales, on the order of a gyroradius, is generated by the streaming of the CRs along the mean magnetic field, leading to the resonant generation of MHD waves. This so-called streaming instability [48, 51] happens because of a small scale anisotropy in the distribution function of the CRs in the frame of the waves due to the preferential propagation of CRs along the field. A growing MHD wave field leads to a stronger pitch angle scattering of the particles and hence isotropizes the distribution function. Since the waves are essentially frozen into the plasma, preferential scattering in the forward direction leads to momentum transfer from the CRs to the gas via the waves as a mediator. We will discuss the astrophysical implications in the context of GWs in Sect. 4.

In summary, turbulence is responsible for efficient mixing, as well as for generating structures, which are coupled non-linearly, on all scales in the ISM. It redistributes the energy from large to small scales, but also inverse cascades are possible, as e.g. in 2D turbulence.[1] In compressible turbulence, dissipation can also occur through shocks at all scales. Whereas scaling relations give some insight e.g. into the energy distribution, the evolution of non-linear structures in high Reynolds number flows like in the ISM require high resolution numerical simulations.

2.2 3D High Resolution Modeling of the Interstellar Medium

Simulating whole galaxies is still beyond the scope of current computer power, because the wide range of structures to be resolved is simply too large, and following the turbulent cascade to the microscale is at present an insurmountable challenge. We have therefore opted for *mesoscale* simulations, in which the computational box contains a representative patch of the ISM, e.g. centred at the solar system, which is large enough on the one hand to include the largest ISM structures, in

[1] Decaying 2D turbulence is characterized by the emergence of coherent vortex structures due to self-organizing processes. These can lead to a distortion of the energy spectrum, in particular on the larger scales.

particular the integral scale at which turbulence is fed in, and small enough on the other hand to achieve sufficient resolution for the most important physical length scales. However, it is presently impossible to resolve the dissipation scale, because for Reynolds numbers of e.g. 10^6 the microscale is $\eta/l_0 = Re^{-3/4}$, which yields $\eta \approx 3 \times 10^{-5} l_0$. We have found the energy injection scale to be $l_0 \sim 100\,\mathrm{pc}$ [19], so that $\eta \sim 3 \times 10^{-3}\,\mathrm{pc}$, which is about two orders of magnitude below our highest resolution of 0.375 pc on a Cartesian grid of $1 \times 1 \times \pm 15\,\mathrm{kpc}$ in x-,y- and z-direction, respectively (for a projection in the $x - z$-plane, see Fig. 1); some older simulations use $z = \pm 10\,\mathrm{kpc}$. If the box size would be smaller, we would not capture the outflow in z-direction (galactic fountain/wind) and could not evolve the ISM for sufficiently long enough time to wipe out the memory of the initial conditions, which are always artificial in a strongly non-linear dynamical system, captured in full swing. The development of subgrid models is still in its infancy, and at present most simulations use numerical instead of molecular viscosity to dissipate the energy. Another important length scale is the cooling length, which is $\lambda_c \sim c_s \tau_c \approx 3 k_B^{3/2}/(\mu \bar{m})^{1/2}\,(T^{3/2}/(n\Lambda(T)))$, where c_s is the isothermal speed of sound, τ_c the radiative cooling time scale, and $\mu, \bar{m}, n, \Lambda(T)$ are the mean molecular weight, the average atomic mass, the particle number density and the interstellar cooling function, respectively. The latter peaks at a temperature of $T \sim 10^5\,\mathrm{K}$ in the hot ISM phase, with a value of $\Lambda(T) \sim 10^{-21}\,\mathrm{erg\,cm^3\,s^{-1}}$, so that $\lambda_c \approx 0.5\,\mathrm{pc}$ for $n = 0.1\,\mathrm{cm^{-3}}$, which is well resolved in our simulations. Below the resolution limit, however, are the coolest and densest regions with e.g. $n = 10^3\,\mathrm{cm^{-3}}$ and $\Lambda(T) \sim 10^{-27}\,\mathrm{erg\,cm^3\,s^{-1}}$ at $T = 100\,\mathrm{K}$, yielding $\lambda_c \approx 1.5 \times 10^{-3}\,\mathrm{pc}$. Since we are not dealing in detail with molecule formation and chemistry in interstellar clouds, this shortcoming is acceptable within the framework of approximations.

It has been found that among the various energy input sources for turbulence in the ISM, SN explosions are the dominant ones [54]. Therefore we model a SN driven ISM. Our model treats a fixed gravitational field provided by the stellar disk with self-gravity and heat conduction included in some of the models, radiative cooling of an optically thin gas in collisional ionization equilibrium (CIE), and uniform heating due to starlight, varying with z [67]. The CIE implementation of radiative cooling uses a tabulated version à la Dalgarno and McCray [15] with an ionization fraction of 0.1 at temperatures below $10^4\,\mathrm{K}$ with a temperature cutoff at 10 K. Our initial model is based on the observed gas distributions in hydrostatic equilibrium, with the vertical distribution of the cool, warm, ionized and hot gases as described by Dickey and Lockman [22], Reynolds [59], and Ferrière [28].

The energy momentum and mass input sources are SNe types Ia, Ib + c and II, which are described by pistons in their Sedov phases, with radii determined by their progenitor masses. These are derived from initial mass functions (IMFs) applied to regions of star formation, which are chosen from the computational domain if their temperatures are below 10 K and the particle density above $100\,\mathrm{cm^{-3}}$; if the explosions occur in the field, no threshold criterion is applied. The SN rates are normalized to the volume of the stellar disk in which a specific SN is found and are taken from Ferrière ([27], see also references therein). The star forming disk has

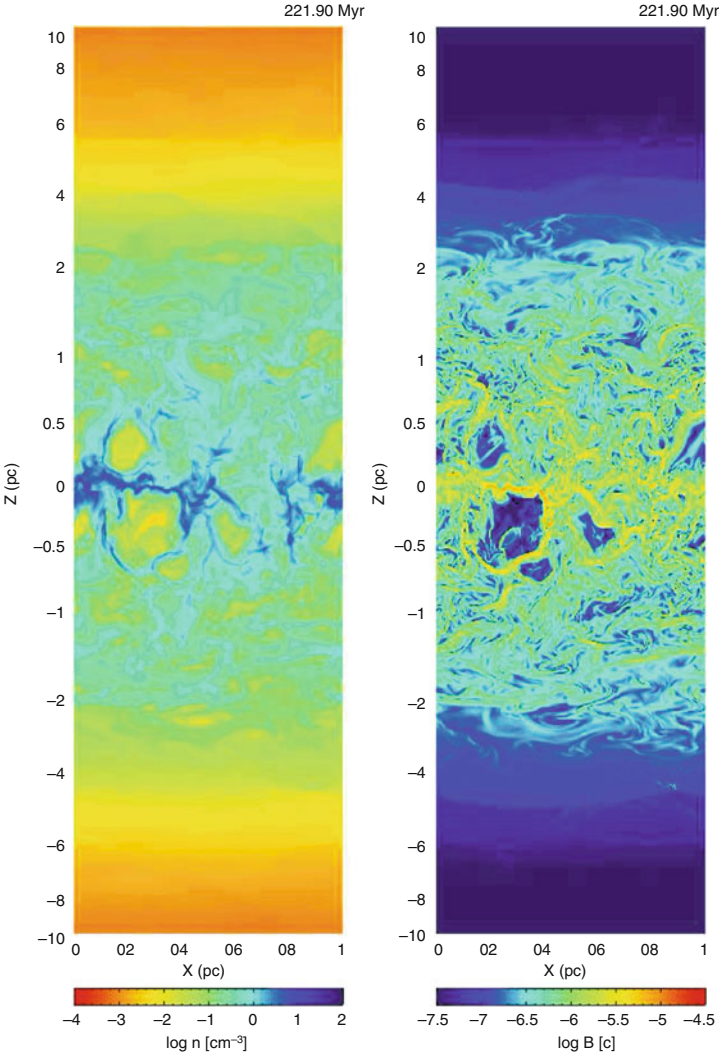

Fig. 1 Vertical slices through the 3D data cube showing the z-distribution of the density (*left*) and magnetic field (*right*) at time $t = 221.9$ Myr; the mean field is 3.1 μ G. The scale above and below ± 0.5 kpc is compressed for better representation. The colour coding is *red* for low/high density/B-field, while *dark blue* refers to the high/low density/B-field. The galactic midplane (at $z = 0$ kpc) becomes severely distorted by the break-out of superbubbles, and the density distribution in the halo is more clumpy than for simulations without magnetic field. The vertical outflow is characterized by large scale coherent B-field structures, e.g. magnetic loops and islands, due to the effect of the magnetic tension forces. The field is very tangled on small scales, and numerical diffusivity will allow for magnetic reconnection at the resolution limit (Figure taken from AB05, reproduced with permission ©ESO)

a radius of 12 kpc for all stellar disks, with their half thicknesses being twice the scale height of the corresponding SNe distributed in the field. The scale height of Type Ia SNe is 325 pc [29], whereas the scale height of Population I stars depends on whether the stars are in the field or in associations. About 40 % of SNe types Ib + c and II are placed randomly in the ISM with an exponential scale height of 90 pc, while 60 % explode in associations with a scale height of 46 pc, following the distribution of the molecular gas in the Galaxy.

2.3 Results

We have performed high resolution numerical 3D simulations without ([16, 21], AB04) and with magnetic field ([20], AB05), following the evolution of structures well into the non-linear regime, for as long as 400 Myr. In both types of simulation, there was always a vertical outflow of gas from the disk into the halo, driven by SN activity in the disk (see Fig. 1). Even for a Galactic SN rate, about 20 % of the halo mass was leaving the vertical extension of the box at $|z| = 10$ kpc. In the disk, structures on all scales are visible, reinforcing the importance of turbulence. Considering the traditional picture of the ISM, which has entered the textbooks, according to which the gas is distributed into distinct stable phases, regulated by SN explosions with mass and energy exchange at constant pressure, our results, in agreement with other authors (e.g. [40, 45]), have led to a change of paradigm.

We find that (i) the hot intercloud medium (HIM) fills only about 20 % of the disk volume (in contrast to 50–70 % of McKee and Ostriker ([56], MO77)), never exceeding 50 % even for an increase in SN rate by a factor of 16, corresponding to a starburst, (ii) it takes about 150 Myr for reaching a dynamical equilibrium at constant SN rate after having established the disk-halo duty cycle, (iii) about 55 % of the mass is in the *thermally unstable* warm neutral medium (WNM), in agreement with observations by Heiles and Troland [36] who find a value of 47 %, (iv) the correlation between magnetic field strength, $B \propto \rho^{1/2}$, the so-called Chandrasekhar-Fermi law [14], does not hold in general, but only marginally for the cold dense regions, (v) between $T \sim 10^2 - 10^6$ K, the flow is dominated by ram pressure, below by magnetic, and above this temperature regime by thermal pressure, (vi) the energy is fed in at an integral scale of ∼75 pc, according to the flattening of the second order structure function [19], which corresponds to the average break-up scale of superbubbles, (vii) turbulent mixing is the most efficient process to distribute ions and chemical elements in the ISM, (viii) clouds are shock compressed layers and thus transient features, (ix) the pressure is not uniform, and its average value is only about $P/k_B \sim 3{,}000\,\mathrm{K\,cm^{-3}}$.

In a turbulent ISM the correlation between high temperatures and low densities/magnetic fields (see Fig. 2) is not as strong and unique as in a medium with laminar flow due to the non-local character of turbulence.

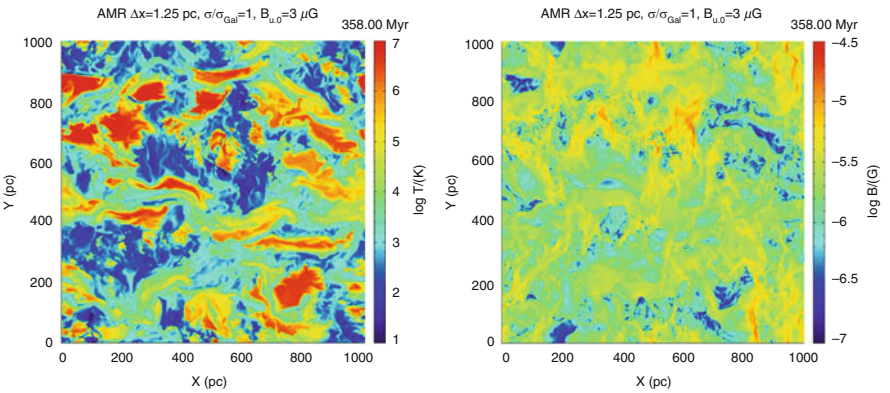

Fig. 2 2D cuts through the galactic midplane at $z = 0$, showing temperature (*left panel*) and magnetic field (*right panel*) after 358 Myr of evolution. The scale is logarithmic and the colour coding is *red*/*blue* for high/low temperatures and B-fields, respectively. High B-fields are usually associated with cold low-β plasma and high inertia. For higher temperature regions such a correlation becomes progressively weaker (Figure taken from AB05, reproduced with permission ©ESO)

3 Non-equilibrium Ionization (NEI) Structure

The simulations in Sect. 2.3 were carried out under the assumption that the ionization structure is always in equilibrium, i.e. collisional ionization is balanced by radiative recombination. This has been state of the art of all 3D simulations of the ISM hitherto. However, even disregarding the dynamics of the medium, i.e. letting the plasma cool isochorically or isobarically, the rates of collisional ionization and radiative recombination do not balance, so that as time goes by, the ionization structure is severely driven out of equilibrium [41, 62].

Consequently, the cooling rates, which depend on the presence of certain ions at a given time, vary as a function of time. Taking into account the dynamics of the plasma, the imbalance becomes even more severe, because adiabatic compression or expansion can change the kinetic temperature of the electrons significantly, while leaving the ionization structure at first unchanged. Hence ionization and recombination can be delayed, if for example a shock or a rarefaction wave passes over a certain fluid element, respectively. It can be shown [11] that fast adiabatic expansion of a plasma, which once was at a temperature of a few 10^6 K can emit X-rays at $\sim 10^4$ K (see Fig. 3). It is important to realize that the dynamical and thermal history of the plasma are inextricable. For instance the dynamics depends on the heating and cooling history and vice versa. Imagine a dynamically expanding plasma, in which the recombination time scale gets prolonged by the density decrease, which "freezes" the ionization stages into the plasma thus altering the cooling rate, which in turn changes the dynamics, closing a feedback loop. In collisional ionization equilibrium (CIE) the presence of an ionization stage of a

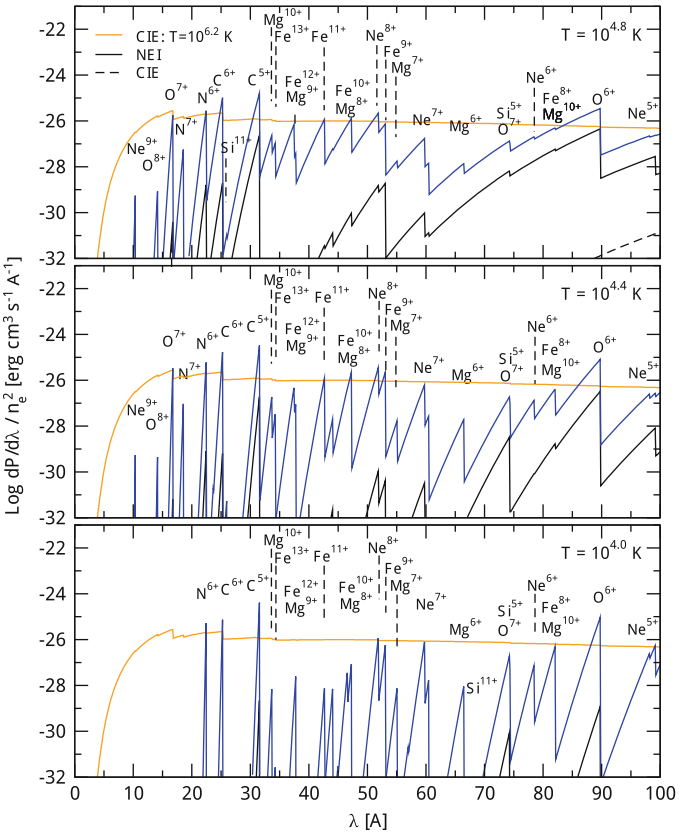

Fig. 3 The resulting NEI spectra at low kinetic electron temperatures from a 3D hydrodynamic simulation of a plasma initially at 10^6 K (see Fig. 4), ranging from $T = 10^{4.8}$ to 10^4 K (*top* to *bottom*), show prominent recombination edges at soft X-ray temperatures, even surpassing at times the CIE emission from a $10^{6.2}$ K(!) plasma (*orange line*); prominent ionization stages are labelled accordingly. The *solid black line* represents the static isochoric NEI spectrum for a plasma initially at 10^9 K. The CIE emission at the temperature indicated is given by the *dashed line*, and is so small that it is only visible in the lower right edge of the upper panel

certain element peaks at a specific temperature, and thus the observation of the most abundant ion in a plasma is a diagnostic for the plasma temperature. In contrast, in a plasma in a NEI state, ions can be present over a wide range of temperatures, e.g. over more than two orders of magnitude [10]. Although the measurement of ionization stages fails to be a reliable temperature proxy, the unique dependence of the thermal on the dynamical history offers the possibility to track the evolution of a plasma and its history.

We have recently managed to couple numerically the ionization structure to the hydrodynamical evolution of the plasma in 3D high resolution simulations of the kind described in Sect. 2.3 ([18] and references therein). A far reaching

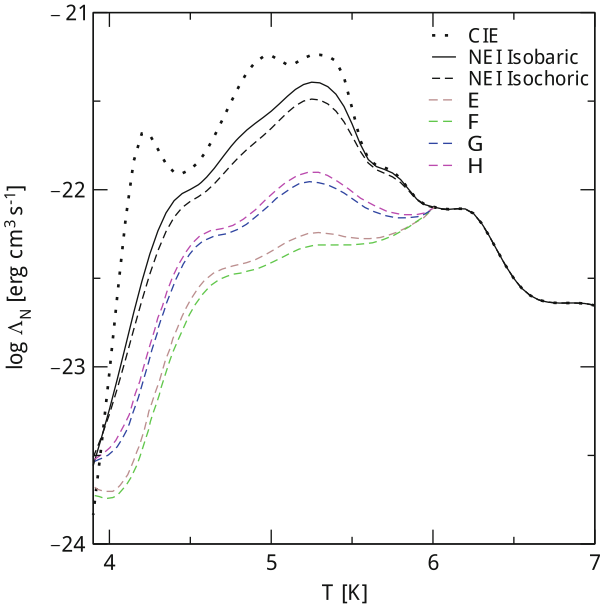

Fig. 4 Comparison of cooling functions, from *top* to *bottom*: standard (CIE) is represented by the *dotted line*, the isobaric and isochoric static (NEI) cooling functions by the *solid* and *dashed lines*, respectively; the coloured lines describe dynamic cooling functions for different thermodynamic cooling paths of the plasma with the labels denoting regions with the same initial temperature of 10^6 K, but having different cooling histories; they correspond from *top* to *bottom* to different regions labeled "H", "G", "E" and "F", respectively in the corresponding NEI simulation. The space and time-dependence of the interstellar cooling function is clearly visible, and differences with respect to CIE can be more than a factor of 10

consequence of these investigations is the insight that cooling is both spatially and temporally dependent, and can differ by more than an order of magnitude from CIE (see Fig. 4). Other striking results from these NEI simulations are (i) an enhanced electron density, especially at lower temperatures, which can very well explain observed pulsar dispersion measures up to 4 kpc in the Galactic plane [17], (ii) an increased concentration of OVI (up to 70 %) in thermally unstable temperature regimes, and (iii) a more realistic distribution of Li-like ions in the local ISM, allowing a better constraint of the age of the Local Bubble.

The largest effects of NEI effects due to delayed recombination can be expected in galactic outflows driven by starbursts [7, 10]. Due to the density decrease out of the plane, upward flows accelerate and lead naturally to fast adiabatic expansion, essentially freezing in high ionization stages, which slowly recombine. The energy thereby released is the ionization energy stored in highly ionized species close to the disk. The resulting halo X-ray spectrum thus mimics an "overionized" plasma, and is well constrained by the dynamics of the starburst driven wind [7].

4 Starburst and Cosmic Ray Driven Galactic Winds

The Galaxy is permeated by magnetic fields and filled with a sea of high energy particles (CRs) having a power law distribution in energy. Since the particles are ultrarelativistic, their light crossing time in the disk is of the order of 10^5 year, which is much less than their residence time in the Galaxy. Since the observed flux is almost isotropic, and the CRs strongly interact with MHD waves, this can only mean that the particles perform a random walk in the Galaxy due to strong pitch angle scattering off magnetic irregularities. This is conveniently described by spatial diffusion, with a particle drift speed of the order of the Alfvén speed. From the amount of secondaries, like e.g. ^{10}Be, resulting from spallation reactions between primaries and interstellar gas, it is known that the CR residence time is of the order of $\tau_r \sim 1.5 \times 10^7$ year, and from the amount of gas that particles have traversed on average ("grammage") before reaching the Earth, it is inferred that they spend most of their time outside the disk in the Galactic halo. Since CRs leave the Galaxy on a time scale τ_r, they have to be constantly replenished by an energy rate of $F_c \sim E_c V_c/\tau_r \approx 4.7 \times 10^{40}\,\mathrm{erg\,s^{-1}}$ for a mean CR energy density of $E_c \sim 0.5\,\mathrm{eV\,cm^{-3}}$ (comparable to the thermal energy density in the ISM) in a CR confinement volume of $V_c \approx 1.8 \times 10^{67}\,\mathrm{cm^3}$, which is given by the cylindrical radius of the star forming disk of 10 kpc and a CR halo extension of 1 kpc in the perpendicular direction. Such a large replenishment rate can only be maintained by sources distributed all over the disk with a considerable energy output like SNRs. Adopting a Galactic SN rate of $\epsilon_{\mathrm{SN}} \sim 2$ per century and a hydrodynamic energy release of $E_{\mathrm{SN}} \sim 10^{51}$ erg, we obtain $F_{SN} \sim \epsilon_{\mathrm{SN}} E_{\mathrm{SN}} \approx 6.7 \times 10^{41}\,\mathrm{erg\,s^{-1}}$; thus about 7 % of the available SN energy has to be converted into the acceleration of particles, a value easily reached by the first order Fermi process (diffusive shock acceleration) as has been demonstrated by numerical simulations (e.g. [5]), who derive a value of up to 20 % for an injection rate of 10^{-4} of suprathermal particles. They also find an energy spectrum power law index of $\gamma = 2.1$ in agreement with observations, which yields $\gamma = 2.7$, with the difference accounting for energy dependent diffusion with a coefficient $\kappa(E) \propto E^{-0.6}$. Given these facts, and their resonant interaction with MHD waves (see Sect. 2), particle transport in the Galaxy and its halo is diffusive as well as advective. The latter is due to momentum transfer from the CRs to the plasma or vice versa via frozen in MHD waves. The secular escape of CRs from the Galaxy leads to a net drift and preferential scattering in the forward direction and thus to streaming of the particles out of the Galaxy. If we are only interested in the pressure force exerted by CRs on the gas, the information about the distribution function may be discarded in favour of the pressure, which is obtained by taking the second order moment over momentum subspace, $p_c = 1/3 \int_0^\infty p\, v f(\mathbf{x}, \mathbf{p}, t)\, d^3p = 4\pi/3 \int_0^\infty p^3\, v f(\mathbf{x}, p, t)\, dp$, where v is the particle speed, for an isotropic momentum distribution, leading to CR hydrodynamics. The hydrodynamic equivalent of the resonant wave generation by CRs is given by

$$\frac{1}{\gamma_c - 1}\frac{\partial p_c}{\partial t} + \nabla \mathbf{F_c} - (\mathbf{u} + \mathbf{v_A})\nabla p_c = 0$$

$$\mathbf{F_c} = \frac{\gamma_c}{\gamma_c - 1}(\mathbf{u} + \mathbf{v_A})\, p_c - \frac{\bar{\kappa}}{\gamma_c - 1}\nabla p_c\,, \tag{6}$$

where $\mathbf{F_c}$ is the CR energy flux density, $\gamma_c = 4/3$ is the adiabatic index for a relativistic CR gas, and $\bar{\kappa}$ is the (Rosseland) mean CR diffusion coefficient. Also the MHD waves exert a pressure on the plasma, which is given by $p_w = \langle(\delta\mathbf{B})^2\rangle/(8\pi)$, where $\delta\mathbf{B}$ is the fluctuation amplitude of the magnetic irregularities. The waves are excited by the CR streaming instability [51], with a resonant wavelength of the order of the particle gyroradius. Their growth rate can be expressed in hydrodynamic form, describing the exchange of energy between particles and waves (e.g. [57]):

$$2\frac{\partial p_w}{\partial t} + \nabla\left(p_w(3\mathbf{u} + 2\mathbf{v_A})\right) = \mathbf{u}\nabla p_w - \mathbf{v_A}\nabla p_c\,. \tag{7}$$

If we add the CR and wave pressure terms as well as their energy flux densities, Eq. (6) and (7), to the set of hydrodynamic equations, we can describe CR and wave driven GWs (for details, see [9] and [69] for including galactic rotation). In the model outlined in the following, the geometry of the outflow is constrained by the magnetic field, which has a component perpendicular to the disk, $\mathbf{B} = (0, 0, B_z)$. The field geometry has to be calculated self-consistently from the CR MHD equations. But the problem can be simplified considerably by introducing a flux tube geometry, which is essentially 1D, where the magnetic field describes a geometry, which is plane parallel near the disk and spherically diverging at distances comparable to the galactic radius R_g; thus the flux tube cross section is given by $A(z) = A_0(1 + (z/R_g)^2)$, while $\nabla \cdot \mathbf{B} = 0$, hence $B_z A(z) = B_0 A_0$, with B_0 and A_0 being the value of the magnetic field and the flux tube area cross section, respectively, at the base of the halo, which is set at $z_0 = 1\,\mathrm{kpc}$ (see [9]). Due to the strong growth of waves because of the CR pressure gradient perpendicular to the disk, one can show that at a distance of about 1 kpc, CR advection starts to dominate diffusion, leading to a change-over in CR transport [8].

In the limiting cases of a starburst, where the flow becomes supersonic close to the disk, or the average flow fed by many generations of superbubbles in the disk, the flow time to the sonic point is less than the energy source life time, and a steady flow is a good description. In other cases, the steady flow has to be interpreted as an average over a sufficiently large number of generations of stars formed in the disk. The existence of steady flows has been verified by time-dependent CR hydrodynamical calculations ([23], henceforth DB12). The solution topology of such flows are well-known from solar and stellar wind theory, although the geometry and the gravitational potential are different here, as well as the additional driving forces by CR and wave pressures. Figure 5 shows the solutions in case of a thermally driven GW, which is appropriate for starbursts, since the flow is mainly driven by the thermal pressure. Such winds are characterized by large mass loss rates and low

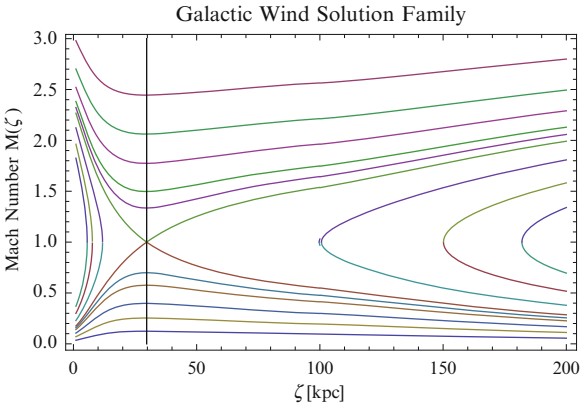

Fig. 5 Solution family of isothermal steady galactic wind flows, showing the Mach number $M(\zeta)$ as a function of normalized vertical distance $\zeta = z/z_0$, from the galactic plane. The curves were calculated for an initial temperature of $T_0 = 2 \times 10^6$ K, a density of $n_0 = 10^{-3}$ cm^{-3}, and a base magnetic field of $B_0 = 10^{-6}$ G at the reference level $z_0 = 1$ kpc, for a Milky Way gravitational potential (including dark matter halo, for details, see Breitschwerdt et al. [9]). The outflow solution is the curve, which starts subsonically at the inner boundary at $\zeta = 1$, passes through a critical point at which the flow becomes sonic, i.e. $M(\zeta) = 1$, at $z_c = 29.7$ kpc (indicated by the *vertical line*), and proceeds supersonically towards a terminal velocity

terminal velocities, whereas winds with less thermal support and/or high densities (and thus strong cooling) are mainly driven by the CRs and the waves, and have typically lower mass loss rates but higher terminal velocities [9]. The growth of waves is very fast, and once $\delta B/B \sim 1$, quasi-linear theory breaks down, and strong damping sets in, resulting in wave dissipation and additional heating of the gas. A self-consistent model can be obtained if the growth of waves is locally balanced by non-linear Landau damping [58], according to which thermal particles are trapped in the beat wave created by two non-linearly coupled Alfvén waves (preferentially traveling along the magnetic field). This also allows to calculate the CR diffusion coefficient.

Outflow solutions start at low Mach numbers close to the disk, pass through a sonic or critical point $M(\zeta) = 1$ (for $\zeta = z/z_0$) and converge asymptotically to a supersonic terminal velocity. Theoretically also transsonic accretion solutions as well as "breeze" flows (remaining always subsonic) are possible (see Fig. 5). The mass loss rate is fixed at the reference level by an initial velocity, if the density is given as a boundary condition (or vice versa), and is for an individual flux tube $dm/dt = \rho_0\, u_0\, A_0$.

How does the flow know, which u_0 it has to pick for a transsonic outflow? The condition that the solution passes through a critical point is that the external pressure p_{ext} at infinity tends to zero. In reality, in starburst galaxies (similar to the solar wind flow) p_{ext} is finite, and the flow has to be accommodated by a termination shock. The critical condition for a steady GW flow is that the total pressure at the critical point

exceeds the external pressure. In the following we will discuss the implication of GWs on the acceleration of CRs beyond the "knee" (Sect. 5), and the contribution of GWs to the metal enrichment of the intracluster medium in clusters of galaxies (Sect. 6).

5 Cosmic Ray Acceleration Beyond the "Knee"

The differential energy spectrum of CRs is given by a broken power law with $N(E)\,dE = K\,E^{-\gamma}\,dE$, with $\gamma = 2.7$ for $10^9 < E < 10^{15}$ eV ("knee"), a steepening to $\gamma = 3.1$ for $10^{15} < E < 10^{18}$ eV ("ankle") and, presumably, a flattening to $\gamma = 2.7$ for $10^{18} < E < 6 \times 10^{19}$ eV, with a final steepening beyond due to the GZK cut-off [33, 68], as a result of π^0/π^+-production via scattering off the cosmic microwave background photons. Whereas there is accumulating evidence, that CR nucleon acceleration up to the knee is achieved by diffusive shock acceleration (DSA) in SNRs (for a classical review see [24]), the acceleration mechanism between the knee and the ankle is still debated.

The maximum attainable energy E_{max} in a cosmic accelerator can be estimated from (i) the magnitude of the induced electric field, which is according to Faraday's law $\nabla \times \mathbf{E} = -(1/c)\partial \mathbf{B}/\partial t$ or to order of magnitude $E/L \sim B/(c\tau) \sim BV_s/(cL)$, considering that the acceleration time scale is $\tau \sim L/V_s$, where L is the scale of the accelerator and V_s the shock velocity, and (ii) the work performed on the particle by the Lorentz force $E_{max} = \int_0^L F_L dx = \int_0^L ZeE dx = ZeBV_sL/c$. Since particle acceleration occurs mainly in the free expansion phase of the SNR while the shock speed is large, $V_s \sim 10^4$ km/s, and the size of the remnant is small, $L \sim 10$ pc, we obtain for a magnetic field of the order 10^{-6} G a value of $E_{max} \sim 4.8 \times 10^2$ erg or $\sim 3 \times 10^{14}$ eV, in agreement with more detailed calculations [13]; note that the gyroradius at this energy is already $r_g = \Gamma m v_\perp c/(ZeB) = pc/(ZeB) \approx 0.32$ pc for a proton, and due to the random walk of particles, the size of the acceleration region must be at least two times the gyroradius [37], before they are eventually convected downstream of the shock; here $v_\perp$, Γ are the velocity component perpendicular to the magnetic field and the Lorentz factor, respectively. Therefore DSA of particles in SNRs can explain the spectrum up to the knee, and up to $\sim 10^{16}$ eV for iron nuclei with $Z = 26$, but not further. One way of carrying on with DSA is to look at B-field amplification, as has been suggested by Völk and Biermann [65] for SN explosions into the compressed shell of a progenitor stellar wind bubble with a high azimuthal B-field strength, or with significant excitation of waves upstream of the forward shock [4]. It has indeed been reported on the basis of rapid X-ray variability in a young SNR [64], that fluctuations in synchrotron brightness of relativistic electrons imply a B-field amplification by a factor of 100 or more. The term $\mathbf{v_A} \nabla p_c$ in Eq. (7) is responsible for wave growth, which is very fast. In a SNR forward shock, $V_s \gg v_A$, and since the shock width is also small compared to its radius, we can it treat as planar with quantities across

it not varying in time appreciably. Hence $(V_s/8\pi)\partial(\delta B)^2/\partial x \sim v_A \partial p_c/\partial x$ or $(\delta B)^2/B^2 \sim (V_s/v_A)p_c/(\rho V_s^2)$. As we have seen, in SNRs the CR pressure can be $\sim$10 % of the kinetic energy density, i.e. $p_c \sim 0.1\rho V_s^2$, and since $V_s > 10^3\, v_A$, this shows that wave growth upstream of the shock is possible due to CR streaming, and $\delta B/B \sim 10^3$, resulting in $E_{max} \sim Z \times 10^{17}$ eV. This estimate, as has been shown in [53], has to be replaced by an analysis of the turbulent non-linear wave spectrum, because quasi-linear theory breaks down for $\delta B/B \geq 1$. While this offers an attractive possibility of extending DSA in SNRs to higher energies, it is not clear why a spectral steepening should occur beyond the knee. A possible explanation could be that the number of sources, accelerating particles to energies beyond the knee, is limited, because (i) only SNRs in the free expansion phase are capable to reach very high energies, if the field is amplified, and, (ii) the maximum values require explosions into a pre-structured medium by stellar winds.

The smooth transition between the spectra before and after the knee at precisely the energy where DSA in SNRs ceases, argues for a Galactic rather than an extragalactic acceleration source, while the spectral steepening supports a change in accelerator. We have shown that DSA in GW shocks offers such a possibility (see DB12). As shown in Sect. 2.3, even at moderate Galactic SN rates, there is a constant flow of gas into the halo with some fraction escaping as a wind. Time-dependence of the SFR, and hence also the SN rate in the disk, leads to the propagation of shocks into the halo (see Fig. 6). Since these shocks are long-lived (of the order of $10^7 - 10^8$ year), the maximum attainable energy is $E_{max} = ZeBV_sL/c = ZeBV_s^2t/c \sim 3 \times 10^{16} - 3 \times 10^{17}$ eV, for shock speeds $V_s \sim 1{,}000$ km/s (see Fig. 7), and B-fields of $\sim 10^{-6}$ G. Figure 7 shows that the speed of both the forward and reverse shock can be constant for a long time. The reason is because in a wind flow the distance the shock has travelled is $z_s \propto t^{3/(5+\beta)}$, with the upstream density $\rho(z) \propto z^\beta$. At distances $L \sim R_g$, the flux tubes open up, $A(z) \propto z^2$, and since the background fluid quickly reaches a flow speed, $u(z) \sim const.$, it follows that $\rho(z) \propto 1/(u(z)A(z)) \propto 1/z^2$, and $\beta = -2$. Thus the shock speed is $dz_s/dt = V_s =$ const., in agreement with Fig. 7. Thus in contrast to DSA in a SNR, the shocks (both forward and reverse) remain strong over a long time, and particles can remain over a sufficiently long time in the accelerator to reach high maximum energies.

But there is a further advantage of this acceleration mechanism: even higher energies can be reached if the particles, which are injected into the flow, are CRs already pre-accelerated in SNRs in the Galactic disk. This also enables a smooth transition to the highest energies, with particles being convected downstream back to the disk, where they can be observed; note that the GW termination shock, which is located at large distances from the disk, and has also been invoked as a site of particle acceleration to energies beyond the knee [39], faces in the opposite direction. The maximum momentum $p_{\max}$ to be attained can be estimated in the test particle picture with $dp_{\max}/dt \sim p_{\max}/\tau_{\rm acc}$ (e.g. [24]), where $\tau_{\rm acc} =\simeq 4\kappa(p)/V_s^2$, and the momentum dependent diffusion coefficient is given by $\kappa(p) \simeq (1/3)\,(mc^3)/(ZeB_0^2 z_0)\, V_s^2\, t^2\, p$ (for details see DB12). This can be

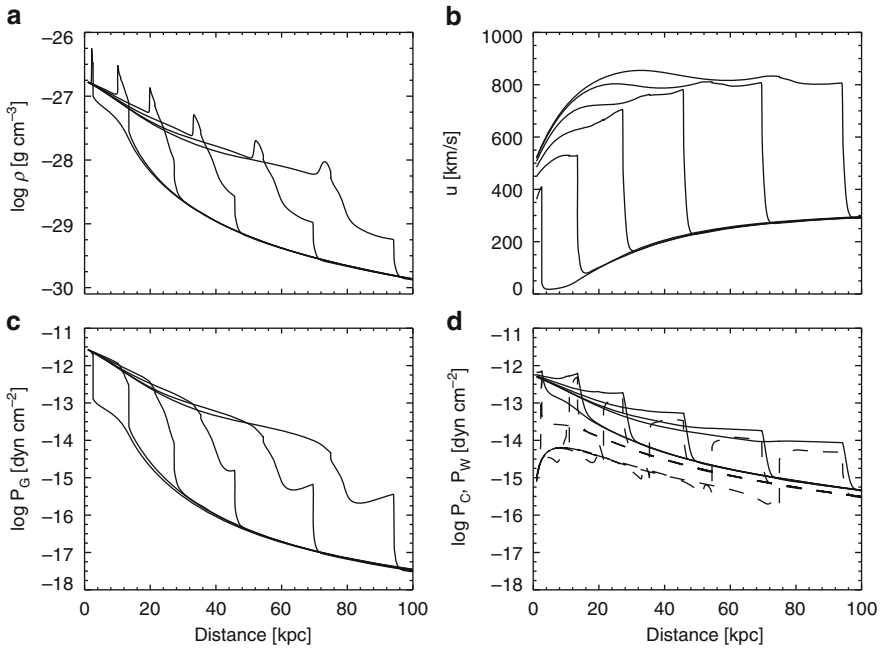

Fig. 6 Galactic wind flow profiles in the flux tube representing the geometry of the wind are shown out to a distance of 100 kpc at six different times between at 3.4×10^6, 2.0×10^7, 3.6×10^7, 5.4×10^7, 7.7×10^7 and 1.0×10^8 years for initial parameters at the base level (boundary conditions) $z_0 = 1$ kpc. The background wind flow is given by a flux tube opening parameter $R_g = 15$ kpc, and $\rho_0 = 1.67 \times 10^{-27}$ g cm^{-3}, $p_{g0} = 2.76 \times 10^{-13}$ dyne cm^{-2}, $p_{c0} = 10^{-13}$ dyne cm^{-2}, $p_{w0} = 4.0 \times 10^{-16}$ dyne cm^{-2}, $B_0 = 10^{-6}$ G, $\kappa = 10^{29}$ cm^2 s^{-1} for the gas density, gas, CR and wave pressures, vertical magnetic field component and CR diffusion coefficient parallel to the field, respectively. The gravitational potential corresponds to a Miyamoto-Nagai potential including a dark matter halo; for details see DB12. At $t = 0$, both the gas and cosmic ray pressures are increased by a factor of 10 at the inner boundary of the flux tube, representing SN explosions in the underlying disk. In panel (**a**) we show the density, in panel (**b**) the fluid velocity with the forward and reverse shock waves showing up as prominent features, in (**c**) the gas pressure, and in (**d**) both the CR (*solid line*) and the MHD wave (*dashed line*) pressures, respectively (Figure taken from DB12, reproduced with permission ©ESO)

straightforwardly integrated to $p_{\max} = p_0 + A(1/t_0 - 1/t)$, with the integration constant $A = 3Z\,e\,B_0\,z_0^2/(4mc^3)$. The result is shown in Fig. 8, where the increase in momentum due to DSA can be seen both for the forward and the reverse shock. The CR energy may be considerably boosted by multiple shocks propagating through the galactic halo as a consequence of time-dependent star formation in the disk. It is noteworthy that the acceleration is quite fast, and the maximum momentum is reached within $z = 10$ kpc. Thus the particle flux back to the disk will be still significant, and geometrical dilution does not seem to be a problem.

For starburst galaxies, which is rather a phase in galactic evolution than a morphological type, this effect becomes most pronounced. We have simulated a

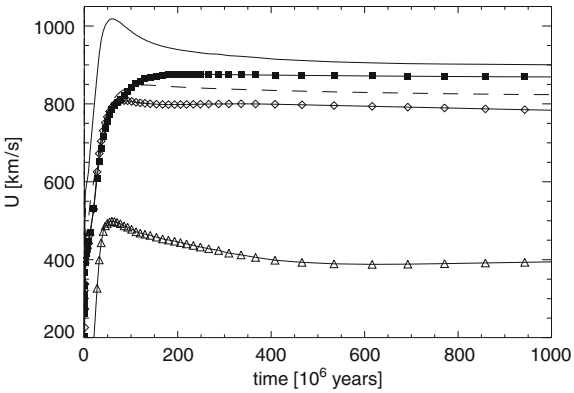

Fig. 7 Flow velocities associated with galactic wind structures (cf. Fig. 6), given in the rest frame of the galaxy. The following curves can be distinguished: velocities of forward shock (*solid line*), reverse shock (*dashed line*), upstream and downstream velocity of the reverse shock (*filled squares* and *open triangles*, respectively), and the upstream velocity (three diffusion lengths, $\tilde{\kappa}/V_s$, ahead of the shock) of the forward shock (*open diamonds*). Note that constant speeds are attained at distances less than 50 kpc (corresponding to time scales of less than 7×10^7 year) (Figure taken from DB12, reproduced with permission ©ESO)

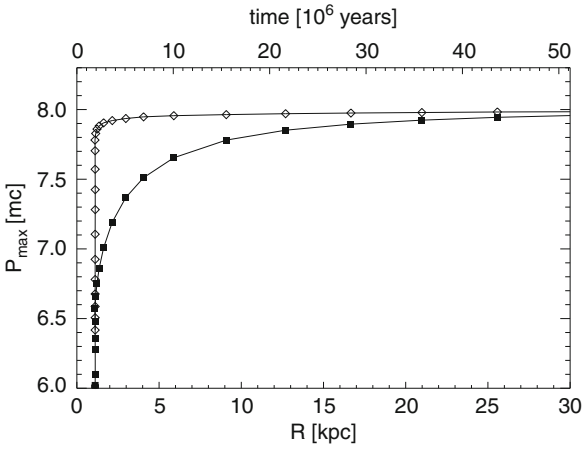

Fig. 8 Particle acceleration at the forward (*filled squares*) and both forward and reverse (*open diamonds*) shocks. The maximum momentum $p_{\max}$ is given in units of $[mc]$ as a function of distance from the disk and the acceleration time, respectively. $p_{\max}$ is already reached within a few kpc distance from the disk, corresponding to about 10^7 year (Figure taken from DB12, reproduced with permission ©ESO)

starburst by increasing the gas and cosmic ray pressures at the base of the halo by a factor of 10 and keeping them constant. The results are qualitatively the same as in Fig. 6, which shows as a result of nonlinear gas and CR hydrodynamics, the gas density, the velocity and the CR and MHD wave pressures, respectively. For example the gas density profile (panel (a)) nicely reveals the different waves travelling in the flow at six different times. From left to right one can distinguish the reverse shock, a rarefaction wave, contact discontinuity and the forward shock. In panel (d) one can see, not surprisingly, that the CR dominates the wave pressure,

because the waves are generated at the expense of the CRs by the streaming instability, and that both are dominating the gas pressure at larger distances. Looking more closely at the shocks, one may note that due to the non-linear back-reaction from the CRs on the gas near the shock as the site of acceleration, there is a CR precursor due to particle diffusion upstream. Particle acceleration occurs at both the forward and the reverse shock. However, particles accelerated at the latter have to diffuse back to the disk, which acts as a filter on lower energy CRs not being able to propagate backwards because of energy dependent diffusion. This will change the power law index.

Observationally, in the nearby starburst galaxy NGC 253, which has been seen in X-rays to exhibit a large scale galactic halo [3], circum-nuclear emission has also been detected in γ-rays with H.E.S.S. [2] and with Fermi LAT (as well as in M 82, Abdo et al. [1]). The emission can be explained by the interaction of CRs with the interstellar gas and radiation fields. The relativistic electron populations in these two starburst galaxies have been found already some time ago by nonthermal radio continuum emission [35, 47].

6 Galactic Winds in Clusters of Galaxies

GWs are a natural phase of galaxy evolution, and their strength will be modulated by the SFR of the underlying galactic disk. These winds can reach considerable distances and will eventually be shocked by the finite pressure of the intergalactic medium (IGM), as well as by nearby galaxies, resulting in the formation of bow shocks. It should be borne in mind that these winds carry chemically enriched material, transported from the underlying star forming or starburst regions in the disk into the halo and eventually into the IGM. It is thus possible to account for metal absorption lines in the IGM. If the galaxies are in groups or in clusters, GWs will contribute to the high metallicities, up to about $Z/Z_{\odot} \sim 0.3$ [30], measured in the intracluster medium (ICM). The most important processes for metal enrichment in the ICM, leaving the possibility of direct pollution by SN explosions in the ICM aside, are ram pressure stripping and GWs. The former is more efficient towards the centre of the cluster, because of the increase of ICM density. A simple criterion has been given by Gunn and Gott [34], according to which ISM in galaxies is stripped, if the ram pressure exceeds the gravitational restoring force, $\rho_{\rm IGM} v_{\rm gal}^2 > 2\pi G \Sigma_* \Sigma_g$; here $\rho_{\rm IGM}$, $v_{\rm gal}$, Σ_*, Σ_g, denote the IGM gas density, the velocity of the galaxy with respect to the cluster centre of mass, and the surface densities of the stars and gas in the galaxy, respectively. On the other hand, GWs, at least if they are steady, are suppressed near the cluster centre, if the external pressure exceeds the total pressure (gas, CRs and waves) at the sonic point of the flow. In contrast to ram pressure stripping the mass ejection rate does not depend on the ICM density, and thus winds will be more efficient at larger distances from the cluster centre (see [60]). This is also reflected by the substructure in the ICM metal distribution due to infall of

groups and small clusters, where again GWs offer a natural explanation when ram pressure stripping is weak.

7 Summary and Conclusions

Star formation is the motor of galactic structure and evolution. The interaction between stars, in particular the high mass tail of the IMF, and the ISM via HII regions, stellar winds and SN explosions changes the state of the gaseous disk profoundly. Since the medium is highly compressible and turbulent, structures occur on all scales, and a substantial amount of the mass is in thermally unstable temperature regimes. The long-term evolution can only be followed by high resolution numerical simulations, which are capable of tracing the non-linear interaction of compressive and Alfvén waves (in case of a strongly magnetized medium).

Due to their comparable energy densities, a dynamical coupling between plasma, magnetic field and CRs has to be taken into account. It is thus possible to transfer momentum from the CRs to the gas, and assist the thermal pressure in driving a GW, thereby injecting mass, momentum and energy into the IGM. Since the outflow consists of material which has a higher metallicity than the average ISM, the chemical enrichment of the ISM will be slowed down. In addition, galaxies are also exposed to infall due to primordial gas from galaxy formation and tidal interactions with neighbouring galaxies, like e.g. the Magellanic clouds in case of the Milky Way. Again, this results in a dilution of the metallicity in the galaxy, because the infalling gas has usually a (much) lower metallicity than a large accreting spiral. The description of infall is a lot easier than outflow, because it just appears as a source of mass and momentum in the continuity and momentum equations, respectively, and adds some kinetic energy to the galaxy because of the release of its potential energy. The infalling gas may exhibit cometary-like tails and bow shocks if it interacts with the outflowing gas. Whereas in the local universe inflow may be just a contaminant by diluting somewhat the interstellar metallicity, it was by far the dominant process in the early universe. We will explore these processes in more detail in the future.

Acknowledgements DB thanks the organizers for their invitation, and Olaf Reimer for many useful comments that helped to improve the manuscript.

References

1. Abdo, A.A., and the Fermi/LAT Collaboration (2010), ApJ, 709, L152
2. Acero, F., and the H.E.S.S. Collaboration (2009), Science, 326, 1080
3. Bauer, M., Pietsch, W., Trinchieri, G., Breitschwerdt, D., Ehle, M., Freyberg, M. J., Read, A. M. (2008), A&A, 489, 1029
4. Bell, A.R., Lucek, S.G. (2001), MNRAS, 321, 433
5. Berezhko, E.G., Yelshin, V.K., Ksenofontov; L.T. (1994), APh, 2, 215

6. Boldyrev, S. (2005), ApJ, 626, L37
7. Breitschwerdt, D. (2003), Rev. Mex. Astron. Astrophys., 15, 311
8. Breitschwerdt, D., Dogiel, V.A., Völk, H.J. (2002), A&A 385, 216
9. Breitschwerdt, D., McKenzie, J.F., Völk, H.J. (1991), A&A 245, 79
10. Breitschwerdt, D., Schmutzler, T., (1999), A&A, 347, 650
11. Breitschwerdt, D., Schmutzler, T. (1994), Nature 371, 774
12. Cen, R., Ostriker, J.P. (1999), ApJ, 514, 1
13. Cesarsky, CJ., Lagage, P.O. (1983), A&A, 125, 249
14. Chandrasekhar, S., Fermi, E. (1953), ApJ, 118, 113
15. Dalgarno, A., McCray, R. A. (1972), ARA&A, 10, 375
16. de Avillez, M.A. (2000), MNRAS, 315, 479
17. de Avillez, M.A., Ashgekar, A., Breitschwerdt, D. Spitoni, E. (2012), MNRAS, 423, L107
18. de Avillez, M.A., Breitschwerdt, D. (2012), ApJ, 756, L3
19. de Avillez, M.A., Breitschwerdt, D. (2007), ApJ, 665, L35
20. de Avillez, M.A., Breitschwerdt, D. (2005), A&A, 436, 585 (AB05)
21. de Avillez, M.A., Breitschwerdt, D. (2004), A&A, 425, 899 (AB04)
22. Dickey J. M., & Lockman F. J. (1990), ARA&A 28, 215
23. Dorfi, E.A., Breitschwerdt D. (2012), A&A, 540, 77 (DB12)
24. Drury, L. O'C. (1983), Rep. Prog. Phys., 46, 973
25. Elmegreen, B. G., Scalo, J. (2004), ARA&A, 42, 211
26. Elsässer, W. M. (1950), Phys. Rev., 79, 183
27. Ferrière, K. M. (2001), Rev. Mod. Phys., 73, 1031
28. Ferrière, K. M. (1998), ApJ, 503, 700
29. Freeman, K. C. (1987), ARA&A, 25, 603
30. Fukazawa, Y., Kawano, N., Kawashima, K. (2004), ApJ, 606, L109
31. Fukugita, M., Peebles, P.E.J. (2004), ApJ, 616, 643
32. Goldreich, P., Sridhar, S. (1995), ApJ, 438, 763
33. Greisen, K., (1966), Phys. Rev. Letters, 16, 748
34. Gunn, J.P., Gott, J.R.. (1972), ApJ, 176, 1
35. Heesen, V., Beck, R., Krause, M., Dettmar, R.J. (2009), A&A, 494, 563
36. Heiles, C., Troland, T. H. (2003), ApJ, 586, 1067
37. Hillas, A.M. (1984), ARA&A, 22, 425
38. Iroshnikov, P.S. (1963), AZh, 40, 742 (1964, Soviet Astron., 7, 566)
39. Jokipii, R., Morfil, G.E. (1985), ApJ, 290, L1
40. Joung, M.K.R., MacLow, M.M. (2006), ApJ, 653, 1266
41. Kafatos, M. (1973), ApJ, 182, 433
42. Kennicut, R.C. (1998), ARA&A, 36, 189
43. Klypin, A., Zhao, H., Somerville, R. (2002), ApJ, 573, 597
44. Kolmogorov, A. N. (1941), Akad. Nauk SSSR Dokl., 30, 299
45. Korpi M. J., Brandenburg A., Shukurov A., Tuominen I., Nordlund A. (1999), ApJL, 514, 99
46. Kraichnan, R.H. (1965), Phys. Fluids, 8, 1385
47. Kronberg, P.P., Biermann, P., Schwab, F.R. (1981), ApJ, 246, 751
48. Kulsrud, R.M., Pearce, W.D. (1969), ApJ, 156, 445
49. Landau, L.D., Lifshitz, E.M. (1959), *Fluid Mechanics*, Vol. 6, Pergamon Press
50. Larson, R.B. (1981), MNRAS, 194, 809
51. Lerche, I. (1967), ApJ, 147, 689
52. Lilly, S.J., Le Fevre, O., Hammer, F., Crampton, D. (1996), ApJ, 460, L1
53. Lucek, S.G., Bell, A.R. (2000), MNRAS, 314, 65
54. Mac Low, M.-M., Klessen, R. S. (2004), Rev. Mod. Phys. 76, 125
55. Madau, P., Ferguson, H.C., Dickoinson, M.E. et al. (1996), MNRAS, 333, L65
56. McKee, C. F., Ostriker, J. P. (1977), ApJ, 218, 148 (MO77)
57. McKenzie, J. F., Völk, H.J. (1982), A&A, 116, 191
58. Ptuskin, V.S., Zirakashvili, V.N., Völk, H.J., Breitschwerdt, D. (1997), A&A 371, 774
59. Reynolds R. J. (1987), ApJ, 323, 118

60. Schindler, S., Kapferer, W., Domainko, W., Mair, M., van Kampen, E., Kronberger, T., Kimeswenger, S., Ruffert, M., Mangete, O., Breitschwerdt, D. (2005), A&A, 453, L25
61. Schmidt, M. (1959), ApJ, 129, 243
62. Shapiro, P.R., Moore, R.T. (1976), ApJ, 207, 460
63. Silk, J. (2003), MNRAS, 343, 249
64. Uchiyama, Y., Aharonian, F.A., Tanaka, T., Takahashi, T., Maeda, Y. (2007), Nature, 449, 576
65. Völk, H.J., Biermann, P.L. (1988), ApJ, 249
66. von Weizsäcker, C.F. (1951), ApJ 114, 165
67. Wolfire, M. G., McKee, C. F., Hollenbach, D., Tielens, A. G. G. M., & Bakes, E. L. O. (1995), ApJ, 443, 152
68. Zatsepin, G.T., Kuz'min, V.A. (1966), JETPL, 4, 78
69. Zirakashvili, Breitschwerdt, D., V.N., Ptuskin, V.S., Völk, H.J. (1996), A&A 311, 113

Stellar Populations in the Galactic Center

G. Bono, N. Matsunaga, L. Inno, E.P. Lagioia, and K. Genovali

Abstract We discuss the stellar content of the Galactic Center, and in particular, recent estimates of the star formation rate (SFR). We discuss pros and cons of the different stellar tracers and focus our attention on the SFR based on the three classical Cepheids recently discovered in the Galactic Center. We also discuss stellar populations in field and cluster stars and present some preliminary results based on near-infrared photometry of a field centered on the young massive cluster Arches. We also provide a new estimate of the true distance modulus to the Galactic Center and we found 14.49 ± 0.02(standard) ± 0.10(systematic) mag ($7.91 \pm 0.08 \pm 0.40$ kpc). Current estimate agrees quite well with similar photometric and kinematic distance determinations available in the literature. We also discuss the metallicity gradient of the thin disk and the sharp change in the slope when moving across the edge of the inner disk, the Galactic Bar and the Galactic Center.

G. Bono (✉)
Dipartimento di Fisica, Universita' di Roma Tor Vergata, Via della Ricerca Scientifica 1, 00133 Roma, Italy

INAF– Osservatorio Astronomico di Roma, via Frascati 33, 00040 Monte Porzio Catone, Italy

Science visitor, European Souther Observatory, Karl-Schwarzschild-Str. 2 85748 Garching bei München, Germany
e-mail: bono@roma2.infn.it

N. Matsunaga
Department of Astronomy, School of Science, The University of Tokyo, 7-3-1 Hongo, Bunkyo-ku, Tokyo 113-0033, Japan
e-mail: matsunaga@astron.s.u-tokyo.ac.jp

L. Inno · E.P. Lagioia · K. Genovali
Dipartimento di Fisica, Universita' di Roma Tor Vergata, Via della Ricerca Scientifica 1, 00133 Roma, Italy
e-mail: laura.inno@roma2.infn.it; eplagioia@roma2.infn.it; katia.genovali@roma2.infn.it

D.F. Torres and O. Reimer (eds.), *Cosmic Rays in Star-Forming Environments*, Astrophysics and Space Science Proceedings 34, DOI 10.1007/978-3-642-35410-6_9,

The difference becomes even more compelling if we take into account that metal abundances are based on young stellar tracers (classical Cepheids, Red Supergiants, Luminous Blue Variables). Finally, we briefly outline the possible mechanisms that might account for current empirical evidence.

1 Introduction

The Galactic Bulge and the Galactic Center play a crucial role in constraining the formation and the evolution of the Galactic spheroid. Recent numerical simulations indicate that the Milky Way formed Inside-Out, this means that the bulge harbors the oldest Galactic populations [20]. This theoretical framework is soundly supported by recent photometric investigations [88] suggesting that stellar populations in the Galactic Bulge are mainly old ($\sim$11 Gyr). On the other hand, the Galactic Center together with the super-massive black hole, harbors, very young stars (a few Myr, [25, 73]), compact star clusters and massive molecular clouds [44].

Although current knowledge of the innermost components of the Galactic spheroid is quite solid, we still lack quantitative constrains concerning their kinematic structure and their chemical enrichment history. In particular, we still lack firm estimates of the edge between the thin disk and the Galactic Bulge. Moreover and even more importantly, current predictions suggest that a presence of a bar-like structure is crucial to support the high rate of star formation present in the Nuclear Bulge. Indeed, it is the bar-like structure to drag the gas and the molecular clouds from the inner disk into the Nuclear Bulge [4, 38, 39].

A more quantitative understanding of this phenomenon will have an impact into the formation and the evolution of classical bulges and pseudo-bulges. The latter are considered disk-like stellar components slowly evolving in galaxy centers, whereas the former are considered the aftermath of galaxy mergers [40]. The chemical evolution of the thin disk in the solar circle has been investigated using different stellar tracers and optical spectroscopy (Cepheids: [46, 63], open cluster: [11]). The same outcome applies for the Galactic Bulge [5, 89]. The chemical enrichment in the Galactic Center is still in its infancy [17, 60].

In the following we discuss recent findings concerning stellar populations in the Galactic Center. In particular, we will focus our attention on recent estimates of the star formation rate (Sect. 2.1) and on recent findings concerning field and cluster stellar populations (Sect. 2.2). Moreover, we will discuss in Sect. 3 recent determinations of the distance to both the Galactic Center and the Galactic Bulge. The metallicity distribution will be discussed in Sect. 4 while in Sect. 5 we briefly outline future perspective for photometric and spectroscopic investigations.

2 Stellar Populations and Star Formation in the Galactic Center

2.1 Star Formation

The star formation rate (SFR) across the Galactic Center was estimated by Genzel et al. [30] and more recently by Yusef-Zadeh et al. [85], they found that it was constant during the last few tens of Myr. The latter investigation is based on a paramount analysis of multiband data: NIR (2MASS), MIR (SPITZER), submillimeter (SCUBA) and radio (VLA). These data were used to fit the spectral energy distribution of Young Stellar Objects and on the basis of their ages they provided solid constraints on the recent SFR. On the other hand, [80], by using NIR (DENIS) and MIR (ISOGAL) observations and Asymptotic Giant Branch stars as stellar tracers, found that the SFR was enhanced in the nuclear bulge more than 200 Myr ago and almost continuous till present times. By using deep NIR color-magnitude diagrams based on NICMOS at HST, [25] found that the present day enclosed mass within 30 pc of the Galactic Center, the star counts and the shape of the K-band luminosity function support a continuous star formation history with a rate of $\sim 0.02\, M_{\odot}\, \mathrm{year}^{-1}$. This finding is also consistent with the presence of the three young massive clusters located inside the central 50 pc. The above investigations are somehow hampered by uncertainties affecting distance determinations and by the relevant changes of the extinction across the Galactic Center. Moreover, both individual and ensemble age estimates based on the above tracers might be affected by possible systematic uncertainties. Classical Cepheids present several advantages when compared with other stellar tracers.

1. **Easy targets** – Classical Cepheids are bright stars and they can be easily recognized by using either the Bailey diagram (luminosity amplitude vs. period) or the Fourier parameters of light curves.
2. **Distance indicators** – Classical Cepheids are very robust primary distance indicators. NIR Period-Luminosity relations and Period-Wesenheit relations are marginally affected by metallicity effects and by differential reddening.
3. **Evolutionary status** – Their evolutionary status is well established. They are intermediate-mass stars during central helium burning and hydrogen shell burning. They are evolving along the so-called blue loop and obey to well defined Period-Age and Period-Color-Age relations [8]. In particular, once the chemical composition has been fixed and we neglect the width in temperature of the instability strip, longer is the pulsation period younger is the age of the Cepheid.
4. **Pulsation properties** – Their pulsation behavior is also well established [7]. They pulsate in the fundamental, first overtone and as mixed pulsators (topology of the Cepheid instability strip). They obey to well defined Period-Color relations. This means that their apparent colors can be adopted to provide an independent estimate of the reddening.

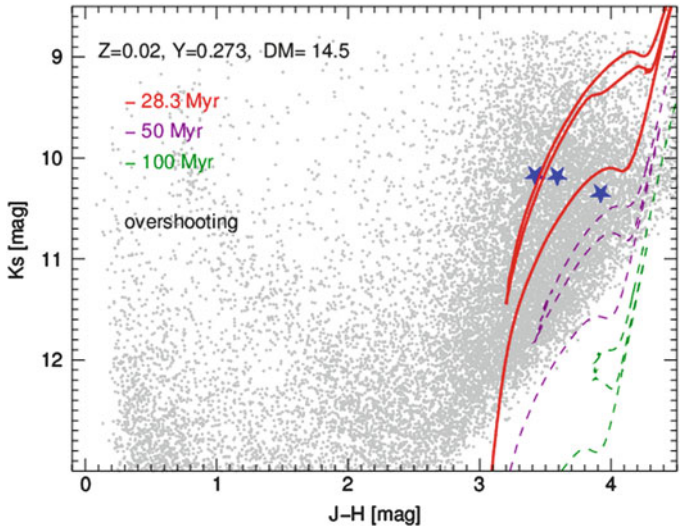

Fig. 1 Comparison between the NIR photometry of the Galactic Center, collected with the NIR camera SIRIUS at the 1.4 m telescope IRSF in South Africa, and stellar isochrones. The *blue stars* mark the position of the three classical Cepheids recently discovered by Matsunaga et al. [56]. *Solid* and *dashed lines* display isochrones with ages ranging from 28.3 Myr (*red*) to 100 Myr (*green*) and solar chemical composition (BASTI data base). Isochrones plotted in this figure account for a mild convective core overshooting during central hydrogen burning phases. Predictions were plotted by assuming a true distance modulus of 14.5, an extinction $A_K = 2.5$ mag and the reddening law by Nishiyama et al. [62]

However, they are far from being ideal stellar tracers, since they also have some indisputable disadvantages.

1. **Time series** – The identification does require homogeneous time series data over time intervals ranging from a few days to more than 100 days.
2. **Multiband observations** – The use of their mean colors does require well sampled light curves in at least two different bands.
3. **Pulsation amplitude** – Their pulsation amplitude steadily decreases when moving from the optical to the NIR bands. The difference is mainly caused by the fact that optical bands are more sensitive to temperature variations, while the NIR bands to radius variations.

On the basis of the above circumstantial evidence and on the discovery of three classical Cepheids with pulsation periods of the order of 20 days, located within 40 parsecs of the central black hole, [56] provided a solid estimate of the SFR. On the basis of the lack of classical Cepheids with shorter periods they estimated that approximately 25 million years ago the star formation rate in this region increased relative to the period of 30–70 million years ago. In order to further constrain the age of the newly discovered Galactic Center Cepheids, we decide to use an independent approach. Figure 1 shows the NIR (K_S vs. $J - H$) Color-Magnitude Diagram of

the Galactic Center region based on NIR images collected with SIRIUS at the 1.4 m telescope IRIS in South Africa.

To constrain the age of the Cepheids we adopted the stellar isochrones available in the BaSTI data base[1] [66, 67]. In particular, we selected isochrones at solar chemical composition (global metallicity, $Z = 0.02$; primordial helium, $Y = 0.273$) accounting for mild convective core overshooting during central hydrogen burning phases and for a canonical mass loss rate. The ages range from 28 (solid red) to 100 (dashed green) Myr. We also adopted a distance modulus of $\mu = 14.5$ mag (see Sect. 3) and the K-band extinction suggested by Matsunaga et al. [56] and the reddening law by Nishiyama et al. [61]. The comparison between stellar isochrones and observed classical Cepheids (blue stars) indicate that their age is of the order of 28 Myr. This estimate agrees quite well with the age based on the Period-Age relation (20–30 Myr). It is worth mentioning that age estimates based on the comparison in the CMD between data and isochrones do depend on uncertainties distance and reddening estimates. Moreover, they are affected by uncertainties in the treatment of mass loss rate and in the efficiency of internal mixing [69]. The age estimates based on the Period-Age relations of classical Cepheids are also affected by uncertainties affecting the mass-luminosity relation, but they appear to be more robust concerning individual age determinations [8].

2.2 Stellar Populations

In two seminal investigations concerning the stellar populations in the Galactic Center, dating back to more than 20 years ago, [65] and [58] performed a NIR survey (the pixel scale was 0.278 arcsec and the filed of view $\approx 71 \times 71$ arcsec) of the central 30 pc using IRAC@2.2m ESO/MPG telescope. They provided firm empirical constraints on the role played by the different stellar components. They found that low-mass ($M < 1\ M_{\odot}$) stars are the main contributor to the dynamical mass (90 %), while they only contribute a minor fraction of the K-band flux, namely the 6 %. On the other hand, intermediate- and high-mass stars contribute with only the 6 % of the dynamical mass, but with almost the 90 % of the K-band flux. By using NIR, MIR, millimeter (IRAM) and radio (MPIfR) observations, [44] confirmed the previous finding, and indeed they found that 70 % of the optical-UV flux comes from massive stars. Moreover, they also provided an estimate of the dynamical mass and they found that it is $M \approx 1.4 \times 10^9\ M_{\odot}$.

The recent literature concerning the young massive star clusters in the Galactic Center is even more flourishing. Detailed spectroscopic investigations of high-mass stars in the Central Cluster and in Arches have been provided by using the integral field spectrograph SINFONI at ESO/VLT [54, 55]. A similar analysis was recently performed by Liermann et al. [47] for Wolf–Rayet stars along the nitrogen sequence

[1]The interested reader is referred to http://albione.oa-teramo.inaf.it/

centrally located in the Quintuplet cluster. They found that their sample is quite bright, but with relatively cool effective temperatures. Interestingly enough, they also found that these objects together with similar objects in Arches and in the Galactic Center form a distinct group in the Hertzsprung-Russell diagram. Deep NIR CMDs for Arches and Quintuplet have been provided by Figer et al. [23, 24] using NICMOS at HST. They reached a limiting magnitudes between 19 and 20.5 in the F160W and F205W bands and estimated that the cluster age ranges from 2 ± 1 Myr (Arches) to 4 ± 1 Myr (Quintuplet).

A more detailed NIR photometric analysis of the Arches stellar content was recently provided by Espinoza et al. [22]. They adopted NACO Adaptive Optic camera at ESO/VLT to perform very accurate and deep photometry, they found that a Salpeter–like power law cannot be discarded for the Initial Mass Function (IMF) of Arches. This is a very interesting finding, since previous investigations [37, 76] suggested a top–heavy IMF for this cluster. The empirical scenario is becoming even more interesting due to the ongoing discoveries of new clusters. By using images collected with NICMOS at HST and low-resolution spectra with ISAAC at ESO/VLT, [19] identified a new young massive cluster located at the far end of the Galactic Bar.

In order to constrain the field and the cluster stellar populations in the Galactic Center, we started a long term project aimed at providing a detailed census of the young-, the intermediate- and the old populations. We are facing two important problems in dealing with a quantitative analysis of the stellar populations in the Galactic Center: (a) heavy differential extinction affecting both field and cluster stars; (b) transformations into a standard photometric system becomes a difficult problem in presence of strong reddening variations [22]. To properly address the latter problem, we performed accurate NIR photometry across the Arches cluster by using a set of J (82), H (45) and K_S (45) images collected with SOFI at ESO/NTT. The entire data set includes both low- (0.288 arcsec/px, FoV $= 4.9 \times 4.9$ arcmin) and high- (0.144 arcsec/px, FoV $= 2.5 \times 2.5$ arcmin) resolution mode. The photometry was performed by using DAOPHOT and ALLFRAME ([75], and references therein). The final photometric catalog was calibrated into the 2MASS photometric system by using local standards [43]. Figure 2 shows a preliminary H, $H - K$ Color-Magnitude diagram (CMD) of the cluster region located within 2 arcmin from the center.

The comparison between theory and observations was performed by using young cluster isochrones at solar chemical composition. The solid lines show isochrones with ages ranging from 30 to 100 Myr. The isochrones were computed using evolutionary tracks that account for mild convective core overshooting. The isochrones were plotted by adopting a true distance modulus of 14.48 ± 0.13 mag, an extinction in the K-band of $A(K_S) = 2.5$ mag and the reddening law by Nishiyama et al. [61]. A glance at the data plotted in this figure shows that the blue stars located at $H - K_S \sim 1.4$ are cluster young main sequence stars (see Fig. 4 in [26]). However, a detailed comparison between theory and observations does require an appropriate subtraction of field stars by using nearby control fields.

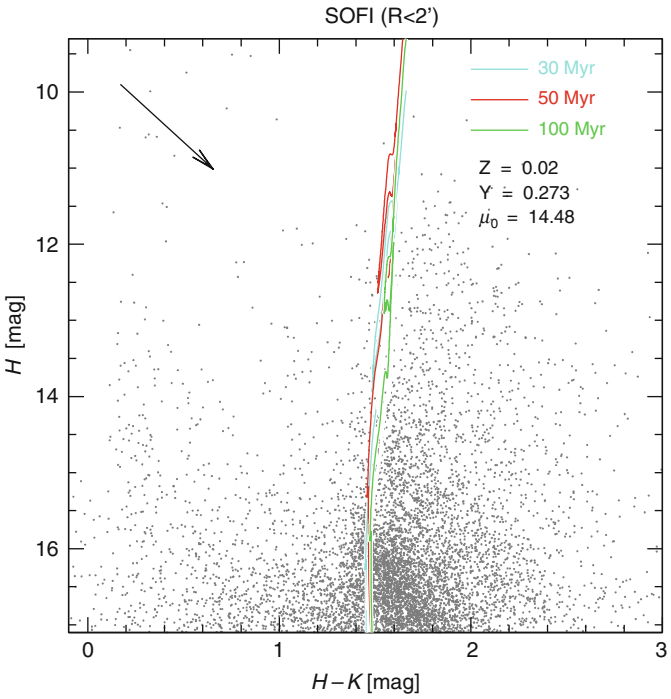

Fig. 2 Comparison between the NIR photometry of the young cluster Arches collected with the NIR camera SOFI at NTT/ESO in La Silla, and stellar isochrones. Note that are only plotted stars located within 2 arcmin from the cluster center. The *solid lines* show young (30 Myr) isochrones at solar chemical composition (BaSTI data base). The adopted distance modulus of 14.5, the K-band extinction $A_K = 2.5$ mag and the reddening law are the same as in Fig. 1. The *black arrow* shows the reddening vector

3 The Distance to the Galactic Center

In the recent literature distance estimates to the Galactic Center are often mixed with distance determinations to the Galactic Bulge. However, current evaluations concerning the edge of the inner disk suggest d $\sim 5 \pm 1$ kpc. Photometric and astrometric distances to the Galactic Center have been recently reviewed by Matsunaga et al. [57] (and references therein). They found that both photometric and kinematic estimates cluster around 8 kpc. This means that distance determinations to the Galactic Bulge do depend on the density profile and on the radial distribution of the adopted standard candle. It is plausible to assume that the two sets of distance determinations may differ at the 20 % level.

In order to provide a quantitative estimate of the difference we decided to provide a new distance determination to the Galactic Center by using NIR and MIR Period-Wesenheit relations for the three new classical Cepheids in the Galactic Center. The use of the PW relation has several indisputable advantages when compared with Period-Luminosity relations [9].

Table 1 Nuclear Bulge Cepheid distances

Star	$\mu^{a}_{WJK_s}$	μ^{a}_{WJH}	$\mu^{a}_{WHK_s}$	μ^{b}_{mean}
a	14.69 ± 0.05	14.55 ± 0.05	14.53 ± 0.05	14.57 ± 0.03
b	14.51 ± 0.05	14.32 ± 0.05	14.30 ± 0.05	14.46 ± 0.03
c	14.53 ± 0.05	14.48 ± 0.05	14.41 ± 0.05	14.42 ± 0.03

[a]Distance modulus based on the zero-point calibration obtained by the predicted FU PW relations for Galactic Cepheids provided by Marconi et al. [53]. The associated error is the standard deviation from the theoretical PW relation. The color coefficients of the adopted PW relations are the following: $\frac{A_K}{E(J-K_S)} = 0.50$; $\frac{A_H}{E(J-H)} = 1.42$; $\frac{A_K}{E(H-K_S)} = 1.44$; [61]

[b]The weighted average of the three distance modulus estimations

1. **Reddening uncertainty** – The PW relations are independent of uncertainties affecting reddening estimates.
2. **Instability strip topology** – The PW relations are independent of the pulsator distribution inside the instability strip, since they account for the width in temperature.
3. **Linearity** – They are almost linear over the entire period range [35], since they mimic a PLC relation.
4. **Mixing length** – The dependence of the PW relations (slope and zero-point) on the adopted mixing-length parameter is negligible.
5. **Chemical composition** – The slopes of both NIR and optical-NIR PW relations appear to be independent of chemical composition for metallicities ranging from $Z = 0.004$ (Small Magellanic Cloud) to $Z = 0.02$ (Milky Way). The adopted helium content Y, at fixed metallicity and mass-luminosity relation, only affects the zero-point of the PW relations.

However, the PW relations also have some indisputable disadvantages.

1. **Reddening law** – The Wesenheit magnitudes rely on the assumptions that the reddening law is universal [36]. Thus, distance estimates based on PW relations do depend on the reddening law adopted to estimate the extinction coefficients.
2. **Multiband photometry** – The PW relations require time series data in two different bands.

The distance of the Cepheids in the Galactic Center are derived using the PW relations in the three NIR bands (JHK_S). We have defined the three Wesenheit magnitudes adopting the color coefficients given in Table 1. By using the theoretical models provided by Marconi et al. [53], we have computed the following PW relations:

$$W(JK_s) = -(2.802 \pm 0.002) - (3.205 \pm 0.002) \times \log P$$

$$W(JH) = -(2.971 \pm 0.00) - (3.361 \pm 0.007) \times \log P$$

$$W(HK_s) = -(2.714 \pm 0.003) - (3.123 \pm 0.003) \times \log P$$

with standard deviations of 0.03, 0.01 and 0.04 mag.

The mean JHK_S magnitudes of the Cepheids are given in [56]. The difference between the predicted and the observed value of the Wesenheit magnitude gives the true distance modulus of each Cepheid. The distance moduli obtained in each band and the error-weighted average are listed in Table 1. The associated error is due to the standard deviation from the theoretical PW relation and also to the error on the total-to-selective extinction ratio, as given in [61]. The derived distances agree quite well with the independent determinations provided by Matsunaga et al. [56]. Our results are independent of the extinction correction, therefore, we obtain a mean distance modulus for the three Cepheids in the Galactic Center of 14.49 ± 0.02(standard) $\pm$ 0.10(systematic) mag with a small intrinsic error. The systematic error accounts for uncertainties in the zero-point of the NIR PW relations and in the reddening law [35]. Thus, we found a mean distance of $7.91 \pm 0.08 \pm 0.40$ kpc to the Galactic Center that is in very good agreement with the distance to the Galactic Center based on the S2 orbit around the central black hole (8.28 ± 0.35 kpc, [31]) and with the parallax of Sgr B (7.9 ± 0.8 kpc, [71]).

4 Metallicity Distribution in the Galactic Center

The iron and the α-element abundance gradients across the Galactic disk are fundamental observables to constrain the chemical enrichment of disk stellar populations [3, 46, 50–52, 63]. They also play a key role in constraining the physical assumptions adopted in chemical evolution models [13, 15, 68]. The most recent theoretical and empirical investigations brought forward three open issues:

1. **Stellar tracers** – Empirical evidence indicates that different stellar tracers do provide different slopes. Metallicity gradients based on Cepheids, provide slopes ranging from -0.05 dex kpc^{-1} [2, 12, 42, 45, 49, 50, 82] to -0.07 dex kpc^{-1} [46]. More recently, [63] using iron abundances for 265 classical Cepheids – based either on high-resolution spectra or on photometric metallicity indices – and Galactocentric distances ranging from $R_G \sim 5$ to $R_G \sim 17$ kpc, found an iron gradient of -0.051 ± 0.004 dex kpc^{-}1. By using an even more large sample of over 400 classical Cepheids, [52] found a gradient of -0.062 ± 0.002 dex kpc^{-1}. A similar gradient was also found by Friel et al. [28] by using a sample of 40 open clusters located between the solar circle and $R_G \sim 14$ kpc, namely -0.06 dex kpc^{-1}. On the other hand, [10] by using new metallicities for five old open clusters located in the outer disk ($12 \leq R_g \leq 21$ kpc) and the sample adopted by Friel et al. [28] found a shallower iron gradient: -0.018 dex kpc^{-1}. The slope of the metallicity gradient based on oxygen abundances of HII regions – with Galactocentric distances ranging from 5 to 15 kpc – is similar to the slope based on Cepheids (-0.04 dex kpc^{-1}, [21]). The difference between the different tracers, might be due to the age difference between the different tracers (young vs. intermediate-age).

2. **Linear slope** – By using a sample of 76 open clusters with distances ranging from 6 to 15 kpc, it was suggested by Twarog et al. [78] that a proper fit to the metallicity distribution does require two zones. The inner disk for Galactocentric distances ranging from 6 to 10 kpc and the outer disk for distances larger than 10 kpc. This hypothesis was supported by Caputo et al. [12], Luck et al. [49], and Andrievsky et al. [3]. More recently, [63] found for the two zones a slope of $-0.130 \pm 0.015\,\mathrm{dex\,kpc^{-1}}$ for the inner disk ($R_G < 8$ kpc) and a slope of $-0.042 \pm 0.004\,\mathrm{dex\,kpc^{-1}}$ for the outer disk. Data plotted in Fig. 3 support the above results. We adopted the same abundances provided by Pedicelli et al. [63], but we used new individual distances based on NIR Period-Wesenheit relations [35] instead of NIR Period-Luminosity relations. Current findings indicate that young tracers do show evidence of a sharp steepening of the slope in the inner disk and a mild flattening of the gradient in the outer disk.
3. **Local inhomogeneities** – There is mounting empirical evidence that abundance inhomogeneities are present not only across Galactic quadrants, but also on smaller spatial scales. Pedicelli et al. [63] found that the iron abundance of the Cepheids belonging to the two overdensities located in the second and in the fourth quadrant, covers a range in metallicity similar to the range in metallicity covered by the global gradient (see also [45, 50, 51]).

Figure 3 shows the position of bright supergiants in two Galactic Center young clusters – Arches and Quintuplet – by Najarro et al. [59, 60] (cross) and Galactic Center field supergiants by Davies et al. [17] (open square). The open diamonds display the position of the two Scutum Red Supergiant clusters by Davies et al. [18] located at the end of the Galactic Bar. A glance at the data plotted in this figure discloses that stars located in the Galactic Center have a solar iron abundance, whereas the average iron abundances are subsolar by 0.2–0.3 dex for the stars located along the Galactic Bar. This means that we are facing a stark discrepancy between the metallicity gradient based on classical Cepheids and the above iron abundances.[2] Plain leading arguments based on the extrapolation of both the global and the inner disk metallicity gradient would imply a super-solar iron abundances approaching the Galactic Center [17]). This discrepancy has already been noted in the literature and [16] suggested that the slope of the metallicity gradient should become shallower for Galactocentric distances smaller than 5 kpc. In principle there is no plausible reason why it should be extrapolated from the inner disk to the Galactic Center. Solid empirical evidence suggest that the Galactic Bulge is dominated by an old (11 Gyr) stellar population with a secondary intermediate-age (a few Gyr) stellar component [88]. Moreover and even more importantly, recent spectroscopic investigations based on high-resolution spectra indicates that the stellar populations in the Galactic Bulge range from metal-intermediate ([Fe/H] ~ -1) to super solar ([Fe/H] $\sim +0.5$) with a broad main peak [Fe/H] ≈ 0.2 [33, 88, 89].

[2]The interested reader is referred to the Table 2 of [17] for a detailed list of the most recent metallicity estimates of the Galactic Center.

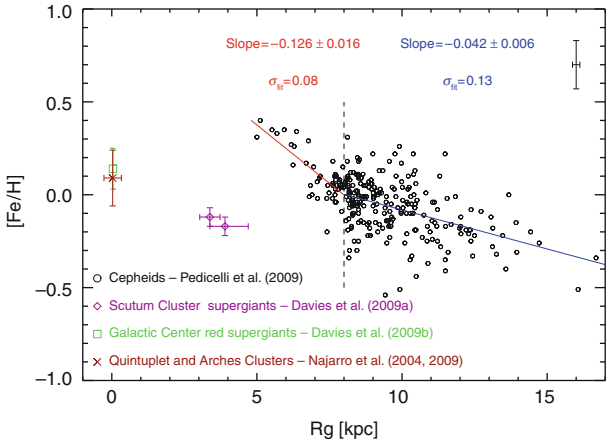

Fig. 3 Galactic iron gradient as a function of the Galactocentric distance. *Empty circles* mark the Galactic Cepheid sample by Pedicelli et al. [63]. The *solid lines* display the metallicity gradient for Cepheids located either inside (*red*, 50 objects) or outside (*blue*, 215 objects) the solar circle (RG < 8 kpc, *vertical dashed line*). The slopes and the standard deviations of the linear fits are also labeled. The error bars in the *top right corner* shows the typical uncertainties in iron abundance and in distance. The two *purple diamonds* display the metallicity of two supergiants located in the Scutum cluster [17], while the *brow cross* the metallicity of the young cluster Quintuplet [60] and the *green square* the metallicity of the red supergiants observed by Davies et al. [18] in the Galactic Center

4.1 Transition Between the Galactic Bulge and the Galactic Center

Quantitative constraints concerning the edge between the inner disk and the Bulge and the edge between the Bulge and the Galactic Center are hampered by lack of accurate distance determinations (see Fig. 4). The above scenario is further complicated by the possible presence of the Galactic Bar. We are facing the evidence that the region located between the Galactic Center and the inner disk is characterized by the lack of star forming regions, of giant HII regions and of young open clusters [17]. On the other hand, Galactic Legacy Mid-Plane Survey Extraordinaire (GLIMPSE) survey based on 30 million mid-infrared (SPITZER) sources identified a linear bar passing through the Galactic Center with half-length $R_{bar} = 4.4 \pm 0.5$ kpc.

Theoretical [4, 27] and observational [1, 86, 87] investigations indicate that the abundance gradient in barred galaxies is shallower than in unbarred galaxies. The typical explanation for this trend is that the bar is dragging gas from the inner disk into the Galactic Center [38]. The pileup of the new fresh material triggers an ongoing star formation activity till the dynamical stability of the bar. In passing we note that the three new Cepheids discovered in the inner disk is supporting the evidence that star formation events might have occurred on an area broader

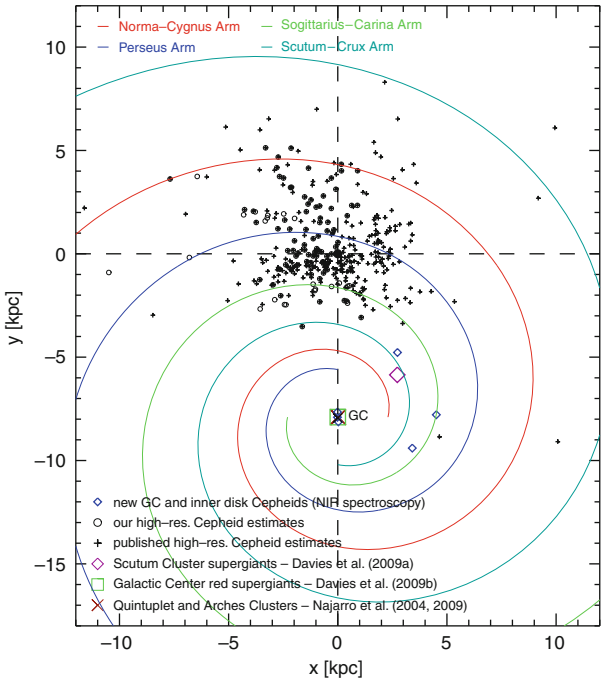

Fig. 4 Same as the Fig. 3, but projected onto the Galactic plane. Together with the known classical Cepheids by Pedicelli et al. [63] have also been plotted the three classical Cepheids discovered by Matsunaga et al. [56] in the Galactic Center (*diamonds*) and the three classical Cepheids recently discovered by Matsunaga et al. [57] in the inner edge of the thin disk (*squares*). The four spiral arms according to the Galactic model of Vallée et al. [79] are plotted with different colors (see labels)

than the near end of the Galactic Bar. A more quantitative understanding of this phenomenon has an impact into the formation and the evolution of classical bulges and pseudo-bulges. The latter are considered disk-like stellar components slowly evolving in galaxy centers, whereas the former are considered the aftermath of galaxy mergers [40, 41, 56].

One of the key consequences of the above scenario is that the typical metallicity distribution along the Galactic Bar and in the Galactic Center should be quite similar to the metallicity distribution in the inner disk. The main advantage in current analysis is that we are using stellar tracers with similar ages, since both Supergiants, Luminous Blue Variables (LBVs) and Cepheids are either massive or intermediate–mass stars. Their evolutionary lifetime is typically shorter than 100 Myr. This evidence seems to support the hypothesis that the occurrence of the bar might not be the main culprit in shaping the metallicity gradient between the inner disk and the Galactic Center. Indeed, current numerical simulations suggest that the timescale within which the radial motion of the gas smooths the actual abundance gradient is of the order of a few hundred Myrs. Part of the azimuthal

variations currently observed across the Galactic disk might be caused by changes in the abundance patterns between the spiral arms and the inter-arm regions [38] and by the clumpiness of the star formation episodes. However, the kinematics of the above stellar tracers is quite limited, since they evolve in situ. This working hypothesis is supported by a very large set of Cepheid abundances provided by Luck et al. [51,52]. They found no evidence of azimuthal variations in an annulus of 1 kpc around the sun. The statistics concerning the Galactic Cepheids located in the inner disk is quite limited, and indeed only a handful of Cepheids are known with Galactocentric distances smaller than 6 kpc. However, in a recent investigation [64] by using high-resolution, high S/N ratio spectra confirmed the super metal-rich nature of four of them [3]. The hypothesis suggested by Davies et al. [17] that the wind of metal-intermediate bulge stars might mix with metal-rich gas present along the bar and the Galactic Center to produce a chemical mixture close to solar appears also very promising. However, to our knowledge we still lack firm empirical evidence on how the winds of bulge stars might fall in the Galactic Center. The infall of metal-poor gas in the Galactic Center appears an even more plausible channel to explain current abundance patterns [48,81]. This is the so-called biased infall scenario [14] in which the infall of gas takes place more rapidly in the innermost than in the outermost regions (inside-out disk formation).

The abundance pattern of α-elements is even more puzzling, since accurate measurements indicate solar abundances, and therefore consistent with typical thin disk stars [18]. However, different tracers (B-type stars, red supergiants, classical Cepheids, HII regions) do provide slightly different mean values, suggesting a broad distribution ([17], and references therein). In this context, it is worth mentioning another piece of evidence concerning the thin disk. Accurate abundance estimates of α-elements in a sizable sample of classical Cepheids indicates that the α(Ca, Mg, Si)-to-iron ratio attains, within the errors, a constant value across the disk [45, 50]. This evidence once confirmed has two relevant implications:

1. **Chemical enrichment** – the chemical enrichment in the last few hundred Myrs across the Galactic disk seems to be driven by core collapse supernovae.
2. **Galactic Center** – the same outcome applies to the Galactic Center, since current estimates suggest a solar composition for both the iron and the α-elements.

5 Future Perspectives

The content of the previous sections further underline the paramount effort undertaken by the astronomical community both from the theoretical and the observational point of view to constrain the stellar populations, the SFR and the chemical enrichment of the Galactic Center. During the last few years the multi-wavelength approach also provided a comprehensive picture of the physical mechanisms driving the formation and the evolution of disks and bulges [32, 41]

However, we still lack firm constraints concerning the geometry and the kinematics at the interface between inner disk, Bulge and Center. The quoted properties of stellar populations in the Bulge and in the Center bring forward that old stellar tracers, such as RR Lyrae, appear to be solid beacons to trace the 3D structure of the innermost Galactic regions. A detailed map of the RR Lyrae in the Galactic Bulge has been performed by OGLE [77], but we still lack a detailed census of RR Lyrae variables in the Galactic Center.

Moreover, we still lack detailed kinematic constraints concerning outer and the inner Lindblad resonance and of the corotation radius [44, 83, 84]. Recent estimates are mainly based on gas kinematics [6, 34, 70], but estimates based on stellar tracers are not available yet. The occurrence of peculiar radial motions at the ending points of the Galactic Bar would also provide the optimal target selection to constrain the chemical enrichment of these regions. It is clear that the second generation instruments at ESO/VLT, such as the KMOS spectrograph [74], appear to be an optimal facility to constrain the kinematics in crowded and highly reddened fields. The field of view is slightly larger than 7 arcmin in diameter and are available 24 integral field units (IFU). The wavelength coverage ranges from 0.8 to 2.5 μm with a medium spectral resolution (R $\sim$ 3500). This new observing facility will provide detailed kinematic maps for both cluster and field stars and chemical abundances for a relevant fraction of the Galactic Center. In this context the next generation of Extremely-Large-Telescopes (European-ELT [E-ELT],[3] the Thirty Meter Telescope [TMT][4] and the Giant Magellan Telescope [GMT][5]) will also play a key role due to their high spatial resolution and high NIR sensitivity. The same applies for JWST.[6]

The comparison between theory and observations presented in Fig. 2 has to be considered as a preliminary step in the understanding of stellar populations across the Arches cluster. The transformation of broad band photometry of highly reddened regions into a standard photometric system is a thorny problem both in the optical [73] and in the NIR [22] regime. This problem becomes even more compelling for the Galactic Center, since recent findings based on the color of red clump stars indicate a flattening of the reddening law towards this region [29, 60].

Acknowledgements It is a pleasure to thank M. Fabrizio for a detailed and critical reading of an early version of this manuscript. One of us GB thanks ASTROMUNDUS and the Department of Astronomy, University of Belgrade for their warm hospitality. We are indebted to the great patience and the constant support from the editors. This work was partially supported by the PRIN MIUR 2011 (P.I. M. Marconi). We are grateful to Jorgen Melnik for the detailed reading of an early draft of this manuscript, and in particular for drawing to our attention the thorny problems connected with NIR photometric calibration.

[3] http://www.eso.org/public/teles-instr/e-elt.html

[4] http://www.tmt.org/

[5] http://www.gmto.org/

[6] http://ircamera.as.arizona.edu/nircam/

References

1. Allard, E. L.; Knapen, J. H.; Peletier, R. F.; Sarzi, M.: The star formation history and evolution of the circumnuclear region of M100. Mont. Notic. Royal Astron. Soc. **371**, 1087 (2006)
2. Andrievsky, S. M.; et al.: Using Cepheids to determine the galactic abundance gradient. III. First results for the outer disc. Astron. & Astroph. **392**, 491 (2002)
3. Andrievsky, S. M.; Luck, R. E.; Martin, P.; Lépine, J. R. D.: The Galactic abundance gradient from Cepheids. V. Transition zone between 10 and 11 kpc. Astron. & Astroph. **413**, 159 (2004)
4. Athanassoula, E.: The existence and shapes of dust lanes in galactic bars. Mont. Notic. Royal Astron. Soc. **259**, 345 (1992)
5. Barbuy, B.; et al.: VLT-FLAMES analysis of 8 giants in the bulge metal-poor globular cluster NGC 6522: oldest cluster in the Galaxy?. Analysis of 8 giants in NGC 6522. Astron. & Astroph. **507**, 405 (2009)
6. Brand, J., & Blitz, L.: The Velocity Field of the Outer Galaxy. Astron. & Astroph. **275**, 67 (1993)
7. Bono, G.; Marconi, M.; Stellingwerf, R. F.: Classical Cepheid Pulsation Models. I. Physical Structure. Astroph. J. Suppl. **122**, 167 (1999)
8. Bono, G.; Marconi, M.; Cassisi, S.; Caputo, F.; Gieren, W.; Pietrzynski, G.: Classical Cepheid Pulsation Models. X. The Period-Age Relation. Astroph. J. **621**, 966 (2005)
9. Bono, G.; Caputo, F.; Marconi, M. & Musella, I.: Insights into the Cepheid Distance Scale. Astroph. J. **715**, 277 (2010)
10. Carraro, G.; et al.: Old open clusters in the outer Galactic disk. Astron. & Astroph. **476**, 217 (2007)
11. Carraro, G.; Costa, E.; Ahumada, J. A.: Photometric Characterization of the Galactic Star Cluster Trumpler 20, Astron. J. **140**, 954 (2010)
12. Caputo, F.; Marconi, M.; Musella, I.; Pont, F.: Pulsational constraints to the metallicity gradient in the Galactic disk. Astron. & Astroph. **372**, 544 (2001)
13. Cescutti, G.; Matteucci, F.; François, P.; Chiappini, C.: Abundance gradients in the Milky Way for α elements, iron peak elements, barium, lanthanum, and europium. Astron. & Astroph. **462**, 943 (2007)
14. Chiappini, C.; Matteucci, F.: A new Picture for the Galaxy Formation. Astrophysics and Space Science, **265**, 425 (1999)
15. Chiappini, C.; Matteucci, F.; Romano, D.: Abundance Gradients and the Formation of the Milky Way. Astroph. J. **554**, 1044 (2001)
16. Cunha, K.; et al.: Chemical Abundances of Luminous Cool Stars in the Galactic Center from High-Resolution Infrared Spectroscopy. Astroph. J. **669**, 1011 (2007)
17. Davies, B.; et al.: The Chemical Abundances in the Galactic Center from the Atmospheres of Red Supergiants. Astroph. J. **694**, 46 (2009a)
18. Davies, B.; et al.: Chemical Abundance Patterns in the Inner Galaxy: The Scutum Red Supergiant Clusters. Astroph. J. **696**, 2014 (2009b)
19. Davies, B.; et al.: A newly discovered young massive star cluster at the far end of the Galactic Bar. Mont. Notic. Royal Astron. Soc. **419**, 1860 (2012)
20. Debattista, V. P.; Mayer, L.; Carollo, C. M.; Moore, B.; Wadsley, J.; Quinn, T.: The Secular Evolution of Disk Structural Parameters. Astroph. J. **645**, 209 (2006)
21. Deharveng, L.; Peña, M.; Caplan, J.; Costero, R.: Oxygen and helium abundances in Galactic HII regions - II. Abundance gradients. Mont. Notic. Royal Astron. Soc. **311**, 329 (2000)
22. Espinoza, P.; Selman, F. J.; Melnick, J.: The massive star initial mass function of the Arches cluster. Astron. & Astroph. **501**, 563 (2010)
23. Figer, D. F.; McLean, I. S.; Morris, M.: Massive Stars in the Quintuplet Cluster. Astroph. J. **514**, 202 (1999)
24. Figer, D. F.; et al.: Massive Stars in the Arches Cluster. Astroph. J. **581**, 258 (2002)
25. Figer, D. F.; Rich, R. M.; Kim, S. S.; Morris, M.; Serabyn, E.: An Extended Star Formation History for the Galactic Center from Hubble Space Telescope NICMOS Observations. Astroph. J. **601**, 319 (2004)

26. Figer, D. F.; et al.: Discovery of an Extraordinarily Massive Cluster of Red Supergiants. Astroph. J. **643**, 1166 (2009)
27. Friedli, D.; Benz, W.: Secular evolution of isolated barred galaxies. II. Coupling between stars and interstellar medium via star formation. Astron. & Astroph. **301**, 649 (1995)
28. Friel, E. D.; et al.: Metallicities of Old Open Clusters. AJ **124**, 2693 (2002)
29. Fritz, T. K.; Gillessen, S.; Dodds-Eden, K., et al.: Astroph. J. **737**, 73 (2011)
30. Genzel, R.; Eckart, A.; Ott, T.; Eisenhauer, F.: On the nature of the dark mass in the centre of the Milky Way. Mont. Notic. Royal Astron. Soc. **291**, 219 (1997)
31. Gillessen, S.; et al.: Monitoring Stellar Orbits Around the Massive Black Hole in the Galactic Center. Astroph. J. **692**, 1075 (2009)
32. Graham, A. W., & Guzmán, R.: HST Photometry of Dwarf Elliptical Galaxies in Coma, and an Explanation for the Alleged Structural Dichotomy between Dwarf and Bright Elliptical Galaxies. Astronomical Journal. **125**, 2936 (2003)
33. Hill, V.; et al.: The metallicity distribution of bulge clump giants in Baade's window. Astron. & Astroph. **534**, 80 (2011)
34. Honma, M., & Sofue, Y.: Rotation Curve of the Galaxy. Publications of the Astronomical Society of Japan, **49**, 453 (1997)
35. Inno, L.; et al.: On the distance of the Magellanic Clouds using Cepheid NIR and optical – NIR period – Wesenheit relations. Astroph. J. **764**, 84 (2013)
36. Inno, L.; et al.: The Classical Cepheid Distance scale in the NIR bands. Journal of Physics: Conference Series. **383**, 012008 (2012)
37. Kim, S. S.; et al.: The Arches Cluster Mass Function. Astroph. J. **653**, 113 (2006)
38. Kim, S. S.; Saitoh, T. R.; Jeon, M.; Figer, D. F.; Merritt, D.; Wada, K.: Nuclear Star-forming Ring of the Milky Way: Simulations. Astroph. J. **735**, 11 (2011a)
39. Kim, J.; et al.: Galaxy Formation with Self-consistently Modeled Stars and Massive Black Holes. I. Feedback-regulated Star Formation and Black Hole Growth. Astroph. J. **738**, 54 (2011b)
40. Kormendy, J.; Kennicutt, R. C.: Secular Evolution and the Formation of Pseudobulges in Disk Galaxies. Ann. Rev. Astron & Astroph. **42**, 603 (2004)
41. Kormendy, J.; Fisher, D. B.; Cornell, M. E.; Bender, R.: Structure and Formation of Elliptical and Spheroidal Galaxies. Astroph. J. Suppl. **182**, 216 (2009)
42. Kovtyukh, V. V.; Wallerstein, G.; Andrievsky, S. M.: Galactic Cepheids. I. Elemental Abundances and Their Implementation for Stellar and Galactic Evolution. Publ. Astron. Soc. Pacific **117**, 1173 (2005)
43. Lagioia, E.P.; et al.: Deep and accurate near infrared photometry of the young massive cluster Arches. in preparation
44. Launhardt, R.; Zylka, R.; Mezger, P. G.: The nuclear bulge of the Galaxy. III. Large-scale physical characteristics of stars and interstellar matter. Astron. & Astroph. **384**, 112 (2002)
45. Lemasle, B.; François, P.; Bono, G.; Mottini, M.; Primas, F.; Romaniello, M.: Detailed chemical composition of Galactic Cepheids. A determination of the Galactic abundance gradient in the 8–12 kpc region. Astron. & Astroph. **467**, 283 (2007)
46. Lemasle, B.; François, P.; Piersimoni, A.; Pedicelli, S.; Bono, G.; Laney, C. D.; Primas, F.; Romaniello, M.: Galactic abundance gradients from Cepheids. On the iron abundance gradient around 10–12 kpc. Astron. & Astroph. **490**, 613 (2008)
47. Liermann, A.; et al.: The Quintuplet cluster. II. Analysis of the WN stars. Astron. & Astroph. **524**, 82 (2010)
48. Lubowich, D. A.; et al.: Deuterium in the Galactic Centre as a result of recent infall of low-metallicity gas. Nature **405**, 1025 (2000)
49. Luck, R. E.; et al: The galactic abundance gradient from Cepheids. IV. New results for the outer disc. Astron. & Astroph. **401**, 939 (2003)
50. Luck, R. E.; Kovtyukh, V. V.; Andrievsky, S. M.: The Distribution of the Elements in the Galactic Disk. AJ **132**, 902 (2006)
51. Luck, R. E.; et al.: The Distribution of the Elements in the Galactic Disk. II. Azimuthal and Radial Variation in Abundances from Cepheids. AJ **142**, 51 (2011a)

52. Luck, R. E.; Lambert, D. L.: The Distribution of the Elements in the Galactic Disk. III. A Reconsideration of Cepheids from l = 30° to 250°. AJ **142**, 136 (2011b)
53. Marconi, M.; Musella, I.; & Fiorentino, G.: Cepheid Pulsation Models at Varying Metallicity and $\Delta Y/\Delta Z$. Astroph. J., **632**, 590 (2005)
54. Martins, F.; et al.: Stellar and wind properties of massive stars in the central parsec of the Galaxy. Astron. & Astroph. **468**, 233 (2007)
55. Martins, F.; et al.: The most massive stars in the Arches cluster. Astron. & Astroph. **478**, 219 (2008)
56. Matsunaga, N.; Kawadu, T.; Nishiyama, S.; Nagayama, T.; Kobayashi, N.; Tamura, M.; Bono, G.; Feast, M. W.; Nagata, T.: Three classical Cepheid variable stars in the nuclear bulge of the Milky Way. Nature **477**, 188 (2011)
57. Matsunaga, N.; et al.: Cepheids another short period variables near the Galactic centre. Mont. Notic. Royal Astron. Soc. submitted (2012)
58. Mezger, P. G.; Zylka, R.; Philipp, S.; Launhardt, R.: The nuclear bulge of the Galaxy. II. The K band luminosity function of the central 30 PC. Astron. & Astroph. **348**, 457 (1999)
59. Najarro, F.; et al.: Metallicity in the Galactic Center: The Arches Cluster. Astroph. J. **611**, 105 (2004)
60. Najarro, F.; et al.: Metallicity in the Galactic Center: The Quintuplet Cluster. Astroph. J. **691**, 181 (2009)
61. Nishiyama, S.; et al.: Interstellar Extinction Law in the J, H, and Ks Bands toward the Galactic Center. Astroph. J. **638**, 839 (2006)
62. Nishiyama, S.; et al.: Interstellar Extinction Law Toward the Galactic Center III: J, H, KS Bands in the 2MASS and the MKO Systems, and 3.6, 4.5, 5.8, 8.0 ?m in the Spitzer/IRAC System. Astroph. J. **696**,1407 (2009)
63. Pedicelli, S.; Bono, G.; Lemasle, B.; et al.: On the metallicity gradient of the Galactic disk. Astron. & Astroph. **504**, 81 (2009)
64. Pedicelli, S.; et al.: New Baade-Wesselink distances and radii for four metal-rich Galactic Cepheids. Astron. & Astroph. **518**, 11 (2010)
65. Philipp, S.; et al.: The nuclear bulge. I. K band observations of the central 30 PC. Astron. & Astroph. **348**, 768 (1999)
66. Pietrinferni, A.; Cassisi, S.; Salaris, M.; Castelli, F.: A Large Stellar Evolution Database for Population Synthesis Studies. I. Scaled Solar Models and Isochrones. Astroph. J. **612**, 168 (2004)
67. Pietrinferni, A.; Cassisi, S.; Salaris, M.; Castelli, F.: A Large Stellar Evolution Database for Population Synthesis Studies. II. Stellar Models and Isochrones for an α-enhanced Metal Distribution. Astroph. J. **642**, 797 (2006)
68. Portinari, L.; Chiosi, C.: On radial gas flows, the Galactic Bar and chemical evolution in the Galactic Disc. Astron. & Astroph. **355**, 929 (2000)
69. Prada Moroni, P. G.; et al.: On the Evolutionary and Pulsation Mass of Classical Cepheids. III. The Case of the Eclipsing Binary Cepheid CEP0227 in the Large Magellanic Cloud. Astroph. J. **749**, 108 (2012)
70. Reid, M. J.; Menten, K. M.; Zheng, X. W. et al.: Trigonometric Parallaxes of Massive Star-Forming Regions. VI. Galactic Structure, Fundamental Parameters, and Noncircular Motions. Astroph. J. **700**, 137 (2009)
71. Reid, M. J.; Menten, K. M.; Zheng, X. W. et al.: A Trigonometric Parallax of Sgr B2. Astroph. J. **705**, 1548 (2009)
72. Selman, F.; Melnick, J.; Bosch, G.; Terlevich, R.: Astron. & Astroph. **341**, 98 (1999)
73. Serabyn, E.; Morris, M.: Sustained star formation in the central stellar cluster of the Milky Way. Nature **382**, 602 (1996)
74. Sharples, R.; Bender, R.; Agudo Berbel, A.; et al.: Recent Progress on the KMOS Multi-object Integral Field Spectrometer. The Messenger, **139**, 24 (2010)
75. Stetson, P. B.: The center of the core-cusp globular cluster M15: CFHT and HST Observations, ALLFRAME reductions PASP **106**, 250 (1994)

76. Stolte, A.; et al.: The Arches Cluster: Evidence for a Truncated Mass Function? Astroph. J. **628**, 113 (2005)
77. Soszyński, I.; Dziembowski, W. A.; Udalski, A. et al.: The Optical Gravitational Lensing Experiment. The OGLE-III Catalog of Variable Stars. XI. RR Lyrae Stars in the Galactic Bulge. Acta Astronomica. **61**, 1 (2011)
78. Twarog, B. A.; et al.: Some Revised Observational Constraints on the Formation and Evolution of the Galactic Disk. AJ **114**, 2556 (1997)
79. Vallée, J. P.: The Spiral Arms and Interarm Separation of the Milky Way: An Updated Statistical Study. AJ **130**, 569 (2005)
80. van Loon, J. T.; et al.: Infrared stellar populations in the central parts of the Milky Way galaxy. Mont. Notic. Royal Astron. Soc. **338**, 857 (2003)
81. Wakker, B. P.; et al.: Accretion of low-metallicity gas by the Milky Way. Nature **402**, 388 (1999)
82. Yong, D.; et al.: Elemental Abundance Ratios in Stars of the Outer Galactic Disk. III. Cepheids. AJ **131**, 2256 (2006)
83. Yuan, C.: Relationships Between Active Galactic Nuclei and Starburst Galaxies.ASP Conference Series. **31**, 127 (1992)
84. Yuan, C. & Kuo, C.-L.: Bar-driven Spiral Density Waves and Accretion in Gaseous Disks.Astroph. J. **486**, 750 (1997)
85. Yusef-Zadeh, F.; et al.: Star Formation in the Central 400 pc of the Milky Way: Evidence for a Population of Massive Young Stellar Objects. Astroph. J. **702**, 178 (2009)
86. Zánmar Sánchez, R.; Sellwood, J. A.; Weiner, B. J.; Williams, T. B.: Modeling the Gas Flow in the Bar of NGC 1365. Astroph. J. **674**, 797 (2008)
87. Zaritsky, D.; Kennicutt, R. C.; Huchra, J.P.: H II regions and the abundance properties of spiral galaxies. Astroph. J. **420**, 87 (1994)
88. Zoccali, M., Renzini, A., Ortolani, S., et al.: Age and metallicity distribution of the Galactic bulge from extensive optical and near-IR stellar photometry. Astron. & Astroph. **399**, 931 (2003)
89. Zoccali, M.; et al.: The metal content of bulge field stars from FLAMES-GIRAFFE spectra. I. Stellar parameters and iron abundances. Astron. & Astroph. **486**, 177 (2008)

The Cosmic-Ray Dominated Region of Protoplanetary Disks

G. Chaparro Molano and I. Kamp

Abstract We investigate the chemical evolution in the midplane of protoplanetary disks in the region 1 AU $\leq r \leq$ 10 AU, focusing on cosmic ray induced processes. These processes drive the chemical pathways of formation of gas phase molecules which later can be adsorbed onto the surface of grains. We improve on previously existing chemical models by treating the interaction of cosmic rays with the gas/grain environment in a way that is consistent with the local conditions. This means including the effects of dust aggregation in the disk and the extinction of cosmic ray induced UV photons by the gas. We conclude that the effects of cosmic ray UV flux enhancement brought about by grain growth are as relevant as their extinction by gas species. Thus we identify CO, CO_2, SiO, S and O_2 as the main species that contribute to the gas extinction in these regions. The implementation of this method seeks to complete other models that use steady state estimations of the chemical composition of the disk.

1 Introduction

Cosmic rays play a role in ionizing the material and driving the chemistry in protoplanetary disks, which has been largely underestimated. This is specially true in the region where they can be most relevant: the cold environment of the midplane of protoplanetary disks. This region is known to be opaque to stellar UV and X ray photons [27] and for this reason it has the reputation of being a dead zone. However, the region of the midplane located at $z/r < 0.05$ and $1 < r < 10$ AU can in fact be dominated by cosmic ray processing, as they penetrate above column densities of $\Sigma \sim 150\,\mathrm{g\,cm^{-2}}$ [19, 23]. Steady state chemical models applied to

G.C. Molano (✉) · I. Kamp
Kapteyn Astronomical Institute, Postbus 800, 9747 AV Groningen, The Netherlands
e-mail: chaparro@astro.rug.nl

D.F. Torres and O. Reimer (eds.), *Cosmic Rays in Star-Forming Environments*, Astrophysics and Space Science Proceedings 34, DOI 10.1007/978-3-642-35410-6_10,

these regions cannot fully describe the chemical evolution of the midplane, as the chemical relaxation timescale can be up to 10^8 years [27], which is longer than the lifetime of the disk [9].

Current chemical models of protoplanetary disks do include to a large extent the effects of cosmic rays [18, 22, 24–27]. However, the effects of the local gas opacity and grain growth are for the most part overlooked, as the parameters for estimating cosmic ray photoionization/dissociation rates are usually taken from molecular cloud literature [10, 28].

Our goal is to identify the main contributors to the extinction of cosmic ray induced UV (CRUV) photons in different regions of the midplane ($r = 1$–10 AU) of a disk of a T Tauri star. We implement a time dependent calculation of the CRUV photo rates that includes the extinction provided by the dust and also by gas species, which depend on their relative abundances. We implement this method in our time dependent chemical rate equation solver `chem_compact`. This code is benchmarked against steady state chemical abundances from the ProDiMo solver [27] and against observed cometary ice abundances [4, 7].

2 Cosmic Ray Induced UV Photons

Besides direct ionization of gas phase species cosmic rays can ionize the medium by inducing a UV field that comes from secondary ionization of molecular hydrogen. The process, known as the Prasad Tarafdar mechanism [15], starts when an electron, with a typical energy of 30 eV, is released after the cosmic ray ionization of an H_2 molecule. This electron then hits another (neutral) H_2 molecule, which leaves it in an excited electronic state [16, 21]. The emission probability profile of CRUV is obtained from the transition probability of the first three excited electronic levels ($B\ ^1\Sigma_u^+$ and $C\ ^1\Sigma_u$). In the subsequent decay to excited vibrational states of the ground electronic level, Lyman and Werner photons are emitted in the 90–170 nm range.

Cosmic ray induced UV photons can be absorbed by the material in the local environment where they are generated. Both gas and dust can absorb these photons and become a source of local extinction, but this depends on the local density and temperature conditions. For instance, at 10 AU most of the material is frozen on the surface of dust grains and therefore the extinction of CRUV depends entirely on the local dust properties. Thus, in such gas poor environments the CRUV photoprocesses will not be affected by the composition of the gas and the chemistry can be described in a fairly straightforward way.

The rate of CRUV photoprocesses depends on the shape of the photon emission probability from every cosmic ray ionization of H_2:

$$k_{\mathrm{CU},i} = \zeta_{\mathrm{H_2}} \frac{n_{\mathrm{H_2}}}{n_{\langle \mathrm{H} \rangle}} \gamma_i \ ; \ \ \gamma_i = \int_{1.76\,\mathrm{PHz}}^{3.28\,\mathrm{PHz}} \frac{P(\nu)\sigma_i(\nu)}{\sigma_{\mathrm{tot}}(\nu)}\, d\nu \ . \tag{1}$$

P is the emission probability profile of a CRUV photon, σ_i is the photoprocess cross section, and $\sigma_{\rm tot}$ is the total (gas+dust) cross section. This cross section includes the information of the relative gas abundances and cross sections of all other gas phase species. This expression implicitly includes a shielding effect, which can be important in regions where high density/temperature combinations create a gas rich environment. From Eq. (1) we can define the frequency averaged opacity as:

$$\langle \kappa_i \rangle = \frac{\int F(\nu)\kappa_i(\nu)\, d\nu}{\int F(\nu)\, d\nu} \,. \tag{2}$$

The shape of the radiation field that dissociates or ionizes a species $F(\nu)$ not only depends on the CRUV emission probability, but also on the CRUV extinction of all other species $\sigma_{\rm tot}(\nu)$, which leads to the frequency dependent opacity $\kappa_i(\nu)$:

$$F(\nu) = \frac{P(\nu)}{\sigma_{\rm tot}(\nu)} \;;\; \kappa_i(\nu) = \xi_i \sigma_i(\nu) \frac{n_{\langle \rm H \rangle}}{\rho_{\rm gas}} \,. \tag{3}$$

Here $\rho_{\rm gas} = n_{\langle \rm H \rangle} \mu m_{\rm H}$ (μ being the mean molecular weight). This formula for the opacity yields units of cm^2 per gram gas. Using Eq. (3) the expression for the opacity can be rewritten as:

$$\langle \kappa_i \rangle = \frac{\xi \gamma_i}{\gamma_0 \mu m_{\rm H}} \;;\; \gamma_0 = \int \frac{P(\nu)}{\sigma_{\rm tot}(\nu)}\, d\nu \,. \tag{4}$$

The grain size distribution in a protoplanetary disk has larger grains in protoplanetary disks than in molecular clouds because of grain growth [8]. An increase in the average grain size will decrease the combined area per unit volume, which means that grains will become less efficient in absorbing incoming UV photons. From a typical protoplanetary disk dust size distribution $f(a) \sim a^{-p}$, where a is the dust radius ($0.1\,\mu{\rm m} \leq a \leq 10\,\mu{\rm m}$) we calculate the maximum CRUV photon flux in a gas poor region of a protoplanetary disk to be $N_{\rm CU} \simeq 386{,}000$ photons cm^{-2}s^{-1}. This value is 40 times larger than in molecular clouds, compared to previous estimates of 10^4 photons cm^{-2}s^{-1} [20].

3 Chemical Model

The code `chem_compact` is our VODE based [5] gas/grain chemical rate equation solver. In it we include a reaction network based mostly on the UMIST06 database for astrochemistry [28] and including H_2 formation on grains [6] and ad/desorption reactions: Adsorption and thermal and stellar UV photodesorption from [2, 13, 14], cosmic ray direct and induced UV photo- desorption from [11, 17]. We consider 67 chemical species composed of 8 elements.

Table 1 Physical conditions in relevant gas rich-regions, from the ProDiMo simulation [27]

r (AU)	T (K)	$n_{\langle H \rangle}$ (cm^{-3})
1	80	10^{14}
3–5	65	10^{12}
7–8	40	10^{11}

The initial conditions for our disk model were obtained by running our chemical evolution code under molecular cloud conditions ($T = 20$ K, $n_{\langle H \rangle} = 10^6\,\mathrm{cm}^{-3}$) from atomic, low metallicity abundances. The resulting abundances after 10^7 year were used as initial conditions. We use low metal initial abundances because Si, Fe, and Mg form dust grains before the formation of the disk.[1]

In order to estimate the effects of gas opacity in the CRUV photoprocess rates and therefore in the chemical evolution, we replace the relevant rates from the UMIST [28] database with our own rates, Eq. (1). As these rates depend on ξ_i, we recalculate them at every timestep as the solver yields new values for the gas abundances.

3.1 Chemistry in Gas-Rich Regions

The gas-rich regions of the disk probed in our models are listed in Table 1. In the regions studied, the dominant species are CO (gas) and H_2O (ice) consistently, while O_2, O, SiO, CO_2, and CH_4 are the secondary carriers of carbon, silicon and oxygen. The opacity is mostly provided by O_2, SiO, CO_2, and S, where SiO and O_2 are the species that dominate the opacity. From Figs. 1 and 2 we can see that the evolution of SiO and O_2 correspond to changes in the opacity. For this reason, here we will showcase the interaction between those species. We can see that the correlation between the chemical evolution and the opacity is very complex, and the variations are not linear in nature. This shows that the chemical evolution obtained when considering the effects of gas opacity is not simply halfway between low and a high CRUV field conditions, but it has to be studied in a case by case basis.

In Fig. 2 we can see that at 1 AU after 10^4 year the gas opacities rise, while the dust opacity remains constant. The late O_2 enhancement seen in Fig. 1 implies that it is providing most of the CRUV gas extinction, and thus SiO absorbs less CRUV photons. Thus, as the opacity fraction provided by dust grains is reduced, O_2 self shields and it slows down atomic oxygen formation via photodissociation of SiO. This causes a rebound effect after 10^5 year, as O_2 needs a constant supply of atomic oxygen for its formation.

At 3–5 AU from the central star the temperature is lower than at 1 AU. Thus, SiO is now mostly in the ice phase, while retaining a small presence in the gas. It is kept at a stable but low level throughout the simulation. This implies that OH

[1] This is what sightlines show where the absorption lines of these metals are measured from various clouds against a bright background star [12].

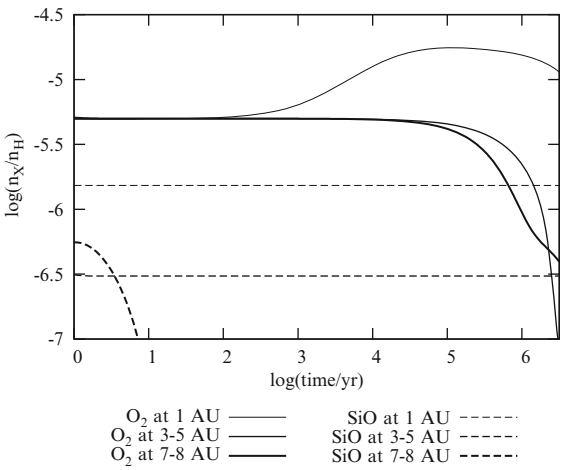

Fig. 1 Chemical abundance evolution

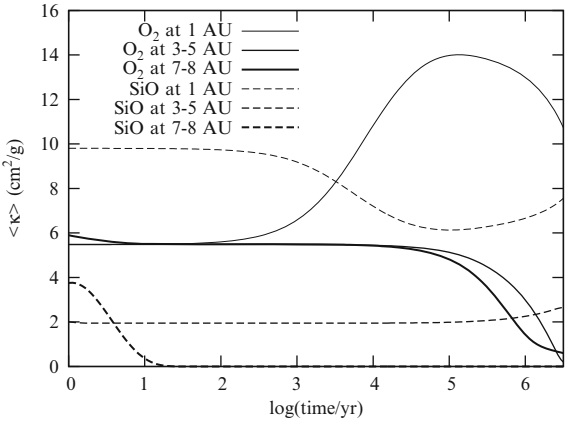

Fig. 2 CRUV gas opacity vs. time. For reference, the dust opacity is 68 cm^2/g (gas)

formation from SiO is not as efficient as it was at 1 AU. The low OH formation rate cannot sustain the formation of O_2 because the oxygen in it is lost to H_2O. The consequent decrease in O_2 opacity causes the CRUV photorates to increase for other molecules, as it allows more CRUV photons to dissociate or ionize other species. This is evidenced in Fig. 2, as the SiO opacity increases as the O_2 opacity decreases. Now CH_4 CRUV photodissociation becomes very efficient at forming CH_2, which reacts with OH faster than any other OH reaction. This exacerbates the depletion of O_2, as seen at the end of the simulation in Fig. 1. The gas opacity in this region is about a third less than in the 1 AU region, which is caused by the lack of efficient O_2 formation and the freeze out of SiO.

As we can see from the chemical evolution plot in Fig. 1, at 7–8 AU SiO is completely frozen after only 1 year, with negligible gas phase abundances, even though the chemical evolution for the other significant species remains more or less the same. However, the lack of SiO in the gas phase impacts the late formation of

H_2O that appears at lower distances. Since O_2 is not consumed in the formation of water, its depletion is not as dramatic as in the 3–5 AU region. The gas opacity here is very similar to that observed at 3–5 AU (Fig. 2), except for the absence of SiO opacity due to freeze out, which enhances the CRUV rates for all other species, including CO.

The longevity granted to SiO in our efficient CRUV induced OH formation models in the disk midplane has repercussions beyond the midplane of the disk. Following [1], the vertical drift timescale $\tau_{\rm vd}$ of a molecule that moves up to a distance $z = \lambda$ above the midplane can be estimated using the disk viscosity. A simple calculation for $\lambda = 0.1$ AU, corresponding to the $A_V = 1$ region (at $r = 1$ AU) of the disk yields that $\tau_{\rm vd} \simeq 280$ year. An SiO molecule can survive for approximately 10^3 year (if $\chi = 1$) or 1 year (if $\chi = 10^3$) before being photodissociated by the stellar UV field at the $A_V = 1$ region. Therefore, in the optimistic (former) case it is possible for SiO to accumulate around $A_V = 1$ and to be detectable. However, since the region where SiO is being formed has a small radial extent ($r \leq 1 - 5$ AU), its detection could prove to be very difficult.

3.2 Chemistry at 10 AU

In this region the environment is cold enough (20 K, at a density of $10^{10}\,{\rm cm}^{-3}$) to allow us to study the chemical evolution without taking into account the gas opacity [7]. Under these conditions, the CRUV rate constant takes the familiar form:

$$k_{{\rm CU},i} = \frac{\zeta_{\rm H_2}}{\sigma^{\rm UV}_{\langle {\rm H} \rangle}(1-\omega)} \int_{1.76\,{\rm PHz}}^{3.28\,{\rm PHz}} P(\nu)\sigma_i(\nu)\,d\nu \ . \tag{5}$$

This is the expression that is frequently used in models that include CRUV photoprocesses [10,21,28], mostly because it is valid for ISM and molecular cloud conditions (low gas abundances). This formula is very convenient for computing the chemical rate equations, as everything in the rate constant can be calculated beforehand.

After 10^6 years the ice content resembles what is observed in cometary ices [3,4], where H_2O ice is followed by CO and CO_2 ice and, to a lesser degree, CH_4 ice. In our model, CH_4 ice is formed only after water ice formation has become so efficient that it takes away most of the oxygen from CO and leaves the carbon free to form other molecules. This suggests that the CH_4 ice found in comets may have been formed at a late stage of the disk evolution.

We present a comparison between measured cometary ice abundances and our resulting ice abundances in Table 2. Our resulting ice ratios are very close to the cometary values when using a cometary carbon-to-oxygen ratio. This happens because a fraction of the total carbon may be stored in the core of dust grains in our model. These results fit the cometary $n_{\rm CO\#}/n_{\rm H_2O\#}$ and $n_{\rm CO_2\#}/n_{\rm H_2O\#}$ ratios closely, which means that the relative abundances of ice species can be predicted by our model.

Table 2 Ice ratios in comets compared to our results

Ratio	Cometary measurements[a]	c_c[b]: [C/O] = 0.16 10^7 year
$n_{CO_2\#}/n_{CO\#}$	<0.6	0.43
$n_{CO\#}/n_{H_2O\#}$	<0.2	0.14
$n_{CO_2\#}/n_{H_2O\#}$	0.02–0.12	0.06
$n_{CH_4\#}/n_{H_2O\#}$	0.003–0.015	<0.001

[a] Abundances compiled from cometary measurements in [3, 4]

[b] Ratios from our `chem_compact` model

4 Conclusions

We have included the information of the gas opacity of all molecules that are photoprocessed by cosmic ray induced UV photons in our chemical evolution model. By studying the impact that the gas opacity of individual species has on the chemistry and viceversa, we can build a simplified tool that includes the most important species while understanding the underlying relationship between the opacity and the chemistry. As some opacities rise, an important shielding effect appears and the CRUV photoprocess rates change. This affects the chemical formation pathways for both gas and ice phase species.

The most important species that contribute to the gas opacity are O_2, SiO, Si, CO and CO_2, in a consistent manner throughout the 1–8 AU region of the disk midplane. We find that the opacities of O_2, SiO (and CO_2 in the warm regions around 1 AU) are the most variable in time and hence are the ones that require most attention, and whose effects cannot be easily dismissed. As the CO and S abundances remain more or less constant in those regions, their opacity remains fairly constant as well. Thus, future models must include this treatment of CRUV gas and dust opacity while only considering the contribution of the most significant species that our models yield for the probed regions of the disk.

Finally, we found that if SiO is steadily created in the midplane at long timescales, it can drift vertically upwards and accumulate around the $A_V = 1$ region, thus suggesting a possibility for future detections of SiO in protoplanetary disks.

References

1. Aikawa, Y. 2007, ApJL, 656, L93
2. Aikawa, Y., Miyama, S. M., Nakano, T., & Umebayashi, T. 1996, ApJ, 467, 684
3. Bockelée-Morvan, D., Crovisier, J., Mumma, M. J., & Weaver, H. A. 2004, The composition of cometary volatiles, ed. Festou, M. C., Keller, H. U., & Weaver, H. A., 391–423
4. Bockelée-Morvan, G. 2010, in Physics and Astrophysics of Planetary Systems, EAS Publication Series No. 41, 313–324
5. Brown, P. N., Byrne, G. D., & Hindmarsh, A. C. 1989, SIAM J. Sci. Stat. Comput., 10, 1038

6. Cazaux, S. & Tielens, A. G. G. M. 2002, ApJL, 575, L29
7. Chaparro Molano, G. & Kamp, I. 2012, A&A, 537, A138
8. D'Alessio, P., Calvet, N., & Hartmann, L. 2001, ApJ, 553, 321
9. Fedele, D., van den Ancker, M. E., Henning, T., Jayawardhana, R., & Oliveira, J. M. 2010, A&A, 510, A72
10. Gredel, R., Lepp, S., Dalgarno, A., & Herbst, E. 1989, ApJ, 347, 289
11. Hasegawa, T. I. & Herbst, E. 1993, MNRAS, 261, 83
12. Jenkins, E. B. 2009, ApJ, 700, 1299
13. Leger, A., Jura, M., & Omont, A. 1985, A&A, 144, 147
14. Öberg, K. I., van Dishoeck, E. F., & Linnartz, H. 2009, A&A, 496, 281
15. Prasad, S. S. & Tarafdar, S. P. 1983, ApJ, 267, 603
16. R. Riahi, Ph. Teulet, Z. Ben Lakhdar, & A. Gleizes. 2006, Eur. Phys. J. D, 40, 223
17. Roberts, J. F., Rawlings, J. M. C., Viti, S., & Williams, D. A. 2007, MNRAS, 382, 733
18. Semenov, D., Hersant, F., Wakelam, V., et al. 2010, A&A, 522, A42
19. Semenov, D., Wiebe, D., & Henning, T. 2004, A&A, 417, 93
20. Shen, C. J., Greenberg, J. M., Schutte, W. A., & van Dishoeck, E. F. 2004, A&A, 415, 203
21. Sternberg, A., Dalgarno, A., & Lepp, S. 1987, ApJ, 320, 676
22. Thi, W.-F., Woitke, P., & Kamp, I. 2011, MNRAS, 412, 711
23. Umebayashi, T. & Nakano, T. 1981, PASJ, 33, 617
24. Visser, R., Doty, S. D., & van Dishoeck, E. F. 2011, A&A, 534, A132
25. Visser, R., van Dishoeck, E. F., Doty, S. D., & Dullemond, C. P. 2009, A&A, 495, 881
26. Walsh, C., Millar, T. J., & Nomura, H. 2010, ApJ, 722, 1607
27. Woitke, P., Kamp, I., & Thi, W. 2009, A&A, 501, 383
28. Woodall, J., Agúndez, M., Markwick-Kemper, A. J., & Millar, T. J. 2007, A&A, 466, 1197

The Central Regions of Local (U)LIRGs Viewed with Big Radio Eyes

Miguel Ángel Pérez-Torres

Abstract I review some of the main results obtained by our team in the last few years on high-angular resolution radio studies of nearby Luminous and Ultra-Luminous Infrared Galaxies (LIRGs and ULIRGs, respectively). These galaxies are expected to form stars at rates $\gtrsim$(10–100) $M_\odot$ year^{-1}, and produce core-collapse supernovae at rates $\gtrsim$(0.3–3) year^{-1}. (U)LIRGs are also expected to be bright at radio wavelengths, thanks to the ubiquitous Far-Infrared Radio correlation, which makes high-angular resolution ($\lesssim 0.1''$) radio observations an excellent tool for probing the inner $\simeq$100 pc region of local (U)LIRGs. I justify the need for this high-angular resolution radio studies of local (U)LIRGs and, among other results, I present the impressive discovery of an extremely prolific supernova factory in the central $\sim$150 pc of the galaxy Arp 299-A (D = 45 Mpc) and the monitoring of a large number of very compact radio sources in it, the detection and precise location of the long-sought AGN in Arp 299-A and, more recently, the evidence for the existence of nuclear disks ($\lesssim$100 pc in size) in starburst galaxies from their radial distribution of supernovae. All those results show that very-high angular resolution studies of nearby (U)LIRGs are of high relevance for the comprehension of both local and high-z starbursting galaxies.

1 Introduction

The study of galaxies at the highest infrared luminosities, i.e., Luminous $10^{11}\,L_\odot \leq L_{IR} \leq 10^{12}\,L_\odot$) and Ultra-Luminous ($L_{IR} \geq 10^{12}\,L_\odot$) Infrared Galaxies (LIRGs and ULIRGs, respectively) is relevant for many reasons:

M.Á. Pérez-Torres (✉)
IAA-CSIC, Glorieta de la Astronomía s/n, 18008 Granada, Spain
e-mail: torres@iaa.es

D.F. Torres and O. Reimer (eds.), *Cosmic Rays in Star-Forming Environments*, Astrophysics and Space Science Proceedings 34, DOI 10.1007/978-3-642-35410-6_11,

1. (U)LIRGs account for about 10 % of the total radiant energy production and provide ∼20 % of all the high-mass star-formation in the local universe (e.g., [6]).
2. The bulk of the energy radiated by ULIRGs is infrared emission from warm dust grains heated by a central power source, or sources, whose nature (AGN, starburst, or both) is often unknown, but whose evolution is likely to be related.
3. Essentially all LIRGs above $\sim 10^{11.4}\,L_{\odot}$ appear to be interacting galaxies and all ULIRGs seem to be advanced merger systems. Thus they may represent an important stage in the formation of quasi-stellar objects (e.g., [46]).
4. (U)LIRGs are also of cosmological relevance, as they bear many similarities with star-forming galaxies at high-z (e.g. local UV-bright starbursts are good analogs to Lyman Break Galaxies (e.g. [34]).
5. Finally, (U)LIRGs are ideal laboratories to study the complex ecosystems of stars, gas, Black Holes, the interstellar medium (ISM), and test massive star and black-hole starbursts evolution, or probe the Initial Mass Function (IMF) of the high-mass stars.

2 The Dust Heating Central Source: AGN Versus SB

As mentioned above, the bulk of the energy radiated by ULIRGs is infrared emission from warm dust grains heated by a central power source, or sources. The critical question concerning these galaxies is whether the dust in the central regions ($r \lesssim 1$ kpc) is heated by a starburst or an active galactic nucleus (AGN), or a combination of both. Mid-infrared spectroscopic studies on samples of ULIRGs (e.g. [19]) suggested that the vast majority of these galaxies were powered predominantly by recently formed massive stars, with a significant heating from the AGN only in the most luminous objects [52]. Veilleux et al. also found that at least half of ULIRGs are probably powered by both an AGN and a starburst in a circumnuclear disk or ring. These circumnuclear regions are typically located at radii $r \lesssim 700$ pc from the nucleus of the galaxy, and also contain large quantities of dust. Those facts (compactness of the emission and dusty environments) prevent to gain much insight into the nature of the central source, either from optical, or infrared observations.

2.1 The Need of High-Angular Radio Observations of (U)LIRGs

Why radio observations? Those largely dusty environments imply huge extinctions in the optical, and even in the infrared, which prevents the direct detection of recent starburst activity, e.g., via supernova explosions. The advantage of observing in radio is that these wavelengths are not affected by dust obscuration, thus allowing to see the activity within those deeply buried regions.

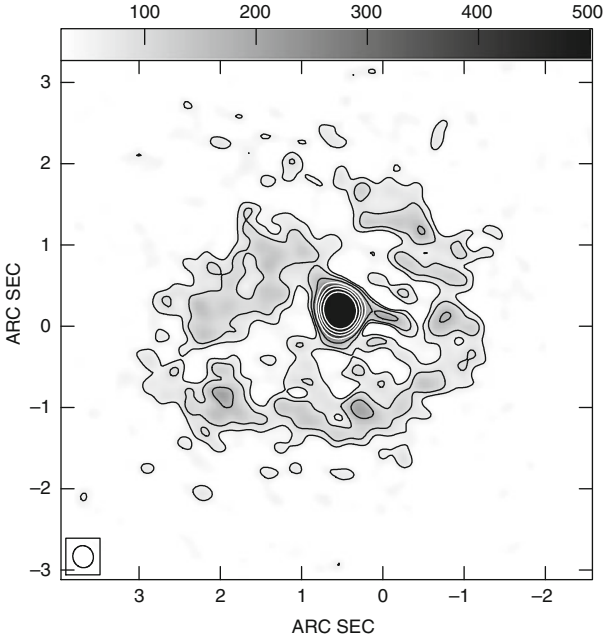

Fig. 1 The LIRG Mrk 331 (D = 75 Mpc) imaged at 8.46 GHz with the VLA on December 2006 (unpublished image). The synthesized FWHM beam is a Gaussian beam of size $0.27'' \times 0.25''$. Contour levels are drawn at $(3, 3\sqrt{3}, 9, \ldots) \times 19\mu$Jy beam^{-1}, the off-source rms of the image, and the peak of brightness is 7.3 mJy beam^{-1}, and corresponds to the bright spot in the central region of the galaxy. $1''$ corresponds to 357 pc (See text for details)

Why high-angular resolution? At a typical distance of 100 Mpc to a local (U)LIRG, $1''$ corresponds to a linear size of about 500 pc. Therefore, if one aims at spatially resolving the circumnuclear regions of (U)LIRGs to understand in detail the ongoing processes in the central regions of those monsters, sub-arcsecond resolution is a must. This makes an excellent case for high-angular resolution radio observations of (U)LIRGs, since current radio interferometric arrays provide sub-arcsecond angular resolution (EVLA, MERLIN) or even milliarcsecond resolution, using Very Long Baseline Interferometry (VLBI).

How do (U)LIRGs look in radio? The central kiloparsec region of many nearby (U)LIRGs shows a distribution of their radio emission typically consisting of a compact ($\lesssim$200 pc), high surface brightness, central radio source corresponding to an active nuclear region (whether powered by an AGN, or a nuclear starburst), immersed in a low surface brightness circumnuclear, extended ($\simeq$1 kpc) halo [13].

As an example, I show in Fig. 1 an 8.46 GHz VLA image of the LIRG Mrk 331. At a distance of D = 75 Mpc to Mrk 331, $1''$ corresponds to a linear size of 357 pc. Note that all radio emission is concentrated in a region whose angular size is less that $3''$ in diameter, or less than 1 kpc. The total 8.5 GHz flux density is of $\simeq$29.3 mJy, corresponding to a monochromatic radio luminosity of $\sim 1.6 \times 10^{29}$ erg s^{-1} Hz^{-1}.

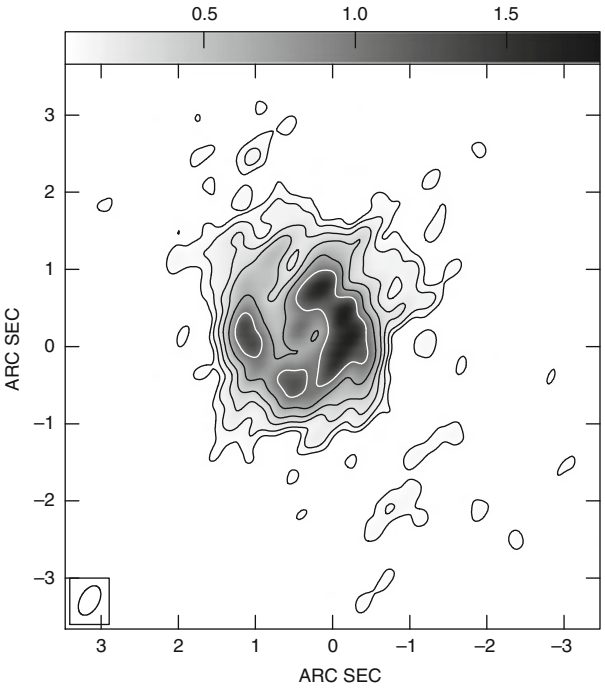

Fig. 2 The LIRG NGC 1614 (D = 65.6 Mpc) imaged at 8.46 GHz with the VLA on June 2006 (unpublished image). The synthesized FWHM beam is a Gaussian beam of size $0.42'' \times 0.24''$. Contour levels are drawn at $(3, 3\sqrt{3}, 9, \ldots) \times 22\,\mu\text{Jy beam}^{-1}$, the off-source rms of the image, and the peak of brightness is 1.78 mJy beam $^{-1}$, and corresponds to a bright spot in the circumnuclear ring of star-formation. $1''$ corresponds to 320 pc (See text for details)

It often happens also that the high-surface brightness is not at the central $\sim$200 pc region, but on a prominent circumnuclear ring where a burst of recent star formation is ongoing. Figure 2 shows an 8.46 GHz VLA image of the LIRG NGC 1614. At the distance of D = 65.6 Mpc to NGC 1614, $1''$ corresponds to a linear size of 320 pc. As with Mrk 331, all radio emission is concentrated in a region less than 1 kpc in size. The total 8.5 GHz flux density is of $\simeq$32.9 mJy, corresponding to a monochromatic radio luminosity of $\sim 1.8 \times 10^{29}$ erg s^{-1} Hz^{-1}, and I note that unlike the case of Mrk 331, where the circumnuclear ring is very faint, about 90 % of the radio luminosity from NGC 1614 comes from a prominent circumnuclear ring which is at a distance of $\sim$250 pc from the nucleus of the galaxy.

Based on those high-angular radio observations, it is evident that, contrary to what we would have thought from a lower-resolution image, most of the starburst activity happening in NGC 1614 is actually taking place in this ring. By converting the measured flux density into a brightness temperature, $T_{\rm b}$, we would find out that this temperature is, in most regions of the ring, much higher than the thermal temperature of the plasma around the massive stars, implying a non-thermal (synchrotron) origin for the radio emission. The natural explanation for

this non-thermal emission is that it is due to recent explosions of core-collapse supernovae (CCSNe) and supernova remnants (SNRs), which implies that most of the starburst activity is still ongoing ($t \lesssim 40$ Myr) in the ring of NGC 1614.

Some of the most spectacular examples where high-sensitivity, high-resolution radio observations have been extremely important in studying both the nuclear and circumnuclear include, among others, the discovery of individual supernovae, e.g. SN 2000 feet, one of the brightest radio supernovae ever, which exploded in the circumnuclear starburst region of the LIRG NGC 7469 [1, 11, 39], or the discovery of large populations of radio supernovae and supernova remnants in the nuclear regions of the ULIRGs Mrk 273 [4] and Arp 220 [37], and of the LIRG Arp 299 [39], using VLBI observations. In this review, I will discuss in detail Arp 299.

3 Radio as a Direct Tracer of Massive Star-Formation in (U)LIRGs, Near and Far

A large fraction of the massive star-formation at both low- and high-z has taken place in (U)LIRGs [29, 30]. Indeed, by applying evolutionary stellar models (e.g. [26]) to bursts of age 10–100 Myr, and adopting a standard IMF, one can obtain the SFR as a function of $L_{\rm FIR}$ [25]:

$$\mathrm{SFR} \approx 17.2 \left(\frac{\mathrm{L_{FIR}}}{10^{11}\,\mathrm{L_\odot}} \right) \mathrm{M_\odot\ year^{-1}} \tag{1}$$

While the compact, centrally located radio emission in these galaxies might be generated by a point-like source (AGN), or by the combined effect of multiple RSNe and supernova remnants (SNRs), e.g., the evolved nuclear starburst in Arp 220 ([37] and references therein) and M 82, it seems now well established that in the circumnuclear regions of those objects there is an ongoing burst of star formation producing core-collapse supernovae (CCSNe, Type Ib/c and Type II SNe) at a high rate (e.g. NGC 7469 [11]; Arp 299 [35]; NGC 6240 [18]; Arp 220 [37]; IRAS 18293-3413 [33, 41]; IRAS 17138-1017 [22, 38]). Therefore, a powerful tracer for (recent) starburst activity in (U)LIRGs is the detection of core-collapse supernovae (CCSNe).

Since stars more massive than $\mathrm{M} \gtrsim 8\,\mathrm{M_\odot}$ explode as CCSNe, the observed rate at which those stars die ($r_{\rm CCSN}$) can be used as a direct measurement of the current star formation rate (SFR) in galaxies, and may provide unique information about the initial mass function (IMF) of the high-mass stars. Indeed, if for the sake of simplicity we assume a constant star-formation rate for a starburst, it can be shown that (e.g. [39])

$$r_{\rm CCSN} = \int_{m_{\rm SN}}^{m_u} \Phi(m)\, dm = SFR \left(\frac{\alpha - 2}{\alpha - 1} \right) \left(\frac{m_{\rm SN}^{1-\alpha} - m_u^{1-\alpha}}{m_l^{2-\alpha} - m_u^{2-\alpha}} \right) \tag{2}$$

where *SFR* is the (constant) star formation rate in $M_\odot$ year^{-1}, m_l and m_u are the lower and upper mass limits of the initial mass function (IMF, $\Phi \propto m^{-\alpha}$), and m_{SN} is the minimum mass of stars that yield supernovae, assumed to be 8 $M_\odot$ (e.g., [47]).

While the rate at which stars die in normal galaxies is rather low (e.g., one SN is expected to explode in the Milky Way every ∼50 year), the CCSN rate in luminous and ultraluminous infra-red galaxies (LIRGs, $L_{IR} \equiv L[8-1{,}000\,\mu m] \geq 10^{11}\,L_\odot$; and ULIRGs, $L_{IR} \geq 10^{12}\,L_\odot$; [46]) is expected to be at least one to two orders of magnitude higher than in normal galaxies, and hence detections of SNe in (U)LIRGs offer a promising way of determining the current star formation rate in nearby galaxies. In fact, by combining Eqs. 20 and 26 from Condon [12] -who assumes a Miller-Scalo IMF- one can obtain

$$r_{CCSN} \approx 0.37 \left(\frac{L_{FIR}}{10^{11}\,L_\odot} \right) \text{year}^{-1} \tag{3}$$

where $L_{FIR} = L[40-400\,\mu m]\,L_\odot$. [31] found an empirical relation between the (constant) CCSN rate and $L[8-1,000\,\mu m]$ for starburst galaxies, which yields a similar value to that obtained by [12]:

$$r_{CCSN} \approx 0.27 \left(\frac{L_{FIR}}{10^{11}\,L_\odot} \right) \text{year}^{-1} \tag{4}$$

where in both equations it is assumed that there is no AGN contribution to the IR luminosity.

Equations (1), (3) and (4) clearly show that (U)LIRGs are prolific star-forming factories, with LIRGs having typical values of SFRs and core-collapse supernova rates of ∼(17–170) $M_\odot$ year^{-1} and $r_{CCSN} \sim (0.3-3.0)$ year^{-1}, respectively, and ULIRGs in excess of those upper ends.

However, the direct detection of CCSNe in the extreme densities of the central few hundred pc of (U)LIRGs is, as pointed out earlier, extremely difficult since emission in the visual band suffers very significant extinction in those regions, which contain large amounts of dust, and can at best yield only a lower limit to the true value of r_{CCSN}. Fortunately, radio is not affected by dust absorption. Moreover, significant radio emission from CCSNe is expected -as opposed to thermonuclear SNe- as the interaction of the SN ejecta with the circumstellar medium (CSM) gives rise to a high-energy density shell, which is Rayleigh-Taylor unstable and drives turbulent motions that amplify the existing magnetic field in the presupernova wind, and efficiently accelerate relativistic electrons, thus enhancing the emission of synchrotron radiation at radio wavelengths [7].

Thus, starburst activity in the circumnuclear regions of LIRGs ensures both the presence of a high number of massive stars and a dense surrounding medium, so bright radio SNe are expected to occur. Those SNe can be detected, even in the innermost regions of (U)LIRGs, by means of high angular resolution (≤0.05 arcsec), high-sensitivity (≤0.05 mJy) radio searches of CCSNe, as radio emission is unaffected by dust extinction, and the angular resolution yielded by

current Very Long Baseline Interferometry (VLBI) arrays, of the order of a few milliarcsec at cm-wavelengths, is able to detect individual radio supernovae at large distances in the local Universe (e.g. Arp 220, [37]; Arp 299, [5,42]; see also Fig. 6).

3.1 Are SNe in Starburst Environments Intrinsically Different?

At conferences, I have been asked this question several times, and the reasoning goes as follows: Since the ambient conditions where SNe explode in (U)LIRGs are extreme, in comparison with those encountered in nearby, normal galaxies (e.g., number densities of the insterstellar medium of $10^3\,\mathrm{cm}^{-3}$, rather than $\sim 1\,\mathrm{cm}^{-3}$), could the supernovae exploding there be intrinsically different?

I show in Fig. 3 a set of images of the LIRG NGC 7469 and its supernova SN 2000ft taken from Pérez-Torres et al. [42]. SN 2000ft resulted in one of the brightest radio supernovae ever with a peak radio luminosity of $\sim 2 \times 10^{28}\,\mathrm{erg\,s^{-1}\,Hz^{-1}}$ at 8.4 GHz [11]. It exploded in the circumnuclear region of NGC 7469, at a distance of $\sim$600 pc from the center of its host galaxy, and its evolution went in a pretty standard way (see Fig. 4), typically seen for radio supernovae in nearby, normal galaxies. The "only" remarkable aspect was that the SN was never detected at low frequencies ($\nu \lesssim 1.6$ GHz), which was interpreted as being due to a foreground absorber present in the galaxy, i.e., an H II region. This is not surprising, considering the large amount of H II regions that exist in starburst galaxies. Foreground absorbers have been also found close to a few other radio supernovae in nearby, normal galaxies.

Thanks to this spectacular radio monitoring, many things were learnt about the properties of the supernova progenitor, the circumstellar medium (CSM) and the interstellar medium (ISM). For example, Pérez-Torres et al. [42] found $\dot{M} \lesssim (4.7-5.1) \times 10^{-5}\mathrm{M}_\odot\,\mathrm{year}^{-1}$ for SN 2000ft, typical of a red supergiant progenitor star. Those authors also found that the radio emission from SN2000ft was driven by its interaction with the CSM, rather than with the ISM.

In fact, the duration of the radio SN phase (when the radio emission is governed by interaction between the ejecta and its circumstellar medium, CSM) is limited by the extent of the expanding presupernova wind, since the latter eventually reaches a radius where its ram pressure, $\rho_w\, v_w^2$, equals the external pressure of the interstellar medium (ISM), P_{ISM} [9]. For a spherically symmetric, steady wind ($\rho_w \propto r^{-2}$), this radius is

$$r_w \approx 0.18\, \dot{M}_{-4}^{1/2} v_{w1}^{1/2} p_7^{-1/2}\,\mathrm{pc} \tag{5}$$

where $p_7 = P_{ISM}/k$ is the ISM pressure in units of $10^7\,\mathrm{cm}^{-3}\,\mathrm{K}$, which is the estimated pressure for the central region of the starburst in M 82 ([8]). Once the ram pressure goes below P_{ISM}, the core-collapse supernova enters its supernova remnant (SNR) phase, and its radio emission is no longer powered by the interaction with the CSM, but rather with the ISM. At this stage, the density encountered by the SN would be constant, which would result in a significant flattening of the radio emission, or even an increase, i.e., a departure from the general, steep decline

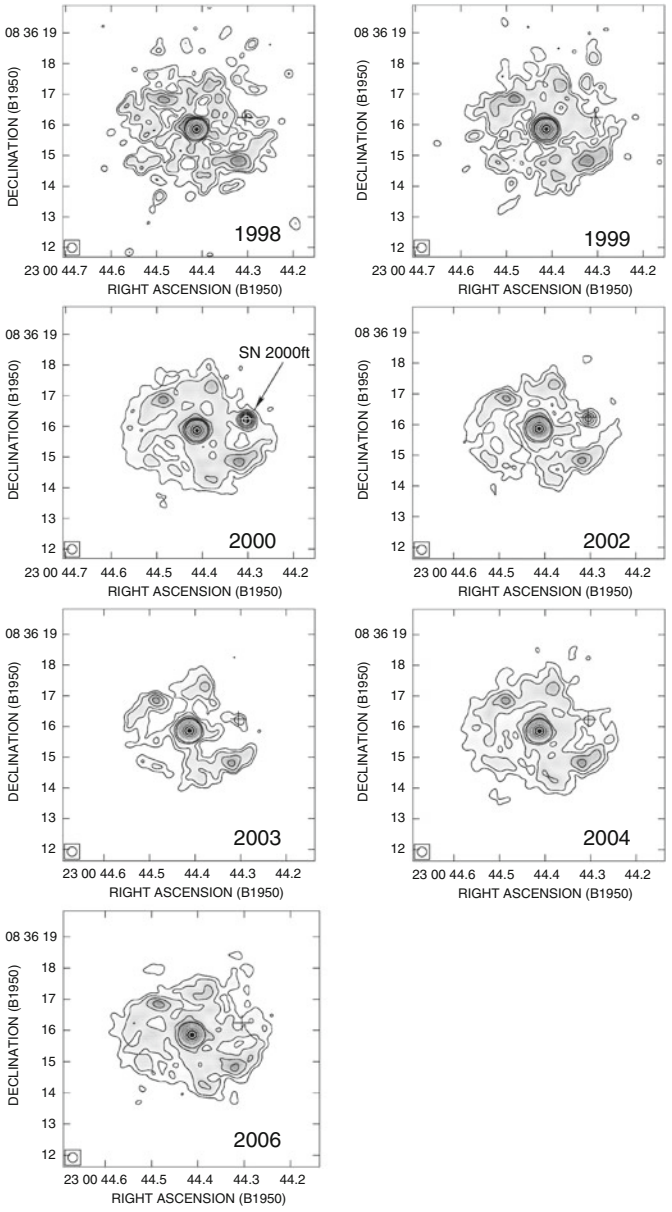

Fig. 3 Total intensity radio images of the SN 2000ft and its host galaxy LIRG NGC 7469, obtained at 8.4 GHz with the VLA in A-configuration, which cover a time baseline of almost 8 years (from 8 April 1998 till 5 February 2006). The maps have been spatially convolved to obtain the same circular Gaussian beam of size $0.31''$, to be able to compare adequately all the images. The contour levels are drawn at $(3, 3\sqrt{3}, 9, \ldots) \times 25\mu\mathrm{Jy\,beam}^{-1}$, which is the highest off-source rms of all the maps (corresponding to the 1998 and 1999 epochs). The peaks of brightness correspond to the nucleus of NGC 7469. The cross corresponds to the position of the peak of SN 2000ft in the 2,000 image.

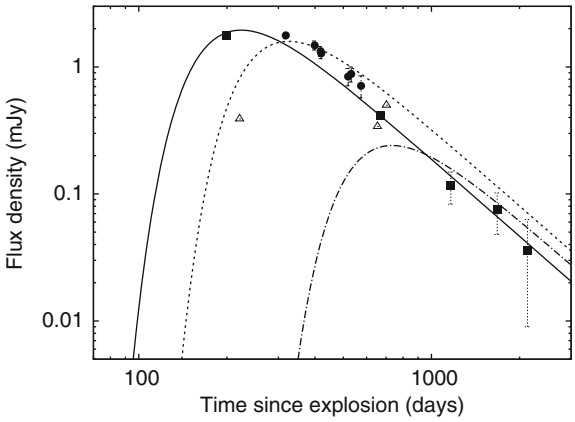

Fig. 4 Radio light curve of SN 2000ft at 8.4 GHz (*filled squares*), 5.0 GHz (*filled circles*), and 1.6 GHz (*upper limits*; *open triangles*), along with the resulting light curve fits (8.4 GHz, *solid line*; 5.0 GHz, *dotted line*; 1.4 GHz, *dashed-dotted line*) of the parameterized model described in Pérez-Torres et al. [42]. Note that the late time data ($t \gtrsim 1{,}000$ days) follows genuinely a steep power-law decline

observed in the early times of the optically thin phase of SN 2000f. No such thing has been observed for SN 2000ft, which confirms its radio emission is still due to CSM interaction, not to interaction with the ISM. In other words, it is still a (young) SN, not a radio supernova remnant (RSN).

Strong starburst activity in the circumnuclear regions of (U)LIRGs implies both the presence of a high number of massive stars and a dense surrounding medium, so bright radio SNe are expected to occur [7, 10], and high-resolution radio observations have shown that highly extinguished CCSNe do exist in the circumnuclear ($r \lesssim 1$ kpc) regions of local (U)LIRGs [11, 22, 28, 35, 41, 48]. Therefore, VLBI observations can place strong constraints on the properties of star formation in the dust-enshrouded environments encountered in (U)LIRGs.

3.2 Arp 220

One of the most remarkable cases among (U)LIRGs is the prototypical ULIRG Arp 220. Its central region is composed of two radio nuclei, each of them hosting a large number of compact components, mostly identified with young SNe and SNRs (see, e.g., [37]) and Fig. 5). The radio light curves of many of those SNe appeared to be stable over periods $\geq$5 year, indicating their interaction with a dense ISM [44]. The eastern nucleus hosts 20 RSNe, while the western one hosts 29 RSNe, and it is about three times brighter, suggesting that there might be a differential free-free absorption in the nuclei [28].

Recently, Parra et al. [37] have detected many of the compact components in Arp 220 at frequencies above 1.6 GHz, and their spectra indicate the presence of both relatively young SNe along with SNRs. Moreover, the radio supernova rate found by Parra et al. [37] seems to coincide with the expected CCSN rate (4 SN/year) as inferred from Arp 220 infrared luminosity. Since all the new RSNe are very bright,

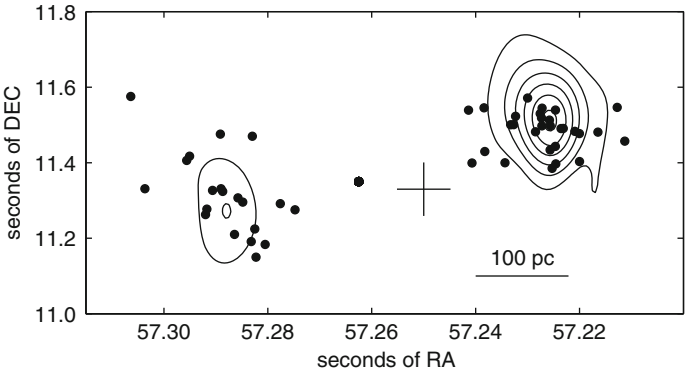

Fig. 5 Overall view of the Arp 220 nuclear region. *Filled circles* are the corrected positions of the 49 compact sources at 18 cm catalogued by [28]. Contours show a 6 cm delay–rate map ("Single baseline snapshot image") obtained from a 10 min scan with the Ar–Eb baseline in project EP049. Contours are drawn 500 μJy apart starting from 500 μJy. The data was tapered in time and frequency to reduce sidelobes, resulting in a delay–rate beam of FWHM ∼200 mas and a map noise of ∼42 μJy. The *cross* indicates the reference position RA(J2000.0) = $15^{\rm h}34^{\rm m}57.^{\rm s}25$, DEC(J2000.0) = $+23°30'11.''33$

indicating they are Type IIn-like SNe (whose progenitor stars are very massive), this may indicate a top-heavy IMF for the stars in the nuclei of Arp 220.

3.3 Arp 299

Arp 299 consists of two interacting galaxies (IC 694 and NGC 3690), which are in an early merger stage [24]. At a luminosity distance of 44.8 Mpc [15] for $H_0 = 73\,{\rm km\,s^{-1}\,Mpc^{-1}}$, Arp 299 has an infrared luminosity $L_{\rm IR} \approx 6.7 \times 10^{11} L_\odot$ [45], which almost qualifies it as a ULIRG. The innermost ∼150 pc nuclear region of Arp 299-A (see Fig. 6) is heavily dust-enshrouded, thus making the detections of SNe very challenging even at near-infrared wavelengths. Yet, Arp 299 hosts recent and intense star-forming activity, as indicated by the relatively high frequency of supernovae discovered at optical and near-infrared wavelengths in its outer, much less extinguished regions [16, 27, 32, 43, 51, 54].

The brightest component at infrared and radio wavelengths is IC 694 (A in the top panel of Fig. 6; hereafter Arp 299-A), which accounts for ∼50 % of the total infrared luminosity of the system, and ∼70 % of its 5 GHz radio emission [35]. Numerous H II regions populate the system near star-forming regions, which implies that star formation has been occurring at a high rate for past ∼10 Myr [2]. Given that IC 694 accounts for most of the infrared emission in Arp 299, it is the region that is most likely to contain new SNe [13]. Since optical and near-infrared observations are likely to miss a significant fraction of CCSNe in the innermost regions of

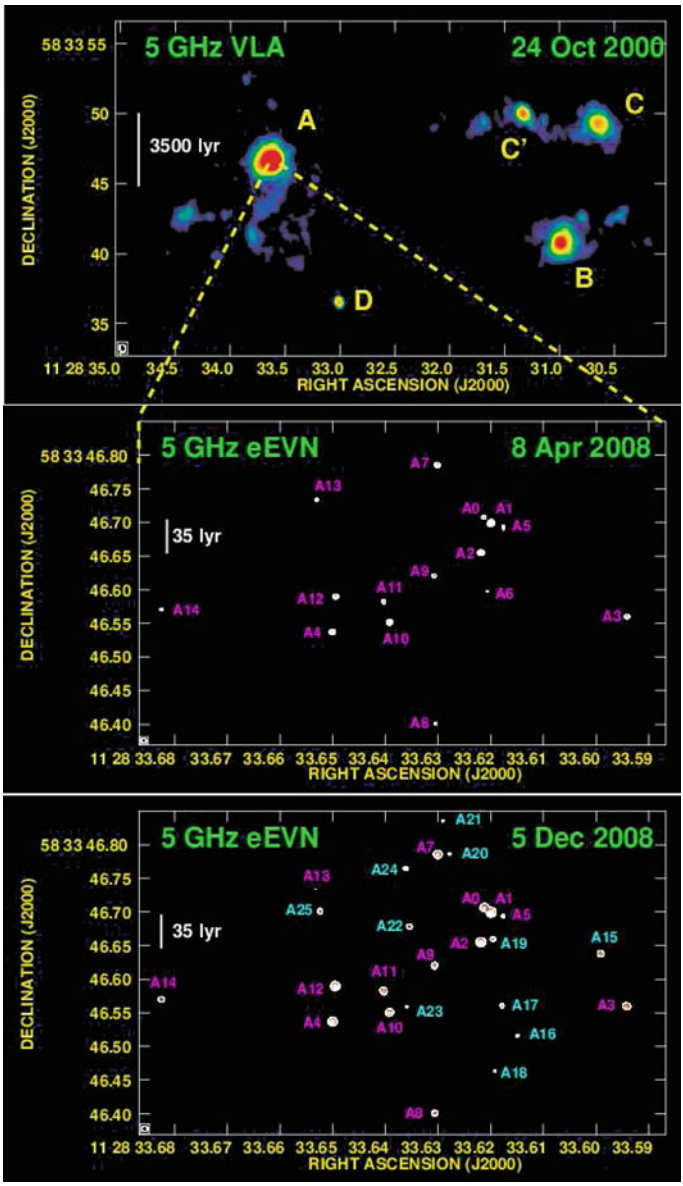

Fig. 6 *Top:* 5 GHz VLA archival observations of Arp 299 on 24 October 2000, displaying the five brightest knots of radio emission in this merging galaxy. *Middle* and *bottom*: Contour maps drawn at five times the r.m.s. of our 5 GHz eEVN observations of the central 500 light years of the luminous infrared galaxy Arp 299-A on 8 April 2008 and 5 December 2008, revealing a large population of relatively bright, compact, non-thermal emitting sources. The size of the FWHM synthesized interferometric beam was (0.6 × 0.4 arcsec) for the VLA observations, and (7.3 × 6.3 milliarcsec) and (8.6 × 8.4 milliarcsec) for the EVN observations on 8 April 2008 and 5 December 2008, respectively. To guide the reader's eye, we show in *cyan* the components detected only at the 5 December 2008 epoch

Arp 299-A due to high values of extinction ($A_V \sim 34 - 40$ Gallais et al. [17] and Alonso-Herrero et al. [2]) and the lack of the necessary angular resolution, radio observations of Arp 299-A at high angular resolution, high sensitivity are the only way of detecting new CCSNe and measuring directly and independently of any model its CCSN and star formation rates. Very Long Baseline Array (VLBA) observations carried out during 2002 and 2003 resulted in the detection of five compact sources [35], one of which (A0) was identified as a young SN.

4 The AGN-Starburst Connection in Arp 299-A

As mentioned in the introduction of this contribution, the dusty nuclear regions of luminous infra-red galaxies (LIRGs) are heated by either an intense burst of massive star formation, or an active galactic nucleus (AGN), or a combination of both. Disentangling the contribution of each of those putative dust-heating agents is a challenging task, and direct imaging of the innermost few pc can only be accomplished at radio wavelengths, using very high-angular resolution observations.

My team and I started to monitor the A-nucleus of the interacting starburst galaxy Arp 299, using very long baseline interferometry (VLBI) radio observations at 1.7 and 5.0 GHz [42]. Our aim was to characterize the compact sources in the innermost few pc region of Arp 299-A, as well as to detect recently exploded core-collapse supernovae. We imaged with milliarcsecond resolution the inner 8 pc of the nuclear region in Arp 299-A, using contemporaneous EVN observations at 1.7 and 5.0 GHz [40], and the summary of those results is shown in Fig. 7. At 5.0 GHz, we detect components A0, A1, and A5, as previously detected by Pérez-Torres et al. [39]. At 1.7 GHz, A1 and A5 are also detected, but not A0. In addition, two new components between A1 and A5 (A1b and A1c) are detected at 1.7 GHz, forming a complex.

The morphology, spectral index, radio luminosity, and radio-to-X ray luminosity ratio of the A1–A5 complex are consistent with that of an LLAGN, and rules out the possibility that it consists of a chain of young RSNe and SNRs in a young SSC. We therefore concluded that A1 is the long-sought AGN in Arp 299-A. Since Arp 299-A had long been thought of as a pure starburst, our finding of a buried, low-luminosity AGN in its central region, coexisting with a recent burst of starformation, suggests that both a starburst and AGN are frequently associated phenomena in mergers. In this case, our result is likely to have an impact on evolutionary scenarios proposed for AGN and the triggering mechanism of activity in general.

We note that component A0, previously identified as a young RSN by Neff et al. [35], is not seen at our low-frequency observations, which implies there must be a foreground absorbing H II region, which precludes its detections at frequencies $\lesssim$1.7 GHz. It is remarkable that this RSN exploded at the mere (deprojected) distance of 2 pc from the putative AGN in Arp 299-A, which makes this supernova one of the closest to a central supermassive black hole ever detected. This result may also be relevant to accreting models in the central regions of galaxies, since it is not

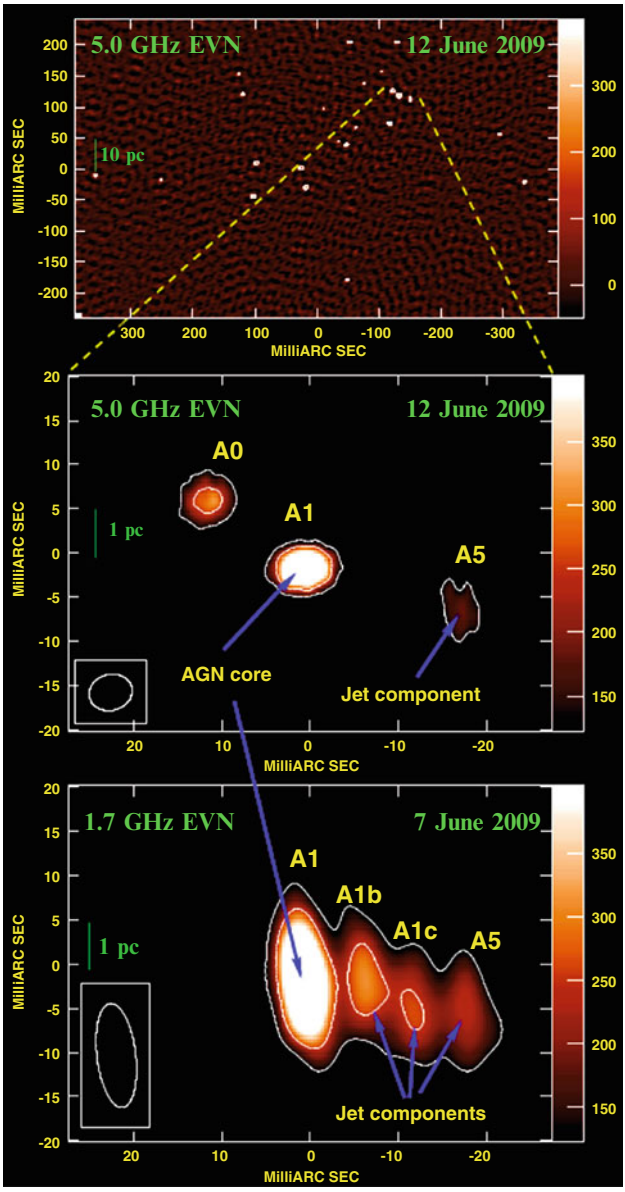

Fig. 7 *Top:* 5.0 GHz full EVN image of the central 150 pc region of the luminous infrared galaxy Arp 299-A (= IC 694), displaying a large number of bright, compact, nonthermal emitting sources, mostly identified with young RSNe and SNRs. The image center is at RA 11:28:33.63686 and DEC 58:33:46.5806. *Middle* and *bottom*: Blow-ups of the inner 8 pc of the nuclear region of Arp 299-A, as imaged with the full EVN at 1.7 and 5.0 GHz. The image center is at RA 11:28:33.61984 and DEC 58:33:46.7006 in both panels. The morphology, spectral index and luminosity of the A1–A5 region are very suggestive of a core-jet structure. The color scale goes from −50 μJy/b up to 400 μJy/b in the *top panel* and from 125 to 400 μJy/b in the *middle* and *bottom panels*. Contours are drawn at five and ten times the off-source r.m.s. noise

easy to explain the existence of very massive, supernova progenitor stars so close to an AGN. While seemingly contradictory, this could explain the low-luminosity of the AGN we see in Arp 299-A. In fact, since massive stars shed large amounts of mechanical energy into their surrounding medium, thereby significantly increasing its temperature, those massive stars would hinder the accretion of material to the central black hole, which could in turn result in a less powerful AGN than usual. (See also [21] and the contribution of Herrero-Illana et al. to these proceedings.)

5 Energy Budget in (U)LIRGs and Equipartition Magnetic Field

Since essentially all of the observed radio emission in the central regions of (U)LIRGs is of synchrotron origin (see Sect. 2.1), we can estimate a minimum total energy in magnetic fields, electrons, and heavy particles and a minimum magnetic field for them. In fact, if we assume equipartition (magnetic field energy is approximately equal to the total particle energy), then the minimum total energy is [36]

$$E_{\rm min}^{\rm (tot)} = c_{13}\,(1+k)^{4/7}\,\phi^{3/7}\,R^{9/7}\,L^{4/7} \tag{6}$$

where L is the radio luminosity of the source between ν_1 and ν_2, R is a characteristic size, c_{13} is a slowly-dependent function of the observed radio spectral index, α, ϕ is the fraction of the supernova's volume occupied by the magnetic field and by the relativistic particles (filling factor), and k is the ratio of the (total) heavy particle energy to the electron energy. This ratio depends on the mechanism that generates the relativistic electrons, ranging from $k \approx 1$ up to $k = m_p/m_e \approx 2{,}000$, where m_p and m_e are the proton and electron mass, respectively. A value of $k \simeq 100$ seems appropriate for most galaxies [3]. For the sake of simplicity, I will use a value of $\alpha = -0.7$, which is a typical radio synchrotron spectral index. The value of the function c_{13} is $\sim 2.4 \times 10^4$ (for $\alpha = -0.7$, $\nu_1 = 30\,$MHz and $\nu_2 = 30\,$GHz). The characteristic size of the synchrotron emitting region in (U)LIRGs varies from case to case, although the most compact starbursts, typically residing in ULIRGs, i.e., advanced mergers, have sizes of $\sim$100–200 pc, an for the sake of simplicity we will use here a nominal value of $R = 100\,$pc. Here, we will fix the filling factor, ϕ to a value of 0.5.

The total (synchrotron) radio luminosity between $\nu_1 = 30\,$MHz and $\nu_2 = 30\,$GHz (for $\alpha = -0.7$) can be written as

$$L_{\rm R} \approx 5 \times 10^{39} \left(\frac{S_{\nu,0}}{10\,{\rm mJy}}\right) \left(\frac{D}{100\,{\rm Mpc}}\right)^2 {\rm erg\,s^{-1}} \tag{7}$$

where $S_{\nu,0}$ is the flux density, in mJy, at a reference frequency.

With these values, the minimum total energy enclosed in a 100 pc region of a (U)LIRG at a nominal distance of 100 Mpc with $S_{\nu,0} = 10$ mJy is

$$E_{\rm min}^{\rm (tot)} \approx 1.9 \times 10^{53} (1+k)^{4/7} \left(\frac{\phi}{0.5}\right)^{3/7} \left(\frac{R}{100\,{\rm pc}}\right)^{9/7} \left(\frac{D}{100\,{\rm Mpc}}\right)^{14/7} {\rm erg} \quad (8)$$

The value of the magnetic field that yields $E_{\rm min}^{\rm (tot)}$ is then equal to

$$B_{\rm min} \approx 128\,(1+k)^{2/7} \left(\frac{\phi}{0.5}\right)^{-2/7} \left(\frac{R}{100\,{\rm pc}}\right)^{-6/7} \left(\frac{L_{\rm R}}{5 \times 10^{39}\,{\rm erg\ s^{-1}}}\right)^{2/7} \mu{\rm G} \quad (9)$$

where we have set $c_{12} = 10^7$ in the above equation, for simplicity. Since $1 \leq k \leq 2{,}000$, $E_{\rm min}^{\rm (tot)}$ is then between 2.8×10^{53} erg and 1.5×10^{55} erg, and equals 2.7×10^{54} erg for our nominal value of $k = 100$. The corresponding values of the equipartition magnetic field lie then between $\sim$156 μG (electrons dominate) and $\sim$1.1 mG (heavy particles dominate), and equals $\sim$0.5 mG for our nominal value of $k = 100$. We see that the energy contained in the central, compact regions (size $\lesssim$100 pc) of (U)LIRGs are huge, and the magnetic fields in those ambients are expected to be significant, since the above estimates are lower limits to the real values of the magnetic fields.

6 Magnetic Field and Radiation Fields in (U)LIRGs

We have just seen that the minimum equipartition total energy in the form of particles and magnetic field emitting by synchrotron radio emission within the central $\sim$100 pc of a (U)LIRG is huge. In particular, the magnetic field is expected to be significantly larger than in normal galaxies, where on average has a value of $\sim$5 μG, and hence is expected to play a significant role in the physics of those objects. Similarly, since the bolometric luminosity of those beasts is dominated by radiative emission at IR wavelengths, it is also expected that the radiative field plays a significant role. But which is the main player here: the radio synchrotron, or the radiative field?

In the previous section we obtained that a typical magnetic field for the central $\sim$100 pc of a (U)LIRG is $\sim$500 μG (assuming $k \approx 100$). Therefore, we can write the energy density of the magnetic field as

$$U_{\rm B} = B^2/8\pi \approx 1.0 \times 10^{-8} \left(\frac{B}{500\,\mu{\rm G}}\right)^2 {\rm erg\,cm^{-3}} \quad (10)$$

Since the bolometric luminosity of (U)LIRGs is dominated by the emission at infrared wavelengths, the energy density of the radiation field is therefore dominated by the IR luminosity, and can be written as follows:

$$U_{\rm rad} \approx \frac{\rm L_{ir}}{c\,R^2} \approx 1.3 \times 10^{-7} \left(\frac{L_{\rm ir}}{10^{11}\,L_\odot}\right) \left(\frac{R}{100\,{\rm pc}}\right)^{-2} {\rm erg\,cm^{-3}} \qquad (11)$$

Thus, IC losses are likely to dominate the central ∼100 pc regions of (U)LIRGs, in magnetic fields are close to minimum equipartition estimates. We note, though, that it may well be that equipartition does not hold in those compact regions. For example, [49] suggest that minimum equipartition estimates are not reliable, if the nuclear disks in the central regions of (U)LIRGs are magnetic field supported. In the former case, i.e., when the pressure of the magnetic field is large enough to compete with that of the gas in the nuclear disk, the implied magnetic fields would be high enough so that synchrotron losses would dominate over IC losses. I refer the reader to Thompson et al. [49].

7 Tracing the Radial Distribution of Supernovae Using High-Angular Radio Observations

The last topic in this review of radio continuum observations of (U)LIRGs deals with using the already existing high-angular resolution radio data of three starburst galaxies, aimed at studying the radial distribution of supernovae in the central few hundred pc and eventually relate this information with co-evolutionary scenarios of black hole growth and nuclear disks.

The activity in the central regions of luminous and ultra-luminous infrared galaxies (LIRGs, $10^{11} L_\odot \leq L_{\rm IR} < 10^{12} L_\odot$, and ULIRGs, $L_{\rm IR} \geq 10^{12} L_\odot$, respectively) is powered by either accretion onto a supermassive black hole (SMBH), and/or by a burst of activity due to young, massive stars. It has been found that LIRGs and ULIRGs are associated with interacting and merging galaxies, respectively, and the interaction between the galaxies is assumed to provide large amounts of dense molecular gas that eventually reach the central regions of the galaxies, where they are responsible for triggering massive star formation and possibly accretion onto an SMBH, Di Matteo et al. [14]. However, not all the accumulated gas is expected to be accreted directly onto the putative SMBH, since the removal of the angular momentum of the gas is very inefficient [50]. The angular momentum that is not removed will then permit the accreted gas to form a reservoir, namely a nuclear disk in the central ∼100 pc around the AGN, e.g., Wada and Norman [53] and Kawakatu et al. [23]. Furthermore, if the gas in the nuclear starburst is dense enough, vigorous star formation is expected to occur, which can be detected via, e.g., high-angular resolution observations of recently exploded supernovae, e.g., in the LIRG Arp 299 [39]; or the ULIRG Arp 220 [28].

Table 1 Scale length parameters for the galaxies discussed in this paper

Nucleus	$\tilde{h}_{\rm SN}/10^{-3}$	$h_{\rm SN}$ (pc)	γ
Arp 299-A	$1.9^{+1.9}_{-0.8}$	$29.3^{+29.6}_{-13.7}$	$1.1^{+0.2}_{-0.2}$
Arp 220 East	$3.1^{+2.0}_{-0.9}$	$22.2^{+14.4}_{-6.2}$	$1.0^{+0.2}_{-0.3}$
Arp 220 West	$3.4^{+1.6}_{-1.5}$	$24.4^{+11.2}_{-10.8}$	$0.8^{+0.3}_{-0.2}$
Arp 220 E + W	$3.3^{+0.7}_{-0.9}$	$23.4^{+4.7}_{-6.6}$	$0.8^{+0.1}_{-0.2}$
A299 + A220	$2.0^{+0.3}_{-0.4}$	$20.9^{+2.6}_{-2.3}$	$0.9^{+0.1}_{-0.1}$
M82	$\left(2.8^{+0.9}_{-0.7}\right) \times 10^1$	$144.4^{+21.5}_{-17.5}$	–
H09 sample	$\left(2.9^{+0.2}_{-0.1}\right) \times 10^2$	–	–

All quoted uncertainties correspond to 90 % confidence limit intervals, to which a systematic error was added in the cases of Arp 220 east, Arp 220 west, and M 82, owing to the uncertainty in the precise location of their centers

Kawakatu et al. [23] proposed an scenario for (U)LIRGs, where a nuclear disk is supported by the turbulent pressure of SNe. In their model, the turbulence due to supernova activity transports the angular momentum toward the central pc-scale region. One of the implications of the model developed by Kawakatu et al. [23] is that the BH growth rate depends on the spatial distribution of both young stars and SNe in the nuclear disk. In particular, detailed hydrodynamical simulations by Wada and Norman [53] required that, if the disk followed a power-law density profile with radius, $\Sigma^{SN} = \Sigma_0^{SN}(r/r_{\rm out})^{-\gamma}$, the value of γ had to be equal to 1.0.

We used high-angular radio observations from the literature, as well as data obtained by us, of three starburst galaxies in the local universe (M82, Arp 299-A, and Arp 220) to analyze the radial distribution of CCSNe/SNRs in their central few hundred parsecs, which may have strong implications for the (co)-evolution of AGN and (nuclear) starbursts in galaxies, in general. More specifically, we aimed at testing the predictions by Wada and Norman [53].

Our main results are summarized in Table 1 and Fig. 8, where we show the radial distribution of SNe in our three starburst galaxies and, for comparison, also for spiral galaxies (from the Hakobyan et al. [20] sample; hereafter H09), along with the fits to these data. We note the clear existence of three different regimes: one characterized by a very steep profile of the surface number density of SNe, which is typical of strong, nuclear starbursts (Arp 299− A + Arp 220); a second, less steep profile, as indicated for the (circum)nuclear starburst in M82; and a third, flatter profile, which is typical of very large disks, such as those in spiral galaxies (H09 sample). These results suggest that the surface density of SNe, hence of available gas to convert into stars, reaches a maximum in the vicinities of the SMBH in LIRGs and ULIRGs. We also show in col. 4 of Table 1 the fits to a power-law disk profile, consistent with the fiducial value of $\gamma = 1$ used by Wada and Norman [53] and Kawakatu et al. [23] for the nuclear disk, and appears to yield further support to the modelling of nuclear disks and co-evolutionary scenarios of BH and starbursts in (U)LIRGs. I refer the reader to Alonso-Herrero (2012) and (Herrero-Illana, Pérez-Torres and Alberdi these proceedings) for details on the modelling of the radial distribution of SNe in the central regions of (U)LIRGs.

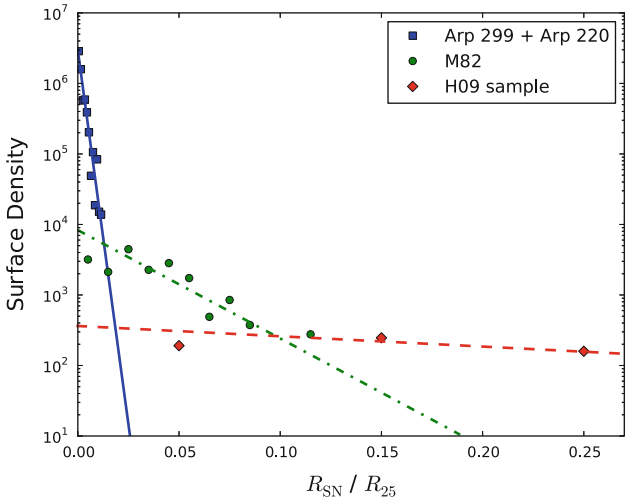

Fig. 8 Radial distribution of SNe for (nuclear) starbursts and spiral galaxies. The data correspond to the combined Arp 299-A + Arp 220 sample (*blue squares*), M82 (*green circles*), and a sample of spiral galaxies (*red diamonds*) from [20] (H09). The fitted lines are for Arp 299-A + Arp 220 (*solid line*), M82 (*dotted-dashed line*), and H09 (*dashed line*). For the sake of clarity, only the innermost part of the H09 sample is shown in the plot. (From [21]); see also Herrero-Illana, Pérez-Torres and Alberdi, these proceedings)

8 Summary

High-angular radio observations are relevant for studies of (U)LIRGs in the local universe as those objects are embbeded in extremely dusty environments, which imply huge extinctions in the optical, and even in the infrared, thus preventing the direct detection of recent starburst activity, e.g., via supernova explosions. Radio is not affected by dust obscuration, thus allowing to see the activity within those deeply buried regions. At the typical distances of $\sim$100 Mpc to a local (U)LIRG, $1''$ corresponds to a linear size of about 500 pc. Therefore, to spatially resolve the circumnuclear regions of (U)LIRGs to understand in detail the ongoing processes in their central regions, sub-arcsecond resolution is a must. Current radio interferometric arrays provide sub-arcsecond angular resolution (EVLA, MERLIN) or even milliarsecond resolution, using Very Long Baseline Interferometry (VLBI), and thus they become a very powerful tool to study (U)LIRGs.

Here, I have presented just some of the results obtained by our team, including the impressive discovery of an extremely prolific supernova factory in the central $\sim$150 pc of the galaxy Arp 299-A (D = 45 Mpc) and the monitoring of a large number of very compact radio sources in it, the detection and precise location of the long-sought AGN in Arp 299-A and, more recently, the evidence for the existence of nuclear disks ($\lesssim$100 pc in size) in starburst galaxies from their radial distribution

of supernovae. All those results show that very-high angular resolution studies of nearby (U)LIRGs are of high relevance for the comprehension of both local and high-z starbursting galaxies.

References

1. Alberdi, A., Colina, L., Torrelles, J. M., et al. 2006, ApJ, 638, 938
2. Alonso-Herrero, A., Rieke, G. H., Colina, L., et al. 2009, ApJ, 697, 660
3. Beck, R. & Krause, M. 2005, Astronomische Nachrichten, 326, 414
4. Bondi, M., Perez-Torres, M.-A., Dallacasa, D., & Muxlow, T. W. B. 2005, MNRAS, 361, 748
5. Bondi, M., Perez-Torres, M. A., Herrero-Illana, R., & Alberdi, A. 2012, A&A, 539, A134
6. Brinchmann, J., Charlot, S., White, S. D. M., et al. 2004, MNRAS, 351, 1151
7. Chevalier, R. A. 1982, ApJ, 259, 302
8. Chevalier, R. A. & Clegg, A. W. 1985, Nature, 317, 44
9. Chevalier, R. A. & Fransson, C. 2001, ApJ, 558, L27
10. Chugai, N. N. 1997, Ap&SS, 252, 225
11. Colina, L., Alberdi, A., Torrelles, J. M., Panagia, N., & Wilson, A. S. 2001, ApJ, 553, L19
12. Condon, J. J. 1992, ARA&A, 30, 575
13. Condon, J. J., Huang, Z.-P., Yin, Q. F., & Thuan, T. X. 1991, ApJ, 378, 65
14. Di Matteo, P., Combes, F., Melchior, A.-L., & Semelin, B. 2007, A&A, 468, 61
15. Fixsen, D. J., Cheng, E. S., Gales, J. M., et al. 1996, ApJ, 473, 576
16. Forti, G., Boattini, A., Tombelli, M., Herbst, W., & Vinton, G. 1993, IAU Circ., 5719, 3
17. Gallais, P., Charmandaris, V., Le Floc'h, E., et al. 2004, A&A, 414, 845
18. Gallimore, J. F. & Beswick, R. 2004, AJ, 127, 239
19. Genzel, R., Lutz, D., Sturm, E., et al. 1998, ApJ, 498, 579
20. Hakobyan, A. A., Mamon, G. A., Petrosian, A. R., Kunth, D., & Turatto, M. 2009, A&A, 508, 1259
21. Herrero-Illana, R., Perez-Torres, M. A ., & Alberdi, A. 2012, A&A, 540, L5
22. Kankare, E., Mattila, S., Ryder, S., et al. 2008, ApJ, 689, L97
23. Kawakatu, N. & Wada, K. 2008, ApJ, 681, 73
24. Keel, W. C. & Wu, W. 1995, AJ, 110, 129
25. Kennicutt, Jr., R. C. 1998, ARA&A, 36, 189
26. Leitherer, C. & Heckman, T. M. 1995, ApJS, 96, 9
27. Li, W.-D., Li, C., Wan, Z., Filippenko, A. V., & Moran, E. C. 1998, IAU Circ., 6830, 1
28. Lonsdale, C. J., Diamond, P. J., Thrall, H., Smith, H. E., & Lonsdale, C. J. 2006, ApJ, 647, 185
29. Magnelli, B., Elbaz, D., Chary, R. R., et al. 2009, A&A, 496, 57
30. Magnelli, B., Elbaz, D., Chary, R. R., et al. 2011, A&A, 528, A35
31. Mattila, S. & Meikle, W. P. S. 2001, MNRAS, 324, 325
32. Mattila, S., Monard, L. A. G., & Li, W. 2005, IAU Circ., 8473, 1
33. Mattila, S., et al. 2007, ApJ, 659, L9
34. Meurer, G. R., Heckman, T. M., Lehnert, M. D., Leitherer, C., & Lowenthal, J. 1997, AJ, 114, 54
35. Neff, S. G., Ulvestad, J. S., & Teng, S. H. 2004, ApJ, 611, 186
36. Pacholczyk, A. G. 1970, Radio astrophysics. Nonthermal processes in galactic and extragalactic sources
37. Parra, R., Conway, J. E., Diamond, P. J., et al. 2007, ApJ, 659, 314
38. Pérez-Torres, M. A., et al. 2008, CBET, 1392, 2
39. Pérez-Torres, M. A., Alberdi, A., Colina, L., et al. 2009a, MNRAS, 399, 1641
40. Pérez-Torres, M. A., Alberdi, A., Romero-Canizales, C., & Bondi, M. 2010, A&A, 519, L5
41. Pérez-Torres, M. A., Mattila, S., Alberdi, A., et al. 2007, ApJ, 671, L21

42. Pérez-Torres, M. A., Romero-Canizales, C., Alberdi, A., & Polatidis, A. 2009b, A&A, 507, L17
43. Qiu, Y. L., Qiao, Q. Y., Hu, J. Y., & Li, W.-D. 1999, IAU Circ., 7088, 2
44. Rovilos, E., Diamond, P. J., Lonsdale, C. J., Smith, H. E., & Lonsdale, C. J. 2005, MNRAS, 359, 827
45. Sanders, D. B., Mazzarella, J. M., Kim, D.-C., Surace, J. A., & Soifer, B. T. 2003, AJ, 126, 1607
46. Sanders, D. B. & Mirabel, I. F. 1996, ARA&A, 34, 749
47. Smartt, S. J. 2009, ARA&A, 47, 63
48. Smith, H. E., Lonsdale, C. J., Lonsdale, C. J., & Diamond, P. J. 1998, ApJ, 493, L17
49. Thompson, T. A., Quataert, E., Waxman, E., Murray, N., & Martin, C. L. 2006, ApJ, 645, 186
50. Umemura, M. 2001, ApJ, 560, L29
51. van Buren, D., Jarrett, T., Terebey, S., et al. 1994, IAU Circ., 5960, 2
52. Veilleux, S., Sanders, D. B., & Kim, D.-C. 1999, ApJ, 522, 139
53. Wada, K. & Norman, C. A. 2002, ApJ, 566, L21
54. Yamaoka, H., Kato, T., Filippenko, A. V., et al. 1998, IAU Circ., 6859, 1

Evidence of Nuclear Disks from the Radial Distribution of CCSNe in Starburst Galaxies

Rubén Herrero-Illana, Miguel Ángel Pérez-Torres, and Antxon Alberdi

Abstract Galaxy-galaxy interactions are expected to be responsible for triggering massive star formation and possibly accretion onto a supermassive black hole, by providing large amounts of dense molecular gas down to the central kiloparsec region. Several scenarios to drive the gas further down to the central $\sim$100 pc, have been proposed, including the formation of a nuclear disk around the black hole, where massive stars would produce supernovae. Here, we probe the radial distribution of supernovae and supernova remnants in the nuclear regions of the starburst galaxies M82, Arp 299-A, and Arp 220, by using high-angular resolution ($\lesssim$0.″1) radio observations. We derived scale-length values for the putative nuclear disks, which range from $\sim$20–30 pc for Arp 299-A and Arp 220, up to $\sim$140 pc for M82. The radial distribution of SNe for the nuclear disks in Arp 299-A and Arp 220 is also consistent with a power-law surface density profile of exponent $\gamma = 1$, as expected from detailed hydrodynamical simulations of nuclear disks. This study is detailed in Herrero-Illana, Perez-Torres, and Alberdi [11].

1 Introduction

The activity in the central regions of luminous and ultra-luminous infrared galaxies (LIRGs, $10^{11} L_{\odot} \leq L_{\rm IR} < 10^{12} L_{\odot}$, and ULIRGs, $L_{\rm IR} \geq 10^{12} L_{\odot}$, respectively) is powered by either accretion onto a supermassive black hole (SMBH), and/or by a burst of activity due to young, massive stars. It has been found that LIRGs and ULIRGs are associated with interacting and merging galaxies, respectively, and the interaction between the galaxies is assumed to provide large amounts of dense

R. Herrero-Illana (✉) · M.Á. Pérez-Torres · A. Alberdi
Instituto de Astrofísica de Andalucía (IAA-CSIC), Glorieta de la Astronomía, s/n, 18008, Granada, Spain
e-mail: herrero@iaa.es; torres@iaa.es; antxon@iaa.es

D.F. Torres and O. Reimer (eds.), *Cosmic Rays in Star-Forming Environments*, Astrophysics and Space Science Proceedings 34, DOI 10.1007/978-3-642-35410-6_12,

molecular gas that eventually reach the central regions of the galaxies, where they are responsible for triggering massive star formation and possibly accretion onto an SMBH [8]. However, not all the accumulated gas is expected to be accreted directly onto the putative SMBH, since the removal of the angular momentum of the gas is very inefficient [19]. The angular momentum that is not removed will then permit the accreted gas to form a reservoir, namely a nuclear disk in the central $\sim$100 pc around the AGN [12, 21]. Furthermore, if the gas in the nuclear starburst is dense enough, vigorous star formation is expected to occur, which can be detected via, e.g., high-angular resolution observations of recently exploded supernovae (e.g., in the LIRG Arp 299 [17], or the ULIRG Arp 220 [13]).

Kawakatu et al. [12] proposed an scenario for (U)LIRGs, where a nuclear disk is supported by the turbulent pressure of SNe. In their model, the turbulence due to supernova activity transports the angular momentum toward the central pc-scale region. One of the implications of the model developed by Kawakatu et al. [12] is that the BH growth rate depends on the spatial distribution of both young stars and SNe in the nuclear disk.

We have used high-angular radio observations from the literature, as well as data obtained by us, of three starburst galaxies in the local universe (M82, Arp 299-A, and Arp 220) to analyze the radial distribution of CCSNe/SNRs in their central few hundred parsecs, which may have strong implications for the (co)-evolution of AGN and (nuclear) starbursts in galaxies, in general, and in (U)LIRGs in particular.

2 The Radial Distribution of SNe in Nuclear Starbursts

The radial distribution of SNe[1] on galactic scales has been thoroughly studied [2, 3, 10, 20]. Optical observations have been very useful for this purpose, as dust extinction plays a minor role in the external regions of most galaxies. However, the dust-enshrouded environments of the nuclear regions in (U)LIRGs, as well as the need for milliarcsecond angular resolution to pinpoint individual SNe, have prevented this kind of studies in the central regions of local (U)LIRGs. Fortunately, both issues – obscuration and (angular) resolution – can be overcome by means of Very Long Baseline Interferometry (VLBI) radio observations of the central regions of (U)LIRGs, since radio is dust-extinction free, and VLBI provides milliarsecond angular resolution.

2.1 Methods

We used VLBI observations to probe the radial distribution of SNe in the nuclear regions of Arp 299-A and Arp 220, as well as MERLIN, VLA, and

[1] We will use here the term SNe to denote both CCSNe and SNRs.

VLBI observations towards M82. For each galaxy, we fitted the surface density profile of the SNe to two different disk profiles: (i) an exponential disk, $\Sigma^{SN} = \Sigma_0^{SN} \exp(-\tilde{r}/\tilde{h}_{\rm SN})$, and (ii) a disk with a power-law density profile with radius, $\Sigma^{SN} = \Sigma_0^{SN}(r/r_{\rm out})^{-\gamma}$. The first case (exponential disk) assumes that the SN distribution follows the radial surface-brightness density in spiral disks, while the second one (power-law disk) was used to probe the profiles predicted by numerical simulations [21]. The notation follows the one used in Hakobyan et al. [10], where Σ_0^{SN} is the surface density of SN at the center, $\tilde{r}$ is the normalized radius, and $r_{\rm out}$ is the radius of the farthest SN analyzed, considered here to be the outer boundary of the putative nuclear disk. The main parameters that are obtained from those fits are the scale length, $\tilde{h}_{\rm SN}$, and the index of the power-law profile, γ, of the putative nuclear disks in the central regions of these galaxies.

Following a similar analysis as the one described in [10] (hereafter, H09), we determined the number of sources in concentric rings around the center of the galaxy and fitted the data to both an exponential and a power-law disk, as described above.

Since the supernova samples for all our three galaxies are of relatively small size, resulting in some small size bins, the actual uncertainties in the fits could be larger than formally obtained from a single fit. To assess the robustness of our fitting procedure, we performed a series of Monte Carlo (MC) simulations. For each galaxy, we generated 10,000 mock supernova samples, whose values were uniformly distributed within the uncertainty of each data point, and fitted them. In this way, we obtained a distribution of 10,000 different fitting values for the scale-length parameter, $\tilde{h}_{\rm SN}$, and the power-law index, γ, for each galaxy. This approach allowed us to obtain more reliable values of those parameters, since no assumption was made about the Gaussianity of the distributions of both the scale length and power-law index, or of their errors. We then used the median value of the distribution of our MC values to characterize $\tilde{h}_{\rm SN}$ and γ, and set the uncertainty in these parameters at the 90 % confidence level. To test our method, we reanalyzed the sample of H09 for 239 CCSNe within 216 host galaxies, and obtained a value of $\tilde{h}_{\rm SN} = 0.29^{+0.02}_{-0.01}$, which is in excellent agreement with their estimate, and confirms the robustness of our analysis.

2.2 Results

We outline the results obtained for each individual galaxy.

2.2.1 Arp 299-A

Arp 299-A ($D = 44.8$ Mpc) is one of the two interacting galaxies of the LIRG Arp 299. The sample of SNe used for our study comes from both observations from the European VLBI Network (EVN) at 5.0 GHz, presented in Pérez-Torres [17] and in Bondi et al. [4], as well as from published data obtained with the Very Long

Baseline Array (VLBA) at 2.3 and 8.4 GHz by Ulvestad [18]. The existence and precise location of the low luminosity AGN in Arp 299-A was reported by Pérez-Torres [16], hence its position was used to calculate accurate de-projected distances for all SNe in the nuclear region of Arp 299-A. The sample has a total of 31 sources. However, although there are sources at distances as far as $\tilde{r} = 11.4 \times 10^{-2}$, only one source is further than $\tilde{r} = 6.6 \times 10^{-2}$, so the latter value of $\tilde{r}$ was used as the limiting radius for our study, giving a final number of 30 sources. The scale length obtained using the non-linear fit is $\tilde{h}_{\rm SN} = 1.6 \times 10^{-3}$, with a standard deviation of 0.5×10^{-3}. After performing the MC analysis, we obtained a final value $\tilde{h}_{\rm SN}$ of $\left(1.9^{+1.9}_{-0.8}\right) \times 10^{-3}$.

2.2.2 Arp 220

Arp 220 is a merging system at 77 Mpc, and the closest and most well-studied ULIRG. High-angular resolution radio observations from its two nuclear regions were first obtained by Lonsdale et al. [13] using global VLBI, who found a total of 49 radio supernovae in both the east (20) and west (29) nuclei. We used the position of the peak flux density from a delay-rate VLBI map as the estimated position for the center of each galactic nucleus [15]. One of the compact sources in the Arp 220 east nucleus is at a much larger distance than the rest of them, which we did not use in our fit, thus limiting the normalized radii to $\tilde{r} = 0.011$. Therefore, a total of 48 SNe were considered in the fits, which we carried both separately, for each nucleus, and for the combined data set. Similarly, we performed MC simulations for each of the two nuclei, as well as for the combined sample In this way, we obtained a scale-length for the east and west nuclei of $\left(3.1^{+2.0}_{-0.7}\right) \times 10^{-3}$ and $\left(3.4^{+1.5}_{-0.9}\right) \times 10^{-3}$, respectively, and a combined scale-length for Arp 220 is $\left(3.3^{+0.6}_{-0.4}\right) \times 10^{-3}$. To quantify the effect of the uncertain position of the putative AGNs, we shifted them 100 times randomly around our nominal position, given by the peak flux density, by a maximum value of $\sigma_{(RA,DEC)} = \mathrm{FWHM}/(2\,\mathrm{S/N})$, where FWHM is the full-width at half maximum, and S/N is the signal-to-noise ratio, resulting in 4.2 mas for the east nucleus and 1.4 mas for the west one, and then fitted to the data. The maximum differences obtained were considered as a systematic error, which we added to our nominal values, such that the combined scale length became $\tilde{h}_{\rm SN} = \left(3.3^{+0.7}_{-0.9}\right) \times 10^{-3}$.

2.2.3 Combination of Arp 299-A and Arp 220

The normalized radii of Arp 299-A and Arp 220 (both east and west nuclei) are comparable. We can thus combine every source prior to the analysis to obtain an average scale-length parameter with smaller errors to help characterize both nuclear starbursts. The scale length obtained for the combined samples is $\tilde{h}_{\rm SN} = \left(2.0^{+0.3}_{-0.2}\right) \times 10^{-3}$. The original non-linear fit is shown in Fig. 1 and our MC analysis results are shown in Fig. 2. After taking into account systematic errors due to the uncertainty in the precise location of the AGNs of the Arp 220 east and west nuclei, the final value for the scale length is $\tilde{h}_{\rm SN} = \left(2.0^{+0.3}_{-0.4}\right) \times 10^{-3}$.

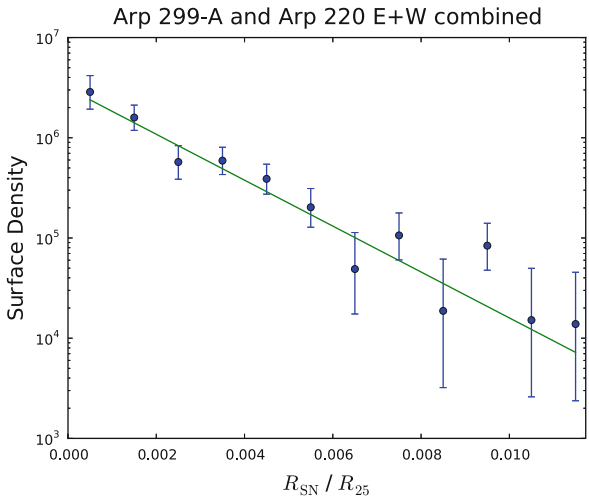

Fig. 1 Non-linear fit of the surface density profile of the combined sample of SNe from both Arp 299-A and Arp 220

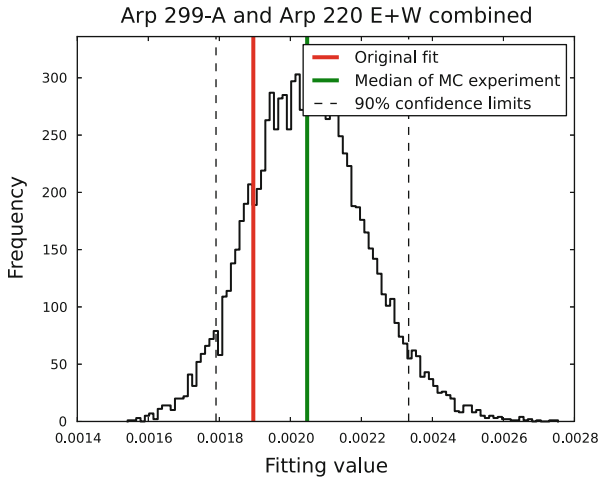

Fig. 2 MC histogram of $\tilde{h}_{SN}$ for the combined sample of SNe from Arp 299-A and the two nuclei of Arp 220. The original non-linear fit is shown in *red*, and the median of the distribution created with the MC simulation is shown in *green*. The *dashed lines* correspond to the 90 % confidence level interval

2.2.4 M82

At a distance of 3.2 Mpc, M82 is the prototypical starburst galaxy, which has been the target of many observations at high-angular resolution. For our analysis, we combined sources catalogued as SNe (or SNR) detected by Wills [23], Allen et al. [1], McDonald et al. [14], Fenech et al. [9], and Brunthaler et al. [5]. These comprise observations at several frequencies with MERLIN, VLA, and VLBA, including a

Table 1 Scale length parameters for the studied galaxies

Nucleus	$\tilde{h}_{\rm SN}/10^{-3}$	$h_{\rm SN}$ (pc)	γ
Arp 299-A	$1.9^{+1.9}_{-0.8}$	$29.3^{+29.6}_{-13.7}$	$1.1^{+0.2}_{-0.2}$
Arp 220 East	$3.1^{+2.0}_{-0.9}$	$22.2^{+14.4}_{-6.2}$	$1.0^{+0.2}_{-0.3}$
Arp 220 West	$3.4^{+1.6}_{-1.5}$	$24.4^{+11.2}_{-10.8}$	$0.8^{+0.3}_{-0.2}$
Arp 220 E + W	$3.3^{+0.7}_{-0.9}$	$23.4^{+4.7}_{-6.6}$	$0.8^{+0.1}_{-0.2}$
A299 + A220	$2.0^{+0.3}_{-0.4}$	$20.9^{+2.6}_{-2.3}$	$0.9^{+0.1}_{-0.1}$
M82	$\left(2.8^{+0.9}_{-0.7}\right) \times 10^{1}$	$144.4^{+21.5}_{-17.5}$	–
H09 sample	$\left(2.9^{+0.2}_{-0.1}\right) \times 10^{2}$	–	–

All quoted uncertainties correspond to 90 % confidence limit intervals, to which a systematic error was added in the cases of Arp 220 east, Arp 220 west, and M82, owing to the uncertainty in the precise location of their centers.

total of 39 sources. Since no AGN has yet been discovered in M82, we instead used the radio kinematic center of M82 [22] as the position of its nucleus. The scale length obtained with the MC simulation is $\tilde{h}_{\rm SN} = \left(2.8^{+0.4}_{-0.3}\right) \times 10^{-2}$. Although the radio kinematic center is likely to be very close, if not exactly coincident, with the putative nucleus of M82, we nevertheless quantified the effect that an error in the position chosen as the nucleus of M82 would have in the fits. In particular, we shifted our fiducial position for the nucleus by up to 20 pc in several directions, and then fitted the data. The maximum differences were considered as a systematic error, which we added to our nominal value, thus yielding $\tilde{h}_{\rm SN} = \left(2.8^{+0.9}_{-0.7}\right) \times 10^{-2}$.

3 Discussion and Summary

Our main results are summarized in Table 1 and Fig. 3, where we show the scale lengths, index of the power-law SN profile, and the radial distribution of SNe for the three galaxies discussed here, as well as for the sample of spiral galaxies from H09.

We note that the scale lengths for the exponential disk fits to the radial distribution of SNe in the nuclear regions of the starburst galaxies, are at least an order of magnitude smaller that those obtained by H09 for the whole disks of spiral galaxies. In particular, $\tilde{h}_{\rm SN}$ is two orders of magnitude smaller in the case of Arp 299-A and Arp 220. Correspondingly, the physical sizes inferred for the scale lengths of the nuclear disks (col. 3 in Table 1) are much smaller than for galactic disks: ∼20–30 pc for Arp 299-A or Arp 220, which is similar to the size derived for the nuclear starburst of the LIRG NGC 7469, (30–60 pc; [6]), using CO interferometric observations, and ∼160 pc for M82, which is also similar to the scale-length of the nuclear disk in the ULIRG/QSO Mrk 231 [7].

We show in Fig. 3 the radial distribution of SNe in our three starburst galaxies and, for comparison, also for spiral galaxies (from the H09 sample), along with

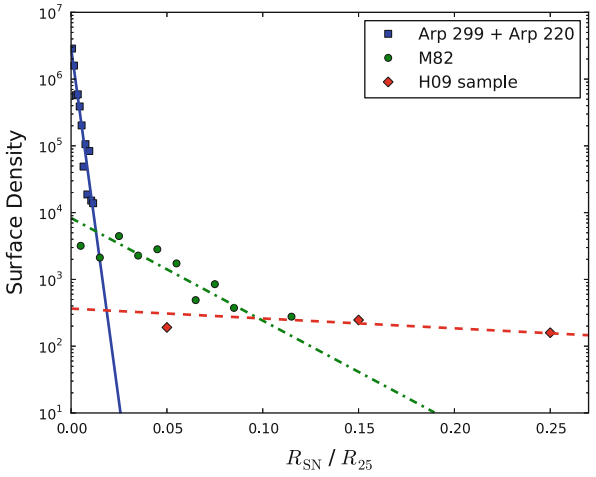

Fig. 3 Radial distribution of SNe for (nuclear) starbursts and spiral galaxies. The data correspond to the combined Arp 299-A + Arp 220 sample (*blue squares*), M82 (*green circles*), and the H09 sample of spiral galaxies (*red diamonds*), and the *fitted lines* are for Arp 299-A + Arp 220 (*solid line*), M82 (*dotted-dashed line*), and H09 (*dashed line*). For the sake of clarity, only the innermost part of the H09 sample is shown in the plot. See also the contribution by Pérez-Torres, this volume

the fits to these data. We note the clear existence of three different regimes: one characterized by a very steep profile of the surface number density of SNe, which is typical of strong, nuclear starbursts (Arp 299-A + Arp 220); a second, less steep profile, as indicated for the (circum)nuclear starburst in M82; and a third, flatter profile, which is typical of very large disks, such as those in spiral galaxies (H09 sample). These results suggest that the surface density of SNe, hence of available gas to convert into stars, reaches a maximum in the vicinities of the SMBH in LIRGs and ULIRGs. We also show in col. 4 of Table 1 the fits to a power-law disk profile, consistent with the fiducial value of $\gamma = 1$ used by Wada et al. [21] and Kawakatu et al. [12] for the nuclear disk, and appears to yield further support to their modeling.

We have modeled for the first time the radial distribution of SNe in the nuclear starbursts of M82, Arp 299-A, and Arp 220, and derived scale-length values for exponential disks, which are in the range between $\sim$20 and $\sim$140 pc. We have also modeled these SNe distributions as power-law disk profiles, and found that they agree with state-of-the art numerical simulations of nuclear disks around SMBHs. We interpret our results as evidence of nuclear disks around the centers, i.e., AGNs, of starburst-dominated galaxies and also support for evolutionary scenarios where a nuclear disk of size $\lesssim$100 pc is formed in LIRGs and ULIRGs [12]. In particular, the scale-length obtained for the LIRG Arp 299-A and the LLAGN nature of its SMBH [16], suggests that its nuclear disk is likely supported by gas pressure, such that the accretion onto the SMBH is smaller than for a turbulent-supported disk. It is very likely that this is also the case for the ULIRG Arp 220. Future deep VLBI observations of a significantly large sample of (U)LIRGs, which would result in

the discovery of new SN factories, will be of much use for deriving statistically significant results on the size of nuclear disks, and thus setting useful constraints on (co)-evolutionary scenarios.

References

1. Allen, M. L. & Kronberg, P. P. 1998, ApJ, 502, 218
2. Anderson, J. P. & James, P. A. 2009, MNRAS, 399, 559
3. Bartunov, O. S., Makarova, I. N., & Tsvetkov, D. I. 1992, A&A, 264, 428
4. Bondi, M., Perez-Torres, M. A., Herrero-Illana, R., & Alberdi, A. 2012, ArXiv
5. Brunthaler, A., Menten, K. M., Reid, M. J., et al. 2009, A&A, 499, L17
6. Davies, R. I., Tacconi, L. J., & Genzel, R. 2004a, ApJ, 613, 781
7. Davies, R. I., Tacconi, L. J., & Genzel, R. 2004b, ApJ, 602, 148
8. Di Matteo, P., Combes, F., Melchior, A.-L., & Semelin, B. 2007, A&A, 468, 61
9. Fenech, D. M., Muxlow, T. W. B., Beswick, R. J., Pedlar, A., & Argo, M. K. 2008, MNRAS, 391, 1384 Freeman, K. C. 1970, ApJ, 160, 811
10. Hakobyan, A. A., Mamon, G. A., Petrosian, A. R., Kunth, D., & Turatto, M. 2009, A&A, 508, 12l59
11. Herrero-Illana, R., Perez-Torres, M. A., & Alberdi, A. 2012, A&A, 540, L5
12. Kawakatu, N. & Wada, K. 2008, ApJ, 681, 73
13. Lonsdale, C. J., Diamond, P. J., Thrall, H., Smith, H. E., & Lonsdale, C. J. 2006, ApJ, 647, 185
14. McDonald, A. R., Muxlow, T. W. B., Wills, K. A., Pedlar, A., & Beswick, R. J. 2002, MNRAS, 334, 912
15. Parra, R., Conway, J. E., Diamond, P. J., et al. 2007, ApJ, 659, 314
16. Perez-Torres, M. A., Alberdi, A., Romero-Canizales, C., & Bondi, M. 2010, A&A, 519, L5
17. Perez-Torres, M. A., Romero-Canizales, C., Alberdi, A., & Polatidis, A. 2009, A&A, 507, L17
18. Ulvestad, J. S. 2009, AJ, 138, 1529
19. Umemura, M. 2001, ApJ, 560, L29
20. van den Bergh, S. 1997, AJ, 113, 197
21. Wada, K. & Norman, C. A. 2002, ApJ, 566, L21
22. Weliachew, L., Fomalont, E. B., & Greisen, E. W. 1984, A&A, 137, 335
23. Wills, K. A., Pedlar, A., Muxlow, T. W. B., & Wilkinson, P. N. 1997, MNRAS, 291, 517

GeV Gamma-Ray Emission from Normal and Starburst Galaxies

Jürgen Knödlseder

Abstract With the launch of the *Fermi* satellite and the advent of modern air-Cherenkov telescopes such as H.E.S.S. and VERITAS, star-forming galaxies have become a new class of gamma-ray sources that extend the study of cosmic-ray physics from the Milky Way to external galaxies. So far, eight star-forming galaxies have been observed at GeV energies (SMC, LMC, Milky Way, M 31, M 82, NGC 253, NGC 1068, and NGC 4945) while two have been seen at TeV energies (M 82, NGC 253). In this paper, I review the observational status of the GeV observation of these galaxies, and I summarize the conclusions that have been drawn from these observations on cosmic-ray physics in normal and starburst galaxies.

1 Introduction

The Earth is permanently bombarded by a flux of charged particles, being primarily composed of atomic nuclei. The composition of the atomic nuclei follows closely that of the solar system matter, with a few notable exceptions, such as the overabundance of Li, Be and B, and other elements lighter than Fe. Electrons occur only with an abundance of about 1 % in the particle flux, positrons are ten times less frequent.

This high-altitude radiation, discovered by Victor Hess in a series of balloon flights one century ago [1], is today known as cosmic rays. As we will demonstrate later, we know that these cosmic rays are ubiquitous in our Galaxy. The typical energy density of Galactic cosmic rays amounts to $\sim$1 eV/cm^3 which is comparable to the energy density of starlight, of interstellar magnetic fields, and of the kinetic energy density of interstellar gas. Cosmic rays are thus an energetically important

J. Knödlseder (✉)
IRAP, 9, avenue Colonel-Roche, 31028 Toulouse Cedex 4, France
e-mail: jurgen.knodlseder@irap.omp.eu

D.F. Torres and O. Reimer (eds.), *Cosmic Rays in Star-Forming Environments*,
Astrophysics and Space Science Proceedings 34, DOI 10.1007/978-3-642-35410-6_13,

constituent of our Galaxy that affect the physical state of the interstellar medium (ISM) by heating and ionizing its atomic and molecular phases [2]. Cosmic rays also contribute to supporting interstellar gas against gravity [3], and are thought to alter the spectrum of interstellar turbulence as they get reaccelerated by draining energy from magnetohydrodynamic waves [4]. In addition, cosmic rays are essential for the Parker dynamo mechanism, which may be the source of the large-scale magnetic fields in galaxies like the Milky Way [5, 6].

The cosmic rays that are observed at Earth span an enormous energy range from about 10^7 eV to above 10^{20} eV per nuclei. At the lowest energies ($\lesssim$10 GeV per nuclei), cosmic rays are affected by interactions with the solar wind, so only little is known about the precise cosmic-ray flux in this domain. Ionization by low-energy cosmic rays is important for the chemical processes operating inside dense molecular clouds, where Lyman photons cannot penetrate [7]. Ultimately, cosmic rays are therefore likely responsible for the emergence of life. At the highest energies (>10 EeV per nuclei), the gyroradius of cosmic rays in the typical Galactic magnetic field of 3 μG exceeds the thickness of the Galactic plane, so the particles are difficult to retain within the Milky Way. Particles at the very highest energies are thus generally believed to originate from extragalactic sources, yet the nature of these sources and the physical mechanism responsible for particle acceleration is still subject to much debate [11].

The origin of the Galactic component is also a matter of very active research. Following an energetic argument formulated by Ginzburg and Syrovatskii [8], supernova explosions could provide the necessary energy to maintain a steady state cosmic-ray flux in our Galaxy. The shock waves created by supernova explosions in the ISM provide a prolific environment for particle acceleration [9]. Observation of nonthermal hard X-ray emission from supernova remnants (SNRs) demonstrates that electrons are accelerated in these shocks up to energies of 100 TeV [10]. Gamma-ray observations are suggestive of hadron acceleration in a number of SNRs, although a definite proof for hadron acceleration by SNRs is still missing [11]. Alternative sources of cosmic rays comprise the shocks generated by the stellar winds of massive stars, pulsars and their wind nebulae [12, 13].

Cosmic rays in our Galaxy are best traced by high-energy gamma-ray emission (0.1–100 GeV). The interactions of cosmic-ray particles with the interstellar medium leads to broad-band gamma-ray emission that can be traced throughout the entire Galaxy. Three physical processes contribute significantly to the diffuse high-energy gamma-ray emission from our Galaxy.

Firstly there is neutral pion decay, which dominates the gamma-ray luminosity of the Milky Way at GeV energies. Neutral pions (π^0) are a product of hadronic interactions in the interstellar medium, mainly cosmic-ray protons colliding with the nuclei of hydrogen atoms of the interstellar gas, although also heavier nuclei contribute. After a mean lifetime of 8.4×10^{-17} s, π^0 decays into two gamma-ray photons with energies of 67.5 MeV in the rest frame of the pion. This energy will be substantially Doppler shifted with respect to the Earth rest frame due to the large kinetic energies of the π^0 mesons in the cosmic rays. For energies that are large compared to the π^0 rest mass of 135 MeV, the gamma-ray spectrum mimics

the cosmic-ray spectrum, and thus provides a directly measure of the cosmic-ray particle spectrum.

Secondly there is inverse Compton emission that arises from the interaction of cosmic-ray electrons with the interstellar radiation field and the cosmic microwave background radiation. The main contributions to the interstellar radiation field come from stars (emitting from near-infrared to ultraviolet wavelengths) and dust (emitting in the mid- to far-infrared domain) [14]. The index α of the resulting gamma-ray spectrum relates to the index δ of the electron spectrum through $\alpha = (\delta + 1)/2$, with a cutoff due to the Klein-Nishina effect that typical arises at energies of $\sim$50 TeV. Thus, for proton and electron distributions with comparable spectral indices, the inverse Compton emission is harder than the π^0 decay emission, and hence it should dominate the Galactic diffuse emission at TeV energies.

Thirdly there is non-thermal (or relativistic) Bremsstrahlung that arises when cosmic-ray electrons interact with the electrostatic field of atomic nuclei. The gamma-ray spectrum mimics the cosmic-ray spectrum, and thus it provides a directly measure of the cosmic-ray particle spectrum. The index α of the resulting gamma-ray spectrum mimics again that of the particles (i.e. $\alpha = \delta$). While at GeV energies relativistic Bremsstrahlung is believed to be negligible, it may become dominant at energies below the π^0 creation threshold [15] (but see Strong et al. [16] who argue that relativistic Bremsstrahlung is negligible in the MeV energy range).

Figure 1 illustrates the contribution of the three components to the Galactic diffuse emission as seen from the inner Galaxy by the Large Area Telescope (LAT) aboard the *Fermi* satellite after 21 months of observations [17]. In addition to the diffuse emission components, the figure also shows the point source (orange, dotted) and isotropic background (brown, long-dash-dotted) contributions, which are negligible. Neutral pion decay (red, long-dashed) dominates the Galactic diffuse emission, followed by relativistic Bremsstrahlung (cyan, dash-dotted) at energies $\lesssim$2 GeV and inverse Compton emission (green, dashed) at higher energies. Within the systematic uncertainties of the analysis (grey area), the model explains the data reasonably well, although some significant deviations occur above a few tens of GeV.

Figure 2 shows the 0.2–100 GeV gamma-ray allsky map as seen by *Fermi*-LAT over the same 21 months of observations [17]. About $\sim$80 % of the photons in this map are attributed to cosmic-ray interactions in our Galaxy, visible as a bright and diffuse emission structure running along the Galactic plane. The remaining photons arise from individual sources, situated either in or outside our Galaxy. Among the Galactic sources we find pulsars and their wind nebulae, supernova remnants, globular clusters, binary systems composed of a compact object and a high-mass stellar component, and one nova [84]. The extragalactic sources are all galaxies. Most of them are powered by a supermassive black hole in their centre and show radio jets; they manifest as blazars or radio galaxies [18]. A handful of the galaxies are powered by cosmic rays. These are either normal galaxies in the Local Group of galaxies, or nearby starburst galaxies [19].

The gamma-ray emissions from these normal and starburst galaxies probe cosmic-ray properties and cosmic-ray physics in different systems and environments. Nearby systems can eventually be resolved, allowing to infer the cosmic-ray

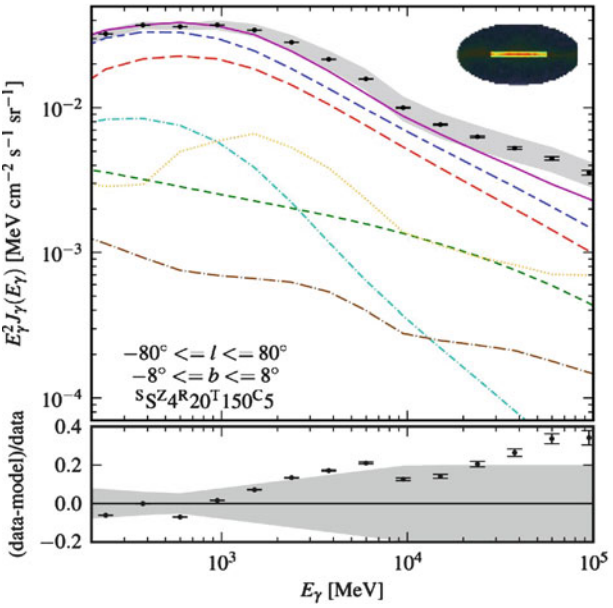

Fig. 1 *Fermi*-LAT spectrum of the diffuse gamma-ray emission from the inner Galaxy (*black points*) compared to a spectral model [17]. The model has been split into three basic emission components: π^0 decay (*red*, *long-dashed*), inverse Compton emission (*green*, *dashed*), and relativistic Bremsstrahlung (*cyan*, *dash-dotted*). Also shown is the total diffuse galactic emission (*blue*, *long-dash-dashed*) and total emission (*magenta*, *solid*) including sources (*orange*, *dotted*) and isotropic background (*brown*, *long-dash-dotted*). The *gray region* represents the systematic error in the *Fermi*-LAT effective area. The *bottom panel* shows the fractional residual (data-model)/data

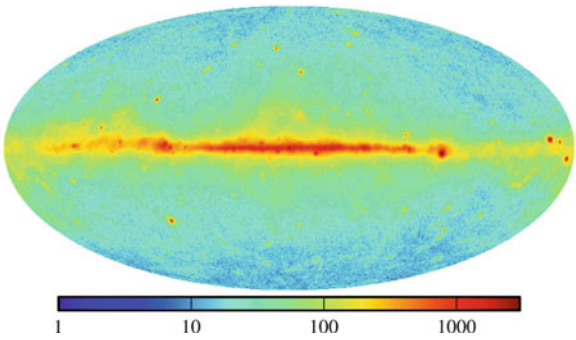

Fig. 2 High-energy gamma-ray (0.2–100 GeV) allsky map obtained by *Fermi*-LAT after 21 months of observations [17]

density distribution in the galaxy. We will demonstrate this with the recent *Fermi*-LAT observations of the Large Magellanic Cloud [20]. Even if not resolved, the integrated gamma-ray luminosity of the galaxy bears some information about the average cosmic-ray density, allowing to compare cosmic-ray injection rates to

galaxy properties. We will demonstrate this by comparing the gamma-ray properties of the normal and starburst galaxies detected by *Fermi*-LAT [19,21]. And measuring the gamma-ray spectra provides information about the cosmic-ray particle spectra and the emission components in the galaxies, allowing for inferences about cosmic-ray physics and diffusion. This will be illustrated by discussing the gamma-ray spectra of the normal and starburst galaxies detected in high-energy or very high-energy gamma-ray so far [19].

2 Some Historical Remarks

High-energy gamma-ray emission from the plane of our Galaxy has been predicted in the late 1940s and early 1950s [22–25], and a first gamma-ray sky map (made out of 22 events!) has been derived from data of the Explorer XI satellite, indicating a putative "tendency for the events to cluster about the galactic plane" [26]. A clear detection of the Galactic plane emission has been achieved with the OSO-3 satellite in the late 1960s, measuring an intensity above 100 MeV of 5×10^{-4} ph cm^{-2} s^{-1} rad^{-1} towards the inner Galaxy. This intensity was in excess of expectations based on the cosmic-ray density observed at Earth, indicating a "remarkably great increase" of the cosmic-ray density towards the inner regions of the Galaxy [27]. Based on the 621 sky events measured by OSO-3, a first sky map that clearly evidenced the Galactic plane was presented by Kraushaar et al. [28].

Following these early results, the SAS-2 and COS-B satellites considerably deepened our view of the Galaxy in high-energy gamma-rays. Variations of the cosmic-ray density throughout the Galactic disk were needed to explain the observational data [29], and overall, gamma-ray intensity variations along the Galactic plane appeared now clearly related to the spiral arm structure of the Milky Way [30]. The evidence was growing that cosmic-ray nuclei of a few GeV were likely of Galactic origin [31]. Gamma-rays were established as a tracer of the total gas column density in the local ISM [32], and were even used to map the still poorly known molecular hydrogen distribution of the Galaxy [33]. Once the molecular hydrogen had been mapped accurately using large-scale CO surveys [34], the gamma-ray observations were used to calibrate the CO-to-H_2 conversion factor [35]. Using the kinematic information in the radio surveys of neutral and molecular hydrogen, [36] derived for the first time the radial distribution of high-energy gamma rays in the outer Galaxy, suggesting that the density of GeV cosmic-ray nuclei remains surprisingly constant beyond the solar circle. The studies have subsequently been extended to the entire Galaxy [37, 38], confirming the weakness of the radial cosmic-ray density gradient. From the distribution of potential cosmic-ray sources (e.g., SNRs or pulsars) in the Galaxy a much steeper radial gradient had been predicted, and until now, the weakness of the radial cosmic-ray density gradient, known as the "cosmic-ray gradient problem", is not satisfactorily explained (see below).

With the launch of the EGRET telescope aboard the Compton Gamma-Ray Observatory (CGRO) in 1991, precision measurements of Galactic diffuse

gamma-ray emission became possible. EGRET enabled for the first time studies of individual molecular clouds which showed that the CO-to-H_2 conversion factors and gamma-ray emissivities are comparable between the clouds and the intercloud medium [39–41]. The analysis of data from the entire Galaxy indicated that no significant spectral variations exist below 4 GeV, suggesting that the cosmic-ray electron to proton ratio does not vary significantly throughout the Galaxy [42]. At higher energies, the data indicate some spectral variations which may arise from cosmic-ray diffusion and/or escape processes. Most features of the observed gamma-ray emission have been reproduced using a model that assumed coupling between the matter and cosmic-ray densities, based on arguments of dynamic balance between matter, magnetic fields and cosmic rays [43]. Only above 1 GeV, the observed flux exceeded the model prediction by a significant amount, a feature named the "GeV excess" [42]. An alternative modeling approach, called GALPROP, has been developed [14, 44]. This model emphasizes cosmic-ray propagation calculations and a larger inverse Compton contribution to the gamma radiation, and using plausible assumptions about enhanced cosmic-ray densities with respect to the local measurements, it was able to explain the GeV excess. More recently, Grenier and Casandjian [45] used EGRET data to evidence the need for an additional gas component that is unseen in radio observations to explain the morphology of the GeV gamma-ray emission. This unseen gas is referred to as the "dark gas" component.

Besides our own Galaxy, EGRET detected also for the first time an external normal galaxy in GeV gamma-rays: the Large Magellanic Could (LMC) [46]. The signal from this Galaxy had been searched for since the early days of gamma-ray astronomy [26], but only EGRET had sufficient sensitivity to capture the faint emission. The few photons detected from the LMC combined with the limited angular resolution of EGRET did not allow for a spatial mapping of the emission, yet it was inferred that the emission morphology is consistent with that of the radio emission. The integrated gamma-ray flux seen from the LMC was consistent with predictions based on a model using the principles of dynamic balance and containment [47], and from this agreement, [46] concluded that the level of cosmic rays in the LMC is comparable to that in our Galaxy.

In contrast, the Small Magellanic Cloud (SMC) was not detected by EGRET. The upper-limit thus derived allowed to clearly dismiss a metagalactic origin for the bulk of cosmic rays with energies 10^{15}–10^{16} eV [48], settling a long standing question in cosmic-ray physics.

No other normal galaxy was seen by EGRET, and also the most actively star-forming galaxies, such as starbursts, luminous or ultraluminous infrared galaxies (LIRGs or ULIRGs), escaped detection. Upper limits on the flux from the Andromeda galaxy (M 31) have been published by Sreekumar et al. [49], upper limits for other galaxies can be derived from Fig. 3 of Hartman et al. [50]. Also the stacking analysis of EGRET observations at the positions of LIRGs and ULIRGs did not reveal any evidence for gamma-ray emission from this class of objects [51].

3 The Milky Way

Fermi-LAT provides a view of the entire gamma-ray sky from 30 MeV to beyond 100 GeV with a sensitivity surpassing that of EGRET by more than an order of magnitude [52]. It is thus an excellent instrument to study the diffuse gamma-ray emission from our Galaxy.

One of the first observations of the telescope was the non-confirmation of the GeV excess observed by EGRET. The *Fermi*-LAT spectrum that is observed at intermediate Galactic latitudes is in fact consistent with diffuse emission models based on the measured cosmic-ray spectra [53]. The same is true for the spectrum observed from the inner Galaxy (see Fig. 1). The GeV excess was thus explained as a systematic error in the calibration of the EGRET telescope.

The emissivity of nearby atomic hydrogen was also found to agree with expectations assuming measured cosmic-ray spectra [54], confirming earlier analyses by SAS-2, COS-B and EGRET that, however, were hampered by the uncertain subtraction of point-source contributions.

Analysis of data for the second [55] and third Galactic quadrants [56] confirmed the cosmic-ray gradient problem, showing that the decrease of the gamma-ray emissivity towards the outer Galaxy is smaller than expected from cosmic-ray diffusion models. The problem is particularly visible in all sky residual maps that are obtained after subtracting plausible cosmic-ray diffusion models that had been fitted to the *Fermi*-LAT data from the observed diffuse Galactic emission (see Fig. 3). Towards the outer regions of the Galaxy (i.e. towards the left and right boundaries of the maps), significant positive emission residuals remain along the Galactic plane, irrespectively of the model assumptions. The fractional residuals are generally smaller towards the inner region of the Galaxy, which is no surprise because this area shows the strongest signal on the sky, and hence is driving the parameter fit. The main message that can be retained from Fig. 3 is that we still do not understand the large scale distribution of the gamma-ray emissivity in the Galaxy, which can be due to our limited understanding of cosmic-ray physics (source distribution, diffusion properties, size of cosmic-ray halo), or due to our incomplete knowledge of the interstellar gas distributions and densities, or due to both.

In addition to the enhanced emission towards the outer Galaxy, the all sky residual maps show notable excess emission above and below the Galactic centre direction. Towards the north, the residual emission is dominated by emission correlated with Loop I, a nearby giant radio loop spanning over 100° and centered on the Sco-Cen OB association [57]. The Loop I emission may be the inverse Compton counterpart of the synchrotron emission seen in the Haslam 408 MHz radio map [58], with possible contributions from π^0 decay gamma rays associated with neutral hydrogen [60].

Superimposed on the Loop I emission, and also visible south of the Galactic plane, is an emission excess with a bipolar structure that obeys a harder gamma-ray spectrum than the diffuse emission from the Galactic plane [59]. This bipolar structure has been dubbed the "Fermi bubbles" and presents $\sim$5 % of the total

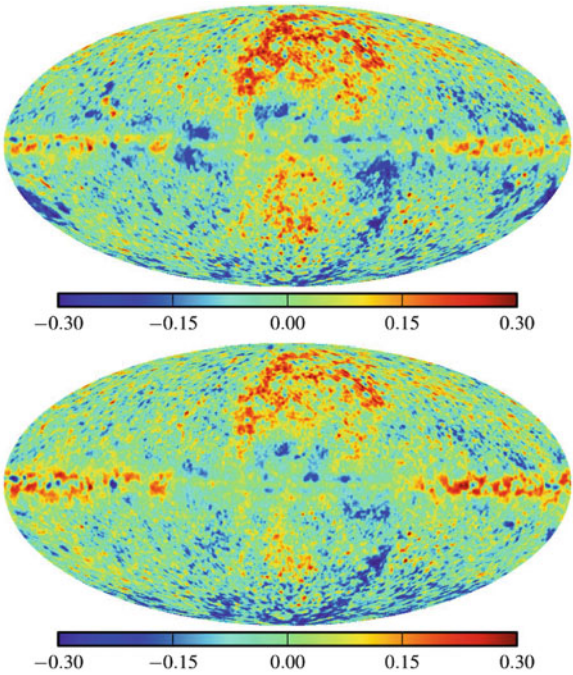

Fig. 3 Gamma-ray residuals (data-model)/model for the energy range 0.2–100 GeV for two GALPROP models of Galactic diffuse emission [17]. For the *top* model a vertical halo scale height of 4 kpc has been assumed, the radial cosmic-ray source density has been based on the Galactic distribution of supernova remnants, and a spin temperature of 150 K has been assumed. For the *bottom* model the vertical halo scale height has been set to 6 kpc, the radial cosmic-ray source density has been based on the Galactic distribution of pulsars, and the neutral hydrogen has been assumed to be optically thin

Galactic gamma-ray luminosity between 0.1 and 100 GeV [60].[1] The gamma-ray emission in this structure seems most likely to originate from inverse Compton scattering, since the required electron cosmic-ray population can also naturally generate the WMAP haze as a synchrotron signal. ROSAT X-ray measurements suggest that the bubbles are hot and hence underdense regions, and thus argue against the gamma rays originating from bremsstrahlung or π^0 decay [60]. The origin of the bipolar structure is much less clear. Scenarios tempting to explain the creation of the bipolar structure invoke a recent activity period of the supermassive black hole at the Galactic centre [60, 62, 63], a recent starburst towards the Galactic centre [60, 64], or more exotic phenomena like annihilating dark matter [65, 66]. In this context it should be mentioned that the possible detection of a 130 GeV gamma-ray line in *Fermi*-LAT data of the Galactic centre [68] considerably stimulates the ideas about dark matter annihilating in the central regions of the Milky Way. On the other hand, [67] recently identify a gamma-ray cocoon feature within the southern bubble, a jet-like feature along the cocoon's axis of symmetry, and another directly opposite the Galactic centre in the north. If the detection of such a jet-like feature is

[1] The discovery paper [59] called this emission the "Fermi haze", in analogy to the "WMAP haze" that has been discovered by the same group in the data of the Wilkinson Microwave Anisotropy Probe (WMAP) [61].

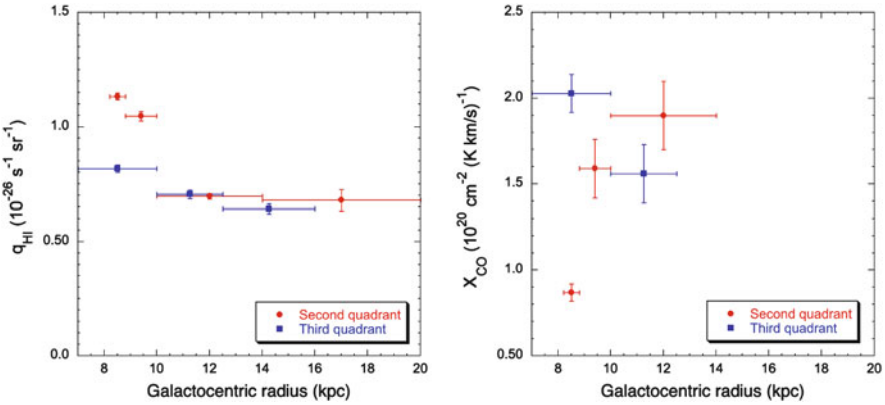

Fig. 4 Gamma-ray emissivities >200 MeV (*left panel*) and CO-to-H_2 conversion factors (*right panel*) as function of Galactocentric radius as determined using *Fermi*-LAT data for the second and third Galactic quadrant [55, 56]. A spin temperature of 125 K has been assumed to derive the values

confirmed, the hypothesis that the Fermi bubbles are the result of recent AGN-like activity at the centre of our Galaxy would be considerably strengthened.

But let's come back to the cosmic-ray gradient problem. The left panel of Fig. 4 shows the >200 MeV gamma-ray emissivities as function of Galactocentric radius that have been derived for the second and third Galactic quadrant using *Fermi*-LAT data [55, 56]. In the right panel we show the CO-to-H_2 conversion factors $X_{\rm CO}$ that have been computed from the CO to H I emissivity ratio using $X_{\rm CO} = q_{\rm CO}/(2\,q_{\rm HI})$. The left panel illustrates the rather shallow decline of gamma-ray emissivities beyond 10 kpc which suggests a small cosmic-ray gradient in the outer Galaxy. In contrast, H I emissivity values in the solar vicinity show quite some dispersion. One may be tempted to conclude that the dispersion suggests variations in the local cosmic-ray density, but a comparison with the right panel indicates an alternative explanation. Regions with high H I emissivity show a surprisingly low $X_{\rm CO}$ ratio, which may indicate that $q_{\rm HI}$ has been overestimated by the analysis. In the general analysis procedure, which goes back to the COS-B era [36], a linear combination of gas map templates is fitted to the data. The parameters that are adjusted are the normalization factors $q_{\rm HI}$ and $q_{\rm CO}$, representing the emissivity of neutral and molecular hydrogen, respectively (in practice, additional components are added to represent dark gas, the isotropic background, and point sources in the field [55]). As the fit matches the templates to the data, an increase of $q_{\rm HI}$ leads necessarily to a reduction of $q_{\rm CO}$, making $X_{\rm CO}$ very sensitive to the precise balance between $q_{\rm HI}$ and $q_{\rm CO}$. Both parameters are well defined if the morphology of the gas templates is very distinctive, but increasing crosstalk is seen for H I and CO maps that show strong resemblance (see for example Fig. 3 in [41]). The impact of the spin temperature on derived H I column densities, and the possible presence of dark gas considerably complicates the situation [69]. It remains to be seen whether these effects can

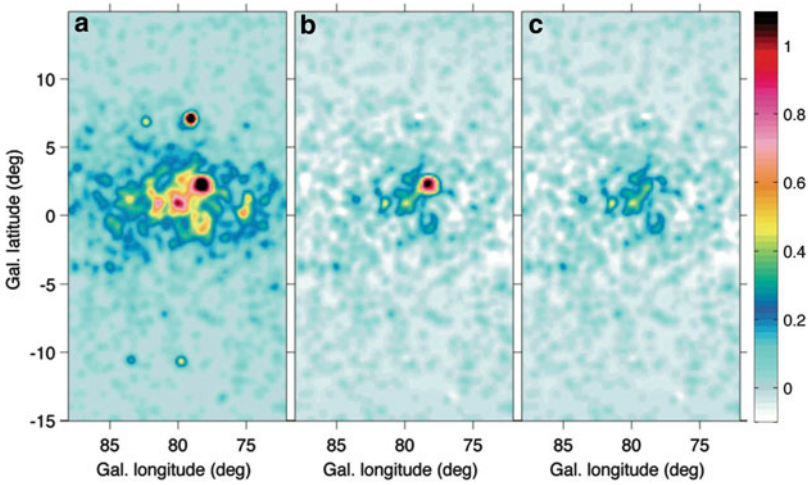

Fig. 5 *Fermi*-LAT counts maps in the 10–100 GeV band smoothed with a $\sigma = 0.25^\circ$ Gaussian kernel [71]. From *left* to *right*, the panels show the total emission (**a**), the emission after subtraction of the interstellar background and all known sources but γ Cygni (**b**), and after further removal of the extended emission from γ Cygni (**c**)

explain some of the features seen in Fig. 4. In the meantime, claims of $X_{\rm CO}$ gradients and variations [41, 55, 69] should be considered with caution.

Massive star forming regions have been postulated since a while as potential sites of cosmic-ray induced gamma-ray emission [12, 72], and recent observations with the Milagro Gamma Ray Observatory in the TeV domain have been interpreted as evidence for active cosmic-ray sources accelerating hadrons in the Cygnus X region [73]. Using 2 years of *Fermi*-LAT data, [70] have investigated the diffuse gamma-ray emission from the Cygnus region, and find a gamma-ray emissivity and $X_{\rm CO}$ factor that is in agreement with the values measured in the local interstellar medium. So despite the conspicuous star formation activity and high masses of the interstellar clouds, the cosmic-ray population in the Cygnus complex averaged over a few hundred parsecs appears similar to that of the local interstellar space.

Nevertheless, above 10 GeV, an additional hard spectral component has been evidenced in the *Fermi*-LAT data that spatially correlates well with the interstellar cavity that has been carved out through ionization, radiation pressure, and the winds of the massive stellar population of the Cyg OB2 cluster [71]. Figure 5 presents three maps of the Cygnus region, showing the residuals after progressively removing known emission components. The excess remaining in the right panel (C) coincides well with the Cygnus superbubble. The total 1–100 GeV luminosity of this excess has been estimated to $(9 \pm 2) \times 10^{34}$ erg s^{-1} [71], which is surprisingly small compared to the mechanical wind power of 4×10^{38} erg s^{-1} that is available from the Cyg OB2 association [74]. If Cyg OB2 were at the origin of the observed emission, only $\sim$0.02 % of its available kinetic power would be tapped to produced the observed gamma-ray emission.

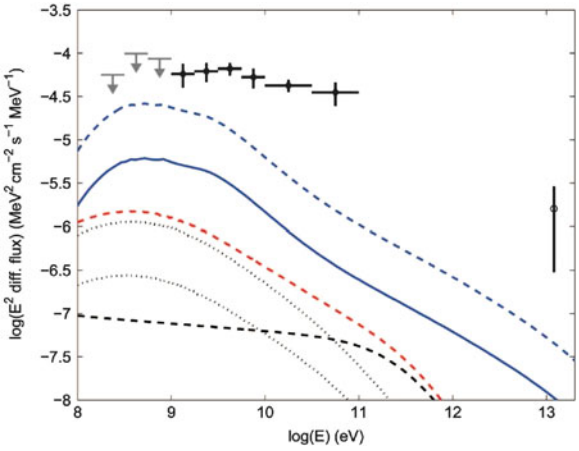

Fig. 6 Energy spectrum of the cocoon emission [71]. The 1σ errors are statistical, 2σ upper limits are given below 1 GeV. The *open circle* shows the Milagro flux, integrated over $78.7^\circ < l < 81.7^\circ$ and $-0.4^\circ < b < 2.6^\circ$, and corrected for the extrapolated contribution of the TeV J2032+4130 source at energies >10 TeV. The *blue curves* show the expected π^0 decay emission based on the locally measured cosmic-ray spectrum pervading the ionized gas for electron densities $10\,\mathrm{cm}^{-3}$ (*solid*) and $2\,\mathrm{cm}^{-3}$ (*dashed*). The *black curves* show the expected inverse Compton emission based on the locally measured cosmic-ray spectrum, upscattering the stellar light from Cyg OB2 (*upper dotted curve*), NGC 6910 (*lower dotted curve*), and the interstellar radiation present in the PDRs (*dashed curve*). The *red curve* sums all inverse Compton emissions

The energy spectrum of the excess emission is presented in Fig. 6, demonstrating the hardness of the spectrum when compared to Galactic diffuse emission components. The expected contributions of π^0 decay and inverse Compton emission based on the locally measured cosmic-ray spectrum are superimposed as lines, illustrating that the observed emission is in excess of and harder than model predictions using plausible assumptions on gas densities and interstellar radiation fields in the region. The excess argues for an additional cosmic-ray component to be present in Cygnus, the hardness points to freshly accelerated particles [71]. Interestingly, although separated by a large gap without any data, the flux point obtained by Milagro seems to fit the extrapolation of the *Fermi*-LAT spectrum to TeV energies.

It remains to be seen whether the cocoon of freshly accelerated cosmic rays detected by *Fermi*-LAT in the Cygnus superbubble can indeed be explained by cosmic-ray acceleration in the stellar winds of the massive OB stars of young stellar clusters. More such cocoons should be found within our Galaxy to confirm this scenario, yet Cyg OB2 is one of the most massive young stellar clusters known in our Galaxy, and definitely the closest one of such mass, hence other potential candidates may be too faint to be detectable by current instruments. *Fermi*-LAT has however detected gamma rays from another massive star cluster situated in the nearby LMC galaxy [20], and we now turn to these observations to see how they fit in our global understanding of cosmic-ray acceleration and propagation in the Milky Way.

4 The Large Magellanic Cloud

As targets for studies of cosmic-ray physics, nearby galaxies have the advantage of being viewed from outside, and so line of sight confusion, which complicates studies of emission from the Galactic disk, is diminished. This advantage is, however, somewhat offset by the limitations of angular resolution and sensitivity of the instrument. The LMC is thus an excellent target for studying the link between cosmic-ray acceleration and gamma-ray emission since the galaxy is nearby ($D \approx 50$ kpc; [75, 76]) and thus reasonably bright, has a large angular extent of $\sim 8°$ and thus is easily resolvable, and is seen at a small inclination angle of $i \approx 20° - 35°$ [77, 78], which avoids source confusion. In addition, the LMC is relatively active, housing many supernova remnants, bubbles and superbubbles, and massive star-forming regions that are all potential sites of cosmic-ray acceleration.

Fermi-LAT has provided the first spatially resolved gamma-ray image of the LMC [20], that is presented in Fig. 7. A striking feature of this image is that the gamma-ray emission does not correlate well with the gas distribution of the galaxy. Under the conventional assumption that a galaxy is filled up with a "sea" of cosmic-ray particles that is homogenized through the effects of convection and diffusion in galactic magnetic fields [79], one would predict that the gamma-ray image of the LMC should in first order be a proxy of the gas distribution in the galaxy, modulated eventually by a large scale cosmic-ray density gradient. In contrast, a substantial fraction of the LMC surface area appears devoid of gamma rays, and the emission shows considerable structure, with a single bright feature dominating the image. Interestingly, this features coincides with 30 Doradus, one of the most active starburst regions in the entire Local Group of galaxies [80].

A comparison of the observed distribution of gamma rays to tracers of interstellar emission components has revealed that the emission morphology correlates well with the ionized gas component, while neutral atomic or molecular hydrogen show considerably different morphologies [20]. This result even holds if the 30 Doradus region is excluded from the correlation analysis. This finding does not imply, however, that the gas with which the cosmic rays interact is necessarily ionized, it simply shows that the spatial distribution of the LMC gamma-ray emissivity resembles the spatial distribution of ionized gas. As interstellar ionization is primarily provided by UV photons from O stars (i.e. stars with masses $>20\,M_\odot$), the distribution of ionized gas traces the distribution of O stars. Consequently, the gamma-ray emissivity of the LMC correlates with the distribution of O stars.

The shortcut of attributing this correlation to cosmic-ray production by O stars is appealing, but in view of the results obtained for our own Galaxy, and in particular those of the Cygnus region [70, 71], some caution is appropriate. Cyg OB2 houses about 120 O stars [81], which is, within a factor of a few comparable to the number of O stars found in 30 Doradus [82]. The kinematic energy input of the stars in 30 Doradus should therefore also be comparable to the input provided by the Cyg OB2 stars, say about $\sim 10^{39}$ erg s^{-1}, which is in line with studies of the kinematic structure of the region [83]. The observed >100 MeV gamma-ray flux

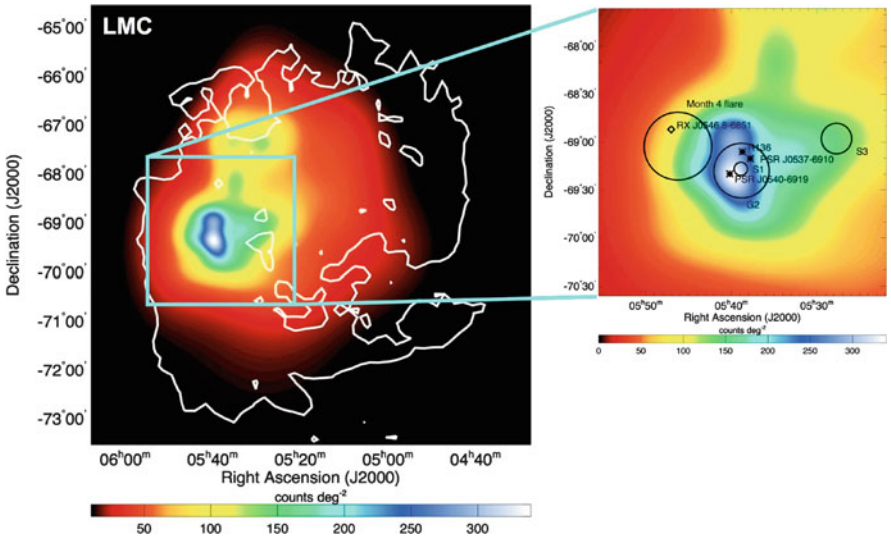

Fig. 7 *Fermi*-LAT image of the Large Magellanic Cloud. The image is based on a background subtracted counts map that has been adaptively smoothed to remove image noise. In the *left panel*, the colors show the gamma-ray emission while the *white contour* shows the outline of the LMC as traced by neutral hydrogen. The *right panel* shows a zoom into the 30 Doradus region. The *circles* indicate the locations of source components that have been fitted to the data. The *stars* mark the positions of potential gamma-ray emitting sources. The location of an observed flare in the area is also indicated (The figure has been adapted from Abdo et al. [20])

from 30 Doradus amounts to $(4.6 \pm 0.5) \times 10^{-11}\,\mathrm{erg\,s^{-1}\,cm^{-2}\,sr^{-1}}$, corresponding to a luminosity of $(1.4 \pm 0.1) \times 10^{37}\,\mathrm{erg\,s^{-1}}$. Thus, about $\sim$1 % of the mechanical luminosity of 30 Doradus are required to explain the observed gamma-ray emission. Although not excessive, this fraction is 50 times larger than the fraction inferred from the cocoon emission in Cygnus [71]. So if the 30 Doradus gamma rays are attributed to cosmic rays, there must be something fundamentally different in 30 Doradus compared to the most massive star-forming regions in the Milky Way.

But maybe there exists a simpler explanation. Massive star forming regions are rich in remnants of stellar explosions, such as supernova shells or pulsars. In particular, pulsars are known to be bright gamma-ray emitters that form the dominant GeV source population of normal galaxies [84], and numerous pulsars are found in the Galactic star forming regions Cygnus and Carina. Pulsars are also known in 30 Doradus, two of them being among the three most powerful pulsars known (PSR J0537−6910 and PSR J0540−6919). Although no gamma-ray pulsations have so far been detected from these objects [20], it would be surprising if pulsars would not contribute to the gamma-ray emission seen from 30 Doradus. The question is: can pulsars explain most of the gamma-ray flux seen from 30 Doradus?

The Crab is the most powerful gamma-ray pulsar known in the Milky-Way, yet with a $>$100 MeV gamma-ray luminosity of $\sim 6 \times 10^{35}\,\mathrm{erg\,s^{-1}}$ [85], it could

only account for ∼1/20 of the observed luminosity from 30 Doradus. Thus, at the distance of the LMC, the Crab would only be a faint source, barely detectable with *Fermi*-LAT. Explaining the 30 Doradus emission with pulsars would either require tens of Crab-type pulsars in that area, or one pulsar which is at least ten times more luminous in gamma rays than the Crab. There is indeed some headroom for the existence of more luminous gamma-ray pulsars, as the Crab only converts a tiny fraction (∼0.1 %) of its rotational power into gamma rays [85]. In this context we note that H.E.S.S. recently detected TeV gamma rays from the pulsar wind nebula of PSR J0537−6910 in 30 Doradus [86], inferring a TeV luminosity for the nebula that is ∼14 times superior to that of the Crab nebula at TeV energies. If the nebula TeV luminosity is linked to the pulsar GeV luminosity (which is not implausible because both are powered by the spin-down of the pulsar), PSR J0537−6910 would be a prime candidate to explain the GeV emission observed by *Fermi*-LAT from 30 Doradus. Ongoing searches for pulsations from this object in *Fermi*-LAT data may allow to settle this question in the future.

It should also be mentioned that owing to the large extension of the LMC, blazars lying along the line of sight behind the galaxy may also contribute to the observed signal. For the sensitivity reached during the first *Fermi*-LAT analysis of the LMC, it has been estimated that 1 and 2 background blazars may exist within the boundaries of the galaxy, and indeed, a flare of gamma-ray emission had been observed near 30 Doradus that could indicate some blazar activity towards this general direction [20]. While a flaring signal can be easily excluded from the data (as has been done by Abdo et al. [20]), steady emission from unknown background sources can only be distinguished from the overall LMC on basis of possible spectral differences. Nevertheless, it should be mentioned that no gamma-ray emission from known blazars in the field of the LMC has been detected by Abdo et al. [20].

Having all these caveats in mind, and excluding the 30 Doradus region from the analysis due to the uncertain origin of the emission, the remaining overall emission of the LMC can be interpreted in the context of cosmic-ray induced gamma-ray emission. In that way, Abdo et al. [20] derived an average >100 MeV gamma-ray emissivity of $\sim 0.4 \times 10^{-26}$ ph s^{-1} sr^{-1} H-atom^{-1} which is about a factor of ∼4 lower than the value measured in the local interstellar medium of the Milky Way [54]. The average cosmic-ray density in the LMC amounts thus to only ∼25 % of the cosmic-ray density observed near Earth. This lower density can be explained by an either lower cosmic-ray production rate in the LMC with respect to our Galaxy, or by an easier escape of the cosmic rays into the intergalactic medium.

5 The Small Magellanic Cloud

While before the launch of the *Fermi* satellite only upper limits had been derived on gamma-ray emission from the SMC [48], the LAT achieved a first detection of the galaxy [87]. Figure 8 shows the gamma-ray map of the SMC that has been obtained using 17 months of *Fermi*-LAT data, with contours tracing H I column

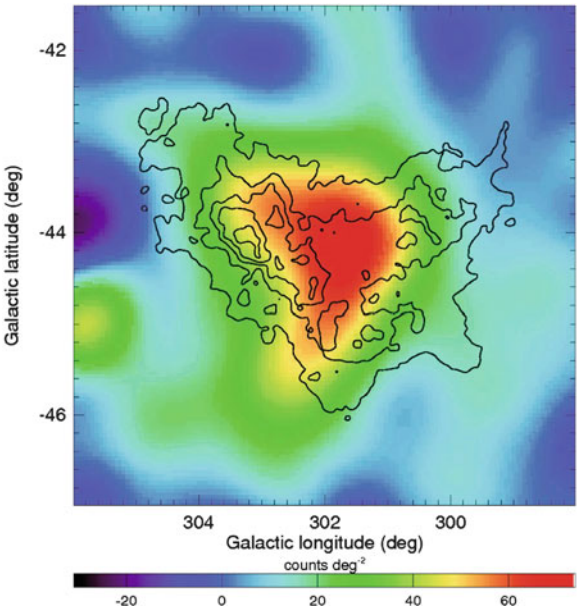

Fig. 8 *Fermi*-LAT image of the SMC in the 200 MeV–20 GeV energy band after subtraction of the celestial background [87]. The image has been smoothed by a 2D Gaussian kernel with $\sigma = 0.4°$. The SMC is traced by H I column density contours

density superimposed. The observed gamma-ray emission is clearly centred on the galaxy, and extends over an area of $\sim$3° in diameter. Owing to the faintness of the signal combined with the small angular size of the galaxy, only limited information is so far available concerning the spatial distribution of the emission. Nevertheless, no clear correlation between the gamma-ray emission and the distribution of either neutral gas or ionized gas is observed. A possible link of the gamma-ray emission with supergiant shells has been pointed out [87].

Under the assumption that all emission can be attributed to cosmic-ray interactions with the interstellar medium, the observed integrated >100 MeV flux of $(3.7 \pm 0.7) \times 10^{-8}$ ph cm^{-2} s^{-1} implies an average cosmic-ray density in the SMC of $\sim$15 % of the value measured locally in the Milky Way. Interestingly, the estimated star formation rate per unit volume in the SMC is comparable, or even larger, than that of the Milky Way, so the rate with which cosmic rays are injected in the galaxy per unit volume should be at least as large as the Galactic value. The apparently lower average cosmic-ray density in the SMC then implies that the cosmic-ray confinement time is lower or the cosmic-ray diffusion coefficient is larger in comparison to the Milky Way. Alternatively, non steady-state scenarios or the confinement of cosmic-ray in the hot and tenuous interiors of large superbubbles may also account for the observations without implying cosmic-ray densities below the Galactic one [87].

In any case, the relatively low gamma-ray flux combined with the observed star formation rate implies that the contribution of point sources to the overall gamma-ray emission could be significant in the SMC. By making plausible assumptions on the average luminosity and the expected number of gamma-ray pulsars that

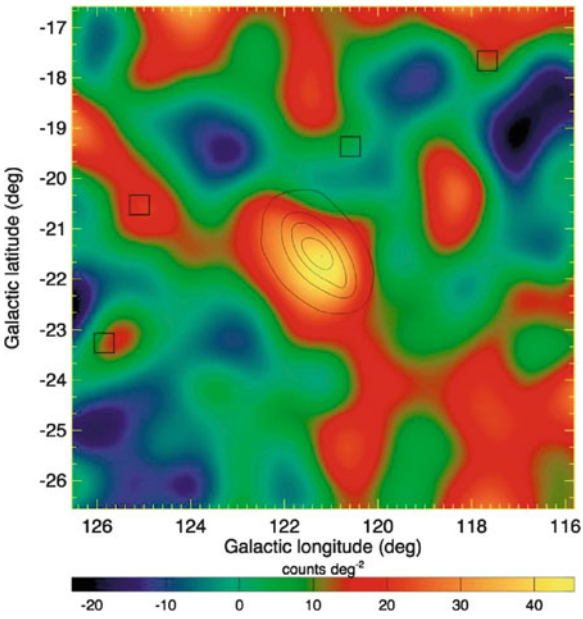

Fig. 9 *Fermi*-LAT image of M 31 in the 200 MeV–20 GeV energy band after subtraction of the celestial background and nearby point sources [21]. The image has been smoothed by a 2D Gaussian kernel with $\sigma = 0.5^\circ$. M 31 is traced by contours of 100 μm infrared emission that have been convolved with the LAT point spread function. The *square symbols* indicate the locations of the point sources that have been subtracted from the data

may be present in the SMC, [87] estimate that between ∼25 and 100 % of the observed flux may be attributed to the combined emission of gamma-ray pulsars. If pulsars contribute indeed significantly to the emission, the average cosmic-ray density deduced from the observations would be even lower, reinforcing the idea that cosmic-ray escape from the SMC is amplified with respect to our Galaxy.

6 Other Local Group Galaxies

Fermi-LAT has also provided the first detection of gamma-ray emission from the nearby Andromeda galaxy [21]. Figure 9 shows the image of the region around M 31 that has been derived using almost 2 years of continuous sky survey observations. With a significance of 5σ, the signal is at the limit of what is detectable by the LAT. Although the gamma-ray image indicates some elongation of the emission that follows the morphology of the galaxy, the current data can not allow to discriminate between point-like and extended emission.

Assuming that the entire gamma-ray emission originates from cosmic-ray interactions with the interstellar medium of M 31, the observations indicate an average cosmic-ray density that amounts to about half of the Galactic value [21]. As the estimated average star formation rate of M 31 is inferior to that of the Milky Way by about the same factor, the lower cosmic-ray density in M 31 is readily explained by a lower cosmic-ray injection rate in that galaxy.

Gamma-ray emission has also be searched for in the Local Group galaxies M 33 [21], M 81, M 83, IC 342, Maffei 1, Maffei 2, and M 94 [88] without any significant detection. The derived upper limits for these galaxies are fully compatible with a scenario where the gamma-ray luminosities scale with the integrated star formation rates in star-forming galaxies (see below).

7 Starburst Galaxies

For the first time, *Fermi*-LAT has also detected GeV gamma-ray emission from starburst galaxies. First from the well known prototypical galaxies M 82 and NGC 253 [89], later also from NGC 1068 and NGC 4945 [90]. While for the first two objects it is widely accepted that the observed gamma-ray emission originates in cosmic-ray interactions with the interstellar medium of these galaxies, contributions from the active nucleus can not be excluded for NGC 1068 and NGC 4945 [90]. M 82 [91] and NGC 253 [92] have also been detected at TeV energies using ground-based Cherenkov telescopes, providing thus a wide spectral coverage of the gamma-ray emission that allow for inferences about the cosmic-ray spectrum to be made.

The gamma-ray luminosities of the starburst galaxies are clearly in excess to those of the Milky Way, M 31, the LMC and the SMC, reinforcing the idea that the cosmic-ray densities increase with increasing star formation rate of a galaxy [89]. Theoretically predicted gamma-ray spectra [93–97] agree reasonably well with the observations, although the observed spectra are not extremely constraining, owing to the faintness of the gamma-ray flux seen at GeV and TeV energies.

While in the Milky Way, most cosmic-ray protons are believed to escape the Galaxy before being able to scatter inelastically off the ISM nuclei, generating π^0 meson, the dense ISM in starburst galaxies may provide a thick target to cosmic-ray protons that converts a substantial fraction of the cosmic-ray energy into pionic gamma rays [98]. Starburst galaxies have thus been suggested to be proton calorimeters [99]. Proton calorimetry would manifest by relatively hard spectral indices of $\Gamma \approx 2.0 - 2.4$ while proton escape leads to softer spectra with $\Gamma \approx 2.7$, as is observed for the Milky Way [100]. The fact that starburst galaxies are both detected at GeV and TeV energies points indeed towards relatively hard gamma-ray spectra, supporting the hypothesis that starburst galaxies are proton calorimeters. Alternatively, strong advective cosmic-ray losses, produced for example by strong galactic winds, will also produce hard gamma-ray spectra, so the question of whether starburst galaxies are indeed proton calorimeters is not yet definitely settled [100].

It should also be mentioned that contributions of point sources, in particular at TeV energies, may complicate the picture [100, 101]. The large star formation rates encountered in the cores of starburst galaxies will also result in large populations of supernova remnants and pulsar wind nebulae (PWNe). Although estimates based on the gamma-ray luminosities of Galactic PWNe imply that $\sim 10^4$–10^5 such objects

would be needed to contribute significantly to the GeV–TeV emission seen from M 82 and NGC 253, in cannot be ruled our that PWNe in starbursts are much more radiatively efficient in gamma rays that in the Milky Way, for example through stronger inverse Compton losses [100].

8 The Gamma-Ray Population of Starforming Galaxies

Taking together the four galaxies from the Local Group (Milky Way, M 31, LMC, and SMC) and the four starburst galaxies (M 82, NGC 253, NGC 1068, and NGC 4945), a first sample of gamma-ray emitting star-forming galaxies exists that spans five orders of magnitude in star formation rate and gamma-ray luminosity. Figure 10 shows the 1–100 GeV gamma-ray luminosities of this sample as function of the radio continuum (RC) luminosity at 1.4 GHz. The latter is an excellent tracer of the star formation rate (SFR), which is shown as the upper abscissa according to Eq. 2 of [102]. The plot shows also the 95 % confidence upper flux limits that have been obtained from the *Fermi*-LAT analysis for a sample of 69 dwarf, spiral, and luminous and ultraluminous infrared [19]. Obviously, there exists a good correlation between the integrated GeV gamma-ray luminosity and the integrated SFR of the galaxies, and also the upper limits are consistent with the correlation. A power law fit to the data (shown as red line) results in a slope of $\sim$1.1, suggesting that the relation between GeV luminosity and SFR is slightly non-linear. Still, it is striking that the relation seems to hold from the SMC dwarf galaxy, with its low cosmic-ray density that may indicate a substantial loss of cosmic-ray particles, to NGC 1068, which is proposed to be a proton calorimeter [100].

For reference, Fig. 10 shows as red dashed line the expected gamma-ray luminosity of a galaxy in the calorimetric limit. To derive this line, it has been assumed that 10 % of the kinetic energy released in a core-collapse supernova (taken to be 10^{51} erg) go into cosmic-ray nuclei. In this simplistic picture, none of the galaxies reaches in fact the calorimetric limit, and the slight non-linearity of the observed correlation may be interpreted as an increase of the calorimetric efficiency from $\sim$10–20 % for dwarf galaxies to $\sim$30–50 % for starburst galaxies [19]. In this scenario, the physical conditions for cosmic-ray escape vary surprisingly little among the galaxies, despite their large diversity in size, interstellar mass and density, and star formation rate.

Figure 11 presents a compilation of the observed GeV–TeV gamma-ray spectra for all eight galaxies [19]. The spectra are expressed in absolute luminosity, illustrating the wide spread in gamma-ray power among the detected objects. For the Milky Way, instead of a measured spectrum, a global model is shown that has been adjusted to *Fermi*-LAT data of diffuse Galactic gamma-ray emission (as we're observing our Galaxy from inside, it is not possible to make a model-independent estimation of the Galactic gamma-ray luminosity). The figure illustrates that the more luminous galaxies also have comparatively harder gamma-ray spectra. Whereas the power-law

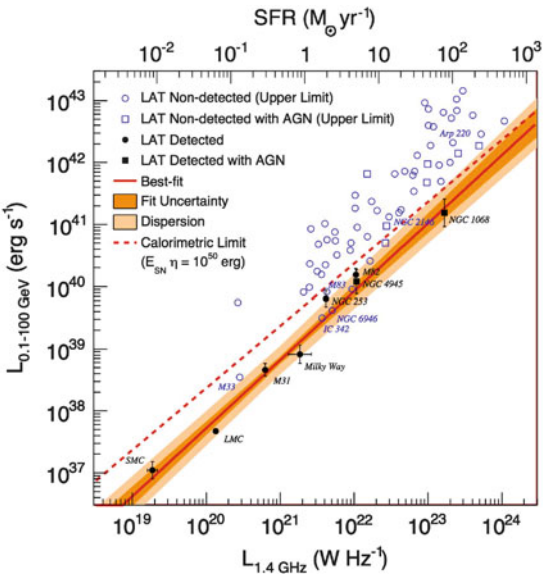

Fig. 10 Gamma-ray luminosity versus RC luminosity at 1.4 GHz. Galaxies significantly detected by the LAT are indicated with *filled symbols*, galaxies with gamma-ray flux upper limits are marked with *open symbols*, galaxies hosting AGN are shown with *square markers*. The upper abscissa indicates SFR estimated from the RC luminosity. The best-fit power law relation is shown by the *red solid line* along with the fit uncertainty (*darker shaded region*), and intrinsic dispersion around the fitted relation (*lighter shaded region*). The *dashed red line* represents the expected gamma-ray luminosity in the calorimetric limit assuming an average CR luminosity per supernova of 10^{50} erg [19]

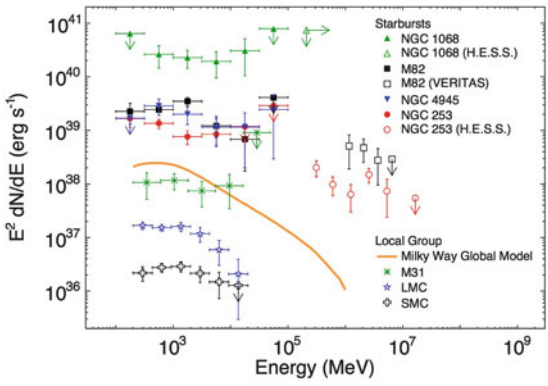

Fig. 11 Gamma-ray luminosity spectra of star-forming galaxies detected by the LAT and imaging air-Cherenkov telescopes [19]

spectral indices of M 82 and NGC 253 are 2.2–2.3 extending to TeV energies, the spectra of the LMC and SMC steepen above ∼2 GeV.

Although star-forming galaxies are intrinsically faint sources, they are numerous in the Universe, and their combined emission may give rise to a diffuse background of cosmic gamma-ray radiation that carries an imprint of the past star formation

history [103]. Following the discovery of GeV and TeV emission from starburst galaxies, the possible contribution of star-forming galaxies to the diffuse background radiation has attracted increasing attention. Estimates based on the resolved population of blazars observed by *Fermi*-LAT suggest that less than 30 % of the diffuse extragalactic background originates from blazars [104], making a perceptible contribution from starburst galaxies to the diffuse gamma-ray background plausible. By combining the relationship between gamma-ray luminosity and SFR with an estimate of the SFR evolution with redshift derived from non-AGN galaxies [19,105] estimate that star-forming galaxies contribute to about $\sim$10 % to the diffuse gamma-ray background, with the bulk of the emission arising from galaxies with redshifts $z < 1.5$. This estimate is still too low to explain the extragalactic gamma-ray background, suggesting that important aspects of these populations are not included in current models and/or that other high-energy source classes or diffuse processes contribute a significant fraction of the observed gamma-ray intensity.

9 Conclusions and Outlook

With the launch of the *Fermi* satellite and the advent of the modern air-Cherenkov telescope systems H.E.S.S. and VERITAS, star-forming galaxies have become a new class of gamma-ray sources that extend the study of cosmic-ray physics from the Milky Way to external galaxies. So far, eight star-forming galaxies have been observed at GeV energies (SMC, LMC, Milky Way, M 31, M 82, NGC 253, NGC 1068, and NGC 4945) while two have been seen at TeV energies (M 82, NGC 253). The galaxies detected at TeV energies have amongst the highest SFRs in the sample, suggesting that gamma-ray spectra harden with increasing SFR.

The gamma-ray observations have confirmed the general ideas about cosmic-ray acceleration in galaxies, and a clear correlation between star formation activity and gamma-ray luminosity has been established. However, with the first spatially-resolved gamma-ray images that are now available for the LMC and SMC, new challenges arise. Explaining the emission morphology of the LMC, and in particular, explaining the absence of gamma-ray emission from particularly dense regions of the interstellar medium may possibly require some revision of our ideas about cosmic-ray diffusion and penetration in dense clouds. Point source contributions may also be more important than previously thought, and cannot be neglected when studying the gamma-ray emission of galaxies, in particular if they are not spatially resolved.

The continuing observations of the *Fermi* satellite will probably provide more detections of star-forming galaxies in the near future. More data will also allow refining the gamma-ray spectra of the brighter systems, providing more stringent constraints on the cosmic-ray spectra in the galaxies. The freshly installed H.E.S.S. II telescope will close the gap between the GeV and TeV energy domains, and in the recent future, an unprecedented spectrum of NGC 253 promises an improved understanding of the cosmic-ray physics in that galaxy.

The new generation Cherenkov Telescope Array CTA will provide a further significant step forward. CTA will measure the diffuse gamma-ray emission surrounding nearby ($\sim$1 kpc) and powerful (a few 10^{50} erg) sources of cosmic rays in the Milky Way. Massive molecular clouds located in the vicinity of cosmic-ray sources will be detectable even to larger distances, comparable with the distance of the Galactic centre [106]. The detection of the overall diffuse galactic emission due to the cosmic-ray sea in the Milky Way will be challenging, but with a sufficient accumulation of observing time, advances are also expected in this area. Beyond our own Galaxy, CTA will provide unprecedented spectra of starburst galaxies, and further objects may be detected, such as the ULIRG Arp 220, providing insights into the cosmic-ray physics of the most extreme environments in the Universe.

References

1. Hess, V. F., Physik. Zeit., 12, 1084
2. Ferrière, K. M. 2001, Rev. Mod. Phys., 73, 1031
3. Ferrière, K. M. 1998, ApJ, 497, 759
4. Ptuskin, V. S., Moskalenko, I. V., Jones, F. C., Strong, A. W., & Zirakashvili, V. N. 2006, ApJ, 642, 902
5. Hanasz, M., Kowal, G., Otmianowska-Mazur, K., & Lesch, H. 2004, ApJ, 605, L33
6. Hanasz, M., Otmianowska-Mazur, K., Kowal, G., & Lesch, H. 2009, A&A, 498, 335
7. Indriolo, N., Fields, B. D., & McCall, B. J. 2009, ApJ, 694, 257
8. Ginzburg, V. L., & Syrovatskii, S. I. 1964, The Origin of Cosmic Rays
9. Ellison, D. C., Drury, L. O'C., Meyer, J.-P. 1997, ApJ, 487, 197
10. Koyama, K., Petre, R., Gotthelf, E. V., et al. 1995, Nature, 378, 255
11. Aharonian, F., Bykov, A., Parizot, E., Ptuskin, V., & Watson, A. 2012, Space Science Reviews, 166, 97
12. Cesarsky, C. J., & Montmerle, T. 1983, Space Science Reviews, 36, 173
13. Fang, K., Kotera, K., Olinto, A. V. 2012, ApJ, 750, 118
14. Strong, A. W., Moskalenko, I. V., & Reimer, O. 2000, ApJ, 537, 763
15. Strong, A. W., Bennett, K., Bloemen, H., et al. 1996, A&AS, 120C, 381
16. Strong, A. W., Diehl, R., Halloin, H., et al. 2005, A&A, 444, 495
17. Ackermann, M., Ajello, M. Atwoord, W. B., et al. 2012, ApJ, 750, 1
18. Ackermann, M., Ajello, M., Allafort, A., et al. 2011, Ap7, 743, 171
19. Ackermann, M., Ajello, M., Allafort, A., et al. 2012, ApJ, accepted (arXiv:1206.1346)
20. Abdo, A. A., Ackermann, M., Ajello, M., et al. 2010, A&A, 512, 7
21. Abdo, A. A., Ackermann, M., Ajello, M., et al. 2010, A&A, 523, 2
22. Feenberg, E., & Primakoff, H. 1948, Phys. Rev., 73, 449
23. Hayakawa, S. 1952, Prog. Theor. Phys., 8, 571
24. Hutchinson, G. W. 1952, Philos. Mag., 43, 847
25. Morrison, P. 1958, Il Nuovo Cimento, 7, 858
26. Kraushaar, W. L., & Clark, G. W. 1962, Phys. Rev. Lett., 8, 106
27. Clark, G. W., Garmire, G. P., & Kraushaar, W. L. 1968, ApJ, 153, 203
28. Kraushaar, W. L., Clark, G. W., Garmire, G. P., et al. 1972, ApJ, 177, 341
29. Strong, A.W., Wdowczyk, J., & Wolfendale, A. W. 1973, ICRC, 1, 463
30. Bignami, G. F., Fichtel, C. E., Kniffen, D. A., & Thompson, D. J. 1975, ApJ, 199, 54
31. Dodds, D., Strong, A. W., & Wolfendale, A. W. 1975, MNRAS, 171, 569
32. Fichtel, C. E., Simpson, G. A., & Thompson, D. J. 1978, ApJ, 222, 833
33. Strong, A. W., Bignami, G. F., Bloemen, J. B. G. M., et al. 1982, A&A, 115, 404

34. Dame, T. M., Ungerechts, H., Cohen, R. S., et al. 1987, ApJ, 322, 706
35. Lebrun, F., Bennett, K., Bignami, G. F., et al. 1983, ApJ, 274, 231
36. Bloemen, J. B. G. M., Bennett, K., Bignami, G. F., et al. 1984, A&A, 135, 12
37. Bloemen, J. B. G. M., Strong, A. W., Mayer-Hasselwander, H. A., et al. 1986, A&A, 154, 25
38. Strong, A. W., Bloemen, J. B. G. M., Dame, T. M., et al. 1988, A&A, 207, 1
39. Hunter, S.D., Digel, S. W., De Geus, E. J., & Kanbach, G. 1994, ApJ, 436, 216
40. Digel, S. W., Hunter, S.D., & Mukherjee, R. 1995, ApJ, 441, 270
41. Digel, S. W., Grenier, I., Heithausen, A., Hunter, S.D., & Thaddeus, P. 1996, ApJ, 463, 609
42. Hunter, S. D., Bertsch, D. L., Catelli, J. R., et al. 1997, ApJ, 481, 205
43. Bertsch, D. L., Dame, T. M., Fichtel, C. E., et al. 1993, ApJ, 416, 587
44. Strong, A. W., Moskalenko, I. V., & Reimer, O. 2004, ApJ, 613, 962
45. Grenier, I. A., Casandjian, J.-M., & Terrier, R. 2005, Science, 307, 1292
46. Sreekumar, P., Bertsch, D. L., Dingus, B. L., et al. 1992, ApJ, 400, L67
47. Fichtel, C. E., Özel, M. E., Stone, R. G., & Sreekumar, P. 1991, ApJ, 374, 134
48. Sreekumar, P., Bertsch, D. L., Dingus, B. L., et al. 1993, Phys. Rev. Lett., 70, 127
49. Sreekumar, P., Bertsch, D. L., Dingus, B. L., et al. 1994, ApJ, 426, 105
50. Hartman, R. C., Bertsch, D. L., Bloom, S. D., et al. 1999, ApJS, 123, 79
51. Cillis, A. N., Torres, D. F., & Reimer, O. 2005, ApJ, 621, 139
52. Atwood, W. B., Abdo, A. A., Ackermann, M., et al. 2009, ApJ, 697, 1071
53. Abdo, A. A., Ackermann, M., Ajello, M., et al. 2009, Phys. Rev. Lett., 103, 251101
54. Abdo, A. A., Ackermann, M., Ajello, M., et al. 2009, ApJ, 703, 1249
55. Abdo, A. A., Ackermann, M., Ajello, M., et al. 2010, ApJ, 710, 133
56. Ackermann, M., Ajello, M., Baldini, L., et al. 2011, ApJ, 726, 81
57. Casandjian, J., & Grenier, I. 2009, in *2009 Fermi Symposium*, arXiv:0912.3478
58. Haslam, C. G. T., Salter, C. J., Stoffel, H., & Wilson, W. E. 1982, A&AS, 47, 1
59. Dobler, G., Finkbeiner, D. P., Cholis, I., Slatyer, T., & Weiner, N. 2010, ApJ, 717, 825
60. Su, M., Slatyer, T. R., & Finkbeiner, D. P. 2010, ApJ, 724, 1044
61. Finkbeiner, D. P. 2004, ApJ, 614, 186
62. Cheng, K.-S., Chernyshov, D. O., Dogiel, V. A., Ko, C.-M., Ip., W.-H. 2011, ApJ, 731, 17
63. Zubovas, K., & Nayakshin, S. 2012, MNRAS, 424, 666
64. Crocker, R. M., & Aharonian, F. 2011, Phys. Rev. Lett., 106, 101102
65. Malyshev, D., Cholis, I., & Gelfand, J. D. 2010, 722, 1939
66. Dobler, G., Cholis, I., & Weiner, N. 2011, ApJ, 741, 25
67. Su, M., & Finkbeiner, D. P. 2012, ApJ, 753, 61
68. Weniger, C. 2012, arXiv:1204.2797
69. Ackermann, M., Ajello, M., Allafort, A., et al. 2012, ApJ, in press (arXiv:1207.0616)
70. Ackermann, M., Ajello, M., Allafort, A., et al. 2012, A&A, 538, 71
71. Ackermann, M., Ajello, M., Allafort, A., et al. 2011, Science, 334, 1103
72. Montmerle, T. 1979, ApJ, 231, 95
73. Abdo, A. A., Allen, B., Aune, T., et al. 2008, ApJ, 688, 1078
74. Martin, P., Knödlseder, J., Meynet, G., & Diehl, R. 2010, A&A, 511, A86
75. Matsunaga, N., Feast, M. W., & Menzies, J. W. 2009, MNRAS, 397, 933
76. Pietrzynski, G., Thompson, I. B., Graczyk, D., et al. 2009, ApJ, 697, 862
77. Kim, S., Staveley-Smith, L., Dopita, M. A., et al. 1998, ApJ, 503, 674
78. Van der Marel, R. P. 2006, in *The Local Group as an Astrophysical Laboratory*, ed. M. Livio, & T. M. Brown (Cambridge University Press), 47
79. Aharonian, F. 2004, in *22nd Texas Symposium on Relativistic Astrophysics*, ed. by Pisin Chen, Elliott Bloom, Greg Madejski, Vahe Patrosian, p. 43
80. Pineda, J. L., Ott, J., Klein, U., et al. 2009, ApJ, 703, 736
81. Knödlseder, J. 2000, A&A, 360, 539
82. Brandl, B. R. 2005, in *Starbursts: From 30 Doradus to Lyman Break Galaxies*, ed. by R. de Grijs and R. M. González Delgado. Astrophysics & Space Science Library, Vol. 329. Dordrecht: Springer, 2005, p.49
83. Chu, Y.-H., & Kennicutt, R. C. Jr. 1994, ApJ, 720, 737

84. Nolan, P. L., Abdo, A. A., Ackermann, M., et al. 2012, ApJS, 199, 31
85. A. A. Abdo, M. Ackermann, M. Ajello, M., et al. 2010, ApJ, 708, 1254
86. Komin, N., Djannati-Atai, A., Gallant, Y., et al. 2011, in *32nd International Cosmic Ray Conference*, arXiv:1201.0639v1
87. Abdo, A. A., Ackermann, M., Ajello, M., et al. 2010, A&A, 523, A46
88. Lenain, J.-P., & Walter, R. 2011, A&A, 535, 19
89. Abdo, A. A., Ackermann, M., Ajello, M., et al. 2010, ApJL, 709, L152
90. Lenain, J.-P., Ricci, C., Trler, M., Dorner, D., et al. Walter, R. 2010, A&A, 524, A72
91. Acciari, V. A., Aliu, E., Arlen, T., et al. 2009, Nature, 462, 770
92. Acero, F., Aharonian, F., Akhperjanian, A. G., et al. 2009, Science, 326, 1080
93. Domingo-Santamaria E., & Torres, D. F. 2005, A&A, 444, 403
94. Persic, M., Rephaeli, Y., & Arieli, Y. 2008, A&A, 486, 143
95. de Cea del Pozo, E., Torres, D. F., & Rodriguez Marrero, A. Y. 2009, ApJ, 698, 1054
96. Lacki, B. C., Thompson, T. A., Quataert, E. 2010, ApJ, 717, 1
97. Rephaeli, Y., Arieli, Y., & Persic, M. 2010, MNRAS, 401, 423
98. Pohl, M. 1994, A&A, 287, 453
99. Thompson, T. A., Quataert, E., & Waxman, E., 2007, ApJ, 654, 219
100. Lacki, B. C., Thompson, T. A., Quataert, E., Loeb, A., & Waxman, E. 2011, ApJ, 734, 107
101. Mannheim, K., Elsässer, D., Tibolla, O. 2012, APh, 35, 797
102. Yun, M. S., Reddy, N. A., & Condon, J. J. 2001, ApJ, 554, 803
103. Pavlidou, V., & Fields, B. D. 2002, ApJ, 575, L5
104. Abdo, A. A., Ackermann, M., Ajello, M., et al. 2010, ApJ, 720, 435
105. Rodighiero, G., Vaccari, M., Franceschini, A., et al. 2010, A&A, 515, A8
106. Acero, F., Bamba, A., Casanova, S., et al. 2012, APh, in press

Nonthermal Emission from Star-Forming Galaxies

Yoel Rephaeli and Massimo Persic

Abstract The detections of high-energy γ-ray emission from the nearby starburst galaxies M 82 & NGC 253, and other local group galaxies, broaden our knowledge of star-driven nonthermal processes and phenomena in non-AGN star-forming galaxies. We review basic aspects of the related processes and their modeling in starburst galaxies. Since these processes involve both energetic electrons and protons accelerated by SN shocks, their respective radiative yields can be used to explore the SN-particle-radiation connection. Specifically, the relation between SN activity, energetic particles, and their radiative yields, is assessed through respective measures of the particle energy density in several star-forming galaxies. The deduced energy densities range from $\mathcal{O}(10^{-1})$ eV cm^{-3} in very quiet environments to $\mathcal{O}(10^{2})$ eV cm^{-3} in regions with very high star-formation rates.

1 Introduction

High star formation (SF) and supernova (SN) rates in starburst (SB) galaxies (SBGs) boost the density of energetic nonthermal particles, whose main constituents are protons and electrons. Coulomb, synchrotron and Compton energy losses by the electrons, and the decay of pions following their production in energetic

Y. Rephaeli (✉)
School of Physics and Astronomy, Tel Aviv University, Tel Aviv, 69978, Israel

Center for Astrophysics and Space Sciences, University of California, San Diego, La Jolla, CA 92093-0424, USA
e-mail: yoelr@wise.tau.ac.il

M. Persic
INAF/Osservatorio Astronomico di Trieste and INFN-Trieste, via G.B.Tiepolo 11, I-34143 Trieste, Italy
e-mail: persic@oats.inaf.it

D.F. Torres and O. Reimer (eds.), *Cosmic Rays in Star-Forming Environments*, Astrophysics and Space Science Proceedings 34, DOI 10.1007/978-3-642-35410-6_14,

proton interactions with protons in the ambient gas, result in emission over the full electromagnetic spectrum, from radio to very high-energy (VHE, $\geq$100 GeV) γ-rays. The relatively high intensity emission in SBGs, as compared with emission form 'normal' star-forming galaxies (SFGs), makes nearby members of this class the most likely non-AGN targets for γ-ray telescopes, such as *Fermi* and the (Cherenkov arrays) H.E.S.S., MAGIC, and VERITAS.

Interest in γ-ray emission from SFGs clearly stems from the prospects for improved understanding of the origin and propagation mode of energetic electrons and protons and their coupling to interstellar media. This interest has been enhanced by recent detections of the two nearby SBGs M82 & NGC253 by *Fermi* [1] and, respectively, by H.E.S.S [5] and VERITAS [6]. M31, the closest normal spiral galaxy, was also detected by *Fermi* [2].

A realistic estimate of the expected γ-ray emission requires a detailed account of all relevant energy loss processes of energetic electrons and protons as they move out from the central SB source region into the outer galactic disk. Calculations of the predicted X-γ-ray spectra of nearby galaxies were made long ago with varying degree of detail (e.g., [22, 28, 46, 61]). A more quantitative numerical approach was initiated by Arieli and Rephaeli [11], who used a modified version of the GALPROP code [44, 45] to solve the Fokker-Planck diffusion-convection equation (e.g., [41]) in 3D with given source distribution and boundary conditions for electrons and protons. This numerical treatment was implemented to predict the high-energy spectra of the two nearby galaxies M82 ([52], hereafter PRA) and NGC253 ([58], hereafter RAP). The predictions made in these papers agree well with observations made with Fermi and TeV arrays, as will be discussed in the next section.

Particle acceleration and propagation in galactic environments are largely similar in all SFGs. What mainly distinguishes a SBG from a normal SFG is the dominance of a relatively small central region of intense star formation activity. The overall validity of the numerical treatments of the two nearby SBGs provides a solid basis for generalizing the model to SFGs in general.

We briefly review the calculation of steady-state particle spectra and their predicted radiative spectra for the above two nearby SBGs, and discuss similar calculations for conditions in a SFG. The particle energy density can be determined in several different ways. In order to assess and gauge the SN-energetic particle connection we compare estimates of the energetic proton (which dominate the) energy density in SFGs by three different methods, finding overall agreement, which provides further evidence for the validity of the basic approach.

2 Particle and Radiation Spectra in Starburst Galaxies

Acceleration in SN shocks by the first-order Fermi process yields a power-law distribution with index $q \geq 2$ (e.g., [55]) in a very wide energy range, from a value close to the mean thermal energy of the gas particles (in non-relativistic shocks) to a very high value ($\geq 10^{14}$ eV). The accelerated proton-to-electron (p/e)

density ratio, N_p/N_e, in the source (either the SB or the full disk) region can be calculated assuming charge neutrality [15, 64]. This ratio reaches its maximum value, $(m_p/m_e)^{(q-1)/2}$ (for $q > 1$; m_e and m_p are the electron and proton masses), over most of the relevant range of particle energies, $E > 1$ GeV. (For the dependence of this ratio on particle energy, and more discussion on this and other relevant physical processes, see PRA and references therein.)

The electron density in the source region, N_e, is inferred from radio measurements (of the same region); by adopting the theoretically expected expression $N_p/N_e = (m_p/m_e)^{(q-1)/2}$, the proton density N_p can be deduced. The fit to the radio data provides both the normalization of the electron spectrum and the *actual* value of q, which is found to be somewhat larger than 2, even in the central SB region. In this procedure the electron population is composed of both primary and secondary electrons, with the latter self-consistently determined by accounting for the pion yield of energetic protons with protons in the gas. We note that the theoretically predicted value of the density ratio is valid in the source region, where energy equipartition is more likely to be attained since the relevant processes couple particles and fields more effectively than in the rest of galactic disk.

The particle spectral distributions evolve differently as they propagate out from their acceleration region. Typically, the electron spectrum is most directly deduced from measurements of synchrotron radio emission. The inferred spectrum can be related to the source spectrum through a solution of the kinetic equation describing the propagation modes and energy losses by electrons and protons as they move out from their acceleration region. A very useful detailed description of the time-dependent spectro-spatial distribution of protons, diffusing out of a region with a discrete population of acceleration sites, was recently given by Torres et al. [77]. This study elucidates the explicit dependence of the distribution on distance from the acceleration site, energy loss time, and the diffusion coefficient. It also follows the temporal evolution of the distribution towards a steady state.

Since the estimated duration of a SB phase is $\sim 10^8$ year, a timescale which is much longer than any of the relevant energy loss or propagation timescales for electrons and protons, in (essentially) all treatments a steady state is assumed to be attained. Since the calculation of particle steady-state spectra requires inclusion of all the important energy loss mechanisms and modes of propagation, the treatment is necessarily numerical. We have employed the code of Arieli and Rephaeli [11], which is based on a modified version of the GALPROP code [44, 45], to solve the kinetic equation for $N_i(\gamma, R, z)$, where $i = e, p$, γ is the Lorentz factor, and R and z are the 2D spatial radius and the coordinate perpendicular to the galactic plane. The exact Fokker-Planck diffusion-convection equation (e.g., [41]) was solved in 3D with given source distribution and boundary conditions for electrons and protons. In addition to diffusion with an energy dependent coefficient, particles are assumed to be convected by a galactic wind with spatially varying velocity.

The dominant energy losses of high-energy electrons are synchrotron emission and Compton scattering by the FIR and optical radiation fields; these processes (obviously) depend on the mean strength of the magnetic field, B, and the energy density of the radiation fields, respectively. At energies below few hundred MeV,

electrons lose energy mostly by Coulomb interactions with gas particles. At low energies proton losses are dominated by Coulomb interactions with gas particles. Protons with kinetic energy above the (range of) pion masses ($\sim$140 MeV) lose energy mainly through interactions with ambient protons, yielding neutral (π^0) and charged ($\pi^{\pm}$) pions. Neutral pions decay into photons, while decays of $\pi^{\pm}$ result in energetic $e^{\pm}$ and neutrinos. The proton and (total) electron components are coupled through the production of secondary electrons in π^- decay (following their creation in *pp* interactions).

Measured synchrotron radio spectra provide the critically important information on the particle spectra and their overall normalization: Fitting the predicted radio emission to measurements fixes normalization of the steady state electron and – based on a theoretical prediction – proton energy distributions. From these measurements alone the electron density and mean magnetic field cannot be separately determined. To do so it is usually assumed that particle and magnetic field energy densities are equipartitioned. In our numerical treatment this approach necessitates an iterative procedure to solve for N_e, N_p, and the field strength at the center, B_0, given a measured value of the radio flux.

Particles diffuse and are convected out of their source region. Diffusion is likely to be random walk against magnetic field inhomogeneities, with an estimated value of $\sim 3 \times 10^{28}$ cm^2/s for the central diffusion coefficient. Convection is by galactic wind with a typical velocity of $\sim$500 km s^{-1} [71] in the source region. Based on Galactic cosmic-ray MHD wind models, we assume that the convection velocity increases linearly with distance from the disk plane (e.g. [86]).

The other quantities needed to calculate the steady state distributions of electrons and protons are the densities of neutral and ionized gas in the central SB region and throughout the disk, the central value of the (mean) magnetic field and its spatial profile across the disk, and energy densities of ambient radiation fields (including the CMB). As discussed in PRA, it is assumed that magnetic flux is conserved in the IS ionized gas, so that the mean strength of the field can be related to the local ionized gas density, n_e, using the scaling $B \propto n_e^{2/3}$ [56]. If instead energy equipartition is assumed, and the magnetic energy density is scaled to the thermal gas energy density, then the proportionality relation is $B \propto n_e^{1/2}$. In our work we have taken the ionized gas density profile to be $n_e \propto exp(-z/z_0)/(1 + (R/R_0)^2)$, typically with $R_0 = 1.5$ kpc, and $z_0 = 0.5$ kpc (as deduced for NGC 253 by Strickland et al. [70]).

Given the measured radio fluxes from the central and full disk regions of the two nearby SBGs M82 and NGC253, shown in Fig. 1 for the latter galaxy, and values of all the above quantities, the steady state particle spectra and their radiative yields were calculated using the modified GALPROP code. Here we present the results of this work; more details on the method and values of the input parameters can be found in PRA and RAP (Fig. 2).

The high-energy photon spectra of NGC253 are shown in Fig. 3 (from RAP). Emission levels depend mostly on values of the proton to electron ratio in the source region, on the magnetic field, gas density, and their spatial profiles. The basic normalization of the electron density is provided by the measured radio emission in

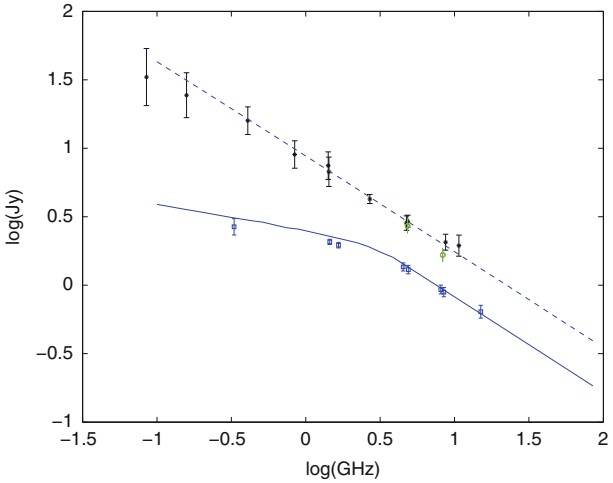

Fig. 1 Spectral fits to radio measurements of the SB and entire disk regions of NGC 253 (RAP). The *solid line* is a fit to the emission from the SB region; the *dashed line* is a fit to the emission from the entire disk. Data are from Klein et al. [36] (*black dots*), Carilli [16] (*blue squares*), and Heesen et al. [30] (*green circles*)

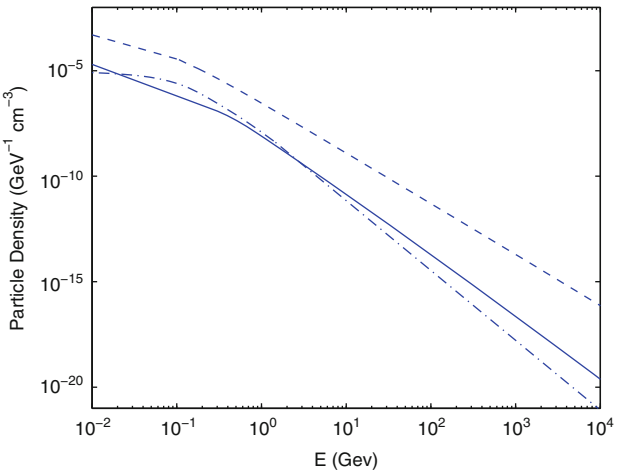

Fig. 2 Primary proton (*dashed line*), primary electron (*solid line*), and secondary electron (*dashed-dotted line*) spectral steady state density distributions in the central SB region NGC 253 (RAP)

the source region; the variation of the electron spectrum across the disk is largely determined by synchrotron losses. Uncertainty in the estimated level of emission is largely due to the steep dependence of the electron density on the field. As argued by RAP, the central value of the (mean) magnetic field is unlikely to be appreciably higher than the value deduced in N253 (and also in M82), $B_0 \sim 200\,\mu$G. A lower

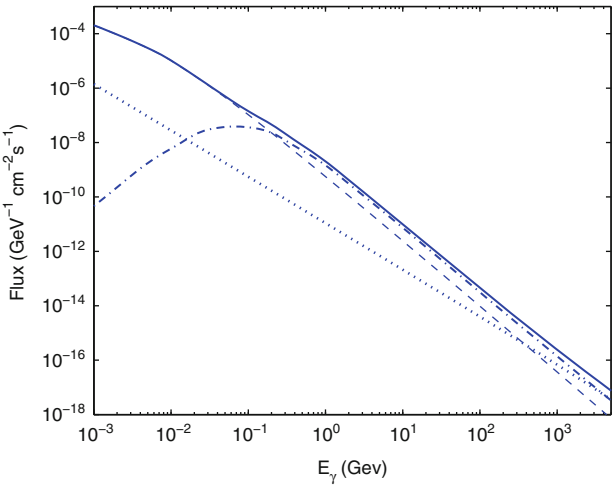

Fig. 3 High-energy emission from the disk of NGC 253. Radiative yields are from Compton scattering off the FIR radiation field (*dotted line*), electron bremsstrahlung off ambient protons (*dashed line*), π^0 decay (*dashed-dotted line*), and their sum (*solid line*)

field value would result in a reduced proton density and a lower rate of π^0 decays. For a given radio flux the electron density would have to be correspondingly higher, resulting in higher bremsstrahlung and Compton yields, roughly compensating for the lower level of hadronic emission. Emission from π^0 decay depends linearly on the ambient proton density in the central disk region.

Detailed modeling of high-energy emission from M82 by PRA preceded its detection by VERITAS [5] and *Fermi* [1]. These observations are shown in Fig. 4 (from Abdo et al. [1]), together with theoretical predictions including that of PRA. The detected flux level agrees well with that predicted by PRA and by de Cea et al. [20]. Results from our similar treatment of the steady-state particle and radiation spectra of NGC253 were presented in RAP. The estimated high energy fluxes for this galaxy (RPA, [22, 46]) were also in the range measured by *Fermi* [1], and – in the TeV region – by the HESS telescope [6], given the substantial observational and modeling uncertainties. These observational results and predicted spectra are shown in Fig. 5 (adopted from Abdo et al. [1]); our integrated spectrum and estimated 1σ uncertainty region are marked by the dashed blue lines (inserted into the original figure). These two SBGs are the only extragalactic non-AGN sources that were detected at both GeV and TeV energies. The FIR luminosities of these galaxies are at or somewhat below the nominal level for SBGs; clearly, their apparent high brightness is due to their proximity.

A few other local and nearby galaxies were also detected at high energies: LMC [3], SMC [4], Andromeda (M31; [2]), and the composite Sy2/SB galaxies NGC 1068 and NGC 4945 [40]. The emission in these galaxies is mostly hadronic γ-ray emission, except for NGC 1068 where emission from the active nucleus may

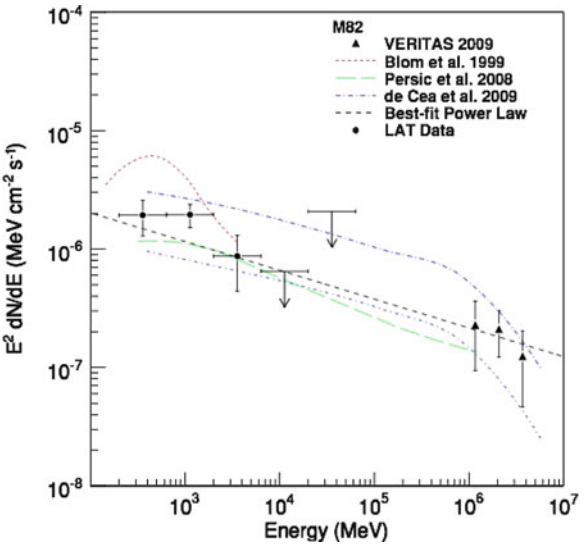

Fig. 4 High-energy emission from M82. VERITAS [5] and *Fermi* measurements are shown together with predicted spectra (Figure is reproduced from Abdo et al. [1])

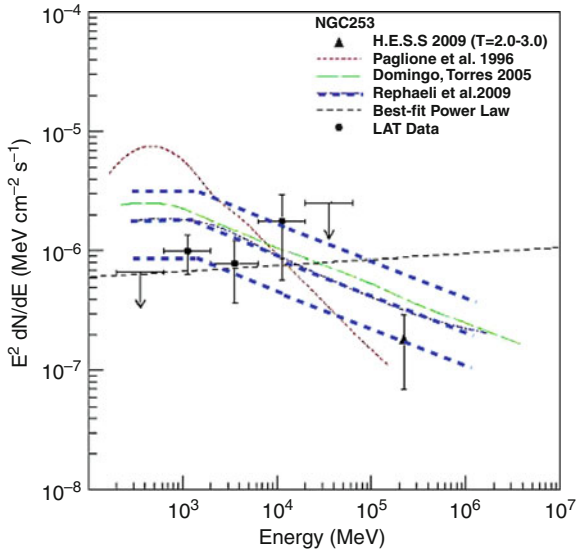

Fig. 5 High-energy emission from the disk of NGC 253. *Fermi* and H.E.S.S measurements are shown together with predicted spectra (The figure is reproduced from Abdo et al. [2]; the added *dashed blue lines* show our predicted spectrum with the estimated range of 1σ uncertainty)

be dominant. Among galaxies whose detected high energy emission is powered by stellar activity, Arp 220 has the highest SFR in the local universe, yet an attempt to detect it by MAGIC [10] was not successful due to its relatively large distance.

3 Estimates of Cosmic-Ray Energy Density

Active star formation in galaxies leads to acceleration of protons and electrons via the Fermi-I diffusive shock acceleration mechanism in SN remnants. Under equilibrium conditions in a galaxy, a minimum-energy configuration of the magnetic field and the energetic particles may be attained. Energy densities of particles and magnetic fields may then be in approximate equipartition, implying that the energetic proton energy density, $U_{\rm p}$, can be deduced from the detected level of synchrotron radio emission. In this *radio-based* approach $U_{\rm p}$ can be estimated if the source size, distance, radio flux, and radio spectral index are known.

In a *γ-based* approach, $U_{\rm p}$ can be obtained from the measured GeV–TeV spectral flux, which is mostly due to p-p interactions, as described the previous section. Only recently have such measurements become possible, at present only for ten sources.

In the *SN method*, with an assumed fraction of SN kinetic energy that is channeled into particle acceleration, $U_{\rm p}$ can be estimated if the size of the star-forming region and SN rate are known, as well as an estimate for the proton residence timescale from the presence (or absence) of a galactic wind emanating from the star-forming region. This timescale is largely determined by the advection timescale ($\sim 10^5$ year) in SBGs, and by the π^0-decay timescale ($\sim 10^7$ year) in low-SFR (quiescent) galaxies.

Expanding on our previous work [50], we show that the three methods give consistent results for U_p for a sample of ten galaxies with widely varying levels of star formation activity, from very quiescent to extreme SBs. These are the only galaxies of their kind for which γ-ray data, in addition to radio data and SN rates, are available (see Table 1).

3.1 Particles and Magnetic Field

The population of NT electrons consists of primary (directly accelerated) and secondary (produced via $\pi^{\pm}$ decays) electrons. While the exact form of the steady-state electron energy spectrum is not a single power law, at high energies the flattening of the spectrum due to Coulomb losses can be ignored, justifying the use of the approximate single power-law form. The combined (primary plus secondary) electron spectral density distribution is then

$$N_{\rm e}(\gamma) \;=\; N_{e,0}\,(1+\chi)\,\gamma^{-q}, \tag{1}$$

where the electron Lorentz factor γ is in the range $\gamma_1 \le \gamma \le \gamma_2$, $N_{e,0}$ is a normalization factor of the primary electrons, χ is the secondary-to-primary electron ratio, and $q \ge 2$ is the spectral index. Ignoring the contribution of low-energy electrons with $\gamma < \gamma_1$, the electron energy density is $U_{\rm e} = N_{\rm e,0}\,(1+\chi)\,m_{\rm e}c^2 \int_{\gamma_1}^{\gamma_2} \gamma^{1-q}{\rm d}\gamma$, where γ_2 is an upper cutoff whose exact value is irrelevant in the limit of interest, $\gamma_2 \gg \gamma_1$. For $q > 2$ and $\gamma_2 \gg \gamma_1$,

Table 1 Star-forming galaxies: the data

Object	D_L^{a} (Mpc)	r_s^{b} (kpc)	$f_{1\,\mathrm{GHz}}^{c}$ (Jy)	α_{NT}^{d}	$n_{\mathrm{e,th}}^{e}$ (cm^{-3})	L_{TIR}^{f} (erg/s)	SFR^{g} ($\mathrm{M}_\odot$/year)	ν_{SN}^{h} (year^{-1})	M_{gas}^{i} ($\mathrm{M}_\odot$)	L_γ^{j} (erg/s)	Notes
Arp 220	74.7	0.25	0.3	0.65	300	45.75	253	3.5	$9.24^{+0.10}_{-0.11}$	<42.25	SB
M 82	3.4	0.23	10.0	0.71	200	44.26	8.2	0.25	$9.37^{+0.09}_{-0.14}$	$40.21^{+0.10}_{-0.13}$	SB
NGC 253	2.5	0.20	5.6	0.75	400	44.23	7.7	0.12	$9.20^{+0.10}_{-0.11}$	$39.76^{+0.14}_{-0.19}$	SB
Milky Way	–	4.4	–	–	0.01	43.75	2.5	0.02	$9.81^{+0.12}_{-0.16}$	$38.91^{+0.12}_{-0.15}$	Quiescent
M 31	0.78	4.5	4.0	0.88	0.01	42.98	0.43	0.01	$9.88^{+0.11}_{-0.15}$	$38.66^{+0.09}_{-0.10}$	Quiescent
M 33	0.85	2.79	3.30	0.95	0.03	42.68	0.22	0.003	$9.35^{+0.13}_{-0.19}$	<38.54	Quiescent
LMC	0.049	2.4	285.0	0.84	0.01	42.45	0.13	0.002	$8.86^{+0.12}_{-0.18}$	$37.67^{+0.05}_{-0.05}$	Quiescent
SMC	0.061	1.53	45.3	0.85	0.01	41.45	0.01	0.001	$8.66^{+0.03}_{-0.06}$	$37.04^{+0.11}_{-0.14}$	Quiescent
NGC 4945	3.7	0.22	5.5	0.57	300	44.02	4.7	0.1–0.5	$9.64^{+0.10}_{-0.40}$	$40.30^{+0.12}_{-0.16}$	SB+Sy2
NGC 1068	16.7	1.18	6.6	0.75	300	45.05	50	0.2–0.4	$9.71^{+0.11}_{-0.19}$	$41.32^{+0.15}_{-0.23}$	SB+Sy2

[a] Distance (from Ackermann et al. [7])

[b] Effective radius of star-forming region. See text. Data are from Persic and Rephaeli [50] and refs. therein (Arp 220, M 82, NGC 253), Beck and Gräve [14] (M 31), Tabatabaei et al. [73] (M 33), Weinberg and Nikolaev [82] (LMC), Wilke et al. [83] (SMC), Moorwood and Oliva [43] (NGC 4945), and Spinoglio et al. [66] (NGC 1068)

[c] 1 GHz flux density. Data are from Persic and Rephaeli [50] and refs. therein (Arp 220, M 82, NGC 253)), Beck and Gräve [14] (M 31), Tabatabaei et al. [73] (M 33), Klein et al. [35] (LMC), Haynes et al. [29] (SMC), Elmouttie et al. [24] (NGC 4945), and Kühr et al. [37] (NGC 1068)

[d] Non-thermal spectral radio index. Data are from Persic and Rephaeli [50] and refs. therein (Arp 220, M 82, NGC 253), Beck and Gräve [14] (M 31), Tabatabaei et al. [73] (M 33), Klein et al. [35] (LMC), Haynes et al. [29] (SMC), Elmouttie et al. [24] (NGC 4945), and Kühr et al. [37] (NGC 1068)

[e] Thermal electron density. Data are from Roy et al. [62] (Arp 220), Petuchowski et al. [53] (M 82), Kewley et al. [34] and Corral et al. [18] (NGC 253), Cox [19] (Milky Way), Beck [13] (M 31), Tabatabaei et al. [74] (M 33), Points et al. [54] (LMC), Sasaki et al. [63] (SMC), Spoon et al. [67] (NGC 4945), and Kewley et al. [34] (NGC 1068)

[f] Total IR [i.e., (8–1,000) μm] luminosity, in log (from Ackermann et al. [7])

[g] Star formation rate, from $\mathrm{SFR} = L_{\mathrm{IR}}/(2.2 \times 10^{43}\,\mathrm{erg/s})$ [33]

[h] Core-collapse SN rate. Data are from Persic and Rephaeli [50] and references therein (Arp 220, M 82, NGC 253), Diehl et al. [21] (Milky Way), van den Bergh and Tammann [80] (M 31, M 33, SMC, LMC; see also Pavlidou and Fields [47]), Lenain et al. [40] and references therein (NGC 4945, NGC 1068). For NGC 1068 we also computed an upper limit to the SN rate ($\nu_{\mathrm{SN}} \leq 0.39$) using Mannucci et al.'s [42] formula $\nu_{\mathrm{SN}} = (2.4 \pm 0.1) \times 10^{-2}[L_{\mathrm{FIR}}/(10^{10} L_\odot)]\,\mathrm{year}^{-1}$, being $f_{\mathrm{FIR}} = 1.26 \times 10^{-11}(2.58\, f_{60} + f_{100})\,\mathrm{erg\,cm^{-2}\,s^{-1}}$ (see [31]) with $f_{60} \simeq 190$ Jy and $f_{100} \simeq 277$ Jy

[i] Gas mass (neutral plus molecular hydrogen: $M_{\mathrm{HI}} + M_{\mathrm{H_2}}$), in log. Data are from: Torres [76] for Arp 220; Abdo et al. [1] for M 82, NGC 253, and the Milky Way; Abdo et al. [2] for M 31 and M 33; Abdo et al. [3] for the LMC; Abdo et al. [4] for the SMC; and Lenain et al. [40] for NGC 4945 and NGC 1068

[j] High-energy (>100 MeV) γ-ray luminosity, in log (from Ackermann et al. [7]).

$$U_{\rm e} \simeq N_{e,0}(1+\chi)m_{\rm e}c^2\gamma_1^{2-q}/(q-2)\,. \tag{2}$$

For a population of electrons (specified by Eq. 1) traversing a homogeneous magnetic field of strength B in a region with (a spherically equivalent) radius $r_{\rm s}$ located at a distance d, standard synchrotron relations yield

$$N_{\rm e,0}(1+\chi) \;=\; 5.72\times10^{-15}\;\psi\;a(q)^{-1}\;B^{-\frac{q+1}{2}}\;250^{\frac{q-1}{2}} \tag{3}$$

where the scaled flux is $f_{1\,\rm GHz}$ Jy, $a(q)$ is defined and tabulated in, e.g., Tucker [78], and $\psi \equiv (\frac{r_{\rm s}}{0.1\,\rm kpc})^{-3}(\frac{d}{\rm Mpc})^2(\frac{f_{1\,\rm GHz}}{\rm Jy})$. Use of Eq. (2) then yields

$$U_{\rm e} \;\simeq\; \frac{2.96}{(1+\chi)}\times10^{-22}\,250^{\frac{q}{2}}\;\psi\;\frac{\gamma_1^{-q+2}}{(q-2)\;a(q)}\;B^{-\frac{q+1}{2}}\,. \tag{4}$$

In order to compute $U_{\rm e}$ from Eq. (4) we need to specify γ_1 and B. To do so we make the following assumptions:

(i) The low-energy limit of the electron power-law spectrum, γ_1, marks the transition (for decreasing energy) from Coulomb [57] to synchrotron losses. For an electron of energy γ, the synchrotron loss rate is

$$\left(\frac{{\rm d}\gamma}{{\rm d}t}\right)_{\rm syn} \;=\; -\,1.30\times10^{-21}\gamma^2\left(\frac{B}{\mu G}\right)^2{\rm s}^{-1} \tag{5}$$

whereas the Coulomb loss rate is

$$\left(\frac{{\rm d}\gamma}{{\rm d}t}\right)_{\rm coul} \;=\; -\,1.2\times10^{-12}n_{\rm e,th}\left[1.0+\frac{\ln(\gamma/n_{\rm e,th})}{75}\right]{\rm s}^{-1}\,. \tag{6}$$

[57]. We then simply assume that electrons lose energy via Coulomb scattering for $\gamma<\gamma_1$ and via synchrotron cooling for $\gamma>\gamma_1$.

(ii) The particle energy density is in equipartition with that of the magnetic field, $U_{\rm p}+U_{\rm e}=B^2/8\pi$. In terms of the p/e energy density ratio, κ, the equipartition condition is $U_{\rm p}[1+(1+\chi)/\kappa]=B^2/8\pi$, so that

$$B \;=\; \left[\frac{7.44\times10^{-21}}{1+\chi}\left[1+\frac{\kappa}{1+\chi}\right]\frac{\gamma_1^{2-q}\,250^{q/2}\,\psi}{(q-2)\;a(q)}\right]^{\frac{2}{5+q}}\,. \tag{7}$$

Inserting Eq. (7) into Eq. (5) we get $(\frac{{\rm d}\gamma}{{\rm d}t})_{\rm syn}\propto\gamma_1^{2(9-q)/(5+q)}$. Once the value of $n_{\rm e,th}$ is specified (see Table 1), by equating Eqs. (5) and (6) we deduce γ_1.

The secondary-to-primary electron ratio χ, which appears in Eq. (7), depends on the injection p/e number ratio, $r_{p/e}=(m_{\rm p}/m_{\rm e})^{(q_{\rm inj}-1)/2}$, and on the gas optical thickness to p-p interactions. Given the branching ratios in p-p collisions, only a

third of these collisions produce electrons. The mean free path of CR protons due to p-p interactions in a medium of density $n_{\rm p}$ is $\lambda_{\rm pp} = (\sigma_{\rm pp} n_{\rm p})^{-1}$; for protons with kinetic energy $T \sim$ few TeV the cross section is $\sigma_{\rm pp} \simeq 50\,{\rm mb} = 5 \times 10^{-26}\,{\rm cm}^2$ [12]. For a typical SB ambient gas density $n_{\rm p} \simeq 150\,{\rm cm}^{-3}$, $\lambda_{\rm pp} \sim 43\,{\rm kpc}$. The probability for a single CR proton to undergo a pp interaction in its 3D random walk through a region of radius $r_{\rm s} \sim 0.25\,{\rm kpc}$ (also typical of SB nuclei) is then $\sqrt{3}\, r_{\rm s}/\lambda_{\rm pp} \simeq 0.01$. Thus, in a typical SB environment, characterized by relatively strong non-relativistic shocks ($q_{\rm inj} = 2.2$), the secondary to primary electron ratio is $\chi = \chi_0 \sqrt{3}\, (r_{\rm s}/\lambda_{\rm pp}) \simeq 0.3$. In a more quiescent environment, with typical values $n_{\rm p} \simeq 1\,{\rm cm}^{-3}$ and $r_{\rm s} \sim 2.5\,{\rm kpc}$, $\chi \simeq 0.03$. The higher value found in SBs is in approximate agreement with results of detailed numerical starburst models for energies $\gtrsim$10 MeV (plotted in, e.g., [20, 46, 58, 76]).

To compute the p/e energy density, κ, we assume power-law spectra: (i) The electron spectral index $q_{\rm e}$ is deduced from the measured radio index α, generally $q_{\rm e} = 2\alpha + 1$. (ii) The proton spectral index is assumed to be close to the injection value, $q_{\rm p} \sim q_{\rm inj} \simeq 2.1$–$2.2$, for the dense SB environments hosted in the central regions of some galaxies, and equal to the leaky-box value, $q_{\rm p} = q_{\rm inj} + \delta \simeq 2.7$ (where $\delta \simeq 0.5$ is the diffusion index) for more quietly star forming galaxies.

Finally, we obtain an explicit expression for $U_{\rm p}$:

$$U_{\rm p} = \frac{1}{8\,\pi}\left[1 + \frac{1+\chi}{\kappa}\right]^{-1}\left[\frac{7.44 \times 10^{-21}}{1+\chi}\left[1 + \frac{\kappa}{1+\chi}\right]\frac{\gamma_1^{2-q}\, 250^{q/2}\, \psi}{(q-2)\, a(q)}\right]^{\frac{4}{5+q}}. \quad (8)$$

Using Eq. (8), values of $U_{\rm p}$ can be obtained from the relevant observational quantities for our sample galaxies; these values are listed in Table 2. The quantities in Eq. (8) are usually well determined for our sample galaxies, except for the p/e energy density ratio κ, for which a spectral index, $q_{\rm p}$, must be assumed. Given its possible values (i.e., $q_{\rm p} \simeq 2.1$–2.2 in SB regions, and $q_{\rm p} \simeq 2.1$–2.2 for quiescent galaxies), the uncertainty in the spectral index, $\delta q_{\rm p} \simeq 0.1$, translates to a factor of $\sim$2 uncertainty on κ, i.e. typically an uncertainty of $\sim$50 % on $U_{\rm p}$ as deduced from Eq. (8).

3.2 *Energetic Particles and γ-Ray Emission*

Based on the calculation of γ-ray emission from SFGs outlined in Sect. 1, $U_{\rm p}$ can be estimated directly from recent measurements of the nearby galaxies. In SBGs, such as M 82 and NGC 253, the central SB region (referred to also as the source region) with a radius of $\sim$200–300 pc is identified as the main site of particle acceleration. The injected particle spectrum is assumed to have an index $q = 2$, the theoretically predicted $N_{\rm p}/N_{\rm e}$ ratio is adopted, and equipartition is assumed. A measured radio index $\alpha \simeq 0.7$ in the source region implies $q = 2\,\alpha + 1 \simeq 2.4$ there, indicating a substantial steepening due to diffusion ($D \propto \gamma^{-\delta}$), that cause the steady-state particle spectral index to be $q_0 + \delta$ above some break energy. The procedure is

Table 2 Star-forming galaxies: Proton energy densities[a]

Object	γ-ray meth.	Radio meth.	SN meth.	Other meth.	r_s (kpc)	τ_{res} (year)
Arp 220	–	1,027	1,142	–	0.25	2.0E+4
M 82	250[b,d]	250	234	–	0.23	4.5E+4
NGC 253	220[c,d]	230	213	–	0.20	6.7E+4
Milky Way	1[e]	–	1.2	1[k]	4.4	2.0E+7
	6[f]	–	5	–	0.2	2.5E+6
M 31	0.36[g]	0.22	0.7	–	4.5	2.5E+7
M 33	< 0.43[g]	0.38	0.7	–	2.8	2.0E+7
LMC	$0.21 - 0.31$[h]	0.22	0.4	–	2.5	4.4E+7
SMC	0.15[i]	0.39	1.1	–	1.5	1.4E+7
NGC 4945	200[j]	201	215	–	0.22	4.5E+4
NGC 1068	–	65	61	–	1.2	1.0E+6

[a] Values are in eV cm^{-3}
[b] Acciari et al. ([5]; see also [20, 52])
[c] Acero et al. [6]
[d] Abdo et al. [1]
[e] Strong et al. [72]
[f] Aharonian et al. [9]
[g] Abdo et al. [2] and Drury et al. [23] for M 33
[h] Abdo et al. [3]
[i] Abdo et al. [39]
[j] Lenain et al. [40]
[k] Webber [81]

similar when star formation does not (largely) occur in a burst in the nuclear region, but proceeds more uniformly across the disk.

For a source with ambient gas number density n_{gas}, proton energy density U_p, and volume V, the integrated hadronic emission from pp-induced π^0 decay is

$$L_{\geq E}^{[q]} = \int_V g_{\geq E}^{[q]}\, n_{gas}\, U_p\, dV \ \ s^{-1}\,, \tag{9}$$

with the integral emissivity $g_{\geq \epsilon}^{[\eta]}$ in units of photon s^{-1}(H-atom)$^{-1}$(eV/cm^3)$^{-1}$ [23]. Thus, U_p can be determined from measurements of $L_{\geq \epsilon}$ and $n_{gas}(r)$, and the particles steady-state energy distributions can be numerically calculated in the context of the convection-diffusion model.

In addition to the high-energy detections of the two local SBGs M 82 and NGC 253 [1, 5, 6], several galaxies with low SFR were also detected by the *Fermi* telescope. (i) the Andromeda galaxy M 31 [2], with $U_p \simeq 0.35\,\mathrm{eV\,cm^{-3}}$; (ii) the Large Magellanic Cloud (LMC) whose average spectrum, either including or excluding the bright star-forming region of 30 Doradus, suggests $U_p \simeq 0.2$–$0.3\,\mathrm{eV\,cm^{-3}}$ [3]; (iii) SMC for which $U_p \simeq 0.15\,\mathrm{eV\,cm^{-3}}$ was deduced [4]. For the Milky Way, the modeling of the Galactic diffuse HE emission along the lines

outlined above requires an average $U_{\rm p} \simeq 1\,{\rm eV\,cm^{-3}}$ [8, 72]. Our values for $U_{\rm p}$ determined from the measured GeV–TeV fluxes are listed in Table 2.

3.3 Energetic Particles and Supernovae

The SN origin of energetic particles suggested early on; as a test of this hypothesis, we estimate of $U_{\rm p}$ by combining the SN rate with the proton residence time, $\tau_{\rm res}$, assuming a fiducial value for the fraction of SN kinetic energy that is channeled to particle acceleration. The residence time is determined from the p-p interaction time, and the two propagation timescales of advection and diffusion:

(i) The energy-loss timescale for *pp* interactions, $\tau_{\rm pp} = (\sigma_{\rm pp} c n_{\rm p})^{-1}$; for protons with kinetic energy $E \gtrsim 10$ TeV for which $\sigma_{\rm pp} \simeq 50\,{\rm mb}$, this timescale is

$$\tau_{\rm pp} \simeq 2 \times 10^5 \left(\frac{n_{\rm p}}{100\,{\rm cm^{-3}}}\right)^{-1} {\rm year}\,. \tag{10}$$

(ii) Particle advection out of the disk mid-plane region in a fast SB-driven wind occurs on a timescale $\tau_{\rm adv}$ determined from the advection velocity for which we adopt (except where noted otherwise) the nominal value $v_{\rm adv} \sim 1{,}000\,{\rm km\,s^{-1}}$, deduced from measurements of the terminal outflow velocity of ∼1,600–2,200 km s^{-1} in M 82 ([69]; see also [17, 65]). For a homogeneous distribution of SNe within the SB nucleus of radius $r_{\rm s}$, the advection timescale is

$$\tau_{\rm adv} \simeq 7.5 \times 10^4 \left(\frac{r_{\rm s}}{0.3\,{\rm kpc}}\right) \left(\frac{v_{\rm out}}{1{,}000\,{\rm km\,s^{-1}}}\right)^{-1} {\rm year}\,. \tag{11}$$

(iii) As noted in the previous section, diffusion is likely to be random walk against magnetic field inhomogeneities, with an estimated central diffusion coefficient, $D \sim 3 \times 10^{28}\,{\rm cm^2/s}$, assuming a magnetic coherence scale of $\lambda \sim 1\,{\rm pc}$. Thus, diffusion out of the central 0.5 kpc is estimated to occur on a timescale

$$\tau_{\rm diff} \simeq 3 \times 10^6 \left(\frac{r_{\rm s}}{0.3\,{\rm kpc}}\right)^2 \left(\frac{\lambda}{1{\rm pc}}\right)^1 {\rm year}\,. \tag{12}$$

Now, since the weighted residence time is

$$\tau_{\rm res}^{-1} = \tau_{\rm pp}^{-1} + \tau_{\rm adv}^{-1} + \tau_{\rm diff}^{-1}\,, \tag{13}$$

it is expected that – under typical conditions in central SB regions – p-p collisions and advection, more so than diffusion, effectively determine the survival there of energetic protons.

During $\tau_{\rm res}$, the number of SN is $\nu_{\rm SN}\tau_{\rm res}$; the kinetic energy deposited by each of these into the ISM is $E_{\rm ej} = 10^{51}$ erg [85]. Arguments based on the energetic particle

energy budget in the Galaxy and SN statistics suggest that a fraction $\eta \sim 0.05$–0.1 of this energy is available for accelerating particles (e.g., [32]). Thus, the proton energy density can be expressed as

$$U_{\rm p} \;=\; 85\,\Big(\frac{\nu_{\rm SN}}{0.3\,{\rm year}^{-1}}\Big)\,\Big(\big(\frac{\tau_{\rm res}}{3\times 10^4\,{\rm year}}\Big)\,\Big(\frac{\eta}{0.05}\;\frac{E_{\rm ej}}{10^{51}\,{\rm erg}}\Big)\,\Big(\frac{r_{\rm s}}{0.3\,{\rm kpc}}\Big)^{-3}\;\;{\rm eV\;cm^{-3}}. \tag{14}$$

The resulting values of $U_{\rm p}$ in the sample galaxies are listed in Table 2.

4 Discussion

Detections of VHE γ-ray emission associated with ongoing star formation in M 82 and NGC 253 add significant new insight on the enhanced energetic electron and proton contents in SBGs, and on their propagation in disks of spiral galaxies. The common star-driven nature of NT phenomena in the wide class of non-AGN SFGs implies that energetic particle densities and radiation fields are self-similarly scaled with SF activity, from quiescent systems to intense SBGs, in spite of the wide range of intrinsic physical conditions in these systems.

We have briefly outlined our treatment of the steady state spectro-spatial distributions of energetic electrons and protons in SFGs, exemplified in the case of the two nearby SBGs M 82 and NGC 253. This approach is based on a numerical solution of the diffusion-convection equation for particle distribution functions, following the evolution from the acceleration sites throughout the disk as the particles lose energy and propagate outward. Key observational normalization is based on measurements of radio synchrotron emission which, through an initial (theoretically assumed) N_p/N_e ratio provides also the normalization of the proton component. Assuming equipartition then allows to relate the local value of the mean magnetic field to the particle energy densities. The numerical solution of the diffusion-convection equation is based on an iterative procedure to determine the particle densities and mean field strength in the galactic center, and evolve these quantities by accounting for all relevant energy losses, and normalizing central values of these quantities by fitting to the measured radio spectrum from the central galactic (or SB) region. The quantitative viability of this approach is confirmed by the good agreement between the predicted high energy emission from M 82 and NGC 253 and measurements with *Fermi*, H.E.S.S., and VERITAS.

Significant detections of the NT emission from above two SBGs at lower (below 100 keV) X-ray energies, as would be expected by the currently operational NuSTAR telescope, will provide additional spectral coverage that will allow separating out the spectral electron and proton components. NuSTAR is the first X-ray telescope with capability to resolve this emission; if this is indeed achieved, important new insight will be gained on the evolution of the electron spectro-spatial distribution across the disks of these nearby SBGs.

The three methods we have discussed to estimate energetic particle energy densities are clearly not independent. The γ-ray method and the radio method are coupled through the p/e ratio at injection, through the secondary-to-primary electron ratio, and through the imposed condition of particle-field equipartition. The SN method is not independent of the γ-ray method either, because both depend on the proton residence time, although – unlike the γ-ray and radio methods – it does not depend on the particle radiative yields but on the statistics of core-collapse SN. Also, the three methods do not stand on equal footing: with the γ-ray, radio, and SN methods we, respectively, either *measure*, *infer*, and or *estimate* the value of U_p. A substantial agreement among estimates based on the three methods is found for most of the galaxies in Table 1. The only exceptions are the SMC and NGC 1068. As for the former, the proton confinement volume could be small, so that most particles diffuse out to intergalactic space [4]. If so, the γ-ray method yields the (lower) *actual* proton energy density, whereas the radio and SN methods estimate the (higher) *produced* amount. NGC 1068 hosts a prototypical Seyfert-2 nucleus (e.g., [84]) surrounded by a spherical circumnuclear SB shell with external radius of 1.5 kpc and thickness 0.3 kpc, and mass $3.4 \times 10^9\,\mathrm{M}_\odot$ [66]; its implied energy density is $U_\mathrm{p} \approx 65\,\mathrm{eV\,cm^{-3}}$ from both the radio and SN methods. [We note that Lenain et al. [40] suggested that the HE emissions of the above two SB and Sey II galaxies NGC 4945 and NGC 1068 are powered by, respectively, star formation and AGN activity.]

A debated aspect of proton energy loss and propagation times is whether the former is shorter than the latter; if so, the system is said to be a 'proton calorimeter' (e.g., [38, 39]). No galaxy in the above sample is found to be in the calorimetric limit; the two SBGs M 82 and NGC 253 would seem to be only marginally close to this limit. The presence of fast, SB-driven galactic winds advecting energetic particles out of the disk seems to be a ubiquitous feature in SBGs, limiting the degree at which they can be calorimetric. More generally, it is known that energetic particles do diffuse out of non-AGN SFGs, as evidenced also by significant radio emission [26], and possibly also high energy NT X-ray emission [59] from large central regions of galaxy clusters. The estimated intracluster particle (and indeed also the magnetic) energy densities are sufficiently high, suggesting origin in the cluster galaxies.

Based on the reasonable hypothesis that local SB galaxies resemble young galaxies which were particularly abundant in the early universe, their contributions to the X-γ-ray backgrounds are of obvious interest (e.g., [59]). Calculations of the superposed emission from SBGs [27, 39, 48, 49, 68, 75] indicate that this emission constitutes at least a tenth of these backgrounds.

References

1. Abdo, A.A., et al. (LAT Collaboration) 2010a, ApJL, 709, L152
2. Abdo, A.A., et al. (LAT Collaboration) 2010b, A&A, 523, L2
3. Abdo, A.A., et al. (LAT Collaboration) 2010c, A&A, 512, A7

4. Abdo, A.A., et al. (LAT Collaboration) 2010d, A&A, 523, A46
5. Acciari, V.A., et al. (VERITAS Collaboration) 2009, Nature, 462, 770
6. Acero, F., et al. (HESS Collaboration) 2009, Science, 326, 1080
7. Ackermann, M., et al. (LAT Collaboration) 2012, ApJ, 755, 164
8. Ackermann, M., et al. (LAT Collaboration) 2011, ApJ, 726, 81
9. Aharonian, F., et al. (HESS Collaboration), 2006, Nature, 439, 695
10. Albert, J., et al. (MAGIC Collaboration) 2007, ApJ, 658, 245
11. Arieli, Y., & Rephaeli, Y. 2007, unpublished
12. Baltrusaitis R.M., et al. 1984, PRL, 52, 1380
13. Beck R. 2000, in "The Interstellar Medium of M 31 and M 33", eds. E.M.Berkhuijsen, R.Beck, R.A.M.Walterbos (Aachen: Shaker), p.171 (astro-ph/0009455)
14. Beck, R., & Gräve, R. 1982, A&A, 105, 192
15. Bell, A.R. 1978, MNRAS, 182, 443
16. Carilli C.L. 1996, A&A, 305, 402
17. Chevalier, R.A., & Clegg, A.W. 1985, Nature, 317, 44
18. Corral P., Hollenbach D.J., Lord S.D., et al. 1994, ApJ, 423, 223
19. Cox D.P. 2005, ARA&A, 43, 337
20. de Cea Del Pozo, E., Torres, D.F., & Rodriguez Marrero, A.Y. 2009, ApJ, 698, 1054
21. Diehl R., Halloin H., Kretschmer K., et al., 2006, Nature, 439, 45
22. Domingo-Santamaría, E., & Torres, D.F. 2005, A&A, 444, 403
23. Drury, L.O'.C., Aharonian, F.A., & Völk, H.J. 1994, A&A, 287, 959
24. Elmouttie M., Haynes R.F., Jones, K.L., et al. 1997, MNRAS, 284, 830
25. Enomoto, R., et al. 2008, ApJ, 683, 383
26. Ferrari, C. Govoni, F., Schindler, S., Bykov, A., & Rephaeli, Y. 2008, Space Science Reviews, 134, 93
27. Fields, B.D., Pavlidou, V., & Prodanovic, T. 2010, ApJ, 722, L199
28. Goldshmidt, O., & Rephaeli, Y. 1995, ApJ, 444, 113
29. Haynes, R.F., Klein, U., Wayte, S.R., et al. 1991, A&A, 252, 475
30. Heesen, V., Beck, R., Krause, M., Dettmar, R.J. 2008, A&A, 494, 563
31. Helou G., Khan I.R., Malek L., Boehmer L. 1988, ApJS, 68, 151
32. Higdon, J.C., Lingenfelter, R.E., & Ramaty, R. 1998, ApJ, 509, L33
33. Kennicutt, R.C. Jr. 1998, ARAA, 36, 189
34. Kewley L.J., Heisler C.A., Dopita M.A., et al. 2000, ApJ, 530, 704
35. Klein, U., Wielebinski, R., Haynes, R.F., & Malin, D.F. 1989, A&A, 211, 280
36. Klein U. et al. 1983, å127, 177
37. Kühr H., Witzel A., Pauliny-Toth I.I.K., Nauber U. 1981, A&AS, 45, 367
38. Lacki, B.C., Thompson, T.A., & Qataert, E. 2010, ApJ, 717, 1
39. Lacki, B.C., Thompson, T.A., Quataert, E., Loeb, A., & Waxman, E. 2011, ApJ, 734, 107
40. Lenain J.-P., Ricci C., Türler M., Dorner D., Walter R. 2010, A&A, 524, 72L
41. Lerche, I., & Schlickeiser, R. 1982, MNRAS, 201, 1041
42. Mannucci F., Maiolino R., Cresci G., et al. 2003, A&A, 401, 519
43. Moorwood A.F.M. & Oliva E. 1994, Apj, 429, 602
44. Moskalenko I.V, & Strong A.W. 1998, ApJ, 493, 694
45. Moskalenko I.V, Jones, F.C., Mashnik, S.G., Ptuskin, V.S., & Strong, A.W., 2003, ICRC, 4, 1925
46. Paglione, T.A.D., Marscher, A.P., Jackson, J.M., & Bertsch, D.L. 1996, ApJ, 460, 295
47. Pavlidou, V., & Fields, B.D. 2001, ApJ, 558, 63
48. Pavlidou, V., & Fields, B.D. 2002, ApJ, 575, L5
49. Persic, M., & Rephaeli, Y. 2003, A&A, 399, 9
50. Persic, M., & Rephaeli, Y. 2010, MNRAS, 403, 1569
51. Persic, M., & Rephaeli, Y. 2012, in preparation
52. Persic, M., Rephaeli, Y., & Arieli, Y. 2008, A&A, 486, 143 (PRA)
53. Petuchowski SJ, Bennett CL, Haas MR, et al. 1994, ApJ, 427, L17
54. Points S.D., Chu Y.-H., Snowden S.L., Smith R.C. 2001, ApJS, 136, 99

55. Protheroe, R.J., & Clay, R.W. 2004, PASA, 21, 1
56. Rephaeli, Y. 1988, Comm. Ap., 12, 265
57. Rephaeli, Y. 1979, ApJ, 227, 364
58. Rephaeli, Y., Arieli, Y., & Persic, M 2010, MNRAS, 401, 473
59. Rephaeli, Y., Gruber, D.E., Persic, M., & MacDonald, D. 1991, ApJ, 380, L59
60. Rephaeli, Y., Nevalainen, J., Ohashi, T., & Bykov, A. 2008, Space Science Reviews, 134, 71
61. Romero, G.E., & Torres, D.F. 2003, ApJ, 586, 33
62. Roy A.L., Oosterloo T., Goss W.M., Anantharamaiah K.R. 2010, A&A, 517, A82
63. Sasaki, M., Haberl, F., & Pietsch, W. 2002, A&A, 392, 103
64. Schlickeiser, R. 2002, Cosmic Ray Astrophysics (Berlin: Springer), p.472
65. Seaquist, E.R., & Odegard, N. 1991, ApJ, 369, 320
66. Spinoglio L., Malkan M.A., Smith H.A., et al. 2005, ApJ, 623, 123
67. Spoon H.W.W., Koornneef J., Moorwood A.F.M., Lutz D., Tielens A.G.G.M. 2000, A&A, 357, 3000
68. Stecker, F.W., & Venters, T.M. 2011, ApJ, 736, 40
69. Strickland, D.K., & Heckman, T.M. 2009, ApJ, 697, 2030
70. Strickland et al. 2002, ApJ, 568, 689
71. Strickland, D.K., Ponman, T.J., & Stevens, I.R. 1997, A&A, 320, 378
72. Strong, A.W., Porter, T.,A., Digel, S.W., et al. 2010, ApJ, 722, L58
73. Tabatabaei F.S., Beck R., Krügel E., et al. 2007, A&A, 475, 133
74. Tabatabaei F.S., Krause M., Fletcher A., Beck R. 2008, A&A, 490, 1005
75. Thompson, T.A., Quataert, E., Waxman, E. 2007, ApJ, 654, 259
76. Torres, D.F. 2004, ApJ, 617, 966
77. Torres, D.F., Cillis, A., Lacki, B., & Rephaeli, Y. 2012, MNRAS, 423, 822
78. Tucker, W. 1975, *Radiation Processes in Astrophysics* (Cambridge, MA: MIT Press)
79. Ulvestad 2000, AJ, 120, 278
80. van den Bergh, S., & Tammann, G.A. 1991, ARAA, 29, 363
81. Webber, W.R. 1987, A&A, 179, 277
82. Weinberg, M.D., & Nikolaev, S. 2001, ApJ, 548, 712
83. Wilke, K., Stickel, M., Haas, M., et al. 2003, A&A, 401, 873
84. Wilson, A.S., & Ulvestad, J.S., 1982, ApJ, 263, 576
85. Woosley, S.E., & Weaver, T.A. 1995, ApJS, 101, 181
86. Zirakashvili, V.N., Breitschwerdt, D., Ptuskin, V.S., & Voelk, H.J. 1996, A&A, 311, 113

Cosmic Ray Acceleration in W51C Observed with the MAGIC Telescopes

Ignasi Reichardt, Emiliano Carmona, Julian Krause, Rebecca Gozzini, and Fabian Jankowski on behalf of the MAGIC Collaboration

Abstract We present the observations of the W51 complex with the MAGIC telescopes. After collecting more than 50 h of good quality data, we are able to measure the energy spectrum between 75 GeV and 5.5 TeV, and to fit it with a single power law with an index of $2.58 \pm 0.07_{\mathrm{stat}} \pm 0.22_{\mathrm{syst}}$. We look for underlying structures by means of detailed morphological studies that allow us to locate the majority of the emission around the interaction point between W51C and W51B, where shocked molecular and atomic gas is found. We also find a feature extending towards the pulsar wind nebula candidate CXO J192318.5 + 140305. The possible contribution of this pulsar wind nebula candidate, assuming a point-like source adds up to 20 % of the overall emission. The broad band spectral energy distribution of the whole gamma-ray source can be explained with a simple hadronic model that implies proton acceleration at least up to 100 TeV. The outcome of the modeling, together with the morphology of the source, suggests that we indeed observe ongoing acceleration of ions in the interaction zone between supernova remnant and cloud.

I. Reichardt (✉)
IFAE, Edifici C7b E-08193 Bellaterra, Spain
e-mail: ignasi@ifae.cat

E. Carmona
Max-Planck-Institut für Physik, D-80805 München, Germany

Centro de Investigaciones Energéticas, Medioambientales y Tecnológicas (CIEMAT), Madrid, Spain

J. Krause
Max-Planck-Institut für Physik, D-80805 München, Germany

R. Gozzini · F. Jankowski on behalf of the MAGIC Collaboration
Deutsches Elektronen-Synchrotron (DESY), D-15738 Zeuthen, Germany

D.F. Torres and O. Reimer (eds.), *Cosmic Rays in Star-Forming Environments*, Astrophysics and Space Science Proceedings 34, DOI 10.1007/978-3-642-35410-6_15,

1 Introduction

W51 is a massive molecular complex [6] at a distance of ∼5.5 kpc [21]. Three main components are identified in radio continuum images: the star-forming regions W51A and W51B and, superposed to the south-eastern boundary of W51B, the supernova remnant (SNR) W51C. The estimated age of the SNR W51C is 30 kyr [11]. Evidence of interaction between W51C and W51B is provided by several observations. Most crucial of them are the existence of two 1,720 MHz OH masers [9] and the detection of about 10^3 solar masses of atomic gas at a velocity shifted between 20 and 120 km s^{-1} with respect to its ambient medium [14]. The high-velocity atomic gas exhibits a counterpart in high density molecular gas clumps [15] sharing the same location and velocity shift. In [14, 15] it is shown that the shocked gas is displayed in a thin layer in the interface between the SNR shell, as delimited by the X-ray image from *ROSAT* and the *unshocked* molecular gas. This can be taken as the existence of a J-type shock penetrating the dense gas in a particular region of W51B, whereas in the location of the 1,720 MHz OH masers the shock should be continuous (C-type). Moreover, recent measurements [7] showed over-ionization of the gas in W51B in certain locations close to W51C coinciding with the shocked gas. This excess in ionization implies the existence of an intense flow of freshly accelerated cosmic rays (CRs) that, through proton-proton collisions, ionize the hydrogen in the adjacent cloud. However, ∼0.2° South-East to the shocked gas region, a hard X-ray source CXO J192318.5 + 140305 is detected. This object was first resolved by *ASCA* [12] and later confirmed by *Chandra* [13]. Its X-ray spectrum, together with its morphology, suggests that it is a possible pulsar wind nebula (PWN) associated with the SNR. Therefore, the presence of CXO J192318.5 + 140305 plays a role in the interpretation of the gamma-ray emission from the W51 region.

An extended source of gamma rays coincident with W51C was first detected by the H.E.S.S. telescopes with an integral flux above 1 TeV of about 3 % that of the Crab Nebula [8]. Also, the Large Area Telescope (LAT) on board the *Fermi* satellite detected an extended source between 200 MeV and 50 GeV coincident with the H.E.S.S. source [1]. Moreover, the reanalysis of the archival MILAGRO data after the release of the first *Fermi* catalog revealed a 3.4σ excess with median energy of 10 TeV coincident with the *Fermi*/LAT source [2]. The modeling done by Abdo et al. [1] of the spectral energy distribution (SED) of W51C disfavors leptonic models and suggests a hadronic origin for the emission. However, the object from which the gamma rays originate has not yet been identified within the W51 field, and the gamma-ray spectrum has so far been precisely measured only up to some tens of GeV. In what follows we will present the outcome of the observations with the MAGIC telescopes.

2 Observations

The MAGIC telescopes consist of two 17 m diameter Imaging Atmospheric Cherenkov Telescopes located at the Roque de los Muchachos observatory, La Palma (Spain), at the height of 2,200 m a.s.l. MAGIC detects gamma rays between 50 GeV and several tens of TeV, with a sensitivity[1] of 0.8 % of the Crab Nebula flux at energies >300 GeV, see [4].

MAGIC observed W51 in 2010 and 2011, collecting 53 h of effective dark time in the zenith angle range from 14° to 35°. Observations were carried out in the so-called *wobble* mode, meaning that the telescopes are pointing to positions displaced 0.4° around the centroid of the *Fermi*/LAT source W51C,[2] which allows a better background estimation. All data were taken in stereoscopic mode, recording only events which triggered both telescopes. The data analysis was performed using the MARS analysis framework [4, 17, 19].

3 Results

A source of gamma rays with energy above 150 GeV is detected with a significance of 11.4 σ. The detection significance is estimated using Eq. 17 in [16], where ON events are those reconstructed at an angular distance $\theta < 0.265°$ with respect to the centroid of the *Fermi*/LAT source. The background is estimated by averaging the events with the same angular constraint, but with respect to each of the equivalent camera position in each *wobble* pointing. The signal radius of $\theta < 0.265°$ is defined in order to include all the emission evident in the relative flux map. See [5] for a detailed explanation about the signal estimation.

The centroid of the emission is found in the coordinates $\alpha = 19.382 \pm 0.001$ h, $\delta = 14.191 \pm 0.015°$. This deviates by 0.04° from the position reported by *Fermi*/LAT. At energies above the threshold, $E > 150$ GeV, the point spread function (PSF) of the MAGIC telescopes is 0.085° [4]. We measure [5] the intrinsic extension of the source to be $0.12 \pm 0.02_{\text{stat}} \pm 0.02_{\text{syst}}$ degrees, which is well beyond the PSF. Taking into account the extension of the source, we conclude that the MAGIC and the *Fermi*/LAT sources are coincident.

We extracted the energy spectrum [3, 5] of the gamma-ray emission, and we found that between 75 GeV and 5 TeV it is well described ($\chi^2/\text{NDF} = 5.26/6$) by a power law with a photon index of $\Gamma = 2.58 \pm 0.07_{\text{stat}} \pm 0.22_{\text{syst}}$, and a normalization constant at 1 TeV of $N_0 = (9.7 \pm 1.0_{\text{stat}}) \times 10^{-13} \text{cm}^{-2}\text{s}^{-1}\text{TeV}^{-1}$. The systematic error on the flux normalization is 15 %, which includes the systematic

[1] Sensitivity is defined here as the minimal integral flux to reach 5 σ excess in 50 h of observations, assuming a spectral index like that of the Crab Nebula.

[2] RA = 19.385 h, DEC = 14.19°.

uncertainties of the effective area (11 %) and the background calculation. In addition, the systematic uncertainty in the energy scale is estimated to be 17 % at low (∼100 GeV) and 15 % at medium (∼250 GeV) energies [4].

The integrated flux above 1 TeV is equivalent to ∼3 % of the flux of the Crab Nebula above the same energy, in agreement with the previous flux measurement by the H.E.S.S collaboration [8]. The spectral index measured by MAGIC connects smoothly with the one measured by *Fermi*/LAT above 10 GeV [20], which is $\Gamma = 2.50 \pm 0.18_{\text{stat}}$. Therefore, the emission from W51 can be described by a single power law between 10 GeV and 5.5 TeV.

The PSF of the MAGIC telescopes improves with energy until a saturation value of 0.054° at energies above 1 TeV [4]. We compared the morphology of the source at energies above 300 GeV (where the PSF is 0.075°) with that seen above 1 TeV. In both cases the location of the source and its extension (taking into account the different PSF of both energy ranges) is the same, and are compatible with the values obtained for the analysis above 150 GeV.

The map above 1 TeV is seen in Fig. 1, where the colour scale represents relative flux[3] and the cyan contours represent isocurves of test statistics (TS).[4] The shape of the source is elongated, showing a tail towards the lower left, coincident with the possible PWN CXO J192318.5 + 140305. The maximum of the emission coincides with the shocked-gas region, represented by the red dashed circle. We note that, in any case, the VHE emission does not strictly follow the SNR shell (as seen from the 21 cm continuum emission represented by green contours). The tail seen towards the PWN rises the question of a possible substructure in the emission.

In order to investigate the source for underlying structures, we projected on a line the unsmeared excess distribution of the source along a strip in two energy ranges. The strip is 2° long and is divided in 40 bins of 0.05° each. The orientation of the strip is defined by the position of the PWN candidate and the centroid of the shocked clouds identified by Koo and Moon [15] (RA = 19.380 h, DEC = 14.19°). The width of the strip is defined by two PSF on each side of the line connecting both features, which means 0.3° and 0.216° for the energy ranges from 300 to 1,000 GeV and above 1,000 GeV, respectively. We fitted the projection in each energy range alternatively using a Gaussian function and the sum of two Gaussian functions. The projection of events between 300 and 1,000 GeV has χ^2/d.o.f. values of 28/17 for the single Gaussian fit and 18/14 for the double Gaussian fit, whereas the projection of events above 1,000 GeV has χ^2/d.o.f. values of 16/17 for the single Gaussian fit versus 12/14 for the double Gaussian fit. While poor statistics do not allow to exclude any scenario, it is remarkable that the maxima of the double Gaussian fit in both cases coincides (within statistical errors) with the positions of the shocked

[3]Relative flux means excess events over background events. This quantity accounts for acceptance differences between different parts of the camera.

[4]This TS is Li&Ma significance applied on a smoothed and modeled background estimation. Its null hypothesis distribution mostly resembles a Gaussian function, but in general can have a somewhat different shape or width.

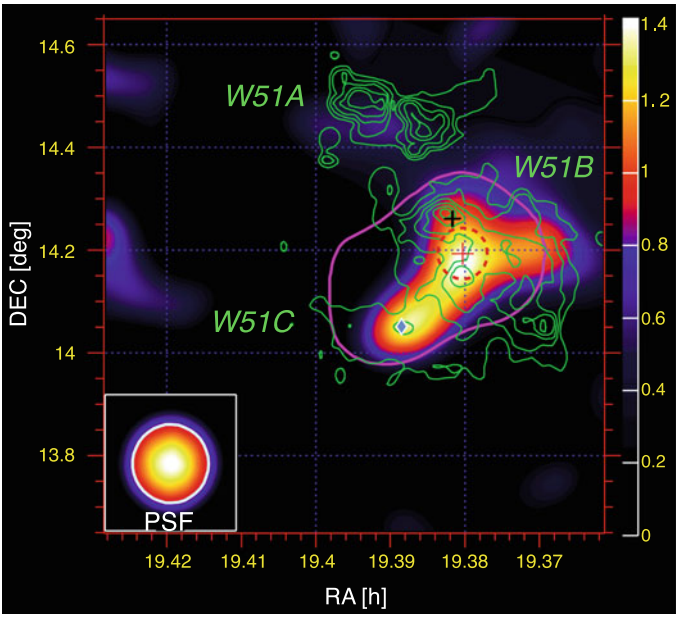

Fig. 1 Relative flux map >1 TeV. *Green* contours represent the 21 cm radio continuum emission [14]. The *blue diamond marks* the position of CXO J192318.5 + 140305 [13] and the *black cross* the position of the 1,720 MHz OH masers [9]. The *red dashed ellipse* represents the region of shocked gas [15]. The shape of the source detected by *Fermi*/LAT is displayed by the *pink* contour. The color scale (*blue* to *red*) represents the relative flux as measured with MAGIC. Cyan contours are TS isocurves, starting at 3 and increasing by 1 per contour

clouds and CXO J192318.5 + 140305. See [5] for a sketch of the projected strip and the Gaussian fits.

We also investigated a possible spatial variation of the spectral properties of the detected signal. To do so, we extracted the spectra above 350 GeV of two regions. The first region was defined to cover the shocked clouds with centroid at RA = 19.380 h, DEC = 14.19°; this will be called the *cloud* region. The second was defined by the position of CXO J192318.5 + 140305 and will be called the *PWN* region.

We use an integration radius of 0.1°. We compared the same analysis on data of the Crab Nebula and find that such a region contains at least 70 % of the excess from a point-like source above 300 GeV. The distance between the chosen positions is 0.19°. Therefore, there is an area of overlap of 1.7 % compared with the integration area of each region, which we consider negligible. The combined areas of both regions represent about 57 % of the area used to determine the overall spectrum. In the *cloud* region the emission is well described by a power law with a flux normalization at 1 TeV of $N_{\text{cloud}} = (4.3 \pm 0.9_{\text{stat}}) \times 10^{-13}\,\text{cm}^{-2}\,\text{s}^{-1}\,\text{TeV}^{-1}$, which implies an integrated flux above 350 GeV equivalent to 1.2 % that of the Crab Nebula. The spectral index of the *cloud* region is $-2.4 \pm 0.5_{\text{stat}}$ and agrees within

statistical uncertainties with the spectral index of the overall emission. Following the same procedure for the *PWN* region we obtain a flux equivalent to 0.7 % that of the Crab Nebula, which represents about a 20 % of the overall emission. The spectral shape of the *PWN* between 350 GeV and 2 TeV can also be well described by a power law, with a spectral index of $-2.5 \pm 0.6_{\text{stat}}$ and a flux normalization at 1 TeV of $N_{PWN} = (2.3 \pm 0.8_{\text{stat}}) \times 10^{-13} \text{cm}^{-2}\text{s}^{-1}\text{TeV}^{-1}$.

4 Discussion

Statistics are not sufficient to clearly discriminate between an extended source or two individual sources from a morphological or a spectral point of view. However, the fact that there is no region of dense gas close to the PWN makes difficult to explain the enhancement of TeV emission in this area under the assumption of uniform CR density. On the other hand, non-thermal X-ray emission which could help to trace the relativistic electron population was found around CXOJ192318.5+140305 [12, 13]. In order to assess whether the VHE emission can be originated by the PWN candidate only, we consider the estimated rate of rotational energy loss $\dot{E} = 1.5 \times 10^{36}\,\text{erg}\,\text{s}^{-1}$ [13] obtained with the empirical relation from Seward and Wang [22]. Given the observed luminosity of the order of $\sim 10^{36}\,\text{erg}\,\text{s}^{-1}$ reported in [1], it seems unlikely that the PWN alone is the source of all gamma-ray emission. This assumption would require an extremely high efficiency in the conversion from rotational energy into gamma rays. The *PWN* region can account for the 20 % of the gamma-ray emission confined in a point-like source, whereas the brightest part is the *cloud* region. If we consider a 20 % of the overall emission to be originated by the PWN, it comes out that a $\dot{E}$ conversion into gamma rays of the order of 10 % is needed, which is in agreement with the generally accepted value.

For the reasons above, we assume that the contribution of the possible PWN is in any case small. This assumption introduces an error in the flux normalization of about 20 % in case part of the emission originates from the PWN candidate. This uncertainty lies within the statistical and systematic errors of the MAGIC measurement. The approach taken in the following modelling is to assume a single particle distribution producing the emission we observe. We refer to [5] for the details on the model setup and fitting procedure. We will only mention here that we consider separate scenarios in which one of the following emission process dominates over the others: pion decay, inverse Compton or Bremsstrahlung. The model discussed here is obtained using as equilibrium particle spectra a broken power law with an exponential cut-off, both for electrons and protons.

First we consider the case where the emission is dominated by leptonic emission mechanisms. We find the same problems already reported by Abdo et al. [1], namely that it cannot reproduce the radio and gamma-ray data simultaneously. Furthermore these models need an unusually high electron to proton ratio of the order of one. Instead, when we model the emission with pion decay as the dominant process, both

radio and gamma-ray emission can be reasonably reproduced [5]. The parameters that provide the best model are:

- Electron to proton ratio: $K_e/K_p = 1/80$
- Steepening of the spectrum after the break: $\Delta s = 1.2$[5]
- Break energy: $E_{\rm br} = 10\,{\rm GeV}$
- Cutoff energy for electrons: $E_{{\rm cut},e} = 0.1\,{\rm TeV}$
- Cutoff energy for protons: $E_{{\rm cut},p} = 120\,{\rm TeV}$
- Average magnetic field: $B = 53\mu\,{\rm G}$
- Average particle density: $n = 10.0\,{\rm cm}^{-3}$
- Energy contained in accelerated electrons: $W_e = 0.069 \times 10^{50}\,{\rm erg}$
- Energy contained in accelerated protons: $W_p = 5.8 \times 10^{50}\,{\rm erg}$

The total kinetic energy of the particles was integrated for $E_{\rm kin} > 100\,{\rm MeV}$ both for electrons and protons.

The luminosity of W51C in the energy range 0.25 GeV–5.0 TeV, which is roughly the energy range of the *Fermi* and MAGIC data, is $L_\gamma \approx 1 \times 10^{36}\,{\rm erg\,s}^{-1}$, assuming a distance of 5.5 kpc. Compared to the hadronic model suggested in [1], the main difference is the index of the particle distribution after the break, which is more precisely determined by the data presented here. The index we obtain is harder, and explains the gamma-ray data up to the end of the MAGIC spectrum. A cut-off energy of $E_{{\rm cut},p} \geq 100\,{\rm TeV}$ is needed to fit the MAGIC data, indicating the existence of protons at least to this energy. However, our model is far from the hint of emission observed by MILAGRO at 35 TeV which, if confirmed at this flux level, would require the introduction of an additional component at the highest energies.

We also derive that about 11 % of the mass of the molecular cloud is inside the SNR interaction volume. The explosion energy of the SNR has been estimated in [11] as $E_{\rm SN} \approx 3.6 \times 10^{51}$ erg. Therefore, the total amount of kinetic energy in electrons and protons is about 16 % of the explosion energy of the supernova. This fraction is just slightly higher than the value normally assumed, of around 10 %, of the explosion energy converted into CRs to maintain the observed flux of Galactic CRs [10]. The proton to electron ratio is not far from value observed at earth of $K_p/K_e \approx 50$ [23].

The morphology described in this work shows that the gamma-ray emission is originated very close to the acceleration site of the radiating particles due to the high density of the surrounding medium. The unusually high ionization reported by Ceccarelli et al. [7] close to the maximum VHE emission region indicates the presence of freshly accelerated low-energy protons. The missing emission towards the edges of the cloud could be explained with a lower diffusion coefficient in the shocked cloud region, or with a shielding effect, either of which is possible in a surrounding medium of high density.

[5]The radio measurements in [18] indicate a spectral index of $\alpha_r \approx -0.26$ (as defined by $S_\nu \propto \nu^{\alpha_r}$). This can be attributed to electrons emitting synchrotron radiation and fixes the initial power-law index of the electron spectrum to $s \approx 1.5$. We adopt this value both for electrons and protons.

5 Conclusions

MAGIC has performed a deep observation of a complex Galactic field containing the star-forming regions W51A and W51B, the SNR W51C and the possible PWN CXO J192318.5 + 140305. We are able to restrict the emission region to the zone where W51C interacts with W51B and, in particular, to the region where shocked gas is observed. This clearly pinpoints the origin of the emission to the interaction between the remnant and the molecular cloud. The MAGIC relative flux map shows a feature extending towards this possible PWN. However, the existence of two independent, resolved sources cannot be statistically established from the analysis of the morphology, neither significant spectral differences between the two regions are found.

We have produced a physically plausible model of the emission of the SNR by considering a spherical geometry and uniform distribution of the ambient material. We note that this system is clearly anisotropic (as seen in the multi-wavelength data), and more detailed modeling may achieve a better description of the source. We find that the VHE emission from W51C cannot be explained by any of the considered leptonic models. The emission is best described when neutral pion decay is the dominant process. In the proposed model, the SNR has converted about 16 % of the explosion energy into kinetic energy for proton acceleration and the emission zone engulfs a 10 % of a molecular cloud of 10^5 solar masses. To achieve a good description of the gamma-ray spectrum, protons are required to reach at least an energy of the order of 100 TeV to produce the observed emission.

The morphology of the source cannot be explained by CRs diffusing from the SNR to the cloud. It can instead be qualitatively explained with VHE gamma-ray emission being produced at the acceleration site of CRs. This involves ongoing acceleration of CRs or re-acceleration of already existing CRs at the shocked cloud region.

Given that W51C is one of the most luminous Galactic sources at gamma-ray energies, the results presented here add further evidence towards the confirmation of supernova remnants as main contributors to the CR flux up to energies of at least 100 TeV.

References

1. A. A. Abdo *et al.* [Fermi LAT collaboration], Astrophys. J. **706**, L1 (2009) [arXiv:0910.0908 [astro-ph.HE]].
2. A. A. Abdo *et al.*, Astrophys. J. **700**, L127 (2009) [Erratum-ibid. **703**, L185 (2009)] [arXiv:0904.1018 [astro-ph.HE]].
3. J. Albert *et al.* [MAGIC Collaboration], Nucl. Instrum. Meth. A **583**, 494 (2007) [arXiv:0707.2453 [astro-ph]].
4. J. Aleksic *et al.* [MAGIC Collaboration], Astropart. Phys. **35**, 435 (2012) [arXiv:1108.1477 [astro-ph.IM]].
5. J. Aleksic *et al.* [MAGIC Collaboration], A&A *in press* [arXiv:1201.4074 [astro-ph.HE]].

6. J. M. Carpenter and D. B. Sanders, Astron. J. **116**, 1856 (1998) [arXiv:astro-ph/9806298].
7. C. Ceccarelli, P. Hily-Blant, T. Montmerle, et al. 2011, ApJL, 740, L4
8. A. Fiasson, V. Marandon, R. C. G. Chaves & O. Tibolla, 2009, in Proceedings of the 31st ICRC, Lodz, http://icrc2009.uni.lodz.pl/proc/pdf/icrc0889.pdf
9. A. J. Green, D. A. Frail, W. M. Goss & R. Otrupcek, 1997, AJ, 114, 2058
10. A. M. Hillas 2005 J. Phys. G: Nucl. Part. Phys. 31 R95 doi:10.1088/0954-3899/31/5/R02
11. B.-C. Koo, K.-T. Kim & F. D. Seward, 1995, ApJ, 447, 211
12. Koo, B.-C., Lee, J.-J. & Seward, F. D. 2002, AJ, 123, 1629
13. B.-C. Koo, J.-J. Lee, F. D. Seward & D.-S. Moon, 2005, ApJ, 633, 946
14. B.-C. Koo, & D.-S. Moon 1997, ApJ, 475, 194
15. B.-C. Koo, & D.-S. Moon 1997, ApJ, 485, 263
16. T. P. Li and Y. Q. Ma, Astrophys. J. **272**, 317 (1983).
17. S. Lombardi, K. Berger, P. Colin, A. D. Ortega, S. Klepser and f. t. M. Collaboration, arXiv:1109.6195 [astro-ph.IM].
18. D.-S. Moon, & B.-C. Koo 1994, Journal of Korean Astronomical Society, 27, 81
19. A. Moralejo *et al.*, arXiv:0907.0943 [astro-ph.IM].
20. D. Paneque et al., in Proceedings of the Fermi Symposium, Rome 2011
21. M. Sato, M. J. Reid, A. Brunthaler and K. M. Menten, Astrophys. J. **720**, 1055 (2010) [arXiv:1006.4218 [astro-ph.GA]].
22. F. D. Seward & Z.-R. Wang 1988, ApJ, 332, 199
23. J. A. Simpson, Ann. Rev. Nucl. Part. Sci. **33**, 323 (1983).

Cosmic Rays and Molecular Clouds

Stefano Gabici

Abstract This paper deals with the cosmic-ray penetration into molecular clouds and with the related gamma–ray emission. High energy cosmic rays interact with the dense gas and produce neutral pions which in turn decay into two gamma rays. This makes molecular clouds potential sources of gamma rays, especially if they are located in the vicinity of a powerful accelerator that injects cosmic rays in the interstellar medium. The amplitude and duration in time of the cosmic–ray overdensity around a given source depend on how quickly cosmic rays diffuse in the turbulent galactic magnetic field. For these reasons, gamma-ray observations of molecular clouds can be used both to locate the sources of cosmic rays and to constrain the properties of cosmic-ray diffusion in the Galaxy.

1 Introduction: The Supernova Remnant Paradigm for the Origin of Galactic Cosmic Rays

Cosmic Rays (CRs) [1–4] are charged and energetic particles that hit the Earth's atmosphere from above. The flux of CRs, once corrected for the effect of solar modulation, is constant in time and corresponds to a local energy density of $w_{CR} \approx 1\,\mathrm{eV/cm^3}$. Remarkably, this is comparable to the energy density of both magnetic field and thermal gas in the interstellar medium. CRs are mainly protons, with approximately 10 % of Helium, and 1 % of both heavier nuclei and electrons. Their differential energy spectrum is a steep and featureless power law $N_{CR} \propto E^{-s}$ with slope $s \approx 2.7$, and ≈GeV particles are the main contributors to the total CR energy density. The slope of the spectrum slightly steepens to $s \approx 3$ at an energy

S. Gabici (✉)
AstroParticule et Cosmologie, Université Paris Diderot, CNRS/IN2P3, CEA/IRFU, Observatoire de Paris, Sorbonne Paris Cité, 10, rue Alice Domon et Léonie Duquet, 75205, Paris Cedex 13, France
e-mail: Stefano.Gabici@apc.univ-paris7.fr

D.F. Torres and O. Reimer (eds.), *Cosmic Rays in Star-Forming Environments*, Astrophysics and Space Science Proceedings 34, DOI 10.1007/978-3-642-35410-6_16,

of $\approx 4 \times 10^{15}$ eV and this spectral feature is called the CR knee. The CR spectrum continues up to energies of the order of $\approx 10^{20}$ eV, but here we restrict ourselves to considering particles with energies below the knee, which can be confined by the interstellar magnetic field and thus are certainly of galactic origin. Finally, the arrival directions of CRs are extremely isotropic in the sky. The isotropy is of the order of $\approx 10^{-3}$ for particle energies above ≈ 1 TeV, where local (i.e. heliospheric) effects can be neglected, and depends very weakly on the particle energy for energies up to the knee. The high level of isotropy is due to the diffusion of CRs in the turbulent galactic magnetic field, which isotropizes the trajectories of particles and prevents a direct identification of CR sources based on the observed arrival direction of particles. This is the reason why indirect observational evidences, such as the detection of photons produced by CR interactions with the ambient medium, are needed in order to locate the sites of CR acceleration. *To date, the sources of galactic CRs are still not firmly identified.*

A connection between CRs and supernovae was first proposed by Baade and Zwicky in 1934 [5] and still remains the most popular explanation for the origin of galactic CRs. In its modern version (see [6] for a review), the supernova paradigm for the origin of cosmic rays mainly relies on a consideration based on the energy required to maintain the observed flux of CRs against their escape from the Galaxy. The overabundance of Li, Be, and B in CRs with respect to the abundances measured in the solar system, where they are virtually absent,[1] can be explained as the result of spallation of heavier CR nuclei by interstellar gas. The amount of matter, or grammage, that CRs with an energy of $\gtrsim$GeV need to traverse to produce the observed amount of Li, Be, and B is equal to $\mu \approx 5\,\mathrm{g/cm^2}$. This corresponds to a confinement time in the galactic disk of $t_d = \mu/\rho c \approx 3 \times 10^6$ year, where ρ is the mean gas density in the disk (≈ 1 particle per cubic centimeter) and c is the speed of light. Assuming that the CR intensity is constant in both time and space within the galactic disk, which has a radius of $R_{mw} \approx 15\,\mathrm{kpc}$ and a thickness h of a few hundred parsecs, one can estimate the CR luminosity of the Galaxy as $W_{CR} = [w_{CR}(\pi R_{mw}^2)h]/t_d \approx 10^{41}$ erg/s. This has to be compared with the total power from supernova explosions in the galaxy $P_{SN} = \nu_{SN} E_{SN} \approx 10^{42}$ erg/s, where $\nu_{SN} \approx 3$/century is the supernova rate in the Galaxy and $E_{SN} \approx 10^{51}$ erg is the typical supernova explosion energy. It is evident form these figures that *supernovae, or something related to them, may be the sources of CRs if $\approx 10\,\%$ of their explosion energy is somehow converted into accelerated particles.*

A mechanism for the acceleration of particles that operates at supernova remnant (SNR) shocks was proposed in the late seventies, when it was realized that particles can be accelerated at shock waves via a first-order Fermi mechanism [7–9]. A characteristic prediction of these models is a differential energy spectrum for the accelerated particles which is a power law with slope close to $\approx E^{-2}$. Power law spectra of relativistic particles have indeed been observed in SNRs,

[1] Li, Be, and B are not synthesized in stars, and their standard abundance is very low, being mainly determined by primordial nucleosynthesis.

both through X-ray (see e.g. [10, 11]) and gamma-ray (e.g. [12, 13]) observations and this is considered an evident manifestation of shock acceleration at expanding SNR shock waves. The X-ray emission is unambiguously interpreted as the synchrotron radiation from relativistic electron, while the gamma ray emission can be interpreted either as inverse Compton scattering of electrons or decay of neutral pions generated in hadronic interactions between CRs and ambient gas. As discussed in the following, *the ambiguity between the hadronic or leptonic origin of the observed gamma-ray emission from SNRs is one of the main obstacles in proving (or disproving) the fact that SNRs are indeed the sources of CRs.*

Another issue that needs to be explained is the absence of features in the CR spectrum up to the energy of the CR knee, which is the mild steepening of the spectral slope observed at a particle energy of a few PeVs. The featureless of the spectrum up to that energy suggests that the sources that are responsible for the acceleration of the bulk of the CRs in the Galaxy (≈GeV particles) are probably able to accelerate particles all the way up to the knee. In fact, assuming that several classes of sources contribute significantly to the CR spectrum at different particle energies and create such a featureless power law spectrum, though not impossible, would require an *ad hoc* fine tuning which seems quite unreasonable. In other words, *if SNRs are the sources of galactic CRs, most likely they have to act as particle PeVatrons* (see e.g. [14]).

Finally, the question on the origin of galactic CRs cannot be considered answered until we understand the details of their propagation in the interstellar medium (for recent reviews see e.g. [15, 16]). Measurements of the grammage that CRs must traverse while propagating from the sources to the Earth can be performed at different CR particle energies. Such measurements clearly point toward an energy dependent grammage, and thus an energy dependent confinement time of CRs in the Galaxy, with higher energy particles escaping faster, according to $t_{esc}(E) \propto E^{-\delta}$, with $\delta \approx 0.3 \ldots 0.6$. By assuming that CRs of all energies travel, on average, a distance h before leaving the Galaxy, the escape time can be converted into a spatial diffusion coefficient $D \approx h^2/t_{esc} \approx D_0(E/10\ \mathrm{GeV})^{\delta}$, with $D_0 \approx 10^{28} \ldots 10^{29}\,\mathrm{cm}^2/\mathrm{s}$ [15, 16]. If CR sources inject in the Galaxy $Q_{CR}(E)$ particles with energy E per unit time, with a power law spectrum $Q_{CR}(E) \propto E^{-\alpha}$, then the equilibrium spectrum of CRs in the Galaxy is: $N_{CR} \propto Q_{CR}(E) \times t_{esc} \propto E^{-\alpha-\delta}$. The observed slope of the CR spectrum is $N_{CR} \propto E^{-2.7}$, which gives: $\alpha \approx 2.1 \ldots 2.4$. Thus, *the slope of the injection spectrum of CRs in the Galaxy has to be close to, but definitely steeper than 2*.

At this point, another remark is needed. If the diffusion coefficient grows too fast with energy, i.e. if δ is closer to ≈0.6 rather than to ≈0.3, CRs with energies close to the knee would escape the Galaxy too quickly to be isotropized by the galactic magnetic field. In this scenario one would expect a high level of anisotropy at high energies, in contrast with what is observed. Thus, best–bet reference values for the spectral slope at injection of CRs and for the slope of the diffusion coefficient are probably $\alpha \approx 2.4$ and $\delta \approx 0.3$, which are consistent with both the chemical and isotopic abundances of CRs and their isotropy.

The reason why the SNR hypothesis for the origin of galactic CRs is the most trusted and investigated scenario (but see e.g. [17] and [18] for a different and radically different perspective, respectively) is the fact that within this framework, most of the observational requirements can be explained within a reasonable accuracy. As said above, the total energy budget is not an issue, provided that the efficiency of particle acceleration is of the order of $\approx 10\,\%$. X-ray and gamma-ray observations clearly show that a mechanism capable of accelerating particles up to (at least) hundreds of TeVs operates at SNR shocks, and the characteristics of the observed radiation fit quite well with predictions of shock acceleration theory. Moreover, recent developments in our understanding of the CR-induced amplification of the magnetic field at shocks suggest that SNRs might be able to accelerate particles up to the energy of the knee [19] and inject them in the interstellar medium with a spectrum slightly steeper than E^{-2} (see e.g. [20] or [21, 22] for two ways to steepen the spectral slope above $\alpha = 2$), as required to explain the observed spectrum of CRs. Also the CR chemical composition is reproduced with fair agreement with observations [23], while for what concerns the CR anisotropy the agreement between predictions and data is consistent within a factor of a few [24, 25], if a weak dependence on energy of the diffusion coefficient is adopted, i.e. $\delta \approx 0.3$. However, in this latter case a comparison is less straightforward given that the level of anisotropy may be dominated by the exact location of the few nearest CR sources.

Despite all these very encouraging facts, it has to be kept in mind that we are still missing a conclusive and unambiguous proof of the fact that SNRs, as a class of objects, accelerate CRs and inject them in the interstellar medium at the rate required by observations. This review is an attempt to describe how gamma-ray observations, and in particular gamma-ray observations of molecular clouds, might finally lead to prove (or falsify) the SNR paradigm for the origin of CRs.

2 Gamma-Rays from Supernova Remnants

CRs in the Galaxy undergo proton–proton hadronic interactions with the interstellar gas and produce neutral pions. The threshold energy for pion production is $E_p \approx 280\,\mathrm{MeV}$, where E_p is the kinetic energy of the incoming CR. Each pion then decays into two gamma-ray photons which, for energies well above the threshold, have a typical energy equal to $\approx 0.1 \times E_p$ [26–28]:

$$p + p \longrightarrow p + p + \pi^0$$
$$\pi^0 \longrightarrow \gamma + \gamma$$

Being the product of the decay of a particle of mass m_{π^0}, the resulting differential energy spectrum of gamma rays exhibits a pronounced peak at an energy $\approx m_{\pi^0}/2 \approx 70\,\mathrm{MeV}$. At energies larger than that, the gamma ray spectrum roughly

mimics the spectrum of the CRs. The energy loss time of CRs due to proton-proton interactions is determined by the interaction cross section $\sigma_{pp} \approx 40\,\mathrm{mb}$ and inelasticity $\kappa \approx 0.45$. Since these quantities depend weakly on particle energy, the energy loss time virtually depends on the gas density only and reads (e.g. [29]):

$$\tau_{pp} = \frac{1}{n_{gas} c \kappa \sigma_{pp}} \approx 6 \times 10^7 \left(\frac{n_{gas}}{1\ \mathrm{cm}^{-3}}\right)^{-1}\ \mathrm{yr} \tag{1}$$

Charged pions can also be generated in proton–proton interactions, and the final products of their decay are electrons, positrons, neutrinos, and antineutrinos. Electrons and positrons can in turn produce gamma rays via inverse Compton scattering or Bremsstrahlung. Finally, also CR electrons, often referred to as *primary electrons*, to distinguish them from the ones (*secondaries*) generated in proton–proton interactions, can produce gamma rays through the same mechanisms. Among all these mechanisms for the production of gamma rays, the decay of neutral pions is the dominant one in producing the prominent diffuse gamma-ray emission observed in the GeV energy range from the galactic disk [30, 31]. Such a strong diffuse emission constitutes an unavoidable background in searches for galactic sources of GeV gamma-rays. On the other hand, due to the steepness of the CR spectrum, the diffuse TeV emission from the galactic disk is expected to be too weak to become an issue for present day Cherenkov telescopes, and for this reason in the following we focus mainly on the TeV energy domain.

A way to use gamma-ray observations in order to test the SNR hypothesis for the origin of CRs was proposed in 1994 [32, 33]. If SNR are the sources of CRs, $\approx$10 % of the explosion energy of each supernova in the Galaxy has to be converted, on average, into CRs. The typical explosion energy is $\approx 10^{51}$ erg, and it does not vary much from supernova to supernova. Thus, on average one might expect to find $W_{CR}^{tot} \approx 10^{50}$ erg in form of CRs in a SNR. For simplicity, let's assume that at the SNR shock particles are accelerated with a differential spectrum $N_{SNR} \propto E^{-2}$ which extends from $\approx$GeV to $\approx$PeV energies. This gives a CR energy spectrum inside the SNR equal to $W_{CR} \approx N_{SNR}(E)E^2 \approx 7 \times 10^{48}$ erg. Then the gamma-ray flux from the SNR due to neutral pion decay is also a power law in energy with slope $\propto E_\gamma^{-2}$ and can be roughly estimated in this way:

$$F_\gamma(E_\gamma)E_\gamma^2 \approx \frac{W_{CR}\, c_{p\to\gamma}}{\tau_{pp}\,(4\pi d^2)} \approx 10^{-11} \left(\frac{W_{CR}^{tot}}{10^{50}\mathrm{erg}}\right)\left(\frac{n_{gas}}{1\ \mathrm{cm}^{-3}}\right)\left(\frac{d}{1\ \mathrm{kpc}}\right)^{-2}\ \mathrm{erg/cm^2/s} \tag{2}$$

where $c_{p\to\gamma} \approx 0.1$ is the average fraction of the proton energy transferred to the gamma-ray photon and d is the SNR distance. In computing the gamma-ray flux it has been assumed that the ambient gas with density n_{gas} is compressed at the strong SNR shock by a factor of 4. Moreover, any leptonic contribution to the gamma-ray emission (i.e. inverse Compton scattering and Bremsstrhalung from both primary and secondary electrons) has been neglected.

The hadronic gamma-ray flux predicted from Eq. 2 is well within the detection capability of the Cherenkov telescopes that currently operate in the TeV energy domain: H.E.S.S., MAGIC, and VERITAS. In other words, if SNR are the sources of CRs, some of them must have been detected by Cherenkov telescopes. This claim remains substantially correct, thought less striking [34], even if one assumes a steeper spectrum $\approx E^{-2.1...2.4}$ for the accelerated particles, a choice more consistent with CR data (see Sect. 1). Indeed, roughly half a dozen of isolated (i.e. not associated with a molecular cloud) SNRs have been detected in TeV gamma rays (for reviews see [12, 13]), and this fits well with the above mentioned predictions. However, electrons are also accelerated at shocks, as demonstrated by the X-ray synchrotron emission observed from a number of SNRs. Thus, a competing leptonic mechanisms, namely inverse Compton scattering off photons of the cosmic microwave background radiation, could also account for the observed TeV emission. This means that the detection of SNRs at TeV energies cannot be considered as a proof of the fact that SNRs are indeed the sources of CRs, but only as an additional consistency check of that scenario.

The question about the hadronic or leptonic nature of the TeV emission from SNRs constitutes one of the most discussed issues in gamma-ray astronomy. A key parameter which regulates the predominancy of one contribution over the other is the magnetic field in the shock region. If the field is significantly stronger than $\approx 10\,\mu$G, then the observed synchrotron X-rays can be explained by a relatively meagre number of electrons, which would produce unappreciable TeV inverse Compton emission. Conversely, if the value of the magnetic field is smaller than or comparable to $10\,\mu$G the much larger number of electrons needed to explain the X-ray emission will also suffice to explain the whole observed TeV emission. Thus, the value of the magnetic field at the shock is a crucial parameter of the problem, and its determination would allow us to unveil the nature of the gamma ray emission.

Observational evidence has been found for the presence of very strong magnetic fields of the order of $\approx 100\,\mu\text{G}...1\,\text{mG}$ in several SNRs. Such evidences come from X-ray observations of narrow synchrotron filaments located at the position of the shock [35–37], or of very fast temporal variations of the synchrotron emission from small knots within the SNR [38, 39]. In both cases, a strong magnetic field is needed to reduce the synchrotron cooling time of electrons down to values that would explain both the fast variability and the small thickness of filaments, since in such a strong magnetic field electrons would radiate all their energy before reaching large distances downstream of the shock. The importance of these measurements is the fact that they point towards a very efficient acceleration of CR protons and nuclei, which seem to be the only plausible source for the field amplification. On the other hand, it has to be noted that the regions in which field amplification has been measured constitute a very small fraction of the entire SNR shell, and thus little can be said about the average value of the field on larger scales, and also on the global CR acceleration efficiency from the whole shock.[2] In other words, the

[2] At least one exception to this exists, which is the SNR Cas A, for which a high value ($\approx 300\,\mu$G) of the average magnetic field in the whole shell region has been determined [40, 41].

average field could be much smaller than the one measured in knots and filaments, and this would be in agreement with a leptonic interpretation of the gamma-ray emission from SNRs.

Another way to discriminate between the hadronic or leptonic origin of the observed gamma-ray emission from SNRs is by measuring the spectral slope of the gamma-ray spectrum from the GeV to the TeV energy range. SNR shocks are expected to accelerate particles, both hadrons and leptons, with a differential spectrum which is close to a power law $N(E) \propto E^{-\gamma}$. By using a very simple toy–model it can be shown that the spectrum of the CRs that escape the SNRs and are injected in the interstellar medium is expected to be, very roughly, $\approx E^{-2}$ if $\gamma < 2$ and $\approx E^{-\gamma}$ if $\gamma > 2$ [42–45]. Thus, to satisfy the requirements from CR data, we adopt here values of γ in the range $2.1 \ldots 2.4$. This would result in a relatively steep (i.e. steeper than E^{-2}) hadronic gamma-ray emission due to proton-proton interactions with a spectrum $E_\gamma^2 F_\gamma^{pp}(E_\gamma) \propto E_\gamma^2 N(E/c_{p\to\gamma}) \approx E_\gamma^{-0.1\ldots0.4}$. To compute the spectrum resulting from the inverse Compton scattering of accelerated electrons one has to keep in mind that in the leptonic scenario for the gamma–ray emission a weak magnetic field is required in order not to overshoot the observed X–ray fluxes. Thus, synchrotron energy losses can be neglected and the spectrum of electrons does not change and remains $E^{-\gamma}$. In this case, the differential energy spectrum of the inverse Compton scattering emission is a power law with index $(\gamma + 1)/2 \approx 1.55 \ldots 1.7$, resulting in a spectral energy distribution equal to $E_\gamma^2 F_\gamma^{IC} \approx E_\gamma^{0.3\ldots0.45}$, which is significantly harder than E^{-2}. This spectral difference – a hard spectrum for the leptonic emission and a soft one for the hadronic – can be used to distinguish between the two scenarios. To do this, GeV observations by the Fermi satellite are of crucial importance since they can be combined with TeV observations to obtain a broad band gamma–ray spectrum.

Indeed, Fermi detected several young SNRs. Observations of the SNR RX J1713.7-3946, the most prominent TeV bright SNR, revealed a very hard spectral energy distribution with index close to 1.5, suggesting that for this particular SNR the gamma-ray emission is most likely leptonic [46]. Conversely, the gamma-ray spectrum observed from the historical SNR Tycho is a power law with slope $\approx$2.3, pointing towards an hadronic origin of the emission [47, 48]. The case of Vela Jr., another TeV bright young SNR, is less clear, since neither the hadronic nor the leptonic model can be ruled out based on gamma–ray data only [49]. Similar conclusions can be reached for the SNR Cas A, for which an hadronic origin of the gamma–ray emission seems favored, but a leptonic one (based on relativistic Bremsstrahlung) cannot be completely ruled out [50]. To complete the picture, some remarks are in order: first of all, the fact that the emission from RX J1713.7-3946 seems to be leptonic does not mean that that SNR is not an accelerator of CR protons. In fact, if the ambient density close to the SNR is low, at the level of $\approx 0.1\,\mathrm{cm}^{-3}$, then the expected hadronic gamma–ray emission would fall below the observed one even for quite high acceleration efficiency of $\approx$30 % [46]. Thus, the evidence for leptonic emission cannot be considered as an argument against CR acceleration at SNRs. The second remark is that a hadronic interpretation for the emission from RX J1713.7-3946 has been pushed forward in [51, 52], while a

leptonic one for Tycho has been presented in [53]. This indicates that an unanimous agreement on the interpretation of the gamma–ray emission from young SNRs is not reached yet, even for the best studied sources.

X–ray observations can also help in discriminating between hadronic and leptonic models. In fact, the first convincing evidence in favor of the leptonic origin of the gamma rays from the SNR RX J1713.7-3946 came from the non-detection of X–ray lines in its spectrum. The idea is that if one wants to explain the gamma–ray emission as the result of hadronic interactions, a high density for the ambient gas has to be assumed. This would also enhance the thermal emission from the shocked gas, and X–ray lines should appear on top of the synchrotron X–ray spectrum. Their absence in the observed spectrum cannot be accounted for in hadronic models [54], unless two distinct zones (one for the production of gamma–rays and one for the production of thermal radiation) are invoked [51].

Finally, Fermi also detected several old SNRs, with an age of $\approx 10^4$ year (e.g. [55, 56]). In most cases the gamma–ray emission is likely to have a hadronic origin. This is because a leptonic interpretation would require an unreasonable total energy in form of accelerated electrons (e.g. [55]). For old SNRs, the velocity of the shock is quite small, of the order of 100 km/s, and these objects are very often interacting with dense molecular clouds. Both these things may inhibit the acceleration (or reacceleration [57]) of particles. On one side, the acceleration rate is small for slow shocks and in addition to that, the neutral gas in the molecular cloud can damp the magnetic field turbulence and reduce the scattering rate of particles, which is a key ingredient for their acceleration [58]. Thus, old SNRs are not expected to accelerate CRs all the way up to the knee and, in agreement with this expectation, their TeV gamma–ray spectrum, when measured, is generally quite steep.

To conclude, there is now growing consensus on the fact that SNRs are capable of accelerating CR protons up to GeV–TeV energies. Also, there is quite convincing indication for proton acceleration above TeV energies from at least one young SNR (Tycho), while in another case (RX J1713.7-3946) the gamma–ray emission is most likely leptonic, and we cannot say much on CR acceleration efficiency from gamma–ray data only. Moreover, the high values of the magnetic field inferred from X-ray observations of several young SNRs seem to require that efficient CR acceleration operates at least at some locations in those shocks. Unfortunately, we are still missing convincing and direct observational evidence for the fact that SNRs accelerate particles up to the knee. A conclusive proof (or confutation) of the SNR paradigm for the origin of CRs will hopefully come soon, with the advent of new gamma–ray facilities like CTA, HAWK or LHAASO [59–61], which will dramatically increase the amount and quality of data.

In the next sections, it will be shown how present and future gamma–ray observations of molecular clouds can contribute in solving the problem of CR origin. In particular, if a massive cloud is located at or close to the SNR shock, the gamma–ray emission due to neutral pion decay is strongly enhanced due to the presence of a thick target. This would enhance the probability to detect the hadronic emission and thus allow the identification of SNRs as sources of CRs. Moreover, in at least two cases, the SNRs W28 [62, 63] and W44 [64], some gamma–ray emission is

detected from outside of the SNR shell, and coincident with the position of dense gas clouds. In another case, the SNR IC 443, the centroids of the GeV and TeV emissions are not coincident, but significantly displaced [65]. To interpret these observations, CR escape from the SNR shells and energy dependent propagation of CRs have been often invoked. This suggests that gamma–ray observations of molecular clouds could also be used to study and constrain the propagation of CRs close to their sources, about which very little is known.

3 Molecular Clouds as Cosmic Ray Barometers

Consider a molecular cloud (MC) with mass $M_5 = (M/10^5 M_\odot)$ at a distance $d_{\rm kpc} = (d/{\rm kpc})$ from the observer. Let us further assume that the CR intensity in the region of the Galaxy where the MC is located is the same as the one measured at the Earth. Under these circumstances, an expression similar to Eq. 2 can be written to describe the expected integral gamma-ray flux due to proton–proton interactions in the MC [66, 67]:

$$F_\gamma(>E_\gamma) \approx 2\times 10^{-13}\,\delta\,\left(\frac{M_5}{d_{\rm kpc}^2}\right)\left(\frac{E_\gamma}{\rm TeV}\right)^{-1.7}\,{\rm cm}^{-2}{\rm s}^{-1} \tag{3}$$

where a multiplicative factor of $\approx$1.5 has been applied to account for the contribution to the emission from nuclei heavier than hydrogen both in CRs and ambient gas [68]. The factor δ accounts for possible deviations of the CR intensity with respect to the one measured at the Earth, and under the assumption (quite reasonable, within a factor of a few) of homogeneity of the CR intensity in the Galaxy it is equal to 1. By assuming that the MC has an average density of $\approx$100 cm^{-3} one can estimate its apparent size as: $\vartheta_{cl} \approx 1^\circ M_5^{1/3}/d_{\rm kpc}$. MCs characterized by $\delta = 1$ (i.e. no CR overdensity with respect to the CR background) have been often referred to as *passive* clouds [69], to indicate the absence of particle acceleration inside or in the vicinity of the cloud.

From the discussion above it follows that: (i) MCs are expected to be quite extended TeV gamma–ray sources, since Cherenkov telescopes have an angular resolution of $\vartheta_{res} \approx 0.1^\circ$, (ii) Cherenkov telescopes of current generation, with an integral sensitivity for point sources of the order of $\Phi(>1\,{\rm TeV}) \approx 10^{-12}$ cm^{-2} s^{-1}, which worsen as $\approx \vartheta_{cl}/\vartheta_{res}$ for extended sources, cannot detect passive MCs unless they are much more massive than $10^5 M_\odot$ and/or very close to the Earth, (iii) the future TeV gamma–ray facility CTA, the Cherenkov Telescope Array, will improve the sensitivity by a factor of 5–10 and will be able to detect passive clouds with masses $\gtrsim 10^5 M_\odot$ only if they are located within a distance of $\lesssim$1 kpc or so [70].

If the assumption $\delta = 1$ is relaxed, and gamma rays are detected from a MC, Eq. 3 can be used to determine the actual value of δ at the location of the cloud, provided that the mass and distance of the MC are known. If not only the intensity of CRs, but also their spectral distribution differs from the local one, δ becomes

an energy dependent quantity. Overdensities of CRs of the order of $\delta > 10$, or masses well above $10^5 M_\odot$ are needed in order to detect TeV photons from MCs with telescopes of present generation. This is illustrated with a few examples below.

The molecular cloud complex located in the inner Galaxy and named *galactic centre ridge* has been detected by H.E.S.S. [71] as a diffuse TeV emission extending for $\approx 1^\circ$ or so around the galactic centre. The spatial distribution of the gamma–ray emission correlates well with the gas density in the region, which is derived from the observations of the CS emission line [72]. This suggests that the emission is of hadronic origin, the dense gas being the target for CR interactions. A detection has been possible because the large distance of $\approx$8.5 kpc is compensated by the very large gas mass of the complex, equal to a few times $10^7 M_\odot$. The differential spectrum of the gamma–ray emission can be fitted by a power lax with index $\approx$2.3, which indicates that the spectrum of the CRs responsible for that gamma–ray emission is much harder than the CR galactic background, which is $\approx E^{-2.7}$. Moreover, from the measured gamma–ray flux at 1 TeV it can be inferred that the intensity of $\approx$10 TeV CRs in the galactic centre region is enhanced by a factor of $\approx 3 \ldots 10$ with respect to the background. The hard spectrum, coupled with the enhanced intensity of CRs implies that some recent event of particle acceleration took place in that region.

Another similar example is represented by the massive MCs located in the vicinity of the SNR W28 [62]. These clouds have a total mass of $\approx 10^5 M_\odot$ and the system (SNR and MCs) is located at a distance of $\approx$2 kpc. The MCs have been detected in TeV gamma rays by H.E.S.S. and a CR overdensity of the order of $\delta \approx 10 \ldots 30$ has been inferred. As it will be discussed in Sect. 6, the most natural interpretation of that emission is that the CRs in excess of the background have been accelerated by the SNR W28, have escaped the site of acceleration and are still diffusively confined in the region. The enhanced intensity of CRs coupled with the presence of the dense clouds can explain the observed gamma–ray emission.

In the GeV energy domain these kind of studies are more difficult because of the worse angular resolution (a fraction of a degree) of current instruments and most of all because of the very intense diffuse emission from the galactic disk that constitutes an important background in the search of gamma–ray sources. However, studies of the diffuse emission and of prominent clouds or cloud complexes remain feasible, and could provide information on the large scale distribution of CRs (see e.g. [73]). The Fermi collaboration performed a study of the diffuse emission from some specific regions in the galactic plane characterized by the presence of dense gas, like the Cassiopeia and Cepheus region [74] and the third galactic quadrant, where the Local and Perseus arms can be observed [75]. From the knowledge of the spatial distribution of the gas along the line of sight, the spatial distribution of $\approx$GeV CRs has been inferred. No significant spectral variation up to the outer Galaxy has been found, meaning that the spectrum of $\approx$GeV CRs is, on large galactic scales, quite constant. The CR intensity has been found to have a weak dependence on galactocentric distance, even weaker than the one predicted by standard propagation models such as GALPROP [76]. This means that the CR intensity is not expected to vary a lot (i.e. more than a factor of a few) over galactic scales.

It is clear from the examples described above how gamma–ray observations of MCs can be used to measure the CR intensity in specific regions of the Galaxy. For this reason, MCs have been sometimes referred to as *CR barometers* and are now considered important tools to locate the position of galactic accelerators of CRs (e.g. [14, 29, 73, 77–79]). In fact, the importance of the gamma–ray emission from MCs was first realized in connection to the estimate of the masses of MCs [66]. These masses are estimated from the intensity of emission lines of some molecules, most notably the carbon monoxide, CO, which is the second most common molecule in the interstellar medium after molecular hydrogen, and it is much easier to detect. The line intensity gives the mass of the CO in the cloud, which can be converted to the total mass, largely dominated by molecular hydrogen, through a conversion factor, X_{CO}, which unfortunately is not very well constrained [80]. The idea to use gamma–rays to estimate the mass of MCs is based on the assumption of spatial homogeneity of CRs in the Galaxy, which would allow to use the gamma–ray flux observed from MCs to calibrate the X_{CO} conversion factor. This can be easily understood from Eq. 3 with $\delta = 1$. Very recently, the Fermi collaboration performed a study of the massive and nearby Orion MCs [81] and obtained interesting constraints on the value of X_{CO}, pointing towards a non–linear relation between the densities of carbon monoxide and molecular hydrogen.

Thus, it is clear from what said above that gamma–ray bright MCs can be used as CR barometers with one main caveat: the uncertainty on the value of X_{CO}, which is used to determine the mass of the cloud, translates in an uncertainty on the value inferred for the CR overdensity δ from the gamma–ray flux of the cloud. Despite that, MCs can still be used to measure variations in the CR intensity in the Galaxy. First of all, spectral measurements are not affected by the uncertainty in the determination of the mass. As an example, the hard gamma–ray spectrum observed from the galactic centre ridge implies that the CRs that produce that gamma–ray emission have a different spectrum, and thus intensity, with respect to the galactic CR background. Second, large overdensities of CRs of the order of a few tens, as the one inferred for the clouds in the vicinity of the SNR W28, can hardly be ascribed solely to an erroneous determination of the mass of the cloud.

One last issue that needs to be discussed concerns the penetration of CRs into MCs. So far, it has been implicitly assumed that CRs can freely penetrate MCs and that the CR intensity inside a cloud is equal to the one immediately outside. In fact, this assumption is valid only when the time it takes CRs to diffuse across the cloud is shorter than the CR energy loss time (see e.g. [82]).

To check whether this is true or not, in the left panel of Fig. 1 [83] the characteristic time scales for diffusion and energy losses have been plotted as a function of the particle energy for a giant molecular cloud with total mass $M_{cl} = 10^5 M_\odot$ and radius $R_{cl} = 20$ pc. Assuming a flat density profile the density is $n_{gas} \sim 120\,\mathrm{cm}^{-3}$. The magnetic field is assumed to be $B_{cl} = 20\,\mu\mathrm{G}$. The dotted line refers to proton energy losses, which are dominated by ionization losses at energies below $\sim$1 GeV and by inelastic proton–proton interactions at higher energies. The solid line represents the electron energy loss time. The three different power law behaviors reflect the dominance of ionization, Bremsstrahlung and synchrotron

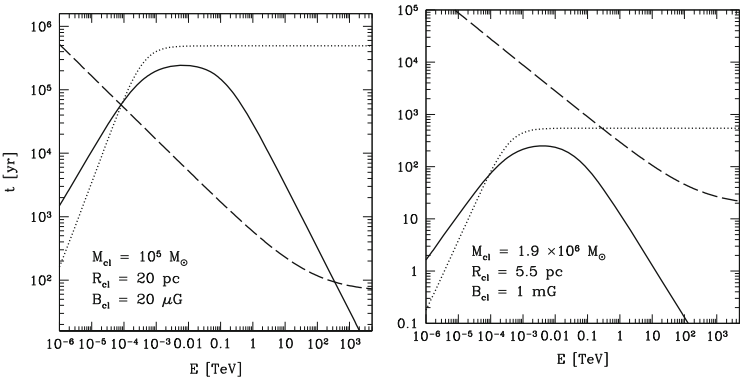

Fig. 1 *Left panel*: relevant time scales for CR propagation inside a molecular cloud with mass $M_{cl} = 10^5 M_\odot$, radius $R_{cl} = 20$ pc, and magnetic field 20 μG. Assuming a flat density profile the density is $\sim 120\,\mathrm{cm}^{-3}$. The *dashed line* represents the CR propagation time scale over a distance R_{cl}. The *dotted line* represents the energy loss time for CR protons (ionization losses are relevant below 1 GeV, inelastic proton-proton interaction at higher energies) while the *solid line* refers to the energy loss time for CR electrons, including ionization losses, Bremsstrahlung losses and synchrotron losses, which dominate at low, intermediate and high energies respectively. *Right panel*: same as the *left panel*, but for the specific case of the SgrB2 cloud with mass $1.9 \times 10^6 M_\odot$, radius 5.5 pc and magnetic field 1 mG. This implies an average density of $1.1 \times 10^5\,\mathrm{cm}^{-3}$ (see text for an explanation of the choice of parameters adopted) (Figure from [83])

losses at low, intermediate and high energies, respectively. Finally, the dashed line represents the propagation time over a distance equal to the cloud radius. The propagation time has been estimated as $t_d \approx R_{cl}^2/(6\,D)$ with a diffusion coefficient equal to $D = 10^{28}(E/10\ \mathrm{GeV})^{0.5}\ (B/3\,\mu\mathrm{G})^{-0.5}\ \mathrm{cm}^2/\mathrm{s}$, a value consistent with CR data. The deviation from a power law behavior at high energies indicates the transition from a diffusive to a straight line propagation.

For proton energies above the threshold for pion production ($E_{th} \sim 280$ MeV), the propagation time is always shorter than the energy loss time. This means that CR protons which produce both gamma rays and secondary electrons can freely penetrate the cloud and their flux is not attenuated due to energy losses. The propagation time for CR electrons is also shorter than the energy loss time for particle energies between $E \sim 100$ MeV and a few hundreds of TeV. This implies that, within this energy range, the secondary electrons produced inside the cloud quickly escape, and have little effect on the non-thermal emission from the cloud. On the other hand, extremely energetic electrons with energies above a few hundreds TeVs radiate all their energy in form of synchrotron photons before leaving the cloud. In a typical magnetic field of a few tens of microGauss, these electrons emit synchrotron photons with energy: $E_{syn} \approx 1(B_{cl}/10\ \mu\mathrm{G})(E/100\ \mathrm{TeV})^2$ keV. Thus, the most relevant contribution from secondary electrons to the cloud non thermal emission falls in the hard X-ray band.

The properties of giant molecular clouds located in the galactic centre region can differ significantly from the average figures reported above. As an example, we plot in the right panel of Fig. 1 the typical time scales for the SgrB2 cloud. This is a very massive cloud located at 100 pc (projected distance) from the galactic centre. The cloud virial mass is $M_{SgrB2} = 1.9 \times 10^6 M_\odot$ [84] and a magnetic field at the milliGauss level has been measured in the outer envelope of the cloud complex [85]. The mass distribution can be fitted with a radial gaussian density profile with $\sigma = 2.75$ pc [84]. To compute the curves plotted in Fig. 1 (right panel), we assumed a cloud radius of $R_{SgrB2} = 2\sigma = 5.5$ pc, which encloses $\approx$95 % of the total cloud mass. This gives an average density of $n_{gas} = 1.1 \times 10^5\,\mathrm{cm}^{-3}$ (roughly a factor of 2 below the central density). It is evident from the right panel of Fig. 1 that the SgrB2 cloud is remarkably different from a typical giant molecular cloud. In particular, the very high values of the magnetic field and of the gas density make the energy loss time of CR protons significantly shorter than the propagation time for energies below a few hundred GeVs. Moreover, for CR electrons the energy loss time is always shorter than the propagation time. This means that CR protons with energies up to few hundred GeVs cannot penetrate the molecular cloud, as they do in the cases considered in the left panel of Fig. 1. Primary CR electrons cannot penetrate the cloud, while secondary CR electrons produced inside the cloud in hadronic interactions cannot leave the cloud and radiate all their energy close to their production site. These characteristics make SgrB2 a very peculiar objects whose modeling needs a specific treatment.

A detailed study of the effects of CRs exclusion from giant MCs on their gamma ray emission have been discussed in detail in [82] and the main results can be summarized as follows: CRs are expected to penetrate freely giant MCs unless the diffusion coefficient inside the cloud is substantially reduced (i.e. at least a factor of 100…1,000) with respect to the average galactic one. An exception to this is the SgrB2 MC, characterized by an unusually large mass and density which would prevent CRs penetration due to strongly enhanced energy losses.

Now that the issue of the CR penetration inside MCs has been addressed, it is possible to discuss the situation in which a MC is located in the vicinity of a CR accelerator, and attempt to predict the gamma–ray spectrum resulting from the interactions between the CRs that escaped the accelerator and the dense gas in the cloud. As stressed above, the detection of such emission can be used to locate the sources of CRs, but also to study their propagation properties on spatial scales of the order of the distance between the CR source and the MC.

4 Molecular Clouds/Supernova Remnant Associations: Expected Cosmic-Ray and Gamma-Ray Spectra

After escaping the acceleration site (e.g. a SNR shock), CRs interact with the ambient gas and produce neutral pions that in turn decay into gamma rays. The production of such radiation is enhanced if a large amount of dense gas (e.g. a

massive MC) is present in the vicinity of the source of CRs. The CR background in the Galaxy has a steep differential spectrum with slope $s \approx 2.7$ and an energy density equal to $E^2 N_{CR}(E) \approx 6 \times 10^{-3} (E/\mathrm{TeV})^{-0.7} \mathrm{eV\ cm^{-3}}$. Due to the steepness of the spectrum, an excess in the CR intensity with respect to the CR background would appear more easily at higher ($\approx$TeV) than at lower ($\approx$GeV) energies. For this reason we focus here on the energy domain probed by Cherenkov instruments, which corresponds to photon energies $\gtrsim 100\,\mathrm{GeV}$.

To be more specific, consider now a SNR which releases in a single impulsive event $\approx 10^{50}\ W_{50}\,\mathrm{erg}$ of CRs protons in the interstellar medium, with a differential spectrum $N_{SNR}(E) \propto E^{-\alpha}$. If we assume that SNRs indeed are the sources of galactic CRs, then we know from the constraints coming from CR data (see Sect. 1) that, on average, $W_{50} \approx 1$ and α has to be in the range $\approx 2.1 \ldots 2.4$. For example, for a CR spectrum with slope 2.4 this corresponds to a total differential spectrum equal to: $E^2 N_{SNR}(E) \approx 2 \times 10^{60} W_{50} (E/\mathrm{TeV})^{-0.4}\,\mathrm{eV}$. If CR diffusion proceeds isotropically, at a given time t after escaping the SNR particles with a given energy E occupy (roughly uniformly) a spherical region of radius $R \approx \sqrt{6\,D(E)\,t}$ surrounding the SNR, where D is the diffusion coefficient. It follows that the energy density of runaway CRs with an energy of 1 TeV exceeds the one in the background if CRs have propagated up to a distance $R_* \lesssim 140\ W_{50}^{1/3}$ pc from their source. If one takes $D_{gal} = 10^{29}\,\mathrm{cm^2/s}$ as a reference value for the galactic diffusion coefficient of CRs with energy of 1 TeV, then the time on which an excess of CRs is present around the SNR is $t_* \approx R_*^2/(6\,D_{gal}) \approx 10^4$ year. Therefore, the search for gamma ray emission from molecular clouds located close to SNRs has to be focused on regions of size 100–200 pc around SNRs not much older than $\approx 10^4$ years. These figures, together with the spectrum and the intensity of the gamma–ray emission, change if the diffusion coefficient in the vicinity of the SNR differs significantly from its average value D_{gal}, and this suggests that these kind of studies might be used to constrain the diffusion properties of CRs close to their sources. This is very important, because from CR data only a value of the diffusion coefficient averaged over a large volume in the Galaxy can be inferred, and little is known on its spatial variations on small scales.

One reason to expect a smaller diffusion coefficient close to CR sources is connected to the presence of the CRs themselves. This is because CRs that escape the source can generate magnetic turbulence via streaming instability and such turbulence can in turn confine CRs, reducing the diffusion coefficient [86–88]. Under these circumstances, the CR diffusion becomes a non–linear process [89,90]. It follows that observational constraints on the diffusion coefficient can shed light on the plasma instabilities through which CRs generate magnetic turbulence.

Following [29], we consider two different scenarios for the escape and propagation of CRs away from the source: in the first one CRs are released in the interstellar medium in a single impulsive event occurring at a time $t = 0$, while in the second one CRs are continuously released over a time interval Δt. In a rough approximation, these two scenarios describe two possible (and opposite) ways in which SNRs may release CRs in the interstellar medium: in an almost impulsive

event at some stage of the dynamical evolution of the SNR, or continuously over an extended time interval (e.g. the whole Sedov phase). These two extreme and definitely idealized scenarios should account for our little knowledge on the actual way in which CRs escape SNRs [45].

In both scenarios, the propagation of CR protons in the interstellar medium can be described by the diffusion equation:

$$\frac{\partial f}{\partial t} = D\,\nabla^2 f + Q \tag{4}$$

where $f(E, R, t)$ is the differential energy distribution of CRs at a given time t and at a distance R from the source, $D(E) \propto E^{-\delta}$ is the CR diffusion coefficient, assumed to be isotropic and spatially homogeneous, and $Q(E, R, t)$ is the CR injection term. Energy losses have been neglected because, as can be estimated from Eq. 1, for the typical densities of the interstellar medium the energy loss time far exceeds the CR confinement time in the Galaxy. Moreover, we do not consider here CR electrons because they are expected to suffer severe synchrotron losses at the SNR shock. Such strong energy losses might prevent them to escape the shock until the very late phases of the SNR evolution.

For an impulsive injection of CRs in the interstellar medium, the injection term reads: $Q = N_{SNR}(E)\delta(R)\delta(t)$, where we have assumed a point like source. Here, $N_{SNR}(E) \propto E^{-\alpha}$ represents the number of particles of energy E which escape the SNR and is normalized to $\int \mathrm{d}E\; N_{SNR}(E)\; E = W_{CR}$, where $W_{CR} = 10^{50}\; W_{50}$ erg is the total energy in form of escaping CRs. Under these assumptions the solution of Eq. 4 is [29]:

$$f(E, R, t) = \frac{N_{SNR}(E)}{\pi^{3/2} R_d^3} \exp\left[-\left(\frac{R}{R_d}\right)^2\right] \tag{5}$$

where $R_d = \sqrt{4\,D\,t}$ is a characteristic diffusion distance, i.e. the distance that particles with energy E can cover in a time t. Thus, if we consider a specific energy E, for distances smaller than R_d Eq. 5 can be approximate, neglecting factors of order unity, as: $f \approx W_{CR}/R_d^3$ which means that CRs are distributed roughly homogeneously within a spherical region of radius R_d. If a MC is located at a given distance $d_{SNR/MC}$ from the SNR, by using the definition of the diffusion distance R_d it is possible to estimate the minimum energy E_* of CRs that can diffuse up to the cloud in a time t: $d_{SNR/MC} = \sqrt{4\,D(E_*)\,t}$. This means that for energies well above E_* the CR energy spectrum is a power law $f \propto N_{SNR}(E)/D(E)^{3/2} \propto E^{-\alpha-3\delta/2}$, while a sharp low energy cutoff suppress the spectrum below E_*. Then, for photon energies above $E_\gamma^* \approx 0.1 E_*$, the neutral pion decay gamma–ray spectrum from the cloud exhibit the same spectral shape as the CR spectrum, while below that energy one expects to see a spectrum close to the one produced by a monoenergetic distribution of protons, which is flat: $\propto E_\gamma^0$ [26–28].

To describe a continuous injection of CRs, the appropriate injection term is: $Q = Q_{SNR}(E)\delta(R)$, with $Q_{SNR} \propto E^{-\alpha}$ as the injection spectrum. Assuming that the injection lasts for a sufficiently long time, the steady state solution of Eq. 4 can be found and reads:

$$f(E, R) = \frac{Q_{SNR}(E)}{4\pi D(E) R} \tag{6}$$

Thus, in this case CRs are not uniformly distributed but their intensity decreases with the distance from the source as $\propto 1/R$ and their spectrum is $\propto E^{-\alpha-\delta}$. The steady state solution is applicable when the duration of the injection is much longer than the diffusion time of CRs $t \approx R^2/(6\ D)$. Considerations similar to the ones made for the impulsive source can be made to infer the spectral shape of the gamma rays produced by the runaway CRs.

It must be remembered that, when computing the gamma–ray emission from a MC located in the vicinity of a CR accelerator, also the (unavoidable!) contribution from the CR background has to be considered. This would add a soft and steady component to the gamma–ray emission which would often dominate the emission in the GeV energy range.

In [83], the gamma–ray spectrum due to proton–proton interactions in a MC was computed for different distances from a nearby SNR and for different times after the supernova explosion. In these work, the SNR is assumed to inject $\approx 3 \times 10^{50}$ erg in form of CRs, with a spectrum $\propto E^{-2}$. To mimic an energy dependent escape of particles from the SNR, particles of energy E are assumed to escape after a time $t_{esc} \propto E^{-\omega}$, with ω chosen in a way to have particles with energy 4×10^{15} eV (the CR knee) escaping the SNR at the beginning of the Sedov phase, and particles with energy 1 GeV escaping at the end of the Sedov phase. Thus, the CR distribution around the SNR can still be described by Eq. 5 with a modified definition of the diffusion distance: $R_d = \sqrt{4\ D(E)\ (t - t_{esc}(E))}$, that takes into account that CRs with different energies are released at different times.

The main finding is that concave gamma–ray spectra may be produced in a MC located in proximity of a SNR, as the result of the decay of neutral pions produced in CR interactions. Such concavity reflects the shape of the underlying CR spectrum, which consists of the superposition of two components: the galactic CR background, characterized by a steep spectrum, and the CRs coming from the nearby SNR, which exhibit a hard spectrum. With this respect, the distance between the SNR and the MC $d_{SNR/MC}$ plays a crucial role. This is because, the larger the distance between the SNR and the cloud, the lower the level of the CR flux coming from the SNR. Moreover, also the time evolution of the emission from a cloud changes with $d_{SNR/MC}$ since the time it takes a particle with given energy to cover such a distance scales as $t \sim d^2_{SNR/MC}/D$, where D is the diffusion coefficient.

In Fig. 2 the total gamma ray spectrum from a MC is shown as a function of the distance between the SNR and the cloud. The cloud mass is $10^5 M_\odot$ and the distance from the SNR is 50, 100, and 200 pc for the left, central and right panel, respectively. The solid, dotted, and dashed lines refer to the emission for 2,000,

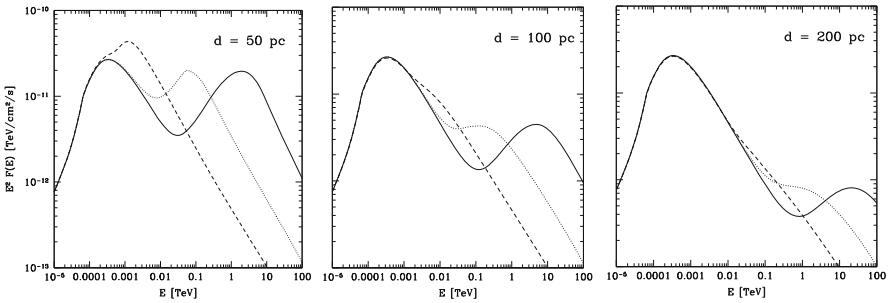

Fig. 2 Total gamma ray emission from a molecular cloud of mass $10^5 M_{\odot}$ located at a distance of 1 kpc. The distance between the MC and the SNR is 50, 100, and 200 pc for *left*, *centre*, and *right panel*, respectively. The *solid*, *dotted*, and *dashed lines* refers to the emission at a time 2,000, 8,000, and 32,000 years after the explosion

8,000, and 32,000 years after the supernova explosion. It is evident from Fig. 2 that a great variety of gamma–ray spectra can be produced. In almost the entirety of the cases considered, the gamma ray–emission is characterized by the presence of two pronounced peaks. The low energy peak, located in the GeV domain is steady in time and it is the result of the decay of neutral pions produced in hadronic interactions of background CRs in the dense intercloud gas. The high energy peak is the result of hadronic interactions of CRs coming from the nearby SNR, and thus it is moving in time to lower and lower energies, as CRs with lower energies can reach the MC at later times. Both the relative intensity and position of the two peaks depend on the distance between the SNR and the cloud. Interestingly, the GeV emission from the cloud is affected by the presence of the nearby SNR only at late times after the explosion and only if the distance from the SNR is comparable or smaller than $\approx$50 pc (see Fig. 2, left panel). In all the other cases the GeV emission is always the result of the interactions of background CRs and thus, at least in this case, observations of molecular clouds in the GeV gamma ray domain cannot be used to infer the presence of a CR accelerator located at a distance greater that $\approx$50 pc from the cloud.

Besides the results described above, a large amount of theoretical and phenomenological work has been carried out by several research groups in order to describe the gamma–ray emission from SNR/MC associations, and the reader is referred to e.g. [91–93] for a list of relevant publications.

In the next Sections, the results derived here will be applied to two scenarios. In Sect. 5 it will be shown how the detection of multi–TeV gamma rays from MCs can be used to identify the location of CR PeVatrons in the Galaxy, while in Sect. 6 the gamma–ray emission detected from the MCs in the vicinity of the SNR W28 will be modeled and a value for the CR diffusion coefficient will be derived as an output of the modeling.

5 An Application: Gamma–Ray Emission from Molecular Clouds and the Origin of Galactic Cosmic Rays Up to the Knee

As said in the Introduction, if SNRs are the sources of galactic CRs, they have to accelerate them all the way up to the CR knee, at $\sim 4 \times 10^{15}$eV $= 4$ PeV. In other words, they must act as CR PeVatrons. If this is indeed the case, SNRs are expected to emit gamma–rays due to hadronic interactions between the accelerated CRs and the interstellar medium swept up by the shock wave with a spectrum extending up to photon energies of hundreds of TeV.

The detection of a SNR in gamma rays with energies up to hundreds of TeV would constitute a decisive and unambiguous indication of acceleration of PeV protons. Because of the Klein-Nishina effect (e.g. [94]) the efficiency of inverse Compton scattering in this energy band is dramatically reduced. Therefore unlike other energy intervals, the interpretation of gamma-ray observations at these energies is free of confusion and reduces to the only possible mechanism – decay of secondary π^0-meson. Although the potential of the current ground-based instruments for detection of such energetic gamma-rays is limited, it is expected that the next generation arrays of imaging Cherenkov telescopes, exploring a broad energy region extending up to the multi–TeV energy range will become powerful tools for this kind of studies.

It should be noted that the number of SNRs currently bright in >10 TeV gamma rays is expected to be rather limited. Multi–PeV protons can be accelerated only during a relatively short period of the SNR evolution, namely, at the end of the free–expansion phase/beginning of the Sedov phase, when the shock velocity is high enough to allow a sufficiently high acceleration rate. When the SNR enters the Sedov phase, the shock gradually slows down and correspondingly the maximum energy of the particles that can be confined within the SNR decreases. This determines the escape of the most energetic particles from the SNR [42]. Thus, unless our theoretical understanding of particle acceleration at SNR is completely wrong, we should expect an energy spectrum of CR inside the SNR approaching PeV energies only at the beginning of the Sedov phase, typically for a time $\lesssim$1,000 years. When the remnant enters the Sedov phase, the high energy cutoffs in the spectra of both protons and gamma rays gradually moves to lower energies, while the highest energy particles leave the remnant [42].

Here we suggest to search for multi–TeV gamma-rays generated by the CRs that escape the SNR. A molecular cloud located close to the SNR can provide an effective target for production of gamma–rays. The highest energy particles ($\sim$few PeV) escape the shell first. Moreover, they diffuse in the interstellar medium faster than low energy particles. Therefore they arrive first to the cloud, producing there gamma rays with very hard energy spectra. Note that an association of SNRs with clouds is naturally expected, especially in star forming regions [77]. The duration of the gamma-ray emission in this case is determined by the time of propagation of CRs from the SNR to the cloud, which in turn depends on the value

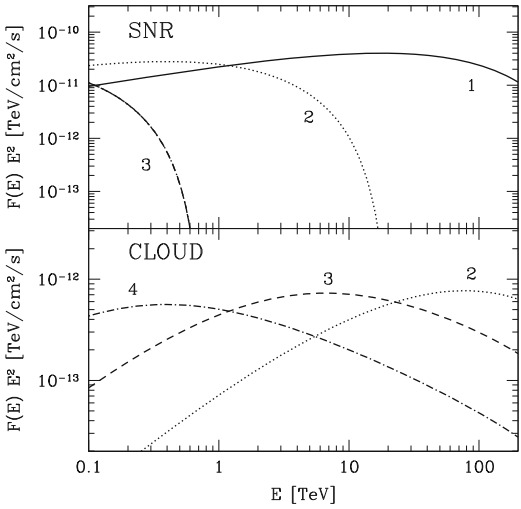

Fig. 3 Gamma–ray spectra from the SNR (*top*) and from a cloud of $10^4 M_\odot$ located 100 pc away from the SNR (*bottom*). The distance is 1 kpc. Curves refer to different times after the explosion: 400 (curve 1), 2,000 (2), 8,000 (3), 3,200 (4) year (Figure from [14])

of the CR diffusion coefficient in the vicinity of the SNR. It is a very well known fact that the CR diffusion coefficient at specific locations in the Galaxy is very poorly constrained from observations, and theoretical predictions are still far from giving solid and reliable estimates for this quantity. However, it is often believed that the CR diffusion coefficient in the vicinity of CR sources might be suppressed with respect to the average galactic one due to CR streaming instability [87, 88]. This CR-induced instability would increase the magnetic turbulence and in turn suppress the diffusion of CRs themselves. Therefore the gamma-ray emission of the cloud may last much longer than the emission of the SNR itself. This makes the detection of delayed gamma-ray signal from clouds more probable. The detection of these multi–TeV gamma-rays from nearby clouds would thus indicate that the nearby SNR in the past was acting as an effective CR PeVatron.

The top panel of Fig. 3 [14] shows the predicted energy spectrum of gamma-ray emission from a SNR produced by interactions of accelerated protons with ambient medium, calculated for typical parameters characterizing SNRs: an explosion energy equal to 10^{51} erg, an ambient density of $1\,\mathrm{cm}^{-3}$ and and initial shock velocity of 10^9 cm/s. The bottom panel shows the emission from a cloud of mass $M_{cl} = 10^4 M_\odot$ located at a distance $d_{cl} = 100$ pc away from the SNR. The distance of the SNR is assumed $D = 1$ kpc and different curves refer to different times after the supernova explosion. The efficiency of CR acceleration at the SNR shock is regulated by the parameter ξ_{CR} (the ratio between the CR pressure at the shock to the shock ram pressure), which is assumed to be equal to 0.3 and constant during the SNR evolution. Finally, we assume a value of the diffusion coefficient equal to $D_{ISM} = 3 \times 10^{29} (E/1\ PeV)^{0.5} \mathrm{cm}^2/\mathrm{s}$, which is significantly suppressed with respect to the extrapolation at PeV energies of the average galactic one, which is measured at much lower energies.

Early in the Sedov phase (curve 1, 400 year after the explosion), the gamma-ray spectrum from the SNR is hard and extends up to $\gtrsim$100 TeV, revealing the acceleration of PeV particles. Conversely, the gamma-ray flux from the cloud is extremely weak, because for the epoch of 400 year after the explosion CRs do not have sufficient time to reach the cloud. The emission of $\gtrsim$100 TeV photons from the SNR lasts a few hundreds years, and after that the cutoff in the gamma-ray spectrum moves to lower energies (curves 2, 3, and 4 correspond to the epochs of 2×10^3, 8×10^3, and 3.2×10^4 year after the explosion). As time passes, CRs finally reach the cloud and produce there gamma rays when interacting with the dense cloud environment. This makes the cloud an effective multi–TeV gamma-ray emitter, with a flux at the sensitivity level of next generation Cherenkov telescopes operating in that energy range. As lower and lower energy particles reach the cloud, the peak of the gamma-ray emission shifts accordingly towards lower energies, first $\approx$TeV, then $\approx$GeV, at flux levels which can be probed by ground based instruments and by Fermi.

As discussed in the previous Section, the shape of the gamma–ray spectrum is naturally explained as follows: at a time t, only particles with energy above E_*, given by $d_{SNR/MC} \approx \sqrt{6 D_{ISM}(E_*) t}$, reach the cloud. Thus the CR spectrum inside the cloud has a sharp low energy cutoff at E_*. The corresponding gamma-ray spectrum exhibits a prominent peak at the energy $\approx 0.1\, E_*$.

The multi-TeV hadronic gamma-ray emission from the cloud is significantly weaker than the one from the SNR, but its detection might be easier because of its longer duration ($\lesssim 10^4$ year versus few hundreds years). Moreover, the leptonic contribution to the cloud emission is likely to be negligible. Electrons accelerated at the SNR cannot reach the cloud because they remain confined in the SNR due to severe synchrotron losses. Secondary electrons can be produced in the cloud, but they cool mainly via synchrotron emission in the cloud magnetic field $\sim 10 \div 100\ \mu G$ [85]. This makes the production of $\gtrsim$TeV gamma rays due to inverse Compton scattering and non–thermal Bremsstrahlung negligible.

To conclude, the acceleration of CRs up to the knee in SNRs can be unambiguously revealed by means of observations of multi-TeV gamma rays and neutrinos coming from the SNR and nearby MCs. The emission from the clouds is weaker than the one from the SNR, but may last much longer, depending on the actual value of the diffusion coefficient, and this might significantly enhance the probability of detection. Gamma rays are emitted with fluxes detectable by currently operating and forthcoming instruments. Since the gamma-ray spectra from clouds are extremely hard, gamma-ray telescopes operating up to very high energies ($\gtrsim$10 TeV), like the Cherenkov Telescope Array, would be the best instruments for this kind of study.

6 Another Application: Constraining the Diffusion Coefficient in the Region Surrounding the Supernova Remnant W28

W28 is an old SNR in its radiative phase of evolution, located in a region rich of dense molecular gas with average density $\gtrsim 5\,\mathrm{cm}^{-3}$. At an estimated distance of ≈ 2 kpc the SNR shock radius is ≈ 12 pc and its velocity ≈ 80 km/s (see e.g. [95]). By using the dynamical model from [96] and assuming that the mass of the supernova ejecta is $\sim 1.4\,M_\odot$, it is possible to infer the supernova explosion energy ($E_{SN} \approx 0.4 \times 10^{51}$ erg), initial velocity ($\approx$5,500 km/s), and age ($t_{age} \approx 4.4 \times 10^4$ year).

Gamma ray emission has been detected from the region surrounding W28 both at TeV [62] and GeV energies [63, 97], by *HESS*, *FERMI*, and *AGILE*, respectively. The TeV emission correlates quite well with the position of three massive molecular clouds, one of which is interacting with the north-eastern part of the shell (and corresponds to the TeV source HESS J1801-233), and the other two being located to the south of the SNR (TeV sources HESS J1800-240 A and B) . The masses of these clouds can be estimated from CO measurements and result in ≈ 5, 6, and $4 \times 10^4 M_\odot$, respectively, and their projected distances from the centre of the SNR are ≈ 12, 20, and 20 pc, respectively [62]. The GeV emission roughly mimics the TeV one, except for the fact that no significant emission is detected at the position of HESS J1800-240 A.

Here, we investigate the possibility that the gamma ray emission from the W28 region could be the result of hadronic interactions of CRs that have been accelerated in the past at the SNR shock and then escaped in the surrounding medium [98].[3] To do so, we follow the approach described in Sect. 4 and in [83], which we briefly summarize below.

For each particle energy E we solve the diffusion equation for CRs escaping the SNR. For simplicity we treat the SNR as a point like source of CRs and we consider an isotropic and homogeneous diffusion coefficient: $D \propto E^\delta$. A value of $\delta = 0.5$ is found to provide a good fit to data (see below), though reasonably good fits can be obtained also for values in the range $\delta = 0.3 - 0.7$. The solution of the diffusion equation gives the spatial distribution of CRs around the source f_{CR}, which is roughly constant up to a distance equal to the diffusion radius $R_d = \sqrt{4\,D\,t_{diff}}$, and given by $f_{CR} \propto \eta E_{SN}/R_d^3$, where η is the fraction of the supernova explosion energy converted into CRs, and t_{diff} is the time elapsed since CRs with energy E escaped the SNR. For distances much larger than R_d the CR spatial distribution falls like $f_{CR} \propto \exp(-(R/R_d)^2)$, as expected for diffusion (see Eq. 5). Following the approach described in [83], we assume that CRs with energy 5 PeV (1 GeV) escape the SNR at the beginning (end) of the Sedov phase, at a time ~ 250 year ($\sim 1.2 \times 10^4$ year) after the explosion, and that the time integrated CR spectrum injected in the interstellar medium is $\propto E^{-2}$. In this scenario, particles with lower

[3] This scenario has been described in a number of recent papers [99–102].

and lower energies are released gradually in the interstellar medium [42], and we parametrize the escape time as: $t_{esc} \propto E^{-\alpha}$ which, during the Sedov phase, can also be written as $R_s \propto E^{-2\alpha/5}$, where R_s is the shock radius at time t_{esc} and $\alpha \sim 4$. From this it follows that the assumption of point like CR source is good for high energy CRs only ($\sim$TeV or above), when R_s is small, but it becomes a rough approximation at significantly lower energies. This is because low energy particles are believed to be released later in time, when the SNR shock radius is large (i.e. non negligible when compared to R_d).

We now provide a simplified argument to show how we can attempt to constrain the diffusion coefficient by using the TeV gamma ray observations of the MCs in the W28 region. The time elapsed since CRs with a given energy escaped the SNR can be written as: $t_{diff} = t_{age} - t_{esc}$. However, for CRs with energies above 1 TeV (the ones responsible for the emission detected by HESS) we may assume $t_{esc} << t_{age}$ (i.e. high energy CRs are released when the SNR is much younger than it is now) and thus $t_{diff} \sim t_{age}$. Thus, the diffusion radius reduces to $R_d \sim \sqrt{4\ D\ t_{age}}$. We recall that within the diffusion radius the spatial distribution of CRs, f_{CR}, is roughly constant, and proportional to $\eta E_{SN}/R_d^3$. On the other hand, the observed gamma ray flux from each one of the MCs is: $F_\gamma \propto f_{CR} M_{cl}/d^2$, where M_{cl} is the mass of the MC and $d \approx 2$ kpc is the distance of the system. Note that in this expression F_γ is calculated at a photon energy E_γ, while f_{CR} is calculated at a CR energy $E_{CR} \sim 10 \times E_\gamma$, to account for the inelasticity of proton-proton interactions. By using the definitions of f_{CR} and R_d we can finally write the approximate equation, valid within a distance R_d from the SNR:

$$F_\gamma \propto \frac{\eta\ E_{SN}}{(D\ t_{age})^{3/2}} \left(\frac{M_{cl}}{d^2}\right).$$

Estimates can be obtained for all the physical quantities in the equation except for the CR acceleration efficiency η and the local diffusion coefficient D. By fitting the TeV data we can thus attempt to constrain, within the uncertainties given by the errors on the other measured quantities (namely, E_{SN}, t_{age}, M_{cl}, and d) and by the assumptions made (e.g. the CR injection spectrum is assumed to be E^{-2}, while the energy dependence of D is assumed to scale as a power law of index $\delta = 0.5$), a combination of these two parameters (namely $\eta/D^{3/2}$). The fact that the MCs have to be located within a distance R_d from the SNR can be verified a posteriori. Given all the uncertainties above, our results have to be interpreted as a proof of concept of the fact that gamma ray observations of SNR/MC associations can serve as tools to estimate the CR diffusion coefficient. More detection of SNR/MC associations are needed in order to check whether the scenario described here applies to a whole class of objects and not only to a test-case as W28. Future observations from the Cherenkov Telescope Array will most likely solve this issue.

Figure 4 shows a fit to the *HESS* data for the three massive MCs in the W28 region. A simultaneous fit to all the three MCs is obtained by fixing a value for $\eta/D^{3/2}$, which implies that the diffusion coefficient of particle with energy 3 TeV (these are the particles that produce most of the emission observed by *HESS*) is:

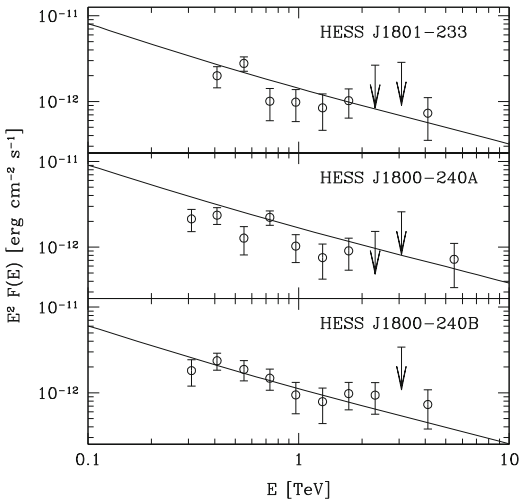

Fig. 4 Simultaneous fit to the three TeV sources detected by HESS in the W28 region. Gamma ray spectra have been calculated by using the parameterizations by Kamae et al. [28], where a multiplicative factor of 1.5 has been applied to account for the contribution to the emission from nuclei heavier than H both in CRs and in the interstellar medium (Figure from [98])

$$D(3\ \mathrm{TeV}) \approx 5 \times 10^{27} \left(\frac{\eta}{0.1}\right)^{2/3} \mathrm{cm}^2/\mathrm{s}\,. \tag{7}$$

This value is significantly smaller (more than an order of magnitude) than the one normally adopted to describe the diffusion of ∼TeV CRs in the galactic disk, which is $\approx 10^{29}$ cm^2/s. This result remains valid (i.e. a suppression of the diffusion coefficient is indeed needed to fit data) even if a different value of the parameter δ is assumed, within the range 0.3…0.7 compatible with CR data. As an example, an acceleration efficiency $\eta = 30\,\%$ corresponds to a CR diffusion coefficient of $D \sim 10^{28}$ cm^2/s, which in turn gives a diffusion distance for 3 TeV particles of $R_d \approx 80$ pc. This means that the results in Fig. 4 are valid if the physical (not projected) distances between the MCs and the SNRs do not significantly exceed R_d. Small values of the diffusion coefficient have been also proposed by Giuliani et al. [97], Fujita et al. [99], Li and Chen [101], and Yan et al. [102]. Note that, since we are considering gamma rays in a quite narrow (about one order of magnitude) energy band around ≈1 TeV, we can actually constrain the diffusion coefficient of CRs with energy ≈3–30 TeV, and we cannot say much about the energy dependence of the diffusion coefficient on a broad energy interval.

In principle, observations by *FERMI* and *AGILE* might be used to constrain the diffusion coefficient down to GeV particle energies. However, in this energy band the uncertainties are more severe because of the following reasons: (i) low energy CRs are believed to be released late in time, when the SNR shock is large, and thus the assumption of point-like source is probably not well justified (see [100] for a model that takes into account the finite size of the SNR); (ii) for the same reason, we can no longer assume that $t_{diff} \sim t_{age}$, as we did for high energy CRs. In other words, we need to know the exact time at which CRs with a given energy escape the SNR. Though some promising theoretical studies exist (see [45] and references therein), our knowledge of the escape time of CRs from SNRs is still quite limited.

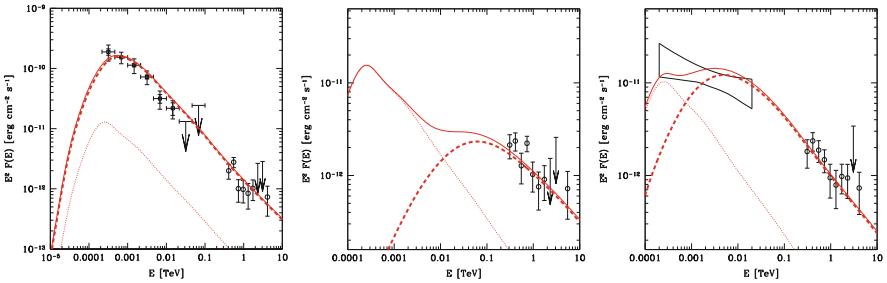

Fig. 5 Broad band fit to the gamma ray emission detected by *FERMI* and *HESS* from the sources HESS J1801-233, HESS J1800-240 A and B (*left* to *right*). *Dashed lines* represent the contribution to the gamma ray emission from CRs that escaped W28, *dotted lines* show the contribution from the CR galactic background, and *solid lines* the total emission. Distances to the SNR centre are 12, 65, and 32 pc (*left* to *right*). *FERMI* and *HESS* data points are plotted in *black*. No GeV emission has been detected from HESS J1800-240 A (Figure from [98])

Figure 5 shows a fit to the broad band gamma ray spectrum measured from *FERMI* and *HESS*. The three panels refers to (left to right) the sources HESS J1801-233, HESS J1800-240 A and B, respectively. Dashed lines represent the contribution to the emission from CRs that escaped from W28, dotted lines the contribution from background CRs, and solid lines the total emission. Since *FERMI* data refers to the emission after background subtraction, dashed lines have to be compared with data points. The (often non-trivial) background subtraction issue might add another source of uncertainty in the comparison between data and predictions. An acceleration efficiency $\eta = 30\,\%$ and a diffusion coefficient $D = 10^{28}$ cm^2/s at 3 TeV have been assumed, while the distance from the SNR centre is assumed to be (left to right) 12, 65, and 32 pc. Keeping in mind all the above mentioned caveats, it is encouraging to see that a qualitative agreement exists between data and predictions also in the GeV band.

Summarizing, we investigated the possibility that the gamma ray emission detected from the MCs in the region of the SNR W28 is produced by CRs that escaped the SNR. This interpretation requires the CR diffusion coefficient in that region to be significantly suppressed with respect to the average galactic one. Such suppression might be the result of an enhancement in the magnetic turbulence due to CR streaming away from the SNR.

7 Conclusions and Future Perspectives

In this paper, it has been shown how gamma–ray observations of MCs can be used to identify the location of the sources of galactic CRs and to constrain the CR diffusion properties close to the sources. Despite encouraging results from both observations and theory, further work is needed to reach a conclusive evidence in favor (or against) the SNR paradigm for the origin of CRs. Hopefully, this will come with the advent of the next generation of gamma–ray instruments, such as CTA.

The main limitations of the approach presented here are probably connected with the oversimplified assumptions made to describe the way in which particles escape from SNR shocks, which is still not well understood (see [45] and references therein for a discussion) and the way in which they diffuse in the interstellar medium.

Of great relevance is the fact that the presence of a MC interacting with the SNR shock can, one one side, amplify the gamma–ray emission from neutral pion decay [103], but also influence and modify the acceleration mechanism of particles at shocks [57, 104, 105], and even have important effects on their escape [58]. All these aspects need to be further investigated.

Moreover, the assumption of isotropic and homogeneous diffusion of CRs close to their sources is certainly an excessive oversimplification. In fact, CR are expected to diffuse preferentially along, parallel to, the magnetic field lines, the perpendicular transport being determined mainly by the wandering of the magnetic field line CRs are attached to [106, 107]. In adition to that, the CR diffusion along the magnetic field lines is most likely a non–linear process, where CRs themselves generate the magnetic turbulence needed to confine them. Some preliminary work including the effects of anisotropic CR diffusion have been recently published [89, 90, 108, 109], and this promises to become one of the most important developments in this field.

Finally, recent measurements of the CR ionization rate in a MC interacting with the shock of the SNR W51C have been presented [110]. These data reveal an enhancement in the CR ionization rate of about two orders of magnitude with respect to standard values. Such an enhancement might be interpreted as the result of the presence of CRs accelerated at the SNR shock. The SNR/MC system has been also detected in TeV gamma rays [111], and the emission is most likely hadronic. Thus, in this particular system CRs can be studied from $\approx$MeV energies (the most relevant for the ionization of the gas) up to multi TeV energies. In the future, studies of this kind will shed light on the acceleration of CRs at shocks and on their escape over an unprecedented energy range.

Acknowledgements I would like to thank the organizers of the Sant Cougat Forum for Astrophysics, Diego Torres and Olaf Reimer, for their invitation. I also acknowledge support from the EU [FP7–grant agr. n°256464] and from ANR [JCJC Programme].

References

1. Berezinskii, V.S., Bulanov, S.V., Dogiel, V.A., Ginzburg, V.L., Ptuskin, V.S.: Astrophysics of cosmic rays. North-Holland, Amsterdam (1990)
2. Gaisser, T.K.: Cosmic rays and particle physics. Cambridge University Press, Cambridge (1990)
3. Schlickeiser, R.: Cosmic ray astrophysics. Springer, Berlin (2002)
4. Longair, M.L.: High energy astrophysics. Cambridge University Press, Cambridge (2011)
5. Baade, W., Zwicky, F.: PNAS 20, 259 (1934)
6. Hillas, A.M.: J. Phys. G: Nucl. Part. Phys. 31, R95 (2005)
7. Krymskii, G.F.: Soviet Physics 22, 327 (1977)
8. Bell, A.R.: MNRAS 182, 147 (1978)

9. Blandford, R.D., Ostriker, J.P.: ApJ Lett. 221, L29 (1978)
10. Koyama, K., et al.: Nature 378, 255 (1995)
11. Reynolds, S.P.: ARA&A 46, 89 (2008)
12. Aharonian, F.A., Buckley, J., Kifune, T., Sinnis, G.: Rep. Prog. Phys. 71, 096901 (2008)
13. Hinton, J.A., Hofmann, W., ARA&A 47, 523 (2009)
14. Gabici, S., Aharonian, F.A.: ApJ Lett. 665, L131 (2007)
15. Strong, A.W., Moskalenko, I.V., Ptuskin, V.S.: ARNPS 57, 285 (2007)
16. Castellina, A., Donato, F., arxiv:1110.2981
17. Parizot, E., Marcowith, A., van der Swaluw, E., Bykov, A.M., Tatischeff, V.: A&A 424, 747 (2004)
18. Dar, A., de Rjula, A.: Phys. Rep. 466, 179 (2008)
19. Bell, A.R.: MNRAS 353, 550 (2004)
20. Bell, A.R., Schure, K.M., Reville, B.: MNRAS 418, 1208 (2011)
21. Zirakashvili, V.N., Ptuskin, V.S.: AIP Conf. Proc. 1085, 336 (2008)
22. Caprioli, D.: to appear in JCAP – arXiv:1206.1360
23. Ptuskin, V.S., Zirakashvili, V.N., Seo, E.-S.: ApJ 718, 31 (2011)
24. Ptuskin, V.S., Jones, F.C., Seo, E.S., Sina, R.: Adv. Space Res. 37, 1909 (2006)
25. Blasi, P., Amato, E.: JCAP 01, 011 (2012)
26. Dermer, C.D.: A&A 157, 223 (1986)
27. Kelner, S.R., Aharonian, F.A., Bugayov, V.V.: Phys. Rev. D 74, 034018 (2006)
28. Kamae, T., Karlsson, N., Mizuno, T., Abe, T., Koi, T.: ApJ 647, 692 (2006)
29. Aharonian, F.A., Atoyan, A.M.: A&A 309, 917 (1996)
30. Hunter, S.D., et al.: ApJ 481, 205 (1997)
31. Ackermann, M., et al.: ApJ 750, 3 (2012)
32. Drury, L.O'C., Aharonian, F.A., Vólk, H.J.: A&A 287, 959 (1994)
33. Naito, T., Takahara, F.: J. Phys. G: Nucl. Part. Phys. 20, 477 (1994)
34. Cristofari, P., Gabici, S., Terrier, R., Casanova, S, Parizot, E., in preparation
35. Bamba, A., Yamazaki, R., Ueno, M., Koyama, K.: ApJ 589, 827 (2003)
36. Vink, J., Laming, J.M.: ApJ 584, 758 (2003)
37. Völk, H.J., Berezhko, E.G., Ksenofontov, L.T.: A&A 433, 229 (2005)
38. Uchiyama, Y., Aharonian, F.A., Tanaka, T., Takahashi, T., Maeda, Y.: Nature 449, 576 (2007)
39. Uchiyama, Y., Aharonian, F.A.: ApJ 677, L105 (2008)
40. Cowsik, R., Sarkar, S.: MNRAS 191, 855 (1980)
41. Atoyan, A.M., Aharonian, F.A., Tuffs, R.J., Vólk, H.J.: A&A 355, 211 (2000)
42. Ptuskin, V.S., Zirakashvili, V.N.: A&A 429, 755 (2005)
43. Ohira, Y., Murase, K., Yamazaki, R.: A&A 513, A17 (2010)
44. Caprioli, D., Amato, E., Blasi, P.: Astropart. Phys. 33, 160 (2010)
45. Gabici, S.: MmSAI 82, 760 (2011)
46. Abdo, A.A., et al.: ApJ 734, 28 (2011)
47. Giordano, F., et al.: ApJ Lett. 744, L2 (2012)
48. Morlino, G., Caprioli, D.: A&A 538, A81 (2012)
49. Tanaka, T., et al.: ApJ Lett. 740, L51 (2011)
50. Abdo, A.A., et al.: ApJ Lett. 710, L92 (2010)
51. Fukui, Y., et al.: ApJ 746, 82 (2012)
52. Inoue, T., Yamazaki, R., Inutsuka, S.-I., Fukui, Y.: ApJ 744, 71 (2012)
53. Atoyan, A., Dermer, C.D.: ApJ Lett. 749, L26 (2012)
54. Ellison, D.C., Patnaude, D.J., Slane, P., Raymond, J.: ApJ 712, 287 (2010)
55. Abdo, A.A., et al.: ApJ Lett. 706, L1 (2009)
56. Abdo, A.A., et al.: Science 327, 1103 (2010)
57. Uchiyama, Y., Blandford, R.D., Funk, S., Tajima, H., Tanaka, T.: ApJ Lett. 723, L122 (2010)
58. Malkov, M.A., Diamond, P.H., Sagdeev, R.Z.: Nature Comm. 2, 194 (2011)
59. Actis, M., et al.: Exp. Astr. 32, 193 (2011)
60. Sinnis, G.: NIMPA 623, 410 (2010)

61. Cao, Z., et al.: 38th COSPAR Scientific Assembly, p. 2 (2010)
62. Aharonian, F.A., et al.: A&A 481, 401 (2008)
63. Abdo, A.A., et al.: ApJ 718, 348 (2010)
64. Uchiyama, Y., et al.: ApJ Lett. 749, L35 (2012)
65. Abdo, A.A., et al.: ApJ 712, 459 (2010)
66. Black, J.H., Fazio, G.G.: ApJ 185, L7 (1973)
67. Aharonian, F.A.: Ap&SS 180, 305 (1991)
68. Mori, M.: Astropart. Phys.: 31, 341 (2009)
69. Aharonian, F.A.: Space Sci. Rev. 99, 187 (2001)
70. Acero, F., et al., for the CTA consortium: Astropart. Phys., in press
71. Aharonian, F.A., et al.: Nature 439, 695 (2006)
72. Tsuboi, M., Handa, T., Ukita, N.: ApJ Suppl. 120, 1 (1999)
73. Casanova, S., et al.: PASJ 62, 769 (2010)
74. Abdo, A.A., et al.: ApJ 710, 133 (2010)
75. Ackermann, M., et al.: ApJ 726, 81 (2011)
76. Strong, A.W., Moskalenko, I.V.: ApJ 509, 212 (1998)
77. Montmerle, T.: ApJ 231, 95 (1979)
78. Issa, M.R., Wolfendale, A.W.: Nature 292, 430 (1981)
79. Rodriguez Marrero, A.Y., Torres, D.F., de Cea del Pozo, E., Reimer, O., Cillis, A.N.: ApJ 689, 213 (2008)
80. Combes, F.: ARA&A 29, 195 (1991)
81. Ackermann, M., et al.: ApJ, in press (arXiv:1207.0616)
82. Gabici, S., Aharonian, F.A., Blasi, P.: Ap&SS 309, 365 (2007)
83. Gabici, S., Aharonian, F.A., Casanova, S.: MNRAS 396, 1629 (2009)
84. Protheroe, R.J., Ott, J., Ekers, R.D., Jones, D.I., Crocker, R.M.: MNRAS 390, 683 (2008)
85. Crutcher, R.M.: ApJ 520, 706 (1999)
86. Kulsrud, R., Pearce, W.P.: ApJ 156, 445 (1969)
87. Wentzel, D.G.: ARA&A 12, 71 (1974)
88. Cesarsky, C.J.: ARA&A 18, 289 (1980)
89. Ptuskin, V.S., Zirakashvili, V.N., Plesser, A.A.: Adv. Space Res. 42, 486 (2008)
90. Malkov, M.A., Diamond, P.H., Sagdeev, R.Z., Aharonian, F.A., Moskalenko, I.V.: arXiv:1207.4728
91. Torres, D.F., Rodriguez Marrero, A.Y., de Cea del Pozo, E.: MNRAS Lett. 387, L59 (2008)
92. Casanova, S., et al.: PASJ 62, 1127 (2010)
93. Ellison, D.C., Slane, P., Patnaude, D.J., Bykov, A.M.: ApJ 744, 39 (2012)
94. Blumenthal, G.R., Gould, R.J.: Rev. Mod. Phys. 42, 237 (1970)
95. Rho, J., Borkowski, K.J.: ApJ 575, 201 (2002)
96. Cioffi, D.F., McKee, C.F., Bertshinger, E.: ApJ 334, 252 (1988)
97. Giuliani, A., et al.: A&A 516, L11 (2010)
98. Gabici, S., Casanova, S., Aharonian, F.A., Rowell, G.: SF2A2010, p313 – arXiv:1009.5291
99. Fujita, Y., Ohira, Y., Tanaka, S.J., Takahara, F.: ApJ Lett. 707, L179 (2009)
100. Ohira, Y., Murase, K., Yamazaki, R.: MNRAS 410, 1577 (2011)
101. Li, H., Chen, Y.: MNRAS Lett. 409, L35 (2010)
102. Yan, H., Lazarian, A., Schlickeiser, R.: ApJ 745, 140 (2012)
103. Aharonian, F.A., Drury, L.O'C., Völk, H.J.: A&A 285, 645 (1994)
104. Drury, L.O'C., Duffy, P., Kirk, J.G.: A&A 309, 1002 (1996)
105. Reville, B., Kirk, J.G., Duffy, P., O'Sullivan, S.: A&A 475, 435 (2007)
106. Jokipii, J.R., Parker, E.N.: ApJ 155, 777 (1969)
107. Casse, F., Lemoine, M., Pelletier, G.: Phys. Rev. D 65, 023002 (2002)
108. Giacinti, G., Kachelriess, M., Semikoz, D.V.: Phys. Rev. Lett. 108, 261101 (2012)
109. Nava, L., Gabici, S.: in preparation
110. Ceccarelli, C., et al.: ApJ Lett. 740, L4 (2011)
111. Aleksić, J., et al.: A&A 541, A13 (2012)

Molecular and Atomic Gas in the Young TeV γ-Ray SNRs RX J1713.7–3946 and RX J0852.0–4622; Evidence for the Hadronic Production of γ-Rays

Yasuo Fukui

Abstract The interstellar molecular clouds are the site of star formation and also the target for the cosmic ray protons to produce γ-rays via the hadronic process. The interstellar atomic gas is enveloping the molecular clouds and may also be dense enough to affect the γ-ray production. In this chapter, some of the basic properties of the interstellar gas both in molecular and atomic forms will be reviewed. Then, it is presented that two young TeV γ-ray SNRs, RX J1713.7–3946 and RX J0852.0–4622, show good spatial correspondence between the γ-rays and the interstellar protons. The good spatial correspondence provides a support for the hadronic origin of the γ-rays in these SNRs. It is emphasized that both molecular and atomic hydrogen plays a role as targets for cosmic ray (CR) protons. The clumpy distribution of the target interstellar medium (ISM) protons is crucial in the interaction of the supernova shocks with the ISM, whereas models with uniform ISM distribution are not viable. Finally, it is suggested that the dense atomic gas without molecules may occupy the dominant part of the dark gas in the local ISM.

1 Introduction

Recent progress in γ-ray imaging of supernova remnants (SNRs) is remarkable. In particular, several γ-ray telescopes, H.E.S.S., VERITAS, MAGIC, Fermi and AGILE, are obtaining high quality γ-ray images of high-energy objects including SNRs and PWNs in the Galaxy in the last decade (e.g., [11, 12, 18, 39, 78]). It was originally suggested in the middle of the twentieth-century that we are able to observe the γ-rays produced by the hadronic interaction between the cosmic ray

Y. Fukui (✉)
Department of Physics, Nagoya University, Furo-cho, Chikusa-ku, Nagoya, 464-8601, Japan
e-mail: fukui@a.phys.nagoya-u.ac.jp

D.F. Torres and O. Reimer (eds.), *Cosmic Rays in Star-Forming Environments*,
Astrophysics and Space Science Proceedings 34, DOI 10.1007/978-3-642-35410-6_17,

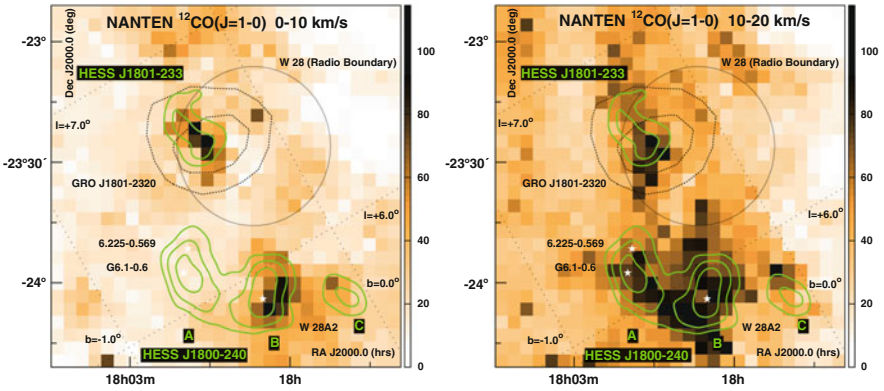

Fig. 1 NANTEN ^{12}CO($J = 1-0$) integrated intensity distribution toward the W28 region (linear scale in K km s^{-1}) with TeV γ-ray significance contours overlaid (*green*) 4, 5, 6σ levels ([4], Fig. 2). The velocity ranges are 0–10 km s^{-1} (*left panel*) and 10–20 km s^{-1} (*right panel*). The radio boundary of W28, GRO J1801–2320 and the location of the HII region W28A2 (*white stars*) are shown in the in the panels

(CR) protons and the interstellar protons which produce neutral pions decaying into γ-rays [37].

The history of observations of the interstellar medium (ISM) spans over more than a half century and observations of the ISM have been made mainly at radio, infrared and optical wavelengths. The HI observations at 21 cm and the CO observations at 2.6 mm provide powerful tools to probe the major neutral component of the ISM. In particular, early CO surveys allowed us to make a comparison between the γ-rays and the molecular protons [19]. The COS-B satellite obtained the γ-ray distribution of the whole sky in the 100 MeV–10 GeV range [50]. The correlation between the γ-rays and CO is good at a degree-scale resolution and was used to derive a X factor ($=N(\mathrm{H}_2)/W(^{12}\mathrm{CO})$) that relates the CO intensity to the proton density [16, 47, 68].

The TeV γ-ray astronomy with ground-based atmospheric Cerenkov telescopes including H.E.S.S. opened a new era by detecting the highest energy γ-rays in the Galaxy. The TeV γ-rays may be produced by the CR protons whose energy is close to the knee and have a potential to probe the highest energy Galactic CRs and the acceleration site. The H.E.S.S. survey of the Galactic plane which detected more than 50 γ-ray sources was compared extensively with the NANTEN CO observations and the region of the W28 SNR was found to show the best spatial correspondence with the TeV γ-rays as shown in Fig. 1 [4]. It however remained as a puzzle why the other γ-ray sources do not show clear correspondence with the CO. For instance, the most remarkable TeV γ-ray SNRs, RX J1713.7–3946 and RX J0852.0–4622, were not identified conclusively to be associated with CO (e.g., [8]). In this chapter, we show that this puzzle has been solved by a careful analysis of the ISM protons including atomic protons.

2 Interstellar Medium

The interstellar medium consists of gas and dust. The mass ratio of the gas and dust is 100:1. The gas is either neutral or ionized. The ionized gas is a minor component in mass, since recombination is rapid in the Galactic disk for the general ionizing UV radiation field from OB stars. Therefore, the neutral gas is the dominant component in mass. The neutral gas is mainly either atomic or molecular hydrogen. Because of the higher cooling rate at higher densities, the denser gas tends to be cooler; the cooling rate is proportional to density squared, whereas the heating rate linearly depends on density.

The atomic gas (HI gas) has a density from 0.1 to 100 cm^{-3} with kinetic temperature from 30 to 3,000 K. It is generally believed that such interstellar medium consists of two dynamically stable phases, either "high temperature and low density" and "low temperature and high density" [67]. It is yet possible that a significant amount of transient HI gas at an intermediate density range exits, since the ISM gas is highly turbulent and far from the dynamically equilibrium (e.g., [46]). It is generally assumed that the HI emission is optically thin as suggested by the non-flat HI line profiles [20], whereas it is possible that there exits opaque HI emission from dense HI. Such HI gas may be important in a shell compressed by the stellar winds in SNRs, although the nature of such HI gas has not been discussed often in the literature.

The molecular gas has density greater than $10^3\,\mathrm{cm}^{-3}$ with typical temperature of 10 K (e.g., [34]). The low temperature is in part due to the efficient molecular cooling and the strong shielding of stellar photons by dust grains. The major heating of the molecular clouds is made by CR protons of a 100 MeV range. The main constituent of the molecular clouds is H_2 but H_2 does not have a radiative transition observable at low temperature of 10 K. We use usually the rotational transition of CO at 2.6 mm wavelength to observe the molecular clouds. The CO transition (rotational quantum number $J = 1 - 0$) can be excited via collision with H_2 at 10 K. H_2 is formed from HI by reactions on dust surface and is then liberated into the interstellar space. There is no reliable tracer for a density range, approximately 100–1,000 cm^{-3}. In this range, CO/H_2 may not be formed yet and HI may be optically thick. It is therefore difficult to see the phase transition from HI to H_2, while future studies may be able to establish CI or CII transitions to trace such a density regime.

The molecular clouds are clumpier than the HI gas and the mass of a molecular cloud ranges from 100 to $10^7\,\mathrm{M}_\odot$. The large clouds having mass greater than $10^5\,\mathrm{M}_\odot$ are called giant molecular clouds (GMCs). The total number of GMCs in the Galaxy is estimated to be 3,000. GMCs are nearly self-gravitating (e.g., [28]). They have long lifetime of a few 10 Myrs [44] and are the formation site of stars of various mass. Ultraviolet radiation and stellar winds of high-mass stars formed in the GMCs ionize and eventually disperse GMCs. Such high-mass stars are the progenitors of SN explosions where the CR rays are accelerated.

3 Gamma-ray SNRs (Supernova Remnants)

The interstellar medium (ISM) is crucial in producing high-energy radiation from supernova remnants. In particular, the protons in the ISM play a role as targets for CR protons to produce γ-rays. CR protons do not emit electromagnetic radiation, whereas a reaction between CR protons and ISM protons produces a neutral pion which decays into two γ-rays. This is the so called hadronic process of γ-ray production and provides a unique probe for the CR protons. Another reaction that produces γ-rays is the leptonic process in which CR electrons energize low energy photons into γ-rays via the inverse Compton effect. Such CR electrons are observed directly via non-thermal synchrotron emission. One of the most important issues related to the γ-ray SNRs is if the γ-rays are produced by the hadronc process or the leptonic process. It is of vital importance to establish the hadronic-origin γ-rays in order to verify the origin of the CRs, a long standing puzzle since 1912 when the CRs were discovered by V. Hess.

If the hadronic process is working, we expect that the spatial distribution of the γ-rays corresponds to that of the ISM protons. Some of the previous efforts however did not find reasonable correspondence between the γ-rays and the ISM in the two most outstanding TeV γ-ray SNRs, RX J1713.7–3946 and RX J0852.0–4622 [6, 8]. These previous works used only mm-wave CO data to estimate the ISM proton distribution. It may however be necessary to include atomic protons also as the target protons if their density is high enough (Sect. 2). We employ the TeV γ-ray observations by H.E.S.S. at angular resolution of 0.1°, as well as the CO and HI data obtained with the NANTEN2 4 m telescope and ATCA (the Australia Telescope Compact Array) combined with the Parkes 64 m telescope, respectively. We present the results of comparisons between the TeV γ-rays and the ISM protons in the two SNRs, RX J1713.7–3946 and RX J0852.0–4622, to demonstrate that the TeV γ-ray distribution well corresponds to the ISM proton distribution where both atomic and molecular protons are taken into account [29, 30].

3.1 RX J1713.7–3946

RX J1713.7–3946 is the brightest TeV γ-ray SNR detected in the Galactic plane survey with H.E.S.S. [5] and is a most promising candidate where the origin of the γ-rays may be established. The γ-rays higher than 10 TeV is detected here, suggesting that the CR protons responsible may have energy close to the knee, 10^{15} eV, if the γ-rays are hadronic. The SNR was discovered in X-rays with ROSAT [57] and soon the X-rays are found to be non-thermal synchrotron emission with no thermal features [45]. TeV γ-rays were first detected by CANGAROO [24] and H.E.S.S. resolved the shell-like TeV γ-ray distribution [3, 6, 7]. Considerable work has been devoted to explore the γ-ray emission mechanisms [1, 2, 6, 12, 22, 23, 25, 43, 54, 56, 60, 70, 80].

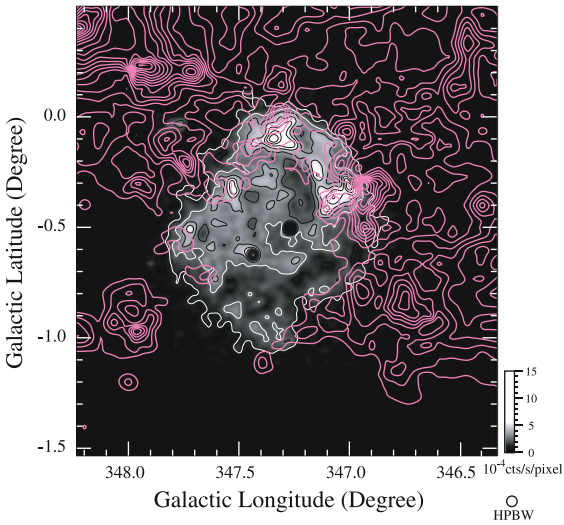

Fig. 2 Overlay map in Galactic coordinates showing a supernova remnant (SNR), RX J1713.7–3946, in gray scale (ROSAT PSPC X-ray Survey [64]; from ROSAT archive database) and the intensity distribution of CO($J = 1 - 0$) emission in *magenta contours*. The intensity is derived by integrating the CO spectra from -11 to $-3\,\mathrm{km\,s^{-1}}$, which is considered to be a velocity component interacting with the SNR. The *lowest contour* level and interval of CO are $4\,\mathrm{K\,km\,s^{-1}}$ [26]

The molecular gas interacting with the SNR was discovered in the CO $J = 1 - 0$ emission in V_{LSR}, the velocity with respect to the local standard of rest, around $-7\,\mathrm{km\,s^{-1}}$. Figure 2 shows that the distribution of the CO emission in RX J1713.7–3946 well correlates with the X-ray distribution [26]; the northwestern rim of the X-ray coincides with the most prominent CO peaks [26, 27, 53, 61]. This X-ray distribution is now interpreted as caused by the interaction between the shock front and the molecular clouds as modeled in the magneto-hydrodynamical (MHD) numerical simulations by Inoue et al. [41]. The correlation provides a robust verification of the physical association of the CO clouds with the SNR shell.

The distance of the SNR was determined to be 1 kpc by using the flat rotation curve of the Galaxy [26]. Studies of X-ray absorption suggested a similar distance 1 kpc under an assumption of uniform foreground gas distribution [45], but the local bubble of HI located by chance toward the SNR makes the X-ray absorption uncertain in estimating the distance [64]. A subsequent careful analysis of the X-ray absorption also favors the smaller distance [17]. At 1 kpc the SNR has a radius of 9 pc and an age of 1,600 years [26, 75] and the expanding shock front has a speed of 3,000 km $\mathrm{s^{-1}}$ [73, 74, 79]. Most recently, [61] showed that the SNR harbors the star forming dense clump peak C (Fig. 3b) and argued that the X-ray intensity is significantly enhanced around the clump due to the shock interaction, reinforcing the association of the molecular gas.

The molecular gas associated with the SNR opened a unique possibility to identify target protons in the hadronic process. We expect the γ-ray distribution mimics that of the interstellar target protons if the hadronic process is working and if the CR distribution is uniform within the SNR. A detailed comparison between the ISM protons and the high-resolution γ-ray image of H.E.S.S. is therefore a useful test of the hadronic scenario.

Figure 3a–c shows the distributions of TeV γ-rays, CO and HI. The velocity range of the interacting gas with the SNR is later confirmed to be -20 to $0\,\mathrm{km\,s^{-1}}$

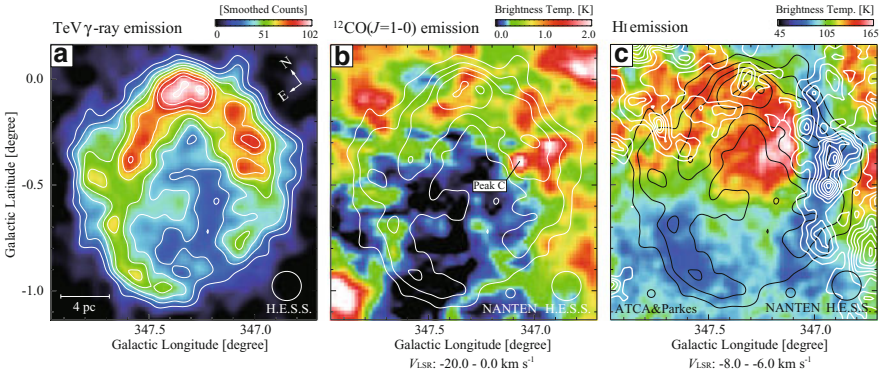

Fig. 3 (**a**) The H.E.S.S. TeV γ-ray distribution of RX J1713.7–3946 in smoothed excess counts above the cosmic-ray background (see Fig. 2 of [7]). Contours are plotted every 10 smoothed counts from 20 smoothed counts. (**b**) Averaged brightness temperature distribution of ^{12}CO($J = 1 - 0$) emission in a velocity range of $V_{\rm LSR} = -20$ to 0 km s^{-1} is shown in color [26, 53]. *White contours* show the H.E.S.S. TeV γ-ray distribution and are plotted every 20 smoothed counts from 20 smoothed counts. (**c**) Averaged brightness temperature distribution of HI emission obtained by ATCA and Parkes in a limited velocity range from $V_{\rm LSR} = -8$ to -6 km s^{-1} [51] is shown in color. *White contours* show the ^{12}CO($J = 1 - 0$) brightness temperature integrated in the same velocity range every 1.0 K km s^{-1} ($\sim 3\sigma$) [29]

and is shown in Fig. 3b [29]. We shall adopt this velocity range hereafter. The TeV γ-rays show a well-defined SNR shell. The CO distribution shows a relatively good correspondence with the TeV γ-rays, whereas in some places the correspondence breaks. The most notable break is seen toward the southeastern rim (SE rim) of the γ-ray shell where no CO is seen. The HI distribution shows that HI is distributed over the entire SNR with a peak in the north, suggesting that a significant amount of HI gas is also associated with the SNR. The HI intensity shows decrease toward the west and southeast in the SNR. The decrease in the west coincides with the CO and represents low-abundance cold HI in the molecular cloud. The decrease in the southeast is different from that, because there is no CO in the SE rim.

Figure 4a shows the HI distribution overlayed on the TeV γ-ray distribution toward the SE rim and Figure 4b shows a typical HI profile and a CO profile in the SE rim at $(l, b) = (347.55°, -0.92°)$. The HI contours show a fairly good correlation with the γ-rays, whereas the HI intensity actually decreases toward the γ-ray enhancements. The HI profile shows a broad dip in a velocity range from -20 to 0 km s^{-1}. We interpret that the dip is due to self-absorption by cool HI associated with the SNR. Such a broad dip is unusual for cold HI dips in typical dark clouds which have generally a narrow linewidth of a few km s^{-1}. In the present case, we ascribe the broad dip as due to the large expanding motion of the HI cavity wall. This HI gas is not seen in CO, indicating that gas density is lower than 10^3 cm^{-3} and that the gas still contains fairly dense HI in the order of 100 cm^{-3} as estimated below. The spin temperature $T_{\rm s}$ of cool HI decreases with density due to the increased atomic line cooling and photon shielding as shown by numerical calculations (e.g.,

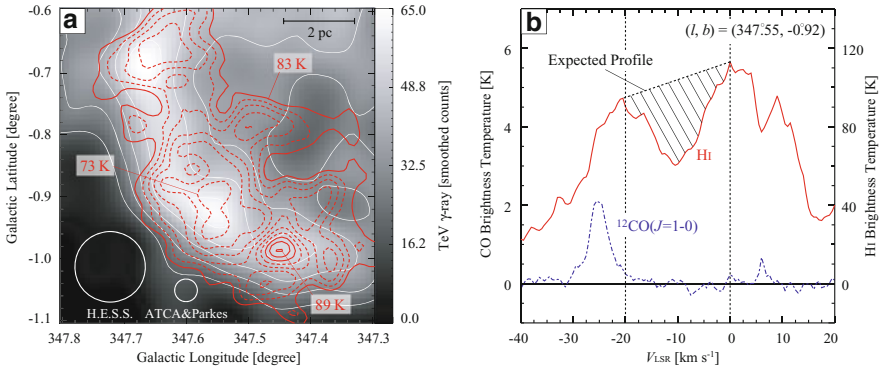

Fig. 4 (**a**) The H.E.S.S. TeV γ-ray distribution toward the SE cloud [7]. *Red contours* show averaged HI brightness temperature distribution in a velocity range from -15 to $-5\,\mathrm{km\,s^{-1}}$ [51]. (**b**) The HI and ^{12}CO($J = 1 - 0$) spectra at $(l, b) = (347.55°, -0.92°)$. The shaded area shows an expected HI profile [29]

Fig. 2 in [35]). This is just consistent with the behavior in Fig. 4a; the decease of the HI brightness indicates higher HI density in the SE rim and the γ-ray count increases with the density increase. By taking reasonable T_s ($\sim$40 K) as inferred from the minimum intensity of HI at the dip bottom, we calculate the HI column density responsible for the self-absorption. Here we adopt a conventional assumption that the background HI emission is interpolated by a straight line (Fig. 4b). We estimate that the HI optical depth is close to 1 and calculate the absorbing HI column density to be $\sim 3 \times 10^{21}\,\mathrm{cm^{-2}}$ (see Fig. 5b), indicating that the SE rim has enhanced HI density. As shown later in Fig. 7, this interpretation of the HI dip is consistent with the visual extinction which also shows enhanced ISM toward the SE rim.

We present below some additional details on derivation of the ISM proton distribution. The molecular column density is calculated by using an X factor to convert the ^{12}CO $J = 1 - 0$ intensity into H_2 column density (Eq. 1) and the error is due to the 3σ noise fluctuations in the CO observations.

$$N(\mathrm{H_2}) = X \cdot W(^{12}\mathrm{CO}) \tag{1}$$

where the X factor, $N(\mathrm{H_2})$ / $W(^{12}\mathrm{CO})(\mathrm{K\,km\,s^{-1}})$, adopted is 2.0×10^{20} $[\mathrm{cm^{-2}/(K\,km\,s^{-1})}]$ (Bertsch et al. 1993). Then, the molecular proton density is given as $N_\mathrm{p}\,(\mathrm{H_2}) = 2N(\mathrm{H_2})$.

The peak HI brightness is usually around 80–100 K in the region except for the regions with HI self-absorption. The brightness is consistent with warm HI with typical spin temperature $T_s \sim$125 K. The atomic proton column density is estimated by assuming that the 21 cm HI line is optically thin as follows [20];

$$N_\mathrm{p}(\mathrm{HI}) = 1.823 \times 10^{18} \int T_\mathrm{b} dV \ \ (\mathrm{cm^{-2}}) \tag{2}$$

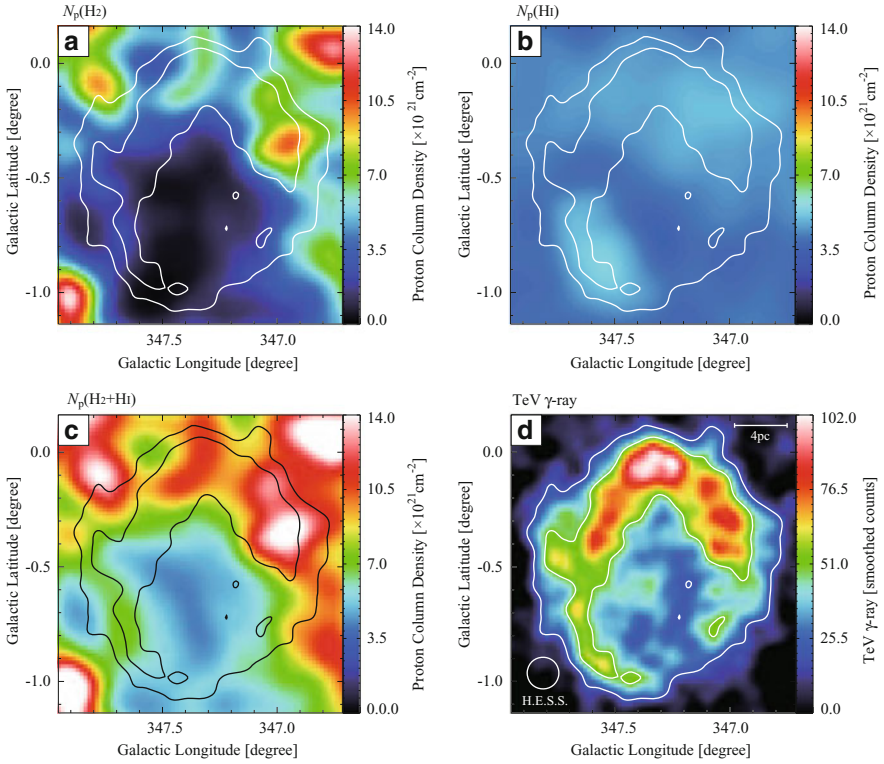

Fig. 5 (**a**) Distributions of column density of ISM protons N_p estimated from ^{12}CO($J = 1 - 0$), $N_p(H_2)$, (**b**) HI emission with correction for the HI self-absorption N_p(H I) and (**c**) $N_p(H_2+HI)$. All the datasets used here are smoothed to HWHM of TeV γ-ray PSH. (**d**) TeV γ-ray distribution. Contours are plotted every 50 smoothed counts from 20 smoothed counts [29]

where T_b (K) and V (km s^{-1}) are the Hz brightness and velocity. The self-absorbing HI column density is added to this in order to obtain the total atomic protons. The noise fluctuations in the HI brightness are very small. The major uncertainty here comes from the uncertainty of T_s of the cool HI and the interpolation of the background HI, but it is smaller than 10^{21} cm^{-2} and do not significantly affect the present estimates of $N_p(H_2+HI)$.

The total ISM proton column density is finally given by the sum as follows;

$$N_p(H_2 + HI) = N_p(H_2) + N_p(HI) \tag{3}$$

The average H_2 density of the CO cloud is around several 100 cm^{-3} and that of the SE rim is around 100 cm^{-3}.

Figure 5 summarizes the results. Figure 5a–d shows $N_p(H_2)$, N_p(HI), $N_p(H_2+HI)$ and TeV γ-rays, respectively. First, we see that there is a significant amount of N_p(HI) (column density is several times 10^{21} cm^{-2}) over the SNR

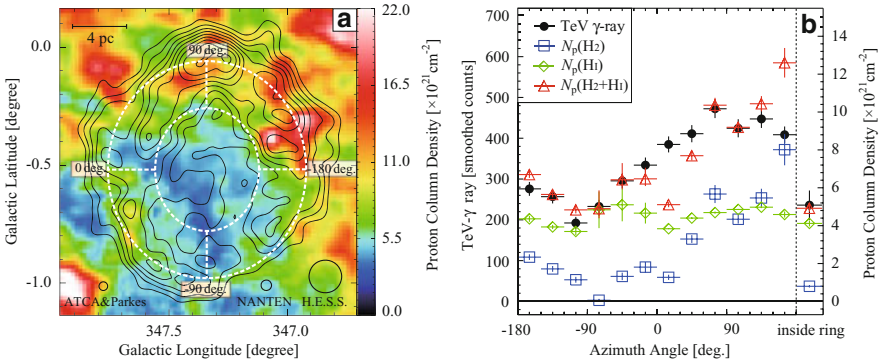

Fig. 6 (**a**) Distributions of column density of the total ISM protons $N_{\rm p}({\rm H_2+HI})$ in a velocity range from -20 to $0\,{\rm km\,s^{-1}}$. Contours are the same as in Fig. 1a. (**b**) Azimuthal distributions of $N_{\rm p}({\rm H_2})$, $N_{\rm p}({\rm HI})$, $N_{\rm p}({\rm H_2+HI})$ and TeV γ-ray smoothed counts per beam between the two elliptical rings shown in Fig. 8a. The proton column densities are averaged values between the rings (see text). Semi-major and semi-minor radii of the outer ring are 0.46° and 0.42°, respectively, and the radii of the inner ring are half of them. The same plots inside the inner ring are shown on the right side of Fig. 8b [29]

particularly toward the SE rim. The total ISM protons show a significant difference by inclusion of the HI and the ISM proton distribution shows a much better correspondence with the γ-ray distribution than the H_2 alone. Figure 6 shows a comparison of the azimuthal angular distribution between $N_{\rm p}$ and γ-rays and we see $N_{\rm p}({\rm H_2+HI})$ shows a good correspondence with the TeV γ-rays. This is the first result which demonstrates a good spatial correspondence between TeV γ-rays and ISM protons at 0.1° angular resolution and proves that a necessary condition for the hadronic scenario is fulfilled in the TeV γ-ray SNR. One of the natural next steps is to extend the method to the other SNRs as shown for RX J0852.0–4622 in the next sub-section.

An important implication of the HI analysis is that the SE rim has enhanced column density in HI as in the TeV γ-rays, whereas the analysis of the HI dip has some uncertainty in $T_{\rm s}$ and the HI background interpolation. In order to make an independent check of the HI column density, we can use other methods to measure the ISM protons. The visual extinction is one of such methods applicable at a distance of 1 kpc. Figure 7a shows that the distribution of the visual extinction is consistent with the HI result in the SE rim, lending another support for the analysis of the HI dip as self-absorption. Figure 7b shows for comparison the sum of the ISM proton distribution including both the foreground ISM protons and those in the SNR. More recently, a new analysis of the Suzaku X-ray data also shows a similar enhanced absorption column density toward the SE rim [63]. Considering all these, we are confident that the $N_{\rm p}({\rm H_2+HI})$ distribution in Fig. 6a is reliable.

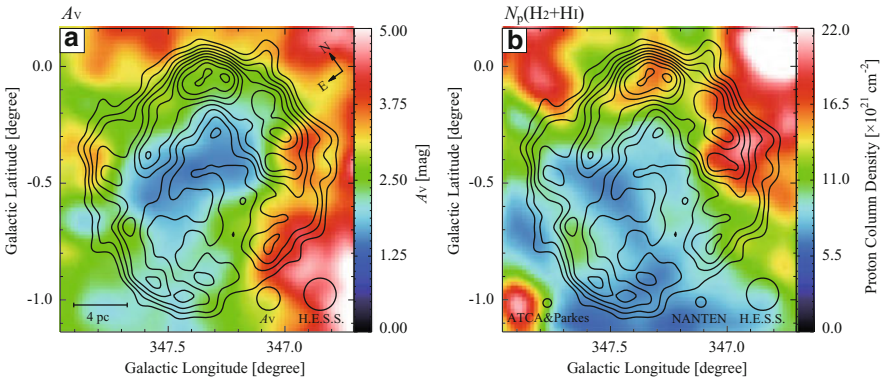

Fig. 7 (**a**)A_V distribution (Dobashi et al. 2005) is shown in color. TeV γ-ray contours are the same as in Fig. 1a. (**b**) Distribution of column density of the total ISM protons estimated from both CO and HI in a velocity range from $V_{LSR} = -20$ to 10 km s^{-1}. Here the HI self-absorption is taken into account. TeV γ-ray contours are the same as in Fig. 1a [29]

3.2 RX J0852.0–4622

RX J0852.0–4622 is another prominent young TeV γ-ray SNR imaged by H.E.S.S. Aschenbach et al. [10] discovered RX J0852.0–4622 as a hard X-ray SNR seen in projection against the Vela SNR in ROSAT All-Sky Survey image. RX J0852.0–4622 and RX J1713.7–3946 share similar properties; they are both young with ages of 1,600–2,000 years and show non-thermal synchrotron shell-like X-ray emission with no thermal features in addition to the strong shell-like TeV γ-rays (Fig. 8a). The apparent large diameter of RX J0852.0–4622, about 2°, is most favorable to test a spatial correspondence between the γ-rays and the ISM at a 0.12° angular resolution (FWHM) of H.E.S.S. There are two more similar shell-like TeV γ-ray SNRs, RCW 86 and HESS J1731–347, but they are small with a size of about 0.5° [9, 40], making it difficult to test the spatial correspondence.

The age and distance of RX J0852.0–4622 have been the subject of debate in the literature. Slane et al. [65, 66] argued that RX J0852.0–4622 is physically associated with the GMC, the Vela Molecular Ridge (VMR, [49, 76]). The distance of the VMR is estimated to be 700 ± 200 pc [48], whereas it is not yet established if the VMR is physically connected to RX J0852.0–4622 (see e.g., [55]). Recently, Katsuda et al. [42] estimated an expansion rate of RX J0852.0–4622 based on two observations separated by 6.5 years made with XMM-Newton toward the northwestern rim of RX J0852.0–4622, and derived an age of 1.7–4.3 $\times$ 10^3 years for the SNR and a distance of 750 pc. We will adopt this distance to RX J0852.0–4622.

In the region of RX J0852.0–4622, the CO clouds are significantly less than in the region of RX J1713.7–3946. This is not surprising since RX J0852.0–4622 is far from the Galactic center where the ISM density is generally lower than in the region of RX J1713.7–3946. Among all the CO features in the direction, we

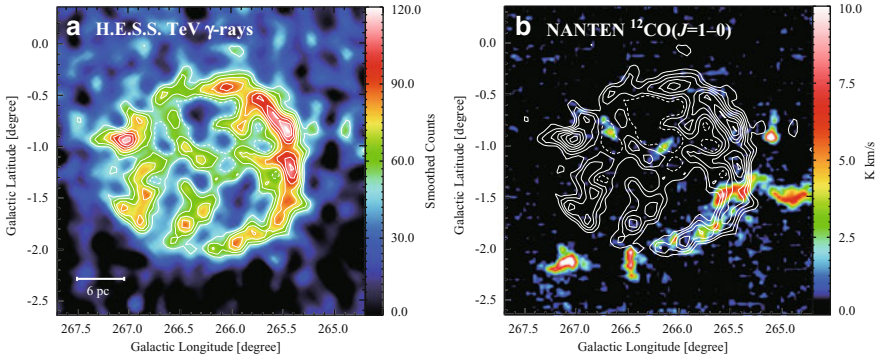

Fig. 8 (**a**) The H.E.S.S. TeV γ-ray distribution of RX J0852.0–4622 in smoothed excess counts (see Fig. 1 of [8]). Contours are plotted every 10 smoothed counts from 50 smoothed counts. (**b**) Integrated intensity distribution of ^{12}CO($J = 1-0$) emission in a velocity range of $V_{\rm LSR} = 24$ to 30 km s^{-1} is shown in color (Moriguchi et al. 2001). *White contours* show the H.E.S.S. TeV γ-ray distribution and are plotted the same as Fig. 8a

find that the CO clouds at 25 km s^{-1} show clear association with the southwestern rim of the SNR (Fig. 8b). Based on this correspondence we have searched for associated CO and HI gas with the SNR shell. Figure 9a shows the total ISM proton distribution in RX J0852.0–4622 derived by combining the associated CO and HI distributions. The velocity range is from 0 to 50 km s^{-1} centered at 25 km s^{-1}, although the Galactic rotation suggests lower velocity less than 10 km s^{-1}. We ascribe this velocity deviation as due to the expansion of a few HI supershells; the SNR RX J0852.0–4622 is located toward an overlapping region among these HI shells and the associated ISM has significant deviation by 50 km s^{-1} at maximum from the pure Galactic rotation. The total associated HI mass is $10^4\,M_\odot$ while that of molecular gas is $10^3\ M_\odot$. So, the associated ISM is dominated by the atomic gas in RX J0852.0–4622. On the other hand, the associated ISM mass in RX J1713.7–3946 is $10^4\ M_\odot$ both in H_2 and HI, respectively. RX J1713.7–3946 is therefore associated with 10 times more molecular gas than RX J0852.0–4622.

We made a Gaussian fitting to the radial TeV γ-ray distribution and determined the best-fit parameters like the radius and width of the shell (Fig. 9a). Figure 9b shows the azimuthal TeV γ-ray distribution [30]. This is obtained by averaging the γ-ray count between the two rings at the 1/3 level of the peak of the Gaussian shell, 0.61° and 0.92° in the radial distribution from the SNR center. The two rings include the major part of the γ-ray shell and Figure 9b represents well the γ-ray azimuthal distribution. We find the correspondence between the total ISM and the TeV γ-rays is reasonably good. This is the second case that shows a good correspondence between the ISM protons and TeV γ-rays. Toward the angle 15° in Fig. 9b there is some excess in the γ-rays. This is due to a PWN located by chance toward this part of the shell, which is not associated with the SNR.

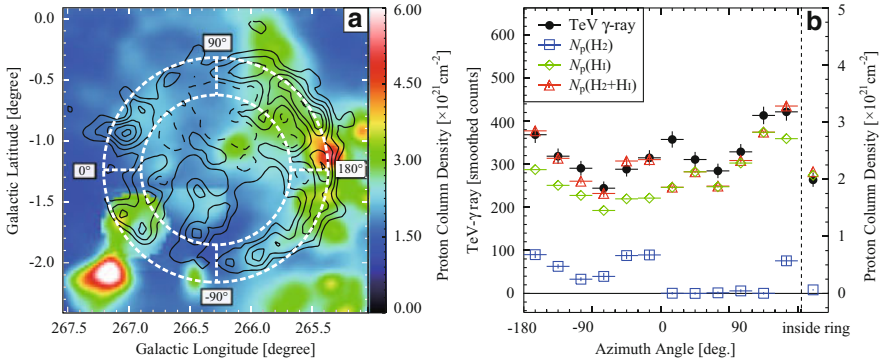

Fig. 9 (**a**) The column density of the ISM proton distribution $N_p(H_2+HI)$ and the contours of TeV γ-rays. The *outer* and *inner circles* are centered at $(l, b) = (266.28°, -1.24°)$ with radii of 0.92° and 0.63°, respectively. (**b**) The azimuthal angles are indicated. The azimuthal distribution of the TeV γ-rays and the ISM protons. The γ-ray counts and the column density of the ISM protons in the two circles in Fig. 9(**a**) are shown at every 30°. The *black dots* show the TeV γ-ray counts and the *blue box* the molecular protons $N_p(H_2)$, the *green box* the atomic protons $N_p(HI)$, and the *red triangle* the total ISM protons $N_p(H_2+HI)$. The right-most point shows the average within the *inner circle* [30]

To summarize this section, we have shown that the ISM proton distribution $N_p(H_2+HI)$ shows a good spatial correspondence with the TeV γ-ray distribution in the two outstanding TeV γ-ray SNRs. This is a step forward in establishing the hadronic origin of γ-rays, whereas the results alone do not reject the leptonic scenario. What remains to be explored is (1) if a leptonic model for the γ-ray production can also explain the observed TeV γ-ray distribution, and (2) if such a hadronic model is consistent with the non-thermal X-ray distribution by the CR electrons.

4 Interaction Between the ISM and the SNR Shock, and the γ-Ray Production

The comparisons between γ-rays and the ISM in the two SNRs in Sect. 3 have led to a picture that the shell-like clumpy ISM consisting of atomic and molecular gas acts as the target for CR protons to produce the hadronic γ-rays. We shall here discuss into more detail the interaction between the SN shock front and the ISM in RX J1713.7–3946. We presume that a similar argument is applicable to RX J0852.0–4622 by considering its properties similar to RX J1713.7–3946 (Sect. 3).

Figure 10a shows a comparison between the non-thermal X-rays and the CO distribution in the northwestern (NW) rim of RX J1713.7–3946 [61]. In the X-ray distribution, the NW rim is particularly intense and this is where the densest CO clumps are located. Figure 10b shows a close-up view toward peak C where a

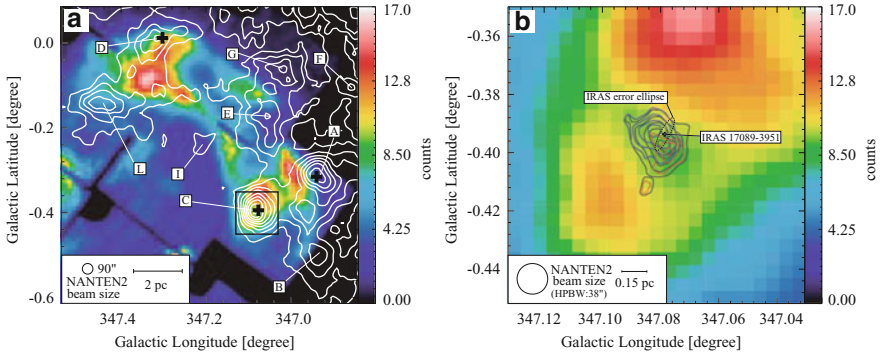

Fig. 10 *Suzaku* XIS (XIS 0 + 2 + 3) mosaic image of RX J1713.7–3946 in the energy bands 1–5 keV in color scale and (**a**) ^{12}CO($J = 2-1$) (**b**) ^{12}CO($J = 4-3$) intensity contours obtained by NANTEN2 ([61], Fig. 5). The area enclosed by the *black box* in (**a**) is shown enlarged in Fig. 9b. Open crosses show the positions of the *IRAS* point sources

protostar with bipolar outflow is located in the center. Figure 10 shows that the X-rays are correlated with CO at pc scale but is anti-correlated at sub-pc scale as shown by that peak C is located toward the local minimum of the X-rays. This behavior is seen in every CO peak within this SNR [62], offering a hint on the details of the interaction.

The initial ISM distribution prior to the SN explosion consists of a wind-evacuated low-density cavity of $\sim$9 pc radius and the cavity wall consists of around ten dense molecular clumps, the cool and dense HI gas as in the SE rim, and the warm HI (Figs. 10 and 11). The interaction with the SN shock waves is taking place in the last several 100 years as estimated from a ratio of $\sim$3 pc/3,000 km s^{-1}. In such a short time scale it is impossible that the molecular clumps are pushed appreciably in space and it is likely that the neutral gas distribution, in particular the molecular distribution, is not significantly affected by the shock interaction. Some of the dense CO clumps located in the inner part of the shell including peak C are likely overtaken by the shock [61]. In addition, the stellar winds likely have stripped off the lower density envelope of the CO clumps, making a steep density gradient at the clump surface. Such a gradient is in fact observed toward peak C by using the sub-mm transitions of CO to trace the radial molecular density distribution [61].

The SN shock front having 3,000 km s^{-1} expansion velocity interacts with the ambient highly clumpy ISM distribution. Many of the previous works on the shock interaction in the SNR assume that the ISM is uniform in density for simplicity (e.g., [23]). If we assume such uniform ISM, in order to produce the observed γ-rays the ISM density has to be increased to at least 10 cm^{-3}. Then, the uniform model predicts that strong thermal X-rays will be emitted by the heating of the ISM in the shock waves. This creates a serious discrepancy with observations since no thermal X-rays are detected. This was one of the major arguments against the hadronic scenario in the RX J1713.7–3946 (e.g., [23]). While the uniform ISM

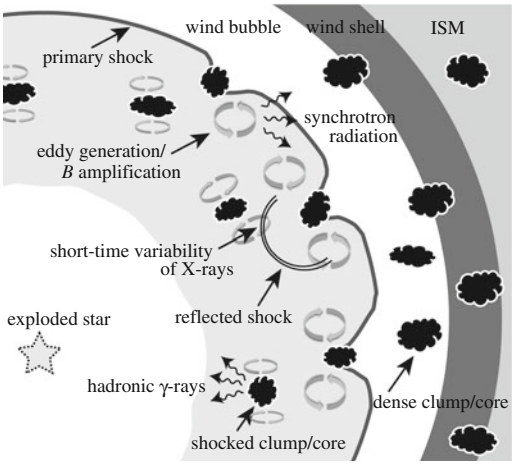

Fig. 11 Schematic picture of the shock-cloud interaction model ([41], Fig. 10). The primary forward shock wave propagates through the cloudy wind bubble, where particle acceleration operates by the diffusive shock acceleration (DSA). The shock waves in the clouds are stalled, which suppresses thermal X-ray line emission. Shock-cloud interactions induce turbulent eddies, which amplifies the magnetic field (∼1 mG) caused by the turbulent dynamo effect and the reverse shocks. Then the synchrotron emissions enhanced around the clouds where magnetic field strength is ∼1 mG around shocked clouds. Also, hadronic γ-rays are emitted from dense clouds illuminated by accelerated protons whose photon index can be $p - 1/2 = 1.5$ for $p = 2$

may be possible as a first approximation, more accurate properties of the interaction strongly depend on the ISM density inhomogeneity. We should therefore adopt more realistic highly inhomogeneous ISM distribution as observed in CO (Fig. 3).

Inoue et al. [41] carried out MHD numerical simulations by considering the clumpy ISM distribution consistent with the observations in RX J1713.7–3946 and discussed the basic aspects of the interaction and the γ-ray and X-ray properties. The interaction between the shock and the CO clumps creates turbulence as simulations indicate (Fig. 12). This turbulence amplifies the magnetic field around the clumps and enhances the synchrotron X-rays. The magnetic field is in the order of 10–100 μG on the average but may be enhanced to the mG order [74]. The shock waves cannot penetrate into the dense molecular clumps and cannot heat them up. This explains the lack of thermal X-rays which happens usually in the other SNRs of lower-density environments. The CR electrons cannot penetrate into the dense clumps since its penetration depth is only in the order of ∼0.1 pc in a given timescale ∼1,000 years [29]. As a result, the X-rays are enhanced around the CO clump but are depressed inside the clumps. This offers an explanation of the pc scale correlation and sub-pc scale anti-correlation between CO and X-rays (Fig. 10). The inside of the cavity is as a whole of very low density due to the stellar winds evacuation, where particle acceleration is efficiently made via diffusive shock acceleration (DSA) to the energy close to the knee (e.g., [11, 15]). CR protons have larger penetration lengths of ∼1 pc than electrons and can interact with the ISM protons inside the

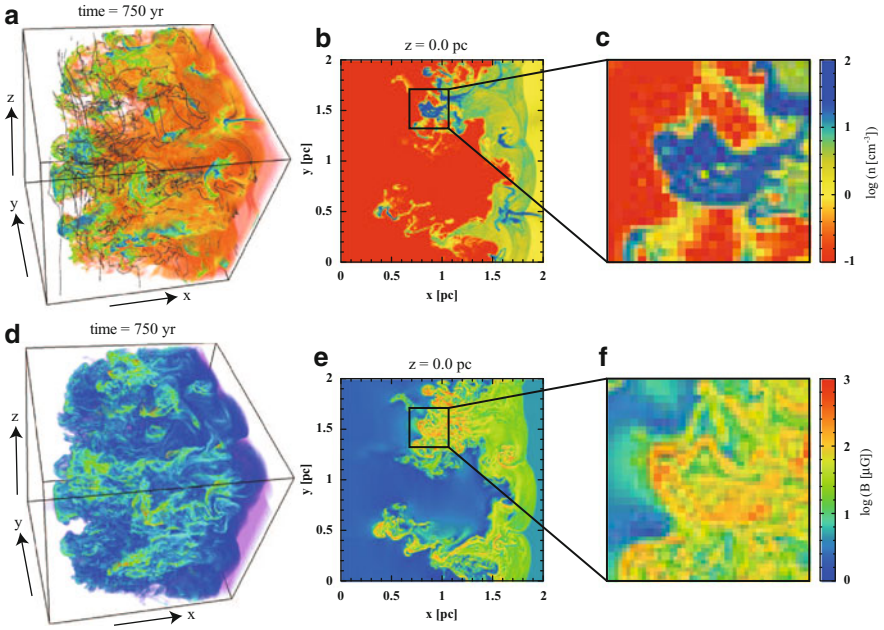

Fig. 12 Results of the numerical simulations between the SN shockwaves on the ISM [41]. The perpendicular shock case at $t = 750$ year after the shock injection [41]. (**a**): number density volume rendering. Regions in *green* and *blue* indicate the density $n \sim 10\,\mathrm{cm}^{-3}$ and $n \geq 30\,\mathrm{cm}^{-3}$, respectively, and the regions in warm colors show the shocked diffuse gas with $n \leq 4\,\mathrm{cm}^{-3}$. Magnetic field lines are represented as *gray lines*. (**b**): two-dimensional number density slice at $z = 0.0\,\mathrm{pc}$. (**c**): close up of the *solid box* in (**b**). (**d**): volume rendering of magnetic field strength. (**e**): slice of magnetic field strength at $z = 0.0\,\mathrm{pc}$. (**f**): close up of the *solid box* in (**e**)

molecular clumps. Such proton-proton reaction explains the γ-ray production and is consistent with the spatial correspondence between the γ-rays and the ISM protons shown in Figs. 6 and 9. The inhomogeneous ISM therefore solves the difficulties in the uniform ISM models by allowing the γ-ray production in the dense clumps as well as the suppression of the thermal X-rays.

In order to have a deeper insight into the γ-ray production, we need to understand the γ-ray energy spectrum. It is usually assumed that CR protons can interact with all the target ISM protons in a SNR, but, to be realistic, penetration of CR protons into the molecular gas is energy dependent for a high density regime like $\sim 10^4\,\mathrm{cm}^{-3}$ or more. The high-energy CR protons can penetrate into the dense clumps, whereas the low-energy protons cannot [31, 80]. This energy dependent penetration makes the lower energy protons interact only with the lower density ISM protons. This reflects in the γ-ray energy spectrum and a harder γ-ray spectrum is expected than in the uniform ISM case.

Figure 13 shows the γ-ray spectrum of RX J1713.7–3946 covering the energy range 10^3–10^8 MeV [1]. This is the combined data of H.E.S.S. and Fermi satellite

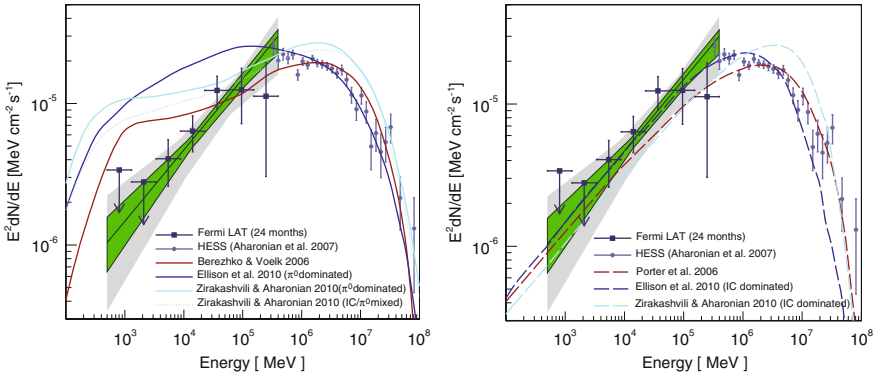

Fig. 13 Energy spectrum and numerical models of RX J1713.7–3946 in GeV to TeV γ-ray spectra taken by the Fermi Large Area Telescope and H.E.S.S. ([1], Fig. 3). Some *solid lines* indicate the numerical model of the hadronic model (π^0-decay spectrum: *left*) and the leptonic model (inverse Compton scattering spectrum: *right*). The *green* region shows the uncertainty band obtained from maximum likelihood fit of the spectrum assuming a power law between 500 MeV and 400 GeV for the default model of the region. The *gray* region depicts the systematic uncertainty of this fit obtained by variation of the background and source models. The *black* error bars correspond to independent fits of the flux of RX J1713.7–3946 in the respective energy bands. *Upper* limits are set at a 95 % confidence level

[1, 7]. RX J1713.7–3946 shows a hard spectrum which is not compatible with the conventional hadronic γ-rays and these authors claimed that the spectrum supports the leptonic scenario. The density- and energy-dependence of the hadronic interaction however indicates that such a hard spectrum is also explained well in the hadronic scenario with highly inhomogeneous ISM distribution as argued into detail by Inoue et al. [41]. Figure 14 shows the γ-ray spectrum in the same energy band with Fig. 13 for RX J0852.0–4622 [71]. This shows a softer spectrum than in Fig. 13 and may be better explained by the hadronic scenario than the leptonic scenario. In connection with the ISM distribution, we note that RX J0852.0–4622 has much less CO clouds than in RX J1713.7–3946. CR protons will therefore interact mainly with the HI gas whose mass is 10 times more than the molecular mass, offering an explanation of the softer spectrum by the hadronic scenario. These two cases suggest that the ISM distribution is crucial in interpreting the γ-ray properties and, in particular, in exploring the hadronic γ-rays.

The identification of target ISM protons in the hadronic scenario allows us to estimate the total CR proton energy $W_{\rm p}$ in these SNRs. By using the relationships which connect the γ-ray counts and the ISM density [6, 7], we estimate that $W_{\rm p}$ is 10^{48} ergs in the two SNRs. This energy corresponds to 0.1 % of the total kinetic energy of a SNR and seems to be ten times less than what is required to explain the CR energy budget of the whole Galaxy. There are a few possibilities to reconcile this discrepancy. The CR energy may yet increase in time with the evolution of a SNR and the total CR energy may become more than estimated above. In W44, a middle-aged SNR, the lower limit of $W_{\rm p}$ is estimated to be 10^{49} erg, ten times

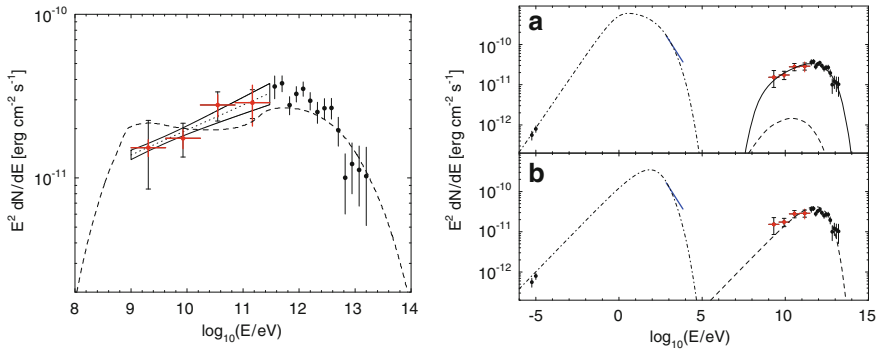

Fig. 14 Energy spectrum and numerical models of RX J0852.0–4622 in GeV to TeV γ-ray spectra taken by the Fermi Large Area Telescope (*red*) and H.E.S.S. (*black*) ([71] Figs. 2 and 3). For the Fermi-LAT points in *left panel*, the *vertical red lines* and the *black caps* indicate statistical and systematic errors, respectively. The *dotted line* shows the best-fit power-law obtained from the maximum likelihood fit for the entire 1–300 GeV band (The butterfly shape is the 68 % confidence region). The *dashed curve* is the π^0-decay spectrum (hadronic model) by Berezhko et al. [13]. Broadband SED of RX J0852.0–4622 with (*a*) the hadronic model and (*b*) the leptonic model. The radio data points and *blue line* indicate the integrated fluxes of the SNR determined based on the 64 m Parkes radio telescope [21] and the the X-ray flux using the ASCA data-set [8]. The *solid*, *dashed*, and *dot-dashed lines* represent contributions from π^0-decays, inverse Compton scattering, and synchrotron radiation, respectively

larger than the present value [12,77]. It is also to be considered that the ISM volume filling factor in a SNR shell may not be 100 %. Particularly, in RX J0852.0–4622 the eastern half of the SNR does not have much ISM, whereas we expect CR protons have a similar number density over the SNR. This suggests that some portion of the CR protons may not be detected in the γ-rays, leading to an under-estimate of W_p by some factor.

In order to better understand the origin of γ-rays in SNRs, we need to have a larger sample of SNRs. A direction is to extend an analysis of the ISM to the middle-aged SNRs like W44, and the other to study smaller TeV γ-ray SNRs like HESS J1731–347 [40]. The latter should be possible with the future instrument CTA at a higher angular resolution of 1 arcmin with higher sensitivity. This will definitely help us to increase the number of samples significantly and provide a better understanding of the γ-ray origin.

5 Dark Gas

An important topic related to the γ-rays originating from the ISM protons is dark gas. The term dark gas is used to represent unseen gas either in HI or CO but is detectable as γ-ray excess [36]. The first observational study of dark gas was made by using the EGRET data toward the local ISM and showed that there is

γ-ray excess, at galactic latitude $5^\circ \leq |b| \leq 80^\circ$, beyond the level which the gas detected by the CO and HI transitions is able to explain. Recently, the Planck satellite provided sensitive mm/sub-mm distributions of the same region and showed that 15 % of the mm/sub-mm dust emission is not explained either by the CO or HI gas [59]. This is also called dark gas. In addition, Planck satellite presents similar dark gas components in the Magellanic Clouds [58]. It is often suggested that dark gas may corresponds to molecular gas with no detectable CO [59], while another possibility discussed is opaque HI gas whose intensity is saturated by moderately large optical depth.

The results of the γ-ray SNR in Sect. 3 suggest that cool HI gas having large optical depth around 1 is responsible for producing part of the γ-rays via the hadronic process. We here discuss that dark gas may correspond to such cool and dense HI gas with relatively large optical depth. Figure 15 shows the HI intensity as a function of HI column density for two spin temperatures $T_s = 100$ and 40 K. The assumption here is that the HI linewidth is $10\,\mathrm{km\,s^{-1}}$. The plot shows that the HI intensity becomes saturated in the HI column density range from 10^{21} to $10^{22}\,\mathrm{cm^{-2}}$. For $T_s = 40$ K, the optical depth of HI is greater than 1 and the typical HI density is around $100\,\mathrm{cm^{-3}}$. These HI column densities correspond to that of the dark gas observed by Planck and we suggest that the purely atomic dense gas is a viable alternative to CO-free molecular gas to explain the dark gas.

We discuss on the time scale of H_2 formation in order to shed another light on the dark gas composition. The H_2 molecules are formed on dust surface with the formation time scale t_{form} given by the Eq. (4) [38].

$$t_{\mathrm{form}} \sim 10^7 \left(\frac{100}{n\ (\mathrm{cm^{-3}})} \right) \ (\mathrm{year}) \tag{4}$$

For density of $n = 100\,\mathrm{cm^{-3}}$, the H_2 formation timescale is 10 Myrs. This is similar to the typical evolutionary timescale of GMCs. On the other hand, the local gas at high galactic latitude where the dark gas is identified is all low column density clouds whose HI column density is in the order of $10^{21}\,\mathrm{cm^{-2}}$. They are surrounding well known local molecular clouds like Ophiuchus and Lupus. The crossing time scale of such ensembles of local clouds, most likely not gravitationally bound, is estimated to be $\sim$1 Myrs as derived from a ratio $10\,\mathrm{pc}/10\,\mathrm{km\,s^{-1}}$ (e.g., see Fig. 4 in [69]). So, the time scale of the surrounding gas is too short to convert HI into H_2. This argues for that the dark gas is dominated by dense HI but not by H_2 without CO. On the other hand, it is conceivable that the envelopes of the GMCs in the Galactic plane may have lifetime long enough to form H_2, and H_2 envelopes without CO may be a viable alternative. Such GMCs are not well sampled in the Galaxy due to heavy contamination in the Galactic plane but the GMCs in the LMC [44] may provide an observable case where the molecular dark gas without CO is dominant. Future careful studies of the dust components will help to clarify the real contents of the dark gas.

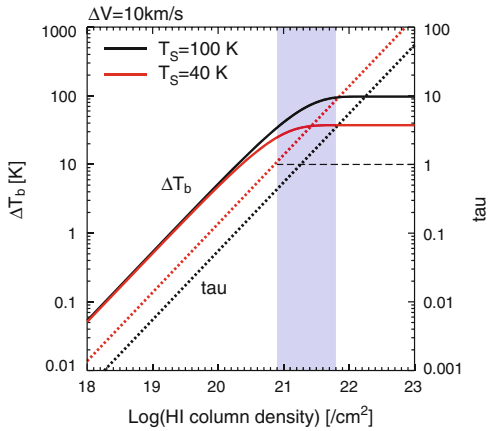

Fig. 15 ΔT_b and τ variations depending on N_p(HI) shown by [72]. Here ΔV of $10\,\mathrm{km\,s^{-1}}$ is assumed. The filled area shows a N_p range of the dark gas [36, 59]

6 Summary

From a view point of high-energy astrophysics, in particular with an emphasis of the origin of γ-rays, we present properties of neutral gas in the interstellar medium and its connection with the γ-ray SNRs.

We first review the gas properties of both atomic and molecular forms as probed by the 2.6 mm CO and 21 cm HI transitions. CO traces dense molecular gas and HI traces lower density atomic gas, whereas either CO or HI may not be a good tracer in an intermediate density regime roughly between 100 and $1{,}000\,\mathrm{cm^{-3}}$.

We then present analyses of the two most remarkable TeV γ-ray SNRs RX J1713.7–3946 and RX J0852.0–4622 and demonstrate that the ISM proton distribution shows a good spatial correspondence with the TeV γ-ray distribution. We argue that this correspondence provides a support for the hadronic scenario of γ-ray production. What remains to be explored is if a leptonic model consistent with the non-thermal X-ray distribution can also explain the observed TeV γ-ray distribution. We describe theoretical numerical simulations of the interaction of the SNR shock waves with the clumpy ISM and discuss that such realistic simulations can explain the observations reasonably well, whereas the uniform ISM models are not viable.

Then, we present a discussion on the dark gas observed in the γ-rays and mm/sub-mm dust emission. We argue that, for the local component of the dark gas in the Galaxy, dense HI gas as observed in RX J1713.7–3946 is a good candidate for the dark gas. The local gas is dominated by low mass clouds and their time scale may be too short to convert HI into H_2. On the other hand, the GMCs in the LMC have larger time scale like 10 Myrs, long enough for H_2 formation, and therefore molecular dominant dark gas is a viable model on the GMC scale.

Finally, we conclude that the ISM plays an essential role in producing the γ-rays and X-rays in the SNR, and the future instruments like CTA, combined with the ISM studies, will achieve tremendous progress in the γ-ray astrophysics of the SNR and the other high-energy objects.

Acknowledgements The author is grateful to the SOC for inviting him to this most stimulating conference. He is grateful to all the collaborators in this project for their invaluable contributions. His special thanks are to Felix Aharonian, Gavin Rowell, Naomi M. McClure-Griffiths, Tsuyoshi Inoue and Shu-ichiro Inutsuka. NANTEN2 is an international collaboration of 10 universities; Nagoya University, Osaka Prefecture University, University of Cologne, University of Bonn, Seoul National University, University of Chile, University of New South Wales, Macquarie University, University of Sydney, and University of ETH Zurich. This work was financially supported by a grant-in-aid for Scientific Research (KAKENHI, No. 21253003, No. 23403001, No. 22540250, No. 22244014, No. 23740149, No. 22740119 and No. 24224005) from MEXT (the Ministry of Education, Culture, Sports, Science and Technology of Japan). This work was also financially supported by the Young Research Overseas Visits Program for Vitalizing Brain Circulation (R2211) and the Institutional Program for Young Researcher Overseas Visits (R29) by JSPS (Japan Society for the Promotion of Science) and by the grant-in-aid for Nagoya University Global COE Program, Quest for Fundamental Principles in the Universe: From Particles to the Solar System and the Cosmos, from MEXT.

References

1. Abdo, A. A., Ackermann, M., Ajello, M., et al. The Astrophysical Journal 734 28 (2011)
2. Acero, F., Ballet, J., Decourchelle, A., et al. Astronomy & Astrophysics 505 157–167 (2009)
3. Aharonian, F. A., Akhperjanian, A. G., Aye, K.-M., et al. Nature 432 75–77 (2004)
4. Aharonian, F., Akhperjanian, A. G., Bazer-Bachi, A. R., et al. Astronomy & Astrophysics 481 401–410 (2008)
5. Aharonian, F., Akhperjanian, A. G., Bazer-Bachi, A. R., et al. The Astrophysical Journal 636 777–797 (2006a)
6. Aharonian, F., Akhperjanian, A. G., Bazer-Bachi, A. R., et al. Astronomy & Astrophysics 449 223–242 (2006b)
7. Aharonian, F., Akhperjanian, A. G., Bazer-Bachi, A. R., et al. Astronomy & Astrophysics 464 235–243 (2007a)
8. Aharonian, F., Akhperjanian, A. G., Bazer-Bachi, A. R., et al. The Astrophysical Journal 661 236–249 (2007b)
9. Aharonian, F., Akhperjanian, A. G., de Almeida, U. B., et al. The Astrophysical Journal 692 1500–1505 (2009)
10. Aschenbach, B. Nature 396 141–142 (1998)
11. Bell, A. R. Monthly Notices of the Royal Astronomical Society 182 147–156 (1978)
12. Berezhko, E. G., Voumllk, H. J. Astronomy & Astrophysics 492 695–701 (2008)
13. Berezhko, E. G., Pühlhofer, G., Voumllk, H. J. Astronomy & Astrophysics 505 641–654 (2009)
14. Bertsch, D. L., Dame, T. M., Fichtel, C. E., et al. Astrophysical Journal 416 587–600 (1993)
15. Blandford, R. D., & Ostriker, J. P. Astrophysical Journal 221 L29-L32 (1978)
16. Bloemen, J. B. G. M., Strong, A. W., Mayer-Hasselwander, H. A., et al. Astronomy & Astrophysics 154, 25–41 (1986)
17. Cassam-Chenai, G., Decourchelle, A., Ballet, J., et al. Astronomy & Astrophysics 427 199–216 (2004)
18. Castro, D., & Slane, P. The Astrophysical Journal 717 372–378 (2010)
19. Dame, T. M., Hartmann, D., & Thaddeus, P. The Astrophysical Journal 547 792–813 (2001)
20. Dickey, J. M., & Lockman, F. J. Annual review of astronomy & astrophysics 28 215–261 (1990)
21. Duncan, A. R., & Green, D. A. Astronomy & Astrophysics 364 732–740 (2000)
22. Ellison, D. C., & Vladimirov, A. The Astrophysical Journal 673 L47-L50 (2008)
23. Ellison, D. C., Patnaude, D. J., Slane, P., & Raymond, J. The Astrophysical Journal 712 287–293 (2010)

24. Enomoto, R., Tanimori, T., Naito, T., et al. Nature 416 823–826 (2002)
25. Fang, J., Tang, Y., & Zhang, L. The Astrophysical Journal 731 32 (2011)
26. Fukui, Y., Moriguchi, Y., Tamura, K., et al. Publications of the Astronomical Society of Japan 55 L61-L64 (2003)
27. Fukui, Y. HIGH ENERGY GAMMA-RAY ASTRONOMY: Proceedings of the 4th International Meeting on High Energy Gamma-Ray Astronomy. AIP Conference Proceedings 1085 104–111 (2008)
28. Fukui, Y., & Kawamura, A. Annual Review of Astronomy & Astrophysics 48 547–580 (2010)
29. Fukui, Y., Sano, H., Sato, J., et al. The Astrophysical Journal 746 82–99 (2012)
30. Fukui, Y et al. in preparation (2013)
31. Gabici, S., Aharonian, F. A., & Blasi, P. Astrophysics & Space Science 309 365–371 (2007)
32. Gast, H., Brun, F., Carrigan, S., et al. arXiv:1204.5860 (2012)
33. Giuliani, A., Cardillo, M. and Tavani, M. arXiv:1111.3592 (2011)
34. Goldsmith, P. F. IN: Interstellar processes; Proceedings of the Symposium, Grand Teton National Park, WY. Dordrecht, D. Reidel Publishing Co., 51–70 (1987)
35. Goldsmith, P. F., Li, D., & Krčo, M. The Astrophysical Journal 654 273–289 (2007)
36. Grenier, I. A., Casandjian, J.-M., & Terrier, R. Science 307 1292–1295 (2005)
37. Hayakawa, S. Progress of Theoretical Physics, 15, 111–121 (1956)
38. Hollenbach, D., & Salpeter, E. E. Astrophysical Journal 163 155
39. Hui, C. M. 2009 Snowbird Particle Astrophysics and Cosmology Workshop (SNOWPAC 2009), 426, 35 (2010)
40. H.E.S.S. Collaboration, Abramowski, A., Acero, F., et al. Astronomy & Astrophysics 531 A81 (2011)
41. Inoue, T., Yamazaki, R., Inutsuka, S.-i., & Fukui, Y. The Astrophysical Journal 744 71 (2012)
42. Katsuda, S., Tsunemi, H., & Mori, K. The Astrophysical Journal 678 L35-L38 (2008)
43. Katz, B., & Waxman, E. Journal of Cosmology & Astroparticle Physics 18 (2008)
44. Kawamura, A., Mizuno, Y., Minamidani, T., et al. The Astrophysical Journal Supplement 184 1–17 (2009)
45. Koyama, K., Kinugasa, K., Matsuzaki, K., et al. Publications of the Astronomical Society of Japan 49 L7-L11 (1997)
46. Koyama, H., & Inutsuka, S.-i. The Astrophysical Journal 564 L97-L100 (2002)
47. Lebrun, F., Bennett, K., Bignami, G. F., et al. Astrophysical Journal 274, 231–236 (1983)
48. Liseau, R., Lorenzetti, D., Nisini, B., Spinoglio, L., & Moneti, A. Astronomy & Astrophysics 265 577–596 (1992)
49. May, J., Murphy, D. C., & Thaddeus, P. Astronomy and Astrophysics Supplement Series 73 51–83 (1988)
50. Mayer-Hasselwander, H. A., Buccheri, R., Kanbach, G., et al. Ninth Texas Symposium on Relativistic Astrophysics 336 211 (1980)
51. McClure-Griffiths, N. M., Dickey, J. M., Gaensler, B. M., et al. The Astrophysical Journal Supplement Series 158 178–187 (2005)
52. Moriguchi, Y., Yamaguchi, N., Onishi, T., Mizuno, A., & Fukui, Y. Publication of the Astronomical Society of Japan 53 1025–1036 (2001)
53. Moriguchi, Y., Tamura, K., Tawara, Y., et al. The Astrophysical Journal 631 947–963 (2005)
54. Morlino, G., Amato, E., & Blasi, P. Monthly Notices of the Royal Astronomical Society 392 240–250 (2009)
55. Pannuti, T. G., Allen, G. E., Filipović, M. D., et al. The Astrophysical Journal 721 1492–1508 (2010)
56. Patnaude, D. J., Slane, P., Raymond, J. C., & Ellison, D. C. The Astrophysical Journal 725 1476–1484 (2010)
57. Pfeffermann, E., & Aschenbach, B. International Conference on X-ray Astronomy & Astrophysics: Rntgenstrahlung from the Universe, 267–268 (1996)
58. Planck Collaboration, Ade, P. A. R., Aghanim, N., et al. Astronomy & Astrophysics 536 A17 (2011a)

59. Planck Collaboration, Ade, P. A. R., Aghanim, N., et al. Astronomy & Astrophysics 536 A19 (2011b)
60. Porter, T. A., Moskalenko, I. V., & Strong, A. W. The Astrophysical Journal 648 L29-L32 (2006)
61. Sano, H., Sato, J., Horachi, H., et al. The Astrophysical Journal 724 59–68 (2010)
62. Sano, H et al. in preparation (2013a)
63. Sano, H et al. in preparation (2013b)
64. Slane, P., Gaensler, B. M., Dame, T. M., et al. The Astrophysical Journal 525 357–367 (1999)
65. Slane, P., Hughes, J. P., Edgar, R. J., et al. YOUNG SUPERNOVA REMNANTS: Eleventh Astrophysics Conference. AIP Conference Proceedings 565, 403–406 (2001a)
66. Slane, P., Hughes, J. P., Edgar, R. J., et al. The Astrophysical Journal 548 814–819 (2001b)
67. Spitzer, L. New York Wiley-Interscience (1978)
68. Strong, A. W., Bloemen, J. B. G. M., Dame, T. M., et al. Astronomy & Astrophysics 207 1–15 (1988)
69. Tachihara, K., Toyoda, S., Onishi, T., et al. Publications of the Astronomical Society of Japan 53 1081–1096 (2001)
70. Tanaka, T., Uchiyama, Y., Aharonian, F. A., et al. The Astrophysical Journal 685 988–1004 (2008)
71. Tanaka, T., Allafort, A., Ballet, J., et al. The Astrophysical Journal Letters 740 L51 (2011)
72. Torii, K., Fukui, Y., Sano, H., et al. The Spectral Energy Distribution of Galaxies, Proceedings of the International Astronomical Union, IAU Symposium 284 389–392 (2012)
73. Uchiyama, Y., Aharonian, F. A., & Takahashi, T. Astronomy & Astrophysics 400 567–574 (2003)
74. Uchiyama, Y., Aharonian, F. A., Tanaka, T., Takahashi, T., & Maeda, Y. Nature 449 576–578 (2007)
75. Wang, Z. R., Qu, Q.-Y., & Chen, Y. Astronomy & Astrophysics 318 L59-L61 (1997)
76. Yamaguchi, N., Mizuno, N., Saito, H., et al. Publications of the Astronomical Society of Japan 51 775–790 (1999)
77. Yoshiike, S et al. submitted to Astrophysical Journal (2012)
78. Zanin, R. arXiv:0912.3671 (2009)
79. Zirakashvili, V. N., & Aharonian, F. Astronomy & Astrophysics 465 695–702 (2007)
80. Zirakashvili, V. N., & Aharonian, F. A. The Astrophysical Journal 708 965–980 (2010)

New Insights on Hadron Acceleration at Supernova Remnant Shocks

Damiano Caprioli

Abstract We outline the main features of nuclei acceleration at supernova remnant forward shocks, stressing the crucial role played by self-amplified magnetic fields in determining the energy spectrum observed in this class of sources. In particular, we show how the standard predictions of the non-linear theory of diffusive shock acceleration has to be completed with an additional ingredient, which we propose to be the enhanced velocity of the magnetic irregularities particles scatter against, to reconcile the theory of efficient particle acceleration with recent observations of gamma-ray bright supernova remnants.

1 Introduction

Supernova remnants (SNRs) have been regarded for many decades now as the sources of Galactic cosmic rays (CRs), both because of their energetics and of the fact that strong shocks are expected to naturally accelerate particles with power-law energy distributions, according to the so-called Fermi mechanism.

Clear-cut evidences of particle acceleration in SNRs have been found many years ago in radio to X-ray synchrotron emission, therefore attesting the presence of *electrons* with energies as high as 10–100 TeV. On the other hand, direct evidences of *proton* acceleration are much less clear: the most prominent signature of hadronic acceleration has been individuated in the γ-ray emission from the decay of neutral pions produced in nuclear interaction between relativistic nuclei and the interstellar medium [13]. The first SNRs detected in the TeV γ-rays, however, did not unravel the question, since in this energy range it is hard to disentangle whether the observed spectrum (typically exhibiting a cut-off around $\sim$10 TeV) is the result either of the

D. Caprioli (✉)
Princeton University, 4 Ivy Ln, Princeton, NJ 08544, USA
e-mail: caprioli@astro.princeton.edu

D.F. Torres and O. Reimer (eds.), *Cosmic Rays in Star-Forming Environments*,
Astrophysics and Space Science Proceedings 34, DOI 10.1007/978-3-642-35410-6_18,

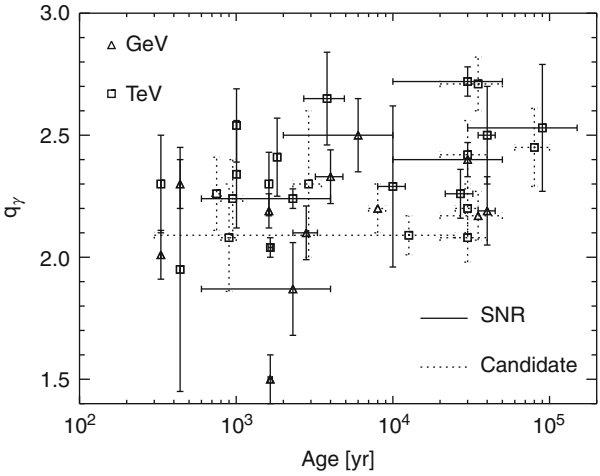

Fig. 1 Slopes q_γ of the γ-ray spectra as inferred in the GeV/TeV band for both confirmed and candidate SNRs, as in the legend (Data from Table 1 in Ref. [4])

hadronic mechanism described above or of inverse-Compton scattering (ICS) of relativistic electrons on some photon background.

Coupling the TeV observations of Cherenkov telescopes as HESS, VERITAS and MAGIC with the GeV observations of the Fermi satellite, however, it has been possible to assess the nature of the emission, at least in some paradigmatic cases: SNR RX J1713.7-3946 turned out to be mostly consistent with a leptonic scenario [1] while, on the contrary, Tycho's SNR has been convincingly modeled according to the hadronic hypothesis [12]. The main element allowing such a distinction is *the slope of the observed γ-ray spectrum*: for a $\propto E^{-q}$ CR energy distribution, ICS is expected to produce a flatter power-law photon spectrum, $\propto E_\gamma^{-(q+1)/2}$, while pion decay and bremsstrahlung produce a spectrum parallel to the parents' one, $\propto E_\gamma^{-q}$.

Both GeV and TeV observations are—in basically all the cases—consistent with spectra steeper than E^{-2}, as showed in Fig. 1 (see Ref. [4] for more details). The only SNRs showing a GeV slope smaller than 2 are in fact the aforementioned RX J1713.7-3946 and Vela Jr., whose emission may be accounted for by invoking a strong photon background making ICS dominate over pion decay. When the spectrum is steeper than E^{-2} across many energy decades, however, a hadronic mechanism is favored, instead since bremsstrahlung is typically negligible in SNRs.

But this behavior has another important consequence in terms of the process responsible for particle acceleration (of both electrons and protons, which share the same spectrum in rigidity): it has to be able to produce particle spectra steeper than E^{-2}. This apparently harmless requirement is at odds with any theory of *efficient* particle acceleration at SNRs developed in the last 30 years since, according to Fermi's mechanism, the expected slope is a function of the shock compression ratio

only, and namely $q = \frac{r+2}{r-1}$. For strong shocks $r = \frac{\gamma+1}{\gamma-1} = 4$, with $\gamma = 5/3$ the gas adiabatic index and, in turn, $q = 2$. When acceleration is efficient, though, one could expect the shock to be modified by the back-reaction of the accelerated particles, whose pressure may become comparable with the ram one. The simplest way to account for this effect is considering that CRs are relativistic particles forming a gas with adiabatic index $\gamma_{cr} = 4/3$, which would provide a compression ratio $r = 7$ and in turn $q = 1.5$. The escape of high-energy particles may in addition make the shock behave as partially radiative, increasing r even further and pushing q down to 1–1.2. In any case, a very solid prediction of the *non-linear theory of diffusive shock acceleration* (NLDSA) is that the CR spectrum has to be invariably flatter than E^{-2} at the highest energies, and being flatter and flatter for larger and larger acceleration efficiencies (for more details on CR modified shocks see, e.g., Ref. [11]).

Therefore, independently of the possible origin (leptonic or hadronic) of the observed GeV emission, Fermi-LAT's observations force us to rethink our theory of CR acceleration, challenging the paradigm which requires SNR shocks to channel fraction as large as 10–30 % of their kinetic energy into accelerated particles in order to be the potential sources of Galactic CRs.

2 Magnetic Field Amplification and Particle Acceleration

A fundamental tile in the mosaic of the comprehension of particle acceleration in (young) SNRs has also come from the detection of narrow X-ray bright rims immediately downstream of their forward shocks. The non-thermal nature of their spectra has been accounted for as due to synchrotron emission of relativistic electrons, while their narrowness (typically less than 0.01 pc) points to magnetic fields as large as a few hundreds μG, almost two orders of magnitude larger than the typical interstellar one. Such an evidence has been welcomed by theorists for several reasons.

- The super-Alfvènic streaming of CRs upstream of the shock has been predicted to lead to the excitation of several magnetic modes via plasma instabilities [2,14].
- A higher level of magnetization enhances particle diffusion and allows the achievement of larger energies, arguably up to a few PeV, namely enough to account for the knee observed in the Galactic CRs detected at Earth [3].
- The pressure in magnetic turbulence may be so large to overcome the gas one, therefore preventing the CR pressure to modify the shock too severely [8].
- Finally, magnetic field self-generation may have a key role also in determining the CR spectral slope, and therefore in reconciling NLDSA theory with γ-ray observations, which is what we want to outline here (also see Ref. [5]).

Without delving into the details of a kinetic theory of plasmas, we can state that, being the accelerated particles and the magnetic fields coupled through resonant scattering, the whole system has to gradually reduce the relative velocity of CRs,

whose diffusion velocity is basically the shock velocity in the upstream reference frame, u, and of magnetic irregularities, whose phase velocity is of the order of the Alfvèn speed, $v_A = B/\sqrt{4\pi\rho}$. In other words, magnetic field amplification might be considered as an inevitable consequence of an efficient CR acceleration while, on the other hand, an enhanced level of magnetization is a necessary condition for an efficient particle diffusion and acceleration: if the initial Alfvènic Mach number $M_A = u/v_A$ is large (as it typically is is in the interstellar magnetic field), it tends to be reduced by a non-linear interplay between particles and fields.

We model such an interplay by adopting the semi-analytic formalism for NDLSA outlined in Ref. [5] and references therein, which proved to be quick but very accurate for non-relativistic shocks [9]. We solve the equations of hydrodynamics coupled with a kinetic description of the non-thermal particles (via the diffusion-convection equation, Eq. 2.5 in Ref. [5]) and a fluid description for the generation of magnetic turbulence via resonant streaming instability (Eq. 2.18 in Ref. [5]). The dynamical feedback of both accelerated particles and amplified magnetic fields are self-consistently retained in this approach, as well as the escape of the highest energy particles from the upstream boundary [7].

The key role of magnetic field amplification in determining the CR spectral slope is to enhance the velocity of the scattering centers, i.e., the phase velocity of the magnetic waves, $\sim v_A \propto \delta B$. Since the compression ratio shaping the CR spectra is not the one of the fluid, but rather the one of the velocity of their scattering centers ahead and behind the shock, when v_A becomes a non-negligible fraction of u, it is in principle possible for diffusive shock acceleration to produce spectra steeper than E^{-2}.

More precisely, the compression ratio felt by the fluid between upstream and downstream is the usual $r = u_u/u_d \geq 4$ for strong, CR modified shocks, while the compression ratio felt by CRs is instead $\tilde{r} = (u_u + v_{A,u})/(u_d + v_{A,d})$. According to the argument above, however, the coupling between CRs and magnetic field is expected to produce waves streaming *against* the fluid in the upstream (in the direction opposite to the CR gradient), while downstream the turbulence should be efficiently isotropised ($v_{A,d} \sim 0$).

The net effect is that $\tilde{r} = (1 - M_{A,u}^{-1})r$ and, in turn, if $M_A(\delta B)$ becomes small enough, the predicted slope of the CR spectrum $q = \frac{\tilde{r}+2}{\tilde{r}-1}$ may become larger than 2, even for strong shocks and large CR pressures. On the other hand, a steeper CR spectrum allocates less pressure (which in turn generates less magnetic field), therefore we need a non-linear calculation to understand which effect dominates the determination of the spectral slope when acceleration is efficient: the pressure in CRs, which makes the shock more compressible, or rather the reduced jump in $\tilde{r}$.

Since CR injection has not been understood from first principles, yet, we cannot but parametrize it: we allow η, i.e., the fraction of particle crossing the shock with a momentum large enough to be injected into the acceleration mechanism, to vary between $\sim 10^{-7}$ and ~ 0.1. Such a large range of injection efficiency reflects different regimes of CR acceleration, spanning from unmodified shocks (where the pressure in CRs, P_{cr} is expected to be negligible with respect to the ram pressure),

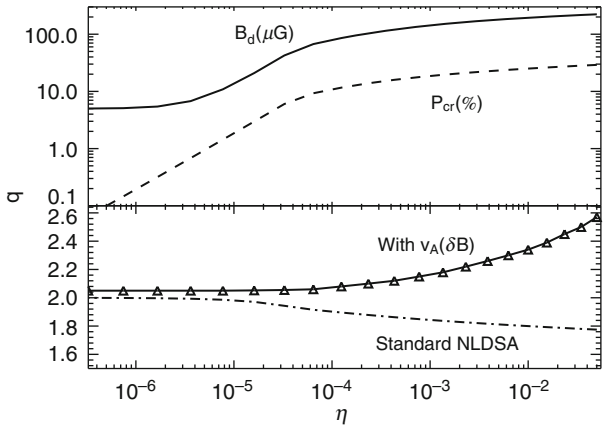

Fig. 2 *Top panel*: pressure in CRs at the shock, P_{cr}, expressed as a fraction of the ram pressure ρu^2, and predicted downstream magnetic field, B_d, as a function of the injection efficiency η. The environmental parameters are those relevant for a typical SNR in the early Sedov stage (see Ref. [5] for more details). *Bottom panel*: CR spectral slope obtained when the Alfvèn velocity is calculated in the self-amplified magnetic field δB (*solid line* with *triangles*) or according to a standard NLDSA theory assuming $M_A(B_0) \gg 1$ (*dot-dashed line*)

to strongly modified ones, in which the shock structure is deeply affected by CRs and in which magnetic field amplification is very effective. At saturation, in fact, we have that $P_B = \delta B^2/8\pi \sim P_{cr}/M_A$ (see §2.1 in Ref. [5] for the exact dependence).

Our results are showed in Fig. 2 for a SNR about 3,000 year old, i.e., in the early Sedov stage. For a much wider discussion of the SNR evolution in terms of its non-thermal content the reader may refer to Refs. [5, 6]. In the top panel, P_{cr} and the downstream field B_d are showed as function of η: they reproduce the test-particle case for $\eta \lesssim 10^{-5}$, show a linear increase for about a decade and finally saturate to about 10–20 % and 100–200 μG, respectively, above $\eta \sim 10^{-4}$.

The very reason of this saturation, which among other things assesses the mild dependence of our findings on η, is that the whole system reacts to high injection efficiencies by steepening the CR spectrum in order to accommodate almost the same energy in non-thermal particles, as demonstrated in the bottom panel of Fig. 2 (solid line). Spectra as steep as $E^{-2.2} - E^{-2.5}$ correspond to the highest acceleration efficiencies and to the fields inferred in the downstream of young shell SNRs (see Fig. 3 in Ref. [5]). The spectral slope obtained is also compared with the one predicted by a two-fluid theory of NLDSA, $q = (3\gamma_{eff} - 1)/2$, where the CR contribution is accounted for via a compression ratio modulated by an effective adiabatic index of the gas + CR fluid [10], namely $\gamma_{eff} = \frac{5+3P_{cr}}{3-3P_{cr}}$ (dot-dashed line in the bottom panel of Fig. 2). It is worth recalling that the latter slope, already clearly inconsistent with the observations reported in Fig. 1, represents an *upper limit* to the one which would be predicted by taking into account also the escape of CRs, which would make the shock partially radiative, in principle increasing r well above 7 [11].

The only way to accommodate the typical efficiencies (10–20 %) required for the SNRs to be the sources of Galactic CRs, and the high levels of magnetization observed (a few 100 μG), with CR spectra steeper than E^{-2} is to modify the standard theory of NLDSA.

We propose here that accounting for the features of the magnetic field produced by the CR streaming is a possible way to build a consistent picture of efficient NLDSA in SNRs, actually reversing the usual trend which relates larger and larger CR acceleration efficiencies with flatter and flatter spectra.

References

1. Abdo, A.A., Fermi LAT Collaboration: Observations of the Young Supernova Remnant RX J1713.7-3946 with the Fermi Large Area Telescope. ApJ 734, 28 (2011)
2. Bell, A.R.: Turbulent amplification of magnetic field and diffusive shock acceleration of cosmic rays. MNRAS 353, 550–558 (2004)
3. Blasi, P., Amato, E., Caprioli, D.: The maximum momentum of particles accelerated at cosmic ray modified shocks. MNRAS 375, 1471–1478 (2007)
4. Caprioli, D.: Understanding hadronic gamma-ray emission from supernovaremnants. JCAP5, 26–+ (2011)
5. Caprioli, D.: Cosmic-ray acceleration in supernova remnants: non-linear theory revised. JCAP, 7, 38 (2012)
6. Caprioli, D., Amato, E., Blasi, P.: The contribution of supernova remnants to the galactic cosmic ray spectrum. APh 33, 160–168 (2010)
7. Caprioli, D., Blasi, P., Amato, E.: On the escape of particles from cosmic-ray modified shocks. MNRAS 396, 2065–2073 (2009)
8. Caprioli, D., Blasi, P., Amato, E., Vietri, M.: Dynamical Effects of Self-Generated Magnetic Fields in Cosmic-Ray-modified Shocks. ApJ Lett 679, L139–L142 (2008)
9. Caprioli, D., Kang, H., Vladimirov, A.E., Jones, T.W.: Comparison of different methods for non-linear diffusive shock acceleration. MNRAS 407, 1773–1783 (2010)
10. Chevalier, R.A.: Blast waves with cosmic-ray pressure. ApJ 272, 765–772 (1983)
11. Malkov, M.A., OC. Drury, L.: Non-linear theory of diffusive acceleration of particles by shock waves. Reports of Progress in Physics 64, 429–481 (2001)
12. Morlino, G., Caprioli, D.: Strong evidence for hadron acceleration in Tycho's supernova remnant. A&A 538, A81 (2012)
13. OC. Drury, L., Aharonian, F., Volk, H.J.: The gamma-ray visibility of supernova remnants. A test of cosmic ray origin. A&A 287, 959–971 (1994)
14. Skilling, J.: Cosmic ray streaming. I - Effect of Alfven waves on particles. MNRAS 172, 557–566 (1975a)

Cosmic Rays in the Orion Bar

Yago Ascasibar, Aura C. Obreja, and Ángeles I. Díaz

Abstract The detailed structure of HII regions and the surrounding photodissociation regions (more precisely, the extent and chemical composition of the ionized, neutral, and molecular layers) poses strong constraints on the intensity of the magnetic field and the presence of cosmic rays. Conversely, an accurate knowledge of these physical parameters is necessary in order to understand the observable properties of nearby regions, as well as those of unresolved, distant star-forming galaxies. Due to its close distance to the Earth and its nearly edge-on geometry, the Orion Bar provides an excellent testbed for detailed photoionization models. We will show that, although the observed structure of the ionized HII region can be reproduced with remarkable accuracy, the agreement in the atomic layer is only qualitative, and the predicted abundances of several molecular species are off by several orders of magnitude. Consistent with previous work, our results hint that the density of cosmic rays is high (well above the Galactic background, though not as large as implied by equipartition arguments), but their role on the molecular chemistry is still unclear. In particular, we consider that cosmic rays alone cannot probably solve all the present discrepancies between models and observations, and a more detailed treatment of the three-dimensional structure of the region is clearly required.

1 Introduction

Galaxy formation is one of the key open questions in Astrophysics and Cosmology. The gravitational collapse of dark matter haloes, as well as their internal structure, have been extensively studied by means of cosmological numerical simulations, and, although some issues (such as e.g. the inner density profile) remain hotly debated, there is broad agreement in the overall picture. However, there is no such

Y. Ascasibar (✉) · A.C. Obreja · Á.I. Díaz
Universidad Autónoma de Madrid, Madrid 28049, Spain
e-mail: yago.ascasibar@uam.es; aura.obreja@uam.es; angeles.diaz@uam.es

D.F. Torres and O. Reimer (eds.), *Cosmic Rays in Star-Forming Environments*,
Astrophysics and Space Science Proceedings 34, DOI 10.1007/978-3-642-35410-6_19,

consensus as far as star formation is concerned. It is clear that the intergalactic gas must fall into the galaxies, cool down, and form a multiphase interstellar medium. It is also generally accepted that stars are born in molecular cloud complexes, whose formation and destruction are regulated by a complex interplay between the radiative cooling and heating of the gas, the gas (and dust) chemistry, and the energy input (winds, turbulence, photons) from the young stellar populations. The details – often swept under the loose denomination of "stellar feedback" – are far from being well understood, though, and many models, with varying degrees of success in reproducing the wealth of observational data, are built by resorting to simple (or sophisticated) recipes describing how the gas is transformed into stars.

In order to understand the *physics* behind stellar feedback, it is necessary to investigate the effects of young stars on their immediate surroundings, paying particular attention to the photodissociation of the molecular reservoir. It is important to note that, in the molecular region, cosmic rays play a crucial role on the structure and dynamics of the nebula, being in some cases the dominant heating mechanism and making a significant contribution to the total pressure. They also determine the gas chemistry, regulating the charge of dust grains and the condensation and destruction of molecular hydrogen, and they are responsible for many of the observational properties of the region, especially in the radio and gamma-ray regimes.

The Orion Bar is an ideal laboratory to explore the effects of radiative stellar feedback, as well as the role of cosmic rays and magnetic fields. Most of the ionizing radiation comes from the star θ^1 Orionis C, located roughly at the centre of the region, and the privileged orientation of the Bar offers an exquisite view of the interface between the ionized, atomic, and molecular layers of the cloud. Ascasibar et al. [5] presented different models of the Orion Bar based on the assumption of hydrostatic equilibrium. Here we provide a summary of the most important results, focusing on the implications for the population of cosmic rays in young star-forming regions.

2 Photoionization Models

We used the public plasma physics code Cloudy[1] (last described in [10]) to model the internal structure of the Orion Bar. The gas is assumed to be in ionization, thermal, and hydrostatic equilibrium at every point, and its properties depend on the ionizing continuum – including the cosmic microwave background, a $T = 39{,}600\,\mathrm{K}$ [15] stellar atmosphere representing ${}^1\theta$ Ori C, and a thermal bremsstrahlung component with $T = 10^6\,\mathrm{K}$ to account for the presence of hot X-ray emitting gas [8] –, the gas density and chemical composition at the illuminated face [6], the geometry of the system, and the energy densities of cosmic rays and magnetic fields.

[1] http://www.nublado.org

The density at the illuminated face is set to $n_0 = 10^{3.2}\,\mathrm{cm}^{-3}$ in all our models, and its variation with distance from the central source is given by the hydrostatic equilibrium condition

$$\frac{1}{\rho(r)}\frac{\mathrm{d}P(r)}{\mathrm{d}r} = a_{rad} - \frac{GM(r)}{r^2} \tag{1}$$

where the total pressure

$$P(r) = P_{\mathrm{gas}} + P_{\mathrm{ram}} + P_{\mathrm{turb}} + P_{\mathrm{mag}} + P_{\mathrm{lines}} \tag{2}$$

includes the thermal component, the uniform (set to zero) and turbulent ($2\,\mathrm{km\,s}^{-1}$) motions of the gas, the magnetic pressure, and the contribution [7, 9] of the trapped emission lines. The pressure gradient has to balance the sum of the outward acceleration, driven by the radiation field, and the inward pull of the gravitational force. The distribution of the gas mass is computed self-consistently by the code, and the θ^1 Ori C multiple system is modelled as a point mass of $50\,\mathrm{M}_\odot$ [14] located at the centre of the region. As shown in [4], gravity plays an important role in the outer regions, setting the total extent of the cloud and thus eliminating one free parameter of the model.

We use a simple parametrization of the geometry of the HII region (the distance from the central star to the illuminated face) that is able to provide a reasonable fit to the emission line data (see [5]). For the magnetic field, we assume a phenomenological relation of the form

$$\frac{B}{B_0} = \frac{n}{n_0} \tag{3}$$

and the abundance of cosmic rays is set to either the Galactic background density or to the value implied by equipartition with the magnetic field. More precisely, we consider the three benchmark cases discussed by Pellegrini et al. [17]:

- Thermal pressure model: $B_0 = 0$, Galactic CR
- Magnetic pressure model: $B_0 = 8\ \mu$G, Galactic CR
- Enhanced cosmic rays: $B_0 = 8\ \mu$G, Equipartition CR

3 Comparison with Observations

In order to test the ability of our models to describe the properties and the structure of the Orion Bar, we compare their predictions with the observed surface brightness profiles of the [SII] $\lambda\,\lambda 6,716+6,731$ Å [17] and Hα [22] emission lines, originated in the HII region, the H_2 S(1 − 0) transition at 2.121 μm [21] from the atomic layer, and the column densities of several species – CO^+ [11, 20], CN [19], SO^+ [11],

SO [13], CS [12, 19], and SiO [18] – that trace the structure of the cloud deep into the molecular region.

In our models, the extent of the HII region is set by the gas density at the illuminated face, the intensity of the ionizing radiation, the distance to the Orion Nebula, and the geometrical configuration of the system. We determine the latter from the (extinction-corrected) surface brightness profiles of the [SII] and Hα lines. The best-fitting values of the parameters describing the geometry have been found by means of the FiEstAS sampling technique [1], a Monte Carlo integration scheme based on the Field Estimator for Arbitrary Spaces (FiEstAS; [2, 3]). It was found that the properties of the ionized region are not very sensitive to the presence of cosmic rays and magnetic fields. The gas pressure, magnetic pressure, and enhanced cosmic rays models yield identical predictions for the gas density, temperature, and emissivity as a function of depth into the cloud. Judging form the quality of the fit, the proposed geometry seems to provide a reasonable description of the Orion Bar up to the ionization front, regardless of the assumptions made concerning the non-thermal components.

Once the geometry is set, the surface brightness profile of the H_2 line, as well as the molecular column densities discussed below, are a genuine prediction of the models. In the atomic region, there is qualitative agreement with the observational data, but none of the scenarios we have considered is able to reproduce the observed H_2 2.121 μm emission at the quantitative level. Although there is some uncertainty associated to the exact amount of dust extinction, our results suggest that the maximum intensity of the line is underestimated by about a factor of 3. In the gas pressure scenario, the separation between the peaks of the [S II] and the H_2 emission is always too small, whereas the magnetic pressure model fails to explain the observed surface brightness even for $A_{2.121\,\mu\mathrm{m}} = 0$. The enhanced cosmic rays model seems slightly more promising, but the precise amount of dust extinction is critical. In addition, the density gradient in the molecular region should be much steeper than predicted by our gravitational models in order to reproduce the observed lack of emission outside the main peak.

Finally, the abundances of different molecular species provide a direct probe of the extent and the physical conditions of the outer, molecular layer, including the amount of cosmic rays present. The comparison between model predictions and observational data is far from straightforward, given the many assumptions made in both fronts, but our results suggest that, at present, they show severe discrepancies. Some molecules (e.g. CO^+, SO) are better reproduced by the enhanced cosmic rays model, while others (e.g. CN) are closer to the predictions of the models with an average Galactic cosmic-ray population. The results for other species (e.g. SO^+) are intermediate between these two cases, and some column densities (e.g. CS, SiO) are overpredicted by several orders of magnitude by all the models considered.

4 Discussion and Conclusions

Even in the Orion Nebula, a paradigmatic example of a low-density star-forming region, cosmic rays and magnetic fields play a crucial role. While the structure of the ionized region is fully determined by the gas properties (density, composition, and geometry) as well as those of the incident radiation field, the intensity of the magnetic field sets the thickness of the atomic layer, where cosmic-ray heating may make a significant contribution to the gas temperature. In the molecular region, cosmic rays are the dominant heating mechanism, and the temperature raises by an order of magnitude (from $\sim$10 to $\sim$100 K) when the abundance of cosmic rays goes from the average Galactic background to the equipartition value. This has a dramatic effect on the chemistry of the molecular region, reflected on the predicted column densities of many molecular species.

Unfortunately, none of our models is able to provide a reasonable match to the observational data. One possible reason is, of course, that they are too simple to describe all the relevant features of the Orion Nebula, and new free parameters are necessary. In particular, variations of the gas density and the intensity of the magnetic field across the illuminated face could have a strong impact on the predicted properties. Alternatively, it is also possible that the models are incomplete because they do not include all the relevant physics. While we do not think that the assumption of hydrostatic equilibrium incurs in severe errors, it seems likely that the dynamics of the nebula may affect the results quantitatively. Some additional uncertainty, affecting both theory and observations, is associated to the values of the different reaction rates, especially in the molecular region. Finally, two major concerns are, on the one hand, that the radiation from nearby stars (see e.g. [16]) or the (extra-)Galactic UV background may play an important role in the outer edge of the Bar, shielded from the photons of θ^1 Ori C. On the other hand, a multiphase description of the gas (e.g. [12, 21]) could be necessary, which would invalidate our approach. Further work is clearly required in order to clarify these issues and gain a better understanding of the role of cosmic rays in star-forming environments.

Acknowledgements We would like to thank the organizers for such a stimulating conference, bringing together people from so many different communities and points of view. Y. Ascasibar receives financial support from project AYA 2010-21887-C04-03 as well as from the *Ramón y Cajal* programme, under contract RYC-2011-09461.

References

1. Ascasibar Y (2008) FiEstAS sampling – a Monte Carlo algorithm for multidimensional numerical integration. Computer Physics Communications 179:881–887, DOI 10.1016/j.cpc.2008.07.011, 0807.4479
2. Ascasibar Y (2010) Estimating multidimensional probability fields using the Field Estimator for Arbitrary Spaces (FiEstAS) with applications to astrophysics. Computer Physics Communications 181:1438–1443, DOI 10.1016/j.cpc.2010.04.011, 1006.1296

3. Ascasibar Y, Binney J (2005) Numerical estimation of densities. MNRAS356:872–882, DOI 10.1111/j.1365-2966.2004.08480.x, arXiv:astro-ph/0409233
4. Ascasibar Y, Diaz AI (2010) Photoionized gas in hydrostatic equilibrium: the role of gravity. MNRAS404:275–282, DOI 10.1111/j.1365-2966.2010.16270.x, 1001.3035
5. Ascasibar Y, Obreja AC, Diaz AI (2011) Hydrostatic photoionization models of the Orion Bar. MNRAS416:1546–1555, DOI 10.1111/j.1365-2966.2011.19151.x, 1106.3990
6. Baldwin JA, Ferland GJ, Martin PG, Corbin MR, Cota SA, Peterson BM, Slettebak A (1991) Phys- ical conditions in the Orion Nebula and an assessment of its helium abundance. ApJ374:580– 609, DOI 10.1086/170146
7. Elitzur M, Ferland GJ (1986) Radiation pressure and emission clouds around active galactic nuclei. ApJ305:35–44, DOI 10.1086/164226
8. Feigelson ED, Getman K, Townsley L, Garmire G, Preibisch T, Grosso N, Montmerle T, Muench A, McCaughrean M (2005) Global X-Ray Properties of the Orion Nebula Region. ApJS160:379–389, DOI 10.1086/432512, arXiv:astro-ph/0506503
9. Ferland GJ, Elitzur M (1984) Radiation pressure and the stability of broad-line region clouds. ApJ285:L11–L14, DOI 10.1086/184354
10. Ferland GJ, Korista KT, Verner DA, Ferguson JW, Kingdon JB, Verner EM (1998) CLOUDY 90: Numerical Simulation of Plasmas and Their Spectra. PASP110:761–778, DOI 10.1086/316190
11. Fuente A, Rodrguez-Franco A, Garca-Burillo S, Martn-Pintado J, Black JH (2003) Observational study of reactive ions and radicals in PDRs. A&A406:899–913, DOI 10.1051/0004-6361:20030712
12. Hogerheijde MR, Jansen DJ, van Dishoeck EF (1995) Millimeter and submillimeter observations of the Orion Bar. 1: Physical structure. A&A294:792–810
13. Jansen DJ, Spaans M, Hogerheijde MR, van Dishoeck EF (1995) Millimeter and submillimeter observations of the Orion Bar. II. Chemical models. A&A303:541
14. Kraus S, Balega YY, Berger J, Hofmann K, Millan-Gabet R, Monnier JD, Ohnaka K, Pedretti E, Preibisch T, Schertl D, Schloerb FP, Traub WA, Weigelt G (2007) Visual/infrared interferom- etry of Orion Trapezium stars: preliminary dynamical orbit and aperture synthesis imaging of the ?1 Orionis C system. A&A466:649–659, DOI 10.1051/0004-6361:20066965, arXiv:astro- ph/0702462
15. Kurucz RL (1979) Model atmospheres for G, F, A, B, and O stars. ApJS40:1–340, DOI 10.1086/190589
16. ODell CR, Harris JA (2010) Spectrophotometry of the Huygens Region of the Orion Nebula, the Extended Orion Nebula, and M 43: Scattered Light Systematically Distorts Conditions Derived from Emission Lines. AJ140:985–1006, DOI 10.1088/0004-6256/140/4/985, 1008.1002
17. Pellegrini EW, Baldwin JA, Ferland GJ, Shaw G, Heathcote S (2009) Orions Bar: Physical Conditions Across the Definitive H + /H0/H2 Interface. ApJ693:285–302, DOI 10.1088/0004-637X/693/1/285, 0811.1176
18. Schilke P, Pineau des Forets G, Walmsley CM, Martin-Pintado J (2001) Observations of SiO to- wards photon dominated regions. A&A372:291–301, DOI 10.1051/0004-6361:20010470
19. Simon R, Stutzki J, Sternberg A, Winnewisser G (1997) Chemical stratification in the Orion Bar region: CN and CS submillimeter observations. A&A327:L9–L12
20. Stoerzer H, Stutzki J, Sternberg A (1995) CO+ in the Orion Bar, M17 and S140 star-forming regions. A&A296:L9+
21. van der Werf PP, Stutzki J, Sternberg A, Krabbe A (1996) Structure and chemistry of the Orion bar photon-dominated region. A&A313:633–648
22. Wen Z, Odell CR (1995) A three-dimensional model of the Orion Nebula. ApJ438:784–793, DOI 10.1086/175123

The FIR-Radio Correlation in Rapidly Star-Forming Galaxies: The Spectral Index Problem and Proton Calorimetry

Todd A. Thompson and Brian C. Lacki

Abstract We review the physics of the FIR-radio correlation (FRC) of star-forming galaxies, focusing on "electron calorimetry" as an explanation. We emphasize the importance of the "spectral index problem"—that galaxies have flatter GHz synchrotron spectra than predicted in the strong-cooling calorimeter limit. We argue that these shallow spectra require significant bremsstrahlung and/or ionization losses for the primary and secondary CR electron/positron populations. This then implies that CR protons suffer strong pionic losses before escape in dense starburst galaxies ("proton calorimetry"), and that these systems should be gamma-ray bright, forming a FIR-gamma-ray correlation. Implications for the diffuse non-thermal cosmic gamma-ray and neutrino backgrounds are mentioned. Caveats and uncertainties, as well as other solutions to the "spectral index problem" such as rapid advection of CRs in starburst superwinds, are highlighted.

1 Introduction

The FIR-radio correlation (FRC) is a nearly linear empirical relation between the GHz radio synchrotron and the far-infrared emission of star-forming galaxies of the form (e.g., [8, 14, 68])

$$\nu L_\nu(\mathrm{GHz}) \sim 10^{-6} L_{\mathrm{FIR}}. \quad (1)$$

T.A. Thompson (✉)
Department of Astronomy and Center for Cosmology & Astro-Particle Physics, The Ohio State University, Columbus, OH, USA
e-mail: thompson@astronomy.ohio-state.edu

B.C. Lacki
Jansky Fellow, Institute for Advanced Study, Princeton, NJ, USA
e-mail: brianlacki@ias.edu

D.F. Torres and O. Reimer (eds.), *Cosmic Rays in Star-Forming Environments*, Astrophysics and Space Science Proceedings 34, DOI 10.1007/978-3-642-35410-6_20,

The radio emission is from high-energy cosmic ray (CR) electrons (and positrons) in the host galaxy's magnetic field, and the FIR emission is from the dust-reprocessed UV/optical photons from massive stars. The FRC was discovered by van der Kruit [63, 64], who plotted the 10 μm and 1.4 GHz fluxes of a small sample of star-forming galaxies and Seyfert nuclei. Helou et al. [19] and de Jong et al. [18] extended this work to a larger sample, finding linear correlations between the 60 μm IRAS flux and the 20 and 6 cm flux, respectively. The compilation of [68] presents the 1.4 GHz–60 μm correlation for ≃1,800 galaxies in the 2 Jy IRAS sample, finding a linear FRC over ∼4 dex in $L_{\rm FIR}$ from local dwarf galaxies to the densest starburst galaxies known.[1] Murphy et al. [40–42] show that the local FRC holds down to sub-kpc scales within individual galaxies. The FRC has also recently been investigated at high z for large populations of star-forming galaxies by Reddy and Steidel [50], Smolčić et al. [58], Sargent et al. [56], Ivison et al. [20], and Mao et al. [36].

Aside from radio-bright AGN, which strongly deviate, there are notably few exceptions to the mean FRC. For example, there is a small population of star-forming galaxies that are radio-dim (or radio-silent) compared to the mean relation, perhaps because of a very young stellar population (e.g., [55]). The Galactic Center is similarly radio-dim with respect to the FRC (e.g., [15, 16]). Among sources at high z, only the submm-selected sources may deviate significantly, and these appear to be radio-bright by a factor of ∼2–3 [24, 39, 43, 65]. In general, normal radio-quiet AGN appear to follow the relation.

The importance of the FRC is several-fold. First, because the FIR emission of a galaxy is a good indicator of its star formation rate (SFR), to the extent that the FRC holds at high z, radio observations provide a measure of the SFRs of galaxies for which FIR observations may not be available. Second, because the GHz emission is largely synchrotron from primary CR electrons and secondary electrons/positrons ($e^{\pm}$) in the magnetic fields of the host galaxies, the FRC constrains the cosmic ray ($U_{\rm CR}$) and magnetic energy densities ($U_{\rm B}$) of galaxies over a large dynamic range in their properties. Since $U_{\rm B}$ and $U_{\rm CR}$ are known to be comparable to the energy density of turbulence and the pressure required for hydrostatic equilibrium in the Galaxy [10], it is of considerable interest to constrain these components of the ISM in galaxies at all redshifts.

Any theory of the FRC clearly must explain the normalization and linearity of the relation over ∼4 dex in $L_{\rm FIR}$. However, there are several ancillary observations that a theory must also contend with. First, the photon energy density ($U_{\rm ph} \sim F/c$), which measures the importance of inverse Compton (IC) losses on starlight for CR $e^{\pm}$, varies by >6 dex along the FRC. Second, as we highlight in Sect. 3, the radio spectral indices at GHz frequencies are fairly shallow for normal Milky Way-like spirals with $\alpha \sim 0.8 - 0.9$ ($F_\nu \propto \nu^{-\alpha}$), and they become even shallower for the compact galaxies that make up the high-luminosity end of the FRC. Third,

[1] For the purposes of this work, we take "starbursts" to be any galaxy with an average gas surface density more than $\sim 200\,{\rm M}_\odot/{\rm pc}^2$.

the average gas density of galaxies varies from ∼0.1 to $10^4\,\mathrm{cm}^{-3}$, implying a large range in the CR $e^{\pm}$ cooling time by ionization and bremsstrahlung losses, if CRs sample mean-density gas. Fourth, several galaxies—notably M82 and NGC 253—have now been observed at GeV and TeV energies [1–3]. Since IC and bremsstrahlung losses by CR $e^{\pm}$ produce gamma-rays, these detections constrain the importance of these interactions for the CR $e^{\pm}$ as a whole. Since CR protons can produce gamma-rays either directly from π^0 decay after inelastic collisions with nuclei in the ISM, or indirectly via secondary $e^{\pm}$ production by $\pi^{\pm}$ decay, and subsequent bremsstrahlung and IC, the gamma-ray detections also constrain CR protons.

Below, we briefly discuss the physics of the FRC, focusing on the arguments for "electron calorimetry" in (essentially) all galaxies, and both electron and "proton calorimetry" in starbursts. Throughout, we emphasize the implications of these arguments for the physics of the FRC, and the caveats and uncertainties in our interpretation.

2 Electron Calorimetry

The standard picture of the FRC is "electron calorimetry" ([33, 60, 66] (T06); [25] (LTQ)). In this picture, the UV/optical light of massive stars is absorbed by dust, producing the FIR emission. The supernovae from the stellar population—or some other process directly coupled to star formation—accelerate primary CR electrons and protons at a fixed energy injection rate per unit mass of stars formed. If the escape time ($t_{\rm escape}$) for CR electrons via diffusion or advection in a galactic wind is then longer than the cooling time ($t_{\rm cool}$) via synchrotron, IC, bremsstrahlung, and ionization losses, and then if a constant fraction of the primary CR electron energy goes into synchrotron, one would expect a linear FRC. In this picture, there is a constant proportionality between every synchrotron photon and every gram of material that ends up in, or is cycled through, stars.

This picture is very appealing because the normalization works out for simple assumptions. Taking a standard IMF with a continuous SFR, and assuming that a constant fraction $\xi_{0.002} = \xi/0.002$ of 10^{51} ergs per supernova goes into CR electrons, the injected electron power is

$$L_{\mathrm{CR}e} \sim 2 \times 10^{-5}\,\xi_{0.002}\,L_{\rm FIR}. \tag{2}$$

For a power-law spectrum of CR electrons of the form $dN/d\gamma_e \propto \gamma_e^{-p}$, with $p \simeq 2-2.4$, and with maximum energy $\gamma_{\rm max} = 10^6 - 10^9$, one estimates the GHz radio luminosity as

$$\nu L_\nu(\mathrm{GHz}) \sim L_{\mathrm{CR}e}/[2\ln(\gamma_{\rm max})] \sim 10^{-6}\,\xi_{0.002} L_{\rm FIR}, \tag{3}$$

close to the observed relation (Eq. 1). As long as p is not too steep, and as long as $\xi \approx$ constant, and as long as synchrotron is either the dominant loss process or a constant fraction of the total losses for all galaxies, the normalization and linearity of the FRC are roughly obtainable, to within an order of magnitude. Because $U_{\rm ph}$ changes dramatically along the FRC for different galaxies, electron calorimetric models are generally driven to $U_{\rm B} \sim U_{\rm ph}$ to keep IC and synchrotron losses in a constant proportion if these two dominate the cooling ([33, 66]; T06; LTQ). Since $U_{\rm ph} \propto F \propto \dot{\Sigma}_\star$, where the latter is the SFR/area, the observed Schmidt law of galaxies ($\dot{\Sigma}_\star \propto \Sigma_g^{1.4}$; [21]) and the rough proportionality $U_{\rm B} \sim U_{\rm ph}$ then imply that $B \propto \dot{\Sigma}_\star^{0.7}$. In LTQ, we find that

$$B \simeq 5\,\mu{\rm G} \left(\frac{\Sigma_g}{10\ {\rm M}_\odot\ {\rm pc}^{-2}} \right)^{0.7} \tag{4}$$

is a reasonable approximation to the expected galaxy-wide magnetic field strength from Milky Way-like galaxies all the way up to the highest surface density ULIRGs, but because our models have strong bremsstrahlung, ionization, and pionic losses, the magnetic field scaling $B \propto \Sigma_g^{0.7}$ is related not only to the form of the Schmidt Law, but also (and more subtely) to the energy dependence of bremsstrahlung cooling. We return to this issue in Sect. 4 below.

3 The Spectral Index Problem

The problem with electron calorimetry comes when one compares the expected GHz spectral indices with those observed. For CR electrons fully cooled by either IC or synchrotron, one expects $\alpha = p/2 \simeq 1 - 1.2$ (e.g., [45]). This follows from the fact that when energy losses dominate, the equilibrium cosmic ray spectrum is $N(\gamma) \propto \gamma^{1-p}/\dot{\gamma}$, where the energy loss rate $\dot{\gamma} \propto \gamma^2$ for both IC and synchrotron. The predicted index is steeper than observed in normal spirals, and much steeper than observed in dense rapidly star-forming galaxies (e.g, [12]). Thus, if CR electron cooling is dominated by synchrotron or IC, and if $t_{\rm cool} < t_{\rm escape}$, as required by calorimetry, then the theory is inconsistent with observations. This tension is particularly acute since the IC and synchrotron cooling timescales ($t_{\rm synch}$ & $t_{\rm IC}$) in the densest starbursts are very short. The fact that these systems are most in violation of the strong-cooling expectation for the radio spectrum is key.

One way to solve this spectral index problem would be to use harder CR injection spectra with $p < 2$, but this option is not widely considered because Fermi shock acceleration is expected to produce spectra with $p \geq 2$ (e.g., [9]), and because such hard spectra are not inferred from observations of supernova remnants.

A second way to solve the spectral index problem, which we favor, is with bremsstrahlung and ionization losses. The shallower energy dependence of these loss processes ($\dot{\gamma} \propto \gamma^1$ and γ^0, respectively) flattens the equilibrium CR

electron/positron particle spectrum, producing a flatter emitted GHz synchrotron spectrum, but only if the timescale for bremsstrahlung or ionization cooling ($t_{\rm brems}$ & $t_{\rm ion}$) is comparable to $t_{\rm synch}$ and/or $t_{\rm IC}$. Prima facie, this solution is particularly appealing since $t_{\rm brems}$ and $t_{\rm ion}$ are inversely proportional to the gas density of the medium, and it is in the densest galaxies that the flattest GHz spectra are seen. In addition, this solution maintains the basic picture of electron calorimetry in the sense that $t_{\rm cool} < t_{\rm escape}$, but again only if $t_{\rm synch}$ and/or $t_{\rm IC}$ are $\sim t_{\rm brems}$ and/or $t_{\rm ion}$ for galaxies. In T06 and LTQ, we explored the physics of this solution to the spectral index problem in detail. As we discuss in Sect. 4, this solution has a number of implications, and it makes several important and testable predictions.

Finally, another way to flatten the CR spectrum is to give up on calorimetry altogether and appeal to advection. By advecting CRs out of the host galaxy's radiation and magnetic fields, one can maintain a flatter synchrotron spectrum. One then requires that $t_{\rm escape} < t_{\rm cool}$. Since $t_{\rm IC}$ alone varies by orders of magnitude among the galaxies along the FRC, such a mechanism would directly constrain $t_{\rm escape}$ as a function of galaxy properties. To preserve the linearity of the FRC over this dynamic range would also likely require fine-tuning, and it would put potentially unrealistic requirements on the power injected into CRs per unit star formation in the brightest systems. We return to this issue in Sect. 5.

4 Implications of the Bremsstrahlung & Ionization Solution

The solution to the spectral index problem sketched in Sect. 3 can only work if $t_{\rm synch}$ and/or $t_{\rm IC}$ are $\sim t_{\rm brems}$ and/or $t_{\rm ion}$ for the GHz-emitting CR $e^{\pm}$ of galaxies. Can this be possible over the very large dynamic range of the FRC? Scaling for CR $e^{\pm}$ radiating at $\nu_{\rm GHz} = \nu/{\rm GHz}$ frequencies, one finds that

$$t_{\rm synch}/t_{\rm ion} \sim 1\, n_{100} B_{100}^{-1} \nu_{\rm GHz}^{-1} \tag{5}$$

and

$$t_{\rm synch}/t_{\rm brems} \sim 3\, n_{100} B_{100}^{-3/2} \nu_{\rm GHz}^{-1/2}, \tag{6}$$

where $n_{100} = n/100\ {\rm cm}^{-3}$ and $B_{100} = B/100\,\mu{\rm G}$. These ratios are remarkable in light of the fact that we know that the magnetic field strengths of galaxies must dramatically increase as a function of density from the $\sim\mu$G magnetic fields of normal spirals to the $\sim$mG magnetic fields of the densest starbursts ([13]; T06). In the electron calorimeter limit, we find that an approximate scaling $B \propto \Sigma_g^{0.7}$, where Σ_g is the gas surface density of the galaxy, is required to reproduce the linearity of the FRC so that $U_{\rm ph}$ is a constant fraction of $U_{\rm B}$ ([33, 66]; T06; LTQ). With this scaling, and taking $\Sigma_g = 2 m_p n h$, where h is the gas scale height, one finds from Eqs (5) and (6) that

$$t_{\rm synch}/t_{\rm ion} \propto n^{3/10} \quad \text{and} \quad t_{\rm synch}/t_{\rm brems} \propto n^{-1/20}. \tag{7}$$

These imply that ionization losses for GHz emitting $e^{\pm}$ are increasingly important as the density of galaxies increase, and that bremsstrahlung losses are important *and a nearly constant fraction of synchrotron losses for starbursts* across the FRC.[2]

We give the details of this mechanism for flattening the radio spectra of dense galaxies and for maintaining the FRC in LTQ. We find that in starburst galaxies the synchrotron losses are sub-dominant with respect to bremsstrahlung by a factor of $\sim$10. In addition, as implied by Eq. (7), ionization plays an increasingly important role in the most dense galaxies. For a fixed injection rate of CRs per unit star formation, the dominant role of bremsstrahlung in high density starburst galaxies eats away at the radio flux, and would cause a deviation from the linear FRC if another process did not step in to "fill in" the missing radio emission. In LTQ, this extra energy is injected from CR protons, which interact with the dense ISM of starbursts and produce π^0 and $\pi^{\pm}$, which decay to gamma-rays, secondary $e^{\pm}$, and neutrinos. The secondary $e^{\pm}$ cool like the primary electrons via synchrotron, IC, bremsstrahlung, and ionization losses and provide the missing radio flux to maintain the FRC.

4.1 Proton Calorimetry: Conspiracy or Physics?

Such a mechanism for "filling in" the radio-emitting CR population with secondary $e^{\pm}$ from protons has the feel of fine-tuning and conspiracy. Note, though, that given the same assumptions that led to Eq. (2), but assuming that $\eta_{0.1} = \eta/0.1$ of the 10^{51} ergs per supernova goes to CR protons, we have that

$$L_{\mathrm{CR}p} \sim 10^{-3}\, \eta_{0.1} L_{\mathrm{FIR}}. \tag{8}$$

If the CR proton population samples an ISM of density n, the characteristic timescale for pion losses is

$$t_{\pi} \sim 5 \times 10^{7}\ \mathrm{year}\ n^{-1}. \tag{9}$$

This timescale is similar to the bremstrahlung and ionization loss times for CR electrons, and thus we expect that if the CR electrons are calorimetric, and if bremsstrahlung and/or ionization dominates their losses, then the CR protons should be calorimetric too. In analogy with electron calorimetry, we expect starburst "proton calorimeters" such that $t_{\pi} < t_{\mathrm{escape}}$. In this limit, all of the protons are converted to pions (and then secondary $e^{\pm}$, gamma-rays, and neutrinos) before escape. Because $\sim 1/6$ of the CR proton energy goes to $e^{\pm}$ and because $\eta/\xi \sim 20 - 100$, in a proton calorimetric galaxy the secondary $e^{\pm}$ are comparable to, or

[2] In T06 we made the similar point that *if* galactic magnetic fields were always in equipartition with respect to gravity then $B^2 \sim 8\pi^2 G \Sigma^2$, and $t_{\mathrm{synch}}/t_{\mathrm{ion}} \propto n^0$ for GHz emitting $e^{\pm}$.

dominate, the primary CR electrons ([54]; T06). And their emissions, in both the radio (via synchrotron) and MeV-TeV (via bremsstrahlung and IC) bands should also be comparable.

In more detail, define the proton calorimetry fraction as $F_{\rm cal}$ and $\tilde{\delta} = (\eta/\xi)(m_p/m_e)^{p-2} \sim 100$, which measures the injected proton-to-electron ratio at high energies (LTQ).[3] The total power into secondary $e^{\pm}$ can be expressed in terms of the power into primary e^{-} radiating at the same frequency as [29]

$$\begin{aligned} \nu L_\nu(\text{secondary } e^{\pm}) &\approx \frac{1}{6} F_{\rm cal}\, \nu L_\nu(\text{protons}) \\ &\approx \frac{\tilde{\delta}}{6} F_{\rm cal}\, \nu L_\nu(\text{primary } e^{-}) \\ &\approx 12.5 \left(\frac{\tilde{\delta}}{75}\right) F_{\rm cal}\, \nu L_\nu(\text{primary } e^{-}). \end{aligned} \tag{10}$$

Thus, as galaxies become increasingly proton calorimetric, the contribution of the secondary $e^{\pm}$ overwhelms the primary e^{-} and dominates the radio emission at GHz frequencies. This effect alone would dramatically increase the radio emission per unit star formation in galaxies, causing strong deviations from the FRC, except that bremsstrahlung losses increase in lock-step with secondary $e^{\pm}$ production from CR proton pion production as $F_{\rm cal}$ goes from $\sim$0.05 to $\sim$1, from normal star-forming galaxies to those perhaps a few times denser than the starburst of M82 ($n \sim 300 - 500\ {\rm cm}^{-3}$).

Even more importantly, because the transition from small $F_{\rm cal}$ to $F_{\rm cal} \sim 1$ occurs over just a few decades in density, one may ask how the FRC persists for starbursts whose ISM density dramatically exceeds this transition density ($\Sigma_g \sim 0.1$ g cm^{-2} for a gas scale height of ~ 100 pc; see, Fig. 2 of [28]). Here, we return to Eq. (7), which shows that *if* the average magnetic field strengths of galaxies scale as $B \propto \Sigma_g^{0.7}$, the ratio of the bremsstrahlung cooling time to the synchrotron cooling time is virtually constant. This is the reason that the LTQ models converge on this scaling for $B(\Sigma_g)$: in order to maintain the linearity and normalization of the FRC over the remarkable dynamic range of the correlation the density dependence of the ratio $t_{\rm brems}/t_{\rm synch}$ must essentially cancel.

Is all of this a conspiracy and/or fine-tuning, or is it just physics? Yes and no. It is not a conspiracy in the sense that *both* ionization/bremsstrahlung loss timescale and the pion loss timescale have a n^{-1} dependence. We thus expect pionic secondary $e^{\pm}$ to be generated in the proportion needed to "fill in" the missing radio flux lost as galaxies become increasingly denser, and $F_{\rm cal} \to 1$. It is also not a conspiracy in the sense that we let the power-law index x in the function $B \propto \Sigma_g^x$ vary in the models

[3]The definition of $\tilde{\delta}$ depends on the shape of the injection spectrum at low energies. The version we quote here is from LTQ, where we assume the spectrum is a power law in total energy, starting at the particles' rest energy.

in order to find what value of x would generate an FRC and preserve it over its full range. One may argue that varying x is fine-tuning, but we prefer to think of the result, $x = 0.7$, as simply a product of fitting a model to data (the FRC), which may have at its root a deep physical connection between the star formation rate surface density and magnetic energy density of galaxies. All of that said, the approximate cancellation of oppositely directed effects discussed above, and in more detail in LTQ, relies on a certain value for η/ξ or $\tilde{\delta} \sim 100$. Is it fine-tuned? It is in our models, of course, where we set this ratio by hand, but it is not in nature, where the ratio is likely determined by the physics of non-relativistic shock acceleration (e.g., [53]).

4.2 Gamma-Ray & Neutrino Luminosities and CR Energy Density of Starbursts

The strong pionic losses required to produce secondary $e^{\pm}$ sufficient to maintain the FRC ensure that proton calorimetric galaxies will be gamma-ray and neutrino bright [6, 17, 35, 46, 61, 62]. Assuming that $t_\pi < t_{\rm escape}$, 1/3 of the CR proton energy ends up in π^0, one predicts that proton calorimeters should have

$$\begin{aligned} L_\gamma &\sim 3 \times 10^{-4} \eta_{0.1} L_{\rm FIR} \\ &\sim 10^{40}\,{\rm ergs\ s^{-1}}\ \eta_{0.1}\,{\rm SFR}/({\rm M_\odot\ year^{-1}}), \end{aligned} \tag{11}$$

a linear FIR-gamma-ray correlation (see [61]), which is roughly consistent with measurements from *Fermi* [4, 28].

The predicted $L_\gamma/L_{\rm FIR}$ ratio provides a test of our explanation of the FRC and proton calorimetry. In [28] we made a detailed comparison of our models with the GeV- and TeV-detected starbursts NGC 253 and M82 and find that $F_{\rm cal} \sim 0.4$ with factor of $\sim$2 uncertainties. Even so, we show that the observed GeV-to-GHz ratio indicates that secondary $e^{\pm}$ dominantly undergo strong non-synchrotron losses, with the implication that bremsstrahlung and ionization for leptons, and by extension pionic losses for CR protons, are strong in NGC 253 and M82.

The argument is as follows. For the sake of simplicity, assume a flat E^{-2} spectrum for the primary CR protons. If the gamma-ray emission is pionic, and if the radio emission is dominated by secondary $e^{\pm}$, as implied by Eq. (10) for $F_{\rm cal} > 0.1$, then [28]

$$\nu F_\nu(E_\gamma) \approx 4\,\nu F_\nu(E_e)\ f_{\rm synch}, \tag{12}$$

where $f_{\rm synch}$ is the fraction of the CR power going into synchrotron and the factor of 4 comes from the fact that two times as much energy goes to gamma-rays as eventually ends up in secondary $e^{\pm}$ combined with the fact that synchrotron distributes emission from each decade of $e^{\pm}$ energy into two decades of frequency. Taking observed values for the radio flux ($\sim$9 Jy at GHz) and the gamma-ray flux ($\simeq 3 \times 10^{-12}$ ergs cm^{-2} s^{-1}), one finds that

$$f_{\rm synch} \sim \frac{1}{8},$$

consistent with strong non-synchrotron cooling. Better data below ∼1 GeV in these systems, and the detection of the ULIRG Arp 220 would put the models on a still firmer footing.

The strong pionic losses predicted in proton calorimetric galaxies implies that the CR energy density is

$$\begin{aligned} U_{{\rm CR}p} &= L_{{\rm CR}p} t_\pi V^{-1} \propto {\rm SFR}/(r^2 h) n^{-1} \propto F/\Sigma_g \\ &\simeq 10^{-10}\ {\rm ergs\ cm^{-3}} \left(\frac{\Sigma_g}{10^3\ {\rm M_\odot\ pc^{-2}}} \right)^{0.4}, \end{aligned} \tag{13}$$

where the last proportionality makes use of the Schmidt Law of [21]: $F \propto \Sigma_g^{1.4}$. Thus, $U_{\rm CR}$ increases by a factor of ∼100 from Milky Way-like galaxies to the densest starbursts, and therefore the CR ionization rate in such systems is expected to be very large compared to standard values in Galactic molecular clouds ([47,48]; LTQ; [30]). However, since the pressure required for vertical hydrostatic equilibrium in a galaxy scales with $P \propto \Sigma_g^2$, Eq. (13) implies that $U_{{\rm CR}p}/P \propto \Sigma_g^{-1.6}$, and therefore that CRs are dynamically weak compared to gravity in starbursts (LTQ), in contrast to low surface density Milky Way-like galaxies.

4.3 *Further Implications: The γ-Ray Background and "Puffy" Starbursts*

Additional implications of proton calorimetry in starbursts and the importance of non-synchrotron cooling for the CR $e^\pm$ population are as follows. First, the FRC should hold to higher redshift than previously thought because IC losses on the CMB, which eventually make galaxies radio-dim, have to compete with all loss mechanisms, not just the sub-dominant synchrotron component [26]. Second, the starburst contribution to the diffuse gamma-ray and neutrino backgrounds should be of order $\sim 10^{-6} \eta_{0.1}$ GeV cm^{-2} s^{-1} str^{-1} integrated above 1 GeV, depending on the fraction of star formation occurring proton calorimetric galaxies over cosmic time (T06; [28,32,61]; see also [49]).

Finally, if indeed galaxy magnetic fields scale as something like $B \propto \Sigma_g^{0.7}$, starbursts of the same Σ_g but different gas scale heights would have the same B, but different average gas densities. This should unbalance our mechanism for "filling in" the missing radio flux caused by strong ionization and bremsstrahlung losses. Thus, all else being equal, "puffy" starbursts should be radio bright with respect to the FRC by a factor of $\sim 2-3$ [26]. This has perhaps been observed in the dynamically hot submillimeter galaxies at high-z [24,39,43,65].

5 Other Solutions to the Spectral Index Problem

5.1 Winds

As mentioned in Sect. 3, galactic-scale winds can flatten radio spectra (e.g., [33]; LTQ). This might well be important for starbursts like M82 and NGC 253 or the LIRGs and ULIRGs, where the radio spectra are flattest, the tension with the simplest version of the calorimeter model is strongest (Sect. 2), and where evidence for large-scale outflows is ubiquitous.

We can put some bounds on this mechanism by considering the maximum cooling time for CR $e^{\pm}$ in star-forming galaxies as set by IC, which is inversely proportional to $U_{\rm ph} \propto F \propto \dot{\Sigma}_{\star}$, the SFR per unit area. Writing $t_{\rm IC}$ for the CR $e^{\pm}$ emitting at GHz, one finds that

$$t_{\rm IC} \simeq 5 \times 10^5 \,{\rm year}\; B_{100}^{1/2}\, \nu_{\rm GHz}^{1/2}\, \dot{\Sigma}_{\star,\,10}^{-1}, \tag{14}$$

where $\dot{\Sigma}_{\star,\,10} = \dot{\Sigma}_{\star}/10 {\rm M}_{\odot}\ {\rm year}^{-1}\ {\rm kpc}^{-2}$ and $B_{100} = B/100\mu{\rm G}$ has been scaled to a value appropriate to an M82-like starburst. If we set this maximum cooling time equal to the wind escape time $t_{\rm wind} \sim h/v_{\rm wind}$, then we can derive the *minimum* wind velocity required to compete with IC losses:

$$v_{\rm wind,\,min} \sim 200\,{\rm km\ s^{-1}} h_{100} B_{100}^{-1/2} \nu_{\rm GHz}^{1/2} \dot{\Sigma}_{\star,\,10}. \tag{15}$$

For a ULIRG-like $\dot{\Sigma}_{\star} \sim 10^3\ {\rm M}_{\odot}{\rm year}^{-1}{\rm kpc}^{-2}$ the limit on $v_{\rm wind}$ increases significantly, but is somewhat mitigated by the much larger ∼mG magnetic field strengths in these systems: $v_{\rm wind,\,min} \sim 6{,}000\,{\rm km\ s^{-1}}\, h_{100} B_{\rm mG}^{-1/2} \nu_{\rm GHz}^{1/2} \dot{\Sigma}_{\star,\,1{,}000}$.

Such a wind speed exceeds those inferred observationally from starbursts and ULIRGs in absorption-line studies of cool gas (e.g., [37]). Although the asymptotic wind speed can approach $\sim 1{,}000 - 3{,}000\,{\rm km\,s^{-1}}$ in models of hot thermally-driven [11]-like outflows from starbursts, within the starburst itself, the flow is subsonic with velocities in the range of $\sim 500\,{\rm km\,s^{-1}}$ (see Fig. 3 of [59]). This increases the advective escape timescale significantly in the region where energetic losses for CRs are the strongest.

In the case of dense and compact ULIRGs, we view these inferred *minimum* escape speeds to be prohibitive. However, in M82-like starbursts $v_{\rm wind,\,min}$ may well be achieved and it is at least worth considering if CRs *only* propagate in the rarified hot ISM, thereby avoiding strong losses before escape and ultimately leading to flatter radio spectra in agreement with observations.

Although such models for the FRC deserve further investigation, there are several issues with any model that would seek to solve the spectral index problem with advection over the full dynamic range of the FRC. These can be summarized as (1) energetics, (2) fine-tuning, and (3) gamma-rays.

The arguments proceed as follows. If most of the primary CR electrons are advected out of the system before cooling significantly via synchrotron, one requires larger values of ξ (Eq. 2) to reproduce the radio emission we see. This would require ξ to increase along the FRC from normal galaxies to starbursts, and in precisely the proportion needed to preserve the linearity of the FRC. This requires the shock acceleration mechanisms of the host galaxy to"know" about the CR escape conditions of the host, which prima facie appears fine-tuned [60]. In addition, since the FRC already requires of order 0.5 % of the energy per supernova to go into primary CR electrons, this mechanism would require a fairly large value for ξ in the densest starbursts.

Similarly, gamma-rays from M82 and NGC 253 are observed. Thus, if the CR protons are advected out of the system without undergoing significant pion losses, one encounters the same problem as with the primary electrons: the total power injected in CR protons (η, Eq. 8) must increase in proportion to the ratio of $t_\pi / t_{\rm wind}$ to preserve the observed gamma-ray emission. If the observed FIR-gamma-ray correlation persists for star-forming galaxies this might prove energetically difficult to achieve in more extreme starbursts like the ULIRGs since the gamma-ray luminosities from M82 and NGC 253 already require $\eta \sim 0.1$, and with $\sim$40 % ($F_{\rm cal} \sim 0.4$) of that power converted to GeV gamma-rays through pionic losses. Although such solutions might be workable for individual galaxies, or galaxies spanning a relatively small dynamic range in properties, it seems difficult to make this work without fine-tuning in the face of the FRC and the gamma-ray detections. Clearly, though, a gamma-ray detection of Arp 220, where $\dot{\Sigma}_\star$, n, and $v_{\rm wind,\,min}$ are much larger than M82 and NGC 253 would make these arguments much stronger.

Like proton calorimetry, one consequence of the wind solution to the spectral index problem would be low $U_{\rm CR}$ in starbursts. In the advection-dominated limit, $U_{\rm CR} \sim L_{{\rm CR}p} t_{\rm escape} V^{-1}$:

$$\begin{aligned} U_{\rm CR} &< 10^{-3} \eta_{0.1} F_{\rm FIR} / v_{\rm wind,\,min} \\ &\sim 4 \times 10^{-10}\ {\rm ergs\ cm^{-3}}\ \dot{\Sigma}_{\star,\,100} (v_{\rm wind}/10^3\ {\rm km/s})^{-1}. \end{aligned} \tag{16}$$

The Schmidt Law implies that a galaxy with $\dot{\Sigma}_{\star,\,100} = 1$ has $\Sigma_g \sim 2\,{\rm g\,cm^{-2}}$ [21], implying a pressure required for hydrostatic equilibrium of $P_{\rm hydro} \sim \pi G \Sigma_g^2 \sim 10^{-6}$ ergs cm^{-3}, or approximately $\sim$3,000 times larger than the maximum on $U_{\rm CR}$ scaled in Eq. (16). For higher $\dot{\Sigma}_\star$, $U_{\rm CR}/P_{\rm hydro}$ decreases further.

5.2 *Free-Free Emission & Absorption*

Thermal bremsstrahlung could flatten the radio spectral slopes of galaxies in two ways. First, Condon et al. [13] argue that the ISM of ULIRGs in the local universe are optically-thick to free-free absorption, which would cause spectral turnovers near or below GHz frequency, flattening the synchrotron spectra as frequency decreases before finally causing it to fall. Second, free-free emission could flatten

the spectra of starbursts at frequencies above 1 GHz, potentially masking a fully-cooled synchrotron spectrum and causing us to infer the importance of relativistic bremsstrahlung in cooling the CR $e^{\pm}$ population.

This solution to the spectral index problem also deserves further exploration. Here, we note several pieces of the relevant observations. The most important is that free-free emission is flat with $\alpha \simeq 0.1$: the 1 GHz thermal flux density should be just $\sim$40 % larger than the thermal 30 GHz flux density. But the spectral indices of starbursts are $\alpha \sim 0.5 - 0.7$ between these frequencies, so the total 30 GHz flux densities are much smaller than those at 1 GHz. Therefore, the total contribution of free-free emission relative to synchrotron at 1 GHz must be small. Furthermore, the spectrum of M82 remains relatively steep with $\alpha \sim 0.5$ even at 10–30 GHz in the starburst core [5, 38, 67], with steeper spectra in the halo above and below the plane [23, 51, 52, 57]. That means nonthermal emission is significant or dominant even at those frequencies, tightening limits on thermal emission further.

Most models fitting to the radio spectrum obtain thermal fractions of a few to $\sim$10 % for the starburst core of M82 (e.g., [23,27,67]). Similar thermal fractions are inferred for normal spiral galaxies [44]. In our current understanding, the amount of free-free emission is related to the number of ionizing photons produced by the starburst. The hottest stars, tracers of recent star formation, are the presumed sources of these photons, so the free-free emission should be directly proportional to the star-formation rate and thus the infrared and synchrotron radio emission, if the photons are effective at ionizing neutral gas. Condon [14] calculated a GHz thermal fraction of $\sim 1/8$ using an estimate of the ionizing photon generation rate. Only some fraction of these photons actually ionize gas—some might escape the starburst entirely or be absorbed by dust, which could reduce the thermal fraction from this value. But how absorption and escape effect the thermal fraction in starbursts is unknown (radio recombination line observations provide another avenue for understanding the interaction between gas and ionizing photons; [22]).

The interpretation of radio spectral indices above and below 1 GHz is undoubtably complicated by the inhomogeneous nature of the ISM, including patchy absorption (e.g., [7, 31]), and radio sources, such as unresolved supernova remnants [34]. Better wide-band data in the 1–30 GHz frequency range would significantly improve constraints on the role of free-free emission in shaping the radio spectra of the densest starbursts. The most useful constraints could potentially be derived from spatially resolved broadband spectral slopes and curvature.

6 Summary

The picture of the FRC in starbursts that emerges from the considerations of this proceedings is significantly more complicated than the simplest picture of calorimetry one might envision: that primary CR electrons cool completely before escape from the host galaxy by synchrotron and that FIR photons are just the reprocessed light from massive stars (Sect. 2). First, the radio spectra of galaxies are too flat, arguing strongly against complete synchrotron cooling acting alone,

or synchrotron and IC acting in tandem, or in any relative proportion. Second, if the gamma-ray luminosities of starbursts like M82 and NGC 253 are dominated by pion decays, then these gamma-rays *must be accompanied* by secondary $e^{\pm}$ from charged pions. If the CR protons are even partly calorimetric ($F_{\rm cal} > 0.2$), which they must be in order to power the gamma-ray flux observed, then secondary $e^{\pm}$ dominate the primary CR electrons (see Eq. 10). Furthermore, a comparison of the GeV power to the GHz power shows that these secondary $e^{\pm}$ cool predominantly via non-synchrotron cooling (Eq. 12). Thus, the only pieces of the simplest version of the calorimeter model that survive are (1) that the CR $e^{\pm}$ (both primary and secondary!) cool completely (but not, predominantly, by synchrotron or IC in starbursts!) before they escape, and that (2) the FIR is indeed dust-reprocessed starlight.[4]

In LTQ we tried to set down a theory of the FRC that would work across its diversity of galaxies and star-formation environments. We found that *if* the magnetic fields of galaxies scale as $B \propto \Sigma_g^{0.7}$ that the linearity and normalization of the FRC is reproduced for standard values of $\tilde{\delta} \propto \eta/\xi$, the ratio of the total energy injected in primary CR protons to that in primary CR electrons. This follows from the density dependence of both bremsstrahlung and pion cooling, the energy dependence of bremsstrahlung energy losses, and the fact that we observe the FRC at a given frequency, and not at a given $e^{\pm}$ energy (see Sect. 4). This theory of the FRC makes a number of predictions. It gives a way of estimating the total contribution of star-forming galaxies to the extragalactic background, it predicts deviations from the FRC at fixed Σ_g as a function of the scale height of the galaxies considered, it predicts a linear FIR-gamma-ray correlation for proton calorimetric galaxies, and it allows for consistency checks among the different wavebands that so far broadly agree with observations.

Different explanations for the spectral index problem, such as strong advection in galaxy-scale winds, or free-free absorption/emission, have their own problems (Sect. 5), which have yet to be fully quantified.

Numerous pieces are still missing. Among them, a gamma-ray detection of Arp 220, the nearest ULIRG, which has exceptionally high gas densities, should provide a strong test of the hypothesis of proton calorimetry. Additionally, better constraints on the gamma-ray emission from M82 and NGC 253 at energies below 1 GeV would constrain the relative importance of pionic gamma-rays, IC, and bremsstrahlung, which would have immediate impact on our interpretation of the radio emission in these systems.

Acknowledgements We thank Eliot Quataert, Eli Waxman, and Avi Loeb for conversations and collaboration. TAT is supported in part by NASA Grant NNX10AD01G. BCL is supported by a Jansky Fellowship from the National Radio Astronomy Observatory. NRAO is operated by Associated Universities, Inc., under cooperative agreement with the National Science Foundation.

[4]There is ample evidence that the FIR is not a direct tracer of star formation at the very low luminosity end of the FRC [8].

References

1. Abdo, A. A., et al. 2010, *ApJL*, 709, L152
2. Acciari, V. A., et al. 2009, *Nature*, 462, 770
3. Acero, F., et al. 2009, *Science*, 326, 1080
4. Ackermann et al. 2012, ApJ, 755, 164
5. Adebahr, B. et al. 2012, arXiv:1209.552
6. Akyuz, A., Brouillet, N., & Ozel, M. E. 1991, *A&A*, 248, 419
7. Anantharamaiah, K. R., Zhao, J.-H., Goss, W. M., & Viallefond, F. 1993, ApJ, 419, 585
8. Bell, E. F. 2003, ApJ, 586, 794
9. Blandford, R., & Eichler, D. 1987, Phys. Rep., 154, 1
10. Boulares, A., & Cox, D. P. 1990, ApJ, 365, 544
11. Chevalier, R. A., & Clegg, A. W. 1985, Nature, 317, 44
12. Clemens, M. S., Vega, O., Bressan, A., et al. 2008, A&A, 477, 95
13. Condon, J. J., Huang, Z.-P., Yin, Q. F., & Thuan, T. X. 1991, ApJ, 378, 65
14. Condon, J. J. 1992, ARA&A, 30, 575
15. Crocker, R. M., Jones, D. I., Aharonian, F., et al. 2011a, MNRAS, 411, L11
16. Crocker, R. M., Jones, D. I., Aharonian, F., et al. 2011b, MNRAS, 413, 763
17. de Cea del Pozo, E., et al. 2009, ApJ, 698, 1054
18. de Jong, T., Klein, U., Wielebinski, R., & Wunderlich, E. 1985, A&A, 147, L6
19. Helou, G., Soifer, B. T., & Rowan-Robinson, M. 1985, ApJL, 298, L7
20. Ivison, R. J., Magnelli, B., Ibar, E., et al. 2010, *A&A*, 518, L31
21. Kennicutt, R. C., Jr. 1998, ApJ, 498, 541
22. Kepley, A. A., Chomiuk, L., Johnson, K. E., et al. 2011, ApJL, 739, L24
23. Klein, U., Wielebinski, R., & Morsi, H. W. 1988, A&A, 190, 41
24. Kovács, A., Chapman, S. C., Dowell, C. D., et al. 2006, *ApJ*, 650, 592
25. Lacki, B. C., Thompson, T. A., & Quataert, E. 2010, *ApJ*, 717, 1 (LTQ)
26. Lacki, B. C., & Thompson, T. A. 2010, *ApJ*, 717, 196
27. Lacki, B. C., & Thompson, T. A. 2010, arXiv:1010.3030
28. Lacki, B. C., Thompson, T. A., Quataert, E., Loeb, A., & Waxman, E. 2011, *ApJ*, 734, 107
29. Lacki, B. C. 2011, Ph.D. Thesis, The Ohio State University
30. Lacki, B. C. 2012, arXiv:1204.2580
31. Lacki, B. C. 2012, arXiv:1206.7100
32. Lacki, B. C., Horiuchi, S., & Beacom, J. F. 2012, arXiv:1206.0772
33. Lisenfeld, U., Voelk, H. J., & Xu, C. 1996, A&A, 306, 677
34. Lisenfeld, U., & Völk, H. J. 2000, A&A, 354, 423
35. Loeb, A., & Waxman, E. 2006, JCAP, 5, 3
36. Mao, M. Y., Huynh, M. T., Norris, R. P., et al. 2011, *ApJ*, 731, 79
37. Martin, C. L. 2005, ApJ, 621, 227
38. Marvil, J., Eilek, J., & Owen, F. 2009, Bulletin of the American Astronomical Society, 41, #418.02
39. Michałowski, M. J., Watson, D., & Hjorth, J. 2010, *ApJ*, 712, 942
40. Murphy, E. J., Braun, R., Helou, G., et al. 2006a, *ApJ*, 638, 157
41. Murphy, E. J., Helou, G., Braun, R., et al. 2006b, *ApJL*, 651, L111
42. Murphy, E. J., Helou, G., Kenney, J. D. P., Armus, L., & Braun, R. 2008, *ApJ*, 678, 828
43. Murphy, E. J., Chary, R.-R., Alexander, D. M., et al. 2009, *ApJ*, 698, 1380
44. Niklas, S., Klein, U., & Wielebinski, R. 1997, A&A, 322, 19
45. Niklas, S., & Beck, R. 1997, A&A, 320, 54
46. Paglione, T. A. D., Marscher, A. P., Jackson, J. M., & Bertsch, D. L. 1996, ApJ, 460, 295
47. Papadopoulos, P. P. 2010, ApJ, 720, 226
48. Papadopoulos, P. P., Thi, W.-F., Miniati, F., & Viti, S. 2011, MNRAS, 414, 1705
49. Pavlidou, V., & Fields, B. D. 2002, *ApJL*, 575, L5
50. Reddy, N. A., & Steidel, C. C. 2004, *ApJL*, 603, L13

51. Reuter, H.-P., Klein, U., Lesch, H., Wielebinski, R., & Kronberg, P. P. 1994, A&A, 282, 724
52. Reuter, H.-P., Klein, U., Lesch, H., Wielebinski, R., & Kronberg, P. P. 1992, A&A, 256, 10
53. Riquelme, M. A., & Spitkovsky, A. 2011, ApJ, 733, 63
54. Rengarajan, T. N. 2005, arXiv:astro-ph/0511156
55. Roussel, H., Helou, G., Smith, J. D., et al. 2006, *ApJ*, 646, 841
56. Sargent, M. T., Schinnerer, E., Murphy, E., et al. 2010, *ApJL*, 714, L190
57. Seaquist, E. R., & Odegard, N. 1991, ApJ, 369, 320
58. Smolčić, V., Schinnerer, E., Zamorani, G., et al. 2009, *ApJ*, 690, 610
59. Strickland, D. K., & Heckman, T. M. 2009, ApJ, 697, 2030
60. Thompson, T. A. et al. 2006, *ApJ*, 645, 186 (T06)
61. Thompson, T. A., Quataert, E., Waxman, E. 2007, *ApJ*, 654, 219
62. Torres, D. F. 2004, *ApJ*, 617, 966
63. van der Kruit, P. C. 1971, A&A, 15, 110
64. van der Kruit, P. C. 1973, A&A, 29, 263
65. Vlahakis, C., Eales, S., & Dunne, L. 2007, *MNRAS*, 379, 1042
66. Völk, H. J. 1989, *A&A*, 218, 67
67. Williams, P. K. G., & Bower, G. C. 2010, ApJ, 710, 1462
68. Yun, M. S., Reddy, N. A., & Condon, J. J. 2001, ApJ, 554, 803

A Possible GeV-Radio Correlation for Starburst Galaxies

S. Schöneberg, J. Becker Tjus, and F. Schuppan

Abstract For star-forming regions, there is a correlation of radio and FIR-emission established. The radio emission is caused by synchrotron radiation of electrons, while the FIR emission is attributed to HII regions of OB stars and hot dust powered by those stars. Another possible correlation for star-forming regions might exist between the aforementioned radio emission and the gamma ray emission in the GeV regime. The GeV gamma ray emission of star-forming regions is dominated by the decay of neutral pions formed in collisions of cosmic ray (CR) protons accelerated at supernova remnants (SNRs) with ambient hydrogen, while the electrons generating the synchrotron emission are assumed to be accelerated at the same SNRs. Assuming the same spectral shape for the CR proton and electron distribution and a fixed ratio of CR protons to electrons, the proton- and electron-calorimetry of the star-forming regions can be tested. Furthermore, this provides a method to derive the magnetic field strength in the star-forming region complementary to the existing methods.

1 Introduction

A plot of the total gamma ray luminosity against the luminosity at 5 GHz for M82 and NGC 253 (both starburst galaxies), NGC 1068 and NGC 4945 (starburst-Seyfert composites) and 30 Doradus in the Large Magellanic Cloud and the Milky Way center reveals a trend, as Fig. 1 shows. To interpret this possible correlation, a theoretical approach is followed: The emission of the objects dealt with is assumed to be dominated by SNRs inside the objects. The detected radio emission is attributed to synchrotron radiation of electrons accelerated at the SNRs, the GeV

S. Schöneberg (✉) · J.B. Tjus · F. Schuppan
Ruhr-Universität Bochum, Fakultät für Physik & Astronomie, 44780 Bochum, Germany
e-mail: ssc@tp4.rub.de

D.F. Torres and O. Reimer (eds.), *Cosmic Rays in Star-Forming Environments*,
Astrophysics and Space Science Proceedings 34, DOI 10.1007/978-3-642-35410-6_21,

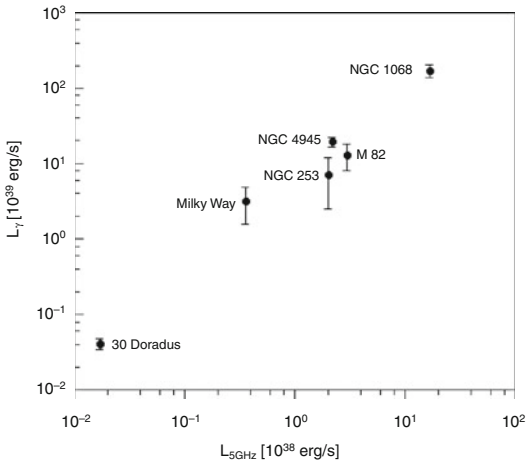

Fig. 1 Correlation between radio luminosity at 5 GHz and the γ-luminosity

gamma rays are caused by the decay of neutral pions formed in collisions of protons accelerated at the SNRs with ambient protons:

$$\mathrm{p_{CR}} + \mathrm{p} \rightarrow \pi^{+/-/0} + X \tag{1}$$

$$\pi^0 \rightarrow \gamma + \gamma \; . \tag{2}$$

Neutrinos are produced from charged pions, where searches are dominated by a background of atmospheric neutrinos so far [2]. Both protons and electrons are probably accelerated at the same site, so it is assumed that their spectra have the same –or a very similar– shape, they only differ by a constant factor

$$\frac{\mathrm{d}N}{\mathrm{d}E_\mathrm{p}} = a_\mathrm{p} \left(\frac{E_\mathrm{p}}{E_0}\right)^{-p}, \quad \frac{\mathrm{d}N}{\mathrm{d}E_\mathrm{e}} = a_\mathrm{e} \left(\frac{E_\mathrm{e}}{E_0}\right)^{-p}, \quad 0.01 \leq \frac{a_\mathrm{e}}{a_\mathrm{p}} \leq 1. \tag{3}$$

To examine the trend in Fig. 1, both radiation processes are investigated in more detail in the following sections.

2 Electron Synchrotron Radiation → Radio Emission

The electron spectral energy distribution is assumed to be a simple power-law:

$$N(E_\mathrm{e})\,\mathrm{d}E_\mathrm{e} = a_\mathrm{e} \left(\frac{E_\mathrm{e}}{m_\mathrm{e}c^2}\right)^{-p} \mathrm{d}E \; . \tag{4}$$

If each electron radiates all its energy at a single frequency ν, the emission coefficient ϵ_ν can be written as:

$$\Rightarrow \epsilon_\nu = a_\mathrm{e} \frac{1}{6} \beta^2 m_\mathrm{e}^2 c^4 \left(\frac{\sigma_\mathrm{T} B}{e} \right) \left(\frac{\nu}{\nu_\mathrm{G}} \right)^\delta \,, \tag{5}$$

$$E = \gamma m_\mathrm{e} c^2, \; \gamma = \left(\frac{\nu}{\nu_\mathrm{G}} \right)^{\frac{1}{2}}, \; \frac{\mathrm{d}E}{\mathrm{d}\nu} = \frac{\nu^{-\frac{1}{2}}}{2\nu_\mathrm{G}^{\frac{1}{2}}} m_\mathrm{e} c^2, \; U_B = \frac{B^2}{8\pi}, \; \delta = (1-p)/2 \,, \tag{6}$$

using the expressions above, where e is the elementary charge, ν_G is the gyrofrequency and σ_T is the Thomson cross-section. In order to obtain the radio luminosity of an object, the emission coefficient is multiplied by the average volume V of an SNR and the number of SNRs, N_SNR in the object:

$$L_\mathrm{Radio} = V N_\mathrm{SNR} \int_{\nu_0}^{\nu_1} \epsilon_\nu(\nu) \, \mathrm{d}\nu \tag{7}$$

$$\mathrm{d}L_\nu = V N_\mathrm{SNR} \, a_\mathrm{e} \frac{1}{6} \beta^2 m_\mathrm{e}^2 c^4 \left(\frac{\sigma_\mathrm{T} B}{e} \right) \left(\frac{\nu}{\nu_\mathrm{G}} \right)^\delta \mathrm{d}\nu \,. \tag{8}$$

By expressing the emission coefficient in terms of energy instead of frequency, the synchrotron flux can be written as:

$$E^2 \frac{\mathrm{d}N}{\mathrm{d}E} = \frac{E}{h} \epsilon(E) = \frac{E}{h} A_\mathrm{e} \frac{1}{6} \beta^2 m_\mathrm{e}^2 c^4 \left(\frac{\sigma_\mathrm{T} B}{e} \right) \left(\frac{E}{h\nu_\mathrm{G}} \right)^\delta \,, \tag{9}$$

where $A_\mathrm{e} = V N_\mathrm{SNR} \, a_\mathrm{e}$.

3 GeV Gamma Rays from pp-Interaction

Following [4], the differential proton flux in each object is derived from gamma ray observations under the assumption that these gamma rays are dominantly formed by pion decay from proton-proton interactions. The spectral shape of the primary proton flux is the same as that of the primary electrons (see Eq. 3) and of the gamma rays from pion decay in the energy range of 300 MeV $< E_\gamma <$ $E_\mathrm{p}^\mathrm{max}/10$. The differential gamma ray luminosity is calculated as:

$$E_\gamma^2 \frac{\mathrm{d}N_\gamma}{\mathrm{d}E_\gamma} = V N_\mathrm{SNR} a_\mathrm{p} n_\mathrm{H} c E_\gamma^2 \int_{E_\mathrm{min}}^{\infty} \sigma_\mathrm{inel}(E_\mathrm{p}) \left(\frac{E_\mathrm{p}}{E_0} \right)^{-p} F_\gamma \left(\frac{E_\gamma}{E_\mathrm{p}}, \, E_\mathrm{p} \right) \frac{\mathrm{d}E_\mathrm{p}}{E_\mathrm{p}} \,. \tag{10}$$

The calculation is done following [4], where the δ-functional approach is used for energies below 100 GeV and the analytical approximation given there is used for higher energies.

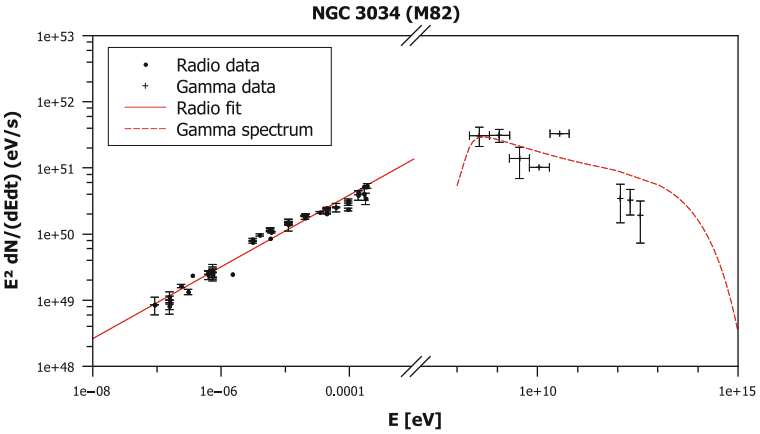

Fig. 2 Modeled partial SED of M82

Table 1 Parameters A_p calculated from Γ-index and gamma ray luminosity, A_e calculated from a fit to the radio data

Source	$\Gamma = p_p$	A_p[1/erg]	δ	p_e	A_e[1/erg]
NGC 1068	2.31 ± 0.13	1.45E + 68	-0.710 ± 0.004	2.421 ± 0.008	1.76E + 69
NGC 4945	2.3 ± 0.1	6.16E + 67	-0.564 ± 0.011	2.129 ± 0.022	7.50E + 66
NGC 253	2.14 ± 0.18	1.00E + 66	-0.525 ± 0.006	2.051 ± 0.012	1.77E + 66
NGC 3034	2.2 ± 0.2	3.20E + 66	-0.457 ± 0.001	1.914 ± 0.002	9.60E + 65

4 Comparison and Conclusions

Combining the spectra as derived from protons and electrons, respectively, allows to model the SED for each object examined. In Fig. 2, this is shown for M82. The gamma ray luminosity L_γ and the spectral index Γ for NGC 4945, 1068 and 3043 given by Lenain et al. [5] and for NGC 253 from [1] are used to calculate $A_p = V N_{SNR}\, a_p$. Using radio data, fits to the radio spectra are made to find the radio synchrotron index δ and the normalization of the primary electron spectrum, A_e, for a magnetic field of $B = 1\,\mu G$. From δ, the spectral index p of the underlying primary electron spectrum is derived. The corresponding values of the calculation are given in Table 1, where $n_H = 100\,cm^{-3}$ was assumed for the calculation of A_p. The quantity A_e depends on the magnetic field as $A_e \propto B^\delta / B$, whereas A_p depends on the average hydrogen density n_H as $A_e \propto 1/n_H$. These expressions can be combined using the inequality in Eq. (3). This allows to determine a possible range of combinations of the magnetic field strength B and the average hydrogen density n_H. This is done in Fig. 3. As can be seen, for each galaxy the observed values for the average hydrogen density and the magnetic field strength lie within the theoretically allowed range, which is the area between the lines corresponding to $a_e/a_p = 0.01$ (dashed black line) and $a_e/a_p = 1$ (solid red line). To test the assumption that the

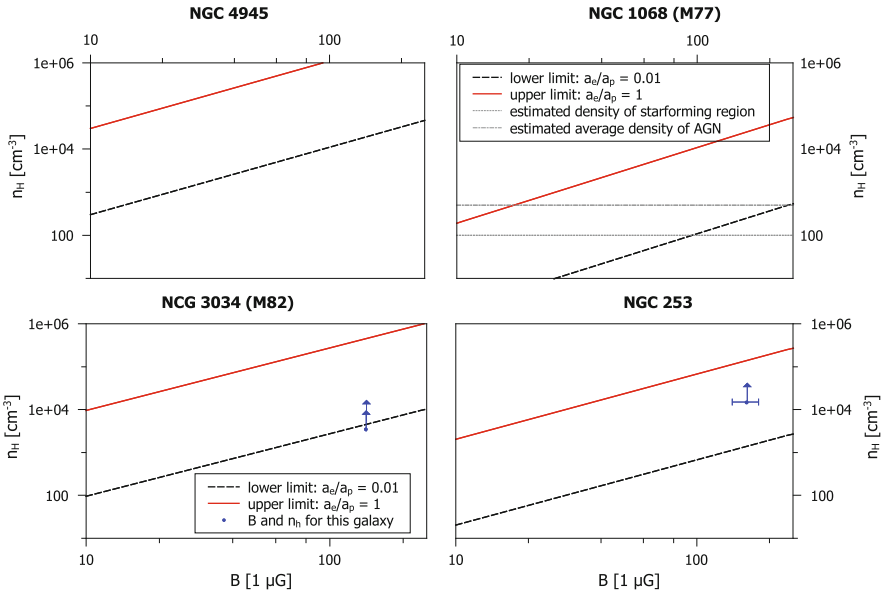

Fig. 3 Possible range of the parameters B and n_{H} for the individual galaxies (Density estimates taken from: [6, 7])

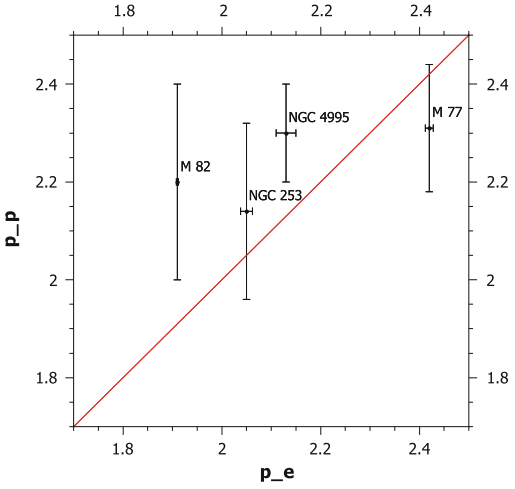

Fig. 4 Spectral index of the proton and electron distribution for each object as derived from gamma or radio data, respectively. The *solid line* represents $p_{\mathrm{p}} = p_{\mathrm{e}}$

energy spectra of protons and electrons have the same shape, the electron and proton spectral indices of the individual galaxies have been calculated and are shown in Fig. 4.

For a given average hydrogen density and an estimate of $a_{\mathrm{e}}/a_{\mathrm{p}}$, this approach could be used to determine the magnetic field strength, complementary to the methods presented in [8] and [3]. For a given average hydrogen density, magnetic

field strength and a fixed ratio for a_e/a_p, this approach could be used to check whether the galaxy is calorimetric for both protons and electrons to the same extent. However, further improvement of the statistics is required to check the possible correlation of GeV gamma rays and radio emission from star-forming regions. Additionally, a more detailed theoretical examination has to be performed to establish this connection and gain new insights. The versatility of such a correlation strongly motivates further investigation in the future.

Acknowledgements We would like to thank B. Adebahr and R.J. Dettmar for helpful and inspiring discussions. We further acknowledge funding from the DFG, Forschergruppe "Instabilities, Turbulence and Transport in Cosmic Magnetic Fields" (FOR1048, Project BE 3714/5-1), the support from Mercator Stiftung, with a contributing grant within the MERCUR project An-2011-0075, from the Junges Kolleg (Nordrheinwestfälische Akademie der Wissenschaften und der Künste) and the support by the Research Department of Plasmas with Complex Interactions (Bochum).

References

1. Abramowski, A. and others: "Spectral analysis and interpretation of the γ-ray emission from the Starburst galaxy NGC 253", arXiv: 1205.5485; submitted to Astroph. Journal (2012)
2. Fedynitch, A., Becker Tjus, J. and Desidiati, P.: "Influence of hadronic interaction models and the cosmic ray spectrum on the high energy atmospheric muon and neutrino flux", arXiv:1206.6710; submitted to Phys. Rev. D. (2012)
3. Heesen, V. and others: "Cosmic rays and the magnetic field in the nearby starburst galaxy NGC 253 III. Helical magnetic fields in the nuclear outflow", Astron. & Astroph. 535, A79 (2011)
4. Kelner, S. R., Aharonian, F. A. and Bugayov, V. V.: "Energy spectra of gamma rays, electrons, and neutrinos produced at proton-proton interactions in the very high energy regime", Phys. Rev. D. 74:3 (2006)
5. Lenain, J.-P. and others: "Seyfert 2 galaxies in the GeV band: jets and starburst", Astron. & Astroph. 524, A72 (2010)
6. Matsushita, S. and others: "Dense and Warm Molecular Gas and Warm Dust in Nearby Galaxies", Publ. of the Astron. Society of Japan 62, 409 (2010)
7. Spinoglio, L. and others: "The Far-Infrared Emission Line and Continuum Spectrum of the Seyfert Galaxy NGC 1068", Astroph. Journal 623, 123 (2005)
8. Thompson, T. A. and others: "Magnetic Fields in Starburst Galaxies and the Origin of the FIR-Radio Correlation", Astroph. Journal 645, 186 (2006)

Shock Acceleration of Relativistic Particles in Galaxy Collisions

U. Lisenfeld and H.-J. Völk

Abstract In a special type of interacting galaxy systems, in which two galaxies collide face-on, radio synchrotron bridges between the two components have been observed. We propose that this radio emission is emitted by relativistic electrons accelerated in shocks produced by gas dynamic interaction of the respective interstellar media during the collision. The sites of acceleration would thus be fundamentally different from most other galaxies where relativistic particles are believed to be accelerated in supernova remnants. We present a model for the radio emission that is able to explain the observed power and spectral index. This kind of process could be relevant, in addition to the cases modelled and discussed here, for galaxies in clusters and groups and for galaxies at high redshift.

1 Introduction

The non-thermal radio emission in galaxies is caused by relativistic electrons moving in a magnetic field and emitting synchrotron radiation. There exists general agreement that these relativistic particles are accelerated in supernova remnants (SNRs). These sites of production establish a close relation between relativistic particles (and their associated radio emission) and recent star formation (SF). An important consequence is that the nonthermal radio emission is a good indicator for recent SF (e.g. [4]), an indicator with the huge advantage of not being affected by extinction. An observational confirmation of this close relation between radio

U. Lisenfeld (✉)
Department of Física Teórica y del Cosmos, Universidad Granada, 18071 Granada, Spain
e-mail: ute@ugr.es

H.-J. Völk
Max-Planck-Institut für Kernphysik, Heidelberg, Germany
e-mail: Heinrich.Voelk@mpi-hd.mpg.de

D.F. Torres and O. Reimer (eds.), *Cosmic Rays in Star-Forming Environments*,
Astrophysics and Space Science Proceedings 34, DOI 10.1007/978-3-642-35410-6_22,

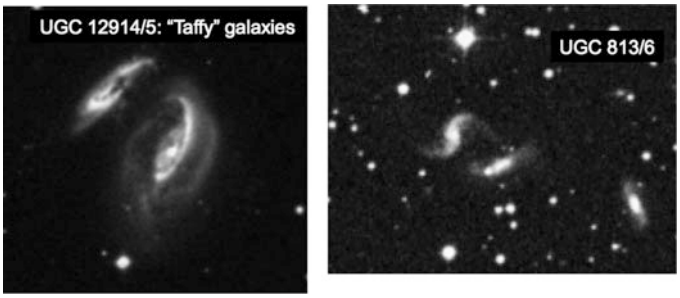

Fig. 1 Images from the Digital Sky Survey (DSS2) of UGC 12194/5 (*left*) and UGC 813/6 (*right*)

emission and SF is the validity of the far-infrared (FIR) radio correlation of galaxies which is followed by all galaxies, except radio-loud AGNs, and which is believed to the driven by SF.

In the present work we are going to present a special type of interacting galaxies, two objects in a face-on collision, which challenges the universal validity of this picture. In these systems there are strong indications for acceleration of relativistic electrons in shocks produced by the gas dynamic interaction of the interstellar media (ISM) during the collision instead of shocks in SNRs. We present a model that is able to explain the radio continuum and the spectral index of the radio bridge. The model has been described in more detail in [8], see also [11] for some extensions and revisions.

2 Face-On Colliding Galaxies

Condon et al. [5] detected a pronounced radio synchrotron bridge in the face-on colliding system UGC 12914/5 (called "Taffy" galaxies). A similar system, UGC 813/6, was observed later by Condon et al. [6] (Fig. 1). Apart from radio continuum emission, a large amount of atomic [5, 6] and molecular gas has also been detected in the bridges [2, 3]. In both systems the two galaxies have experienced a direct, face-on collision some 30 Myr ago, in which the galactic disks collided head-on and interpenetrated each other. The spectral index of the radio emission gradually steepens from the stellar disks with values of 0.7–0.8 to values of 1.3–1.4 in the middle of the connecting gas bridge.

Both systems show excess radio emission with respect to the FIR-radio correlation, deviating by a factor of about 2 from the mean value found for large samples of galaxies (e.g. the FIR flux-limited sample of [12], see Fig. 2). We propose that this excess radio emission is due to acceleration of CR electrons in shocks *not* associated with SF.

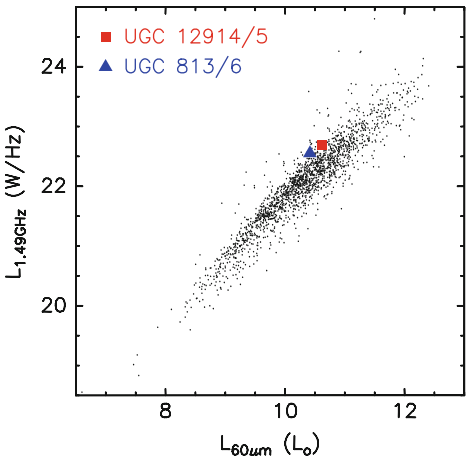

Fig. 2 Radio luminosity at 1.49 GHz vs the luminosity at 60 μm for galaxies from the sample of [12]. The position of UGC 12914/5 and UGC 813/6 are marked

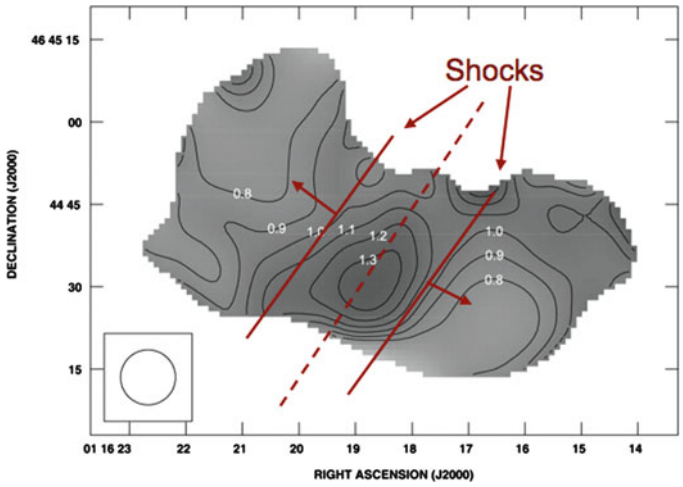

Fig. 3 A spectral index map between 1.49 and 4.9 GHz of the radio emission in UGC 12194/5 from Condon et al. [5]. Overlaid is a schematic view of the shocks that started in the middle between the galaxies when the galaxies collided (*dashed line*) and are propagating into both directions towards the galaxies (the approximate present position is indicated by a *full line*)

3 Modelling the Radio Emission from the Bridges

In a face-on collision, the stellar disks interpenetrate each other without being too much altered. However, the diffuse gas and part of the gas clouds interact hydrodynamically and exchange energy and momentum. The large quantities of atomic and molecular gas that are present in both bridges clearly show that such a gas interaction took place, even though the denser parts of the gas clouds should survive like the stars.

We estimate the total energy produced in this collision by the kinetic energy of the gas. If we assume that half of the gas which is now present in the bridge was previously in one galaxy, and the other half in the other galaxy, then the total energy liberated in a fully inelastic interaction is the kinetic energy of the gas masses.

$$E_{kin} = \frac{1}{2} M_{\rm gas} \left(\frac{v_{\rm coll}}{2}\right)^2, \tag{1}$$

where $M_{\rm gas}$ is the total gas mass in the bridge and $v_{\rm coll}$ denotes the velocity difference of the gas at collision. The factor 1/2 converts this velocity to the velocity difference in the center of mass system (assuming that both gas disks are equally massive). For the gas masses we took into account the HI and H_2 mass, the latter derived from the CO(1-0) considering a Galactic conversion factor of a factor 4 lower value as suggested by Braine et al. [2] and Zhu et al. [13].

During the collision of the ISM, strong, large-scale and supersonic shocks form. A tangential discontinuity will form at the position of the collision and two shocks will propagate in opposite directions (see Fig. 3). In between these shocks the galaxy is filled with post-shock gas. The Mach number of the shocks produced in this collision is comparable to middle-aged supernova remnants in the Sedov phase. Therefore, the particle acceleration efficiency of these shocks is expected to be similar to that of a SNR, i.e. on the order of 10–30 % (e.g. [1]). This is the basic assumption for the model.

We thus assume that 10–30 % of the kinetic energy of the ISM affected by the collision will be available for particle acceleration producing relativistic particles with the same power-law as in SNRs. We furthermore assume that the number of relativistic electrons is about 1 % of that of protons at GeV energies. We then calculate the radio emission produced by these relativistic electrons assuming that they experience synchrotron and inverse Compton losses (adiabatic losses are expected to be small). Choosing the parameters (magnetic field, energy density of the radiation field, time elapsed since the beginning of the collision) based on observations of the system we can reproduce the observed radio synchrotron luminosity and central spectral index of the bridge (for details of the calculations and choice of parameters see [8]).

4 Observational Support for This Model

Why do we believe that the bridge represents radio emission from in-situ accelerated relativistic electrons and not from particles accelerated in SNRs in the disks and dragged or propagated into the bridge? There are various observations that support our scenario.

- The presence of molecular gas in the bridge shows that a gas dynamic interaction of the dense interstellar medium must have taken place. The high relative velocity

of the two systems (500–600 km s^{-1}) implies that the collision was highly supersonic and strong shocks must have formed.
- The presence of shocks has been demonstrated from the observation of strong, shock-excited H_2 emission within the bridge of UGC 12914/5 [9].
- Finally, the fact that the radio emission from the bridge of the two systems produces a deviation from the FIR-radio correlation is highly suggestive for a origin of the radio emission from the bridge that is not associated to recent SF.

If in-situ acceleration of relativistic particles indeed has taken place in the bridge, we also expect hadronic γ-ray emission due to π^0-production by collisions of energetic protons with gas nuclei and subsequent decay into two γ-rays . We estimate the expect γ-ray-flux for UGC 12914/5 to be too low to be detected by present day instruments, mainly due to the large distance of the object. It might, however, be marginally detectable by the future γ-ray instrument *Cherenkov Telescope Array (CTA)* (see [11] for a detailed estimate).

5 Other Systems

We presented a model that can explain the nonthermal radio emission from the bridges of two face-on colliding systems by in-situ acceleration of relativistic particles in shocks produced during a gas dynamic interaction and not in SNRs.

Apart from face-on colliding systems, this mechanism might be relevant for other systems as well. An example are galaxies in clusters and groups. In galaxy clusters, when gas-rich galaxies enter the intracluster medium and get partly stripped of their gas content by tidal interaction or by more direct, hydrodynamic interactions with existing cluster galaxies, gas fragments can be produced [10]. The interaction of these gas fragments with the cold interstellar medium in the cluster galaxies might accelerate relativistic particles in a similar way as described here.

A similar process is most likely taking place in the Hickson Compact Group Stephan's Quintett. In the intragroup medium of this system, a large shock is detected that shows pronounced radio continuum and x-ray emission. Large amounts of molecular gas, traced by CO, have been detected in the shock region [7]. The shock is produced by the collision of ISM from two galaxy group members. The radio continuum has a spectral index of 0.93 [14] which shows that it comes from moderately-aged synchrotron emission, most likely caused by relativistic electrons accelerated in the shock in a similar way as outlined here.

Altogether, the two interacting galaxy pairs discussed here are possibly examples of what might have happened much more frequently at early stages of structure formation, when primordial galaxies had already developed magnetic fields as a consequence of early star formation, but when they were still likely to interact strongly with neighboring structures of a similar character.

Acknowledgements UL acknowledges support by the research projects AYA2007-67625-C02-02 and AYA2011-24728 from the Spanish Ministerio de Ciencia y Educación and the Junta de Andalucía (Spain) grants FQM108.

References

1. Berezhko, E.G., Völk, H.J., 1997, Astropart. Phys., 7, 183
2. Braine, J., Davoust, E., Zhu, M., Lisenfeld, U., Seaquist, E., Motch, C., 2003, A&A, 408, L13
3. Braine, J., Lisenfeld, U., Duc, P.-A., Brinks, E., Charmandaris, V., Leon, S., 2003, A&A, 418, 419
4. Condon, J. J. 1992, ARA&A, 30, 575
5. Condon, J.J., Helou, G., Sanders, D.B., Soifer, B.T., 1993, AJ, 105, 1730
6. Condon, J.J., Helou, G., Jarrett, T.H., 2002, AJ, 123, 1881
7. Guillard, P., Boulanger, F., Pineau des Forts, G., Falgarone, E., Gusdorf, A., Cluver, M. E., Appleton, P. N., Lisenfeld, U., Duc, P.-A., Ogle, P. M., Xu, C. K., 2012, ApJ, 749, 158
8. Lisenfeld, U., Völk, H. J. 2010, A&A, 524, 27
9. Peterson, B. W., Appleton, P. N., Helou, G., Guillard, P., Jarrett, T. H., Cluver, M. E., Ogle, P., Struck, C., Boulanger, F., 2012, ApJ, 751, 11
10. Völk, H.J., Xu, C., 1994, Infrared Phys. Technol., 35, 527
11. Völk, H. J., Lisenfeld, U., 2010, Proceedings of the 25th Texas Symposium on Relativistic Astrophysics, eds: F. M. Rieger, C. van Eldik & W. Hofmann
12. Yun, M.S., Reddy, N.A., Condon, J.J., 2001, ApJ, 554, 803
13. Zhu, M., Gao, Y., Seaquist, E.R., Dunne, L., 2007, AJ, 134, 118
14. Xu, C. K., Lu, N., Condon, J. J., Dopita, M., Tuffs, R. J. 2003, ApJ, 595, 665

Gamma-Rays and Neutrinos from Dense Environments of Massive Binary Systems

W. Bednarek and J. Pabich

Abstract TeV gamma-ray emission has been recently observed from the direction of open clusters containing many massive stars and dense concentrations of matter. We consider the high energy processes occurring within the massive binary systems, and also within their environment, in order to find out whether gamma-rays from hadronic processes might be detectable from such open clusters by the present and future Cherenkov telescopes. We also estimate the accompanying neutrino fluxes which are confronted with the sensitivity of IceCube.

1 Introduction

Open clusters have been suspected as sites for the high energy processes due to the presence of large concentration of matter and also early type compact objects (e.g. massive stars, compact massive binaries, pulsars and their nebulae). In fact, TeV γ-ray emission has been detected from the direction of three open clusters (i.e. Cyg OB 2 – Aharonian et al. [2], Westerlund 2 – Aharonian et al. [1], and Westerlund 1 – Abramowski et al. [4]) and also GeV γ-ray emission extending up to $\sim$100 GeV from the binary system of two massive stars Eta Carinae within the Carina Nebula open cluster complex [3, 8]. This last extraordinary binary system has not been detected up to now in the TeV γ-ray range [5].

We investigate possible radiation processes within and around the massive binary systems surrounded by the large concentrations of matter. It is assumed that nuclei are accelerated in the shocks produced by colliding winds of the binary stars. They can partially disintegrate in the radiation field of massive stars injecting neutrons, protons and surviving nuclei. These hadrons diffuse through

W. Bednarek (✉) · J. Pabich
Department of Astrophysics, The University of Lodz, 90-236 Lodz,ul. Pomorska 149/153, Poland
e-mail: bednar@uni.lodz.pl; pabich@uni.lodz.pl

D.F. Torres and O. Reimer (eds.), *Cosmic Rays in Star-Forming Environments*,
Astrophysics and Space Science Proceedings 34, DOI 10.1007/978-3-642-35410-6_23,

the open cluster producing γ-rays and neutrinos in collisions with the matter. We conclude that such open clusters should emit γ-ray emission with complicated morphology corresponding to the presence of different emission regions which could be investigated by the future Cherenkov Telescope Array (CTA).

2 Acceleration of Hadrons

We consider a massive binary system in which massive stars produce winds with the mass loss rate of the order of $\dot{M}_{\rm WR} = 10^{-5}\dot{M}_{-5}$ M$_\odot$ year^{-1} and velocities of $v_{\rm w} = 10^3 v_3$ km s^{-1}. Density of the wind drops with the distance from the star according to $n_{\rm w}(r) \approx 3.2\times 10^{13}\dot{M}_{-5}/v_3 R_{11}^2 r^2$ cm^{-3}, where $R_{\rm WR} = 10^{11}R_{11}$ cm is the radius of the star, and $r = R/R_{\rm WR}$ is the distance from the star in units of stellar radius. We assume that the binary system is immersed in a relatively dense medium of the open cluster (OC) with density $n_{\rm oc} = 10 n_{10}$ cm^{-3} and with temperature $T_{\rm oc} = 10^4 T_4$ K. At certain distance from the binary system, the pressure of the stellar wind is balanced by the pressure of the thermal gas within the OC. We estimate the radius of the stellar wind cavity in the case of a constant wind velocity, by comparing the energy density of the wind with the energy density of the medium, on $R_{\rm c} \approx 1.1\times 10^{19}[\dot{M}_{-5}v_3/(n_{10}T_4)]^{1/2}$ cm.

We consider the consequences of hadron acceleration within the binary system located in the open cluster. Nuclei (from the stellar winds) can be accelerated on the shock wave which is created within the binary system as a result of collisions of the winds from the massive stars. Significant part of accelerated nuclei escape from the binary system being captured by the wind magnetic field. These nuclei are expected to suffer adiabatic energy losses when the wind expends from the binary system. However, a part of the nuclei should interact injecting relativistic neutrons into the surrounding of the binary system.

Massive stars produce fast and dense winds which can extract significant amount of original mass from the star. In fact, the intensive mass loss rates of the order of a few $10^{-6} - 10^{-4}$M$_\odot$ year^{-1} are characteristic for the Wolf-Rayet (WR) and O type stars. After a few hundred thousand years, the outer parts of the stars are lost and only the inner parts, composed of heavier nuclei, are left. Therefore, the winds of early type stars are expected to be mainly composed from nuclei heavier than hydrogen such as Helium to Oxygen. We estimate the maximum energies of hadrons accelerated in the shock region of colliding winds following the condition considered in [6]. It is assumed that maximum energies are determined by the balance between their acceleration time scale and their advection time scale along the shock structure. The acceleration time scale is given by $\tau_{\rm acc} = E_{\rm h}/\dot{P}_{\rm acc} \approx 0.01 E_{\rm h}/(\chi_{-5}B_3)$ s, where $E_{\rm h}$ is energy of particle per nucleon in GeV, $\chi = 10^{-5}\chi_{-5}$ is the acceleration coefficient and $B_{\rm sh} = 10^3 B_3$ is the magnetic field strength in the acceleration region in G. On the other hand, the advection time scale is estimated by $\tau_{\rm adv} = 3R_{\rm sh}/v_{\rm w} \approx 3\times 10^3 R_{11}/v_3$ where, $R_{\rm sh} = 10^{11}R_{11}/r_{\rm sh}$ is the distance of the

shock from the star and $r_{\rm sh} = R_{\rm sh}/R_{\rm WR}$ is the distance of the shock from the stellar surface in units of stellar radius.

Maximum energies of hadrons accelerated in the shock acceleration process at the shock created in collisions of the stellar winds are then given by $\gamma_{\rm max} \approx 1.3 \times 10^5 R_{11} B_3 v_3 / r_{\rm sh}$ GeV, where $B = 10^3 B_3$ is now the magnetic field strength on the surface of the star and the acceleration coefficient is estimated by $\chi = (v_{\rm w}/c)^2 \approx 10^{-5} v_3^2$. We apply the specific structure of the magnetic field around the massive star defined by Usov and Melrose [9].

In order to have an impression about the role of the fragmentation process of nuclei in the radiation field of massive stars we consider the simple case of their injection from a point-like source not far from the stellar surface, e.g. at the distance of two stellar radii. We calculate the optical depths for fragmentation of nuclei injected at different initial directions and as a function of their energy and selected mass numbers (He, O, Fe). The nuclei are considered to propagate in the vicinity of the representative two massive stars with different parameters: WR stars in the WR 20a binary system and a supermassive star in the Eta Carinae binary system. Note that only nuclei with Lorentz factors above $\gamma_{\rm min}$ can be disintegrated substantially. This critical value can be estimated from $\gamma_{\rm min} = E_\gamma^{\rm th}/3k_{\rm B}T \sim 4 \times 10^4/T_5$, where $E_\gamma^{\rm th} = 2$ MeV is the minimum energy of stellar photon in the nuclei rest frame which is able to disintegrate nuclei, $T = 10^5 T_5$ K is the surface temperature of the star and $k_{\rm B}$ is the Boltzman constant.

We determine the number of nucleons dissolved from nuclei in the disintegration process following paths of nuclei in the magnetic field of the massive star. The magnetic field has complicated structure which is determined by the parameters of the stellar wind and the rotation of the star. We calculate the number of secondary nucleons dissolved from nuclei (neutrons and protons). Some of them collide with the star but some escape from the binary system. We calculate the average number of neutrons, protons and secondary surviving nuclei which escape from the binary system as a function of their energies for three types of primary nuclei (He, O, and Fe). For the considered binaries, significant amount of nucleons can be extracted from Helium and Oxygen nuclei (see details in [7]).

Depending on energy, neutrons can still decay within the stellar wind region or outside it, i.e. already within the open cluster. Protons from neutrons, decaying within the stellar wind, are expected to suffer adiabatic energy losses during the fast expansion of the wind. These protons can be partially transported with the wind to the open cluster. Neutrons with large enough energies mainly decay outside the wind cavity in the volume of the open cluster. Protons from their decay diffuse gradually through the open cluster suffering some collisions with the distributed matter. On the other hand, primary nuclei accelerated within the binary system (and also secondary nuclei and protons from their fragmentation) are captured by the magnetic field in the dense stellar wind. These hadrons can interact with the matter of the wind. As a result of these interactions, additional population of neutrons is produced not far from the vicinity of the binary system where the matter in the stellar wind is still relatively dense. These neutrons decay within or outside the wind cavity

as described above. Moreover, a part of neutrons extracted from nuclei, as a result of their collisions with radiation and matter, can decay within dense clouds which are expected within or close to the open cluster. Protons from their decay can be captured for a long time in a strong magnetic field suffering frequent collisions with the matter.

3 Gamma-Rays from Accelerated Hadrons

We calculate γ-ray spectra produced by hadrons (i.e. nuclei, protons and neutrons) in different regions around the binary system: the wind cavity, the open cluster and the nearby cloud. The method of calculation of the spectra of hadrons in specific regions is described in detail in [7]. In these calculations, we take into account the adiabatic and collisional energy losses of hadrons, the advection process of hadrons with the wind of the massive stars and also the energy dependent decaying process of neutrons in the vicinity of the binary system. For the derived spectra of hadrons, we calculate the spectra of γ-rays produced by them in different regions of the wind cavity, open cluster and the cloud. The absorption of γ-rays produced close to the massive stars is also taken into account. In the case of the open cluster, the γ-ray fluxes depend on the escape of protons from this region which is defined by the parameter $R_{20}^2 B_{-5} n_{30}$, where $R_{\rm oc} = 20 R_{20}$ pc is the radius of the open cluster, $B_{\rm oc} = 10^{-5} B_{-5}$ G its magnetic field and $n = 30 n_{30}\,{\rm cm}^{-3}$ is the density of matter within the open cluster. In the case of a nearby cloud the γ-ray fluxes depend on $R_3^2 B_{-4} n_4$, where $R_{\rm cl} = 3 R_3$ pc is the radius of the cloud, $B_{\rm cl} = 10^{-4} B_{-4}$ G is its magnetic field strength and $n = 10^4 n_4\,{\rm cm}^{-3}$ is its density. As an example, we show the γ-ray spectra for two binary systems with the parameters of the Eta Carinae and WR 20a binary systems (Fig. 1).

Note that due to the absorption process in the stellar radiation, the γ-ray flux from the Eta Carinae wind cavity is predicted on the level below the upper limit recently reported by the HESS collaboration [5]. On the other hand, the γ-ray flux from the open cluster surrounding the Eta Carinae is comparable to the HESS upper limit in the case of the parameter $R_{20}^2 B_{-5} n_{30}$ equal to 10 (see Fig. 1). The emission from the supposed nearby cloud is below this upper limit but above the sensitivity of CTA.

We have also calculated the neutrino spectra produced in hadronic collisions for these two binary systems. It is found that only in the case of the Eta Carinae binary system the spectra produced in the wind cavity are expected to be within the sensitivity of the IceCube telescope and above the Atmospheric Neutrino Background (see Fig. 1). Note however, that in some open clusters a few up to several massive binary systems are observed. In such a case the γ-ray and neutrino fluxes should be proportional to the number of massive binary systems.

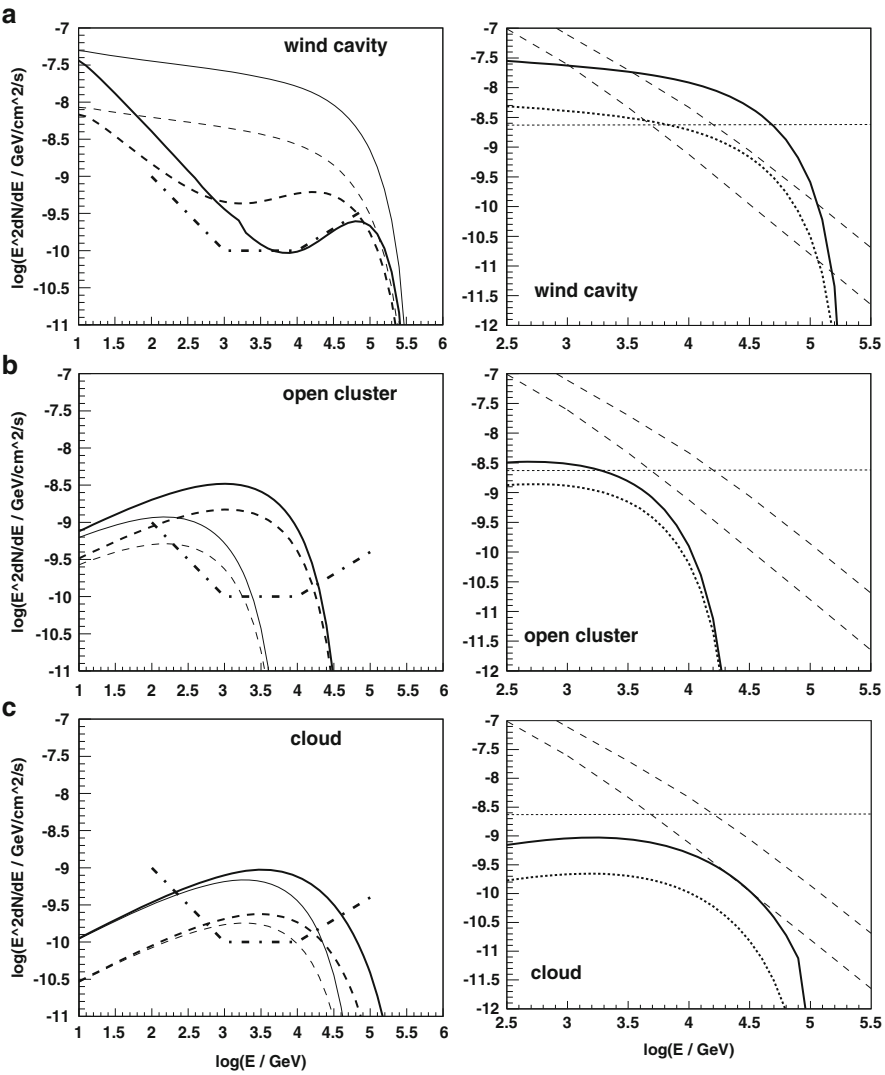

Fig. 1 The spectra of gamma-rays (*left column*) and neutrinos (*right*) produced by nuclei which escaped from the binary system by: (**a**) protons from disintegration of primary nuclei (*upper figures*), (**b**) protons from neutrons (from disintegration of nuclei) decaying outside the wind cavity and colliding with the matter of the wind (*middle*) and (**c**) protons from neutrons decaying within the dense cloud in the vicinity of the binary system (*bottom*), for the binary systems with the parameters of Eta Carinae (*solid curves*) and WR 20a (*dashed*). The γ-ray spectra from the wind cavity are shown by including their absorption in the stellar radiation (*thick curves*) and without absorption (*thin*). The γ-ray spectra from the open cluster are shown for the parameter describing escape of protons from the open cluster equal to $R_{20}^2 B_{-5} n_{30} = 10$ (*thick curves*) and 1 (*thin*) and from the cloud for $R_3^2 B_{-4} n_4 = 1$ (*thick*) and 0.1 (*thin*). It is assumed that 1 % of the stellar wind power goes on acceleration of hadrons. The source is assumed to be at the distance of 2 kpc. The sensitivity of CTA is marked by *dot-dashed curve* and IceCube by the *thin dotted line*. The Atmospheric Neutrino Background is marked by the *thin dashed curves*

4 Conclusions

We considered different sites for production of the TeV γ-rays and neutrinos in hadronic interactions with the matter within the vicinity of the massive binaries immersed in high density regions of the open clusters. Nuclei, expected to be accelerated within the binary system, suffer partial disintegration in the interaction with stellar radiation releasing neutrons and protons. Relativistic neutrons provide efficient mechanism for transporting energy to large distances from the binary system without significant adiabatic energy losses. As an example, we considered two well known very massive binary systems: Eta Carinae and WR 20a. It is concluded that TeV γ-ray emission is expected on the level above the sensitivity of CTA either from the wind cavity created by the wind of the massive stars, or from the open cluster to which nuclei and protons diffuse or neutrons decay, or from the nearby cloud illuminated by relativistic neutrons. Our calculations show that the highest fluxes of the TeV γ-rays should be expected from the large region surrounding the binary system (i.e. the volume of the open cluster) and the lowest from the wind cavity directly surrounding the binary system.

Neutrino fluxes are expected above the sensitivity of the IceCube telescope only in the case of the wind cavity around the binary system with the parameters of the Eta Carinae. Note that estimated fluxes should increase proportionally to the number of the massive binary systems in a specific open cluster. So then, they might be larger by a factor proportional to the number of massive binaries in a specific open cluster.

Acknowledgements This work is supported by the Polish Narodowe Centrum Nauki through the grant No. 2011/01/B/ST9/00411.

References

1. Aharonian, F.A. 2007 A&A, 467, 1075
2. Aharonian, F.A. 2002 A&A, 393, 37
3. Abdo, A. A. et al. 2009 ApJS 183, 46
4. Abramowski, A. et al. 2012a A&A 537, 114
5. Abramowski, A. et al. 2012b MNRAS, arXiv:1204.5690
6. Bednarek, W., Pabich, J. 2011 A&A 530, 49
7. Bednarek, W., Pabich, J. 2012 in preparation
8. Tavani, M. et al. 2009 ApJ 698, L142
9. Usov, V.V., Melrose, D.B. 1992 ApJ 395, 575

Cosmic-Ray-Induced Ionization in Molecular Clouds Adjacent to Supernova Remnants

F. Schuppan, J.K. Becker, J.H. Black, S. Casanova, and M. Mandelartz

Abstract Energetic gamma rays (GeV to TeV photon energy) have been detected toward several supernova remnants (SNR) that are associated with molecular clouds. If the gamma rays are produced mainly by hadronic processes rather than leptonic processes like bremsstrahlung, then the flux of energetic cosmic ray nuclei (> 1 GeV) required to produce the gamma rays can be inferred at the site where the particles are accelerated in SNR shocks. It is of great interest to understand the acceleration of the cosmic rays of lower energy (< 1 GeV) that accompany the energetic component. These particles of lower energy are most effective in ionizing interstellar gas, which leaves an observable imprint on the interstellar ion chemistry. A correlation of energetic gamma radiation with enhanced interstellar ionization can thus be used to support the hadronic origin of the gamma rays and to constrain the acceleration of ionizing cosmic rays in SNR. Using observational gamma ray data, the primary cosmic ray proton spectrum can be modeled for $E > 1$ GeV, and careful extrapolation of the spectrum to lower energies offers a method to calculate the ionization rate of the molecular cloud.

F. Schuppan (✉) · J.K. Becker · M. Mandelartz
Fakultät für Physik & Astronomie, Ruhr-Universität Bochum, 44780 Bochum, Germany
e-mail: florian.schuppan@rub.de

J.H. Black
Department of Earth and Space Sciences,Onsala Space Observatory, Chalmers University of Technology, SE-439 92 Onsala, Sweden

S. Casanova
Unit for Space Physics, North-West University, Potchefstroom 2520, South Africa

D.F. Torres and O. Reimer (eds.), *Cosmic Rays in Star-Forming Environments*, Astrophysics and Space Science Proceedings 34, DOI 10.1007/978-3-642-35410-6_24,

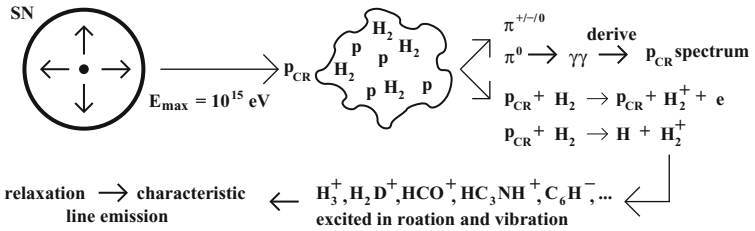

Fig. 1 Sketch of the basic idea

1 Introduction

The origin of cosmic rays (CRs) is one of the central questions in modern astrophysics. In particular, for gamma rays the formation processes are still a matter of debate due to ambiguity of the observations. The detection of the emission of gamma rays in GeV and TeV towards molecular clouds in the direct vicinity of supernova remnants (e.g. [1]) has further fueled the question about the origin of this radiation. In principle, there are three different scenarios by which these particular gamma rays can be formed: bremsstrahlung or inverse Compton scattering of electrons in a leptonic scenario or the formation and – in turn – decay of neutral pions from scattering of CR protons on ambient protons in a hadronic scenario. In most cases, it is not possible to determine which process actually is at work based on the gamma ray spectrum alone. Therefore, correlation studies need to be performed. In the hadronic scenario, CR protons of energies $E > 1$ GeV form neutral pions by deep inelastic scattering on ambient matter, which in turn decay into two gamma rays. It is to be expected that there are also lower energy protons, which are most effective in ionizing hydrogen. Using molecular clouds as tracers for these ionizing lower energy CR protons in spatial correlation with GeV to TeV gamma radiation could offer a strong hint at hadronic origin of the gamma rays, since CR electrons do not penetrate molecular clouds as deeply as CR protons, resulting in a different ionization profile. The ionized molecular hydrogen, H_2^+, triggers a chemical network, forming about 15–20 molecular ions, which are formed in ro-vibrationally excited states (see e.g. [7, 15]). If there is a sufficient amount of these ions formed, i.e. the ionization rate is high enough, the relaxation of these ions results in characteristic line emission, which can be detected as tracer for enhanced ionization [6]. The basic idea is sketched in Fig. 1.

2 Deriving the CR Proton Spectrum

To calculate the ionization rate of the molecular cloud, the primary CR proton spectrum at the source is required. To obtain this, observational data about the gamma radiation from instruments as e.g. FermiLAT can be used. To generate the

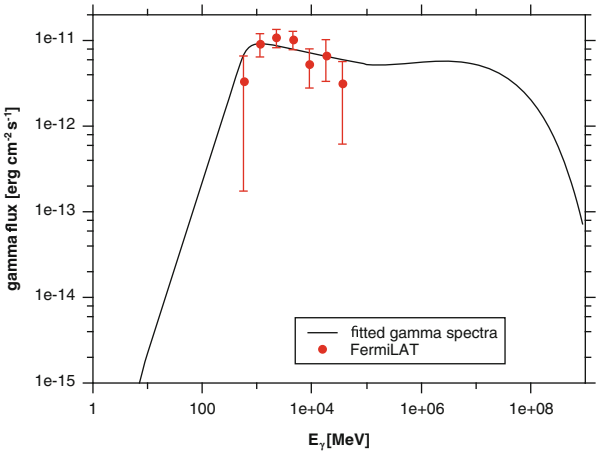

Fig. 2 Gamma ray spectrum from pion decay fitted to gamma ray measurements for G349.7+0.2. Gamma ray measurements from Castro and Slane [8]. Primary CR proton spectral shape assumed: $j_{\mathrm{p}}(E_{\mathrm{p}}) = a_{\mathrm{p}} \left(\frac{E_{\mathrm{p}}}{1\,\mathrm{TeV}}\right)^{-\alpha_l} \exp\left(-\frac{E_{\mathrm{p}}}{1\,\mathrm{PeV}}\right)$. Fit parameters: $\chi^2/\mathrm{dof} = 0.88638$, $a_\gamma = (820.97822 \pm 494.07024)/\left(\frac{n_{\mathrm{H}}}{\mathrm{cm}^{-3}} c\right)\,\mathrm{erg\,MeV^{-2}cm^{-2}\,s^{-1}}$, $\alpha_l = 2.15415 \pm 0.11482$ (To derive a_{p} from a_γ, see [18])

gamma radiation observed, the primary CR proton spectrum at the source can be fitted using a proton-proton interaction model like the one from Kelner et al. 2006 [14] or Kamae 2006 [12, 13]. As input for these models, typically a (broken) power-law in energy with an exponential cutoff is assumed for the primary CR proton spectrum, which forms a spectrum of gamma rays from the decay of neutral pions formed in interactions of the CR protons with ambient matter. An example of the shape of the primary CR proton spectrum is:

$$j_{\mathrm{p}}(E_{\mathrm{p}}) = a_{\mathrm{p}} \left(\frac{E_{\mathrm{p}}}{E_0}\right)^{-\alpha_l} \left(1 + \frac{E_{\mathrm{p}}}{E_{\mathrm{br}}}\right)^{-(\alpha_h - \alpha_l)} \exp\left(-\frac{E_{\mathrm{p}}}{E_{\mathrm{cutoff}}}\right). \quad (1)$$

The fit is performed in such a way that the resulting gamma ray spectrum matches the observational gamma data. Free parameters of the fit are the spectral indices below and above the break energy, α_l and α_h, the break energy E_{br}, the cut-off energy $E_{\mathrm{cut-off}}$ and the normalization of the resulting gamma ray spectrum, a_γ. A fitted gamma ray spectrum for a supernova remnant associated with a molecular cloud is shown in Fig. 2.

Since the threshold energy required for the generation of a single pion is about $130\,\mathrm{MeV}/c^2$ and a primary CR proton of $E_{\mathrm{p}} = 1\,\mathrm{GeV}$ typically gives $\sim 10\,\%$ of its energy to a secondary produced, the primary CR proton spectrum obtained from modeling the GeV–TeV gamma radiation can only be considered known down to energies of about 1 GeV. The ionization cross section of molecular hydrogen, on the other hand, has its peak at 100 keV and declines rapidly towards higher energies

[17], so deriving an ionization rate from the modeled primary CR proton spectrum is not trivial. For $E_\mathrm{p} < 1$ GeV, the spectrum needs to be extrapolated to lower energies carefully, because there is no observational data about this part of the spectrum. In a conservative approach, the primary CR proton spectrum is expected to change from $E_\mathrm{p}^{-\alpha}$ to $E_\mathrm{p}^{-\alpha+3}$ below 1 GeV. Note that the spectral behavior below $E_\mathrm{p} < 1$ GeV has no significant influence on the resulting gamma ray spectrum due to the threshold energy for the production of pions. This modifies the spectral shape of the primary CR proton spectrum as:

$$j_\mathrm{p}(E_\mathrm{p}) = \begin{cases} a_\mathrm{p} \left(\frac{E_\mathrm{lb}}{E_0}\right)^{-\alpha_l} \left(1 + \frac{E_\mathrm{lb}}{E_0}\right)^{-(\alpha_h - \alpha_l)} \exp\left(-\frac{E_\mathrm{lb}}{E_\mathrm{cutoff}}\right) \left(\frac{E_\mathrm{p}}{E_\mathrm{lb}}\right)^{s} & (E_\mathrm{p} \leq E_\mathrm{lb}) \\ a_\mathrm{p} \left(\frac{E_\mathrm{p}}{E_0}\right)^{-\alpha_l} \left(1 + \frac{E_\mathrm{p}}{E_\mathrm{br}}\right)^{-(\alpha_h - \alpha_l)} \exp\left(-\frac{E_\mathrm{p}}{E_\mathrm{cutoff}}\right) & (E_\mathrm{p} > E_\mathrm{lb}), \end{cases} \quad (2)$$

where s is varied from $+1.0$ to $+2.0$, which should offer a lower limit on the spectrum and therefore on the ionization rate. This is due to the fact that an injection spectrum of $\propto p^{-\alpha}$, for a loss term of $\dot{p} \propto p^{-2}$ like ionization losses, would be modified as $\propto p^{3-\alpha}$, and the power law indices for the sources discussed are $s = 1.5$–2.45.

The normalization of the primary CR proton spectrum, a_p, is not trivial to calculate from the resulting gamma ray spectrum normalization a_γ obtained from fitting. In fact, it requires an estimate of the volume of the source, whereas the gamma ray spectrum normalization does not depend on this quantity. It enters either in the cosmic ray density or in the hydrogen density of the cloud. For a more detailed description of the calculation of the primary CR proton spectrum, see Schuppan et al. [18].

3 Predicting the Ionization Rate

Using this spectrum, we can calculate the ionization rate due to primary proton ionization following Padovani et al. [17]. Since the spectral behavior of the primary CR proton spectrum is not precisely known, the ionization rate is calculated for different lower spectral indices s and lower break energies E_lb. The predicted ionization rate only weakly depends on the actual spectral index below the lower break, s, but rather strongly on the lower break energy E_lb. This is due to the strong decline of the ionization cross section of molecular hydrogen for incident proton energies above 100 keV [17]. In our study, we predicted the ionization rates for nine molecular clouds known to be associated with supernova remnants. W49B, in particular, is expected to show signatures of a largely enhanced ionization rate. For at least two objects, the ionization rates are expected to be at least an order of magnitude above the average of Galactic molecular clouds, $\zeta^{\mathrm{H_2}}_{\mathrm{gal.\ aver}} = 2 \times 10^{-16}\,\mathrm{s}^{-1}$ [16]. In this calculation, there are two quantities left as free parameters. The total energy budget in CR protons interacting with the molecular gas, W_p, and the

hydrogen density of the cloud, n_{H}. The product of these quantities is fixed from fitting the resulting gamma ray flux to observational data, $W_{\mathrm{p}} n_{\mathrm{H}} = const.$, but the values of the quantities themselves cannot be derived. Note that this equation can be rearranged in such a way that $W_{\mathrm{p}} n_{\mathrm{H}} = \rho_{\mathrm{p}} V_{\mathrm{cloud}} n_{\mathrm{H}} = \rho_{\mathrm{p}} M_{cloud} = const.$, where ρ_{p} is the energy density of the cosmic ray protons. Therefore, the calculation can be adapted to the quantities for which there are the best estimates available. In our calculations, we chose the fixed value of $n_{\mathrm{H}} = 100\,\mathrm{cm}^{-3}$ as standard value for the clouds. Should future measurements hint at different densities, the results change as $\zeta^{\mathrm{H_2}} \propto n_{\mathrm{H}}^{-1}$.

This work focuses on the ionization due to primary CR protons, neglecting the contribution of primary CR electrons. For a description of the latter, see Padovani et al. [17]. Furthermore, the contribution of secondary electrons from primary ionization events is neglected here, which typically enhances the primary ionization rate by a factor of 1.4–2 [9]. Neglecting these processes, the calculation of the ionization rate is performed following Padovani et al. [17] as:

$$\zeta^{\mathrm{H_2}} = \int_{E_{\mathrm{min}}}^{E_{\mathrm{max}}} j_{\mathrm{p}}(E_{\mathrm{p}}) \sigma_{\mathrm{p}}^{\mathrm{ion}}(E_{\mathrm{p}}) \mathrm{d}E_{\mathrm{p}}\,, \tag{3}$$

where E_{min} is the minimum energy of protons considered to contribute to the ionization rate and $\sigma_{\mathrm{p}}^{\mathrm{ion}}$ is the ionization cross section of molecular hydrogen for protons. E_{max} can be chosen as 1 GeV, increasing it further does not change the resulting ionization rate significantly, due to the rapidly declining ionization cross section for $E_{\mathrm{p}} > 100\,\mathrm{keV}$. The value of E_{min}, however, is of large importance for the result. Generally, protons of kinetic energy $E_{\mathrm{p}} < 100\,\mathrm{keV}$ are not energetic enough to penetrate a cloud of $n_{\mathrm{H}} = 100\,\mathrm{cm}^{-3}$. Due to the rapid decline of the primary CR proton spectra used here towards energies $E_{\mathrm{p}} < E_{\mathrm{lb}}$, a value of $E_{\mathrm{min}} = 10\,\mathrm{MeV}$ is chosen as a conservative approximation [10]. This lower integration limit becomes even more important the lower the value of the lower break energy E_{lb} is. The latter is varied from 30 MeV to 1 GeV in our calculations. Summed up, the larger the lower break energy E_{lb} and the spectral index s below this lower break energy, the lower the resulting ionization rate. In Table 1, the parameters used to calculate the ionization rate for all objects considered are shown. The lower break energy, E_{lb}, was altered, while the spectral index of the primary CR proton spectrum below the lower break energy was chosen as $s = +2.0$ as the most conservative approach. The resulting ionization rate for each object considered depending on the lower break energy is shown in Fig. 3. Changing s from $+2.0$ to $+1.0$ does change the results by a factor of $\sim$1.2 for $E_{\mathrm{lb}} = 30\,\mathrm{MeV}$ up to a factor of $\sim$2 for $E_{\mathrm{lb}} = 1\,\mathrm{GeV}$. This, in combination with the value of the lower break energy, is likely to be the largest uncertainty in the calculation. As can be seen, for $E_{\mathrm{lb}} = 100\,\mathrm{MeV}$, for three objects the predicted ionization rate is at least an order of magnitude above Galactic average for molecular clouds. This choice of the lower break energy E_{lb} might be the most reasonable. However, even for the most conservative scenario, i.e. $E_{\mathrm{lb}} = 1\,\mathrm{GeV}$ and $s = +2.0$, the predicted ionization rate for W49B is orders of magnitude above Galactic average for molecular clouds.

Table 1 Table of parameters used to calculate the ionization rate. All values for W_p are calculated for $n_H \sim 100\,cm^{-3}$ (Gamma ray measurements from: Abdo et al. [1–5] and Castro and Slane [8])

Object	d (kpc)	V_{cloud} (cm^3)	E_0	α_l	α_h or E_{cutoff}	W_p (erg), p of $E_p > 10\,MeV$	Break energy E_{br} (GeV)
W51C	6.0	3.3×10^{60}	1 GeV	1.5	2.9	7.7×10^{49}	15
W44	3.3	5.6×10^{59}	1 GeV	1.74	3.7	9.0×10^{49}	9
W28	2.0	3.2×10^{59}	1 GeV	1.7	2.7	3.3×10^{49}	2
IC443	1.5	4.2×10^{59}	1 GeV	2.0	2.87	2.4×10^{49}	69
W49B	8.0	6.3×10^{56}	1 GeV	2.0	2.7	4.4×10^{50}	4
G349.7+0.2	22.0	2.4×10^{59}	1 TeV	1.7	0.16 TeV	2.2×10^{50}	–
CTB 37A	8.0	1.2×10^{60}	1 TeV	1.7	0.08 TeV	3.7×10^{50}	–
3C 391	7.2	2.5×10^{59}	1 TeV	2.4	100 TeV	3.1×10^{50}	–
G8.7 − 0.1	4.5	9.3×10^{59}	1 TeV	2.45	100 TeV	3.7×10^{50}	–

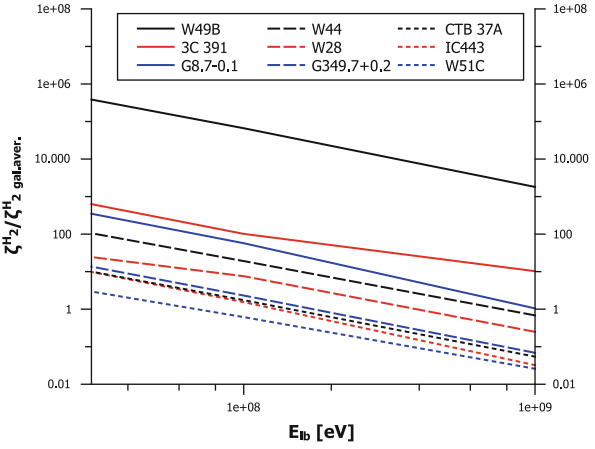

Fig. 3 Predicted ionization rate for all objects considered for different lower break energies E_{lb} of the primary CR protons below $E_p < 1\,GeV$

4 Ionization Signatures

An enhanced ionization rate of molecular and atomic hydrogen triggers a chemical network, forming about 15–20 relatively simple molecular ions. In fully molecular regions, almost every ionization of molecular hydrogen results in formation of an H_3^+ molecular ion. Therefore, the detection of this molecular ion is a very good tracer for the ionization rate in a molecular cloud [11]. With the ionization rate and a few estimates of cloud parameters like the temperature and density, the amounts of molecular ions formed in a certain ro-vibrational state can be derived using a chemical network and a radiative transfer code as e.g. RADEX [19]. In Becker et al. [6], the first predicted spectra of H_2^+, H_3^+, and HeH^+ are shown for a reference model cloud. Similar spectra can be predicted for other molecular ions. In general, the most reactive ions, such as H_2^+, OH^+, and H_2O^+, will be the most direct tracers of high ionization. Such a prediction can be made for each molecular cloud associated with a supernova remnant. The detection of such relaxation lines

in spatial correlation with GeV to TeV gamma radiation is a strong hint at hadronic origin of both signals. The largest uncertainty in the calculation is the shape of the primary CR proton spectrum for energies $E_p < 1\,\mathrm{GeV}$. The estimate chosen here is rather conservative, so the derived ionization rates are actually lower limits. A more precise method to predict ionization rates from CR protons is to propagate the CR protons into the cloud, which will be done in future work. Of particular interest is the prediction of ionization profiles, since the profiles induced by CR ionization are expected to be distinct from those induced by photo-ionization and therefore pinpointing the origin of enhanced ionization, at least near the cloud cores, to cosmic rays. With instruments as the Cherenkov Telescope Array and The Atacama Large Millimeter/submillimeter Array, the spatial resolution to perform the correlation study would be available.

Acknowledgements We would like to thank R. Schlickeiser and P.L. Biermann for helpful and inspiring discussions. We also want to thank Marco Padovani for very helpful comments. JKB, SC and FS acknowledge funding from the DFG, Forschergruppe "Instabilities, Turbulence and Transport in Cosmic Magnetic Fields" (FOR1048, Project BE 3714/5-1) and from the Junges Kolleg (Nordrheinwestfälische Akademie der Wissenschaften und der Künste). JHB is grateful to the Swedish National Space Board for support. We further acknowledge the support by the Research Department of Plasmas with Complex Interactions (Bochum).

References

1. Abdo, A. A. and others: "Fermi LAT Discovery of Extended Gamma-Ray Emission in the Direction of Supernova Remnant W51C", Astroph. J. Lett. 706, L1 (2009)
2. Abdo, A. A. and others: "Gamma-Ray Emission from the Shell of Supernova Remnant W44 Revealed by the Fermi LAT", Science 327, 1103 (2010)
3. Abdo, A. A. and others: "Fermi Large Area Telescope observations of the supernova remnant W28 (G6.4 − 0.1)", Astroph. J. Lett. 718, 348 (2010)
4. Abdo, A. A. and others: "Observation of supernova remnant IC 443 with the Fermi Large Area Telescope", Astroph. J. Lett. 712, 459 (2010)
5. Abdo, A. A. and others: "Fermi-LAT Study of Gamma-ray Emission in the Direction of Supernova Remnant W49B", Astroph. Journal 722, 1303 (2010)
6. Becker, J. K. et al.: "Tracing the sources of cosmic rays with molecular ions", Astroph. J. Lett. 739, L43 (2011)
7. Black, J. H.: "The short but exciting lives of molecular ions in interstellar clouds". In: J. L. Lemaire and F. Combes (eds.), Molecules in Space and Laboratory, (2007)
8. Castro, D. and Slane, P.: "Fermi Large Area Telescope Observations of Supernova Remnants Interacting with Molecular Clouds", Astroph. Journal 717, 372 (2010)
9. Glassgold, A. E. and Langer, W. D.: "Heating of Molecular-Hydrogen Clouds by Cosmic Rays and X-Rays", Astroph. Journal 186, 859 (1973)
10. Indriolo, N. and others: "The Implications of a High Cosmic-Ray Ionization Rate in Diffuse Interstellar Clouds", Astroph. Journal 694, 257 (2009)
11. Indriolo, N. and others: "Investigating the Cosmic-ray Ionization Rate Near the Supernova Remnant IC 443 through H^+_3 Observations", Astroph. Journal 724, 1357 (2010)
12. Karlsson, N. and Kamae, T.: "Parameterization of the Angular Distribution of Gamma Rays Produced by p-p Interaction in Astronomical Environments", Astroph. Journal 674, 278 (2008)

13. Kamae, T. and others: “Parameterization of γ, $e^{+/-}$, and Neutrino Spectra Produced by p-p Interaction in Astronomical Environments”, Astroph. Journal 647, 692 (2006)
14. Kelner, S. R. and others: “Energy spectra of gamma rays, electrons, and neutrinos produced at proton-proton interactions in the very high energy regime”, Phys. Rev. D. 74:3 (2006)
15. McCarthy, M. C. and others: “Laboratory and Astronomical Identification of the Negative Molecular Ion C_6H^-”, Astroph. J. Lett. 652, L141 (2006)
16. Neufeld, D. A. et al.: “Herschel/HIFI observations of interstellar OH^+ and H_2O^+ towards W49N: a probe of diffuse clouds with a small molecular fraction”, Astron. & Astroph. 521, L10 (2010)
17. Padovani, M. and others: “Cosmic-ray ionization of molecular clouds”, Astron. & Astroph. 501, 619 (2009)
18. Schuppan, F. and others: “Cosmic-ray-induced ionization in molecular clouds adjacent to supernova remnants - Tracing the hadronic origin of GeV gamma radiation”, Astron. & Astroph 541, A126 (2012)
19. van der Tak, F. F. S. and others.: “A computer program for fast non-LTE analysis of interstellar line spectra. With diagnostic plots to interpret observed line intensity ratios”, Astron. & Astroph. 468, 627 (2007)

The Consequences of the Interaction of Cosmic Rays with Galactic Center Molecular Clouds

F. Yusef-Zadeh

Abstract We consider that the diffuse GeV, TeV and the FeI 6.4 keV line emission from the inner $2^0 \times 1^0$ of the Galactic center, as observed with Fermi, HESS, Chandra, XMM-Newton and Suzaku, results from the interaction of cosmic ray electrons with the neutral gas and that the emission can be explained in the context of nonthermal bremsstrahlung mechanism. Synchrotron radio emission from this region is measured from multi-frequency radio continuum observations of the Galactic center using the Green Bank Telescope. The interaction of low energy cosmic ray electrons with the gas in the Galactic center infer high values of cosmic ray ionization, heating rates as well as strong FeI Kα line emission at 6.4 keV. The high energy tail of cosmic ray particles interacting with neutral gas produces nonthermal bremsstrahlung emission at GeV γ-rays. The spectrum of diffuse γ-ray emission detected by *Fermi* reflects the energy distribution of electrons producing radio synchrotron emission from the Galactic center.

1 The Role of Cosmic Rays in the Galactic Center

The physical conditions of the ISM at the Galactic center are characterized to be different than those of the Galactic disk. The distributions of the relativistic component traced by nonthermal radio continuum emission and the molecular component are highly concentrated in the central few degrees of the Galactic center. It is then natural to consider the interaction of relativistic electrons and neutral gas and study the chemistry of cosmic ray dominated regions [2, 11]. Diffuse TeV and FeI Kα line emissions have also been detected from Galactic center

F. Yusef-Zadeh (✉)
Department of Physics and Astronomy, Northwestern University, Evanston, IL 60208, USA
e-mail: zadeh@northwestern.edu

D.F. Torres and O. Reimer (eds.), *Cosmic Rays in Star-Forming Environments*,
Astrophysics and Space Science Proceedings 34, DOI 10.1007/978-3-642-35410-6_25,

molecular clouds. These observations taken from radio to TeV energies help bridge a gap in understanding the physical and chemical processes operating at low and high energies.

Given the high concentration of a population of molecular and relativistic gas, we recently investigated the consequences of the cosmic ray interaction with molecular gas. The origin of high energy X-ray and γ-ray emission was explained in the context of bremsstrahlung mechanism [16]. Here, we present highlights of the results of this study and discuss a peculiar cloud G0.11-0.11 as an excellent object for testing the interaction of molecular gas with a magnetized nonthermal filament traced at radio wavelengths.

1.1 Molecular Gas Heating

The reservoir of molecular gas that is distributed in the inner few hundred parsecs of the Galactic center shows an elevated gas temperature compared to that of dust grains. In addition, there is a large concentration of cosmic ray electrons that produce synchrotron radiation from the same region. One consequence of the interaction of cosmic ray electrons with molecular clouds is heating of molecular gas. This heating process is particularly relevant to the unique population of Galactic center molecular clouds showing two different gas temperatures [4]. A two-temperature distribution of molecular clouds is found with the warm ($T_{kin} \sim 200$ K) gas at low H_2 density of $n \sim 10^3\,cm^{-3}$ and cool ($T_{kin} \sim 25$ K) gas to dense cores with $n \sim 10^5\,cm^{-3}$. The high gas temperature of the Galactic center molecular clouds is elevated from 30–50 K up to $T \sim 200$ K [6] and is discrepant with respect to the dust temperature 18–22 K measured from observations of the inner $2^0 \times 1^0$ of the Galaxy [7]. The cause of high temperature molecular gas has been considered to be due to shocks generated as a result of cloud-cloud collisions [12]. However, this mechanism is expected to produce warm gas only at the surface of the clouds where clouds collide with each other. Cosmic rays, on the other hand, have the advantage that they can increase the temperature throughout the cloud, even the heavily shielded dense regions.

The total cooling rate per H_2 molecule is dominated by different molecular species at low and high temperatures. CO rotational cooling dominates below 100 K and scales linearly with H_2 density, whereas H_2 rotational cooling dominates above 100 K and does not scale as strongly with increasing density. The cooling rate can then be mapped to the cosmic ray ionization rate that would supply heat at the same rate. Ionization rates of 10^{-15} and $10^{-14}\,s^{-1}$ would yield gas temperatures of $\sim$100 and $\sim$200 K respectively.

The mass of the molecular nuclear disk is estimated to be $2–6 \times 10^7$ solar mass [8]. The diffuse molecular gas is estimated to have a density of $\sim 100\,cm^{-3}$, as H_3^+ absorption studies indicate [9]. The total energy that needs to be resupplied to keep the gas warm is estimated to be 6×10^{38} erg s^{-1} which is equivalent to one supernova per 7×10^3 years.

1.2 The Production of the FeI Kα *Line Emission*

We recently investigated another consequence of of the cosmic ray interaction via a systematic study of the diffuse 6.4 keV emission coincident with Galactic center molecular clouds [17]. We noted, in particular, a strong correlation between nonthermal radio filaments and molecular clouds. We accounted for the distribution of Kα neutral Fe line emission in terms of the impact of the relativistic particles from local (nonthermal filaments) and diffuse neutral gas, which produces both nonthermal bremsstrahlung X-ray continuum emission and diffuse 6.4 keV line emission. In this picture, the low-energy relativistic particles interacting with neutral gas lose energy as they interact with neutral Fe. The expected Fe Equivalent Width (EW) line is expected to be $\sim$ 2–300 eV for solar abundance. Assuming that diffusion of low energy cosmic ray particles is not hindered by magnetic field fluctuations in molecular clouds, the fluorescent 6.4 keV line emission was predicted to vary on such a time scale unless there is constant acceleration of particles at these energies. It turns out the low energy cosmic ray flux can vary on a short time scale depending on what the density of the medium that the cosmic ray electrons are diffusing through. This is because of ionization losses of electrons diffusing through a molecular cloud. The ionization losses of electrons are particularly dramatic at 100 keV which could diffuse for roughly 5 years in a medium with molecular density of 200 cm^{-3} before they lose most of their energy.

In another model, it is suggested that the 6.4 keV emission results from X-ray irradiation by hypothetical transient source associated with the massive black hole at the Galactic center, Sgr A*, and that we are now seeing its echo in the 6.4 keV line emission [5, 10, 14]. This model can explain many aspects of the time variable emitting clouds at 6.4 keV as well as clouds showing large EWs of 6.4 keV line emission which is >1,000 eV. It is possible that the cosmic ray and X-ray irradiation processes are responsible for production of FeI Kα line emission from Galactic center clouds showing low and high EWs of FeI line, respectively. Future studies can place constraints on the applicability of these two models by investigating the chemistry of the cosmic ray dominated region of the central molecular zone.

One of the most interesting Galactic center molecular clouds showing strong 6.4 keV emission is G0.11-0.11 which is positioned at the edge of the nonthermal filaments of the Arc. This is an important cloud as it can be used to test the cosmic ray irradiation picture. The left panel of Fig. 1 shows contours of the EW (eV) based on Chandra observations and are superimposed on a grayscale continuum image at 20 cm. This figure illustrates the long nonthermal radio filaments that run perpendicular to the Galactic plane as it crosses an HII region G0.18-0.04 or the Sickle nebula. The morphology the eastern edge of the G0.11-0.11 molecular cloud led [15] to argue that radio filaments and G0.11-0.11 are dynamically interacting with each other. Contours of CS (1–0) line emission [15] from G0.11-0.11 are superimposed on a 20 cm image of the filaments and are shown in the right panel of Fig. 1. This figure suggests a strong similarity between the CS and 6.4 keV line distributions, as expected. The EW ranges between $\sim$ 110 to $\sim$ 1,100 eV peaking on

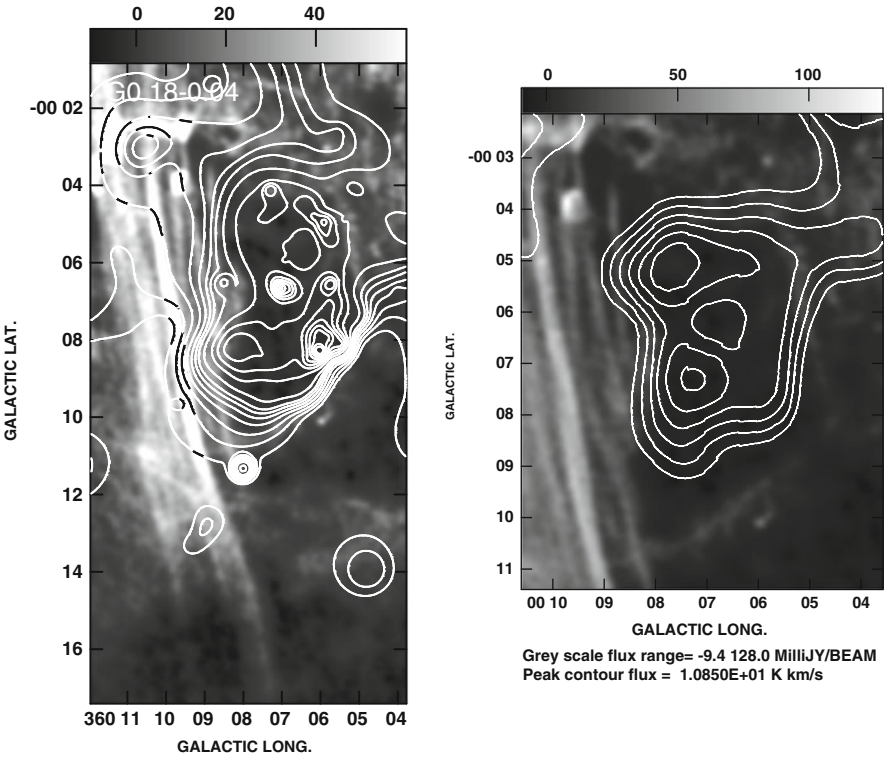

Fig. 1 *Left*: Contours of Equivalent widths of FeI Kα line at 6.4 keV between 110 and 1,100 eV are superimposed on a grayscale continuum image at 1.4 GHz based on Chandra and VLA observations. *Right*: Contours of CS (1-0) emission superimposed on a grayscale continuum image at 1.4 GHz

diffuse and compact sources within the G0.11-0.11 cloud. The low value of the EW of Kα line emission is consistent with the interaction picture. The high value of the equivalent width of FeI 6.4 keV line toward G0.11-0.11 requires a high abundance of iron.

Figure 1 (left) also shows a 6.4 keV cloud with Kα line emission peaking at the location where the longest nonthermal radio filament cross the well-known Sickle HII region G0.18-0.04 at $l = 10.6'$, $b = -3'$. This peak has EW ~ 200 eV and lies at the interface of nonthermal filaments and the 40 km s^{-1} which is associated with the Sickle. The kinematics of ionized gas exactly at the interface between nonthermal filaments and the Sickle at G0.18-0.04 show forbidden velocities ~ -30 km s^{-1} [18]. This anomalous motion of ionized gas in the Sickle can be interpreted in the context of the interaction of the magnetized filaments and the 40 km s^{-1} cloud.

1.3 Diffuse γ-Ray Emission

Recent correlation study of diffuse emission from the Galactic center at multiple wavelengths concluded that the distribution of diffuse γ-ray emission detected by *Fermi* matches best with that of radio continuum emission at 1.45 GHz [16]. It is also known that the distribution of TeV emission traces Galactic center molecular clouds [1]. These correlations suggest that the γ-ray emission is a product of the interaction of cosmic rays with interstellar gas near the Galactic center. We consider that all of the synchrotron-emitting electrons are interacting with the gas. The mechanism for production of γ-ray emission is similar to that invoked to explain the production of Kα line emission except that high energy particles are involved for production of bremsstrahlung γ-ray radiation. We note that the production of GeV photons detected by *Fermi* should have the same spectrum as that seen at radio frequencies without extrapolating the electron energies to higher or lower energies, as they are done to explain the FeI Kα line and TeV emission. To obtain the energy spectrum of electrons, a quantitative estimate of the relative amount of thermal and nonthermal emission from the Galactic center was made by assuming that the two components are spatially mixed from each other following Gregory and Seaquist [13]. The modeling of the data shows that the flux varies $\nu^{-0.25}$ below 3.3 GHz and $\nu^{-1.7}$ above 3.3 GHz, with an unabsorbed nonthermal flux of 2,450 Jy at 325 MHz (see also [3]). Interestingly, a break in the radio spectrum at the transition frequency of 3.3 GHz reflects the break in the spectrum of γ-rays, as measured by *Fermi*. This provides compelling evidence that the interaction of radio emitting GeV electrons with neutral gas is also responsible for production of GeV emission. The change in the spectral index can be attributed to rapid cooling of electrons at high energies (see [16]). As for the contribution of γ-ray emission by Inverse Compton scattering, it turns out to be insignificant compared to nonthermal bremsstrahlung emission from the inner few hundred parsecs of the Galaxy (a more detailed discussion will be given elsewhere).

Acknowledgements I would like to thank my collaborators in this project especially, J. Hewitt, M. Wardle, V. Tatischeff, D. Roberts, W. Cotton, H. Uchiyama, M. Nobukawa, T. G. Tsuru, G. Heinke and M. Royster.

References

1. Aharonian, F., Akhperjanian, A. G., Bazer-Bachi, et al. 2006, Nature, 439, 695
2. Bayet, E., Williams, D. A., Hartquist, T. W. & Viti, S. 2011, MNRAS, 414, 1583
3. Crocker, R. M., Jones, D. I., Melia, F., Ott, J., & Protheroe, R. J. 2010, Nature, 463, 65
4. Hüttemeister, S., Wilson, T. L., Henkel, C., & Mauersberger, R. 1993, A&A, 276, 445
5. Koyama, K., Takikawa, Y., Hyodo, Y., Inui, T., Nobukawa, M., Matsumoto, H., & Tsuru, T. G. 2009, PASJ, 61, 255
6. Lis, D. C., Serabyn, E., Zylka, R., & Li, Y. 2001, ApJ, 550, 761

7. Monlinari, S., Bally, J., Noriega-Crespo, A., Compiegne, M., Bernard, J. P., et al. 2011, ApJ, 735, 33
8. Oka, T., Hasegawa, T., Sato, F., Tsuboi, M., & Miyazaki, A. 1998, ApJS, 118, 455
9. Oka, T., Geballe, T. R., Goto, M., Usuda, T., & McCall, B. J. 2005, ApJ, 632 882
10. Ponti, G., Terrier, R., Goldwurm, A., Belanger, G., & Trap, G. 2011, ApJ, 439, 446
11. Papadopoulos, P. P., Thi, W-F., Miniati, F. & Viti, S. 2011, MNRAS, 414, 1705
12. Rodriquez-Fernandez, N. J., Martin-Pintado, J., Fuente, A., de Vicente, P., Wilson, T. L, & Hüttemeister, S. 2001, A&A, 365, 174
13. Gregory, P. C., & Seaquist, E. R. 1974, ApJ, 194, 715
14. Sunyaev, R.A., Markevitch, M. & Pavlinsky, M. 1993, ApJ, 407, 606
15. Tsuboi, M., Ukita, N., & Handa, T. 1997, ApJ, 481, 263
16. Yusef-Zadeh, F., Hewitt, J. W., Wardle, M., Tatischeff, V., Roberts, D. A., Cotton, W., Uchiyama, H., Nobukawa, M., Tsuru, T. G., Heinke, C. and Royster, M. 2012, submitted to ApJ
17. Yusef-Zadeh, F., Muno, M., Wardle, M., & Lis, D. C. 2007, ApJ, 656, 847
18. Yusef-Zadeh, F., Roberts, D. A., & Wardle, M. 1997, ApJ, L490

Traces of Past Activity in the Galactic Centre

Gabriele Ponti, Mark R. Morris, Regis Terrier, and Andrea Goldwurm

Abstract The Milky Way centre hosts a supermassive Black Hole (BH) with a mass of $\sim 4 \times 10^6\,M_\odot$. Sgr A*, its electromagnetic counterpart, currently appears as an extremely weak source with a luminosity $L \sim 10^{-9}\,L_{Edd}$. The lowest known Eddington ratio BH. However, it was not always so; traces of "glorious" active periods can be found in the surrounding medium. We review here our current view of the X-ray emission from the Galactic Center (GC) and its environment, and the expected signatures (e.g. X-ray reflection) of a past flare. We discuss the history of Sgr A*'s past activity and its impact on the surrounding medium. The structure of the Central Molecular Zone (CMZ), a highly flattened toroid, has not changed significantly since the last active phase of Sgr A*. This relic torus provides us with the opportunity to image the three-dimensional structure of an AGN torus in exquisite detail.

G. Ponti (✉)
Max-Planck-Institut für extraterrestrische Physik, Giessenbachstrasse 1, D-85748, Garching bei München, Germany
e-mail: ponti@mpe.mpg.de

M.R. Morris
Department of Physics and Astronomy, University of California, Los Angeles, CA 90095-1547, USA

R. Terrier
Unité mixte de recherche Astroparticule et Cosmologie, 10 rue Alice Domon et Léonie Duquet, 75205 Paris, France

A. Goldwurm
Service d'Astrophysique (SAp), IRFU/DSM/CEA-Saclay, 91191 Gif-sur-Yvette Cedex, France
Unité mixte de recherche Astroparticule et Cosmologie, 10 rue Alice Domon et Léonie Duquet, 75205 Paris, France

D.F. Torres and O. Reimer (eds.), *Cosmic Rays in Star-Forming Environments*, Astrophysics and Space Science Proceedings 34, DOI 10.1007/978-3-642-35410-6_26,

1 The Galactic Centre (GC)

At approximately 8 kpc ([26, 67, 101, 104, 111, 163, 200, 224, 225, 281, 289]; see Genzel et al. [96] for a review), the GC is by far the closest Galactic nucleus (e.g. Andromeda, the nearest spiral galaxy, is 10^2 times further away). Thus it is an excellent laboratory to directly image, with exquisite resolution, the physical processes that might be occurring in many other galactic nuclei.

In the optical window our view toward the Galactic Centre (GC) is obscured by a thick dust curtain, with more than 30 magnitudes of extinction [16, 17, 233], thus preventing any direct view of it. This dust curtain can be raised by observations in different wavebands; a direct view of the GC can be achieved both at longer and shorter wave-lengths, e.g. in infrared-radio as well as medium-hard ($E \geq 2$–3 keV) X-rays and γ-rays. InfraRed (IR) and radio observations have demonstrated that the GC is very bright and display a stupendous variety of phenomena. On large scales ($\sim 10°$), a large concentration of stars (the so-called Galactic bulge) with a central bar distribution dominates the gravitational potential [31, 78, 319]. The central few hundred parsecs contain several of the most massive molecular clouds of the Galaxy [184] and radio observations reveal arcs and non thermal filaments [181–183, 312], indicating the importance of the Galactic magnetic field for the GC environment [184]. Within the central few parsecs, IR observations have revealed the presence of a dense and luminous star cluster [93–95, 100, 101, 156, 253, 254, 281]. The precise monitoring of stellar motions within 0.5 arcsec of Sgr A* has led to the conclusion that it consists of a compact, dark, central mass concentration of $4 \times 10^6\,M_\odot$, that cannot be anything but a Black Hole ([79, 96, 98, 100, 103] BH [252]).

1.1 X-ray Emission from the GC

The first detections of X-ray sources in the GC date back to the sixties, to the very beginning of X-ray astronomy, when the first short (few minute) observations were made possible with the use of rocket flights [35, 36, 50, 87, 113]. In the 1970s the first soft X-ray satellites (Uhuru, Ariel 5 and HEAO 1) were launched and by the end of the 1970s the first GC soft X-ray images, with arcminute resolution, were obtained thanks to the Einstein (HEAO 2) satellite [296]. Soon after, in the 1980s and early 1990s, coded-mask imaging techniques allowed a similar revolution in the hard X-ray/soft-γ-ray spectral regions with the launch of XRT/SpaceLab2 [258], ART-P/GRANAT [213, 266] and SIGMA/GRANAT [108, 109]. These satellites clearly showed that the soft and hard X-ray emission from the GC region is dominated by bright, variable and transient point sources, mainly X-ray binaries.

Koyama et al. [135], thanks to GINGA data, were the first to discover (in the GC) a 6.7 keV line (Fe XXV), manifested as diffuse and rather uniform emission, resembling the diffuse Galactic ridge emission [292]. Sunyaev et al. [267], using ART-P data, discovered an additional harder and asymmetric component of the

diffuse GC emission. The spatial correlation of this emission with GC Molecular Clouds (MC) prompted the speculation that MC might act as mirrors and this radiation might be reflection of a past flare of a very bright source in the GC (possibly Sgr A* itself). In that case, the authors predicted that the Fe Kα line, associated with the reflection continuum, should soon be detected. Three years later, owing to the high energy resolution of the *ASCA* satellite, the hypothesis of a major X-ray flare in the GC was significantly strengthened by the detection of diffuse Fe Kα line emission from the hard X-ray emitting MC [136]. Finally, ASCA's improved energy resolution in the soft X-ray band allowed also the detection of several high-ionisation emission lines (e.g. of Si, S, Ar, Ca, etc.) associated with a low temperature (T $\sim$ 0.8–1 keV) ionised plasma component pervading the GC.

Since the beginning of this century a new golden age for X-ray astronomy has begun, with the launch of XMM-Newton (1999), Chandra (1999) and Suzaku (2005), three cornerstones in the ESA, NASA and JAXA space projects which have allowed us to take a major step forward in our understanding of the GC X-ray emission.

X-ray observations of the GC show clear evidence for several emission components:

Bright X-ray point sources: For more than three decades it has been possible to image the GC X-ray emission [47, 121, 213, 241, 255, 256, 296]. In particular, during the past decade, intensive *Chandra*, *XMM-Newton*, *RXTE*, *INTEGRAL* and, on an almost daily basis, *Swift* monitoring campaigns have been performed within the central 1.2 square degrees [6, 68–70, 129, 148, 186–188, 272, 294]. Nineteen sources having a 2–10 keV peak luminosity, $L_x \gtrsim 10^{34}$ erg s^{-1}, have been detected in this region so far [70, 298]. It has been possible to identify the brightest ones (about half of the sample) as accreting neutron stars or BH. Two of the 19 sources are persistent (with $L_x \simeq 10^{35-36}$ erg s^{-1}), while the remaining are transients spending years to decades in a quiescent state with $L_x \lesssim 10^{33}$ erg s^{-1} and undergoing short (weeks/months) outbursts with peak luminosity several orders of magnitudes higher. Ten of the 19 bright sources in the central 1.2 square degrees belong to the class of low-luminosity X-ray transients and have never been observed at luminosity higher than $L_x \sim 10^{36}$ erg s^{-1} and only 3 have reached $L_x \gtrsim 10^{37}$ erg s^{-1} [70, 298]. Moreover, no new transients have been found since 2007, suggesting that most X-ray transients recurring on a time scale of less than a decade have now been identified near the GC [69, 70, 121, 187].

Soft X-ray diffuse plasma: A diffuse soft X-ray emission ($E_x \lesssim 4$ keV), traced by the H-like and He-like lines of, e.g., Si, S, Ar and Ca can be best fitted with a low temperature (kT $\sim$ 0.8–1 keV) plasma component that pervades the GC (a small fraction, less than a few percent, of this emission can be ascribed to foreground diffuse soft X-ray emission; [130, 147, 162, 309]). This plasma is bound to the Galaxy. Muno et al. [187], in fact, estimated the sound speed for the soft plasma to be $v_s \sim 500$ km s^{-1}. This plasma will possibly expand to $\sim$1 kpc above the disc, but be bound to the Galaxy (assuming the Breitschwerdt et al. [37] potential). The plasma radiative cooling time within the central 50 pc, is estimated to be 3–6 $\times$ 10^6 year [187]. If about 1 % of the 10^{51} erg of kinetic energy per supernova heats the

plasma (as in the Galactic disc; [128]), it can be sustained by the reasonable rate of one supernova every 10^5 year. Additional soft X-ray emission might be produced by interaction of stellar winds from young and massive stars with the interstellar medium [187] or each other [169] and coronal X-ray sources [58, 82]. The patchy soft plasma distribution, with higher concentrations (up to a factor of 10 variations within 50 pc) towards star forming regions, matches these hypotheses.

Diffuse 6.7 keV (Fe XXV) emission and Galactic ridge X-ray emission: Discovered in the late 1970s [30, 56], the Galactic ridge X-ray emission is one of the largest diffuse features (after the X-ray background) in the 2–10 keV band. With a total X-ray of $L_x = 1 - 2 \times 10^{38}$ erg s^{-1} [220, 276, 294], it is concentrated near the Galactic disc and bulge, extending more than 100° in Galactic longitude and just a few degrees in latitude [227, 292, 293, 304, 305]. With strong emission lines (e.g. Fe XXV and Fe XXVI at 6.7 and 6.97 keV) and a hard X-ray continuum, this emission has a spectrum characteristic of a kT $\sim$ 5–10 keV, optically thin plasma [134, 135, 138, 305, 307]. However, such a hot plasma cannot be gravitationally or magnetically bound to the Galaxy [273], thus it would flow away at a supersonic velocity of few thousands km s^{-1} [322], on a timescale of $\sim 3 \times 10^4$ years [267]. To replenish the energy losses a luminosity (supplied throughout the Galaxy) of 10^{43} erg s^{-1} would be required [273]. At present, no evidence exists for the presence of such a source in the Galaxy.

Alternatively, this diffuse emission might be composed of a large population of initially unresolved, weak point sources [232], as is the extragalactic X-ray background. In support of this hypothesis, it is observed that both the Fe XXV 6.7 keV line and the hard X-ray (3–20 keV) continuum are very well correlated, over the whole Galaxy, with the near IR luminosity (3–4 μm) which traces the stellar mass density [229, 230]. Moreover, thanks to an ultra-deep (1 Ms) *Chandra* observation of a field near the Galactic plane ($l = 0.08°$, $b = -1.42°$, near the GC) with weak interstellar absorption, Revnivtsev et al. [232] resolved more than 80 % of the diffuse 6–8 keV emission into weak discrete sources such as accreting white dwarfs and coronally active stars. Additionally, the luminosity function of these sources is observed to be very similar to the one present in the Solar vicinity [231, 232, 246]. The still unresolved 10–20 % diffuse emission is consistent with being composed of coronally active and normal stars with $L_{2-10\,keV} < 4 \times 10^{29}$ erg s^{-1}, thus below the detection threshold [223]. It now seems clear that the Galactic plane 6.7 keV emission (the so called Galactic ridge diffuse X-ray emission) is mainly composed of weak point sources.

Strong 6.7 keV emission is also present in the GC [135, 203, 304]. As for the Galactic ridge, part of this emission will be produced by accreting white dwarfs and coronally active stars. However, a significant enhancement of 6.7 keV emission, as well as an east-west asymmetry compared to the near IR distributions (tracing point sources), are observed in the central degree [137, 140, 141, 285, 308]. This GC excess of emission (over the best-fit stellar mass distribution model made from near-IR observations and explaining the 6.7 keV emission in the Galactic ridge) is hardly explained by point source origin, requiring a new population of sources with extremely strong Fe XXV line emission [274, 285]. Thus, it has been suggested that

this component might be associated with truly diffuse hot gas [137,285]. The energy required to sustain such hot plasma within the inner 20 pc of the Galaxy is three orders of magnitude smaller than for the entire Galaxy, being $\sim 10^{40}$ erg s^{-1} [187]. Belmont et al. [21] explored the possibility of the hot gas being a gravitationally confined helium plasma. Belmont and Tagger [22], instead, suggested that viscous friction of MC flowing within the hot phase can dissipate energy in the gas and heat it. As for the Galactic plane, *Chandra* can be used to partially resolve the point source contribution to this GC excess of emission. The lower extinction at a distance of 4–9 pc from Sgr A*, allowed Revnivtsev et al. [231] and Yuasa et al. [311] to resolve at least 40 % and possibly the bulk of the total 4–8 keV band GC emission into (as in the Galactic ridge) accreting white dwarfs and coronally active stars. The remaining GC 6.7 keV emission might be associated with supernova remnants, such as Sgr A East [137, 157, 242] which not only show a low temperature (kT $\sim$ 0.8–1 keV) plasma component, but also a significantly hotter (kT $\sim$ 3−4 keV) component producing a harder X-ray continuum and significant Fe XXV line emission.

However, it is difficult to completely rule out that some additional emission might be associated with a hot plasma produced by past energetic events in the GC.

Sgr A*: One of the major drivers for the deep X-ray surveys of the GC during the past half century has been to measure the X/γ-ray emission from the supermassive BH associated with the compact radio source Sgr A* [174, 175]. A weak source has been detected, at the position of Sgr A*, with a 2–10 keV luminosity of only $L_{2-10} = 2 \times 10^{33}$ erg s^{-1} [6], which corresponds to 4×10^{-12} of the Eddington luminosity for a 4×10^6 M$_\odot$ BH. No other BH has ever been detected at such low Eddington ratio. The excellent *Chandra* spatial resolution allowed be resolve at the extent of Sgr A*'s quiescent emission to slightly more than 1" [6], which roughly corresponds to the Bondi radius ([33]; $r_{\rm Bondi} \sim 2 \times 10^5\, r_g$, where $r_g = GM_{\rm BH}/c^2$) and to detect diffuse emission (within 15" radius from Sgr A*) from a non-ionisation-equilibrium plasma [301]. Another major result has been the discovery of Sgr A*'s flaring behaviour, both in X-rays [5, 110] and near-infrared [95,99]. X-ray flares typically occur about once per day, lasting for $\sim 10^{3-4}$ s, during which the X-ray intensity increases by factors up to 160 [220] from the quiescent value, however the bolometric luminosity still remains extremely low. All these observational properties appear to be consistent with Sgr A* accreting stellar wind material captured from nearby stars [52, 63, 65, 173, 222, 235].

In the past decade Sgr A* has been repeatedly observed by *XMM-Newton* and *Chandra* (as well as in IR), accumulating more than 3 Ms exposure (corresponding to almost 2 months) and confirming Sgr A*'s low quiescent-state luminosity. One may wonder whether Sgr A* has always been so underluminous or whether it experienced, in the past, long periods of high-energy activity, that would make the massive black hole of our Galaxy more similar to typical low-luminosity Active Galactic Nuclei, than it appears today.

Diffuse 6.4 keV (Fe Kα) emission: Extended ($\sim 1°$, few 10^2 pc), hard (8–22 keV) X-ray emission elongated along the Galactic plane, corresponding spatially with massive Molecular Clouds (MC) was first detected in the early 1990s thanks to the

ART-P telescope [267]. The authors interpreted this emission as X-ray reflection of a past energetic event in the GC, predicting the presence of the associated fluorescent Fe Kα line.[1] Intense, diffuse and patchy Fe Kα emission, from the same MC, was later measured by ASCA [136], confirming this interpretation. The spatial and temporal variations of the scattered/reflected flux depend on the underlying gas distribution and the past activity of the GC source over a time equal to that taken by the light to cross that region. The presence of massive MC in the inner core of the Galaxy (the so called Central Molecular Zone, CMZ) allows us to put firm constraints on the past activity of the GC over the last $\sim 10^3$ year. This remains true even if other mechanisms can explain the diffuse Fe Kα emission and hard continuum [42, 75, 76, 288, 313, 315].

2 X-ray Reflection

The radiation produced by a powerful X-ray source located close to a MC will interact with the MC material and generate an X-ray reflection component. Hard X-ray radiation entering a MC (with typical hydrogen column density of the order of $N_{\rm H} \sim$ few 10^{22}–10^{24} cm^{-2}; i.e. $\tau \sim$ 0.01–1) produces, in fact, an X-ray reflection spectrum similar to the one shown in Figs. 1 and 2. We describe here the main features of the X-ray reflection from (neutral) MC material. The illuminating source is assumed to have a power-law spectrum with photon index $\Gamma = 2$.

Continuum: Low energy X-ray radiation is mainly absorbed through the photoionisation of hydrogen, helium and the K-electrons of heavy elements. The photoionisation cross section rapidly decreases with frequency: $\sigma_{\rm ph} \sim \nu^{-3}$, thus the Thomson scattering cross section ($\sigma_{\rm T} = 6.65 \times 10^{-25}$ cm^{-2}) already exceeds the photoionisation cross-section per hydrogen atom for photons with energies E > 8–12 keV [14, 25, 38]. At energies E > few keV the photon wavelength is less than the Bohr radius and electrons bound to hydrogen and helium atoms can be treated as free since the recoil energy $\sim h\nu(h\nu/m_e c^2)$ greatly exceeds the ionisation potential of these atoms [14]. High-energy photons lose energy mainly through the recoil effect, transferring it to the electrons at each scattering. The competition between multiple electron (down-) scattering of high-energy photons and photoelectric absorption of low energy photons leads to the characteristic "Compton reflection hump" in the reflection spectrum between 20–100 keV [14, 15, 81, 97, 102, 164, 197]. Figure 1 shows the reflection spectrum from high optical depth ($\tau \gg 1$) MC. A prominent Compton hump is present between 10 and 50 keV. The bottom panel

[1] Even before the Sgr A* case, the (delayed) reflected emission has been discussed (see [46, 266]) for 1E1740.7-2942, one of the two brightest hard X-ray sources in the GC region. During the mid 1990s the source, known to be located inside a molecular cloud [9], was observed in a low state with the flux $\sim$5 times lower than in the bright state. In a set up similar to the one used later for Sgr A*, this fact was used to constrain the optical depth and the size of the cloud from hard X-rays and later from 6.4 keV line [48].

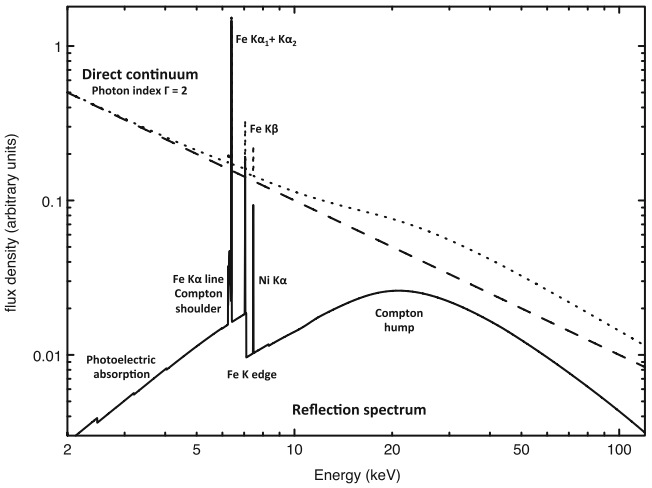

Fig. 1 Typical X-ray reflection spectrum from neutral material with column densities $N_H \gg \sigma_T^{-1} \sim 1.5 \times 10^{24}\text{cm}^2$. The Fe K$\alpha$ doublet + Kβ and Ni Kα lines and the respective Compton shoulders, as well as the K edges and Compton hump are shown (*emission lines* from *lower* atomic number elements which have *lower* EW are not shown) (Figure courtesy of Matt et al. [168])

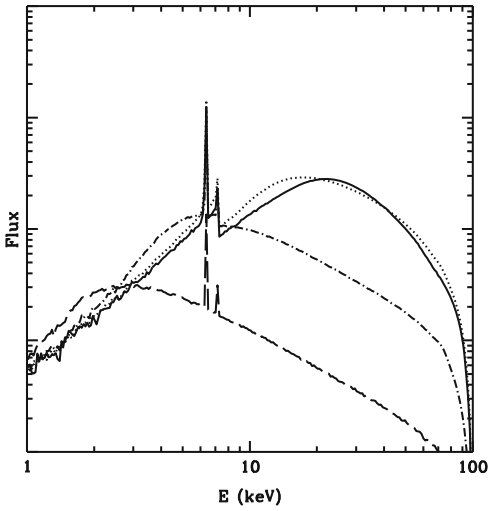

Fig. 2 Reflection spectrum from a molecular cloud (with toroidal geometry and observed face on) for different column densities: 2×10^{22} cm^{-2} (*dashed line*), 2×10^{23} cm^{-2} (*dot-dashed line*), 2×10^{24} cm^{-2} (*dotted line*), 2×10^{25} cm^{-2} (*solid line*). A prominent Compton hump is expected for $\tau \gg 1$, while the high-energy spectrum changes significantly for smaller column density clouds. Almost no Compton hump is visible for $N_H < 2 \times 10^{23}$ cm^{-2} (Figure courtesy of Matt et al. [168])

shows the reflection spectrum from clouds with lower column densities. The reflection spectrum has a very different shape and the Compton hump is less prominent.

Edges and lines: The reflection spectrum does contain jumps corresponding to the K-edges of photo-absorption by heavy elements such as Fe, S, Ar, etc. Due to the high abundance and fluorescent yield of iron, about 30 % of the photons absorbed by photoionisation of iron with energies above the K-shell edge at 7.1 keV give rise to iron K-shell fluorescent photons. The Fe Kα line (2p $\rightarrow$ 1s transition) consists

of two components Kα_1 at 6.404 and Kα_2 at 6.391 keV with branching ratio of 2:1 [11]. The lines have natural widths of $\Delta E \sim 3.5$ eV. High resolution X-ray spectrometers (such as the one provided by X-ray calorimeters) will resolve the doublet and measure with high accuracy any shift due to the cloud motion. For a MC moving at 100 km s^{-1} a 2.1 eV shift is expected. Since the M-shells of neutral iron atoms are populated, the fluorescent Fe Kβ line (3p $\rightarrow$ 1s) at 7.06 keV, with Kβ/Kα ratio = 0.155–0.16 [15, 177, 209, 210], is also expected.

Because both the Fe Kα and reflection continuum intensities are roughly proportional to τ_T and source luminosity the Equivalent Width, EW$_{\rm FeK\alpha}$ is expected to be $\sim$1 keV (for Solar abundances), with only $\sim$30 % variations (from $\sim$0.7 to $\sim$1 keV; see Fig. 3 of Matt et al. [168]) for different MC column densities [168]. The line EW depends also on the system geometry and the iron abundance (A$_{\rm Fe}$). For Solar abundances (A$_{\rm Fe} = 1$) the line EW is $\sim$1 keV against the total reflection continuum [102, 144, 165, 168] and it is expected to vary approximately linearly EW $\sim$ EW(A$_{\rm Fe} = 1$) $\times$ A$_{\rm Fe}^{0.8-0.9}$ for A$_{\rm Fe} << 1$ and saturates for A$_{\rm Fe} >> 1$, EW $\sim$ EW(A$_{\rm Fe} = 1$) [1 + (0.6 − 1.2) $\times$ log(A$_{\rm Fe}$)] [166]. Because of the angular dependence of the Compton effect, the intensity of the scattered continuum (for $\tau \ll 1$) measured at an angle θ with respect to the direction of travel of the incident radiation is expected to be proportional $(1 + cos^2(\theta))$. On the contrary, Fe Kα fluorescence emission is isotropic, thus the observed EW$_{\rm Fe}$ has also a dependence on the system geometry. The K-shell fluorescence yield (Y_Z^K) is an increasing function of atomic number [11], thus weak lines are expected from C, N, O, and Ne ($Y_Z^K \sim 10^{-2}$) as well as Mg, Si and S ($Y_Z^K \sim 10^{-1}$). EW$_{\rm NiK\alpha}$ is estimated to be $\sim$0.05 $\times$ EW$_{\rm FeK\alpha}$ [303].

Compton line shoulders: The recoil upon electron scattering shifts the Fe Kα line photons to lower energies (but this is true for any line). Thus, the initial mono-energetic line spreads downward in energy over two Compton wavelengths ($\Delta E \simeq 2E^2/m_e c^2 = 160$ eV) for each scattering, in this way forming a red wing, the so called "Compton shoulder". The details of the Compton shoulder EW and shape depend on the geometry, and the MC column density. For example, for small scattering angles of X-ray photons the recoil energy is comparable or lower than the ionisation energy [268], leading to modifications of the shape of the Compton shoulder. The motion of the electrons in hydrogen atoms is another important factor causing strong blurring of the low energy wing of the shoulder [268]. However, in most cases the Compton shoulder EW is expected to be roughly 10–20 % of the Fe Kα EW [167, 302].

Polarisation: Thomson scattering on electrons will induce linear polarisation of the reflected emission, even in the case of initially unpolarised radiation. The expected degree of polarisation is given by $P = (1-cos^2\theta)/(1+cos^2\theta)$, where θ is the scattering angle [14, 49]. The detection of polarised light from the MC in the GC will provide a clean test of the X-ray external illumination scenario. Moreover, the scattering angle deduced from polarisation [204, 269] will eventually allow one to determine the MC distance along the line of sight. This is a fundamental parameter for reconstructing the three-dimensional gas distributions in the CMZ and the recent history of GC X-ray emission.

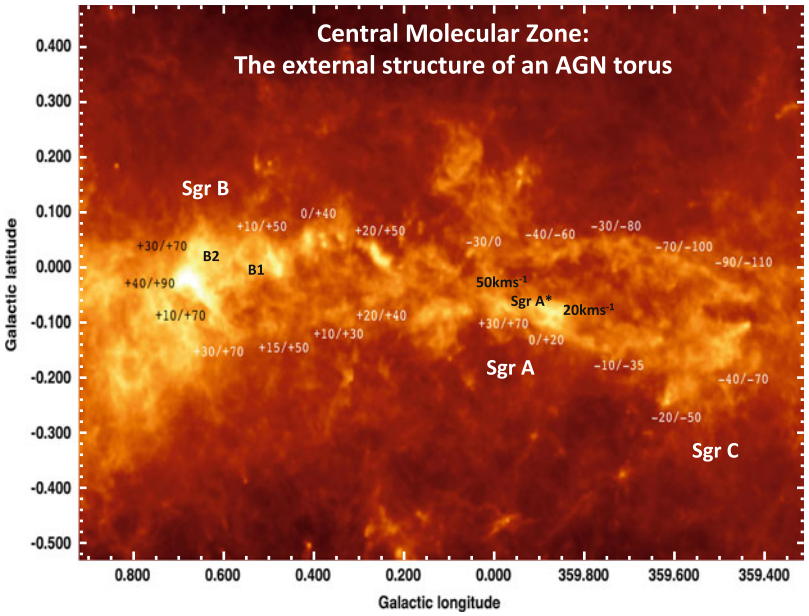

Fig. 3 *Herschel* map of the atomic hydrogen column density distribution of the central ~ 150 pc of the CMZ showing a large part of the the CMZ disc population. The color scale is logarithmic and extends from 4×10^{22} cm^{-2} in the *darkest* regions to 4×10^{25} cm^{-2} in the *brightest* MC cores. Velocity information is taken from CS spectroscopic cubes [283] for the gas counterparts positionally associated with the dense dust clumps. The CMZ disc population appears to have a geometry and location remarkably similar to the one of the AGN molecular torus invoked by AGN unification schemes [286] (Figure courtesy of Molinari et al. [178])

Dust scattering halo: The canonical extinction towards the GC is $A_V \sim 30$ mag, which translates to an X-ray absorbing column density of $N_H \sim 6 \times 10^{22}$ cm^{-2} [88, 221]. The interaction of X-rays with interstellar dust grains leads not only to mere absorption, but also to small-angle scattering, producing a faint and diffuse X-ray halo around the source [158, 208, 221, 238, 280, 299, 300]. Because of the energy dependence of the scattering ($I_{halo} \sim E^{-2}$), dust scattering halos usually appear as a soft power-law component with a fractional intensity of a few to few tens of per cent. The spectral shape of any source in the GC will be modified by the presence of the intervening material. Detailed studies of the dust-scattering halo of bright sources can, in principle, allow one to derive the distribution, along the line of sight, of the scattering material.

2.1 Time Dependent Effects

Depending on the mutual position of the MC and the primary source, substantial evolution of the morphology, flux, equivalent width and shape of the Fe Kα

emission and reflection continuum is expected as a response to a variable primary illuminating source [204, 269]. The light crossing time of the CMZ is t$\sim 10^3$ year, thus monitoring of the reflection component from MC of the CMZ provides constraints on the GC X-ray emission on a similar time-scale and also suggests that the observed present-day X-ray reflection component might be associated with a presently dim source that was brighter in the past [136, 267].

To a first approximation it is possible to place a direct link between the illuminating source luminosity and the fluorescent Fe Kα line flux, assuming isotropic source emission, outside of a cloud with $\tau_T \ll 1$ (see e.g. [269]):

$$F_{\mathrm{FeK}\alpha} = \phi 10^7 \frac{\Omega}{4\pi D^2} \frac{\delta_{Fe}}{3.3 \times 10^{-5}} \tau L_8 \quad (\mathrm{photon\ s^{-1}\ cm^{-2}}), \tag{1}$$

where ϕ is a factor of order unity which weakly depends on the source spectral shape; Ω is the solid angle of the cloud subtended from the location of the primary source; D is the distance to the observer; δ_{Fe} is the iron abundance with respect to hydrogen; τ is the optical depth of the cloud; L_8 is the continuum source luminosity (erg s^{-1}) at 8 keV in the 8 keV wide energy band (see [269] for definition). Thus: $L_8(\mathrm{erg\ s^{-1}}) = 6 \times 10^{38} \times (F_{\mathrm{FeK}\alpha}/10^{-4}) \times (0.1/\tau_T) \times (\delta_{Fe}/3.3 \times 10^{-5})^{-1} \times (R/100\,\mathrm{pc})^2$, where R is the distance from the source to the cloud. If the duration of the source flare is shorter than the cloud light crossing time ($\mathrm{r_{cloud}/c}$), the luminosity estimates should be multiplied by a factor of roughly $\mathrm{r_{cloud}/c}\Delta$t. Because both the Fe K$\alpha$ and reflection continuum intensities are roughly proportional to τ_T and source luminosity the $\mathrm{EW_{FeK}}\alpha$ is expected to be $\sim$1keV (for Solar abundances), with a weak dependence on the MC parameters [168].

Light front scanning the CMZ: The right panel of Fig. 4 shows the situation when the CMZ is illuminated by two very short flares from Sgr A*. The light echo seen from a point different from the source is described by an ellipse, i.e. the locus of points so that the sum of the distances to the source and observer is constant. For an observer at large distance, one focus goes to infinity and the ellipse becomes a parabola. The echo will appear as a parabola, with rotational symmetry about the z-axis, with equation $z/c = (t^2 - (x/c)^2)/2t$, to an observer at infinity [259].

The propagation of an echo in the CMZ allows us to scan the CMZ gas distribution and to perform a tomography of the CMZ. Different patterns of variability are expected for short and long duration flares. In general, the distinction between short and long duration is made on the basis of the light crossing time of the MC and/or MC substructure under investigation. A short duration flare (e.g. months) is expected to produce strong variations of the surface brightness of the Fe Kα line across the MC image, on angular scales corresponding to the typical size of the MC non-uniformities (down to few arcsec); on the other hand, a long duration flare (decades) is expected to reflect the total MC optical depth, which will be much smoother. Monitoring campaigns of the evolution of the Fe Kα morphology (in connection with MC column density maps) will allow a disentangling of these different scenarios.

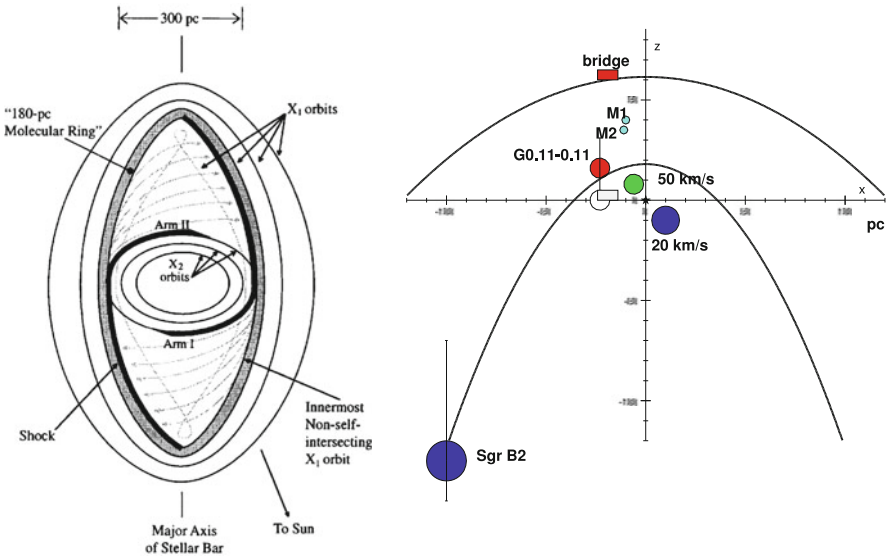

Fig. 4 *(Left panel)* Schematic diagram illustrating the shapes and relative orientations of the X_1 and X_2 orbits and the location of the shocks resulting from the interaction between the innermost X_1 orbit and the outermost X_2 orbit. The arms in the CMZ hypothesized by Sofue [259, 260] are also shown. (Figure courtesy of Morris and Serabyn [184]). *(Right panel)* Sketch of the Galactic plane as seen from the north Galactic pole. Sgr A* is at the vertex and Earth is toward the bottom. Circles represent the hypothesised locations of some MC of the CMZ. Parabolas represent hypothetical light fronts (as seen from Earth) emitted by Sgr A* 100 and 400 year ago (Figure courtesy of Ponti et al. [216])

Superluminal propagation of the echo: The apparent echo expansion velocity over the x-coordinate (see Fig. 4) is equal to or larger than the speed of light for any position ($|\dot{x}/c| = 1 + (ct - |x|)^2/2ct|x|$). Similarly, if the MC is located closer to us than the source, then the echo will scan the MC much quicker than the light-crossing time of the cloud ($\dot{z}/c = 0.5 + x^2/2(ct)^2$, thus $\dot{z} > c$ if $z < 0$, when the MC is in front of the source). Superluminal echos can also be observed in particular geometrical configurations and are mainly linked to the fact that no causal connection is present between the illuminated parts of the MC. The framework is very similar to a projector-screen scenario. The physical variation happens at the level of the projector, for example changing the slide (e.g. taking a time t_s). This variation will appear projected over a distance d_{wall}, thus moving at a velocity $v = d_{wall}/t_s$ which can be $v = d_{wall}/t_s \gg c$ as long as the projector is powerful enough to illuminate a distant enough MC. Observations of superluminal echos have been, and will be, powerful tools to establish the origin of the external illumination of the Fe Kα emission [216].

Propagation of the Fe Kα morphology: The morphology and the time evolution of the Fe Kα emission also provide important constraints, when compared to the MC N_H distribution, on the location of the illuminating source [193, 204, 269].

A general trend appears where the MC starts to light up from the direction of the source and, if the MC is optically thin ($\tau_T \ll 1$), the surface brightness distribution reflects the density distribution in the cloud along the surface of the parabola, disappearing on the time-scale of the flare, convolved with the light crossing time of the cloud. In thicker clouds the light front might not penetrate the denser condensations which will then appear as holes (or cast shadows on the more distant parts of the cloud) in the Fe Kα emissivity if the source is located behind (in front of) the MC [193, 204, 269]. The details of the Fe Kα morphology thus primarily depend on the MC N_H distribution, the duration and light curve of the flare and the source-MC-observer geometry.

Multiple scatterings: Even when the light front has already passed through the MC, multiply scattered photons can still be observed. For example the photons forming Compton shoulders of the lines are created by Thomson scattering of the line photons, thus they will leave the MC with some delay (typically of the order of the light-crossing time of the MC) compared to the primary radiation. Additionally, optically thick and dense MC cores, where multiple scatterings occur, should also still shine for some time after the light front passage. Another effect of multiple scatterings is temporal smoothening of the reflection component to fast source variability happening on time-scales shorter than the typical scattering time.

2.2 X-ray Induced Chemistry and MC Heating

An X-ray light front irradiating a MC is not only expected to produce an X-ray reflection component, but also to interact with molecules, thus inducing chemical reactions. A correlation between the distribution of Fe Kα and rotational line emission from the refractory molecule SiO (with an increase by a factor of $\gtrsim 20$) has been observed by Martín-Pintado et al. [161]. This was an indication that either X-ray irradiation or something associated with it is removing the silicon from dust grains in the form of SiO. Amo-Baladrón et al. [1] confirmed and strengthened this result and suggested that the release of SiO from small grains can occur when hard X-rays deposit their energy in the grains, and heat them locally to high temperature (up to $\sim 10^3$ K).

X-ray irradiation might also be the cause of the high temperature of the MC of the CMZ. Rodríguez-Fernández et al. [237] excluded that X-ray irradiation can be an important source of MC heating. However, they examined present day X-ray luminosities, whereas much brighter past X-ray flares may have occurred at typical intervals much shorter than the cooling time of the MC, so they could be responsible for an important portion of the heating of MC in the GC.

3 The GC Environment

3.1 The Central Molecular Zone

The Central Molecular Zone (CMZ, see Fig. 3) is a thin layer, of about 300×50 pc in size, that contains a total of about $\sim$3–5 $\times 10^7$ $M_\odot$ of dense ($n \sim 10^4$ cm^{-3}), high filling factor ($f \gtrsim 0.1$) molecular material [4, 7, 8, 66, 117, 262, 282, 291], which represents $\sim$ 10 % of the total neutral mass content in the Galaxy [117, 184]. The MC in the CMZ differ considerably from those in the rest of the Galaxy, with higher gas temperatures ($T \sim 70$ K; [117, 170, 180], highly supersonic internal velocities ($\gtrsim$ 15–50 km s^{-1}) and higher densities ($n \sim 10^4$ cm^{-3}). These characteristics are probably deeply related to the special location in the deep gravitational potential of the central bulge, to the GC environment and the past energetic GC activity. For example the high MC densities are probably related to the large tidal shearing present in the CMZ. In fact, as a necessary condition for a cloud at a Galactocentric radius R_G to be stable against tidal disruption, its mean density has to be: $n > 10^4$ cm^{-3} $\times$ [75pc/R_G]$^{1.8}$ [114]. Any lower density MC would be sheared into a tenuous diffuse gas.

The CMZ molecular gas is distributed in giant molecular cloud complexes, with three quarters of the dense clouds located at positive longitudes, three quarters have positive velocities and some have large radial and vertical motions [8]. This distribution and kinematics are clearly inconsistent with both axial symmetry and uniform circular rotation [8, 12, 124, 153, 180] and they suggest two different kinematic MC populations.

The disc population: The most massive, lower velocity ($v \lesssim 100$ km s^{-1}) molecular cloud component (the so called "disc population", [8, 119]) resides close to the Galactic plane in the central 100–200 pc and has filament-like clouds with coherent velocity gradients, suggestive of dust lanes and tidally stretched arcs or arms of gas [8, 250, 259, 261]. We point out here that the CMZ disc population appears to have a toroidal geometry (see Fig. 3; [181]) and a physical scale remarkably similar to the outer parts of the AGN molecular torus invoked by AGN unification schemes [3, 286].

180 pc ring: The second, higher velocity ($v \gtrsim$ 130–200 km s^{-1}) molecular gas component seems to be located in the outer boundary of the CMZ and it appears to form a quasi-continuous ring structure (the so called "180 pc ring") inclined by $\sim$20° with respect to the Galactic plane [153, 154]. Further out, the 180 pc ring connects with a larger structure having a similar tilt, the so called "H I nuclear disc" that contains much of the neutral material (8×10^6 $M_\odot$; [12, 260]) lying between 0.3 and 2 kpc from the nucleus [117, 153, 184]. Thus the outer part of the 180 pc ring appears to mark a transition between H I and H_2 [27].

3.2 The Expanding Molecular Ring

The H I nuclear disk kinematics are highly perturbed, with outward motions of the same order as the rotation velocities. For this reason it was originally interpreted as a radially Expanding Molecular Ring, or EMR [127,248]. Bania [12] proposed that the expansion of this molecular ring was the result of an explosive event at the GC, which occurred $\sim 10^6$ year ago, providing the momentum impulse to $\sim 10^7\,M_\odot$ of nearby gas. There were two main weaknesses of this interpretation. First is the rather extreme energy release required, being of the order of $E \sim 10^{55}$ erg [240, 243], connected with the lack of evidence for the occurrence of such an energetic event. Secondly, the dearth of any clear evidence for interaction between the supposed flood of radially moving molecular material and the non-EMR clouds in the GC region (although Sofue [260] found some indications for shocks as well as gaps in the EMR corresponding to the most prominent clouds in the CMZ). We point out here that the recently discovered *Fermi* bubbles [264] would require, if inflated by accretion onto Sgr A*, a similar energy release $E \sim 10^{55}$ erg occurring on the correct time scale (a few 10^6 year ago). Thus part of the kinematical properties of the Expanding Molecular Ring might be carrying the vestige of a period of intense Sgr A* activity.

However, we need to consider that at the distance of few 10^2 pc from the GC (on the scales of the CMZ and EMR) the gravitational potential is dominated by the stellar component. Nowadays, it is well known that the Galactic bulge has a substantial stellar bar [31,71,78,214,249,309,319] extending to at least 2.4 kpc and with a total mass of 1–3 $\times\ 10^{10}\,M_\odot$. Thus the kinematics of the EMR and CMZ are expected to deviate from axially symmetric circular motion [28]. In fact, gas moving in response to a bar potential tends to settle into elongated orbits (see the left panel of Fig. 4). When the gas is orbiting at radii between that of corotation and that of the inner Lindblad resonance of the bar pattern, it moves on the so-called X_1 orbits (see Fig. 4, [55]), the long axis of which is aligned with the bar. There is an innermost stable X_1 gas orbit inside of which these orbits become self-intersecting, thus likely orbit-crossing and shocks will happen, leading to angular momentum loss and the gas settling into a new family of closed gas orbits, the X_2 orbits, oval-shaped orbits with long axes perpendicular to the bar. In this scenario the H I ring would correspond to the X_1 orbits, the 180 pc ring being the innermost stable X_1 orbit and the inner CMZ disc population the gas residing on the X_2 orbits [27]. A 100 pc elliptical and twisted ring of molecular gas, consistent with residing in X_2 orbits, has been recently revealed by new *Herschel* observations [178], strengthening this interpretation (see Fig. 3).

Probably as a result of the tidal shearing and the associated cloud stability problem [114], the clouds of the CMZ are composed of very clumpy cloud morphology, with about ~ 10 % of the mass in higher density clumps ($\sim 10^5\,cm^{-3}$) embedded in a lower density inter-clump medium ($\sim 10^{3.5}\,cm^{-3}$).

3.3 The CircumNuclear Disc, CND

The inner 5 pc from Sgr A* contains a concentration (with total mass of $\sim 10^{5-6}\,M_\odot$) of dense and warm molecular and atomic gas (the so called CircumNuclear Disc, CND, [18,45,92,116,160,179,206,226]) with a configuration similar to a rotating disc and/or a set of filaments with a tilt of $20-30°$ compared to the Galactic plane and very dense ($n_H \sim 10^{6-8}\,\mathrm{cm}^{-3}$) clumps. The asymmetric CND distribution beyond its inner rim and the presence of also a component of high-velocity ($v \sim \pm 300\,\mathrm{km\,s}^{-1}$) ionised gas, suggest either a transient origin of the CND (produced by e.g. a gravitationally captured, tidally stretched cloud; [223, 320]), or an energetic disruption of a stable disc (e.g. produced by the impact of the Sgr A East supernova remnant upon the disc; [157, 236]). The mass inflow rate of CND gas migrating into the central parsec is $\sim 10^{-2} - 10^{-4}\,M_\odot$ year^{-1} [96, 116, 123, 290], while the accretion rate onto the SgrA* accretion shock (far less gas may actually make it to the Sgr A* event horizon) is estimated to be few $\sim 10^{-6}\,M_\odot$ year^{-1} [6, 65, 301]. This strongly suggests that the present dim period in Sgr A*'s life might be just a temporary phenomenon. The CND provides a reservoir of gas that can be accreted if local processes that cause angular momentum loss can bring material inwards. The ionised "arms" of Sgr A West (the so called mini-spiral) are possibly infalling fragments of the CND that can, on a time scale of $\sim 10^{2-3}$ years, give rise to energetic accretion events.

3.4 The Central Cluster of Young Stars

Within the central parsec, there are several populations of stars. The nuclear cluster, forming 98 % of the observed stars and composed of old ($>10^9$ year), late-type giants and helium burning stars, plus $\sim$200 young ($t = 6 \pm 2 \times 10^6$ year) stars (one of the richest massive star forming regions in the entire Galaxy), forming a strongly warped disc [95, 104, 156, 212, 275]; see [96] for an overview). The tidal shear of the Galactic black hole would impede normal star formation, so for a long time, the presence of the young stars around it gave rise to the "paradox of youth" [98].

It is now believed that they could have formed in situ (see [96] for a review) in a disc either rapidly produced by a massive cloud plunging into Sgr A* (although it seems strange that a molecular cloud reaches the GC at small angular momentum) or slowly building up, but with star formation quenched, until a trigger is reached. Once the disc is formed, rapid dissipation and cooling of fragmented parts of the disc might occur. These clumps would then efficiently form stars [112, 120, 199]. Monte Carlo simulations show that, in this case, the amount of gas accreted through the inner radius of the disc is large enough to provide Sgr A* with the gas to radiate near its Eddington limit throughout the star-formation episode. The ages of the young stars suggest that this event occurred $\sim 6 \pm 2 \times 10^6$ years ago, a time-scale compatible with the formation of the *Fermi* bubbles and the launch of the EMR. Simulations also show that a cloud captured by Sgr A* is expected to form a sheared

and asymmetric circumnuclear disc very closely resembling the observed CND (although the likelihood of such an event needs to be demonstrated). Whichever the process created it, the presence of a massive disc and star formation in the immediate vicinity of the black hole would necessarily be accompanied by a high accretion rate onto Sgr A*. Therefore this star formation would be accompanied by strongly enhanced AGN activity (which, in fact, could have been the trigger for the star formation). Thus, the detailed study of Sgr A*'s environment reveals further hints of a possible glorious past for Sgr A*.

3.5 *Fermi Bubbles and Evidence for Sgr A*'s Jets*

A pair of large scale structures, extending up to 50° (i.e. ∼10 kpc) above and below the Galactic plane and with a width of about 40°, have been recently detected, at γ-ray energies, above a few GeV, thanks to *Fermi* data [264]. These so-called "*Fermi* bubbles" are centered on the core of the Milky Way, they have approximately uniform gamma-ray surface brightness with sharp edges. The bipolar morphology and sharp edges suggest that the *Fermi* bubbles originated by some large episode of energy injection in the GC (e.g., jets originating from AGN activity or nuclear starburst). The bubbles have a luminosity of 4×10^{37} erg s^{-1}, they extend to ∼10 kpc outside the Galactic disc and have an estimated energy content of the order of $\sim 10^{55}$ erg [29, 264]. The *Fermi* bubbles have a hard spectrum extending up to 100 GeV and they seem to be associated with large scale structures observed in X-rays with *ROSAT* [29] and with an excess of radio emission found in *WMAP* data (the so called Galactic haze; [72]). New *Planck* data have recently confirmed the microwave haze to have a morphology consistent with the *Fermi* bubbles. The *Planck* data reveal a hard microwave spectrum consistent with hard synchrotron radiation and excluding free-free emission (Planck collaboration [215]).

The mechanism producing the bubbles is still quite uncertain. Su et al. [264] discussed a possible starburst phase in the GC a few million years ago. A modest, but constant, injection of $\sim 10^{39}$ erg s^{-1} of cosmic rays to the halo is today inferred by the IR luminosity and γ-ray emission from the CMZ [62]. Integrating this emission over $\sim 10^9$ year would produce the correct energy budget [61], however a mechanism to confine the particles for such a long time would be required. Alternatively, the *Fermi* bubbles, X-ray structure and microwave haze might all be produced by an intense AGN phase, with Sgr A* accreting close to the Eddington limit, a few 10^6 year ago [323]. Recently Su and Finkbeiner [265] reported a gamma ray cocoon feature, in the southern *Fermi* bubble, and they produced evidence for a jet-like feature along the cocoon axis with a luminosity of $L_{1-100\,\mathrm{Gev}} \sim 5.5 \pm 0.45$ and $1.8 \pm 0.35 \times 10^{35}$ erg s^{-1} for the cocoon and jet, respectively. If this finding is confirmed, this would strongly support an accretion phase onto Sgr A* that would be therefore associated with a relativistic jet and outflows/winds as generally observed in AGN and stellar mass black holes [3, 83, 218]. For deeper insight into the physics

associated with the *Fermi* bubbles we point the reader to the contribution, in this same volume, by M. Su and R. Crocker.

On a much smaller scale of a few parsec, a faint, collimated linear structure observed at radio wavelength has been recently claimed by Yusef-Zadeh et al. [316]. This feature seems to arise from Sgr A* and to interact with the ionised and molecular material orbiting the supermassive BH. Yusef-Zadeh et al. [316] associate this linear structure to a jet possibly originating a few hundred years ago. Deeper observations are necessary to confirm this feature. A different linear feature pointing to the location of Sgr A* has been noted in X-ray images of the central parsec ([152,190]). The X-ray emission is interpreted as being synchrotron emission produced by a population of highly relativistic electrons created by the shock at the collision point between the jet and the Eastern Arm of the mini-spiral inside the CND [152].

4 Is the GC Fe Kα Emission the Echo of a Past Sgr A* Flare?

The discovery of the Fe Kα line and hard X-ray emission from several massive MC in the CMZ placed on solid ground the idea of this emission is being produced by reflection of a past GC flare [136,267]. Deep *ASCA* observations of Sgr B2, the most massive MC complex in the CMZ, showed many spectral features reminiscent of an X-ray reflection nebula (see Figs. 1, 2, and 5), such as: (i) strong and extended Fe Kα emission with $\sim$1–2 keV EW; (ii) a low-energy cut-off below $\sim$4 keV; (iii) a sharp flux drop consistent with the presence of an Fe K edge [136,191]. Not only spectral, but also morphological evidences has been accumulating. For example, in the Sgr B complex, [191] observed the peak of the extended 6.4 keV emission from Sgr B2 being shifted toward the GC by about $\sim$1–2 arcmin compared to the molecular mass distribution, thus suggesting the presence of an irradiating X-ray source located in the direction of the GC. Assuming that Sgr A* is the illuminating source, they estimated that, a few hundred years ago, it had to be orders of magnitudes brighter than now, with a 2–10 keV luminosity, $L_{2-10} \sim 3\times10^{39}(d/100\,\mathrm{pc})^2\,\mathrm{erg\,s^{-1}}$. A subsequent long *Chandra* observation confirmed these findings (allowing also the detection of the weaker Fe Kβ emission line) and finally, owing to the excellent imaging resolution, the *Chandra* data ruled out the possibility that the 6.4 keV emission was due to unresolved point sources, which contribute less than 3 % of the diffuse Fe Kα emission [193].

The combination of *INTEGRAL*, *ASCA* and *GRANAT* data on Sgr B2, allowed the detection, for the first time, of the Compton hump and the characterisation of the broad band 2–200 keV spectrum (see Fig. 5), which is well fitted by scattered and reprocessed radiation in a cloud of cold gas with abundances about twice Solar (Revnivtsev et al. [228]). Moreover, [228] found no significant variability of the Fe Kα during the 1993–2001 period. They excluded an internal source hypothesis and, based on the intensity of the broad-band spectrum and the cloud

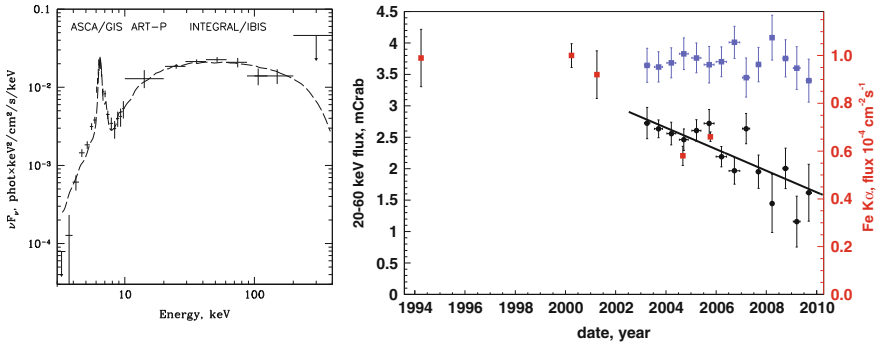

Fig. 5 *(Left panel) ASCA*, $ART - P$ and *INTEGRAL* broad band X-ray spectrum of Sgr B2 (1σ error bars and 2σ *upper* limits). The *dashed line* shows the best fit reflection model convolved with the instrumental resolution. (Figure courtesy of Revnivtsev et al. [228]). *(Right panel) INTEGRAL light curve* of the corrected 20–60 keV Sgr B2 flux in mCrab (*black circles*) and of the secondary calibrator, Ophiuchus cluster (*light blue squares*). Superimposed (*red squares*) are the Fe Kα line fluxes from Inui et al. [122]. A chi-squared test favors a linearly decreasing flux over a constant at the $\sim 4.8\sigma$ level (Figure courtesy of Terrier et al. [279])

column density, they estimated a high luminosity, $L_{2-10/2-200} \sim 0.5/1.5 \times 10^{39}(r/10\,\mathrm{pc})^{-2}(d/100\,\mathrm{pc})^2\,\mathrm{erg\ s^{-1}}$ of the primary illuminating source, active for many years. Such luminosity and period of activity are higher (even higher than the Eddington luminosity for $\mathrm{M_{BH}} = 10\,\mathrm{M_\odot}$) and much longer than the typical values observed in X-ray binaries, thus disfavouring these as possible candidates.

Fe Kα emission has also been detected in a number of other MC, such as Sgr C [192, 257] and small regions in the Sgr A complexes, such as the G0.11-0.11 cloud located close to the radio arc and the bridge [10, 211]. All these Fe Kα clumps are associated with molecular complexes and they have $\mathrm{EW_{FeK\alpha}} \sim$ 1–2 keV, in agreement with a reflection origin. The increased *Suzaku* sensitivity allowed [137] to detect also the Ni Kα emission from several molecular complexes and to discover, in the Sgr B complex, two other X-ray nebulae, M0.74-0.09 and M0.51-0.10 (the latter coincident with Sgr B1). These molecular complexes show a decay of the Fe Kα emission similar to the one observed in Sgr B2, moreover if illuminated by Sgr A* they would require similar luminosity, suggesting that they might be illuminated by the same source irradiating Sgr B2 ([138, 201]; but see also [315]).

4.1 Alternative Mechanisms to Produce FeKα Emission from MC

X-ray irradiation can induce Fe Kα line emission by removal of a K-shell electron rapidly followed by an electronic transition from the L shell to fill the vacancy (see Sect. 2). However, the same process can also be produced by collisional ionisation

induced by accelerated particles, such as low-energy cosmic ray electrons as well as protons/ions. Moreover, the energetic particles, diffusing in dense neutral matter, do produce nonthermal X-rays by atomic collisions as they slow down by ionisation and radiative energy losses (non-thermal bremsstrahlung), thus producing a hard X-ray continuum emission [277, 278, 288].

The physical conditions in the GC are exceptional (see Sect. 3) and make it a special place as regard to particle acceleration. Bright non-thermal radio filaments trace magnetic fields up to a mG [85] and large-scale non-thermal emission suggest the average field to be at least 50 μG [60]. Three of the most massive young star clusters in the Galaxy lie in the CMZ, and intense star formation is taking place there at several sites. It is possible that the density of low-energy cosmic rays is larger in the central regions than in the rest of the Galaxy [23, 74].

Cosmic ray electrons: The presence of strong non-thermal radio filaments in the vicinity of several MC [313, 315] makes it reasonable to consider the presence of a large density of cosmic ray electrons there. This is also supported by the observation of diffuse low-frequency radio emission in the GC region [151] and the high estimates of the ionisation rate compared to the values obtained in the Galactic disc [205]. It has also been suggested [315] that the heating of MC induced by the interaction with cosmic ray electrons might explain the long-standing problem of the origin of the high temperature of the MC within the CMZ [184]. Several authors [277, 278, 288] studied in detail the production of non-thermal lines and X-ray continuum by the interaction of cosmic ray electrons with neutral ambient gas. In most cases the EW of the Fe Kα line is found to be lower than $\sim$0.3–0.5 $\times (A_{\rm Fe}/A_{\odot})$ keV (where $A_{\rm Fe}/A_{\odot}$ is the Fe fractional abundance compared to Solar) and never higher than $\sim 0.6 \times (A_{\rm Fe}/A_{\odot})$ keV, and the continuum radiation should be generally hard ($\Gamma < 1.4$). The production of Fe Kα photons is relatively inefficient. The Fe Kα total luminosity from the CMZ is $\gtrsim 6 \times 10^{34}$ erg s^{-1} [315], thus requiring a power $\gtrsim 2 \times 10^{40}$ erg s^{-1} in cosmic ray electrons (assuming Solar metallicities), which is comparable to that contained in cosmic ray protons in the entire Milky Way [278]. Disfavouring the idea that most Fe Kalpha emission is produced in this way.

Cosmic ray ions/protons: Alternatively, subrelativistic ions propagating through MC can radiate (through inverse bremsstrahlung from the fast ions and classical bremsstrahlung from the secondary knock-on electrons) in the hard X-ray domain and create Fe Kα vacancies [75, 76, 277, 278]. Dogiel et al. [75] proposed that the tidal disruption and subsequent accretion of stars by the central BH (suggested to happen at a rate of one every $\sim 10^4$ year; [270]) could produce the required rate (basically constant on time-scales of centuries) of subrelativistic protons to induce the observed Fe Kα emission. For strong shock acceleration of non-relativistic particles and strong particle diffusion in the cloud, the expected Fe Kα EW is expected to be $\sim$ 0.6–0.8 $\times (A_{\rm Fe}/A_{\odot})$ keV, with an associated continuum having spectral photon index $\Gamma \sim$ 1.3–2. However, fast ions with a soft source spectrum can produce very large EW ($\gg$ 1 keV) and steep ($\Gamma \gg 2$) power-law continuum [76, 278]. In this scenario the Fe Kα line width is expected to be several tens of eV, about one order of magnitude wider than for X-ray reflection or cosmic ray

electron scenario [75, 276]. In fact, the X-ray lines produced by collisions of ions heavier than 4He can be shifted by several tens of eV, significantly broadened and split up into several components [91, 276]. For example, the Fe Kα line produced by impacts of O ions of 1.9 MeV/nucleon is blueshifted by $\sim$50 eV in comparison with the one produced by 5-MeV proton impacts, and has a FWHM of $\sim$100 eV (see [91], Fig. 3.55)

As another alternative, [42] proposed that subrelativistic particles are produced by fast-moving knots resulting from supernova explosions. In fact, fast moving supernova ejecta interacting with dense MC provide a fast conversion of kinetic energy into IR and X-ray radiation with a hard ($\Gamma \sim$ 0–1.5) spectrum and Fe K lines (6.4 and 6.7 keV) with total EW $\sim$ 0.5–0.6 keV. Just $\sim$3 supernova remnants of age less than $\sim 10^3$ year in the GC region could provide the required number of fast moving knots [42].

*4.2 A Christmas Tree Around Sgr A**

A major step forward has been the detection of variability from Fe Kα emitting clouds. The first such detection was reported by Muno et al. [189], who showed a $\sim 2-4\,\sigma$ continuum variability from filamentary ($\sim 0.3 \times 2$ pc) regions that are dominated by Fe Kα emission and coincident with molecular structures near Sgr A [189]. Fast variability is a key factor to discriminate X-ray reflection nebulae from Fe Kα emission induced by cosmic ray interactions with MC [41, 75, 288, 313, 315]. Fast Fe Kα or hard X-ray continuum variability, in fact, rules out the cosmic ray proton scenarios and is barely consistent with the cosmic ray electron models. The variations observed by Muno et al. [189] in the Sgr A complex could be produced by an X-ray binary of $L_X \sim 10^{37}$ erg s^{-1} at a distance of $\sim$7 pc. If, instead, the irradiating source is Sgr A* (thus at, or further away than, the projected distance of 14 pc) then $L_X \gtrsim 10^{38}$ erg s^{-1}. Muno et al. [189] suggested that the flare illuminating these MC in Sgr A might be different from the one irradiating Sgr B2. If these MC were located at their projected distances, such an outburst, in fact, would have occurred $t \gtrsim 60$ year or $t \sim 20$ year ago, before the advent of wide field X-ray monitors, thus it could have been missed [189].

Collecting data from *ASCA*, *Suzaku*, *Chandra* and *XMM-Newton*, Inui et al. [122] and Koyama et al. [139] observed a decline, of the order of $\sim$60 % in $\sim$10 year, of the Fe Kα line flux from both the Sgr B2 and Sgr B1 regions. Using *INTEGRAL* data, [279] measured a 4.8σ variation of the 20–60 keV (the energy of the Compton hump) flux from Sgr B2, starting to decline after the year 2000 (black points in Fig. 5). This confirmed, without inter-calibration effects, the Fe Kα decay (red points in Fig. 5) previously observed. The observed decay time ($t_d = 8 \pm 1.7$ year) is compatible with the light crossing time of the MC core, consistent with reflection but inconsistent with an electron cosmic ray scenario. The spectral index of the illuminating power-law source is found to be $\Gamma = 2 \pm 0.2$. Parallax measurements of the distance of Sgr B2 place it (assuming it is on a nearly circular Galactic orbit)

130 ± 60 pc closer to us than Sgr A* ([224, 225, 239]; but see also [178]). This suggests a mean luminosity for the Sgr A* outburst of $L_X = 1.5\text{–}5 \times 10^{39}\,\mathrm{erg\,s^{-1}}$, occurring $t = 100^{+55}_{-25}$ year ago [279]. New *Suzaku* observations obtained in fall 2009, when compared to previous observations obtained in fall 2005, confirm Sgr B's fading [279] detecting, in 4 year, a reduction in Fe Kα flux and hard (8–10 keV) continuum by a factor 1.9–2.5 from both Sgr B2 and M0.74-0.09 [202]. In particular the variations of these two molecular cores decrease in a synchronised way. The correlation of the variability between the two MC indicates that they share a common external reflection origin [202].

The Sgr A and Sgr B complexes are not the only ones to display Fe Kα variations. The comparison between a *Suzaku* observation in January 2006 and previous *ASCA* and *Chandra* observations suggested variability of the different Fe Kα clumps in the Sgr C complex, all having $\mathrm{EW_{FeK\alpha}} \sim 2.0\text{–}2.2$ keV and clear Fe Kβ [196]. In particular, the clump M359.38-0.00 was not previously observed to emit Fe Kα photons. Moreover, the Fe Kα emission from M359.43-0.07 appeared shifted compared to previous *ASCA* observations, suggesting a reflection origin of this emission [192]. Interestingly, the M359.38-0.00 and M359.47-0.15 clumps correspond to molecular complexes with different line of sight velocities, which are thought to belong to two different arms of the CMZ MC population (see Fig. 4; [196, 245, 259]). This indicates that they most probably have very different line-of-sight distances compared to Sgr A*. This seems to suggest that these two clumps are irradiated by two different beams of radiation, for example by two different flares or by two phases of the same long flare.

The long (more than 1 Ms exposure) *XMM-Newton* monitoring campaign of the Sgr A complex (lasting for almost a decade), led to another important step forward. It allowed the first detection of highly significant ($\sim 4-13\sigma$) Fe Kα variations from several MC in Sgr A [216] as well as the detection of a superluminal echo moving with apparent velocity of $v_{\mathrm{app}} \sim 3\,c$ (see Fig. 6) from a molecular complex called the bridge [114]. The superluminal propagation of the Fe Kα emission strongly suggests an external illuminating source and rules out models based on internal sources and/or cosmic rays (which would have to deal with superluminal motions!).

Contrary to the case of the Sgr B complex, where every clump is consistent with being produced by the same flare, the Fe Kα emitting regions in Sgr A have very different light curves [44, 216]. In some MC the Fe Kα emission is rising, in others it is fading and in some it is constant [44, 216]. It is interesting to note that, as in Sgr B2, the Fe Kα emission from G0.11-0.11 (a MC located close to the radio arc) is fading on a short time scale (comparable to the light crossing time of the MC). If located at its minimal distance from Sgr A* (25 pc) it would require $L_X \gtrsim 10^{39}\,\mathrm{erg\,s^{-1}}$, $t \gtrsim 75$ year ago [216]. These estimates would necessitate a flare of Sgr A* with a luminosity and a difference in time of the same order of magnitude as the one implied by Sgr B2 and B1. Moreover all three of these MC are fading at a rate comparable to the MC light crossing time. This seems to suggest that Sgr B1, B2 and G0.11-0.11 are illuminated by the same flare. On the contrary the bridge (see Fig. 6) shows a clear (13σ) increase of Fe Kα emission, while other MC are consistent with being constant over the *XMM-Newton* monitoring [216]. While the

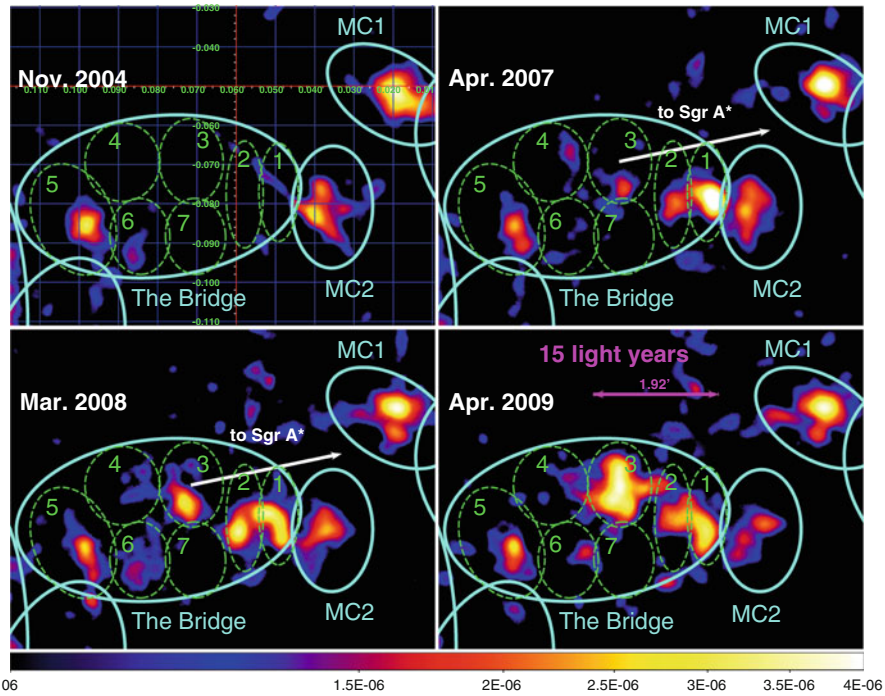

Fig. 6 Fe Kα continuum-subtracted mosaic image of the different EPIC-pn observations of the bridge region. A brightening of regions 1, 2, 3 and 4 is clear. Such variation occurs in a time-scale of about 2–4 years, but on a spatial scale of about 15 light years. This apparent superluminal motion can be explained if the bridge MC is illuminated by a bright ($L > 1.3 \times 10^{38}$ erg s^{-1}) and distant (> 15 pc) X-ray source active for several years. The observation of the superluminal echo cannot be explained by either a single internal source or by low energy cosmic ray irradiation. It is also highly unlikely that the variation is produced by several uncorrelated sources. We note that the illumination starts in the Galactic west and propagates to the east, suggesting that the source is located in the direction of Sgr A* (Figure courtesy of Ponti et al. [216, 217])

flare seems to be passing out of some clouds, it is entering others, or is still in the act of passing through others. The rise, fall, and dwell time scales will all be important for reconstructing the flare profile, and for deciding whether there have been multiple flares within the past several hundred years.

4.3 Which Source of Irradiation?

The very different variability behaviour might indicate that each one of these MC is responding to a different flare of, possibly, separate sources. The observation of a superluminal echo [216] and the synchronised fading of the causally disconnected

regions in the Sgr B complex [202] constrain the mechanism of Fe Kα production to be irradiation from a powerful external source.

As described in Sect. 1.1, only three sources in the central 1.2 square degrees have reached luminosities higher than $L_X \gtrsim 10^{37}$ erg s^{-1} during the past few decades [70, 298]. The highest peak luminosities have been reached by 1A 1742-289 and GRO J1744-28 with $L_X \sim 7 \times 10^{38}$ erg s^{-1} and $L_X \sim 3 \times 10^{38}$ erg s^{-1}, respectively [70]. Both these sources are X-ray transients, thus active only for few weeks-months. No known X-ray binary undergoes such a long outburst with such high mean luminosity [57] as the source irradiating the Sgr B complex. However, this does not exclude that bright X-ray transients, located close enough to a MC, might produce detectable Fe Kα echos. Moreover, it does not exclude a past outburst of an even more extreme version (with even longer recurrence time and higher luminosity) of the peculiar BH X-ray binary GRS1915+105 (a source accreting close to the Eddington rate for more than a decade; [84]). Although this is possible, we believe that a flare from Sgr A* is more plausible and more parsimonious for explaining all of the variability throughout the GC region.

Alternative possibilities involve bright X-ray sources produced by either the passage of the shock wave, generated by the supernova explosion that gave birth to the Sgr A East remnant, over the supermassive BH [157, 236] or the interaction between Sgr A East and the 50 km s^{-1} MC [89]. Fryer et al. [89] performed three-dimensional hydrodynamic simulations of the evolution of Sgr A East and its interaction with surrounding medium (e.g. Sgr A* and the 50 km s^{-1} MC). They found that the passage of the remnant across Sgr A* would have enhanced the accretion rate onto the BH by less than a factor of 2, thus not enough to explain the Fe Kα emission from the CMZ. On the other hand, the first impact of the shock wave with the material in the 50 km s^{-1} MC would have produced a luminosity of $L_{2-200\ \mathrm{keV}} \sim 10^{39}$ erg s^{-1}, decreasing to $\sim 10^{36}$ erg s^{-1} in the following few centuries. The resulting light curve would have, therefore be predicted to have a sharp rise, followed by a very long decay time (a few centuries), dictated by the time-scale for dissipation of kinetic energy [89]. In this scenario the observed rapid and small amplitude Fe Kα variability might be produced by the interaction of the Sgr A East shock with dense matter clumps in the 50 km s^{-1} MC. However, it seems difficult to reconcile the expected slow luminosity decay with the fast decrease of a factor of $\sim$ 3–4 in 5–7 year [202, 279] observed in Sgr B2.

Before attempting to reconstruct the past activity in the GC, we summarise the main limitations and uncertainties associated with the tools that are used.

4.3.1 Uncertainties on the Luminosity Estimates

We try to estimate here the dominant source of uncertainty in the estimation of the primary source's past luminosity. Equation 1 (which assumes isotropic source emission and a cloud with $\sigma_T \ll 1$) provides a direct link between the observed Fe Kα line flux (or upper limit) and luminosity of the source (e.g. Sgr A*), and is the main tool. The luminosity of the source depends linearly on the Fe Kα line

flux and inversely on the distance to the GC. Both are generally well known. The former to better than 10–15 % and the latter to less than 5 %. A higher uncertainty is associated with the knowledge of the Fe abundance, δ_{Fe}, which however can be constrained from the Fe Kα line EW and is expected to have fluctuations of a factor of less than a few. Larger uncertainties are associated with the determination of the cloud optical depth, τ_T, and mainly the solid angle Ω of the cloud from the location of the primary source.

Solid angle: This latter parameter ($\Omega = A_{\rm cloud}/4\pi d^2$) depends on the ratio between the area exposed to the illuminating source ($A_{\rm cloud}$) and the square of the distance (d) between the source and the cloud. Figure 3 shows a large concentration of molecular matter along any direction of the CMZ. In particular, several clouds typically overlap along the line of sight, thus confounding the boundaries between the clouds. Each cloud is expected to move with approximately the same velocity. Thus, thanks to the molecular cloud data cubes that show the MC emission in each velocity range, we can separate the emission from each cloud along the line of sight and accurately measure the correct MC area. MC typically have complex shapes (see Fig. 3) and the area irradiated by the source might be different from the area projected on the image, however we expect this difference to be smaller than a factor of a few.

The dominant uncertainty is associated with the line-of-sight component of the distance between the cloud and Sgr A, to be d_l.* Being the CMZ compact, we expect that for each CMZ cloud, d_l is constrained between the projected distance and $\sim \pm 300$ pc. This generally implies a very large uncertainty that can be as high as 1–2 orders of magnitude. Thus, knowledge of the line of sight distance between the MC and Sgr A*'s plane is key for accurate luminosity estimates. As discussed in Sect. 3 there are several indications of coherent patterns in the MC distributions, from which distances might be derived. However, although these large molecular structures incorporate a significant part of the gas, a further effort is required in order to accurately associate each molecular clump with a line of sight distance. Other methods to determine d_l are based on extinction measurements. Sources distributed uniformly around the GC will appear more extinguished if the MC in question is placed more in the foreground, while MC placed at the far side of the CMZ will contribute little or no absorption.

Ryu et al. [239], assuming that the 6.7 keV and the diffuse soft X-ray plasma (see Sect. 1.1) emission are uniformly distributed around the GC, measured the amount of absorption toward each molecular clump in the Sgr B complex. Seven different spectral components (with an even larger number of free parameters) contribute to the X-ray spectrum, and thus an exceptionally high X-ray spectral quality is required in order to constrain the various components without incurring degeneracies between the different parameters. Moreover, intensity fluctuations of the diffuse soft X-ray plasma (which is known to have a patchy distribution) is likely another source of uncertainty. The distribution of stars in the central $\sim 1^\circ$ is much more uniform. Thus stellar counts in near-IR images can provide reliable constraints on the line of sight distance toward molecular clumps (see, e.g., [107, 114]). Sawada et al. [245] proposed a different method based on the quantitative comparison

between the 2.6-mm CO emission lines and 18-cm OH absorption lines. The GC is an intense and presumably axisymmetric source of diffuse, non-thermal emission at 18-cm, so OH absorption arises preferentially from clouds located in the foreground of the GC. On the other hand, CO emission samples the gas both in front and back of the continuum source equally [245], thus (assuming that the lines are optically thin and that the physical and chemical properties of GC clouds are uniform) the OH/CO ratio for any given cloud provides information about its line-of-sight distance.

The use of the angular dependence of the EW_{Fe} on the angle θ between the direction of the incident radiation and scattered continuum (see Sect. 2) may eventually provide another means of estimating the line-of-sight distances to the Fe Kα emitting MC (see [44]). However, a maximum variation of the EW_{Fe} of $\sim$50 % is expected, thus very solid estimates of MC abundances (producing EW variations of the order of several; see Sect. 2) and N_H (producing EW variations of at least $\sim$30 %; [168]) are required.

Because of physical interactions between the different molecular filaments and streamers, it is easier to estimate the MC distribution in the immediate vicinity of Sgr A* (within the central 15 pc). Coil et al. [51], in fact, suggested that the 20 and 50 km s^{-1} MC are located at less than 15 pc from Sgr A*, just outside the CND, with the former in front and the latter a few pc behind Sgr A* (see also [85]). Perhaps the most promising method for determining the line-of-sight distances of some of the MC containing H_2O maser sources is based on VLBI parallax measurements. Reid et al. [225] measured a distance from the Earth to Sgr B2 of $R_0 = 7.9^{+0.8}_{-0.7}$ kpc and, assuming a circular orbit for Sgr B2, they estimated Sgr B2 to be $\sim$130 pc in front of Sgr A*. Although this measurement roughly agrees with the location estimated by Ryu et al. [239], Molinari et al. [178] suggested an elliptical orbit for Sgr B2 which would be then located *behind* Sgr A*. At the moment, it seems that the line of sight distance of the molecular clumps is the major source of uncertainty in measuring the GC's past activity (influencing both the derived luminosity and time evolution of the event).

Column density. The other major source of uncertainty is in the determination of the cloud column density. Three main ways to determine the MC column densities (N_H) have been used: (1) The N_H can be derived directly from high quality X-ray spectra of each molecular clump. In fact, as long as the column density is lower than the Compton thick limit ($N_H \lesssim \sigma_T^{-1} = 1.5 \times 10^{24}\,\mathrm{cm}^{-2}$) the MC absorption will leave its signature through a clear low energy cut off in the 2–10 keV X-ray spectrum [53]. However, these measurements trace only the total N_H along the line of sight, thus including foreground absorption plus the additional contributions from any MC along the line of sight that are not related to the Fe Kα emitting cloud. Moreover, such measurements are affected by the presence of many additional spectral components (e.g. 6.7 keV emission, soft X-ray plasma, weak point sources) contributing to the observed MC X-ray emission. However, a strong improvement is expected soon thanks to hard X-ray focussing telescopes (such as *NuSTAR* and *Astro-H*) that will enhance, by more than an order of magnitude, the detector sensitivity in the 10 to 80 keV energy band. In fact, in optically thin clouds ($\tau \ll 1$), the shape and intensity of the high energy reflection spectrum depends

strongly (see Fig. 2) on the cloud column density (particularly the Compton hump, see Sect. 2). Combining the information from the low energy reflection cut off, the line intensity and the Compton hump shape, *NuSTAR* and *Astro-H* X-ray spectra will soon provide a more reliable N_H estimate. (2) Alternatively, the N_H can be measured through the intensity of molecular emission lines. Tsuboi et al. [283] provided a formulism (assuming a CS to N_H abundance $X(CS) = 10^{-8}$; [149]) to derive the cloud N_H from the CS line intensity (I_{CS}) : $N_H = \frac{7.5\times10^{11}\times T_{ex}\times I_{CS}}{X(CS)}$, where T_{ex} is the excitation temperature. The great advantage of this method is that it allows us to measure the N_H associated with each single molecular clump. In fact, any intervening material is expected to move at a different velocity, thus the extremely high spectral resolution with which it is possible to measure MC lines allows us to slice the CMZ in different velocity components, and to select MC of interest. However, large uncertainties are associated with T_{ex} and the $X(CS)$ factor, unless detailed modelling is performed. Moreover, at high column densities ($N_H >$ several $\times\ 10^{23}$ cm^{-2}) most molecular lines become self-absorbed and hence are no longer good N_H estimators. (3) Measured the cloud N_H using IR *Herschel* observations. They first estimated the opacity and dust temperature from a pixel-to-pixel fit on the 70–350 μm data, using a dust model [24, 54]. Then, assuming constant dust properties, they converted the opacity to a hydrogen column density ($N_H = N_{HI} + N_{H2}$) using $\tau_{250}/N_H = 8.8 \times 10^{-26}$ cm^2/H. The gas to dust ratio used is valid for the Galactic disc. Uncertainties of a factor of a few are associated with these measurements. In particular, different metallicities with respect to the disc values, would lower the estimated column densities by a factor of a few. Moreover, as with the N_H estimated from X-ray absorption, the column densities derived with this method integrate the effects of dust along the line of sight.

4.4 Sgr A's X-ray Emission History*

The study of the Fe Kα emission from the MC of the CMZ shows strong indications of external irradiation, most probably due to Sgr A*. We also note that: (i) spatially connected structures (such as Sgr B1 and B2 or the bridge) tend to vary in brightness with a coherent pattern; (ii) molecular complexes that appear to be located close together, but display different Fe Kα light curves (such as the bridge, MC1, MC2 and G0.11-0.11; [216]), belong to molecular complexes moving at different line-of-sight velocities. The latter point indicates that these molecular complexes are actually well separated, in three dimensions, despite being close together on the plane of the sky. The different light curves observed from these complexes could then be tracing either different flares or different parts of the same long flare. Moreover, we note that smaller MC generally vary on faster time-scales (with the variation fronts usually propagating close to, or higher than, the speed of light) compared to larger MC. The latter varying on a time scale being typically of the

order of the cloud light crossing time. This suggests that the Fe Kα emission is induced by irradiation by an external source that is variable on both long and short time-scales. Such variability behaviour is usually observed in, for example, sources powered by accretion onto compact objects [19, 20, 133, 171, 219].

Constraints on the GC's past activity are given by the existence of MC that emit Fe Kα and by those clouds that are quiet. Only upper limits to the Fe Kα emission from the MC closest to Sgr A* (the CND, the 20 and 50 km s^{-1} MC; [51]) are observed. If, indeed, the 50 km s^{-1} MC is located 5–10 pc behind Sgr A* [51], then from the estimated column density and the upper limit on the line intensity, we can constrain the mean luminosity of Sgr A* to be lower than $L_{\mathrm{SgrA*}} \lesssim 8 \times 10^{35}$ erg s^{-1} in the past 60–90 year [216]. The observation of approximately constant Fe Kα emission during the past decade, from molecular complexes with sizes smaller than a parsec, indicates that the flare illuminating those clouds lasted more than several years. Moreover, the observation of both a rising and fading phase from some molecular complexes [43, 216] suggests, not surprisingly, some degree of variability of the illuminating source. In fact, the light curves of accretion powered sources are well known to be variable [19, 20, 133, 171, 219].

The uncertainty in the line of sight distance toward the different molecular clouds in the CMZ currently prevents us from putting any firm constraint on the flare history, apart from knowing that Sgr A* underwent one or more flares with luminosities of the order of 10^{39} erg s^{-1} or higher, between $\sim$100 and $\sim$1,000 years ago (and possibly fainter ones). Assuming that Sgr B2 is located $\sim$130 pc in front of Sgr A*, then the flare must have ended $\sim$100 year ago. The Fe Kα evolution of G0.11-0.11 suggests that this cloud is illuminated by the same phase of the flare currently illuminating Sgr B2. Further observations will allow this hypothesis to be tested. Actually, if there is just a single (or a handful) illuminating source, we expect that eventually every MC will reflect the same light curve (convolved with the MC dimension). Therefore, it will eventually be possible to measure the delay of the light curve and hence determine the line of sight distance for each MC. Alternatively, if the line-of-sight to the clouds is known, it will be possible to triangulate the position of the primary source. The light echos provide us with the fantastic opportunity to scan the CMZ and determine its three dimensional distribution.

Although a precise number has not yet been measured, about one third of the MC in the CMZ are Fe Kα active. This suggests that in the past $\sim 10^3$ year (the CMZ light crossing time), Sgr A* was active for a significant fraction of the time. Longer monitoring will clarify if the higher activity was made of several sharp excursions from quiescence to a short lived bright state, or if it involved a more gentle evolving and a longer period of activity. The constraints are still so weak that a single long period of activity is still consistent with the observations ([216], but see [44]). New observing campaigns will provide stronger constraints, allowing us to learn much more about Sgr A*'s past activity.

Is it possible to constrain Sgr A*'s luminosity further in the past? To answer this question, Cramphorn and Sunyaev [59] studied the Fe Kα emission from all the MC in the Galactic disc. None of the MC they observed showed any evidence of Fe Kα emission. This allowed the authors to put several upper limits on Sgr A*'s historical

luminosity. Sgr A*'s average luminosity was found to be lower than $\sim 10^{-(3-4)}$ L_{Edd} since $\sim 4 \times 10^4$ year ago. Obviously the disc of the Milky Way is not completely filled with molecular gas, so gaps in the CO distributions leave unconstrained periods as long as $2-4 \times 10^3$ year. To extend this study even further, Cramphorn and Sunyaev [59] investigated also the more extended HI distribution, allowing them to constrain Sgr A*'s past activity to $L_{SgrA*} < 10^{-2}$ L_{Edd}, in the last $\sim 1 \times 10^5$ year.

To extrapolate even further into the past, different types of tracers of Sgr A*'s luminosity are necessary. The presence of the *Fermi* bubble, the EMR and the disc of young stars within the central parsec, suggest that Sgr A* was radiating close to the Eddington limit ~ 5–6×10^6 years ago.

4.5 *Is All the Fe* Kα *Emission Due to Sgr* A*'s *Flares?*

The measurements of fast Fe Kα flux variations [43, 44, 122, 202, 216, 279] and even the super-luminal propagation of the X-ray echo [216] have excluded a cosmic ray proton/ion origin for this variable component (Fe Kα emission induced by cosmic ray electrons might vary on years timescales; [317]) and cosmic ray electron and internal source for the super-luminal one. This implies that at least part of the Fe Kα radiation has to be produced by a bright external source, most probably Sgr A* (see Sect. 4.3). However, is it plausible to think that all Fe Kα radiation from MC of the CMZ is induced by Sgr A*?

Clear signatures for cosmic ray ion induced Fe Kα emission have been discovered in molecular gas around the Arches cluster [43, 278, 284, 295]. The prominent (EW $\sim$ 1.2 keV) Fe Kα emission has, in fact, been observed to be constant over the past 8 year [43]. Moreover the Fe Kα emission is not well correlated with the molecular gas, forming, instead, a bow shock around the cluster [295]. The Arches cluster is one of the richest and most densely packed massive ($M \sim 5 \times 10^4\,M_\odot$; [118]) star clusters in the Milky Way and is currently moving at highly supersonic speed ($v_{Arch} \sim 200\,km\,s^{-1}$) relative to the bulge stars. Figer et al. [86] and Wang et al. [295] found that the cluster bow shock is interacting with a MC and Tatischeff et al. [278] computed that the shock (assuming a reasonable particle acceleration efficiency of $\sim$3–10 %) could supply enough cosmic ray power to reproduce the Fe Kα emission. Therefore not every Fe Kα active cloud is illuminated by a flare from Sgr A*.

A deep *Suzaku* observation of the molecular cloud G0.162-0.217 revealed a weak Fe Kα line with $EW_{FeK\alpha} \sim 0.2$ keV [90]. The cloud is located at the south end of the Radio Arc [150, 312, 314], a region with, supposedly, enhanced density of cosmic ray electrons. Fukuoka et al. [90] thus proposed that this emission might be induced by cosmic ray electrons.

5 Origin of the Flares-Outbursts

The study of the environment around Sgr A* suggests at least two periods of enhanced activity for the supermassive BH at the Milky Way centre (see Sect. 4.4), the first about $6 \pm 2 \times 10^6$ year ago, with Sgr A* emitting close to the Eddington limit, and the second with a luminosity $1–5 \times 10^{39}\,\mathrm{erg\,s^{-1}}$, which occurred $\sim 10^2$ year ago.

Traces of what triggered the earlier of these accretion events can be found in the close proximity of Sgr A*. The cluster of young stars in the central parsec (see Sect. 3.4) suggests the presence of a very massive disc there, $\sim 6 \times 10^6$ year ago. Some have suggested (although the origin of such disc is still controversial) that this disc might have formed from a MC passing very close to Sgr A*. As a result of tidal disruption and stretching, the cloud would follow a range of intersecting orbits, near the circularisation radius, forming an eccentric, clumpy and filamentary disk. The physical conditions in the disk would allow star formation and accretion onto the BH [34, 96, 244, 318]. Part of the matter in the inner part of this disc would have been accreted, making Sgr A* shine close to the Eddington limit. Part of the disc would have formed massive stars (the central cluster). The outer part of the disc might have been left as a remnant disc and could now comprise what we call the CND (see Sect. 3.3). Finally, a part of the disk would have formed an outflow, such as commonly seen in luminous AGN, perhaps generating both a jet [265] and inflating the *Fermi* bubbles [264].

Somewhat more ambiguous is the physical origin of the enhanced emission that occurred $\sim 10^2$ year ago. Sgr A*'s quiescent X-ray luminosity (see Sect. 1.1) is $L_{2-10\,\mathrm{keV}} = 2 \times 10^{33}\,\mathrm{erg\,s^{-1}}$ [6] and even during the brightest X-ray flare ever observed (in more than 10 years of *XMM-Newton* and *Chandra* monitoring) the X-ray luminosity was only $L_{2-10\,\mathrm{keV}} = 3 \times 10^{35}\,\mathrm{erg\,s^{-1}}$ [220]. The luminosity required to produce the X-ray echo seen from the MC, is $L_{2-100\,\mathrm{keV}} = 1.5–5 \times 10^{39}\,\mathrm{erg\,s^{-1}}$ [279] and is about $\sim 10^4$ times higher than the brightest flare ever observed. This seems to suggest an intrinsic difference between the process producing the daily flaring activity and this major flare-outburst. It is rather surprising then that the required X-ray luminosity can be inferred by simply extrapolating the observed K-band flux distribution, obtained over ~ 10 years of monitoring, to higher fluxes and rare events [73, 297]. This extrapolation to high fluxes and the assumed IR to X-ray conversion involve many assumptions (such as the flare SED and a direct correspondence between the IR and X-ray light curves). Despite these uncertainties, the extrapolation seems to suggest that the X-ray echo is simply an extreme manifestation of the same physical processes that produce the daily flux variability. From a theoretical point of view this conjecture seems plausible. In fact, during normal flux states Sgr A* is thought to accrete from the capture of stellar wind material from nearby stars (see Sect. 1.1). Cuadra et al. [65] suggested that, during this process, cold clumps might sometimes fall into the inner region with an angular momentum low enough to circularise at a very small radius (~ 0.001 arcsec), and create there an accretion disc. Such an event might have enhanced the luminosity

to $L_{Bol} \sim 10^{40}$ erg s^{-1} for a timescale of the order of $\sim 10^2$ year (dominated by the disc viscous timescale; [65]) and have produced the X-ray luminosity required for the observed Fe Kα echo.

Yu et al. [310] suggested, instead, that Sgr A*'s flare could be produced by the shock created by the jet deceleration (and not by accretion) caused by a partial capture of a star by the supermassive BH. This model well reproduces the Fe Kα emission (both the flux and its evolution) of Sgr B2, with a decay time of $\sim$10 year [122, 202, 228, 279]. Zubovas et al. [324] consider the consequences of an asteroid passing within a few astronomical units from Sgr A* and being gravitationally disrupted. Objects with radius $r \sim$ 10–50 km are expected to produce $L_x \lesssim 10^{36}$ erg s^{-1}, thus possibly contributing to Sgr A*'s normal daily flaring activity. However, a planet disruption event (although expected to be much less frequent, e.g. one per $\sim 10^5$ year) might produce flares with $L \sim 10^{41}$ erg s^{-1} for a few tens of years [324]. Alternatively, Sazonov et al. [247] considered gas supply onto Sgr A* via tidal interaction of stars. They estimated that every few 10^4 year, less than 0.1 $M_\odot$ of stellar debris will accrete onto Sgr A* and produce an outburst of $L \sim 10^{42-43}$ erg s^{-1}. A lower luminosity flare could be produced by gas torn off a star that experienced a close collision with another star or a stellar remnant in the nuclear cluster.

Accretion of interstellar material is perhaps a more probable and frequent occurrence because of its larger cross section. In fact, the vicinity of Sgr A* contains several ionised gas streams [321] and numerous blobs of dust and gas [100, 195]. Thanks to the analysis of more than 10 years of infra-red monitoring observations of the stellar orbits of the stars close to Sgr A*, it has been recently discovered that a dense cloud (G2) with a mass of at least $\sim 3\,M_{\rm Earth}$ (estimated from the Brγ luminosity), is now moving (and accelerating) towards Sgr A* [105, 106]. The centre of gravity of the cloud should be at the pericentre (at only 3,100 times the BH event horizon) in mid-2013. Due to the interaction between the gas in the cloud and the ambient material, dynamical instabilities (such as Rayleigh-Taylor and Kelvin-Helmholtz instabilities) will disrupt and fragment the cloud into pieces, some of which might accrete onto Sgr A*. It is predicted that the cloud will not survive the encounter and will generate a small increase in the 2–8 keV luminosity of only one order of magnitude above the quiescent level [39, 251]. However, the cloud origin, mass content and the effects for the future activity of Sgr A* are still highly debated [2, 176, 198]. Murray-Clay and Loeb [194] suggested that this cloud naturally originates from a proto-planetary disc surrounding an undetected low mass star. If so, the mass accreted onto Sgr A* (and thus Sgr A*'s luminosity) might be orders of magnitude higher producing a rare and bright flare. Moreover, such a star will survive the close encounter and possibly regenerate a cloud in time for future pericenter passages. Interestingly the previous passage (if any at all) would have occurred $\sim$ 130-200 yr ago, around the time of the flare that is now illuminating Sgr B2. Further observations of G2 will give us an unprecedented opportunity to study one possible mode of accretion onto a supermassive BH.

6 An AGN Torus in Our Backyard!

Several pieces of evidence suggest that Sgr A* might have undergone a period of AGN activity about 6×10^6 year ago (see Sect. 4.4; [323, 324]). In those conditions the CMZ would have appeared, to an extragalactic observer, to have the properties of a typical AGN torus commonly invoked by AGN unification models [3,286]. In fact, it would have obscured (with column densities up to $N_H \sim 10^{24-25}\,\mathrm{cm}^{-2}$) the direct vision of the central BH to an equatorial observer. At about 50–150 pc the height of the CMZ is about several tens of parsec, thus generating obscuration toward a significant fraction of line of sights. This number is not too dissimilar from the one typically estimated from the fraction of obscured/unobscured AGN [234, 286]. The kinematics of the EMR (see Sect. 3.2) is modified by the influence of the stellar bar potential [28]. However, the radial component of the gas motion could have been generated by the radiation pressure and/or the momentum of an outflow produced by accretion onto Sgr A*, that might have pushed away the molecular material from the accretion disc axis [259, 260], carving two holes of lower extinction. However, along the Galactic disc, where most of the molecular mass is concentrated, the CMZ represents an almost impassable barrier to Sgr A*'s radiation/outflows. The mass of the CMZ is in fact large enough to impede equatorial outflows from Sgr A*, even if accreting at the Eddington limit ($L_{\mathrm{Edd}} \sim 5 \times 10^{44}\,\mathrm{erg\,s}^{-1}$). During the last AGN phase, the inner faces of the inner CMZ clouds would have seen the nuclear continuum (efficiently producing UV and X-ray radiation; [80]) unobscured and be heated by photoionisation, initially to temperatures of $\sim 10^4$ K, then to higher temperatures as their material evaporates away [143]. Part of this gas might have generated an outflowing wind [145, 146], possibly forming a warm absorber component such as observed in UV/X-ray spectra of AGN [32, 126, 142], while the remaining matter would have probably been channelled inwards at a rate sufficient to maintain a steady state against evaporation of the torus inner edge (provided that new material can be fed into the outer edge of the torus; [143]). The luminosity of the nuclear source sets a limit to the survival of dust. Therefore, the so called "dust sublimation radius" is typically assumed to be the inner edge of the molecular torus [13].

The advent of mid and near-IR interferometric observations at VLT and Keck has recently allowed a dramatic improvement in angular resolution. The application of this technique to a few nearby AGN has allowed investigators to marginally and partially resolve the dust sublimation region (the inner edge of the torus) in these objects [40, 125, 131, 132, 172, 271]. Near-IR observations of AGN (tracing hot, $T \sim 10^3$ K, dust emission) reveal geometrically-thin ring radii on sub-parsec ($\sim$0.03–0.5 pc) scales, consistent with the near-IR reverberation radius (the light crossing distance corresponding to the delay between the variabilities in the UV/optical and near-IR; [131, 132]). Moreover, the ring radii present a dependence with source luminosity, as expected for the dust sublimation radii [13, 131, 132]. Mid-IR observations (tracing warm, $T \sim 10^{2-3}$ K, dust) display significantly larger radii with a size going from a fraction up to several parsecs. This clearly indicates a stratification in temperature of the radial structure of the torus, with the hot

near-IR emission tracing the inner torus edge, closer to the irradiating source. IR observations are thus dominated by a central brightness concentration at the scale of the sublimation radius, the bright rim of the innermost dust distribution, and weaker emission from the external, weakly irradiated, part of the torus [131, 132]. More difficult is to determine the structure of the outer, weaker emission or any substructure within these AGN tori.

These results do not contradict the idea that the CND might be the relic of the inner part of the Milky Way AGN torus. Once the intense feeding onto Sgr A* stopped, photo-evaporation halted and the CND has been left as a relic [77] just outside the sublimation radius. The orbital time of the CND material is much shorter than 10^6 year, so it is unlikely that it kept the same shape that it might have had during the AGN phase. After a long period of quiescence, we do not expect to observe remnant radiation from the emitting regions surrounding a typical AGN, i.e. the broad and narrow line regions, the warm absorber, etc. In fact, the recombination timescales of such plasmas are expected to be much shorter than $\sim 10^6$ year [207].

Being only $\sim$8 kpc away (i.e. $\sim$500 times closer than the closest AGN, Cen A), the GC provides us with the unique opportunity to resolve spatially the internal structure of an AGN torus in such exquisite detail. It is expected that the outer CMZ structure has not changed significantly since the last AGN phase ($\sim 6 \times 10^6$ year ago). In fact, a typical MC core, at $\sim$100 pc from the centre, moving at $\sim$100 km s^{-1} (typical orbital velocities of a MC of the CMZ disc population) would require about 10^7 year to complete a full orbit. This suggests that the external structure of the past AGN torus is still preserved in the CMZ. Thus the CMZ can be used as a template to study the structure of the tori of distant AGN and the mass accretion from the outer to inner boundary of AGN tori.

The study of Sgr A*'s surroundings has allowed us to hint at its past activity and the impact of Sgr A*'s emissions on the surrounding matter and star forming regions. Zubovas et al. [323] estimate that, to power the last AGN phase, Sgr A* might have accreted about $\sim 2 \times 10^3\,M_\odot$. This is about one order of magnitude smaller than the estimated mass stored in the CND. The irregular and clumpy structures of the CND, suggest dynamical evolution and episodic feeding of gas towards Sgr A* [155]. The CND appears to be the convergence of the innermost parts of large-scale gas streamers, which are responding to the central gravitational potential well. All these indications suggest that the CND might feed the supermassive BH again. Morris et al. [185] proposed a limit cycle of recurrent nuclear activity where, in the absence of dynamical or radiation pressure from within the CND cavity, viscous disc evolution would cause the inner edge of the CND to shrink, eventually fuelling the BH. The associated burst of radiation would presumably produce shocks and compression of the surrounding gas, possibly inducing a dramatic episode of star formation that could produce a massive cluster like the present central parsec cluster of young stars. The collective winds and radiation pressure from the newly-formed stars and/or AGN accretion, might clear gas from the central region, halting accretion and creating an inner cavity in the CND. The stellar winds from the massive cluster of newborn stars fade out about $\sim 10^7$ year after the star formation

event and, at that point, the inner edge of the CND would start migrate inward again, thus completing the cycle [185].

On larger scales, studies of the CMZ structure also suggest that episodic cloud formation and starbursts in the GC region (with a relaxation oscillator mechanism for quasi-periodic starbursts of $\sim 10^6$–10^7 years; [159, 184, 263]) are a natural result of the interaction between the stellar bar and interstellar gas. This star formation cycle, as well as the cloud kinematics and evolution, can be influenced by Sgr A*'s activity, which in turn will be triggered by matter migrating into its sphere of influence. Therefore, the study of Sgr A*'s past activity and its connection to observable phenomena in the CMZ provide a high-resolution opportunity for studying the AGN feedback phenomenon.

Acknowledgements The authors thank the ISSI in Bern. GP thanks S. Bianchi, E. Churazov, G. Matt, S. Gillessen, V. Tatischeff, T. Dwelly, A. Strong, L. Burtscher, A. Merloni, Y. Tanaka and F. Melia for useful discussion. Part of the work was supported by the French Labex "UnivEarthS".

References

1. Amo-Baladrón, M. A., Martín-Pintado, J., Morris, M. R., Muno, M. P., & Rodríguez-Fernández, N. J. 2009, ApJ, 694, 943
2. Anninos, P., Fragile, P. C., Wilson, J., & Murray, S. D. 2012, arXiv:1209.1638
3. Antonucci, R. 1993, ARA&A, 31, 473
4. Armstrong, J. T., & Barrett, A. H. 1985, ApJS, 57, 535
5. Baganoff, F. K., et al. 2001, Nature, 413, 45
6. Baganoff, F. K., Maeda, Y., Morris, M., et al. 2003, ApJ, 591, 891
7. Bally, J., Stark, A. A., Wilson, R. W., & Henkel, C. 1987, ApJS, 65, 13
8. Bally, J., Stark, A. A., Wilson, R. W., & Henkel, C. 1988, ApJ, 324, 223
9. Bally, J., & Leventhal, M. 1991, Nature, 353, 234
10. Bamba, A., Murakami, H., Senda, A., et al. 2002, arXiv:astro-ph/0202010
11. Bambynek, W., Crasemann, B., Fink, R. W., et al. 1972, Reviews of Modern Physics, 44, 716
12. Bania, T. M. 1977, ApJ, 216, 381
13. Barvainis, R. 1987, ApJ, 320, 537
14. Basko, M. M., Sunyaev, R. A., & Titarchuk, L. G. 1974, A&A, 31, 249
15. Basko, M. M. 1978, ApJ, 223, 268
16. Becklin, E. E., & Neugebauer, G. 1968, ApJ, 151, 145
17. Becklin, E. E., Neugebauer, G., Willner, S. P., & Matthews, K. 1978, ApJ, 220, 831
18. Becklin, E. E., Gatley, I., & Werner, M. W. 1982, ApJ, 258, 135
19. Belloni, T., & Hasinger, G. 1990, A&A, 227, L33
20. Belloni, T., & Hasinger, G. 1990, A&A, 230, 103
21. Belmont, R., Tagger, M., Muno, M., Morris, M., & Cowley, S. 2005, ApJ, 631, L53
22. Belmont, R., & Tagger, M. 2006, A&A, 452, 15
23. Berezinskii, V. S., Bulanov, S. V., Dogiel, V. A., & Ptuskin, V. S. 1990, Amsterdam: North-Holland, 1990, edited by Ginzburg, V.L.,
24. Bernard, J.-P., Paradis, D., Marshall, D. J., et al. 2010, A&A, 518, L88
25. Bethe, H. A., & Salpeter, E. E. 1957, Quantum Mechanics of One- and Two-Electron Atoms, New York: Academic Press, 1957,
26. Bica, E., Bonatto, C., Barbuy, B., & Ortolani, S. 2006, A&A, 450, 105
27. Binney, J., Gerhard, O. E., Stark, A. A., Bally, J., & Uchida, K. I. 1991, MNRAS, 252, 210

28. Binney, J. 1994, NATO ASIC Proc. 445: The Nuclei of Normal Galaxies: Lessons from the Galactic Center, 75
29. Bland-Hawthorn, J., & Cohen, M. 2003, ApJ, 582, 246
30. Bleach, R. D., Boldt, E. A., Holt, S. S., Schwartz, D. A., & Serlemitsos, P. J. 1972, ApJ, 174, L101
31. Blum, R. D., Depoy, D. L., & Sellgren, K. 1995, ApJ, 441, 603
32. Blustin, A. J., Page, M. J., Fuerst, S. V., Branduardi-Raymont, G., & Ashton, C. E. 2005, A&A, 431, 111
33. Bondi, H. 1952, MNRAS, 112, 195
34. Bonnell, I. A., & Rice, W. K. M. 2008, Science, 321, 1060
35. Bowyer, S., Byram, E. T., Chubb, T. A., & Friedman, H. 1965, Science, 147, 394
36. Bradt, H., Naranan, S., Rappaport, S., & Spada, G. 1968, ApJ, 152, 1005
37. Breitschwerdt, D., McKenzie, J. F., & Voelk, H. J. 1991, A&A, 245, 79
38. Brown, R. L., & Gould, R. J. 1970, Phys. Rev. D, 1, 2252
39. Burkert, A., Schartmann, M., Alig, C., et al. 2012, ApJ, 750, 58
40. Burtscher, L., Jaffe, W., Raban, D., et al. 2009, ApJL, 705, L53
41. Bykov, A. M. 2002, A&A, 390, 327
42. Bykov, A. M. 2003, A&A, 410, L5
43. Capelli, R., Warwick, R. S., Porquet, D., Gillessen, S., & Predehl, P. 2011, A&A, 530, A38
44. Capelli, R., Warwick, R. S., Porquet, D., Gillessen, S., & Predehl, P. 2012, A&A, 545, A35
45. Christopher, M. H., Scoville, N. Z., Stolovy, S. R., & Yun, M. S. 2005, ApJ, 622, 346
46. Churazov, E., Gilfanov, M., Sunyaev, R., et al. 1993, ApJ, 407, 752
47. Churazov, E., Gilfanov, M., Sunyaev, R., et al. 1994, ApJS, 92, 381
48. Churazov, E., Gilfanov, M., & Sunyaev, R. 1996, ApJ, 464, L71
49. Churazov, E., Sunyaev, R., & Sazonov, S. 2002, MNRAS, 330, 817
50. Clark, G., Garmire, G., Oda, M., & Wada, M. 1965, Nature, 207, 584
51. Coil, A. L., et al. 2000, ApJ, 544, L111
52. Coker, R. F., & Melia, F. 1997, ApJ, 488, L149
53. Comastri, A. 2004, Supermassive Black Holes in the Distant Universe, 308, 245
54. Compiègne, M., Verstraete, L., Jones, A., et al. 2011, A&A, 525, A103
55. Contopoulos, G., & Mertzanides, C. 1977, A&A, 61, 477
56. Cooke, B. A., Griffiths, R. E., & Pounds, K. A. 1970, Non-Solar X- and Gamma-Ray Astronomy, 37, 280
57. Coriat, M., Fender, R. P., & Dubus, G. 2012, MNRAS, 424, 1991
58. Covino, S., Tagliaferri, G., Pallavicini, R., Mewe, R., & Poretti, E. 2000, A&A, 355, 681
59. Cramphorn, C. K., & Sunyaev, R. A. 2002, A&A, 389, 252
60. Crocker, R. M., Jones, D. I., Melia, F., Ott, J., & Protheroe, R. J. 2010, Nature, 463, 65
61. Crocker, R. M., & Aharonian, F. 2011, Physical Review Letters, 106, 101102
62. Crocker, R. M., Jones, D. I., Aharonian, F., et al. 2011, MNRAS, 413, 763
63. Cuadra, J., Nayakshin, S., Springel, V., & Di Matteo, T. 2005, MNRAS, 360, L55
64. Cuadra, J., Nayakshin, S., Springel, V., & Di Matteo, T. 2006, MNRAS, 366, 358
65. Cuadra, J., Nayakshin, S., & Martins, F. 2008, MNRAS, 383, 458
66. Dahmen, G., Huttemeister, S., Wilson, T. L., & Mauersberger, R. 1998, A&A, 331, 959
67. Dambis, A. K. 2009, MNRAS, 396, 553
68. Degenaar, N., & Wijnands, R. 2009, A&A, 495, 547
69. Degenaar, N., & Wijnands, R. 2010, A&A, 524, A69
70. Degenaar, N., Wijnands, R., Cackett, E. M., et al. 2012, A&A, 545, A49
71. de Vaucouleurs, G. 1964, The Galaxy and the Magellanic Clouds, 20, 195
72. Dobler, G., & Finkbeiner, D. P. 2008, ApJ, 680, 1222
73. Dodds-Eden, K., Gillessen, S., Fritz, T. K., et al. 2011, ApJ, 728, 37
74. Dogiel, V. A., Inoue, H., Masai, K., Schönfelder, V., & Strong, A. W. 2002, ApJ, 581, 1061
75. Dogiel, V., et al. 2009, PASJ, 61, 901
76. Dogiel, V., Chernyshov, D., Koyama, K., Nobukawa, M., & Cheng, K.-S. 2011, PASJ, 63, 535
77. Duschl, W. J. 1989, MNRAS, 240, 219

78. Dwek, E., Arendt, R. G., Hauser, M. G., et al. 1995, ApJ, 445, 716
79. Eisenhauer, F., Schödel, R., Genzel, R., Ott, T., Tecza, M., Abuter, R., Eckart, A., & Alexander, T. 2003, ApJ, 597, L121
80. Elvis, M., Wilkes, B. J., McDowell, J. C., et al. 1994, ApJS, 95, 1
81. Fabian, A. C. 1977, Nature, 269, 672
82. Favata, F., Micela, G., & Sciortino, S. 1997, A&A, 326, 647
83. Fender, R. P., Belloni, T. M., & Gallo, E. 2004, MNRAS, 355, 1105
84. Fender, R., & Belloni, T. 2004, ARA&A, 42, 317
85. Ferrière, K. 2009, A&A, 505, 1183
86. Figer, D. F., Najarro, F., Gilmore, D., et al. 2002, ApJ, 581, 258
87. Fisher, P. C., Johnson, H. M., Jordan, W. C., Meyerott, A. J., & Acton, L. W. 1966, ApJ, 143, 203
88. Fritz, T. K., Gillessen, S., Dodds-Eden, K., et al. 2011, ApJ, 737, 73
89. Fryer, C. L., Rockefeller, G., Hungerford, A., & Melia, F. 2006, ApJ, 638, 786
90. Fukuoka, R., Koyama, K., Ryu, S. G., & Tsuru, T. G. 2009, PASJ, 61, 593
91. Garcia, J. D., Fortner, R. J., & Kavanagh, T. M. 1973, Reviews of Modern Physics, 45, 111
92. Genzel, R., Crawford, M. K., Townes, C. H., & Watson, D. M. 1985, ApJ, 297, 766
93. Genzel, R., Thatte, N., Krabbe, A., Kroker, H., & Tacconi-Garman, L. E. 1996, ApJ, 472, 153
94. Genzel, R., Pichon, C., Eckart, A., Gerhard, O. E., & Ott, T. 2000, MNRAS, 317, 348
95. Genzel, R., Schödel, R., Ott, T., et al. 2003, ApJ, 594, 812
96. Genzel, R., Eisenhauer, F., & Gillessen, S. 2010, Reviews of Modern Physics, 82, 3121
97. George, I. M., & Fabian, A. C. 1991, MNRAS, 249, 352
98. Ghez, A. M., Duchêne, G., Matthews, K., et al. 2003, ApJ, 586, L127
99. Ghez, A. M., et al. 2004, ApJ, 601, L159
100. Ghez, A. M., et al. 2005, ApJ, 635, 1087
101. Ghez, A. M., Salim, S., Weinberg, N. N., et al. 2008, ApJ, 689, 1044
102. Ghisellini, G., Haardt, F., & Matt, G. 1994, MNRAS, 267, 743
103. Gillessen, S., Eisenhauer, F., Fritz, T. K., et al. 2009, ApJ, 707, L114
104. Gillessen, S., Eisenhauer, F., Trippe, S., Alexander, T., Genzel, R., Martins, F., & Ott, T. 2009, ApJ, 692, 1075
105. Gillessen, S., Genzel, R., Fritz, T. K., et al. 2012, Nature, 481, 51
106. Gillessen, S., Genzel, R., Fritz, T. K., et al. 2012, arXiv:1209.2272
107. Glass, I. S., Catchpole, R. M., & Whitelock, P. A. 1987, MNRAS, 227, 373
108. Goldwurm, A., Cordier, B., Paul, J., et al. 1994, Nature, 371, 589
109. Goldwurm, A. 2001, Exploring the Gamma-Ray Universe, 459, 455
110. Goldwurm, A., Brion, E., Goldoni, P., Ferrando, P., Daigne, F., Decourchelle, A., Warwick, R. S., & Predehl, P. 2003, ApJ, 584, 751
111. Groenewegen, M. A. T., Udalski, A., & Bono, G. 2008, A&A, 481, 441
112. Gualandris, A., Mapelli, M., & Perets, H. B. 2012, arXiv:1209.3021
113. Gursky, H., Gorenstein, P., & Giacconi, R. 1967, ApJ, 150, L75
114. Guesten, R., & Downes, D. 1980, A&A, 87, 6
115. Guesten, R., Walmsley, C. M., & Pauls, T. 1981, A&A, 103, 197
116. Guesten, R., Genzel, R., Wright, M. C. H., et al. 1987, ApJ, 318, 124
117. Güsten, R. 1989, The Center of the Galaxy, 136, 89
118. Harfst, S., Portegies Zwart, S., & Stolte, A. 2010, MNRAS, 409, 628
119. Heiligman, G. M. 1987, ApJ, 314, 747
120. Hobbs, A., & Nayakshin, S. 2009, MNRAS, 394, 191
121. in't Zand, J., Verbunt, F., Heise, J., et al. 2004, Nuclear Physics B Proceedings Supplements, 132, 486
122. Inui, T., Koyama, K., Matsumoto, H., & Tsuru, T. G. 2009, PASJ, 61, 241
123. Jackson, J. M., Geis, N., Genzel, R., et al. 1993, ApJ, 402, 173
124. Jackson, J. M., Heyer, M. H., Paglione, T. A. D., & Bolatto, A. D. 1996, ApJ, 456, L91
125. Jaffe, W., Meisenheimer, K., Röttgering, H. J. A., et al. 2004, Nature, 429, 47
126. Kaastra, J. S., Detmers, R. G., Mehdipour, M., et al. 2012, A&A, 539, A117

127. Kaifu, N., Kato, T., & Iguchi, T. 1972, Nature Physical Science, 238, 105
128. Kaneda, H., Makishima, K., Yamauchi, S., et al. 1997, ApJ, 491, 638
129. Kennea, J. A., Burrows, D. N., Campana, S., et al. 2006, The Astronomer's Telegram, 753, 1
130. Kimura, M., Maihara, T., Iwamuro, F., et al. 2010, PASJ, 62, 1135
131. Kishimoto, M., Hönig, S. F., Antonucci, R., et al. 2011, A&A, 527, A121
132. Kishimoto, M., Hönig, S. F., Antonucci, R., et al. 2011, A&A, 536, A78
133. Körding, E. G., Migliari, S., Fender, R., et al. 2007, MNRAS, 380, 301
134. Koyama, K., Makishima, K., Tanaka, Y., & Tsunemi, H. 1986, PASJ, 38, 121
135. Koyama, K., Awaki, H., Kunieda, H., Takano, S., & Tawara, Y. 1989, Nature, 339, 603
136. Koyama, K., Maeda, Y., Sonobe, T., et al. 1996, PASJ, 48, 249
137. Koyama, K., Inui, T., Hyodo, Y., et al. 2007, PASJ, 59, 221
138. Koyama, K., et al. 2007, PASJ, 59, 245
139. Koyama, K., Inui, T., Matsumoto, H., & Tsuru, T. G. 2008, PASJ, 60, 201
140. Koyama, K., Takikawa, Y., Hyodo, Y., Inui, T., Nobukawa, M., Matsumoto, H., & Tsuru, T. G. 2009, PASJ, 61, 255
141. Koyama, K. 2011, The Galactic Center: a Window to the Nuclear Environment of Disk Galaxies, 439, 418
142. Kriss, G. A., Arav, N., Kaastra, J. S., et al. 2011, A&A, 534, A41
143. Krolik, J. H., & Begelman, M. C. 1988, ApJ, 329, 702
144. Krolik, J. H., Madau, P., & Zycki, P. T. 1994, ApJ, 420, L57
145. Krolik, J. H., & Kriss, G. A. 1995, ApJ, 447, 512
146. Krolik, J. H., & Kriss, G. A. 2001, ApJ, 561, 684
147. Kuntz, K. D., & Snowden, S. L. 2008, ApJ, 674, 209
148. Kuulkers, E., Shaw, S. E., Paizis, A., et al. 2007, A&A, 466, 595
149. Irvine, W. M., Goldsmith, P. F., & Hjalmarson, A. 1987, Interstellar Processes, 134, 561
150. LaRosa, T. N., Kassim, N. E., Lazio, T. J. W., & Hyman, S. D. 2000, AJ, 119, 207
151. LaRosa, T. N., Brogan, C. L., Shore, S. N., et al. 2005, ApJ, 626, L23
152. Li, Z., Morris, R. M., & Baganoff, M., 2012, IAU Symposium, Feeding Compact Objects on All Scales, Beijing, China
153. Liszt, H. S., & Burton, W. B. 1978, ApJ, 226, 790
154. Liszt, H. S., & Burton, W. B. 1980, ApJ, 236, 779
155. Liu, H. B., Hsieh, P.-Y., Ho, P. T. P., et al. 2012, ApJ, 756, 195
156. Lu, J. R., Ghez, A. M., Hornstein, S. D., et al. 2009, ApJ, 690, 1463
157. Maeda, Y., Baganoff, F. K., Feigelson, E. D., et al. 2002, ApJ, 570, 671
158. Martin, P. G. 1970, MNRAS, 149, 221
159. Martin, C. L., Walsh, W. M., Xiao, K., et al. 2004, ApJS, 150, 239
160. Martín, S., Martín-Pintado, J., Montero-Castaño, M., Ho, P. T. P., & Blundell, R. 2012, A&A, 539, A29
161. Martín-Pintado, J., de Vicente, P., Rodríguez-Fernández, N. J., Fuente, A., & Planesas, P. 2000, A&A, 356, L5
162. Masui, K., Mitsuda, K., Yamasaki, N. Y., et al. 2009, PASJ, 61, 115
163. Matsunaga, N., Kawadu, T., Nishiyama, S., et al. 2009, MNRAS, 399, 1709
164. Matt, G., Perola, G. C., & Piro, L. 1991, A&A, 247, 25
165. Matt, G., Brandt, W. N., & Fabian, A. C. 1996, MNRAS, 280, 823
166. Matt, G., Fabian, A. C., & Reynolds, C. S. 1997, MNRAS, 289, 175
167. Matt, G. 2002, MNRAS, 337, 147
168. Matt, G., Guainazzi, M., & Maiolino, R. 2003, MNRAS, 342, 422
169. Mauerhan, J. C., Muno, M. P., Morris, M. R., et al. 2009, ApJ, 703, 30
170. Mauersberger, R., Henkel, C., Wilson, T. L., & Walmsley, C. M. 1986, A&A, 162, 199
171. McHardy, I. M., Koerding, E., Knigge, C., Uttley, P., & Fender, R. P. 2006, Nature, 444, 730
172. Meisenheimer, K., Tristram, K. R. W., Jaffe, W., et al. 2007, A&A, 471, 453
173. Melia, F. 1992, ApJ, 387, L25
174. Melia, F., & Falcke, H. 2001, ARA&A, 39, 309
175. Melia, F. 2007, The Galactic Supermassive Black Hole by Fulvio Melia. Princeton University Press, 2007.,

176. Miralda-Escudé, J. 2012, ApJ, 756, 86
177. Molendi, S., Bianchi, S., & Matt, G. 2003, MNRAS, 343, L1
178. Molinari, S., Bally, J., Noriega-Crespo, A., et al. 2011, ApJ, 735, L33
179. Montero-Castaño, M., Herrnstein, R. M., & Ho, P. T. P. 2009, ApJ, 695, 1477
180. Morris, M., Polish, N., Zuckerman, B., & Kaifu, N. 1983, AJ, 88, 1228
181. Morris, M. 1990, Galactic and Intergalactic Magnetic Fields, 140, 361
182. Morris, M., Davidson, J. A., Werner, M., et al. 1992, ApJ, 399, L63
183. Morris, M. 1996, Unsolved Problems of the Milky Way, 169, 247
184. Morris, M., & Serabyn, E. 1996, ARA&A, 34, 645
185. Morris, M., Ghez, A. M., & Becklin, E. E. 1999, Advances in Space Research, 23, 959
186. Muno, M. P., Baganoff, F. K., Bautz, M. W., et al. 2003, ApJ, 589, 225
187. Muno, M. P., et al. 2004, ApJ, 613, 1179
188. Muno, M. P., Bauer, F. E., Bandyopadhyay, R. M., & Wang, Q. D. 2006, ApJS, 165, 173
189. Muno, M. P., Baganoff, F. K., Brandt, W. N., Park, S., & Morris, M. R. 2007, ApJ, 656, L69
190. Muno, M. P., Baganoff, F. K., Brandt, W. N., Morris, M. R., & Starck, J.-L. 2008, ApJ, 673, 251
191. Murakami, H., Koyama, K., Sakano, M., Tsujimoto, M., & Maeda, Y. 2000, ApJ, 534, 283
192. Murakami, H., Koyama, K., Tsujimoto, M., Maeda, Y., & Sakano, M. 2001a, ApJ, 550, 297
193. Murakami, H., Koyama, K., & Maeda, Y. 2001b, ApJ, 558, 687
194. Murray-Clay, R. A., & Loeb, A. 2011, arXiv:1112.4822
195. Mužić, K., Eckart, A., Schödel, R., et al. 2010, A&A, 521, A13
196. Nakajima, H., Tsuru, T. G., Nobukawa, M., et al. 2009, PASJ, 61, 233
197. Nandra, K., & George, I. M. 1994, MNRAS, 267, 974
198. Narayan, R., Özel, F., & Sironi, L. 2012, ApJ, 757, L20
199. Nayakshin, S., Cuadra, J., & Springel, V. 2007, MNRAS, 379, 21
200. Nishiyama, S., Nagata, T., Kusakabe, N., et al. 2006, ApJ, 638, 839
201. Nobukawa, M., Tsuru, T. G., Takikawa, Y., et al. 2008, PASJ, 60, 191
202. Nobukawa, M., Ryu, S. G., Tsuru, T. G., & Koyama, K. 2011, ApJ, 739, L52
203. Nottingham, M. R., Skinner, G. K., Willmore, A. P., et al. 1993, A&AS, 97, 165
204. Odaka, H., Aharonian, F., Watanabe, S., et al. 2011, ApJ, 740, 103
205. Oka, T., Geballe, T. R., Goto, M., Usuda, T., & McCall, B. J. 2005, ApJ, 632, 882
206. Oka, T., Nagai, M., Kamegai, K., & Tanaka, K. 2011, ApJ, 732, 120
207. Osterbrock, D. E., & Mathews, W. G. 1986, ARA&A, 24, 171
208. Overbeck, J. W. 1965, ApJ, 141, 864
209. Palmeri, P., Mendoza, C., Kallman, T. R., Bautista, M. A., & Meléndez, M. 2003, A&A, 410, 359
210. Palmeri, P., Mendoza, C., Kallman, T. R., & Bautista, M. A. 2003, A&A, 403, 1175
211. Park, S., Muno, M. P., Baganoff, F. K., et al. 2004, ApJ, 603, 548
212. Paumard, T., Genzel, R., Martins, F., et al. 2006, ApJ, 643, 1011
213. Pavlinsky, M. N., Grebenev, S. A., & Sunyaev, R. A. 1994, ApJ, 425, 110
214. Peters, W. L., III 1975, ApJ, 195, 617
215. Planck Collaboration, Ade, P. A. R., Aghanim, N., et al. 2012, arXiv:1208.5483
216. Ponti, G., Terrier, R., Goldwurm, A., Belanger, G., & Trap, G. 2010, ApJ, 714, 732
217. Ponti, G., Terrier, R., Goldwurm, A., Belanger, G., & Trap, G. 2011, The Galactic Center: a Window to the Nuclear Environment of Disk Galaxies, 439, 446
218. Ponti, G., Fender, R. P., Begelman, M. C., et al. 2012, MNRAS, 422, L11
219. Ponti, G., Papadakis, I., Bianchi, S., et al. 2012, A&A, 542, A83
220. Porquet, D., Predehl, P., Aschenbach, B., Grosso, N., Goldwurm, A., Goldoni, P., Warwick, R. S., & Decourchelle, A. 2003, A&A, 407, L17
221. Predehl, P., & Schmitt, J. H. M. M. 1995, A&A, 293, 889
222. Quataert, E. 2004, ApJ, 613, 322
223. Quinn, P. J., & Sussman, G. J. 1985, ApJ, 288, 377
224. Reid, M. J., Menten, K. M., Zheng, X. W., et al. 2009, ApJ, 700, 137
225. Reid, M. J., Menten, K. M., Zheng, X. W., Brunthaler, A., & Xu, Y. 2009, ApJ, 705, 1548

226. Requena-Torres, M. A., Güsten, R., Weiss, A., et al. 2012, A&A, 542, L21
227. Revnivtsev, M., Gilfanov, M., Sunyaev, R., Jahoda, K., & Markwardt, C. 2003, A&A, 411, 329
228. Revnivtsev, M. G., et al. 2004, A&A, 425, L49
229. Revnivtsev, M., Sazonov, S., Gilfanov, M., Churazov, E., & Sunyaev, R. 2006a, A&A, 452, 169
230. Revnivtsev, M., Molkov, S., & Sazonov, S. 2006b, MNRAS, 373, L11
231. Revnivtsev, M. G., et al., 2007, *A&A*, 473, 857
232. Revnivtsev, M., Sazonov, S., Churazov, E., et al. 2009, Nature, 458, 1142
233. Rieke, G. H., Rieke, M. J., & Paul, A. E. 1989, ApJ, 336, 752
234. Risaliti, G., Maiolino, R., & Salvati, M. 1999, ApJ, 522, 157
235. Rockefeller, G., Fryer, C. L., Melia, F., & Warren, M. S. 2004, ApJ, 604, 662
236. Rockefeller, G., Fryer, C. L., Baganoff, F. K., & Melia, F. 2005, ApJ, 635, L141
237. Rodríguez-Fernández, N. J., Martín-Pintado, J., Fuente, A., & Wilson, T. L. 2004, A&A, 427, 217
238. Rolf, D. P. 1983, Nature, 302, 46
239. Ryu, S. G., Koyama, K., Nobukawa, M., Fukuoka, R., & Tsuru, T. G. 2009, PASJ, 61, 751
240. Saito, M. 1990, PASJ, 42, 19
241. Sakano, M., Koyama, K., Murakami, H., Maeda, Y., & Yamauchi, S. 2002, ApJS, 138, 19
242. Sakano, M., Warwick, R. S., Decourchelle, A., & Predehl, P. 2004, MNRAS, 350, 129
243. Sanders, R. H. 1989, The Center of the Galaxy, 136, 77
244. Sanders, R. H. 1998, MNRAS, 294, 35
245. Sawada, T., Hasegawa, T., Handa, T., & Cohen, R. J. 2004, MNRAS, 349, 1167
246. Sazonov, S., Revnivtsev, M., Gilfanov, M., Churazov, E., & Sunyaev, R. 2006, A&A, 450, 117
247. Sazonov, S., Sunyaev, R., & Revnivtsev, M. 2012, MNRAS, 420, 388
248. Scoville, N. Z. 1972, ApJ, 175, L127
249. Sellwood, J. A. 1993, Back to the Galaxy, 278, 133
250. Serabyn, E., & Guesten, R. 1987, A&A, 184, 133
251. Schartmann, M., Burkert, A., Alig, C., et al. 2012, ApJ, 755, 155
252. Schödel, R., Ott, T., Genzel, R., et al. 2002, Nature, 419, 694
253. Schödel, R., Eckart, A., Alexander, T., et al. 2007, A&A, 469, 125
254. Schödel, R., Merritt, D., & Eckart, A. 2009, A&A, 502, 91
255. Sidoli, L., Mereghetti, S., Israel, G. L., et al. 1999, ApJ, 525, 215
256. Sidoli, L., Belloni, T., & Mereghetti, S. 2001, A&A, 368, 835
257. Sidoli, L., Mereghetti, S., Treves, A., et al. 2001, A&A, 372, 651
258. Skinner, G. K., Willmore, A. P., Eyles, C. J., Bertram, D., & Church, M. J. 1987, Nature, 330, 544
259. Sofue, Y. 1995, PASJ, 47, 527
260. Sofue, Y. 1995, PASJ, 47, 551
261. Stark, A. A., & Bania, T. M. 1986, ApJ, 306, L17
262. Stark, A. A., & Brand, J. 1989, ApJ, 339, 763
263. Stark, A. A., Martin, C. L., Walsh, W. M., et al. 2004, ApJL, 614, L41
264. Su, M., Slatyer, T. R., & Finkbeiner, D. P. 2010, ApJ, 724, 1044
265. Su, M., & Finkbeiner, D. P. 2012, ApJ, 753, 61
266. Sunyaev, R., Churazov, E., Gilfanov, M., et al. 1991, A&A, 247, L29
267. Sunyaev, R. A., Markevitch, M., & Pavlinsky, M. 1993, ApJ, 407, 606
268. Sunyaev, R. A., & Churazov, E. M. 1996, Astronomy Letters, 22, 648
269. Sunyaev, R., & Churazov, E. 1998, MNRAS, 297, 1279
270. Syer, D., & Ulmer, A. 1999, MNRAS, 306, 35
271. Swain, M., Vasisht, G., Akeson, R., et al. 2003, ApJL, 596, L163
272. Swank, J., & Markwardt, C. 2001, New Century of X-ray Astronomy, 251, 94
273. Tanaka, Y. 2002, A&A, 382, 1052
274. Tanaka, Y. & Yamauchi 2011, JAXA-SP-09-008E, ISSI 1349-113X

275. Tanner, A., Figer, D. F., Najarro, F., et al. 2006, ApJ, 641, 891
276. Tatischeff, V., Ramaty, R., & Kozlovsky, B. 1998, ApJ, 504, 874
277. Tatischeff, V., Duprat, J., Kiener, J., et al. 2003, Phys. Rev. C, 68, 025804
278. Tatischeff, V., Decourchelle, A., Maurin, G., 2012, A&A, in press.
279. Terrier, R., Ponti, G., Bélanger, G., et al. 2010, ApJ, 719, 143
280. Toor, A., Palmieri, T. M., & Seward, F. D. 1976, ApJ, 207, 96
281. Trippe, S., Gillessen, S., Gerhard, O. E., et al. 2008, A&A, 492, 419
282. Tsuboi, M., Handa, T., Inoue, M., Inatani, J., & Ukita, N. 1989, The Center of the Galaxy, 136, 135
283. Tsuboi, M., Handa, T., & Ukita, N. 1999, ApJS, 120, 1
284. Tsujimoto, M., Hyodo, Y., & Koyama, K. 2007, PASJ, 59, 229
285. Uchiyama, H., Nobukawa, M., Tsuru, T., Koyama, K., & Matsumoto, H. 2011, PASJ, 63, 903
286. Urry, C. M., & Padovani, P. 1995, PASP, 107, 803
287. Valinia, A., & Marshall, F. E. 1998, ApJ, 505, 134
288. Valinia, A., Tatischeff, V., Arnaud, K., Ebisawa, K., & Ramaty, R. 2000, ApJ, 543, 733
289. Vanhollebeke, E., Groenewegen, M. A. T., & Girardi, L. 2009, A&A, 498, 95
290. Vollmer, B., & Duschl, W. J. 2002, A&A, 388, 128
291. Walmsley, C. M., Baudry, A., Guilloteau, S., & Winnberg, A. 1986, A&A, 167, 151
292. Warwick, R. S., Turner, M. J. L., Watson, M. G., & Willingale, R. 1985, Nature, 317, 218
293. Warwick, R. S., Norton, A. J., Turner, M. J. L., Watson, M. G., & Willingale, R. 1988, MNRAS, 232, 551
294. Wang, Q. D., Gotthelf, E. V., & Lang, C. C. 2002, Nature, 415, 148
295. Wang, Q. D., Dong, H., & Lang, C. 2006, MNRAS, 371, 38
296. Watson, M. G., Willingale, R., Hertz, P., & Grindlay, J. E. 1981, ApJ, 250, 142
297. Witzel, G., Eckart, A., Bremer, M., et al. 2012, arXiv:1208.5836
298. Wijnands, R., in't Zand, J. J. M., Rupen, M., et al. 2006, A&A, 449, 1117
299. Xiang, J., Lee, J. C., & Nowak, M. A. 2007, ApJ, 660, 1309
300. Xiang, J., Lee, J. C., Nowak, M. A., & Wilms, J. 2011, ApJ, 738, 78
301. Xu, Y.-D., Narayan, R., Quataert, E., Yuan, F., & Baganoff, F. K. 2006, ApJ, 640, 319
302. Yaqoob, T., Murphy, K. D., Miller, L., & Turner, T. J. 2010, MNRAS, 401, 411
303. Yaqoob, T., & Murphy, K. D. 2011, MNRAS, 412, 277
304. Yamauchi, S., Kawada, M., Koyama, K., Kunieda, H., & Tawara, Y. 1990, ApJ, 365, 532
305. Yamauchi, S., & Koyama, K. 1993, ApJ, 404, 620
306. Yamauchi, S., Kaneda, H., Koyama, K., et al. 1996, PASJ, 48, L15
307. Yamauchi, S., Ueno, M., Koyama, K., & Bamba, A. 2008, PASJ, 60, 1143
308. Yamauchi, S., Ebisawa, K., Tanaka, Y., et al. 2009, PASJ, 61, 225
309. Yoshino, T., Mitsuda, K., Yamasaki, N. Y., et al. 2009, PASJ, 61, 805
310. Yu, Y.-W., Cheng, K. S., Chernyshov, D. O., & Dogiel, V. A. 2011, MNRAS, 411, 2002
311. Yuasa, T., Makishima, K., & Nakazawa, K. 2012, ApJ, 753, 129
312. Yusef-Zadeh, F., Morris, M., & Chance, D. 1984, Nature, 310, 557
313. Yusef-Zadeh, F., Law, C., & Wardle, M. 2002, ApJ, 568, L121
314. Yusef-Zadeh, F., Hewitt, J. W., & Cotton, W. 2004, ApJS, 155, 421
315. Yusef-Zadeh, F., Muno, M., Wardle, M., & Lis, D. C. 2007, ApJ, 656, 847
316. Yusef-Zadeh, F., Arendt, R., Bushouse, H., et al. 2012, arXiv:1208.1193
317. Yusef-Zadeh, F., Hewitt, J. W., Wardle, M., et al. 2012, arXiv:1206.6882
318. Yusef-Zadeh, F., & Wardle, M. 2012, Journal of Physics Conference Series, 372, 012024
319. Zhao, H. 1994, Ph.D. Thesis,
320. Zhao, J.-H., Goss, W. M., & Ho, P. T. P. 1995, ApJ, 450, 122
321. Zhao, J.-H., Morris, M. R., Goss, W. M., & An, T. 2009, ApJ, 699, 186
322. Zeldovich, Y. B., & Raizer, Y. P. 1966, New York: Academic Press, 1966, edited by Hayes, W.D.; Probstein, Ronald F.,
323. Zubovas, K., King, A. R., & Nayakshin, S. 2011, MNRAS, 415, L21
324. Zubovas, K., Nayakshin, S., & Markoff, S. 2012, MNRAS, 421, 1315

Fermi Bubble: Giant Gamma-Ray Bubbles in the Milky Way

Meng Su

Abstract Data from the *Fermi*-LAT reveal two gigantic gamma-ray emitting bubble structures (known as the *Fermi* bubbles), extending $\sim 50°$ above and below the Galactic center symmetric about the Galactic plane, with a width of $\sim 40°$ in longitude. The gamma-ray emission associated with these bubbles has a significantly harder spectrum ($dN/dE \sim E^{-2}$) than the inverse Compton emission from known cosmic ray electrons in the Galactic disk, or the gamma-rays produced by decay of pions from proton-ISM collisions. The bubbles are spatially correlated with the hard-spectrum microwave excess known as the *WMAP* haze; the edges of the bubbles also line up with features in the *ROSAT* soft X-ray maps at 1.5–2 keV. The *Fermi* bubble is most likely created by some large episode of energy injection in the Galactic center, such as past accretion events onto the central massive black hole, or a nuclear starburst in the last $\sim$ 10 Myr. Study of the origin and evolution of the bubbles also has the potential to improve our understanding of recent energetic events in the inner Galaxy and the high-latitude cosmic ray population.

1 Introduction

Observations of gamma-ray emission from the inner Galaxy go back decades to *COS-B* [32, 33], and *SAS-2* [14] (see e.g. [6] for a review). Later data from the *EGRET* experiment aboard the *Compton Gamma-ray Observatory* extended to the high-energy side of the π^0 bump [11, 30]. The *Fermi Gamma-ray Space Telescope* launched on June 2008 provides greatly improved data up to $\sim$ 100 GeV, with sufficient angular resolution and sensitivity to map out interesting gamma-ray

M. Su (✉)
Institute for Theory and Computation, Harvard-Smithsonian Center for Astrophysics, 60 Garden Street, MS-10, Cambridge, MA 02138, USA
e-mail: mengsu@cfa.harvard.edu

D.F. Torres and O. Reimer (eds.), *Cosmic Rays in Star-Forming Environments*, Astrophysics and Space Science Proceedings 34, DOI 10.1007/978-3-642-35410-6_27,

structures [3].[1] On the other hand, past activies towards the inner Galaxy have been found in other wavelength. The *Midcourse Space Experiment* combined with *IRAS* data confirms the existence of a limb-brightened bipolar structure, the so called Galactic center lobe (GCL), with origin at the GC on the *degree* scale (see e.g. for a summary of multiwavelength observations of GCL). More evidence of past Galactic center activities have been found in X-ray. Fe Kα echoes from molecular clouds around Sgr A* have been understood as relics of activity in the past few hundred years [24,39]. On a longer timescale, one might expect relics of past activity in high energy cosmic rays (CRs) and hot gas, perhaps far off the disk. The most obvious observables would be e^- CR (visible in inverse Compton gammas and microwave synchrotron) and thermal emission (X-rays).

Electron CRs at 10–100 GeV primarily lose energy in the diffuse interstellar medium (ISM) by (1) emitting microwave synchrotron radiation through interaction with the Galactic magnetic field, and (2) inverse-Compton (IC) scattering on the interstellar radiation field (ISRF), producing gamma rays. The total energy loss rate due to synchrotron is proportional to the magnetic field energy density, $U_{\rm B} = B^2/8\pi$; IC losses are proportional to the ISRF energy density, $U_{\rm ISRF}$, in the Thomson limit (low electron energy), and less in the Klein-Nishina regime where the product of the initial electron and photon energies becomes comparable to the electron mass squared. The electron CRs also lose energy via bremsstrahlung (free-free emission) interactions with the ambient ionized gas, but this is expected to be sub-dominant in the regions of interest.

Indeed, microwave observations also provide intriguing indications of energy release toward the GC. At tens of GHz, the *Wilkinson Microwave Anisotropy Probe* (*WMAP*)[2] provides sensitive degree resolution full sky maps of diffuse microwave emission. By subtracting templates including Galactic Hα, Haslam 408 MHz soft synchrotron, and thermal dust emission to remove the different known emission mechanisms in these maps, a microwave residual excess (named "the microwave haze") with spherical (non-disklike) morphology about $\sim$ 4 kpc in radius toward the GC (visible up to at least $|b| \approx 30°$) has been recognized [15]. It has a spectrum of about $I_\nu \sim \nu^{-0.5}$, harder than typical synchrotron, but softer than free-free. The microwave haze was later interpreted as synchrotron emission from a hard spectrum of e^- cosmic rays. Other hypotheses such as free-free, spinning dust, or thermal dust have failed to explain its morphology, spectrum, or both [12,16].

If the *WMAP* haze is synchrotron radiation from a hard electron population located around the GC, the same CRs would also produce IC scattered gammas, allowing an independent probe of the CR population. IC photons would provide valuable complementary information about the spatial distribution of the e^- CR (given a model for the ISRF), which in turn can constrain hypotheses about their origin. The unprecedented angular resolution and sensitivity of *Fermi*-LAT allows

[1] See also http://fermi.gsfc.nasa.gov/ssc/data/

[2] http://map.gsfc.nasa.gov/

us to probe the gamma-ray counterpart to the microwave haze in detail for the first time.

With *Fermi*-LAT observations, two giant gamma-ray bubbles strongly correlated with the *WMAP* haze structure have been found and named the *Fermi* bubble [13, 37]. This structure extends 50° above and below the GC, with a width of about 40° in longitude. These two "bubble"-like structures have relatively sharp edges and are symmetric with respect to the galactic plane and the minor axis of the galactic disk. The gamma-ray signal reveals similar morphology to the *WMAP* haze, and is also suggestive of a common origin with features in the *ROSAT* X-ray maps at 1.5 keV towards the GC [37].

As we will discuss in detail, the sharp edges, bilobular shape, and apparent centering on the GC of these structures suggest that they were created by some large episode of energy injection in the GC, such as a past accretion onto the central black hole, or a nuclear starburst in the last $\sim$ 10 Myr. It is well known that the GC hosts a massive black hole and massive clusters of recently formed stars [28]. Either of these could potentially provide the necessary energy injection by driving large-scale galactic winds or producing energetic jets; we will outline some of the advantages and disadvantages of each scenario.

2 Fermi-LAT and Fermi Bubble

The Large Area Telescope (LAT; [3, 17]) is the principal scientific instrument on-board the *Fermi Gamma-ray Space Telescope*, which was launched on 2008 June 11, and starting the nominal mission since 2008 August 4. The LAT is a pair-conversion gamma-ray telescope to distinguish gamma-rays in the energy ranging from 20 MeV to more than 300 GeV. It consists of in total 16 modules of tungsten and silicon-strip trackers (4×4 modular array, 12 layers of 3 % radiation length (*Front* or thin section) on top of 4 layers of 18 % radiation length converters (*Back* or thick section)) where high energy gamma rays predominantly convert into electron-positron pairs, and the energy deposition is accurately measured in each crystal to reconstruct the energy of the indicent photon. The tracker/converter system is on top of a calorimeter which contains 96 CsI(Tl) scintillating crystals with 8.6 radiation lengths deep. LAT is surrounded by an anti-coincidence detector that covers the tracker array to distinguish gamma-rays from intense background of energetic CRs, and a programmable trigger and data acquisition system.

The *Fermi* observatory operates primarily in an all-sky scanning survey mode. The spacecraft occupies a low Earth orbit (altitude of 565 km) with an inclination of 25.6°. The LAT provides a wide field-of-view of $\sim$ 2.4 sr, a large effective area of $\sim$ 6,500 cm^2 at 1 GeV, and a point spread function (PSF) about 0.8° for 68 % containment at 1 GeV with variation as function of energy as $E^{-0.8}$ (asymptoting at $\sim$ 0.2° at high energy). It is designed to survey the gamma-ray sky in the energy range from about 20 MeV to several hundreds of GeV. The field of view is so wide that the entire sky may be covered in two orbits by rocking the spacecraft

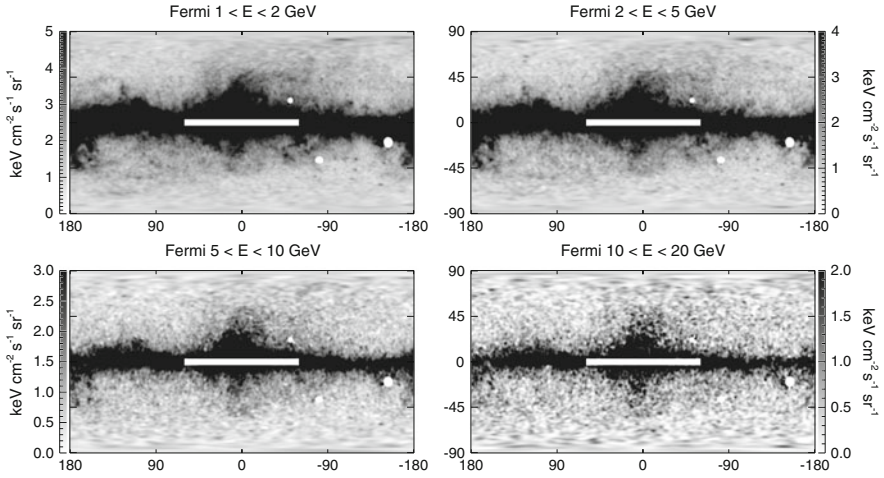

Fig. 1 All-sky *Fermi*-LAT 1.6 year maps in 4 energy bins. Point sources have been subtracted, and large sources, including the inner disk ($-2^\circ < b < 2^\circ, -60^\circ < \ell < 60^\circ$), have been masked [37]

north of zenith on one orbit and south of zenith on the next. Such an observation strategy provides 30 min of livetime on each point in the sky every two orbits in only 3 h. This scan strategy also maximizes observing time while maintaining excellent uniformity.

At low ($\sim$ 1 GeV) energies, and close to the Galactic plane, the gamma-rays observed by *Fermi* are dominated by photons from the decay of π^0 particles, produced by the collisions of CR *protons* with ambient ionized gas and dust in the ISM. Collisions of high energy CR *electrons* with the ISM (primarily protons, but also heavier nuclei) produce bremsstrahlung radiation. The *Fermi* all-sky gamma-ray maps in different energy bands are shown in Fig. 1. In order to uncover the *Fermi* bubble features better, significant π^0 emission, bremsstrahlung, and IC emission from the Galactic disk must be removed. There are three approaches for the foreground removal. One is to use the *Fermi* Diffuse Galactic Model provided by the *Fermi* team.[3] The *Fermi* diffuse Galactic model is a comprehensive model of Galactic gamma-ray emission from the ISM, and serves as a background estimate for point source removal. In this model, the π^0 emission is modeled with maps of interstellar gas: H I from the Leiden/Argentine/Bonn (LAB) Galactic Survey [22] and CO from the CfA composite CO survey [10]. And the model also includes an IC component generated by the `GALPROP` cosmic ray propagation code. `GALPROP` calculates the steady state solution to the diffusion-energy-loss equation, given the 3D gas distribution, interstellar radiation field, B-field model, CR diffusion assumptions, and many other input parameters [34–36]. In Fig. 2, we show the residual maps after subtracting the *Fermi* diffuse Galactic model in different energy

[3] See http://fermi.gsfc.nasa.gov/ssc/data/access/lat/BackgroundModels.html

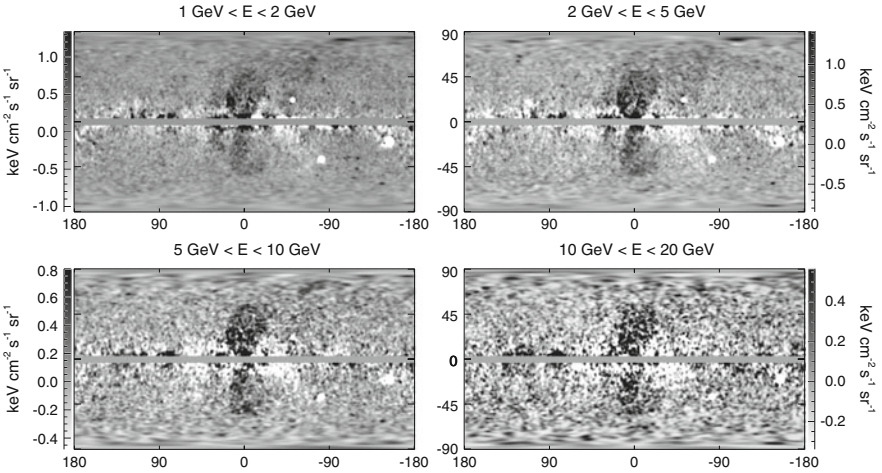

Fig. 2 All-sky residual maps after subtracting the *Fermi* diffuse Galactic model from the LAT 1.6 year maps in 4 energy bins. Two bubble structures extending to $b \pm 50^\circ$ appear above and below the GC, symmetric about the Galactic plane [37]

bins. A double-lobed bubble structure is clearly revealed, with similar morphology in the different energy bins. We note that the bubble is neither limb brightened nor centrally brightened, consistent with a flat *projected* intensity distribution.

The second approach employs a linear combination of templates of known emission mechanisms, using existing maps from multiwavelength observations and/or constructed geometric templates. Since the dominant foreground gamma-rays originate from π^0 gammas produced by CR protons interacting with the ISM, the resulting gamma-ray distribution should be morphologically correlated with other maps of spatial tracers of the ISM. A good candidate is the SFD map of Galactic dust, based on far IR data [29]. The π^0/bremsstrahlung gamma-ray intensity is proportional to the ISM density $\times$ the CR proton/electron density integrated along the line of sight. As long as the CR proton/electron spectrum and density are approximately spatially uniform, the ISM column density is a good tracer of π^0/bremsstrahlung emission. The dust map has some advantages over gas maps: there are no problems with self absorption, no concerns about "dark gas" [18], and the SFD dust map has sufficient spatial resolution (SFD has spatial resolution of $6'$, and LAB is $36'$). On the other hand, SFD contains no velocity information, so it is impossible to break the map into Galactocentric rings. Nevertheless, it is instructive to employ the SFD map to build a very simple foreground model. The goal is to remove foregrounds in a fashion that reveals the underlying structure with as few physical assumptions as possible. In Fig. 3, we show the full sky residual maps at 1–5 and 5–50 GeV after subtracting the SFD dust and the disk model to best reveal the *Fermi* bubble features. Although photon Poisson noise is much greater in the 5–50 GeV map, we identify a *Fermi* bubble structure morphologically similar to the structure in the 1–5 GeV map, present both above and below the Galactic plane.

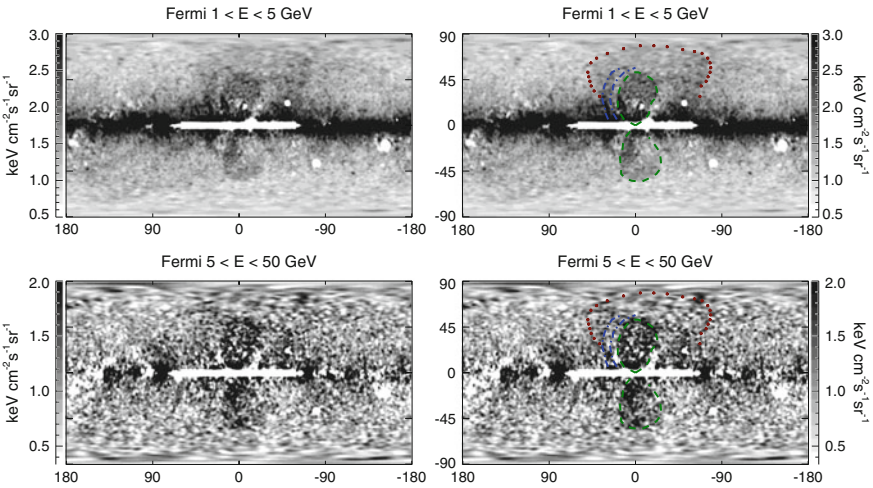

Fig. 3 Full sky residual maps after subtracting the SFD dust and disk templates from the *Fermi*-LAT 1.6 year gamma-ray maps in two energy bins. Point sources are subtracted, and large sources, including the inner disk ($-2^\circ < b < 2^\circ, -60^\circ < \ell < 60^\circ$), have been masked. Two large bubbles are seen (spanning $-50^\circ < b < 50^\circ$) in both cases. *Right panels*: Apparent *Fermi* bubble features marked in color lines, overplotted on the maps displayed in the *left panels*. *Green dashed circles* above and below the Galactic plane indicate the approximate edges of the north and south *Fermi* bubbles respectively. Two *blue dashed arcs* mark the inner (*dimmer*) and outer (*brighter*) edges of the *northern arc* – a feature in the northern sky outside the north bubble. The *red dotted line* approximately marks the edge of *Loop I* [37]

The third approach is taking advantage of the lower energy band 0.5–1.0 GeV *Fermi* map to form a template of a diffusion emission model. It is shown in [37] that the 0.5–1 and 2–50 GeV residual maps after subtracting only the SFD dust map as a template of foreground π^0 gammas. The residual maps should be dominated by IC emission from CR electrons interacting with the ISRF. One can use the 0.5–1 GeV maps as a template of IC emission from high energy electrons scattering *starlight*, and subtract the template from higher energy maps. The *Fermi* bubble is mostly from high energy electron CRs IC scattering on CMB photons, and IR photons at higher energies, which is robust to quite different foreground subtractions.

3 Morphology and Energy Spectrum of the Fermi Bubble

In the *right* panels of Fig. 3, we illustrate the edges of the *Fermi* bubbles and some other features. The *Fermi* bubble has distinct sharp edges, rather than smoothly falling off as modeled in [13]. Besides the two bubbles symmetric with respect to the Galactic plane, we find one giant *northern arc* that embraces half of the north bubble, that extends from the disk up to $b \sim 50$, with ℓ ranging from roughly -40° to 0°. It has a brighter and sharper outer edge in the 1–5 GeV map. On a even larger

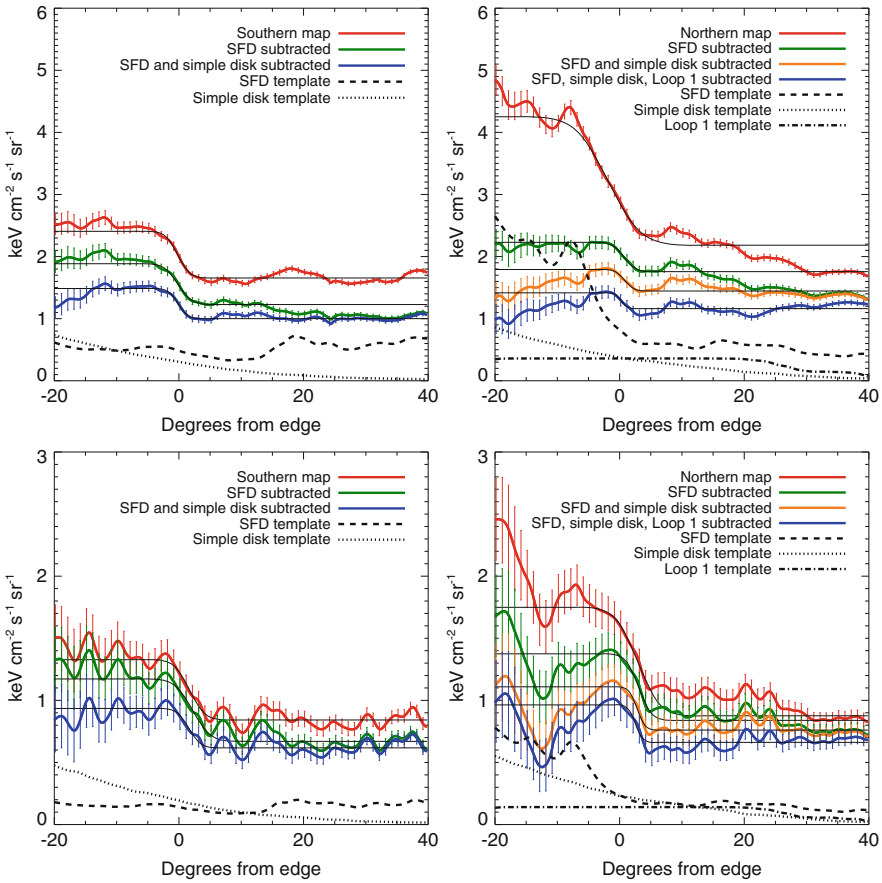

Fig. 4 Intensity as a function of radial distance from the bubble edge, averaged over great circle arcs intersecting the bubble center and lying at $|b| > 28°$. Results are shown for (*left*) the southern bubble, and (*right*) the northern bubble, for (*top*) the averaged 1–2 and 2–5 GeV maps, and (*bottom*) the averaged 5–10 and 10–20 GeV maps. Different lines show the results at different stages of the template regression procedure and the corresponding errors are plotted (see text for an outline of the error analysis) [37]

scale, a fainter structure has been identified extended up to $b \sim 80°$, with ℓ ranging from roughly $-80°$ to $50°$. This large extended structure corresponds to the *North Polar Spur* emission associated with *Loop I* [19].

To illustrate the sharp edges of the bubbles at high latitude more carefully, we show the (projected) intensity profiles along arcs of great circles passing through the estimated centers of the north and south bubbles, and intersecting the bubble edge (as defined in Fig. 3) at $|b| > 28°$. The results are shown in Fig. 4 for the averaged $(1-2)+(2-5)$ GeV maps, and the averaged $(5-10)+(10-20)$ GeV maps. In both energy ranges the edges are clearly visible; in the south, this is true even before

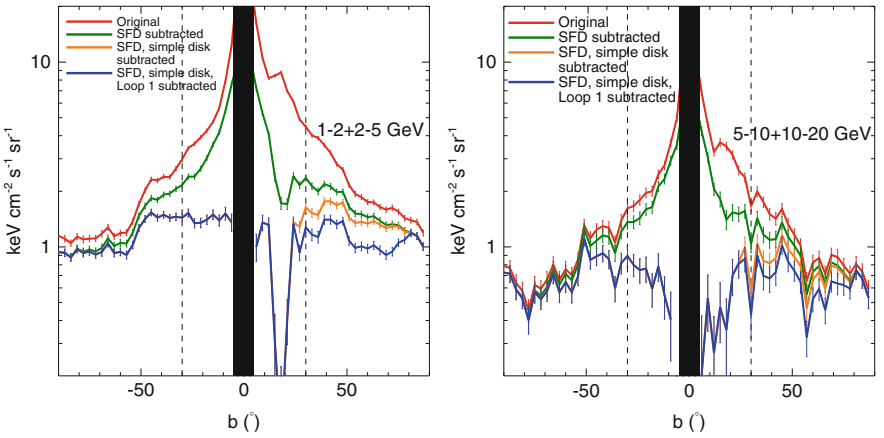

Fig. 5 Intensity averaged over the central 20° in longitude, as a function of latitude, for (*left*) the averaged 1–2 and 2–5 GeV maps, and (*right*) the averaged 5–10 and 10–20 GeV maps. Great circle arcs have been constructed which are perpendicular to the $l = 0$ great circle, extending 10° in each direction (east and west), and the emission is averaged over each such arc; the "b" label corresponding to each arc, and the x-axis of the plot, refers to the value of b at $l = 0$. Different lines show the results at different stages of the template subtraction process. The large oversubtraction at $b \sim 15°$ in the north, especially pronounced in the low-energy data, is associated with a bright feature in the SFD dust map [37]

any templates are subtracted. The intensity profile of the north bubble is strikingly similar to profile of the south bubble. For both of the north and south bubbles, no significant edge-brightening or limb-brightening of the bubbles is apparent from the profiles, the flux is fairly uniform inside the bubbles. In Fig. 5, the intensity profile is shown as a function of latitude from the south to the north pole. We construct great circle arcs perpendicular to the $l = 0$ great circle, extending 10° in each direction (east and west), and average the emission over each such arc. The flatness of the bubbles with latitude (except possibly close to the Galactic plane), and the sharp edges at high latitude, are also revealed (Fig. 6).

Besides the sharp edge of the *Fermi* bubble, its hard energy spectrum is also intriguing. In order to reveal the hardness of the spectrum of the *Fermi* bubbles, and quantitatively study the intensity flatness of the bubble interiors, a careful regression template fitting has been done in [37] by maximizing the Poisson likelihood of a simple diffuse emission model involving 5-templates. The template-correlated spectra for the 5-template fit are shown in Fig. 7. The fitting is done with regions of $|b| > 30°$. In this figure, we show spectra for π^0 emission, bremsstrahlung and inverse Compton scattering calculated using a sample `GALPROP` model (tuned to match locally measured protons and anti-protons as well as locally measured electrons at $\sim 20 - -30$ GeV), as an indication of the expected spectral shapes. The spectra for the SFD and the simple disk template reasonably match the model expectations. The dust map mostly traces the π^0 emission, and the simple disk model resembles a combination of IC and bremsstrahlung emission. The spectrum

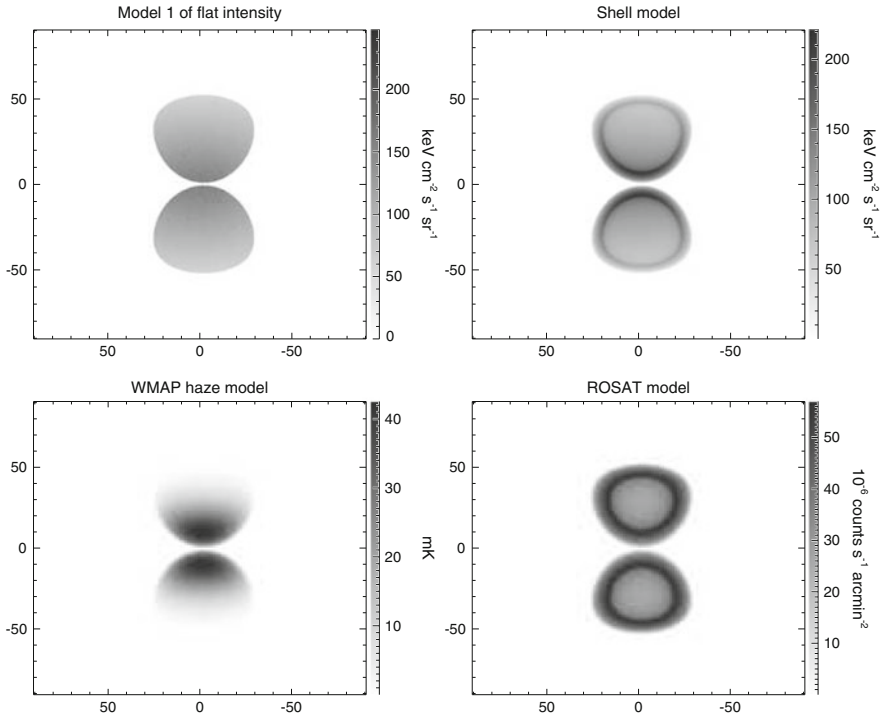

Fig. 6 Projected emission from four emissivity distributions to illustrate the qualitative features of each. *Top left*: A toy model of the *Fermi* bubbles with flat projected intensity. In this model, the volume emissivity (assuming the ISM is optically thin to gamma rays) is proportional to $(R^2 - r^2)^{-1/2}$ for $r < R$, and zero otherwise, where $R = 3.5\,\mathrm{kpc}$ is the approximate radius of the two bubbles, and r is the distance to the center of the north or south bubble. *Top right*: A bubble model with compressed gas shells with a thickness of 0.5 kpc; the electron CR density in the shell is a factor of 5 higher than in the interior of the bubbles. For this model, a limb-brightened edge of the bubbles is clearly visible, a feature which is not seen in the *Fermi* data. *Bottom left*: An illustrative toy model for the *WMAP* haze. The haze synchrotron emissivity depends on the electron CR density and the magnetic field; here we take $B = B_0 e^{-z/z_0}$, where $z_0 = 2\,\mathrm{kpc}$, and show the line of sight integral of this B-field through bubble volume. Even though the synchrotron emissivity is not simply the product of CR density times field strength, this panel suggests that the decreasing intensity of the *WMAP* haze at high latitudes is due to the decay of the Galactic magnetic field away from the Galactic plane. *Bottom right*: A toy model for the *ROSAT* X-ray features. The observed soft X-rays are limb-brightened and we assume all gas is uniformly distributed within a compressed shell, with no contribution from the interior, and X-ray emission is proportional to the gas density squared. The thickness of the shell is 1 kpc [37]

for emission correlated with the *Fermi* bubbles is clearly significantly harder than either of these components, consistent with a *flat* spectrum in $E^2 dN/dE$. This fact coupled with the distinct spatial morphology of the *Fermi* bubbles indicates that the IC bubbles are generated by a *separate* electron component. We also note that the spectrum of the bubble template falls off significantly at energy $< 1\,\mathrm{GeV}$. This

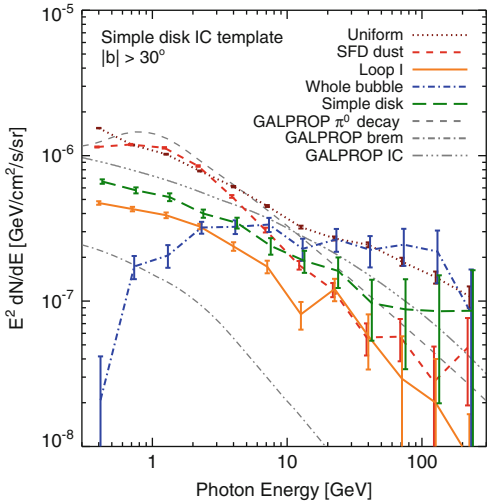

Fig. 7 Correlation spectra for the 5-template fit employing a simple disk model for the IC (and to a lesser degree bremsstrahlung) emission from supernova-shock-accelerated electrons. The SFD-correlated spectrum is shown by the *red short-dashed line* which roughly traces π^0 emission (the *gray dashed line* indicates a GALPROP prediction for π^0 emission). The disk-correlated emission is shown by the *green dashed line*, which traces the soft IC (*gray triple-dot-dashed line*) and bremsstrahlung (*gray dot-dashed line*) component. The spectrum of the uniform emission, which traces the isotropic background (including possible cosmic-ray contamination), is shown as a *dotted brown line*. The *solid orange line* indicates the spectrum of emission correlated with *Loop I*, which has a similar spectrum to the disk-correlated emission. Finally, the *blue dot-dashed line* shows the spectrum correlated with the *Fermi* bubble template. The bubble component has a notably harder (consistent with flat) spectrum than the other template-correlated spectra, and the models for the various emission mechanism generated from GALPROP, indicating that the *Fermi* bubbles constitute a distinct component with a hard spectrum. The fitting is done over the $|b| > 30°$ region. Note that these GALPROP "predictions" are intended only to indicate the expected spectral shape for these emission components, for reference. The correlation coefficients for the SFD map and simple disk model are multiplied by the average value of these maps in the bubble region to obtain the associated gamma-ray emission [37]

feature is robust with respect to the choice of templates. The significant isotropic background is due to extra-galactic emission and charged particle contamination, including heavy nuclei at high energies. The *Fermi* collaboration has measured the extragalactic diffuse emission using additional cuts to reduce charged particle contamination [1]: below $\sim$ 20 GeV the isotropic contribution in our fits is roughly a factor of 2 larger than the extragalactic diffuse emission, but has a similar spectral slope. At energies above $\sim$ 20 GeV the isotropic contribution becomes much harder, which we attribute to charged particle contamination. Using the *Fermi* 0.5–1 GeV residual map (after subtracting the SFD dust map to largely remove the π^0 gammas) as a template of IC emission, similar results have been obtained [37].

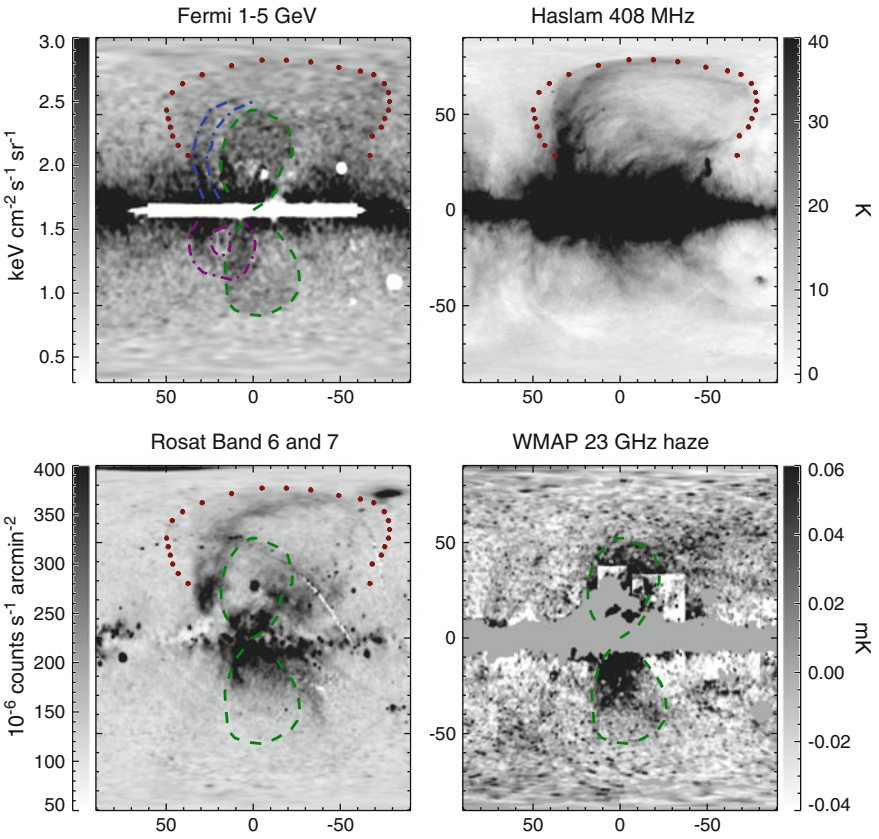

Fig. 8 Comparison of the *Fermi* bubbles with features in other maps. *Top left*: Point-source subtracted 1–5 GeV *Fermi*-LAT 1.6 year map with north and south bubble edges marked with *green dashed line*, and *north arc* in *blue dashed line*. The approximate edge of the *Loop I* feature is plotted in *red dotted line*. *Top right*: The Haslam 408 MHz map overplotted with the same *red dotted line* as the *top left panel*. The *red dotted line* remarkably traces the edge of the bright *Loop I* feature in the Haslam soft synchrotron map. *Bottom left*: the *ROSAT* 1.5 keV X-ray map is shown together with the same color lines marking the prominent *Fermi* bubble features. *Bottom right*: *WMAP* haze at K-band 23 GHz overplotted with *Fermi* bubble edges. The *ROSAT* X-ray features and the *WMAP* haze trace the *Fermi* bubbles well, suggesting a common origin for these features [37]

4 The *Fermi* Bubbles Seen in Other Maps

After a careful search in X-rays, we found interesting large scale feature in *ROSAT* 1.5 keV soft X-ray map, which lines up with the *Fermi* bubbles. The striking similarities of these morphological features, including the *WMAP* microwave haze, strongly suggest a common physical origin for the *Fermi* bubbles, *WMAP* haze, and X-ray edges towards the GC [37] (Fig. 8).

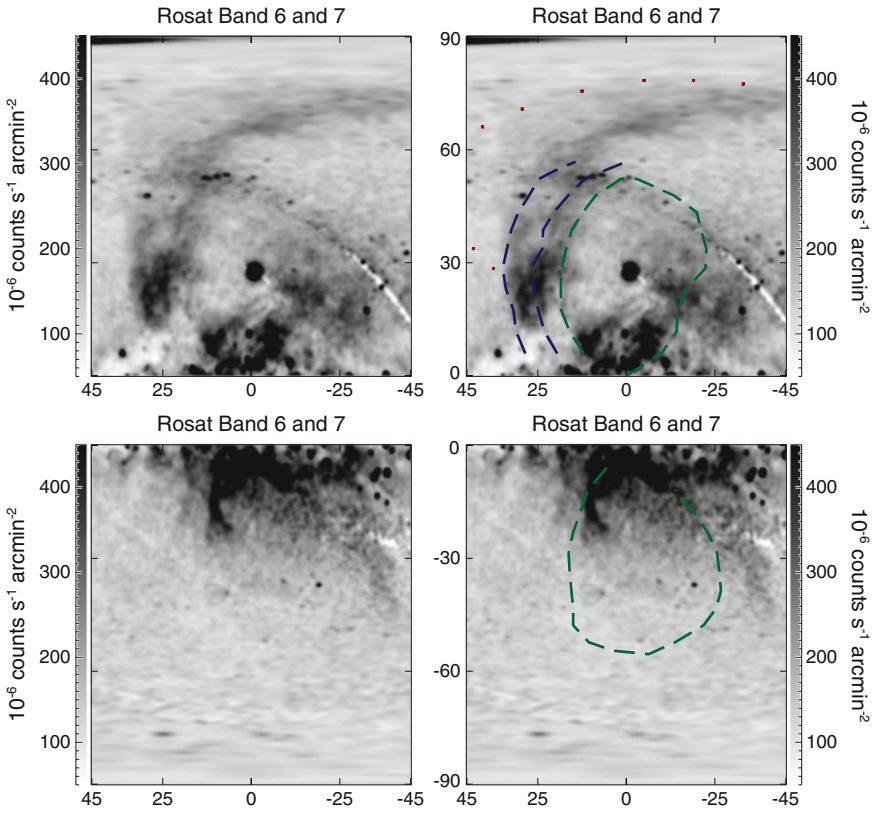

Fig. 9 *Top left*: The *ROSAT* X-ray haze features compared with the *Fermi* bubbles' morphology. *Top row*: The X-ray features of *ROSAT* band 6 and 7 in the north sky towards to the GC (*left panel*) compared with *Fermi* north bubble overplotted with *green dashed line*, *northern arc* feature in *blue dashed line*, and *Loop I* feature in *red dotted line* (*right panel*). *Bottom row*: Same as *top row* but for the south bubble features [37]

4.1 Comparison with ROSAT *X-Ray Features*

The *ROSAT* all-sky survey provides full-sky images at energies from 0.5 to 2 keV.[4] We compare the morphology of the X-ray features in *ROSAT* 1.5 keV map with the edges of the *Fermi* bubbles in detail in Fig. 9. The limb brightened X-ray features align with the edges of both the north and south *Fermi* bubble. Hints of the whole north bubble are also visible in *ROSAT*, as well as two sharp edges in the south that trace the south *Fermi* bubble close to the disk. We show the *ROSAT* 1.5 keV

[4] http://hea-www.harvard.edu/rosat/rsdc.html

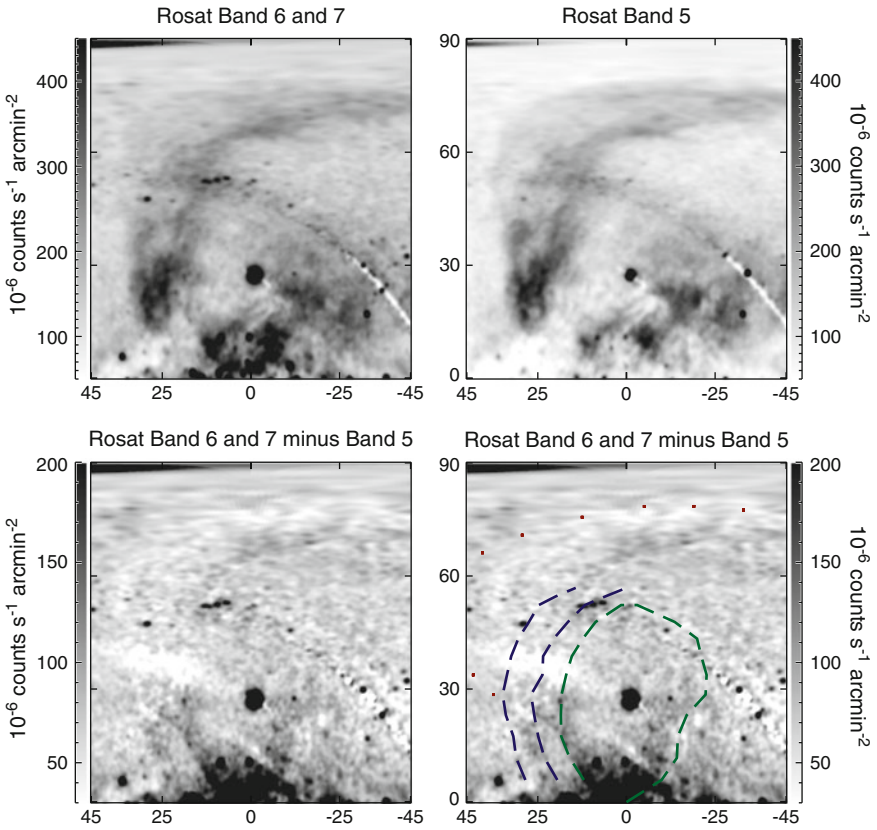

Fig. 10 *Top left*: The *ROSAT* X-ray features in Band 6 and 7. *Top right*: The same region as the *left panel*, but for the *ROSAT* X-ray map in band 5. *Bottom left*: The residual X-ray features after subtracting the *top right* softer Band 5 map from the *top left* harder Band 6 and 7 map. *Bottom right*: The same as the *bottom left panel*, overplotted with the *Fermi* bubble features, the *northern arc*, and *Loop I* features. The residual X-ray features with harder spectrum than the diffuse *Loop I* feature align well with the *Fermi* bubble structures [37]

map overplotted with the edges of the *Fermi* bubbles, the *northern arc*, the *Loop I* features in the *right* panels of Fig. 9. The appearance of the X-ray edges in the *ROSAT* 1.5 keV map, coincident with the *Fermi* bubble edges, strongly supports the physical reality of these sharp edges.

In Fig. 10, we subtract the *ROSAT* 1.0 keV soft X-ray map from the 1.5 keV map to clean up the foreground. We find that the extended *Loop I* feature has a softer spectrum than the X-ray features associated with the bubble edges, and is largely removed in the difference map (*lower left* panel of Fig. 10). The residual features strikingly overlap with the edges of the *Fermi* bubbles (*lower right* panel). No other noticeable large scale features appear in the residual X-ray map which do not appear in the gamma-rays.

4.2 Comparison with WMAP Microwave Haze

The *WMAP* haze is the residual remaining in *WMAP* microwave data after regressing out contributions from thermal dust, free-free, and "soft synchrotron" traced by the Haslam 408 MHz radio survey [19]. Therefore, it is by construction harder than the Haslam-correlated emission. Figure 11 shows a detailed morphological comparison of the south *Fermi* bubble at 1–5 GeV with the southern part of the *WMAP* microwave haze at 23 GHz (K-band). The edge of the *Fermi* bubbles, marked in green dashed line in the *top right* and *lower right* panels, closely traces the edge of the *WMAP* haze. The smaller latitudinal extension of the *WMAP* haze may be due to the decay of the magnetic field strength with latitude. These striking morphological similarities between the *WMAP* microwave haze and *Fermi* gamma-ray bubble can be readily explained if the *same* electron CR population is responsible for both excesses, with the electron CRs interacting with the galactic magnetic field to produce synchrotron, and interacting with the ISRF to produce IC emission.

Besides the similarity of the morphology, the relatively hard spectrum of the *Fermi* bubble also motivates a common physical origin with the *WMAP* haze. Let's simply estimate the microwave synchrotron and gamma-ray ICS signals from one single population of hard electrons distributed in the inner Galaxy, which is helpful to demonstrate that the magnitudes and spectral indices of the two signals are consistent for reasonable parameter values.

For a highly relativistic electron scattering on low energy photons, the spectrum of upscattered photons is given by Blumenthal and Gould [7] and Cholis et al. [9],

$$\frac{dN}{dE_\gamma d\epsilon dt} = \frac{3}{4}\sigma_T c \frac{(m_e c^2)^2}{\epsilon E_e^2}\big(2q\log q + (1+2q)(1-q) + 0.5(1-q)(\Gamma q)^2/(1+\Gamma q)\big) n(\epsilon), \tag{1}$$

$$\Gamma = 4\epsilon E_e/(m_e c^2)^2, \quad q = \frac{E_\gamma}{E_e}\frac{1}{\Gamma(1-E_\gamma/E_e)},$$
$$\epsilon < E_\gamma < E_e\Gamma/(1+\Gamma).$$

Here ϵ is the initial photon energy, E_e is the electron energy, E_γ is the energy of the upscattered gamma ray, and $n(\epsilon)$ describes the energy distribution of the soft photons per unit volume. Where $\Gamma \ll 1$, in the Thomson limit, the average energy of the upscattered photons is given by,

$$\langle E_\gamma \rangle = (4/3)\gamma^2 \langle \epsilon \rangle, \tag{2}$$

where $\gamma = E_e/m_e c^2$ is the Lorentz boost of the electron. In the Klein-Nishina (KN) limit, $\Gamma \gg 1$, the spectrum instead peaks at the high energy end, and the upscattered photon carries away almost all the energy of the electron.

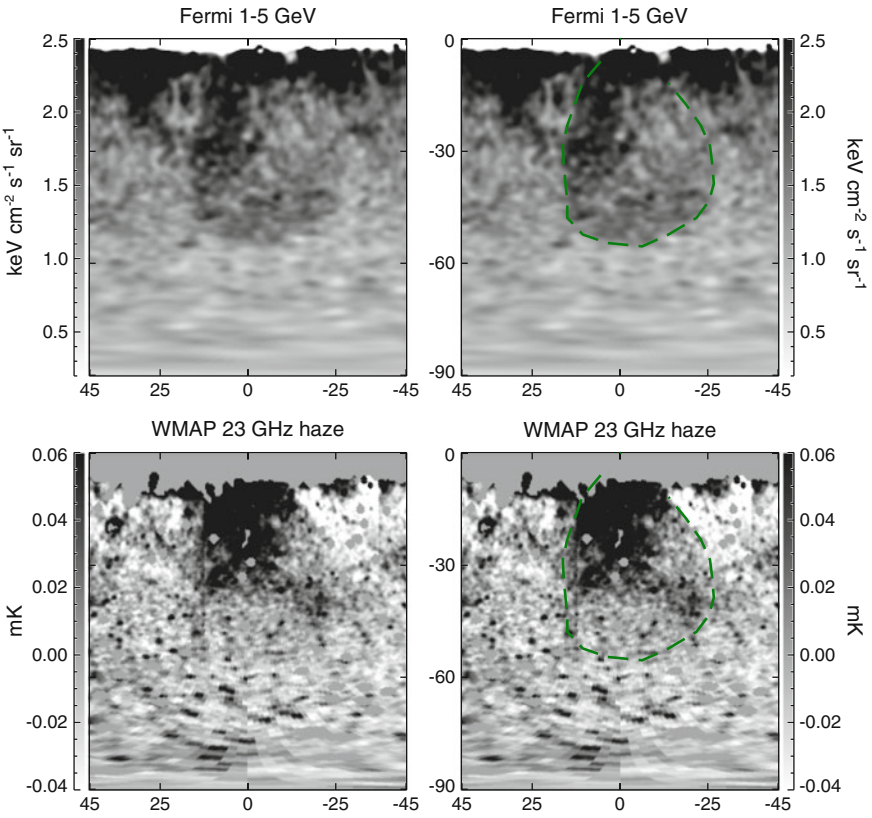

Fig. 11 The *Fermi* bubbles at 1–5 GeV (the residual map obtained by subtracting the SFD dust map and the disk template) compared with the *WMAP* K-band (23 GHz) haze [12]. *Top row*: The 1–5 GeV map with $\ell = [-45°, 45°]$ and $b = [-90°, 0°]$ (*left panel*) with the *Fermi* south bubble edge overplotted in *green dashed line* (*right panel*). *Bottom row*: Same sky region as *top row* but displaying the *WMAP* haze at 23 GHz (*left panel*), with the *Fermi* south bubble edge overplotted in *green dashed line* (*right panel*) [37]

Given a power law steady-state electron spectrum with spectral index γ, the spectral index of the IC scattered gamma rays is $(\gamma + 1)/2$ in the Thomson limit, and $\gamma + 1$ in the extreme KN limit [7]. Photons in the *Fermi* energy range can be produced by scattering of $\mathcal{O}(10 - 100)$ GeV electrons on starlight, which is (marginally) in the KN regime, or by Thomson scattering of much higher-energy electrons on IR or CMB photons. Consequently, the spectral index of gamma rays might be expected to vary with latitude even if the electron spectral index is uniform, becoming harder at higher latitudes where scatterings in the Thomson limit dominate. Closer to the disk, where much of the ISRF energy density is in starlight, IC scatterings are in neither the extreme KN nor Thomson limits, and the spectrum needs to be computed carefully.

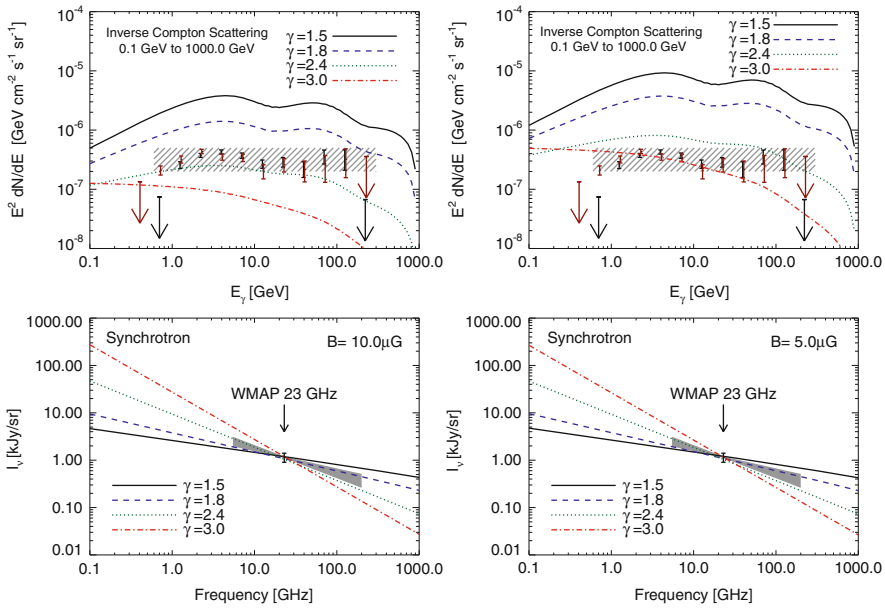

Fig. 12 The estimated spectrum of IC gamma rays (*upper panel*) and synchrotron radiation (*lower panel*) originating from a hard electron spectrum along a line of sight 4 kpc above the Galactic center (i.e. $b \approx 25°$). The steady-state electron spectrum is taken to be a power law, $dN/dE \propto E^{-\gamma}$, with index $\gamma = 1.5$ (*solid black*), 1.8 (*blue dashed*), 2.4 (*green dotted*), and 3.0 (*red dash-dotted*). In all cases the spectrum has a range of [0.1, 1,000] GeV. The interstellar radiation field model is taken from GALPROP version 50p, and the magnetic field is set to be 10 μG for the *left panel* and 5 μG for the *right panel*. The data points in the *upper panels* show the magnitude of the bubble emission obtained from template fitting in Figs. 7 (*brown*) and 13 (*black*) including the "whole bubble" template, as a function of energy. The lowest and highest bins contain 3σ upper limits rather than data points with 1σ error bars, due to the large uncertainties in the haze amplitude at those energies. For reference, a rectangular cross hatch region shows a approximate spectrum in the same place in this and subsequent figures. The data point in the *lower panel* shows the magnitude of the *WMAP* haze averaged over $b = -20°$ to $-30°$, for $|\ell| < 10°$, in the 23 GHz K-band (the overall normalization is chosen to fit this value), and the *gray area* indicates the range of synchrotron spectral indices allowed for the *WMAP* haze by Dobler and Finkbeiner [12]. The same population of hard electrons can consistently generate the *WMAP* synchrotron haze and *Fermi* ICS bubbles [37]

Let's consider a steady-state electron spectrum described by a power law, $dN/dE \propto E^{-\gamma}$, with energy cutoffs at 0.1 and 1,000 GeV. For a region $\sim$ 4 kpc above the Galactic center, we normalize the synchrotron to the approximate value measured by *WMAP* in the 23 GHz K-band [20], $\sim 25°$ below the Galactic plane, and compute the corresponding synchrotron and IC spectra. The *WMAP* haze was estimated to have a spectrum $I_\nu \propto \nu^{-\beta}$, $\beta = 0.39 - 0.67$ [12], corresponding approximately to an electron spectral index of $\gamma \approx 1.8 - 2.4$; Fig. 12 shows the

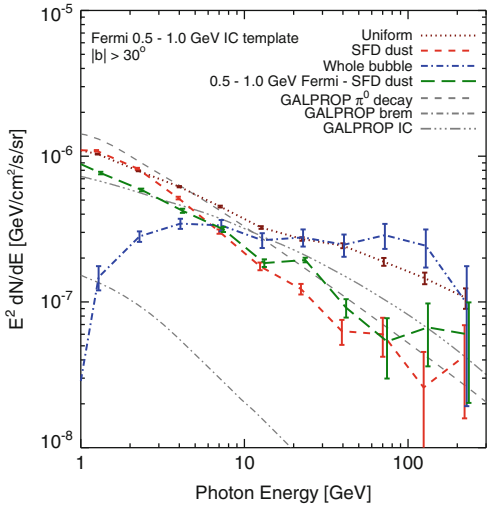

Fig. 13 Same as Fig. 7, but correlation spectra for the 4-template fit employing the *Fermi* 0.5–1 GeV residual map (after subtracting the SFD dust) as a template for the *starlight* IC. The line style is the same as Fig. 7. It is shown that the spectrum correlated with the *Fermi* bubble template (*blue dot-dashed line*) is harder (consistent with flat in E^2dN/dE) than the spectra correlated with the other templates, and the models for the various emission mechanism generated from GALPROP, indicating that the *Fermi* bubbles constitute a distinct gamma-ray component with a hard spectrum. The fitting is done for $|b| > 30°$. As in Fig. 7, the correlation spectra have been normalized to a reference region [37]

calculation for a magnetic field of 10 and 5 μG at 4 kpc above the GC, and electron spectral indices $\gamma = 1.8 - 3$. We can see the good agreement in the case of $\alpha \approx 2 - 2.5$, consistent with the spectrum of the *WMAP* haze.

In the default GALPROP exponential model for the Galactic magnetic field, $|B| = |B_0|e^{-z/z_s}$ with scale height $z_s \approx 2$ kpc, this field strength would correspond to $B_0 \approx 30 - 40\,\mu$G or even higher. This value is considerably larger than commonly used [27]. However, models with a non-exponential halo magnetic field, as discussed by e.g. [2, 38], can have $\sim 10\,\mu$G fields well off the plane.

It's important to note that the extrapolated value of B_0 required to obtain good agreement between the IC and synchrotron amplitudes, in the exponential model, is somewhat higher than found by Dobler et al. [13], who performed the comparison at 2 kpc. This apparent discrepancy originates from the fact that in the haze latitudinal profile given by Hooper et al. [20], the emission falls off rapidly with latitude for $0 > b > -15°$, but then plateaus at $b \sim -15 - 35°$, contrary to expectations based on a B-field profile exponentially falling away from $z = 0$. This suggests either that the magnetic field inside the bubble does not fall exponentially with $|z|$ inside the bubbles, or that the *WMAP* haze contains a significant free-free component at high latitude.

5 Interpretation

The *Fermi* bubbles seem most likely to originate from IC scattering, since the required electron CR population can also naturally generate the *WMAP* haze as a synchrotron signal. The *ROSAT* X-ray measurements suggest that the bubbles are hot and hence *underdense* regions, and thus argue against the gamma rays originating from bremsstrahlung or π^0 decay.

Even though the material in the bubbles is likely high pressure, it is also probably very hot ($\sim 10^7$ K) and has lower gas density than the ambient ISM. This would explain why the *ROSAT* 1.5 keV map shows a "cavity" of soft X-rays toward the center of the *Fermi* bubble structure, like the X-ray cavity in galaxy clusters [26], especially in the north *Fermi* bubble. Furthermore, allowing the *Fermi* bubbles to have lower density than the ambient medium means they would experience a buoyant force moving the bubble material away from the GC, which may help generate the observed morphology. Because π^0 and bremsstrahlung gamma-ray emission both scale as the CR density × the gas density, an underdense region cannot be brighter unless the cosmic ray densities are greatly increased to compensate; for protons, in particular, the propagation lengths are great enough that a proton overdensity cannot reasonably explain the sharp bubble edges observed in the data, if the bubbles are in a steady state.

If the bubbles are expanding rapidly and highly accelerated protons responsible for the gamma-ray emission are trapped behind shock fronts, then sharp edges for the *Fermi* bubbles could occur naturally. However, in the presence of such a shock, electrons would also be accelerated, and would generally produce more gamma-rays than the protons via ICS (since the cooling time for electron CRs is much shorter than the cooling time for proton CRs of comparable energy).

It might be thought that the presence of a bright X-ray edge could lead to a sharp edge in the gamma-ray signal, via IC scattering of electron CRs on the X-ray photons. In the Thomson limit, the energy of IC scattered photons is of order $(\Gamma_e/2)E_e$, with $\Gamma_e = 4E_eE_\gamma/m_e^2$ (where E_γ and E_e are the initial photon and electron energies, respectively, and m_e is the electron mass), and the scattering cross section is independent of the initial electron and photon energies. Thus a higher-energy photon population, leading to a larger value of Γ_e, allows IC gamma-rays at a given energy to originate from lower-energy electrons, which are much more abundant for typical electron spectra with $dN/dE \sim E^{-\gamma}$, $\gamma > 2$. However, in the Klein-Nishina regime where $\Gamma_e > 1$ this picture changes: the energy of scattered photons is determined mostly by the energy of the initial electron, and the cross section scales as $1/\Gamma_e$. Scatterings of ~ 50 GeV electrons already produce ~ 10 GeV gamma rays; when compared to the scattering of 10 GeV electrons on X-rays in the extreme KN limit, the KN suppression of the cross section in the latter case more than counteracts the greater abundance of ~ 10 GeV electrons, unless the electron spectrum is very soft (which is inconsistent with the observed signal).

Similarly, the elongated shape of the *Fermi* bubble structures perpendicular to the Galactic plane suggests that the electron CR distribution itself is extended perpendicular to the plane. The *Fermi* bubble morphology is a strong argument against the

possibility that the *WMAP* haze originates from a disk-like electron distribution with significant longitudinal variation of the magnetic field, as suggested by Kaplinghat et al. [23].

The limb brightening of the X-rays in the *ROSAT* data (as shown in Fig. 9), and the flat intensity profile of the *Fermi* bubbles, suggest the presence of a shell or shock, with increased electron CR density, coinciding with a hot thermal plasma. If the ambient medium several kpc above and below the GC were neutral, then bubbles of ionized gas could produce a void in the H I map. We see no evidence for features aligned with the bubbles in these maps, suggesting that the H I map in this part of the sky is dominated by disk emission, and has nothing to do with the bubbles. If the bubbles are in a static state, the bubble edges should have lower temperature than the bubble interior and thus higher gas density, although shocks or MHD turbulence might lead to higher temperatures at the bubble wall. The X-rays in *ROSAT* may be thermal bremsstrahlung emission, so the emissivity is proportional to the thermal electron density $\times$ ion density. They could also arise from charge exchange reactions occurring when the high-speed gas in the bubbles collides with the denser gas at the bubble edge [31]; this mechanism could explain the pronounced limb brightening of the X-rays. As an alternative explanation, the *ROSAT* X-ray feature might be synchrotron emission from *very high* energy electron CRs. Typically, though, one needs $\sim$ 50 TeV ($\sim$ 5 TeV) electrons with $\sim$ 10 μG (1 mG) magnetic field to produce $\sim$ 1 keV synchrotron photons.

The *Fermi* bubble features do *not* appear to be associated with *Loop I*, a giant radio loop spanning over 100° [25], which is thought to be generated from the local *Sco-Cen* OB association. Detections of *Loop I* in high-energy gamma-rays have been claimed by Bhat et al. [4] and also recently by *Fermi* [8].

The *Fermi* bubbles are morphologically and spectrally distinct from both the π^0 emission and the IC and bremsstrahlung emission from the disk electrons. The *Fermi* bubbles have a distinctly hard spectrum, $dN_\gamma/dE \sim E^{-2}$, with no evidence of spatial variation across the bubbles. As shown in Fig. 12, an electron population with $dN_e/dE \sim E^{-2-2.5}$ is required to produce these gamma rays by IC scattering: this is comparable to the spectrum of electrons accelerated by supernova shocks or polar cap acceleration [5]. However, diffusive propagation and cooling would be expected to soften the spectrum, making it difficult to explain the *Fermi* bubbles by IC scattering from a steady-state population of these electrons (a single brief injection of electrons with $dN/dE \sim E^{-2}$ could generate a sufficiently hard spectrum for the bubbles *if* there was a mechanism to transport them throughout the bubble without significant cooling). The facts strongly suggest that a distinct electron component with a harder spectrum than steady-state SNR generated electrons is responsible for the *Fermi* bubbles and associated signals in the *WMAP* and *ROSAT* data.

How could the electron CRs possess the same hard spectrum everywhere within the bubble and extend up to 10 kpc, while experiencing a steep fall-off at the bubble edge? A large population of CRs might be entrained in large scale Galactic outflows from the GC and enrich the bubbles. CRs could be produced along with jets, or shock accelerated CRs from magnetic reconnection inside the bubble or near its surface. However, it is challenging to produce a flat intensity profile for the bubble

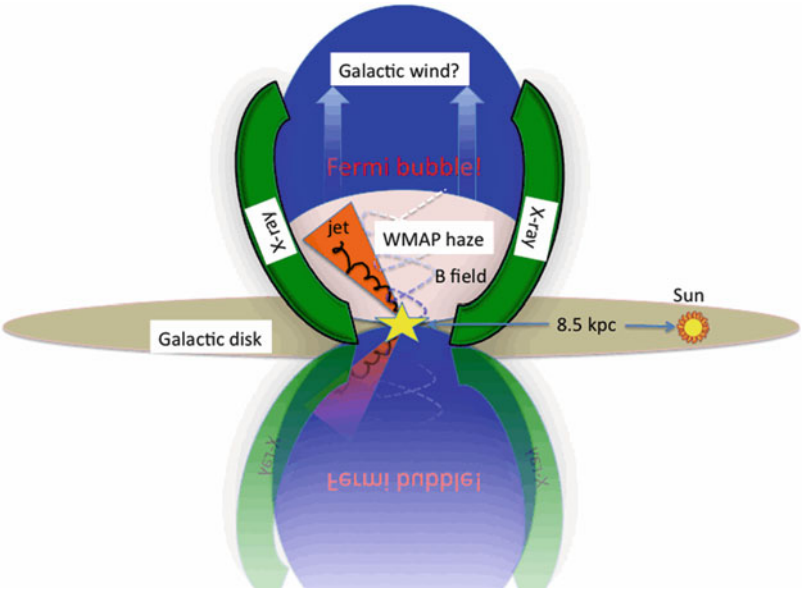

Fig. 14 A cartoon picture to summarize the observations of the *Fermi* bubble structures. Two blue bubbles symmetric to the Galactic disk indicate the geometry of the gamma-ray bubbles observed by the *Fermi*-LAT. Morphologically, we see corresponding features in *ROSAT* soft X-ray maps, shown as green arcs embracing the bubbles. The *WMAP* haze shares the same edges as the *Fermi* bubbles (the pink egg inside the blue bubbles) with smaller extension in latitude. These related structures may have the same physical origin: past AGN activities or a nuclear starburst in the GC (the yellow star) [37]

interior with a sharp edge. The ambient gas should be compressed to a higher density on the shell by shocks (probably also enhancing the magnetic field), and brighter synchrotron emission on the shell would then be expected, but the haze emission observed in *WMAP* is not limb-brightened and shows no evidence for a shell of finite thickness (although we do see shell structure in the X-rays). A cartoon picture summarizing the morphology of the *Fermi* bubbles and associated signals at other wavelengths is shown in Fig. 14.

6 AGN or Starburst Origin?

The *Fermi* bubble structures were likely created by some large episode of energy injection in the GC, such as a past accretion event onto the central MBH, or a nuclear starburst in the last ~ 10 Myr. We have discussed some general possibilities and considerations in this work, and found shortcomings in each scenario; it seems likely that either significant modifications to one of these ideas, or some combination of different mechanisms, will be necessary. Jets originating from AGN activity can potentially accelerate CR electrons to high energies, and transport them

rapidly away from the GC; the cooling time of electrons at 100–1,000 GeV is only 10^{5-6} years, so if the CRs are injected and accelerated only in the GC, a very fast bulk transport mechanism is required to convey them throughout the bubbles before they lose a significant fraction of their energy. However, filling the bubbles completely, with $n = 10^{-2}\,\mathrm{cm}^{-3}$ gas, would require a mass injection of $\sim 10^8$ solar masses, so in any case it is more reasonable for the bulk of the material in the bubbles to be swept up and accelerated as the bubbles expand. Energetic shocks associated with jets can have high Mach number and thus efficiently accelerate CR electrons, producing hard spectra with $dN/dE \sim E^{-2}$, and the total energy required to heat the bubbles is also readily achievable by accretion events onto the central MBH. However, the north-south symmetry of the bubbles has no obvious explanation in the context of an AGN jet: there is no reason for one jet to be oriented perpendicular to the Galactic plane. The large width and rounded shape of the bubbles are also not typical of jets, which are generally much more collimated, although a precessing jet might help explain the wide opening angle of the bubbles. If the central MBH becomes active on a relatively short timescale, the *Fermi* bubbles may be created by a number of past jets, which combine to give rise to the symmetric and uniform *Fermi* bubbles.

An alternate source for the large required energy injection is a nuclear starburst. The wide opening angle of the bubbles is not a problem in this case; the bubble shape is similar to that observed in NGC 3079, and the X-ray features observed by *ROSAT* are similar to those observed in other nearby starburst galaxies. However, no corresponding Hα signal of the *Fermi* bubbles is observed, in contrast to other known starburst galaxies: this problem might potentially be resolved if the Hα-emitting gas has cooled in the time since the starburst phase (gas hot enough to emit the X-rays observed by *ROSAT* has a considerably longer cooling time). Also, generally gas filaments and clumps are observed in the X-rays in starburst galaxies, and it would seem that a relic of a past starburst should become more clumpy with gas clouds and filaments due to cooling of the gas. However, while no such structures are obvious in the *ROSAT* maps, the signal-to-noise is insufficient to place strong constraints. The absence of any such filamentary structures inside the *Fermi* bubbles, on the other hand, argues against a hadronic origin for the bubble gamma ray emission. Hadronic jets might accelerate protons to high energies, and the interactions of these protons with the ISM could then produce hard π^0 gammas and secondary e^+e^-, which would scatter on the ISRF to produce more gamma rays. In this scenario, however, the gamma ray emission should trace the gas density, which we would not expect to be smooth and homogeneous.

In the case of the starburst scenario, the cosmic ray acceleration would be due to shocks at the edge of the bipolar wind. However, the shocks expected in this scenario would be relatively weak and slow-moving, and thus may not be capable of generating a sufficiently hard electron spectrum to reproduce the signal. For example, in first-order Fermi acceleration, a shock Mach number of $\sim$ 3.3 is needed to obtain an electron spectral index of 2.4, as required for the synchrotron explanation of the *WMAP* haze (see e.g. [21]). The *Fermi* bubbles have sharp edges, also suggesting the presence of a shock at the bubble walls. If the CRs producing the

gamma rays have a multi-kpc diffusion length (which is not expected to be the case for 1 TeV electrons, for example), then the edges can still be sharp if the bubble edge is moving outward faster than they can diffuse. If we assume the *Fermi* bubbles are projected structures from three dimensional symmetric blobs towards the GC, the flat intensity profile of the bubbles requires the emissivity to rise at the bubble walls, but remain non-negligible in the bubble interior; the lack of spatial variation in the spectral index may also constrain models where the electrons diffuse long distances from an injection point. Magnetic reconnection in the interior of the bubbles, or some other mechanism such as dark matter annihilation, may help maintain a hard spectrum throughout the bubbles by accelerating existing lower-energy electrons or injecting electrons *in situ*.

Finally, dark matter annihilation or decay, while an effective mechanism for injecting hard electron CRs at high latitudes, cannot *by itself* produce the features in the *ROSAT* X-ray maps correlated with the bubbles, and would not be expected to result in sharp cutoffs in gamma-ray emission at the bubble edges. Large scale astrophysical outflows are required to transport CRs to high latitude and produce observed morphological features of *Fermi* bubbles. On the other hand, we'd like to keep the possibility that dark matter annihilation or decay may be *contributing* to the bubbles, or to gamma-ray emission towards the inner Galaxy that is not well subtracted by either the bubble structure template or the models for known diffuse emission mechanisms. We note that it's not reliable to put constraints on dark matter physics using observed gamma-ray intensity distribution/spectrum towards the Galactic center, as the presence of the *Fermi* bubble implying recent dynamical environment in the inner galaxy. Even if concentrated dark matter distribution produced CRs emitting observable gamma-rays, these CRs would be possibly entrained in the Galactic outflow to higher latitude. Detailed knowledge of the *Fermi* bubbles will be a necessary step before extracting any such dark matter signal.

In the future, The *eROSITA*[5] and *Planck*[6] experiments will provide improved measurements of the X-rays and microwaves, respectively, associated with the *Fermi* bubbles, and so may help discriminate between these scenarios. *eROSITA*, which is expected to launch in 2014, will provide the first imaging all-sky survey of mid-energy X-rays, studying the 0.2–12 keV energy range with $\sim$ 100 eV energy resolution and a PSF of $20''$. The *Planck* satellite, launched in 2009, will greatly improve the measurements of the *WMAP* haze spectrum, and may identify interesting bubble-related features in polarized microwave maps. Future space-borne gamma-ray observations with high energy resolution and large effective area will significantly improve our knowledge of the *Fermi* bubbles at higher energy.

Acknowledgements The author acknowledges Douglas Finkbeiner and Tracy Slatyer for their wonderful collaborations on the discovery paper of the *Fermi* bubbles. Most of the materials in this chapter is based on this paper. The author also acknowledges stimulating conversations with

[5] http://www.mpe.mpg.de/heg/www/Projects/EROSITA/main.html

[6] http://www.rssd.esa.int/index.php?project=Planck

Roland Crocker, Greg Dobler, Martin Elvis, Jonathan Grindlay, Fulai Guo, Christine Jones, Avi Loeb, Sera Markoff, Igor Moskalenko, Ramesh Narayan, Aneta Siemiginowska, Andrew Strong, and Feng Yuan. The author would also like to warmly thank Olaf Reimer and Diego Torres for organizing the 2nd Sant Cugat Forum on Astrophysics, "2012: Cosmic-ray phenomenology in star-forming environments", and their great effort to make the publication of this conference book possible.

References

1. Abdo, A. A., et al. 2010. The Spectrum of the Isotropic Diffuse Gamma-Ray Emission Derived From First-Year Fermi Large Area Telescope Data. Phys. Rev. Lett., 104:101101.
2. Alvarez-Muñiz, J., R. Engel, & T. Stanev 2002. Ultrahigh-Energy Cosmic-Ray Propagation in the Galaxy: Clustering versus Isotropy. ApJ, 572:185–201.
3. Atwood, W. B., A. A. Abdo, M. Ackermann, W. Althouse, B. Anderson, M. Axelsson, L. Baldini, J. Ballet, D. L. Band, G. Barbiellini, J. Bartelt, D. Bastieri, B. M. Baughman, K. Bechtol, D. Bédérède, F. Bellardi, R. Bellazzini, B. Berenji, G. F. Bignami, D. Bisello, E. Bissaldi, R. D. Blandford, E. D. Bloom, J. R. Bogart, E. Bonamente, J. Bonnell, A. W. Borgland, A. Bouvier, J. Bregeon, A. Brez, M. Brigida, P. Bruel, T. H. Burnett, G. Busetto, G. A. Caliandro, R. A. Cameron, P. A. Caraveo, S. Carius, P. Carlson, J. M. Casandjian, E. Cavazzuti, M. Ceccanti, C. Cecchi, E. Charles, A. Chekhtman, C. C. Cheung, J. Chiang, R. Chipaux, A. N. Cillis, S. Ciprini, R. Claus, J. Cohen-Tanugi, S. Condamoor, J. Conrad, R. Corbet, L. Corucci, L. Costamante, S. Cutini, D. S. Davis, D. Decotigny, M. DeKlotz, C. D. Dermer, A. de Angelis, S. W. Digel, E. do Couto e Silva, P. S. Drell, R. Dubois, D. Dumora, Y. Edmonds, D. Fabiani, C. Farnier, C. Favuzzi, D. L. Flath, P. Fleury, W. B. Focke, S. Funk, P. Fusco, F. Gargano, D. Gasparrini, N. Gehrels, F.-X. Gentit, S. Germani, B. Giebels, N. Giglietto, P. Giommi, F. Giordano, T. Glanzman, G. Godfrey, I. A. Grenier, M.-H. Grondin, J. E. Grove, L. Guillemot, S. Guiriec, G. Haller, A. K. Harding, P. A. Hart, E. Hays, S. E. Healey, M. Hirayama, L. Hjalmarsdotter, R. Horn, R. E. Hughes, G. Jóhannesson, G. Johansson, A. S. Johnson, R. P. Johnson, T. J. Johnson, W. N. Johnson, T. Kamae, H. Katagiri, J. Kataoka, A. Kavelaars, N. Kawai, H. Kelly, M. Kerr, W. Klamra, J. Knödlseder, M. L. Kocian, N. Komin, F. Kuehn, M. Kuss, D. Landriu, L. Latronico, B. Lee, S.-H. Lee, M. Lemoine-Goumard, A. M. Lionetto, F. Longo, F. Loparco, B. Lott, M. N. Lovellette, P. Lubrano, G. M. Madejski, A. Makeev, B. Marangelli, M. M. Massai, M. N. Mazziotta, J. E. McEnery, N. Menon, C. Meurer, P. F. Michelson, M. Minuti, N. Mirizzi, W. Mitthumsiri, T. Mizuno, A. A. Moiseev, C. Monte, M. E. Monzani, E. Moretti, A. Morselli, I. V. Moskalenko, S. Murgia, T. Nakamori, S. Nishino, P. L. Nolan, J. P. Norris, E. Nuss, M. Ohno, T. Ohsugi, N. Omodei, E. Orlando, J. F. Ormes, A. Paccagnella, D. Paneque, J. H. Panetta, D. Parent, M. Pearce, M. Pepe, A. Perazzo, M. Pesce-Rollins, P. Picozza, L. Pieri, M. Pinchera, F. Piron, T. A. Porter, L. Poupard, S. Rainò, R. Rando, E. Rapposelli, M. Razzano, A. Reimer, O. Reimer, T. Reposeur, L. C. Reyes, S. Ritz, L. S. Rochester, A. Y. Rodriguez, R. W. Romani, M. Roth, J. J. Russell, F. Ryde, S. Sabatini, H. F.-W. Sadrozinski, D. Sanchez, A. Sander, L. Sapozhnikov, P. M. S. Parkinson, J. D. Scargle, T. L. Schalk, G. Scolieri, C. Sgrò, G. H. Share, M. Shaw, T. Shimokawabe, C. Shrader, A. Sierpowska-Bartosik, E. J. Siskind, D. A. Smith, P. D. Smith, G. Spandre, P. Spinelli, J.-L. Starck, T. E. Stephens, M. S. Strickman, A. W. Strong, D. J. Suson, H. Tajima, H. Takahashi, T. Takahashi, T. Tanaka, A. Tenze, S. Tether, J. B. Thayer, J. G. Thayer, D. J. Thompson, L. Tibaldo, O. Tibolla, D. F. Torres, G. Tosti, A. Tramacere, M. Turri, T. L. Usher, N. Vilchez, V. Vitale, P. Wang, K. Watters, B. L. Winer, K. S. Wood, T. Ylinen, & M. Ziegler 2009. The Large Area Telescope on the Fermi Gamma-Ray Space Telescope Mission. ApJ, 697:1071–1102.
4. Bhat, C. L., M. R. Issa, C. J. Mayer, & A. W. Wolfendale 1985. Acceleration of cosmic rays in the Loop I 'supernova remnant'? Nature, 314:515–517.

5. Biermann, P. L., J. K. Becker, G. Caceres, A. Meli, E.-S. Seo, & T. Stanev 2010. The WMAP Haze from the Galactic Center Region Due to Massive Star Explosions and a Reduced Cosmic Ray Scale Height. ApJ, 710:L53–L57.
6. Bloemen, H. 1989. Diffuse Galactic gamma-ray emission. ARA&A, 27:469–516.
7. Blumenthal, G. R., & R. J. Gould 1970. Bremsstrahlung, Synchrotron Radiation, and Compton Scattering of High-Energy Electrons Traversing Dilute Gases. Reviews of Modern Physics, 42:237–271.
8. Casandjian, J.-M., I. Grenier, & for the Fermi Large Area Telescope Collaboration 2009. High Energy Gamma-Ray Emission from the Loop I region. ArXiv e-prints.
9. Cholis, I., G. Dobler, D. P. Finkbeiner, L. Goodenough, T. R. Slatyer, & N. Weiner 2009. The Fermi gamma-ray spectrum of the inner galaxy: Implications for annihilating dark matter. ArXiv e-prints.
10. Dame, T. M., D. Hartmann, & P. Thaddeus 2001. The Milky Way in Molecular Clouds: A New Complete CO Survey. ApJ, 547:792–813.
11. Dixon, D. D., D. H. Hartmann, E. D. Kolaczyk, J. Samimi, R. Diehl, G. Kanbach, H. Mayer-Hasselwander, & A. W. Strong 1998. Evidence for a Galactic gamma-ray halo. New Astronomy, 3:539–561.
12. Dobler, G., & D. P. Finkbeiner 2008. Extended Anomalous Foreground Emission in the WMAP Three-Year Data. ApJ, 680:1222–1234.
13. Dobler, G., D. P. Finkbeiner, I. Cholis, T. Slatyer, & N. Weiner 2010. The Fermi Haze: A Gamma-ray Counterpart to the Microwave Haze. ApJ, 717:825–842.
14. Fichtel, C. E., R. C. Hartman, D. A. Kniffen, D. J. Thompson, H. Ogelman, M. E. Ozel, T. Tumer, & G. F. Bignami 1975. High-energy gamma-ray results from the second small astronomy satellite. ApJ, 198:163–182.
15. Finkbeiner, Douglas P. 2004a. Microwave ISM Emission Observed by WMAP. Astrophys. J., 614:186–193.
16. Finkbeiner, Douglas P. 2004b. WMAP microwave emission interpreted as dark matter annihilation in the inner Galaxy.
17. Gehrels, N., & P. Michelson 1999. GLAST: The next-generation high energy gamma-ray astronomy mission. Astropart. Phys., 11:277–282.
18. Grenier, I. A., J.-M. Casandjian, & R. Terrier 2005. Unveiling Extensive Clouds of Dark Gas in the Solar Neighborhood. Science, 307:1292–1295.
19. Haslam, C. G. T., C. J. Salter, H. Stoffel, & W. E. Wilson 1982. A 408 MHz all-sky continuum survey. II - The atlas of contour maps. A&AS, 47:1–+.
20. Hooper, Dan, Douglas P. Finkbeiner, & Gregory Dobler 2007. Evidence Of Dark Matter Annihilations In The WMAP Haze. Phys. Rev., D76:083012.
21. Jones, F. C., & D. C. Ellison 1991. The plasma physics of shock acceleration. Space Science Reviews, 58:259–346.
22. Kalberla, P. M. W., W. B. Burton, D. Hartmann, E. M. Arnal, E. Bajaja, R. Morras, & W. G. L. Pöppel 2005. The Leiden/Argentine/Bonn (LAB) Survey of Galactic HI. Final data release of the combined LDS and IAR surveys with improved stray-radiation corrections. A&A, 440:775–782.
23. Kaplinghat, Manoj, Daniel J. Phalen, & Kathryn M. Zurek 2009. Pulsars as the Source of the WMAP Haze. JCAP, 0912:010.
24. Koyama, K., Y. Maeda, T. Sonobe, T. Takeshima, Y. Tanaka, & S. Yamauchi 1996. ASCA View of Our Galactic Center: Remains of Past Activities in X-Rays? PASJ, 48:249–255.
25. Large, M. I., M. J. S. Quigley, & C. G. T. Haslam 1962. A new feature of the radio sky. MNRAS, 124:405–+.
26. McNamara, B. R., & P. E. J. Nulsen 2007. Heating Hot Atmospheres with Active Galactic Nuclei. ARA&A, 45:117–175.
27. Page, L., et al. 2007. Three year Wilkinson Microwave Anisotropy Probe (WMAP) observations: Polarization analysis. Astrophys. J. Suppl., 170:335.
28. Paumard, T., R. Genzel, F. Martins, S. Nayakshin, A. M. Beloborodov, Y. Levin, S. Trippe, F. Eisenhauer, T. Ott, S. Gillessen, R. Abuter, J. Cuadra, T. Alexander, & A. Sternberg 2006.

The Two Young Star Disks in the Central Parsec of the Galaxy: Properties, Dynamics, and Formation. ApJ, 643:1011–1035.
29. Schlegel, David J., Douglas P. Finkbeiner, & Marc Davis 1998. Maps of Dust IR Emission for Use in Estimation of Reddening and CMBR Foregrounds. Astrophys. J., 500:525.
30. Smialkowski, A., A. W. Wolfendale, & L. Zhang 1997. The 'extragalactic' diffuse gamma ray intensity. Astroparticle Physics, 7:21–25.
31. Snowden, S. L. 2009. What Can Be Learned from X-ray Spectroscopy Concerning Hot Gas in the Local Bubble and Charge Exchange Processes? Space Sci. Rev., 143:253–262.
32. Strong, A. W. 1984. COS-B studies of high-latitude gamma rays. Advances in Space Research, 3:87–89.
33. Strong, A. W., H. A. Mayer-Hasselwander, J. B. G. M. Bloemen, W. Hermsen, & F. Lebrun 1987. The final COS-B database - In-flight calibration of sensitivity and instrumental background behaviour. A&AS, 67:283–296.
34. Strong, A. W., & I. V. Moskalenko 1999. The GALPROP program for cosmic-ray propagation: new developments. 4:255–258.
35. Strong, A. W., I. V. Moskalenko, T. A. Porter, G. Jóhannesson, E. Orlando, & S. W. Digel 2009. The GALPROP Cosmic-Ray Propagation Code. ArXiv e-prints.
36. Strong, A. W., I. V. Moskalenko, & V. S. Ptuskin 2007. Cosmic-Ray Propagation and Interactions in the Galaxy. Annual Review of Nuclear and Particle Science, 57:285–327.
37. Su, M., T. R. Slatyer, & D. P. Finkbeiner 2010. Giant Gamma-ray Bubbles from Fermi-LAT: Active Galactic Nucleus Activity or Bipolar Galactic Wind? ApJ, 724:1044–1082.
38. Sun, X. H., W. Reich, A. Waelkens, & T. A. Enßlin 2008. Radio observational constraints on Galactic 3D-emission models. A&A, 477:573–592.
39. Sunyaev, R. A., M. Markevitch, & M. Pavlinsky 1993. The center of the Galaxy in the recent past - A view from GRANAT. ApJ, 407:606–610.

The Fermi Bubbles and Galactic Centre Star Formation

Roland Crocker

Abstract We construct a simple model of the star-formation- (and resultant supernova) driven mass and energy flows through the inner ∼200 pc (in diameter) of the Galaxy. Our modelling is constrained, in particular, by the non-thermal radio continuum and γ-ray signals detected from the region. The region's star-formation activity drives an outflow of plasma, cosmic rays, and entrained, cooler gas. The plasma outflow from the Galactic Centre (GC) reaches a height of a few kpc and is compellingly related to the recently-discovered Fermi Bubbles by a number of pieces of evidence. In general, our investigations explicitly reveal the GC's important role in the Milky Ways wider stellar ecology.

1 Introduction

1.1 A Startling Discovery: The Fermi Bubbles

Surely one of the most exciting discoveries ([11, 40], see Su this volume) in γ-ray astronomy over the last decade is of the Fermi Bubbles (FBs), ∼50°-tall, hard-spectrum emission regions that extend north and south in more-or-less mirror symmetric fashion from the Galactic Centre (GC) at ∼GeV energies. If these structures are truly associated with the GC or the Galactic Bulge – as their very special geometry suggests – they extend a distance approaching 10 kpc from the plane into either Galactic hemisphere, a distance larger than that separating the Solar System from the Galaxy's nucleus. The FBs exhibit a 1–100 GeV γ-ray luminosity of 2×10^{37} erg/s [41] and while their spectra are very hard – $dN_\gamma/dE_\gamma \propto E_\gamma^{-2.1}$ or so – they exhibit a downturn towards $E_\gamma < \sim 1$ GeV on a spectral energy distribution.

R. Crocker (✉)
Max-Planck-Institut für Kernphysik, Saupfercheckweg 1, 69117 Heidelberg, Germany
e-mail: rcrocker@fastmail.fm

D.F. Torres and O. Reimer (eds.), *Cosmic Rays in Star-Forming Environments*,
Astrophysics and Space Science Proceedings 34, DOI 10.1007/978-3-642-35410-6_28,

Anomalous, hard-spectrum microwave emission has also been observed [10, 12, 14] from the inner Galaxy and shown to be roughly coincident with the FBs at lower Galactic latitudes ($|b| \lesssim 30°$). This 'WMAP Haze' has total 22–66 GHz luminosity of a few $\times 10^{36}$ erg/s. Finally, this same region of the sky is bright in apparently thermal X-rays, the Galactic X-ray bulge exhibiting a soft X-ray luminosity approaching a few $\times 10^{39}$ erg/s [31].

The discovery of these completely unanticipated structures has spurred a flurry of theoretical speculation as we now explain.

1.2 What Are the Fermi Bubbles?

There are two fundamental, interwoven questions regarding the FBs:

1. By what process/object(s) are the FBs energised?
2. Are the γ-rays we detect from the FBs dominantly due to (a) inverse Compton (IC) emission from a mysterious population of cosmic ray electrons extending far into the Galactic halo (the 'leptonic scenario') or (b) hadronic collisions between an equally mysterious cosmic ray proton population and ambient gas leading to neutral meson creation and subsequent decay into γ-rays due (the 'hadronic scenario')?

1.2.1 Leptonic Scenarios

As a matter of recent history, the discovery of the WMAP Haze predated that of the γ-ray emission from the FBs. Given that the $F_\nu \propto \nu^{-0.5}$ spectrum of the Haze is naturally interpreted as synchrotron emission from a population of hard-spectrum ($dN_e/dE_e \propto E_e^{-2.0}$) electrons at few $\times 10$ GeV energy, it was rather naturally anticipated that these very same electrons should emit $\sim$GeV γ-ray photons through the process of upscattering starlight in the interstellar radiation field of the Inner Galaxy. So, when anomalous, hard-spectrum emission was detected in Fermi-LAT data covering the inner Galaxy, this emission was naturally interpreted as being due to the inverse-Compton mechanism. Besides, Su et al. [40] affected fore/background removal by regressing out a number of maps at other wavebands from the γ-ray data, including maps that trace the column of gas. This, in normal circumstances, should function to remove the contribution of hadronic γ-ray photons. As I will argue below, such a procedure might not actually remove the hadronic γ-rays for the unusual case presented by the FBs, however. In any case, it seems to have been unanticipated that the anomalous γ-ray emission would extend so very far, $\sim$10 kpc, from the Galactic plane, the significance of this fact being that – so high above the disk – the light field available to be upscattered is the cosmic microwave background (CMB). If the FBs – at least at the higher latitudes – are due to IC upscattering of the CMB into 1–100 GeV energies, 'beam' electrons of energy $>\sim$TeV energy are

now required. And such high-energy electrons cool quickly, in under a Myr [7]. This has the important implication that – in any leptonic scenario for the origin of the FBs – the primary electrons are either transported [16] very quickly from the plane (>3 % the speed of light) or they are accelerated diffusively, in situ, as the result of either first [3] or second-order [25] Fermi acceleration processes. Another point is that the spectrum of the FBs does not seem to evolve measurably as a function of Galactic latitude (at least above $|b| >\sim 20°$ where the spectrum is well-measured); this might be difficult to realise within some leptonic scenarios given that the electron population is cooling quickly and the light-field available for upscattering *is* evolving with distance from the plane.

1.2.2 Hadronic Scenarios

A scenario invoking hadronic emission sidesteps these issues. In particular, cooling of the cosmic ray ions (hereafter, we consider only protons for simplicity) is not an issue because the cooling timescale is so long, $\sim 5\ (n_H/0.01)\ \mathrm{cm}^{-3}$ Gyr, where we have normalised to the rough scale [41] of the plasma density in the FBs as obtained from X-ray observations. As presaged above, Su et al.'s procedure for regressing-out a component from the γ-ray map proportional to the total gas column should normally have accounted for the hadronic emission; why, then, do we even consider the hadronic idea? The point is this procedure assumes the cosmic ray density is uniform, in which case the intensity of γ-rays will simply be proportional to the target gas column along the line-of-sight. The FBs extend very far out of the plane, however, and seem to be related to nuclear activity; both of these should alert us to the possibility that the cosmic ray population inside them may be different from that encountered locally in the Galactic disk. Indeed, again normalising to a rough plasma density of $\sim 0.01\ \mathrm{cm}^{-3}$ the non-thermal proton energy density in the FBs would have to be a $\sim 5\ \mathrm{eV\ cm}^{-3}$ in order to explain their γ-ray luminosity. This is a factor a few larger than in the disk. In addition, given the FBs' hard γ-ray spectrum, the spectrum of this unusual proton population would have to be considerably harder than in the disk, $dN_p/dE_p \propto E_p^{-2.2}$ or so (cf. $dN_p/dE_p \propto E_p^{-2.7}$ in the disk).

Finally we can calculate the power required to be injected into freshly-accelerated, non-thermal protons. This power has a lower limit at the value required to just sustain the proton population in steady state against its radiative losses, in other words a situation in which the FBs are in steady state and constitute a 'thick target' to the protons injected into them, otherwise known as a saturation scenario. This minimum power, as determined by the $L_\gamma \sim 2 \times 10^{37}\ \mathrm{erg/s}$(1–100 GeV) γ-ray luminosity of the FBs, can be roughly calculated to be $3 \times 2 \times 10 \times L_\gamma \sim 10^{39}\ \mathrm{erg/s}$ where these multiplicative pre-factors account for the following: [**3**×] accounts for the three species of roughly equally numerous pions (π^+, π^0, π^-) created per pp collision only one of which decays directly into photons; [**2**×] accounts for others energy losses of the putative proton population (ionisation at low energies and adiabatic losses at all energies); and [**10**×] relates the bolometric energy loss into γ-rays over all energies to the observations between only 1 and 100 GeV.

Such a rate of energy injection is relatively modest – a factor of a few percent of the Galaxy overall cosmic ray luminosity, for instance – but note the following: if we are to be in the saturation regime, requiring steady state, the *pp* loss time must be the minimum timescale in the problem. The FBs, in particular, must have existed for a time $>5\ (n_H/0.01)\ \mathrm{cm}^{-3}$ Gyr and have been fed with a hard-spectrum proton population of time-averaged power $\sim 10^{39}$ erg/s for this sort of timescale. This requirement – which *prima facie* might lead one to abandon this scenario in frustration – is, in fact, met by Galactic centre star-formation which has, as we explain below, been feeding $\sim 10^{39}$ erg/s in cosmic rays into an outflow over Gyr timescales.

We lastly note another important aspect of any hadronic saturation scenario: in such a scenario the volume-emissivity (in any differential volume element) tends to a limiting value *independent* of the gas density within that volume element (which is why regressing-out a map proportional to the gas column may not necessarily remove all hadronic emission). The reason is simple: the steady-state proton population in such a volume element is itself determined by the loss process which is *pp* cooling. Thus, roughly speaking, in that volume element the cosmic ray energy density satisfies $u_p \propto 1/n_H$. On the other hand, the γ-ray luminosity of that element is roughly $\propto u_p \times n_H$; the local gas density thus cancels out. This is as it must be for saturation as – once this situation is reached – the total luminosity of the system is set only by the power injected into the system in the freshly injected cosmic ray protons.

But why am I confident that the GC is currently launching $\sim 10^{39}$ erg/s in hard-spectrum cosmic ray protons into the Galactic bulge (and has been for billions of years)?

2 Intense Star Formation in the Central 200 pc of the Galaxy Drives an Outflow

The inner 200 pc (in diameter) region of the Galaxy presents a peculiar environment, more akin to a star-burst than to conditions typical in the Galactic disk [26]. This much is evident from the various signatures we have for energy densities/pressures in all the components of the GC's ISM that are elevated by up to two orders of magnitude with respect to the Solar System's environment [5, 9, 37]. The ultimate energy source for this high level of activity is all the star-formation going on in this inner region of the Galaxy which accounts for 5–10 % [26] of the Galaxy's massive star formation in a tiny fraction (< 0.05 %) of its volume. In fact, the star-formation areal rate density (in $\mathrm{M}_\odot/\mathrm{year}/\mathrm{kpc}^2$) in the inner 200 pc is $\sim$*3* orders of magnitude larger than the average over the disk. From observations of the star-forming nuclei of external galaxies, this should be quite adequate to generate a large-scale outflow and, indeed, there is much evidence for such an outflow from the GC.

2.1 Morphological Evidence for a GC Outflow

From angular scales $<1°$ up to the tens of degrees – encompassing the GC Spur [18, 33] and the Fermi Bubbles – there is a multitude of evidence for material outflowing from the GC; for a review the reader is directed to Ref. [9]. Here we mention only a subset of the particularly striking evidence. Unsharp-masked, radio continuum maps covering the GC show $\sim 1°$ spurs leaving north and south of the plane [27]. These structures are concentrated above regions displaying the most elevated star-formation rates (and highest molecular gas densities – requisite, of course, to sustain the star-formation); cf. Fig. 1 of Ref. [9]. The emission in these structures contains a significant non-thermal component. In the case of the two of the most dramatic spurs (leaving north from longitudes coincident with the Radio Arc and the Sagittarius C giant molecular cloud and forming the walls of the 'GC Lobe' [32]) this progressively steepens [22] with distance from the plane, a clear signature of an electron population, synchrotron-ageing as it is transported from the plane. Many of these radio continuum structures have counterparts in other wavebands – e.g., few micron emission from dust entrained into these outflows [2, 38] and molecular line emission [34, 36]. X-ray data from ROSAT reveal a limb-brightened biconical outflow structure leaving north and south from the Galactic centre [2, 35] which correlates with both the radio continuum and dust emission (and has been argued to be tracing a star-formation-driven outflow).

2.2 Non-thermal Evidence for a GC Outflow

In addition to this evidence, with collaborators I have been pursuing research that shows the Galactic centre is substantially *under*-luminous in non-thermal emission, in particular, radio continuum emission (tracing synchrotron emission from cosmic ray electrons) and γ-rays (primarily from neutral meson decay tracing the hadronic collisions experienced by cosmic ray protons and heavier ions), given the amount of star formation that is occurring in the region [6, 8, 9]. Another way to say this is that the Galactic centre's radio continuum emission falls far (4σ) short of the expectation generated by the far-infrared–radio continuum correlation (FRC) [44] and its observed far-infrared luminosity. Equally, the GC's γ-ray luminosity is only 10 % at GeV energies – and a measly $\sim$ few % at TeV energies – of the expectation first established theoretically [43] and now – with the advent of *Fermi* – observationally [1] given its FIR output. At the same time the spectrum of the diffuse, non-thermal emission from the GC is very flat, consistent with in situ electron and proton populations that are $dN/dE \sim E^{-2.2}$ or so, much harder than the diffuse emission from the plane.

What is the explanation for these anomalies?

In principle, there are a number of potential explanations for the fact that the system falls off the FRC and is also significantly under-luminous in γ-rays: it might

be, for instance, that supernovae in the GC are intrinsically less efficient cosmic ray accelerators or the system may, in principle, be out of steady state. With regard to the former, we have shown through exhaustive modelling [8, 9] that this is not the case in the GC: perhaps surprisingly given the high (volumetric-average!) gas density in the GC, our global analysis shows that the GC environment is at least typically efficient ($\sim$10 %) in turning injected mechanical energy into non-thermal particles. The latter might be a significant issue if, in particular, the GC system has experienced a recent burst of star-formation on a timescale $\lesssim$10 Myr such that there has not been sufficient time for the most massive stars – which dominate both the thermal radiative output and are the ones whose lives end in supernovae – to go through their lifecycle. The GC's star-formation is bursty when viewed with sufficiently fine resolution in time as witnessed by the discrete massive clusters that inhabit the system. Massive clusters in the GC environment, however, suffer mass segregation and break-up within the strong tidal fields of the region such that within $\sim$10 Myr they become sufficiently dispersed to be invisible against the very high 'background' stellar density [29]; this is significantly shorter that then $\sim$30 Myr lifespan of the least massive stars ($\sim$8 $M_\odot$) whose lives end in core-collapse supernovae. In any case, today at least half of the most massive stars in the GC environment are located outside the three known clusters [24]. Moreover, the star-formation rate in the GC today, $\sim$0.08 $M_\odot$/year ([9] and references therein), is very close to the time-averaged value required to fill out the $\sim 10^9$ $M_\odot$ stellar mass of the Nuclear Bulge over 10 Gyr [21,30]. These considerations imply that the GC's non-thermal deficits are not a result of a non-steady-state situation – so what is going on?

A simple and self-consistent explanation is that the GC region is not a *calorimeter* [42] to either the non-thermal protons or electrons that are accelerated in its environment: these particles are transported away well before they have time to dump their energy radiatively in situ. This transport, moreover, cannot be diffusive because the spectrum of the diffuse, non-thermal radiation that we do detect from the region implies emission from a population of cosmic rays with a hard spectrum, basically consistent with the expectation *at injection* by the accelerators. This means that the transport process has to function equally well at all energies which, of course, will be satisfied if this process is advective: non-thermal particles are removed from the region over a timescale determined by the speed of the outflow. Of course, this finding is in accord with the multi-wavelength morphological evidence discussed above – and, indeed, the firm expectation we have from external star-forming nuclei – that the system is driving an outflow. This has a number of important implications.

2.3 The Environment Experienced by GC Cosmic Rays

Given the amount of power that is going into freshly-accelerated non-thermal particles, on the one hand, and the actual amount of non-thermal radiation we

detect, we can determine a number of parameters describing the environment that the cosmic rays experience as they (largely) escape the system. We know that the outflow velocity experienced by the cosmic rays is the same for both cosmic ray electrons and protons. The environmental parameters that determine the amount of radiative energy loss the cosmic rays experience are, however, different between protons and electrons in general. For the electrons, cooling depends on a number of different processes (dominant in different energy regime) and is, therefore, controlled by a number of different environmental parameters: (path-averaged) gas density controls ionisation and bremsstrahlung cooling, the magnetic field controls synchrotron losses and the ambient light field energy density controls the amount of inverse-Compton emission. For the protons the situation is simpler: the amount of cooling (via hadronic collisions) they experience is only a function of the path-integrated gas density they 'see' as they are removed from the environment.

From this simple consideration one may immediately [6] derive an interesting conclusion: imagine that we have two knobs that control within our GC model (i) the gas density experienced by the escaping protons and (ii) the speed of the outflow removing them from the system. We know, too, the power in protons going into the system and the amount of γ-ray emission we detect, which is held fixed. As the amount of cooling is simply proportional to the gas density, one immediately has the result that, as the outflow velocity is 'dialled-up', the gas density must be correspondingly increased. The outflow velocity, however, cannot be dialled-up without limit, however; the outflow's kinetic energy cannot do more than saturate the total mechanical energy injected into the system (dominantly by the supernovae). This consideration means that the outflow speed has an upper limit at around 1,100 km/s (with a likely speed of a few 100 km/s, very similar to that inferred from external systems); see Fig. 1.

At this velocity, in order that we detect the observationally-determined $\sim$ few % of the expected, calorimetric TeV γ-ray luminosity, the gas density experienced by the protons cannot be higher than a few $\times 10\,\mathrm{cm}^{-3}$ (Fig. 1). This is already less than the volumetric-average gas density in this environment ($\langle n_H \rangle \simeq 120\,\mathrm{cm}^{-3}$) which has the somewhat surprising implication that the population of high-energy $> \sim$10 TeV cosmic ray protons dominantly responsible for the GC's γ-ray emission is not able to penetrate into the densest parts of the GC's molecular clouds (i.e., the cores where the stars are being formed).[1] Similar (though somewhat more complicated) reasoning implies that the electrons 'see' a magnetic field intensity $\sim$100 μG in the GC environment, consistent with an earlier lower limit [5] at 50 μG placed on the large-scale field amplitude in the central few 100 pc of the Galaxy (Fig. 1). On the other hand, from observations of external star-forming nuclei (see, e.g., [39]), we expect that the 'thermalization efficiency' – the fraction of the total

[1]This does not necessarily suggest that cosmic rays are not important in these dense molecular environments: one could easily imagine that the much lower energy cosmic rays responsible for molecular gas ionisation might be accelerated, as an independent population, locally on turbulence within the clouds. I thank Felix Aharonian for making this point to me.

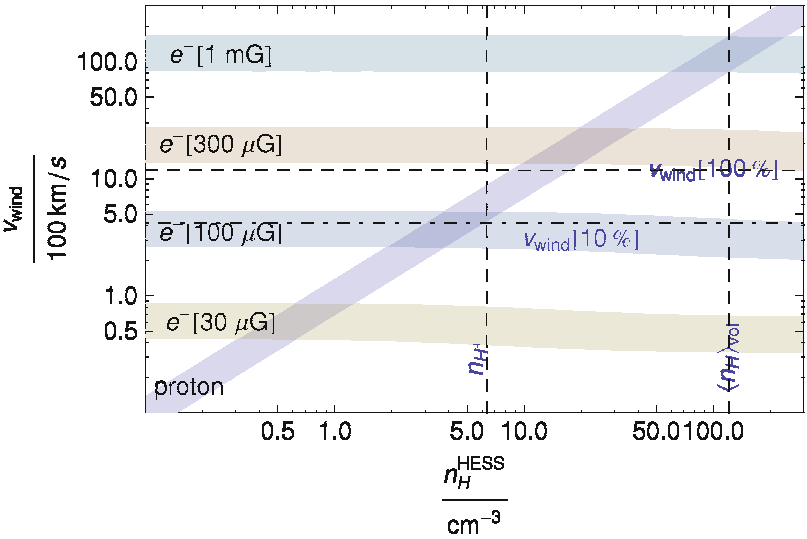

Fig. 1 A plot (after Ref. [6]) showing the inferred gas density as a function of outflow speed given that the proton population loses a few % of its injection energy (see diagonal 'proton' band) and electrons lose ∼10 % of their injection energy in the inner 200 pc region; note that electron cooling is a function of magnetic field (see different bands corresponding to different magnetic field intensities) as well as gas density (controlling ionisation and bremsstrahlung losses of lower-energy electrons) and interstellar radiation field energy density (IC losses). The *dashed horizontal lines* correspond to the maximum wind speed allowed if the kinetic power of the wind saturates the available mechanical power from supernovae (and sub-dominantly, stellar winds) and a wind kinetic power that soaks up 10 % of the injected mechanical power (a rough lower limit according to observations of external, star-forming nuclei). The *vertical dashed bands* show the volumetric average gas density and the gas density just in plasma phase in the region

mechanical power delivered by supernovae and stellar winds that ends up heating of moving the ambient ISM – should not be much less than ∼10 % which suggests that the outflow from the GC cannot have a speed less ∼300 km/s (Fig. 1).

3 The Fermi Bubbles Are Generated by the Galactic Centre's Star-Formation-Driven Outflow

3.1 Joining the Dots

One important implication of this reasoning is that, as we have already belaboured, the vast majority of the CR protons accelerated in the GC region are carried away. Given the timescales, hot plasma and, indeed, 'frozen-in' magnetic fields are also carried away on this outflow. This is where we loop back to the Fermi Bubbles for, as

established above, the proton power required to sustain the γ-ray luminosity of the FBs in saturation is a more-or-less precise match to the proton power our *completely independent* modelling of the inner $\sim$200 pc suggests is carried out of this region on its outflow. This naturally leads one to the conjecture that the GC's star-formation (and consequent supernova) driven outflow is the ultimate power source for the FBs. That the FBs are located to Galactic north and south of the Bubbles and appear to gather down to the plane on $\sim$ few 100 pc scales around the GC is, of course, completely consistent with this idea. Another rather nice point is that the hard-spectrum of the γ-ray emission from the FBs is also accounted-for within this model: by construction, the FBs trap all the cosmic ray protons injected into them. All that happens is that these injected particles proceed to slowly lose their energy in situ in an almost energy-independent fashion (above the pion production threshold). They retain, therefore, the spectrum they had when injected into the base of the FBs which – given they are transported out of the GC advectively – is the same as their distribution at injection by the GC accelerators.

In passing, one notes the contrast between three different, illustrative limiting cases: as already remarked we expect first-order Fermi acceleration sites to deliver cosmic rays into the ISM in a distribution slightly steeper than $dN/dE \propto E^{-2}$; in the plane, because of the energy-dependence of diffusive confinement, this injection distribution is steepened by a further $\sim E^{-0.5}$ (presumably reflecting the spectrum of magnetic turbulence) to produce the steady-state $\propto E^{-2.7}$ spectrum found directly by cosmic ray measurements and inferred from observations of diffuse γ-ray emission from the plane. In contrast, we have claimed, cosmic ray escape from the GC is not governed by diffusion, but rather advection, which works independently of energy. Thus the steady-state cosmic ray distribution in that region – as reflected by the hard spectrum of its non-thermal radiation – is unmodified from the injection spectrum (though note that cosmic ray protons leave the region having lost very little energy on average) Equally, these protons are then injected into the Bubbles – where they proceed to lose all their energy, though very slowly meaning that, again, their distribution simply follows that at injection.

3.2 Issues with the Model

3.2.1 Requisite Long Timescale

The difficulty that this scenario faces, however, is the long timescale already alluded to above – $>$ 5 Gyr! – necessary to establish saturation via pp collisions on the low density plasma environment of the FBs. In other words, we require not only that the GC feeds $\sim 10^{39}$ erg/s into the base of the FBs – which is seems to presently achieve – but also that it has been doing this for many Gyr (to be more exact: the time-averaged power that the GC has been feeding into the FBs over a few Gyr must assume this value – the fact that the currently-inferred cosmic ray power going into

the FBs is close to the time-averaged value is consistent with the statement that the system is more-or-less in steady state).

Does this mean that this scenario is trivially ruled out? It certainly wouldn't make sense for any random position in the disk. But the GC is a geometrically-privileged region – gas is *always* falling through the disk on to this region. The fact that star-formation has been going on – at approximately the current rate – in the *Nuclear* Bulge over the lifetime of the Galaxy [30] (cf. the situation in the larger-scale Galactic Bulge) means that the GC has, indeed, as required, been feeding the FBs CRs at a rate sufficient to power their luminosity for all this time. (One also notes that SNIa amongst the old Galactic bulge stellar population – ten times more massive than the Nuclear Bulge inhabiting the inner 200 pc – will also supply a rather constant and comparable energy input into the inner Galaxy.)

Still, such long timescales do make one uncomfortable. We should look for confirmatory – or at least collaborative – evidence to this scenario. One nicely-consistent point is the following: in addition to CRs, we know that the GC outflow carries away hot plasma and magnetic fields. Given the (time-averaged) supernova rate of one core-collapse event every $\sim$2,000 years, there is an upper limit of 2×10^{40} erg/s to the total power that – in all forms (thermal, kinetic, non-thermal particle, magnetic field) – is carried by this outflow. From the other direction, we can make a rough estimate of the amount of energy that has been expended in inflating the FBs against the pressure ($\sim 4 \times 10^4$ K cm^{-3} [19]) represented by the external ISM, P_{ext}, and supplying their internal energy, i.e., their total enthalpy, $H \equiv \gamma/(\gamma - 1) P_{ext} V_{FB} \gtrsim 3 \times 10^{56}$ erg [17]. The minimum timescale to supply this enthalpy – given the power of the outflow and ignoring all inefficiencies – is > 600 Myr, providing independent confirmation that the star-formation-driven outflow from the GC can inflate the FBs – but necessarily over a long timescale.

3.2.2 Confinement of CRs

The long timescales suggested by the proton saturation scenario point to other issues that must be dealt with. One requirement, of course, is that protons up to at least $\sim$TeV be trapped for the same Gyr timescales mentioned above. This may be partially achieved by diffusive confinement given the evidence that the magnetic field structure inside the Bubbles is highly tangled [10,12,15]. This cannot be the whole answer, however: the FBs seem to have rather well-defined edges [40]. This points to the existence of magnetic walls, defined by a rather regular magnetic field structure with field lines tangential to the surface. In this geometry the gyromotion of charged particles impinging on the walls will swing them around the field lines, returning them to the interior [28]. Such processes seem to occur in bubbles injected – on even larger scales than the FBs – into cluster environments by AGN outflows. Such bubbles must keep their interior hot but rarefied plasma – and likely their cosmic ray – content trapped (and the exterior, colder, denser plasma excluded) for periods of at least 100 Myr (given the relevant buoyant rise times of

such structures). Confining magnetic wall structures, moreover, can naturally result from the 'magnetic draping' phenomenon [13] as the bubbles rise *sub*-sonically through the cluster medium.

Regardless of whether exactly the same mechanism operates for the FBs, we now have evidence for exactly the sort of strong, regular field in part of the walls of the FB required within our scenario to confine the cosmic rays. Polarized microwave emission we have found [18] from the lower part of the eastern edge of the northern Bubble implies synchrotron emission by cosmic ray electrons on a strong ($\gtrsim 10\,\mu$G) and *regular* magnetic field.

3.2.3 Age of the FBs

Another question that naturally presents itself is: how can the structures themselves hang around for so long? If our multi-Gyr timescale is correct, the expansion velocity of the structures can only be of order km/s – much slower than one might naively guess. Such a low speed can only be the result of buoyant rise that would seem to be extremely fine-tuned in terms of the density contrast, η (i.e., the ratio between the densities of the ambient medium and the interior plasma). In general, for bubbles injected into clusters by AGN the density contrast is, initially, extremely large, $\gg 1$ (such bubbles are supported by extremely hot, low density plasma and possibly cosmic rays). Dynamical mechanisms, however, operate so as to entrain extra matter into these bubbles before they rise to heights much exceeding their radii so that $\eta \rightarrow 1$ and they approach neutral buoyancy. The fascinating finding that emerges from modelling of the star-formation GC outflow [9] is that it *always* satisfies $\eta \sim 1 - 10$. The FBs – if inflated by GC star-formation – are expected, therefore, to be buoyant, but only slightly so, so that their inferred long rise times are naturally accounted-for.

4 Continuing Research

4.1 Flat Projected γ-Ray Intensity of FBs

As was first remarked by Su et al. [40] the FBs present a flat *projected* γ-ray intensity; given that we naturally expect the path-length through these structures to change with projected radius from their mid-line, this is non-trivial to achieve and requires generically some increase of the volumetric emission towards the edges of the structures. As has been emphasised [25] our model – with approximately constant volumetric emission – does not achieve this. In fact, of course, our model is single-zone so cannot achieve it, but – by essentially adding extra parameters to the model – one can imagine how an extension of the model would achieve it. We would require that either one or both of the following is realised: (i) the cosmic

ray intensity is systematically larger towards the edges of the FBs than in the centre (as would follow if the magnetic field were systematically more turbulent or stronger there) and (ii) the gas density in the centre of the FBs is so low that saturation is never achieved in this region. Both these would seem to be eminently reasonable modifications of our single zone model.

4.2 Neutrinos from the FBs?

As we originally remarked [7] in any hadronic scenario for the origin of the γ-rays from the FBs, these structures will also be significant sources of high-energy neutrinos, potentially detectable in a future, km^3-scale astrophysical neutrino telescope located in the northern hemisphere. A number of authors (e.g., [4, 23]) have gone on to refine our calculations here and their results confirm the FBs are potentially important sources of astrophysical neutrinos (provided, of course, that they can trap protons to the high energies, $\gtrsim$10 TeV, requisite to the production of detectable neutrinos).

4.3 A Radio Continuum Halo Above the GC?

If this model is correct further observations should reveal a radio continuum flux density of around 20 kJy at 1.4 GHz from an outflow structure around the GC although the size of this structure might be somewhat smaller than that of the Fermi Bubbles (which extend to $\pm 50°$) given the much smaller cooling times of electrons than protons. On the other hand, the radio outflow needs to be bigger than ($6° \times 2°$) because the 'Diffuse Non-thermal Source' [20] detected around the GC on these angular scales does not saturate the FRC as normalised to the FIR luminosity of the GC on $\sim$200 pc size scales [5].

5 Concluding Remarks

The Fermi Bubbles remain a fascinating, unfolding story [41]. They say something profound about the mechanisms that operate within the Galactic nucleus to communicate 'feedback' to the Galaxy-at-large. Whether these processes – in the particular case of the current Milky Way – are primarily energised by star-formation or the super-massive black hole remains a topic for debate as does, indeed, the question of whether the Bubbles' γ-rays are the signatures of high-energy electrons or protons. The reader is urged: *watch this space!*

Acknowledgements RMC would like to thank the co-authors of the papers [6–9, 18] upon which this work is based: Felix Aharonian, David Jones, Casey Law, Fulvio Melia, Tomo Oka, and Juergen Ott. He would also like to thank the organisers for a very stimulating workshop at Sant Cugat and for supporting his attendance.

References

1. Fermi LAT Collaboration, Ackermann, M., Ajello, M., et al. 2012, arXiv:1206.1346
2. Bland-Hawthorn, J., & Cohen, M. 2003, ApJ, 582, 246
3. Cheng, K. S., Chernyshov, D. O., Dogiel, V. A., Ko, C. M., & Ip, W. H. 2011, ApJ, 731, L17
4. Cholis, I. 2012, arXiv:1206.1607
5. Crocker, R. M., Jones, D. I., Melia, F., Ott, J., & Protheroe, R. J. A lower limit of 50 microgauss for the magnetic field near the Galactic Centre, Nature, 463, 65–67 (2010)
6. Crocker, R. M., Jones, D. I., Aharonian, F., et al. 2011a, MNRAS, 411, L11
7. Crocker, R. M., & Aharonian, F. Fermi Bubbles: Giant, Multibillion-Year-Old Reservoirs of Galactic Center Cosmic Rays, Physical Review Letters, 106, 101102 (2011)
8. Crocker, R. M., Jones, D. I., Aharonian, F., Law, C. J., Melia, F., Oka, T., & Ott, J. 2011b, MNRAS, 413, 763
9. Crocker, R. M. 2012, MNRAS, 423, 3512
10. Dobler, G., & Finkbeiner, D. P. 2008, ApJ, 680, 1222
11. Dobler, G., Finkbeiner, D. P., Cholis, I., Slatyer, T., & Weiner, N. 2010, ApJ, 717, 825
12. Dobler, G. A Last Look at the Microwave Haze/Bubbles with WMAP, ApJ, 750, 17 (2012)
13. Dursi, L. J., & Pfrommer, C. 2008, ApJ, 677, 993
14. Finkbeiner, D. P. et al. 2004, ApJ, 617, 350–359
15. Gold, B., et al. 2010, arXiv:1001.4555
16. Guo, F., & Mathews, W. G. 2011, arXiv:1103.0055
17. Hinton, J. A., Domainko, W., & Pope, E. C. D. 2007, MNRAS, 382, 466
18. Jones, D. I., Crocker, R. M., Reich, W., Ott, J., & Aharonian, F. A. 2012, ApJ, 747, L12
19. Kasparova, A. V., & Zasov, A. V. 2008, Astronomy Letters, 34, 152
20. LaRosa, T. N., Brogan, C. L., Shore, S. N., Lazio, T. J., Kassim, N. E., & Nord, M. E. 2005, ApJ, 626, L23
21. Launhardt, R., Zylka, R., & Mezger, P. G. 2002, A&A, 384, 112
22. Law, C. J. 2010, ApJ, 708, 474
23. Lunardini, C., & Razzaque, S. 2012, Physical Review Letters, 108, 221102
24. Mauerhan, J. C., Cotera, A., Dong, H., et al. 2010, ApJ, 725, 188
25. Mertsch, P., & Sarkar, S. 2011, Physical Review Letters, 107, 091101
26. Morris, M., & Serabyn, E. 1996, ARA&A, 34, 645
27. Pohl, M., Reich, W., & Schlickeiser, R. 1992, A&A, 262, 441
28. Pope, E. C. D. 2010, MNRAS, 404, 451
29. Portegies Zwart, S. F., Makino, J., McMillan, S. L. W., & Hut, P. 2002, ApJ, 565, 265
30. Serabyn, E., & Morris, M., Nature, 382, 602 (1996)
31. Snowden, S. L., et al., ApJ, 485, 125 (1997)
32. Sofue, Y., & Handa, T. 1984, Nature, 310, 568
33. Sofue, Y, Reich, W., & Reich, P., 1989, ApJ, 341, 47
34. Sofue, Y. 1996, ApJ, 459, L69
35. Sofue, Y. 2000, ApJ, 540, 224
36. Sofue, Y. 2007, PASJ, 59, 189
37. Spergel, D. N., & Blitz, L. 1992, Nature, 357, 665
38. Stolovy, S., Ramirez, S., Arendt, R. G., et al. 2006, Journal of Physics Conference Series, 54, 176
39. Strickland, D. K., & Heckman, T. M. 2009, ApJ, 697, 2030

40. Su, M., Slatyer, T. R., & Finkbeiner, D. P. 2010, ApJ, 724, 1044
41. Su, M., & Finkbeiner, D. P. 2012, ApJ, 753, 61
42. Thompson, T. A., Quataert, E., Waxman, E., Murray, N., & Martin, C. L. 2006, ApJ, 645, 186
43. Thompson, T. A., Quataert, E., & Waxman, E. 2007, ApJ, 654, 219
44. Yun, M. S., Reddy, N. A., & Condon, J. J. 2001, ApJ, 554, 803

From 10 K to 10 TK: Insights on the Interaction Between Cosmic Rays and Gas in Starbursts*

Brian C. Lacki

Abstract Recent work has both illuminated and mystified our attempts to understand cosmic rays (CRs) in starburst galaxies. I discuss my new research exploring how CRs interact with the ISM in starbursts. Molecular clouds provide targets for CR protons to produce pionic gamma rays and ionization, but those same losses may shield the cloud interiors. In the densest molecular clouds, gamma rays and ^{26}Al decay can provide ionization, at rates up to those in Milky Way molecular clouds. I then consider the free-free absorption of low frequency radio emission from starbursts, which I argue arises from many small, discrete H II regions rather than from a "uniform slab" of ionized gas, whereas synchrotron emission arises outside them. Finally, noting that the hot superwind gas phase fills most of the volume of starbursts, I suggest that it has turbulent-driven magnetic fields powered by supernovae, and that this phase is where most synchrotron emission arises. I show how such a scenario could explain the far-infrared radio correlation, in context of my previous work. A big issue is that radio and gamma-ray observations imply CRs also must interact with dense gas. Understanding how this happens requires a more advanced understanding of turbulence and CR propagation.

*Note by the Editors: This paper has been chosen for the Young Scientist Award of the Sant Cugat Forum on Astrophysics.

B.C. Lacki (✉)
Jansky Fellow of the National Radio Astronomy Observatory, Institute for Advanced Study, Astronomy, Einstein Drive, Princeton, NJ 08540, USA
e-mail: brianlacki@ias.edu

D.F. Torres and O. Reimer (eds.), *Cosmic Rays in Star-Forming Environments*, Astrophysics and Space Science Proceedings 34, DOI 10.1007/978-3-642-35410-6_29,

1 Introduction

Starbursts are detected in synchrotron radio, which is generated from cosmic ray (CR) electrons and positrons ($e^{\pm}$) interacting with magnetic fields [12], and now in gamma rays, which are generated by CR protons colliding with ambient gas and creating pions [1, 3, 4]. While nearby starbursts can be resolved in radio emission, this is not true for the gamma rays. Furthermore, because the gamma rays are a recent discovery, our understanding of CRs is at a basic, phenomenological level. Thus, much of the theoretical work about CRs in starbursts uses one-zone steady-state models [15, 17, 27, 40, 57]. These assume that the interstellar medium (ISM), magnetic fields, and CR injection of starbursts are completely homogeneous – essentially, that starbursts have no structure, which is obviously not true in detail. These kinds of models can help us understand the energetics of CRs in starbursts (which, even a few years ago, was mysterious), but the propagation is treated as a black box.

Some works have expanded from these assumptions, by correlating radio and gamma ray emission and star-formation to constrain CR diffusion [37, 38], by creating 3D steady-state models of CR populations in the Milky Way [53] and the nearby starbursts M82 and NGC 253 [42, 45], or by considering the time- and position- dependent contributions of individual CR accelerators to starbursts' integrated CR spectra [58].

Yet even these approaches are simplifications of what actually happens in starbursts. On small enough scales, the apparently smooth fluctuations in gas density and star-formation resolve into a highly chaotic froth with many phases of vastly different physical conditions (Fig. 1). Molecular gas is highly turbulent in starbursts, leading to strong density fluctuations [25]. In star-forming regions, the overdensities of the molecular gas collapse still further into molecular cores and ultimately into protostars. Newborn O stars and star clusters carve out H II regions. Supernovae and clusters blast bubbles of 10^7–10^8 K plasma which can ultimately fill the volume of a starburst and form into a galactic wind [9, 52]. Pervading these phases are magnetic fields and the CRs themselves.

The interaction between CRs and these different phases must be understood if we are to interpret the results of our phenomenological models. Which phase has the magnetic fields responsible for the radio emission? Which phase provides the target atoms responsible for pionic gamma ray emission? Which phase regulates how CRs are transported spatially? And how do the CRs shape these phases, if at all?

2 How Molecular Clouds Can Stop Cosmic Rays and the Role of Gamma Rays and ^{26}Al

CRs are thought to interact with the bulk molecular ISM, containing most of the gas mass of starbursts, and with some good reason. The observations of gamma rays from starburst galaxies provide evidence that CRs spend some time in dense

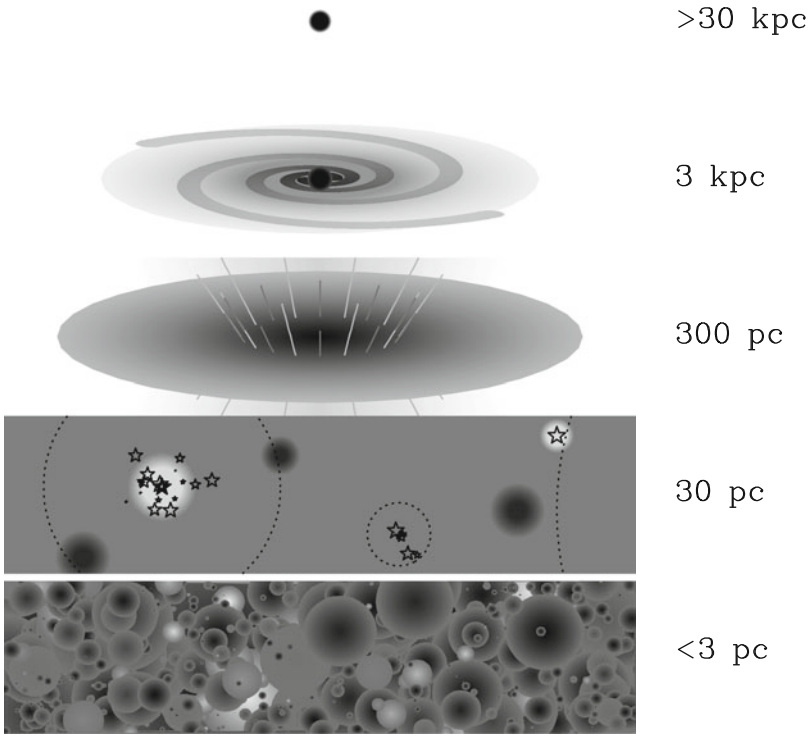

Fig. 1 Starbursts appear more inhomogeneous on smaller scales (the given sizes are to order of magnitude). At large scales (>30 kpc), the galaxy is completely unresolved (as for gamma-ray observations and high-z radio observations). Closer in, we see the resolution of the host galaxy from the starburst (3 kpc) and then the resolved starburst disk with its superwind (300 pc). Then, individual star-forming regions and large molecular cloud complexes become apparent (30 pc). On these scales, how CRs travel from individual accelerators becomes important (*dotted circles*). Finally, on the smallest scales (<3 pc) it becomes clear that the ISM seethes with turbulence and is extremely complex. The overall energetics of CRs in starbursts can be represented by the large-scale view of simple one-zone models. More advanced models take a finer view, simulating large-scale density gradients or the effects of individual CR accelerator regions. Yet, the physics of the CR propagation depends on the chaos of the multiphase ISM on small scales, and so is very poorly understood

(presumably, molecular) gas. Another line of evidence comes from the observed Zeeman splitting of OH lines in Ultraluminous Infrared Galaxies (ULIRGs), which imply that milliGauss magnetic fields are present in OH megamaser regions [46]. These regions occur in dense molecular gas, where the number density is at least 10^4 cm^{-3} and likely 10^{6-7} cm^{-3} [46]. However, magnetic fields require free charges to be frozen into, otherwise the magnetic field lines would slip off the gas through ambipolar diffusion (e.g., [35]). Therefore, we have evidence that something is ionizing the dense molecular gas in ULIRGs. Since UV light is quickly absorbed

and AGNs are not always nearby to provide X-rays, the default assumption is that CRs are ionizing this gas.

The high energy densities of CRs in starbursts can sustain high ionization rates ($\zeta \approx 10^{-16} - 10^{-14}$ sec^{-1}) and heat the gas to high temperatures ($\sim$50–100 K) [41, 54]. The molecular gas in starbursts may represent a "Cosmic Ray Dominated Region" (CRDR). It is not clear, though, how much of the gas the CRs can reach. The problems that face ionizing radiation can be understood by considering other kinds of radiation. Extreme ultraviolet photons interact very strongly with the gas, surrendering much of their power into ionization. Yet that same interaction prevents the photons from going very far: they instead create small highly-ionized H II regions, leaving the majority of the starburst untouched. On the other hand, we never consider Neutrino Dominated Regions, even though neutrinos can penetrate any reasonable column and fill the entire starburst volume. They interact so weakly that their power just escapes the starburst rather than contributing to ionization. To ionize a parcel of gas evenly, we must pick some kind of radiation such that the gas' absorption optical depth is $\sim$1, and this applies to CRs. If CRs interact weakly with the gas, they are blown out by the starburst wind before they can ionize or heat it, or they simply escape through diffusion. If CRs interact strongly with the gas, they lose energy to pionic and ionization losses ("proton calorimetry", [56]), stopping them and shielding the densest regions.

The gamma-ray observations of M82 and NGC 253 indicate that CR protons lose perhaps $\sim$30–40 % of their energy to pionic losses before escaping, implying much stronger losses than in the Milky Way [2, 5, 28]. Moreover, the hard GeV-TeV gamma-ray spectra indicate advective losses which simply remove CRs from the starburst, rather than a high diffusion constant that would let CRs penetrate deep into molecular clouds (e.g., [2]).

The advantage – and trouble – of CRs is that they are deflected by magnetic fields. On the one hand, the effective scattering of CRs lets them build up to large energy densities. On the other, this also means that CRs see a much bigger column than a neutral particle would, stopping them much closer to their sources. The reach of CR ionization thus depends strongly on propagation. But if CRs are not guaranteed to reach all of the molecular gas, we need something else that can.

There *is* a known source of neutral radiation that can ionize the densest molecular gas in starbursts: gamma rays. Above a few MeV, they are stopped by γZ pair production over columns of $\sim$200 g cm^{-2} [8]. The pair $e^{\pm}$ then ionize the gas. Hence, even if CRs are quickly stopped, the bulk gas of the starburst is then likely to be a Gamma Ray Dominated Region (GRDR; Fig. 2). Gamma ray ionization harnesses proton calorimetry: the more strongly the CRs interact with the gas, the higher the energy density of gamma rays is. The gamma-ray ionization rate is

$$\zeta_\gamma \approx F_\gamma \sigma_{\gamma Z} f_{\rm ion}^\gamma / E_{\rm ion} \tag{1}$$

where F_γ is the gamma-ray flux within the starburst, $\sigma_{\gamma Z} \approx 10^{-26}$ cm^2 is the cross section for γZ pair production [8], $f_{\rm ion}^\gamma$ is the efficiency that energy in gamma

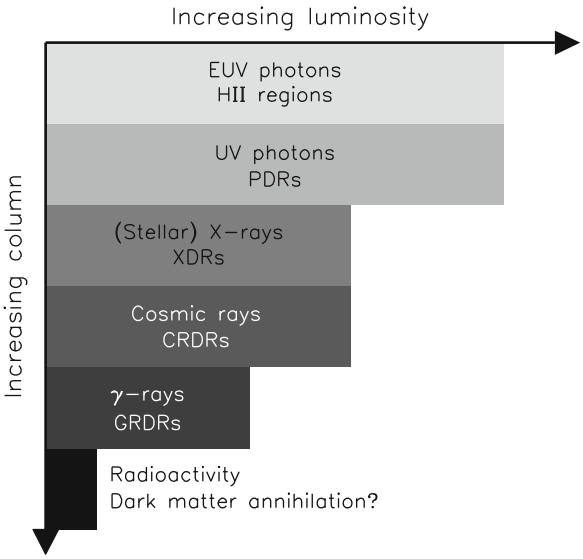

Fig. 2 Different kinds of ionizing radiation are able to penetrate through different columns in the ISM, creating a hierarchy of ionization regions. Starbursts emit many ultraviolet photons but these are stopped very rapidly, resulting small highly-ionized regions. The injected power from gamma rays and radioactivity is small, but it can sustain a low level of ionization everywhere in the ISM

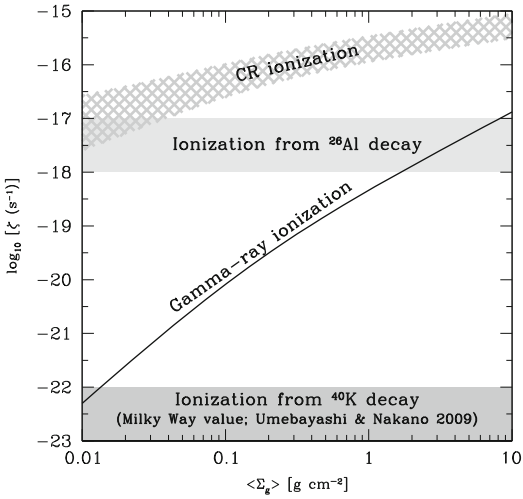

Fig. 3 Comparison of ionization rates from CRs, gamma rays, ^{26}Al, and ^{40}K for starbursts on the Schmidt Law. The CR and ^{26}Al ionization rates depend on their propagation

rays goes into ionizing gas (I assume 0.1, supported by a cascade calculation), and $E_{\rm ion} = 30$ eV [13] is the energy used in each ionization of an atom. F_γ depends on the surface density of star-formation and how proton calorimetric the starburst is – gamma-ray ionization is most effective in very compact ULIRGs like Arp 220.

By using the Schmidt Law [22] to relate gas density to star-formation surface density, I calculate the gamma-ray ionization rate in starbursts. These rates are plotted in Fig. 3: they range from 10^{-22} sec^{-1} at low densities to 10^{-17} sec^{-1}. At the highest gas surface densities, the ionization rates from gamma rays alone

are comparable to those sustained by CRs in Milky Way molecular clouds [29]. Unlike CRDRs, though, GRDRs are not substantially heated by the high energy ionizing radiation. The power dumped by gamma rays is never enough to heat the gas more than a few Kelvin from absolute zero; this is overwhelmed by dust heating, which raises the gas temperature to $\sim$50 K. The coldness of the GRDRs provides a potential observational signature. In molecular lines, the cold GRDRs will appear as shadows against the brighter, hotter CRDR material; the GRDRs should also have a narrower thermal line width [29].

While the gamma-ray ionization rate is high in starbursts like Arp 220, is there anything that can enhance ionization where CRs cannot penetrate in less extreme starbursts? The decay of short-lived radionuclides like ^{26}Al inject MeV particles, ionizing the ISM (long-lived isotopes like ^{40}K sustain only $\zeta \approx 10^{-22}$ sec^{-1}) [59]. The mean abundance X of a radionuclide in the ISM is proportional to the star-formation rate divided by the gas mass, inversely proportional to the gas consumption time. Quicker gas consumption means that more of the gas is converted into stars and ^{26}Al per decay time:

$$X(^{26}\mathrm{Al}) = \frac{M(^{26}\mathrm{Al})}{M_{\mathrm{gas}}} = \frac{\dot{M}(^{26}\mathrm{Al})\tau_{\mathrm{decay}}}{M_{\mathrm{gas}}} \propto \frac{\mathrm{SFR}}{M_{\mathrm{gas}}} = \frac{1}{\tau_{\mathrm{gas}}}. \quad (2)$$

The gas consumption time in starbursts, $\sim$20 Myr in M82 (using the gas mass from [61]), is $\sim$100 times shorter than in the Milky Way [16], implying mean ^{26}Al abundances in starbursts are $\sim$100 times higher [30]. The ^{26}Al alone sustains ionization rates of 10^{-18} sec^{-1} -10^{-17} sec^{-1}. This suggests that ^{26}Al decay ionizes the dense gas in weak starbursts, and gamma rays ionize it in strong starbursts (Fig. 3).

However, if it takes more than a few Myr for the ^{26}Al to mix with the starburst molecular gas, it cannot contribute to ionization [36]. Furthermore, the ^{26}Al may be dumped into the superwind and advected away instead of ionizing molecular gas. On the other hand, the distribution of 1.809 MeV gamma rays from the decay of ^{26}Al in our own Galaxy suggests that it is formed by very massive stars [24]. These very massive stars will not have time to migrate from their star-formation regions, and will likely be near star-forming molecular gas. Like CRs, then, the ionization rate from ^{26}Al nuclei depends on the unknown details of their propagation, something which does not affect gamma rays.

Thus, CRs do not necessarily reach all of the molecular gas in the starbursts. Depending on the unknown propagation of CRs, it is conceivable at least that they leave most of the molecular gas untouched. Ionization from gamma rays and radioactivity may penetrate deeper columns, creating the required free charges to retain magnetic fields. But if CRs are not thoroughly mixed with the molecular gas, are they merely confined to pockets of that gas, or do they spend most of their time in another ISM phase entirely?

3 H II Regions and Starbursts' MHz Radio Spectra: Strömgren Sphere Pudding

The molecular gas ultimately collapses into stars: among the youngest stars are massive O stars that generate ionizing photons. The ionizing luminosity in Lyman continuum photons is actually much greater than the luminosity in CRs; however, these ultraviolet photons interact so strongly with the gas that they never travel far from their birth stars. Thus, instead of the weak but pervasive ionization of CRs or gamma rays, the ultraviolet photons create fully ionized H II regions surrounding O stars with low filling factor (Fig. 2).

The H II regions have two effects on the observed radio spectra: they make the free-free emission observed at high frequencies, and they host free-free absorption at low frequencies [12]. Free-free absorption from individual H II regions is actually observed at low frequencies, both towards the Galactic Center (e.g., [39]) and in the M82 starburst [63]. The free-free emission does not depend much on the geometry of the H II regions. This has led to the adoption of the "uniform slab" assumption, where a uniform density of ionized gas pervades the starburst. However, the geometry matters for calculating the free-free absorption: in reality we have a uniform density, not of *gas*, but of *H II regions*. If the density of H II regions is low enough, on some sightlines there may be no absorption: the H II regions partially cover the starburst (Fig. 4). Furthermore, the nearest H II region on any sightline is buried part way into it. Thus, *if* the synchrotron emitting material is outside the H II regions, some of it remains unobscured at any frequency. In contrast, the radio flux steeply falls towards low frequencies in a truly uniform slab of ionized gas.

The effective absorption coefficient from H II regions is their number density times an effective cross section that depends on their size and opacity. The H II regions can be thought of as Strömgren spheres around super star clusters. I assume these clusters emit ionizing photons for a time $t_{\rm ion}$ in proportion to their mass M and then shut off. Using a super star cluster mass function of $dN/dM \propto M^{-2}\exp(-M/5\times10^6\ {\rm M}_\odot)$ for $M \geq 1{,}000\ {\rm M}_\odot$ (e.g., [34]), I find an effective absorption coefficient of

$$\alpha_{\rm eff} = (120\ {\rm kpc})^{-1}\left(\frac{\rho_{\rm SFR}}{{\rm M}_\odot\ {\rm year}^{-1}\ {\rm kpc}^{-3}}\right)\left(\frac{n_H}{1{,}000\ {\rm cm}^{-3}}\right)^{-4/3}\left(\frac{t_{\rm ion}}{10\ {\rm Myr}}\right) \quad (3)$$

at low frequencies. The H II regions around these SSCs become opaque at a frequency

$$\nu_{\rm ff}^{\rm SSC} = 700\ {\rm MHz}\left(\frac{M}{1{,}000\ {\rm M}_\odot}\right)^{1/6}\left(\frac{T}{10^4\ {\rm K}}\right)^{-3/4}\left(\frac{n_H}{1{,}000\ {\rm cm}^{-3}}\right)^{2/3}; \quad (4)$$

the free-free absorption feature appears in the starburst spectrum around this frequency. If I instead assume that the free-free absorption comes from H II regions around individual O stars with ionizing photon luminosities of $10^{49}\ {\rm sec}^{-1}$,

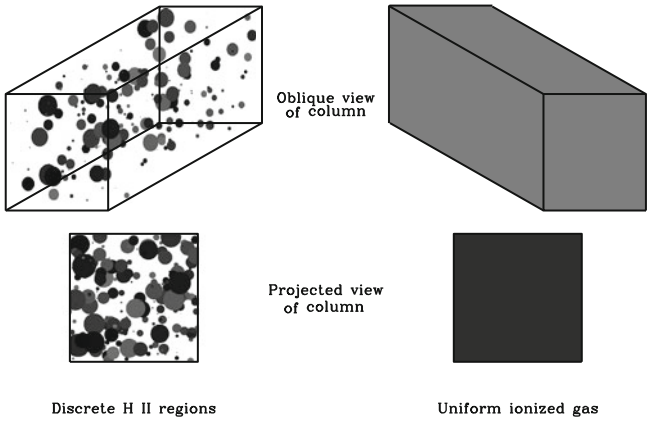

Fig. 4 Illustration of the difference between a uniform density collection of H II regions and a truly uniform ionized gas. In each case, there is free-free absorbing ionized gas which is spread throughout the starburst, so a "uniform slab" model is useful. As the frequency drops to zero, the ionized gas becomes completely opaque. However, not every sightline passes through an H II region on the *left*, as seen by the *white* space in the face-on view: the starburst is partially uncovered. Furthermore, even on sightlines intersecting an H II regions, that ionized gas is at some depth within the starburst (as seen in the oblique view). Thus the H II regions block only a constant fraction of radio emission at low frequency, unlike a uniform gas

then $\alpha_{\rm eff}$ is $\sim$4 times higher. This quantity can then be used in the uniform slab solution to model the actual amount of free-free absorption [31]. I find this effective absorption coefficient is $\alpha_{\rm eff} \approx (0.1 - 1\ {\rm kpc})^{-1}$ as $\nu \to 0$ in M82.

In Fig. 5, I model the radio spectrum of M82 by assuming the free-free absorption and emission comes from Strömgren sphere H II regions around super star clusters. I fit to the number of H II regions, their temperature, and density, as well as the unabsorbed synchrotron spectrum shape using the [62] parameterization:

$$\log_{10}\left(\frac{S_{\rm nt}^{\rm unabs}}{\rm Jy}\right) = \mathcal{A} + \mathcal{B}\log_{10}\left(\frac{\nu}{\rm GHz}\right) + \mathcal{C}\log_{10}\left(\frac{\nu}{\rm GHz}\right)^2 \tag{5}$$

and the amount of free-free emission (including both the free-free emission from the H II regions responsible for the absorption, and a fit component of additional free-free emission):

$$S_{\rm ff}^{\rm unabs} = \mathcal{D}\left(\frac{\nu}{\rm GHz}\right)^{-0.1}. \tag{6}$$

The best-fit model has a spectral index $\mathcal{B} = -0.56$ and an intrinsic synchrotron spectral curvature of $\mathcal{C} = -0.08$. Thermal emission is just 5 % of the 1 GHz flux, even including free-free emission not associated with the absorption. The covering fraction of the H II regions is only 50 %. In this model, the absorbed flux is still 62 % of the unabsorbed flux at low frequencies [31], unlike previous models, where the synchrotron flux drops precipitously below 1 GHz.

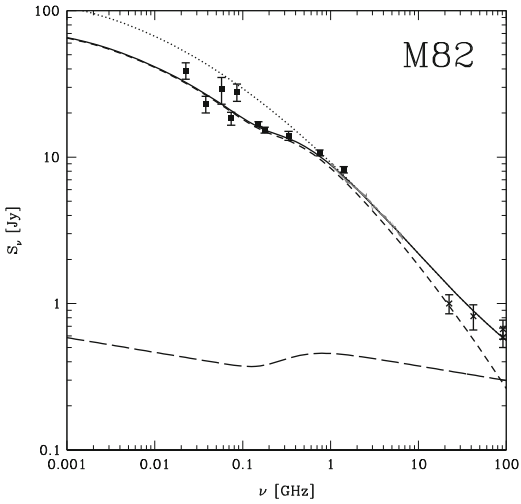

Fig. 5 My fit to the 22 MHz–92 GHz radio spectrum of M82, which assumes that free-free absorption comes from discrete H II regions around super star clusters with O stars. The observed flux is the *solid line* and the unabsorbed flux is the *dotted line*. I also break the observed flux down into its synchrotron (*short-dashed*) and thermal (*long-dashed*) components. Radio data compiled in [31] (from [7, 10, 19, 21, 23, 33, 48], and [62])

I should note, however, that this fit is preliminary, since the beam sizes of the radio data I used in the fit vary widely. Some of the data, particularly the 22.5 and 38 MHz points have extremely large beam sizes ($\sim 1°$), and could easily be contaminated, for example, by the host galaxy of M82. However, the 74 MHz Very Large Array (VLA) sky survey resolved the inner arcminute [10], and the 333 MHz observations by the Giant Metrewave Radio Telescope (GMRT) actually resolved the starburst itself [7]. Both data points are approximately in line with the other data, suggesting that the starburst itself actually is seen at low frequencies. When I redo the fit only including data points with beam sizes smaller than 10 arcmin, the basic conclusion that most of the radio flux is transmitted stands. It would be interesting to measure the spectrum of the starburst with low frequency interferometers like the upgraded Jansky VLA, the GMRT, or the Low Frequency Array (LOFAR).

H II regions naively seem like a good candidate for the location of the CRs: their densities are at least the mean density of the starburst [47], consistent with models; they surround the star-forming regions that may accelerate CRs; and as highly ionized dense plasmas, they have low Alfven velocities, so CRs can self-confine effectively [26]. However, the strong radio emission that seems to be coming from M82 at low radio frequencies constrains this hypothesis – CRs spend some time outside the H II regions.

4 Supernova-Driven Magnetic Fields in the Hot Wind Phase: The Secret of the FIR-Radio Correlation?

So where do CRs spend most of their time? The resolved radio emission appears to be mostly diffuse. If we take that at face value, CRs and the synchrotron emission really do fill most of the starburst. Then the CRs reside in the phase that fills

most of the starburst volume, which is thought to be the hot ($\sim 10^7$–10^8 K) phase that ultimately forms into the wind [20]. Evidence for this gas comes from the observations of 6.7 keV iron line emission from M82; the softer diffuse X-ray emission is mostly thought to be low filling factor gas resulting from when the wind crashes into the galactic halo [51]. This is supported by the evidence for CR advection in M82 and NGC 253 [2, 28]. The picture that arises is that CRs in starbursts are similar to CRs in normal galaxies: the CRs spend most of their time in low density gas that occupies more volume but occasionally diffuse through the high density molecular gas. Pionic gamma rays and secondary $e^{\pm}$ arise during the brief times when the CRs plunge into the molecular gas, but the synchrotron emission arises during the intervals when CRs traverse the diffuse hot phase. Radio emission then mostly traces *magnetic fields in the hot phase*.

What are these fields? The magnetic fields of starbursts are thought to be driven by turbulent dynamos. The energy of supersonic turbulence is injected at some outer scale ℓ, but it rapidly dissipates over a timescale ℓ/σ, where σ is the typical velocity dispersion of the turbulence [50]:

$$U_{\rm turb} = \frac{1}{2}\rho\sigma^2 \approx \frac{\epsilon\ell}{\sigma}, \tag{7}$$

where ρ is the gas density and ϵ is the volumetric energy injection rate. The energy density is then equal to the volumetric energy injection times the dissipation time. I suppose the outer scale of turbulence is the scale height of the starburst, the largest plausible size. Using the central superwind density from [52], I then find $\sigma \approx 2{,}500$ km s^{-1}, indicating weakly supersonic turbulence (for a sound speed $c_S \approx 1{,}500$ km s^{-1}). The magnetic fields are likely amplified until they are in equipartition with turbulent energy [18, 50]. I find for galaxies on the Schmidt law [22], using the energy injection rate from [52],

$$B_{\rm turb}^{\rm hot} \approx 60\varepsilon\ \mu{\rm G}\left(\frac{\Sigma_{\rm SFR}}{{\rm M}_\odot\ {\rm year}^{-1}\ {\rm kpc}^{-2}}\right)^{1/2} \approx 350\varepsilon\ \mu{\rm G}\left(\frac{\Sigma_g}{{\rm g\,cm}^2}\right)^{0.7}. \tag{8}$$

for star-formation and gas surface densities $\Sigma_{\rm SFR}$ and Σ_g respectively, and where ε is a factor of order unity [32].

The radio emission of star-forming galaxies of star-forming galaxies is tightly correlated with its far-infrared (FIR) emission, strongly constraining the effective magnetic fields. In [27], we found a phenomenological scaling of $B_{\rm FRC} \approx 400\ \mu{\rm G}(\Sigma_g/{\rm g\,cm}^2)^{0.7}$ was necessary for this FIR-radio correlation to work. The $B \propto \Sigma_g^{0.7}$ scaling is needed because (1) it keeps the radiation and magnetic fields in equipartition, so the ratio of Inverse Compton and synchrotron cooling times remain constant [60]:

$$\frac{t_{\rm synch}}{t_{\rm IC}} = \frac{U_B}{U_{\rm IC}} \approx \frac{B^2/(8\pi)}{F_{\rm rad}/c} \propto \frac{B^2}{\Sigma_{\rm SFR}} \propto \left(\frac{B}{\Sigma_g^{0.7}}\right)^2, \tag{9}$$

using the [22] Schmidt law ($\Sigma_{\rm SFR} \propto \Sigma_g^{1.4}$). (2) At constant synchrotron frequency (instead of constant electron energy), it preserves the ratio of bremsstrahlung and synchrotron cooling times. The characteristic synchrotron frequency of an electron with energy E_e and charge e is

$$\nu_C = \frac{3E_e^2 eB}{16 m_e^3 c^5} = 1.3\ {\rm GHz} \left(\frac{E_e}{\rm GeV}\right)^2 \left(\frac{B}{100\ \mu{\rm G}}\right) \tag{10}$$

[49]. Plugging that result into formulae for the synchrotron [49] and bremsstrahlung [53] lifetimes give:

$$t_{\rm synch} \approx 1.4\ {\rm Myr} \left(\frac{B}{100\ \mu{\rm G}}\right)^{-3/2} \left(\frac{\nu}{\rm GHz}\right)^{-1/2} \tag{11}$$

$$t_{\rm brems} \approx 310\ {\rm kyr} \left(\frac{n_H}{100\ {\rm cm}^{-3}}\right)^{-1} \tag{12}$$

$$\frac{t_{\rm synch}}{t_{\rm brems}} \approx 4.5 \left(\frac{B}{100\ \mu{\rm G}}\right)^{-3/2} \left(\frac{\nu}{\rm GHz}\right)^{-1/2} \left(\frac{n_H}{100\ {\rm cm}^{-3}}\right) \tag{13}$$

$$\propto B^{-3/2} \nu^{-1/2} n_H . \tag{14}$$

For a given gas scale height, this means that $t_{\rm synch}/t_{\rm brems} \propto (\Sigma_g^{0.7})^{-3/2} \Sigma_g \propto \Sigma_g^{-0.05}$. The $B_{\rm turb}^{\rm hot}$ I quote satisfies these conditions. This suggests that the FIR radio correlation is ultimately powered by the Schmidt Law, causing the hot phase turbulent magnetic fields to have the necessary scaling with mean gas density [32].

This model has interesting implications for whether CRs and magnetic fields are in equipartition with magnetic fields in starbursts. Both CRs and magnetic fields would ultimately have the same power source, the mechanical energy of supernovae. Furthermore, the fraction of supernova power they receive is likely similar (of order tens of percent), with turbulence perhaps receiving a few times more power than the CRs. When the CRs are removed by advection (as seems to be the case in M82 and NGC 253), the residence time for both the CRs and turbulence are also similar. In each case, the residence time is of order a sound-crossing time, with the CR lifetime perhaps being a few times longer than ℓ/σ, because the wind takes some time to accelerate to c_S and beyond. Then equipartition holds between magnetic fields and CRs, even if there is no direct coupling between the two. However, in strongly proton calorimetric galaxies, the residence time of CRs is instead set by pionic loss times that are much shorter than the sound-crossing time: the CR energy density becomes smaller than the magnetic energy density (compare with [27]).

Equipartition seems to work in M82 and NGC 253, as suggested by one-zone models [42,45] and gamma-ray observations [2,43]. However, in Arp 220 and other ULIRGs, equipartition fails if the far-infrared radio correlation is to work [11,55], and one-zone models of the radio emission indicate stronger magnetic fields, a few milliGauss [57], than expected from equipartition. It will be interesting to see if

equipartition actually fails in Arp 220 if it is detected in gamma rays, perhaps with the Cherenkov Telescope Array (CTA; [6]).

While this can explain the magnetic fields, what about the gas density? Previous one-zone models to interpret starbursts' nonthermal emission assume that CRs experience the *mean* (volume-averaged) gas density in the starburst. This can only happen if the CRs leave the hot phase and enter the molecular gas (or possibly H II regions). Interaction with dense gas is needed to flatten the radio spectra through bremsstrahlung and ionization losses [55], though advective escape also flattens spectra. Finally, much of starbursts' radio emission probably comes from pionic $e^{\pm}$ [27, 44]: these are created in dense gas, but they would have to diffuse out into the hot phase to emit radio. How does this mixing of CRs with gas work? Observations of the Galactic Center suggest that CRs *don't* mix with the dense molecular gas there [14], but M82 and NGC 253 seem to be much more efficient at stopping protons [2, 28]. And why does the assumption of mean density seem to work? Only knowledge of how CRs traverse the different phases can answer these questions.

5 Conclusion

The matter in a starburst ISM spans the range of energies from 10 K to 10 TK: cold molecular gas at 10 K, H II regions at 10 kK, the hot wind phase at 10 MK, the MeV ionizing particles from ^{26}Al decay at 10 GK, and the cosmic rays and gamma rays at 10 TK and beyond. The relationship between these phases, and their effects on observables, is complex.

My hypothesis here is that CRs in starbursts spend most of their time in the volume-filling hot phase of the ISM, but they occasionally mix into the molecular gas to efficiently produce gamma rays and pionic $e^{\pm}$. The relatively efficient pionic losses within the molecular phase may shield the densest gas. How this works in detail, like how the competition between the advection in the hot phase and the pionic losses in the molecular gas somehow lets us just use the average gas density of starbursts in one-zone models, is not clear.

Yet the ideas presented here are still simplistic compared to the reality of gas in starbursts. I have considered each phase as if it had a single density and magnetic field, but turbulence creates fluctuations in both of these quantities. Ultimately, to understand CRs in starbursts, we must learn what turbulence does to CRs, gas, and magnetic fields as they interact with each other.

Acknowledgements I am supported by a Jansky Fellowship from the National Radio Astronomy Observatory. The National Radio Astronomy Observatory is operated by Associated Universities, Inc., under cooperative agreement with the National Science Foundation. I would like to acknowledge discussions and comments with Todd Thompson, Padelis Papadopolous, Jim Condon, Rainer Beck, and Diego Torres.

References

1. Abdo, A. A., et al. 2010a, ApJ, 709, L152
2. Abramowski, A., et al. 2012, arXiv:1205.5485
3. Acciari, V. A., et al. 2009, Nature, 462, 770
4. Acero, F., et al. 2009, Science, 326, 1080
5. Ackermann, M., et al. 2012, arXiv:1206.1346
6. Actis, M., Agnetta, G., Aharonian, F., et al. 2011, Experimental Astronomy, 32, 193
7. Basu, A., Mitra, D., Wadadekar, Y., & Ishwara-Chandra, C. H. 2012, MNRAS, 419, 1136
8. Berestetskii, V. B., Lifshitz, E. M., & Pitaevskii, L. P. 1979, *Quantum Electrodynamics*, 2nd ed. (Oxford: Butterworth-Heinemann)
9. Chevalier, R. A., & Clegg, A. W. 1985, Nature, 317, 44
10. Cohen, A. S., Lane, W. M., Cotton, W. D., et al. 2007, AJ, 134, 1245
11. Condon, J. J., Huang, Z.-P., Yin, Q. F., & Thuan, T. X. 1991, ApJ, 378, 65
12. Condon, J. J. 1992, ARA&A, 30, 575
13. Cravens, T. E., & Dalgarno, A. 1978, ApJ, 219, 750
14. Crocker, R. M., Jones, D. I., Aharonian, F., Law, C. J., Melia, F., Oka, T., & Ott, J. 2011, MNRAS, 413, 763
15. de Cea del Pozo, E., Torres, D. F., & Rodriguez Marrero, A. Y. 2009, ApJ, 698, 1054
16. Diehl, R., Halloin, H., Kretschmer, K., et al. 2006, A&A, 449, 1025
17. Domingo-Santamaría, E. & Torres, D. F. 2005, A&A, 444, 403
18. Groves, B. A., Cho, J., Dopita, M., & Lazarian, A. 2003, Publ. Astron. Soc. Australia, 20, 252
19. Hales, S. E. G., Mayer, C. J., Warner, P. J., & Baldwin, J. E. 1991, MNRAS, 251, 46
20. Heckman, T. M., Armus, L., & Miley, G. K. 1990, ApJS, 74, 833
    laxies
21. Israel, F. P., & Mahoney, M. J. 1990, ApJ, 352, 30
22. Kennicutt, R. C. 1998, ApJ, 498, 541
23. Klein, U., Wielebinski, R., & Morsi, H. W. 1988, A&A, 190, 41
24. Knödlseder, J. 1999, ApJ, 510, 915
25. Krumholz, M. R., & McKee, C. F. 2005, ApJ, 630, 250
26. Kulsrud, R., Pearce, W. P. 1969, ApJ, 156, 445
27. Lacki, B. C., Thompson, T. A., & Quataert, E. 2010, ApJ, 717, 1
28. Lacki, B. C., Thompson, T. A., Quataert, E., Loeb, A., & Waxman, E. 2011, ApJ, 734, 107
29. Lacki, B. C. 2012a, arXiv:1204.2580
30. Lacki, B. C. 2012b, arXiv:1204.2584
31. Lacki, B. C. 2012c, arXiv:1206.7100
32. Lacki, B. C. 2012d, in prep.
33. Laing, R. A., & Peacock, J. A. 1980, MNRAS, 190, 903
34. McCrady, N., & Graham, J. R. 2007, ApJ, 663, 844
35. Mestel, L., & Spitzer, L., Jr. 1956, MNRAS, 116, 503
36. Meyer, B. S., & Clayton, D. D. 2000, Space Sci. Rev., 92, 133
37. Murphy, E. J., Helou, G., Kenney, J. D. P., Armus, L., & Braun, R. 2008, ApJ, 678, 828
38. Murphy, E. J., Porter, T. A., Moskalenko, I. V., Helou, G., & Strong, A. W. 2012, ApJ, 750, 126
39. Nord, M. E., Henning, P. A., Rand, R. J., Lazio, T. J. W., & Kassim, N. E. 2006, AJ, 132, 242
40. Paglione, T. A. D., Marscher, A. P., Jackson, J. M., & Bertsch, D. L. 1996, ApJ, 460, 295
41. Papadopoulos, P. P. 2010, ApJ, 720, 226
42. Persic, M., Rephaeli, Y., & Arieli, Y. 2008, A&A, 486, 143
43. Persic, M., & Rephaeli, Y. 2012, arXiv:1201.0369
44. Rengarajan, T. N. 2005, Proc. 29th Int. Cosmic Ray Conf. (Pune), 3
45. Rephaeli, Y., Arieli, Y., & Persic, M. 2010, MNRAS, 401, 473
46. Robishaw, T., Quataert, E., & Heiles, C. 2008, ApJ, 680, 981

47. Rodriguez-Rico, C. A., Viallefond, F., Zhao, J.-H., Goss, W. M., & Anantharamaiah, K. R. 2004, ApJ, 616, 783
48. Roger, R. S., Costain, C. H., & Stewart, D. I. 1986, A&AS, 65, 485
49. Rybicki, G. B. & Lightman, A. P. 1979, *Radiative Processes in Astrophysics*, (New York: Wiley-VCH).
50. Stone, J. M., Ostriker, E. C., & Gammie, C. F. 1998, ApJ, 508, L99
51. Strickland, D. K., & Heckman, T. M. 2007, ApJ, 658, 258
52. Strickland, D. K., & Heckman, T. M. 2009, ApJ, 697, 2030
53. Strong, A. W., & Moskalenko, I. V. 1998, ApJ, 509, 212
54. Suchkov, A., Allen, R. J., & Heckman, T. M. 1993, ApJ, 413, 542
55. Thompson, T. A., Quataert, E., Waxman, E., Murray, N., & Martin, C. L. 2006, ApJ, 645, 186
56. Thompson, T. A., Quataert, E., Waxman, E. 2007, ApJ, 654, 219
57. Torres, D. F. 2004, ApJ, 617, 966
58. Torres, D. F., Cillis, A., Lacki, B., & Rephaeli, Y. 2012, MNRAS, 423, 822
59. Umebayashi, T., & Nakano, T. 2009, ApJ, 690, 69
60. Völk, H. J. 1989, A&A, 218, 67
61. Weiß, A., Neininger, N., Hüttemeister, S., & Klein, U. 2001, A&A, 365, 571
62. Williams, P. K. G., & Bower, G. C. 2010, ApJ, 710, 1462
63. Wills, K. A., Pedlar, A., Muxlow, T. W. B., & Wilkinson, P. N. 1997, MNRAS, 291, 517

Cosmic Ray Driven Dynamo in Spiral Galaxies

Dominik Wóltański, Michał Hanasz, and Kacper Kowalik

Abstract We investigate galactic magnetic field generation by means of direct simulations of magnetized ISM composed of ionized gas, magnetic fields and cosmic rays. We consider galactic disk of interstellar matter rotating under time-dependent galactic gravitational potential due to stars and dark matter particles forming disk, bulge and halo. The seed field is assumed to be of stellar origin and is considered to be supplied by supernovae remnants. As a result of underlying CR-driven dynamo process magnetic field is amplified up to the equipartition level. In the present model we note magnetic field reversals and further temporal changes of magnetic field polarity. We find the strongest magnetic field between spiral arms, which is aligned with the arms. In the presence of a galaxy companion galactic magnetic field evolution proceeds analogously until the merger event, after which magnetic field is disordered. For the simple comparison with real observed galaxies we make synthetic maps of synchrotron emission and show similarities to magnetic field structures observed in spiral galaxies such as NGC 6946.

1 Introduction

Dynamical effects of cosmic ray gas in galactic disks has been pointed by Parker [14], who described the instability of vertically stratified interstellar medium due to buoyancy of weightless components, i.e. cosmic rays and magnetic fields. This is the basis of cosmic ray driven dynamo (CRDD) proposed by Parker [15], which turned out to be a very fast, galactic magnetic fields amplification mechanism in conjunction with the idea of Rees [16] that galactic magnetic field may have a

D. Wóltański (✉) · M. Hanasz · K. Kowalik
Centre for Astronomy, Faculty of Physics, Astronomy and Informatics, Nicolaus Copernicus University, Grudziadzka 5, 87-100 Toruń, Poland
e-mail: minikwolt@astri.umk.pl

D.F. Torres and O. Reimer (eds.), *Cosmic Rays in Star-Forming Environments*, Astrophysics and Space Science Proceedings 34, DOI 10.1007/978-3-642-35410-6_30,

stellar origin. Thus, magnetic fields created and amplified in stars may be supplied to the interstellar medium in stellar winds and supernova bursts and play a role of seed fields required by galactic dynamo action. The first numerical experiments of cosmic ray driven dynamo in local box approximation has been done and studied by Hanasz and collaborators [7, 8]. Global treatment of galactic disk in simulations allowed to achieve an energy equipartition of all three main interstellar medium components: thermal gas, magnetic fields and cosmic ray gas because they are not trapped in a local box any more and can migrate freely. The first global simulation of CRDD has been described by Hanasz and collaborators [9]. The global disk was under an axis-symmetrical, invariable gravitational potential and there was no visible grand-designed structures. However, in the simulation shown by Kulpa-Dybeł and collaborators [12] analytically specified time-dependent non-axis-symmetric gravity component has been added and it was shown that galactic magnetic field can be successfully amplified by CRDD in presence of bars and spiral arms. Here, we present CRDD results achieved in global galactic disk model with live-like gravity from stars and dark matter simulated as n-body particles.

2 Cosmic Ray Driven Dynamo

Cosmic ray driven dynamo is a type of turbulent dynamo where cosmic rays play a crucial role being a source of galactic interstellar turbulence. Cosmic rays enhance the buoyancy effect which triggers vertical magnetic fields loops. This phenomenon is known as the Parker Instability. The loops are twisted by a differential rotation of the ionized ISM component. As a result magnetic configuration favourable for magnetic reconnection may form, where one magnetic polarity is amplified in the disk and other one is carried away by the galactic wind. The dynamo acts until magnetic, cosmic ray and thermal gas energies reach equipartition. Due to galactic wind, which regulate magnetic field morphology and the cosmic ray content in the disk it is important to have an opportunity to examine global dynamo models. Moreover, our idea is to investigate the CRDD process in presence of spiral structure in a gaseous disk, where the global approach is clearly worthy.

In presented models we assume uniform, nucleon-based cosmic ray composition and neglect electrons' contribution. Cosmic rays are treated as a fluid with the adiabatic index $\gamma_{cr} = 14/9$. In the model, cosmic rays are present in the galactic disk at initial stage and are later supplied by supernovae explosions. The dynamical evolution of cosmic rays is determined by the diffusion-advection equation [17]. They move anisotropically, preferably along magnetic field lines. That is described by diffusion tensor based on parallel and perpendicular cosmic ray diffusion coefficients (see [3]) assumed equal to $4.97145 \times 10^{28}\mathrm{cm}^2\mathrm{s}^{-1}$ and $4.97145 \times 10^{26}\mathrm{cm}^2\mathrm{s}^{-1}$, respectively. We chose the most effective resistivity value (see [8]) equal to $3 \times 10^{25}\mathrm{cm}^2\mathrm{s}^{-1}$.

3 Disk Model Description

We perform direct simulations of magnetized ISM composed of gas, magnetic fields and cosmic rays. All gaseous ISM components are equally treated as fully ionized gas which interacts with magnetic fields. We use column density distribution following Ferriere [2]. The distribution is cut off at 20 kpc radius treated as the border of the disk. On the basis of column density distribution along the radius we compute initial gas density vertical profile keeping hydrostatic equilibrium in a given gravity field.

Initially, there is no magnetic field. The source of seed magnetic fields is considered to origin from supernovae remnants that appear in the galactic disk during its evolution. SNR also are sources of cosmic rays. 10% of the typical SN energy (i.e. 10^{51} erg) is considered to transfer to cosmic rays. The initial cosmic ray energy distribution is proportional to gas with the factor $\beta_{cr} = 0$ (models A and B) or $\beta_{cr} = 4$ (model C).

3.1 Gravitational Potential

We consider galactic disk of interstellar matter rotating under time-dependent galactic gravitational potential due to stars and dark matter particles forming disk, bulge and halo. The galactic mass distribution is set in a way that rotation curve is like that of Milky Way. It is very steep for the first kiloparsec of radius and flat farther away. Moreover, by properly chosen bulge to halo mass ratio we avoid early bar formation. We use Hernquist model [10] to randomize positions and initial velocities of mass particles in galaxy model.

The gaseous disk evolution happens in a time-dependent gravitational potential caused by stars and dark matter. We neglect the gravitational contribution of interstellar gas to stars and dark matter motions. We use n-body code to determine dynamical evolution of galaxy composed of stars and dark matter particles collected in a bulge, disk and halo. From gravitational potential values in particles positions we create a mesh by an interpolation. This is performed with the aid of Triangular Shaped Cloud (TSC) method and supplemented by simple linear interpolation along domain boundaries. Resulting gravitational potential distributions on a mesh are additionally interpolated in time and used in the gaseous disk grid simulation.

3.2 Supernovae Bursts Probability Distribution

We assume that supernova explosion probability distribution is a straightforward representation of mass distribution of the gaseous galactic disk. We use the interpretation of Schmidt-Kennicutt law [11, 18] with the exponent 1.4 which describes a

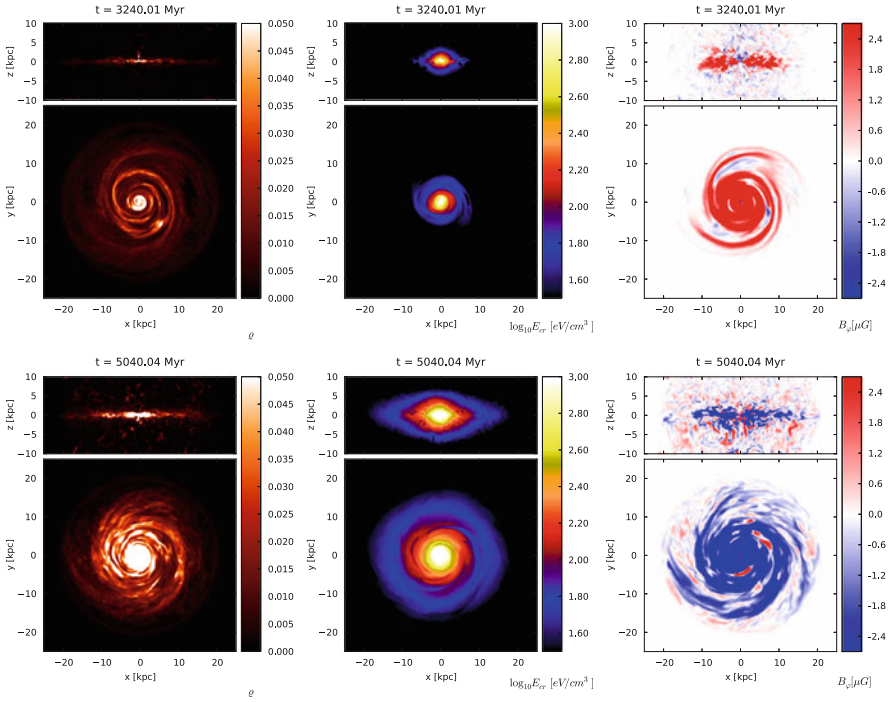

Fig. 1 Evolution of the galactic model B. Meaning of the panels is the same as in Fig. 2. Times in rows are: 3,240 and 5,040 Myr

relation between star formation and molecular gas density. For the numerical reason we add a small correction by setting a lower limit for the mass in a cell below of which there is no contribution to the SNe probability distribution. The supernova bursts frequency (1 SN over 55 years) is taken from [2] as SN type II frequency and is made free to change proportionally to mass contents in the computational domain.

We input dipolar magnetic field source only for the first billion years of galaxy evolution. It is dictated by the necessity of computational cost. However, it should be noted that the contribution of stellar magnetic field during the middle and late stages of galaxy magnetic evolution is negligible.

3.3 Numerical Setup

To determine galactic gravity evolution we use n-body VINE code [13, 19]. We use 6×10^5 particles in n-body galaxy simulation: initially 180,000 of a disk, 60,000 of bulge, 360,000 of halo. The mass of the particle disk is $8.56 \times 10^{10}\ M_\odot$. One disk particle stands for $4.76 \times 10^5\ M_\odot$. The mass of the particle bulge is $2.81 \times 10^{10}\ M_\odot$

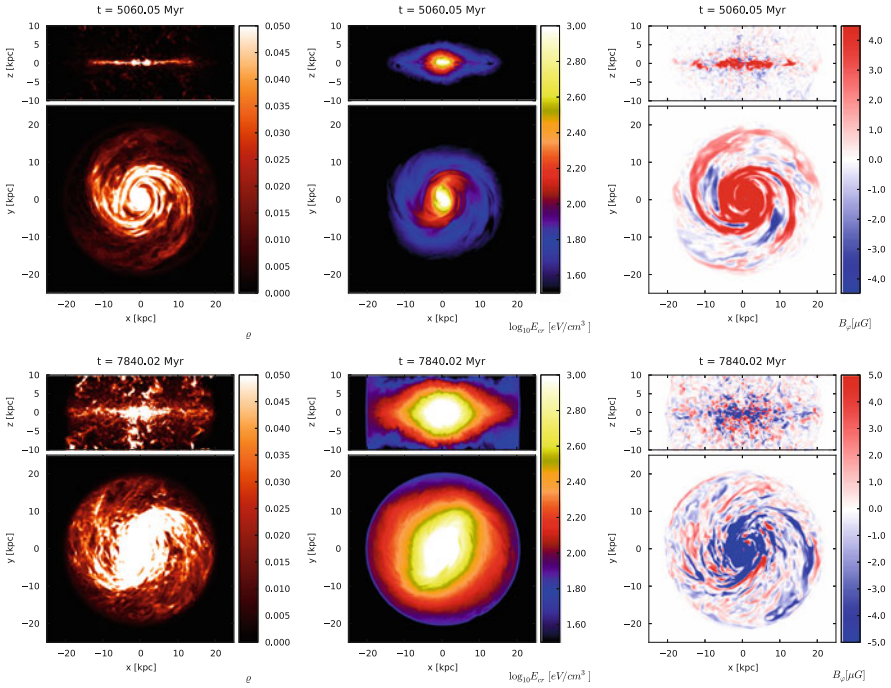

Fig. 2 Evolution of the galactic model A. In subsequent columns there are shown: gas density, logarithm of cosmic ray energy density and azimuthal magnetic field component, respectively. Times in rows are: 5,060 and 7,840 Myr

or $5.62 \times 10^{10}\ M_{\odot}$. The mass of the particle halo is $1.071 \times 10^{11}\ M_{\odot}$. In some cases we have additional 10^4 particles for the secondary galaxy. Then, mass of the satellite is then $4.28 \times 10^{10}\ M_{\odot}$. Every 0.01 Myr the gravitational potential frame is written down to be reused in time in grid simulation.

For the gaseous galactic disk and CRDD simulation we use MHD grid code PIERNIK [4–6]. We keep 100 pc cell resolution. For simulations A and B we set grid $500 \times 500 \times 200$ cells which spans over $50 \times 50 \times 20$ kpc. For the C simulation we set grid $768 \times 768 \times 384$ cells which spans over $76.8 \times 76.8 \times 38.4$ kpc. All the simulations are held up to several billion years of galaxy evolution.

4 Results

We present results of three simulations. Crucial parameters and models' characteristics are gathered in Table 1.

We find magnetic field amplification in the disk up to the equipartition level. The growth of the magnetic field strength is present until about $t = 5$ Gyr and $t = 2.5$ Gyr in the A and B simulations, respectively, reaching values of about 5 μG in the disk.

Table 1 Parameters and characteristics of simulation runs

Model	Grid	Bulge[a]	Satellite[a]	Bar	Reversals	t_{e-fold}
A	$500^2 \times 200$	2.80768 M_{10}	–	late	Yes	240 Myr
B	$500^2 \times 200$	5.61536 M_{10}	–	–	Yes	160 – 200 Myr
C	$768^2 \times 384$	2.80768 M_{10}	4.28 M_{10}	–	Yes	215 – 310 Myr

[a] mas in units $M_{10} = 10^{10}\ M_{\odot}$

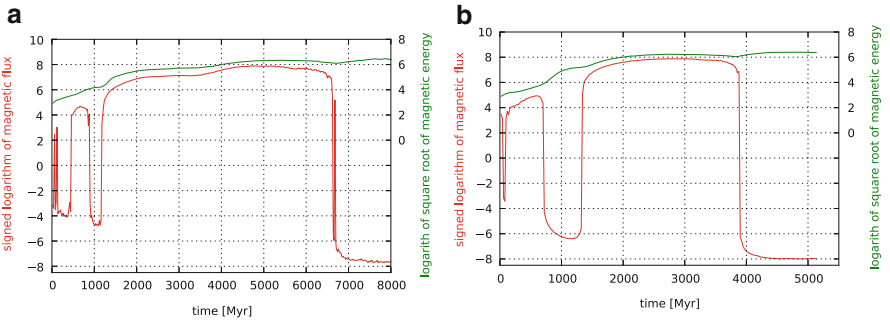

Fig. 3 Magnetic flux (*red bottom lines*) and square root of magnetic energy (*green upper line*) of the simulations A and B (*left* and *right panel*, respectively). The scale on the *left* corresponds to the signum × logarithm of the plotted value. That means there are given the sign of the flux and positive exponents of the flux absolute value

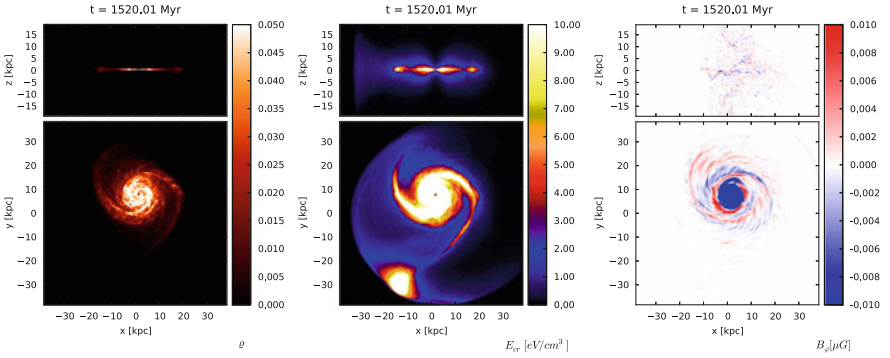

Fig. 4 Density distribution, cosmic ray energy density and azimuthal magnetic field component for the galactic model C for t = 1, 520 Myr

During the amplification phase, magnetic flux and total magnetic energy grow by about 4–5 and 7 orders of magnitude, respectively (see Fig. 3). The average e-folding time of magnetic flux amplification during the first 2 Myr is approximately equal to 160–200 Myr, corresponding to the rotation period at the galactocentric radius $R_g = 5.35 - 8$ kpc. We find several changes of azimuthal magnetic field polarity during amplification phase after which either the positive or negative polarity dominates the disk. In all models we find also late polarity change (6,700 and 3,900 Myr, see Fig. 3) that follow vast reversals of the magnetic field.

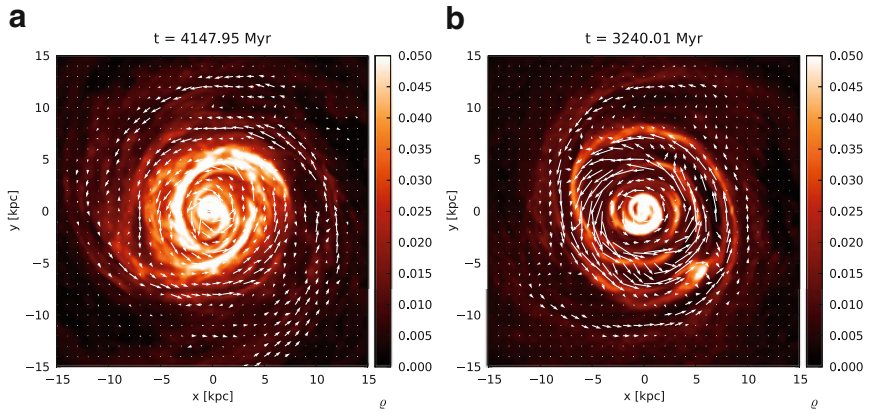

Fig. 5 30 × 30 kpc zoom on the galactic disk with spiral arms for model A (*left panel*, t = 4, 148 Myr) and B (*right panel*, t = 3, 240 Myr). In *red*-to-*white color* scale gas density is shown. Magnetic field vectors are overplotted in *white color*. It can be seen in both cases that the strongest magnetic field is located in interarm regions or on the inner edge of gaseous spiral arms. Magnetic fields are aligned along gaseous arms and form magnetic arms

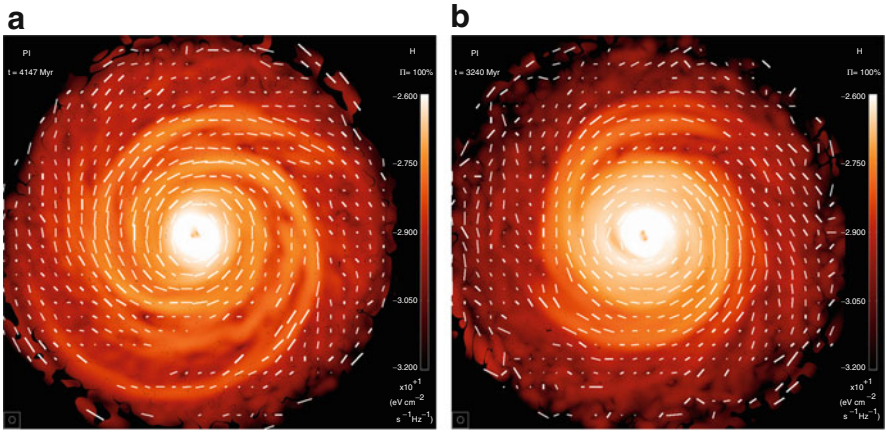

Fig. 6 Synthetic radio maps of logarithm of polarized emission with polarization vectors (models A and B, respectively) for the same stages as in Fig. 5 (model A and B)

In the model A magnetic reversals last for 3.5 Gyr before polarity change and become witnesses of bar formation. In the model B magnetic reversals develop fast and in about 700 Myr lead to magnetic polarity change.

A very important result of presented complex models is that well-developed magnetic field is stronger in the interarm regions. In Fig. 5 we present a map of gas density with magnetic field vectors. It can be seen that vectors are longer between

gaseous arms and simultaneously they are aligned to the arms. This result may become a hint to understand interarm magnetic fields in NGC 6946 [1].

For a direct comparison of our results to observed spiral galaxies we made synthetic maps of polarized intensity of synchrotron emission presented in Fig. 6. We note that our further studies may provide detailed knowledge about strength and morphologies of magnetic fields in spiral galaxies.

Acknowledgements We would like to thank Hanna Kotarba for an assistance and fruitful discussions on n-body galactic models. This work was supported in part by Polish Ministry of Science and Higher Education through the grants 92/N–ASTROSIM/2008/0 and N N203 511038. The computations have been performed on the GALERA supercomputer in TASK Academic Computer Centre in Gdańsk. This work was conducted within POWIEW project supported by the European Regional Development Fund in Innovative Economy Programme (POIG.02.03.00-00-018/08).

References

1. Beck, R., Astron. & Astrophys. 470, 539 (2007)
2. Ferriere, K., Astrophys. J. 497, 759 (1998)
3. Giacalone, J. and Jokipii, J. R., Astrophys. J. 520, 204 (1999)
4. Hanasz, M., Kowalik, K., Wóltański, D. and Pawłaszek, R., arXiv:0812.4839 (2008)
5. Hanasz, M., Kowalik, K., Wóltański, D. and Pawłaszek, R., arXiv:0901.0104 (2009)
6. Hanasz, M., Kowalik, K., Wóltański, D. and Pawłaszek, R., EAS Publ. Series, 42, 275 (2010)
7. Hanasz, M., Otmianowska-Mazur, K., Kowal, G. and Lesch, H., Astron. Nachr. 327, 469 (2006)
8. Hanasz, M., Otmianowska-Mazur, K., Kowal, G. and Lesch, H., Astron. & Astrophys. 498, 335 (2009)
9. Hanasz, M., Wóltański, D. and Kowalik, K., Astrophys. J. Let. 706, L155 (2009)
10. Hernquist, L., Astrophys. J. 356, 359 (1990)
11. Kennicutt, R. C., Jr., Astrophys. J. 498, 541 (1998)
12. Kulpa-Dybeł, K., Otmianowska-Mazur, K., Kulesza-Żydzik, B., Hanasz, M., Kowal, G., Wóltański, D. and Kowalik, K., Astrophys. J. Let. 733, L18 (2011)
13. Nelson, A. F., Wetzstein, M. and Naab, T., Astrophys. J. Supp. 184, 326 (2009)
14. Parker, E. N., Astrophys. J. 145, 811 (1966)
15. Parker, E. N., Astrophys. J. 401, 137 (1992)
16. Rees, M. J., Quart. J. Roy. Astron. Soc., 28, 197 (1987)
17. Schlickeiser, R. and Lerche, I., Astron. & Astrophys. 151, 151 (1985)
18. Schmidt, M., Astrophys. J. 129, 243 (1959)
19. Wetzstein, M., Nelson, A. F., Naab, T. and Burkert, A., Astrophys. J. Supp. 184, 298 (2009)

Nonthermal X-Rays from Low-Energy Cosmic Rays in the Arches Cluster Region

V. Tatischeff, A. Decourchelle, and G. Maurin

Abstract We have studied in detail the production of nonthermal line and continuum X-rays by interaction of accelerated electrons and ions with a neutral ambient gas, and have applied the resulting models to *XMM-Newton* observations of the X-ray emission emanating from the Arches cluster region near the Galactic center. The diffuse X-ray emission prominent in the 6.4 keV Fe Kα line surrounding the very massive cluster is likely excited by low-energy cosmic ray ions produced in the ongoing supersonic collision between the star cluster and an adjacent molecular cloud. The nonthermal emission from this region probably offers at present the best available signature for a source of low-energy hadronic cosmic rays in the Galaxy.

1 Introduction

The Galactic center (GC) region hosts over 10 % of Galactic star formation activity within only < 0.1 % of the volume of the Galactic disk. Three young and very massive stellar clusters are known to reside in the central molecular zone: the Arches

V. Tatischeff (✉)
Centre de Spectrométrie Nucléaire et de Spectrométrie de Masse, IN2P3/CNRS and Univ Paris-Sud, 91405, Orsay Campus, France
e-mail: Vincent.Tatischeff@csnsm.in2p3.fr

A. Decourchelle
Service d'Astrophysique (SAp)/IRFU/DSM/CEA Saclay, Bt 709, 91191, Gif-sur-Yvette Cedex, France

Laboratoire AIM, CEA-IRFU/CNRS/Univ Paris Diderot, CEA Saclay, 91191, Gif sur Yvette, France
e-mail: anne.decourchelle@cea.fr

G. Maurin
Laboratoire d'Annecy le Vieux de Physique des Particules, Univ de Savoie, CNRS, BP 110, 74941, Annecy-le-Vieux Cedex, France
e-mail: gilles.maurin@lapp.in2p3.fr

D.F. Torres and O. Reimer (eds.), *Cosmic Rays in Star-Forming Environments*, Astrophysics and Space Science Proceedings 34, DOI 10.1007/978-3-642-35410-6_31,

(e.g. [5]) and Quintuplet (e.g. [8]) clusters, as well as the nuclear cluster surrounding Sgr A* (e.g. [6]). The three clusters are $\sim$ 2–7 $\times$ 10^6 year old and have masses of $\sim$ 1–4 $\times$ 10^4 $M_\odot$ each.

The Arches cluster differs from the two other young and massive clusters of the GC region by being surrounded by a bright nonthermal X-ray emission prominent in the Fe Kα line at 6.4 keV [2,15,17]. This line is produced by the removal of a K-shell electron in neutral to low-ionized Fe atoms, either by hard X-ray photoionization or by collisional ionization induced by accelerated particles. Several molecular clouds of the central molecular zone emit the 6.4 keV line, most notably Sgr B1, Sgr B2, Sgr C, and clouds located between Sgr A* and the Radio Arc (see [18]). The Fe Kα line from these regions has been interpreted as resulting from photoionization induced by a powerful X-ray flare from the supermassive black hole Sgr A* (e.g. [9, 14]; but see [19]). However, the 6.4 keV line diffuse emission surrounding the Arches cluster is most likely related to the cluster itself. But this radiation is probably not excited by a hard X-ray photoionization source located in the star cluster, because the observed X-ray luminosity of the cluster is about two orders of magnitude short of what would be required for this interpretation. Thus, a likely explanation for this peculiar emission is that it results from the bombardment of molecular gas by low-energy cosmic rays (LECRs) accelerated within or close to the cluster (see also [2, 15, 17]).

We have recently studied in detail the production of nonthermal line and continuum X-rays by interaction of LECR electrons and ions with a neutral ambient medium, and have then used these calculations to interpret *XMM-Newton* observations of the Arches cluster region [13]. We present in the current paper an updated summary of this work, together with some avenues for future research on this topic.

2 XMM-Newton Observations of the Arches Cluster Region

We have considered for our analysis all public *XMM-Newton* EPIC observations encompassing the Arches cluster. The processes of data reduction, map generation, and spectrum extraction are detailed in Tatischeff et al. [13]. A map of the Arches cluster region in the 6.4 keV Fe Kα line is compared in Fig. 1 with a high-resolution image in the H Paschen-α (Pα) line [3, 16]. The Pα line emission is a sensitive tracer of massive stars and their environs. The main diffuse Pα-emitting features in the figure are the eastern Arched filaments, which are thought to be located at edges of molecular clouds photoionized by the adjacent star cluster (see [7]). We see that the 6.4 keV line emission is not well correlated with the Arched filaments, but is concentrated into a region of only a few pc^2 surrounding the star cluster. This strongly suggests that the origin of this emission is related to the cluster itself and not to a distant source such as Sgr A*. The most prominent structure in the X-ray map is composed of two bright knots connected by a faint bridge to the east of the cluster. As already discussed by Wang et al. [17] from *Chandra* observations of this

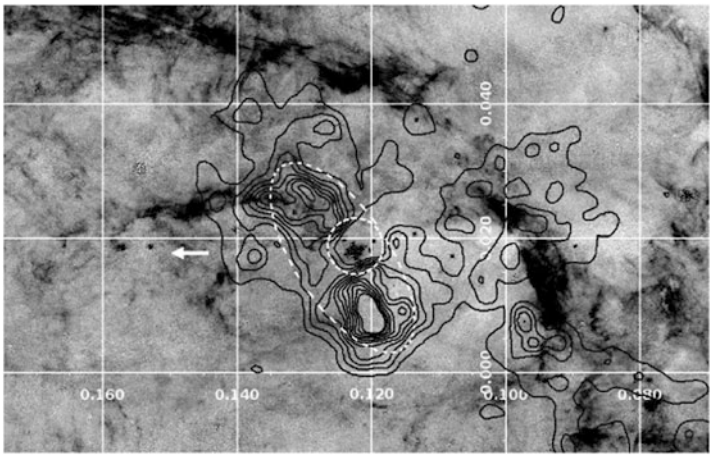

Fig. 1 *XMM-Newton*/EPIC continuum-subtracted 6.4-keV line intensity contours (linearly spaced between 3×10^{-8} and 1.8×10^{-7} photons cm^{-2} s^{-1} arcmin^{-2}) overlaid with a *Hubble Space Telescope*/NICMOS map in the Paschen-α line [3, 16]. EPIC MOS and pn spectra (Fig. 2) were extracted from the region inside the *white dashed ellipse* but outside the *dashed circle* to characterize the bright nonthermal X-ray emission surrounding the Arches cluster. The axis of the map indicate galactic coordinates in degrees. The Arches cluster is located inside the *dashed circle* at $\ell \approx 0.122^\circ$ and $b \approx 0.018^\circ$. The *white arrow* illustrates the observed proper motion of the cluster, which is almost parallel to the Galactic plane [4, 12]. North is up and east is to the *left*

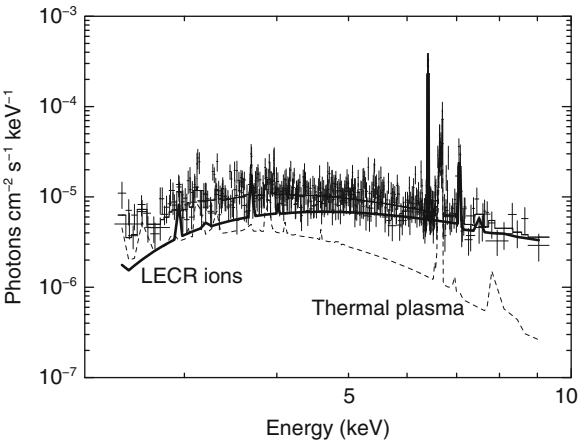

Fig. 2 *XMM-Newton*/EPIC MOS and pn spectra extracted from a broad region around the Arches cluster (see Fig. 1) and the best-fit spectral model assuming that the emission comes from a combination of a collisionally ionization equilibrium plasma (APEC model) and a nonthermal component produced by interactions of LECR ions with a neutral gas. The two emission components are subject to a line-of-sight photoelectric absorption

region, such a morphology is suggestive of a bow shock that may be associated with the supersonic proper motion of the Arches cluster. The direction of motion of the cluster stars relative to the field population is almost parallel to the Galactic plane and directed towards positive longitude [4,12]. The orientation of the bow-shock like structure observed at 6.4 keV is broadly consistent with the cluster proper motion. The evidence that the cluster is presently interacting with a molecular cloud was already discussed by Figer et al. [5].

The diffuse X-ray radiation arising from the environs of the star cluster is composed of a nonthermal component characterized by a hard continuum emission and a strong line at 6.4 keV, plus a thermal plasma component revealed by a line at 6.7 keV from He-like Fe atoms (see Fig. 2). The diffuse thermal emission is thought to be produced by the thermalization of winds from massive stars of the cluster, that merge and expand together to form a bubble of hot gas [17]. The expected temperature of such a cluster wind is consistent with the measured temperature of the thermal component, $kT \sim 2$ keV (see also [1] and references therein).

The nonthermal component can be characterized by a power-law continuum and two Gaussian lines at ~ 6.4 and 7.05 keV to account for the Kα and Kβ lines from neutral to low-ionized Fe atoms (the theoretical Fe Kβ/Kα flux ratio is equal to 13 %). We added an optically thin, ionization equilibrium plasma (APEC, [11]) to model the total X-ray emission. The fit of this model to the data was satisfactory and gave a reduced χ^2 of 1.14. The best-fit index of the power-law component is $\Gamma = 1.6^{+0.3}_{-0.2}$ and the best-fit equivalent width (EW) of the 6.4 keV line with respect to the power-law continuum amonts to 1.2 ± 0.2 keV. These results are compared in the following with model predictions for the production of X-rays by interaction of LECR electrons and ions with a neutral ambient gas.

3 Results and Discussion

In Tatischeff et al. [13], we developed a model in which LECRs are produced in an unspecified acceleration region and penetrate at a constant rate into a nearby cloud of neutral gas. The energetic particles can produce nonthermal X-rays by atomic collisions as they slow down by ionization and radiative energy losses in the ambient medium, and subsequently, they can either stop or escape from the cloud depending on their path length (Λ), which is a free parameter of the model. There are three other free parameters that can be studied from spectral fitting of X-ray data: the minimum energy of the CRs entering the cloud ($E_{\rm min}$), the power-law index of the CR source energy spectrum (s), and the metallicity of the X-ray emission region (Z). We considered the Kα and Kβ lines from ambient C, N, O, Ne, Mg, Si, S, Ar, Ca, Fe, and Ni.

Calculated properties of the X-ray emission produced by LECRs are compared in Fig. 3 with the results obtained from spectral fitting of the *XMM-Newton* data. We fixed for these calculations $\Lambda = 5 \times 10^{24}$ cm^{-2}, which is a typical value for non-relativistic protons propagating in massive molecular clouds of the GC environment (see [13]), and $Z = 1.7 Z_\odot$ ($Z_\odot$ is the solar metallicity), which is consistent with the results of Wang et al. [17]. We see that LECR electrons cannot satisfactorily account for the observed X-ray emission, because the predicted EWs are too low (Fig. 3a). Given that $s \leq 2$ is excluded in the leptonic model by the measured slope of the power-law continuum (Fig. 3c), the measured EW would require a highly super-solar metallicity of the ambient gas ($Z >\sim 3 Z_\odot$), which is not supported by other observations (e.g. [17]). We also see in Fig. 3c that the leptonic model

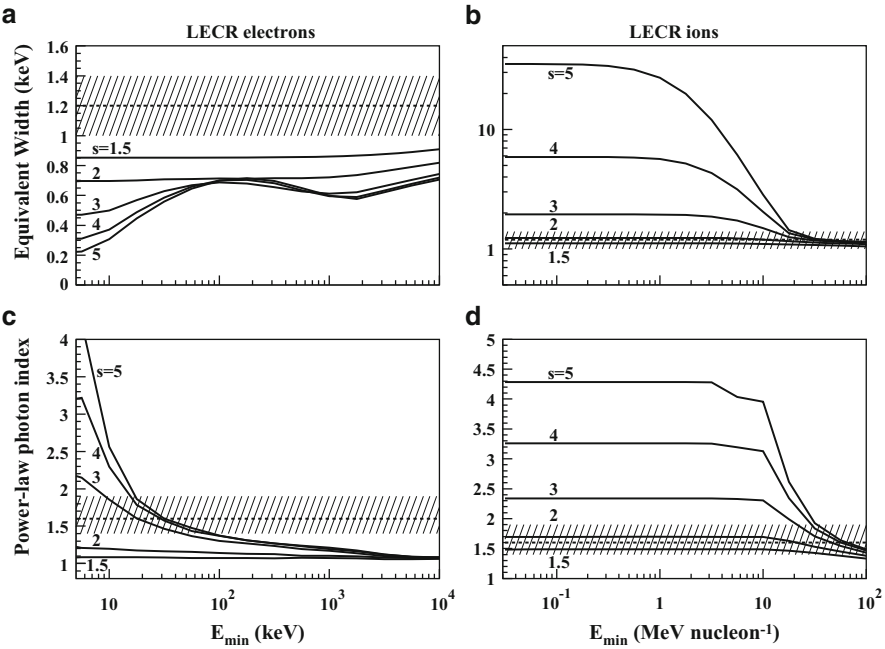

Fig. 3 Comparison of calculated properties of the X-ray emission produced by LECRs (*solid curves*) and observed properties of the X-ray emission detected with *XMM-Newton* from the Arches cluster region (*dashed lines* and *hatched areas* reflecting errors at the 90 % confidence level). Panels (**a**) and (**b**): equivalent width of the 6.4 keV Fe Kα line; panels (**c**) and (**d**): slope of the continuum emission around the 6.4 keV line. The theoretical curves show the results for five values of the CR spectrum index (s), as a function of the CR minimum energy ($E_{\rm min}$). The path length of the CRs in the interaction region is taken to be $\Lambda = 5 \times 10^{24}\,{\rm cm}^{-2}$ and the ambient medium metallicity $Z = 1.7 Z_{\odot}$. Panels (**a**) and (**c**) are for LECR electrons, whereas panels (**b**) and (**d**) are for LECR ions

would require a low CR minimum energy, $E_{\rm min} < 80\,{\rm keV}$, which would imply that suprathermal electrons can freely escape their acceleration region and penetrate into a neutral (or weakly ionized) medium. On the other hand, the measured EW of the Fe K line and the slope of the continuum emission are fully compatible with the predictions of the LECR ion model (Fig. 3b, d). The measured values can be reproduced in this model with any spectral index $s \sim 1.5$–2 and CR minimum energy $E_{\rm min} <\sim 100\,{\rm MeV\ nucleon}^{-1}$.

We have generated models of nonthermal X-ray production by LECRs that can be used in the spectral-fitting software XSPEC for more quantitative comparison with data. As illustrated in Fig. 2, the X-ray emission emanating from the Arches cluster region can be well fitted by a model of LECR ions combined with an optically thin thermal plasma. The best-fit normalization of the nonthermal component allows us to calculate the kinetic power continuously injected in the X-ray production region by CR protons: $(0.2–1) \times 10^{39}\,{\rm erg\ s}^{-1}$. Taking into account the accelerated

α-particles and heavier species, as well as the LECRs with $E < E_{\rm min}$ that do not penetrate into the interaction region, the required total CR power finally amounts to $(0.5–1.8) \times 10^{39}$ erg s^{-1}. In comparison, the total wind power supplied by the massive stars of the Arches cluster is $\sim 4 \times 10^{38}$ erg s^{-1} (see [10]), which is too low to explain the intensity of the nonthermal X-ray emission. The ongoing supersonic collision between the cluster and a molecular cloud is a more likely source for the LECR ions. We estimated in Tatischeff et al. [13] that a total kinetic power of $\sim 2.3 \times 10^{40}$ erg s^{-1} is currently processed in this collision, such that a particle acceleration efficiency of a few percent in the resulting bow shock system would produce enough CR power to explain the X-ray observations. The best-fit index of the CR source spectrum, $s = 1.9^{+0.5}_{-0.6}$, is consistent with this scenario. Deeper observations of this region with X-ray telescopes would allow to better characterize the acceleration process, as well as the effects of LECRs on the interstellar medium.

Acknowledgements We would like to thank Régis Terrier to several useful discussions. G. M. acknowledges financial support from CNES. This work uses observations performed with *XMM-Newton*, an ESA Science Mission with instruments and contributions directly funded by ESA member states and the USA (NASA).

References

1. Capelli, R., Warwick, R. S., Cappelluti, N., Gillessen, S., Predehl, P., Porquet, D., & Czesla, S. 2011a, A&A, 525, L2
2. Capelli, R., Warwick, R. S., Porquet, D., Gillessen, S., & Predehl, P. 2011b, A&A, 530, A38
3. Dong, H., Wang, Q. D., Cotera, A., et al. 2011, MNRAS, 417, 114
4. Clarkson, W. I., Ghez, A. M., Morris, M. R., et al. 2012, ApJ, 751, 132
5. Figer, D. F., Najarro, F., Gilmore, D., et al. 2002, ApJ, 581, 258
6. Genzel, R., Schödel, R., Ott, T., et al. 2003, ApJ, 594, 812
7. Lang, C. C., Goss, W. M., & Morris, M. 2002, AJ, 124, 2677
8. Liermann, A., Hamann, W.-R., & Oskinova, L. M. 2009, A&A, 494, 1137
9. Ponti, G., Terrier, R., Goldwurm, A., Belanger, G., & Trap, G. 2010, ApJ, 714, 732
10. Rockefeller, G., Fryer, C. L., Melia, F., & Wang, Q. D. 2005, ApJ, 623, 171
11. Smith, R. K., Brickhouse, N. S., Liedahl, D. A., & Raymond, J. C. 2001, ApJ, 556, L91
12. Stolte, A., Ghez, A. M., Morris, M., et al. 2008, ApJ, 675, 1278
13. Tatischeff, V., Decourchelle, A., & Maurin, G. 2012, A&A, 546, A88
14. Terrier, R., Ponti, G., Bélanger, G., et al. 2010, ApJ, 719, 143
15. Tsujimoto, M., Hyodo, Y., & Koyama, K. 2007, PASJ, 59, 229
16. Wang, Q. D., Dong, H., Cotera, A., et al. 2010, MNRAS, 402, 895
17. Wang, Q. D., Dong, H., & Lang, C. 2006, MNRAS, 371, 38
18. Yusef-Zadeh, F., Muno, M., Wardle, M., & Lis, D. C. 2007, ApJ, 656, 847
19. Yusef-Zadeh, F., Hewitt, J. W., Wardle, M., et al. 2012, ApJ, 762, 33

The High Altitude Water Čerenkov (HAWC) TeV Gamma Ray Observatory

Eduardo de la Fuente, Tomas Oceguera–Becerra, Guillermo García–Torales, and José Luis García–Luna for the HAWC Collaboration

Abstract The High Altitude Water Čerenkov observatory is a second generation ground based very high-energy γ-ray detector under construction in Sierra Negra, Puebla, México at an altitude of 4,100 m. Higher altitude, improved design and a larger physical size used to reject cosmic ray background, make HAWC 10–20 times more sensitive than its predecessor Milagro. HAWC's large field of view ($\sim$2 sr) and over 90 % duty cycle make it ideal to search for several types of TeV astronomical γ-ray sources, diffuse emission, cosmic anisotropy, and transients. Details and status of HAWC at date, and a galactic star formation application are here presented.

1 Introduction

When high-energy particles or photons ($E > E_c$ where $E_c \sim 600\,\mathrm{MeV/Z}$; E_c is the critical energy and Z the atomic number), called primaries, enter on the Earth's atmosphere ($Z=7$) at altitude of $\sim$30 km, an Extensive Air Shower (EAS) is induced. An EAS is produced by the interaction of primaries with atmospheric nuclei. A primary cosmic ray (usually high energy protons or iron nucleus) produce an EAS with three components: (1) The weak, soft component, or electromagnetic,

E. de la Fuente (✉) · J.L. García–Luna
Dpto. de Física, CUCEI, Universidad de Guadalajara (U de G), México, Av. Revolución 1500 S/R, Guadalajara, Jalisco, México
e-mail: edfuente@gmail.com

T. Oceguera–Becerra
CUCEA, U de G, Zapopan, Guadalajara, Jalisco, México

G. García–Torales
Dpto. de Electrónica, CUCEI, U de G, Guadalajara, Jalisco, México

The HAWC Collaboration

D.F. Torres and O. Reimer (eds.), *Cosmic Rays in Star-Forming Environments*, Astrophysics and Space Science Proceedings 34, DOI 10.1007/978-3-642-35410-6_32,

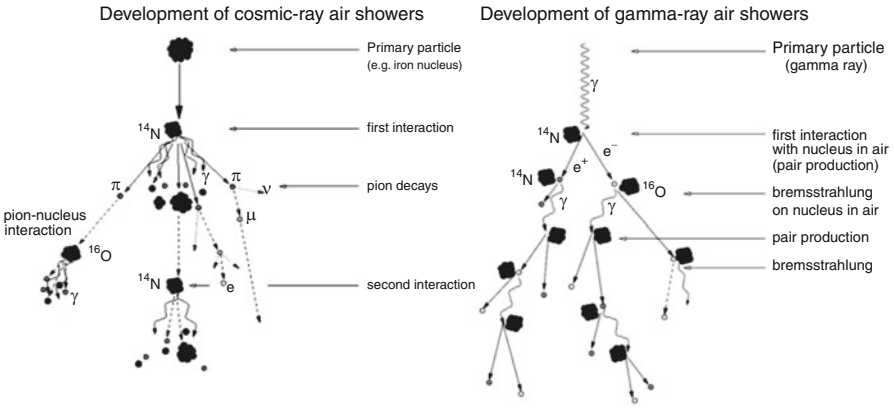

Fig. 1 Extended Air Shower (EAS) diagram. The development of cosmic ray showers (*left*), and gamma-ray showers (*right*). See text for details (Taken from http://www.mpi-hd.mpg.de/hfm/CosmicRay/Showers.html (C) 1999 K. Bernlör)

getting gamma rays through neutral pions decay, (2) The hard component (muon and hadrons), where charged and neutral kaons and pions decay in gamma rays, muons, neutrinos, antineutrinos, and nuclear fragments like protons and neutrons. For example, approximately 20 % of 1 GeV muons produced at 10 km will reach the sea level before decay, and (3) nucleonic component, where high-energy nucleons, desintegration-product nucleons, and nuclear desintegration is present.

On the other hand, if a gamma ray primary hits a nuclei in the Earth's atmosphere, an electron–positron pair production by columbian interaction is presented. These electrical charge particles, interact with other atmospheric nucleus producing secondaries gamma rays via Bremsstrahlung radiation ($e^{\pm} + N \rightarrow e^{\pm} + N + \gamma$). The length scale for the energy loss of e^{-} and photons when interacts with matter (in gr cm^{-2}), is known as the radiation length. When the $e^{\pm}$ from the primary produce a secondary gamma via bremmstrahlung, we obtain one radiation length. When this secondary gamma produce other pair production, and the resulting $e^{\pm}$ gives way to other secondary gamma via Bremmstrahlung, a second radiation length is obtained, and so on. The radiation length X_0, is the distance over which a high energy electron decrease its energy by Bremsstrahlung to $\frac{1}{e}$. The average distance that a high energy photon travels before converting to an $e^{\pm}$ pair is $\sim \frac{9}{7} X_0$, where $X_0 \sim 180 \frac{A}{Z^2} [\frac{g}{cm^2}] \sim 36.6 \frac{g}{cm^2}$; A is the atomic mass. A schematic diagram for the EAS described above is presented in Fig. 1.

When a charged particle (e.g., electrons or muons) from secondaries interacts with a polarized medium, air or water, it can produce Čerenkov radiation because the particle travel faster than light in the medium (Frank–Tamm Theory, 1937). This radiation can be detected by both, Imaging Air Čerenkov Telescopes (IACT's), and Water Čerenkov Detectors (WCD). While IACT's are good telescopes to get high resolution observations, WCDs are excellent as monitoring instruments for transients, AGNs, and large scale structures.

The High Altitude Water Čerenkov (HAWC) observatory is currently under construction at Sierra Negra, Pico de Orizaba National Park, Puebla, México at 19° N, 97° W, with an elevation of 4,100 m above sea level. It is a large water Čerenkov air-shower detector that will consist of 300 large tanks (4.5 m deep × 7.3 m diameter), each containing 200,0001 of highly purified water, covering an area of $\sim 22,000\,\mathrm{m}^2$ which can be seen as a lower limit as in the detection area, particles not coming from zenith can enter through the sides. HAWC is a high-duty cycle, large field of view ($\sim$2 sr) instrument capable of monitoring the gamma ray sky at energies up to 100 TeV. HAWC will provide an unbiased survey of the TeV gamma ray sky like AGNs and GRBs. The sensitivity of HAWC to GRBs is presented by Abeysekara et al. [2], and the unbiased AGN monitoring is discussed by Imram [3]. Also, HAWC can measure the spectra of galactic sources up to 100 TeV, and will map galactic diffuse gamma ray emission detecting galactic sources including pulsars, Pulsar Wind Nebulae, and Supernova Remnants. With 15 times the sensitivity of its predecessor, Milagro, the HAWC Observatory will enable significant detections of Crab-like fluxes each day at a mean energy of 1 TeV. HAWC will also have significant overlap with space and ground-based detectors like MAGIC, VERITAS, NASA–FERMI, etc., which will also offer synergies between them. In Sect. 2 the design and performance of HAWC is discussed, and in Sect. 3, the physics available to do with HAWC is summarized. Details and more information of HAWC are presented in the respective proceedings of the International Cosmic Rays Conference (2011).

2 High Altitude Water Čerenkov Observatory: HAWC

2.1 Detector Design

HAWC will have at least 1200 PMTs, re-using the 900 8 in. hemispherical Hamamatsu photomultipliers (PMTs) from Milagro. Each PMT is deployed at the bottom of a 4.5 (high) × 7.3 (diameter) meters metalic tanks. The 300 tanks arranged in a dense pattern that provides 63 % coverage of the 150 × 150 m instrumented area. Each tank will be instrumented with 4 PMTs; three 8 in. and one 10 in. in diameter, to detect secondary particles from an EAS. If the energy is high enough, the secondaries can arrive at the HAWC detector in a flat plane. The array of water tanks is sensitive to them as they reach the ground. The Čerenkov light produced will be captured by the PMTs, which are sensitive at UV wavelengths. When several tanks observe the same EAS, it is possible to reconstruct the direction of the primary γ-ray that caused the air shower. The layout of HAWC is shown in Fig. 2a. A photo of the site (June 2012) showing the location of the HAWC 30 (tanks) phase and VAMOS;

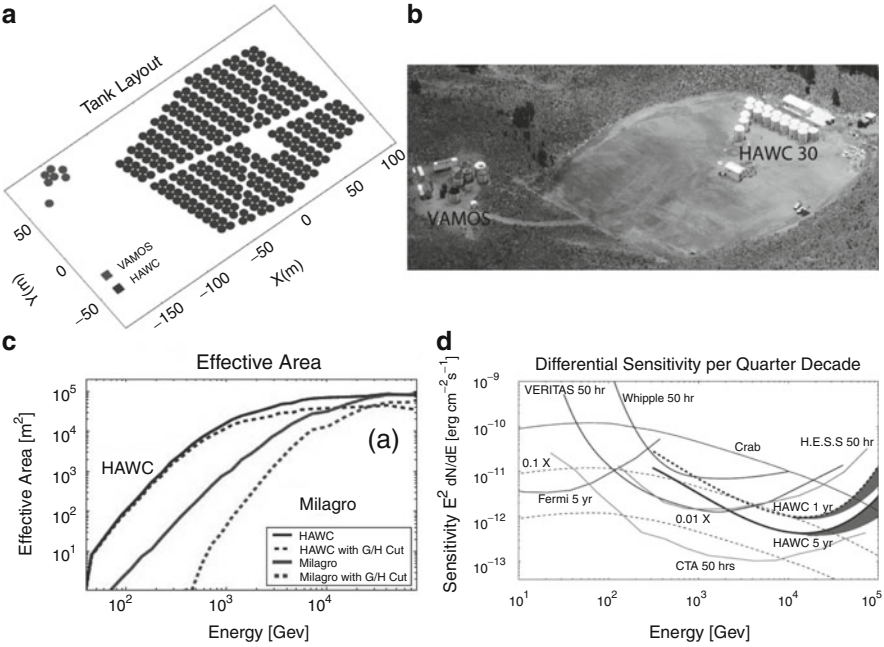

Fig. 2 (**a**) Layout of the VAMOS prototype and the HAWC 300 array. (**b**) Image of the site where HAWC will be placed. The HAWC 30 phase is under construction and it is expected to be operational at the end of 2012. (**c**) Effective area of HAWC along with the effective area of the predecessor experiment Milagro for comparison. Above about 1 TeV, the effective area approaches the geometrical footprint of the experiment and at lower energies the effective area is reduced due to the tendency of lower energy air showers to result in few energetic particles on the ground, (**d**) the sensitivity of HAWC to a Crab-like source compared to other γ-ray observatories. One year HAWC exposure is shown with a *dotted line*, and 5 year exposure is shown with a *solid line*. A total exposure of 50 h is assumed for IACTs, allowing $\sim$15 sources to be surveyed per year with such sensitivity. See Westerhoff et al. in proceedings of the 39th COSPAR Scientific Assembly, 2012

The Verification And Measuring of the Observatory System.[1] VAMOS was built on site in 2011. Six of the tanks were instrumented with 4–7 PMTs per tank.

2.2 Detector Performance

The simulation for HAWC is an extension of the Milagro simulation software package. CORSIKA is used to simulate γ-ray and hadron induced atmospheric showers. A custom detector simulation using GEANT4 is used to propagate the

[1]Technical details and preliminary first results are presented in Proceedings of the 5th International Symposium on High-Energy γ-Ray Astronomy and Proceedings of the Fermi-Swift Conference on Gamma-Ray Bursts, 2012.

secondary shower particles that reach the detector elevation through the HAWC detector. Čerenkov light production is simulated and individual Čerenkov photons are tracked through the detector. Detailed optical modeling of the water (absorption and scattering), reflection and absorption at surfaces, and the PMT response are included. The simulation has been thoroughly tested through comparison with Milagro data. The Milagro electronics utilize the Time-Over-Threshold method for pulse amplitude estimation. The response of this system is simulated by generating a pulse waveform for every detected photon. These simulated pulses are then digitized and converted to amplitude and timing measurements for use by the reconstruction software. HAWC will re-use this electronics where two data acquisition (DAQ) systems are included: The main DAQ system reads out coincident signals in the tanks and reconstructs the direction and energy of individual EAS, and the scaler DAQ counts the hits in each PMT and searches for a statistical excess over the noise of all PMTs. Both systems have different energy sensitivity and are complementary.

The depth and spacing of the PMTs was optimized for γ-ray sensitivity from 1 to 100 TeV. The detector must act as an effective calorimeter in order for the background rejection methods to work properly, so the PMTs need to be sufficiently deep that EM particles are unable to pass close to the photo-cathode and produce large pulses that are not proportional to the deposited energy. We have found that this requires at least 3.5 m of water ($\sim$9 radiation lengths). However, if the PMTs are too deep, the sensitivity (PhotoElectrons/GeV; PEs/GeV) is significantly reduced. At the selected depth of 4 m HAWC detects $\sim$20 PEs/GeV for EM particles and $\sim$30 PEs for through-going muons. The illumination of EM particles is found to be roughly uniform over an area with a radius of 0.75$\times$ depth. This dictates that for a tank of depth 4 m, a radius of $<$3 m is optimal. There is no scientific advantage to making the tanks with diameters smaller than 5 m, but smaller tanks may be more cost effective to produce.

Because the sensitivity of the detector is strongly dependent on the zenith angle of the source being studied, we compute the sensitivity by estimating the number of signal and background events collected during a single transit of the source from horizon to horizon. As a reference source, the Crab is selected. However, since the results are normalized to the Milagro measurements, the sensitivity is nearly independent of the assumed source spectrum. The source declination is selected so that the source passes 15° from zenith as it transits so that a more or less typical sensitivity is estimated. HAWC is 15 % more sensitive to sources that pass through zenith and 20 % less sensitive for sources that transit 25° from zenith. The peak sensitivity of HAWC is at 2 TeV, where we will detect the crab at 75 $\sigma/\sqrt{(year)}$.

The effective area vs. energy plotted for Milagro and HAWC both with and without γ-hadron cuts applied is presented in Fig. 2c. Note that the γ-hadron cut for Milagro severely attenuates the low energy area, but the HAWC γ-hadron separation technique in contrast is much more efficient making HAWC's effective area at low energies $\sim$100 times larger than that of Milagro. In Fig. 2d, the sensitivity of several Čerenkov telescopes is presented. IACTs typically observe sources for 50 h approximately and survey observations are $\sim$10 h. For zenith angles $<$30° the angular dependence of the sensitivity is not significant. However, even with

maximum exposure, an IACT still would not be able to match HAWC sensitivity above 10 TeV. Consequently, most of the HESS sources in the Galactic plane survey are not detected above 10 TeV. HAWC will overcome the latter. For a 1 year survey of the overhead sky, HAWC will have a 5σ point source detection threshold of 40 mCrab. In 4 years, HAWC will survey the viewable sky to the level of 20 mCrab. As stated above, the sensitivity depends on zenith angle, but is not substantially reduced for transit zenith angles $<30°$. The HAWC detector deployed at latitude 19° N will survey 44 % of the entire sky (4π sr) with a sensitivity <50 mCrab and 64 % of the sky with sensitivity <80 mCrab.

3 Physics and Star Formation with HAWC

The HAWC science objectives are: (1) To discover the origin of cosmic rays by measuring gamma ray spectra to 100 TeV. Hadronic sources should have unbroken spectra beyond 30–100 TeV, and the Galactic diffuse gamma rays probe the distant cosmic ray flux; (2) to understand particle acceleration in astrophysical jets with wide field of view and high duty factor observations; and (3) to explore new physics via HAWC's unbiased survey of the sky through understanding of TeV sources and the study of the local TeV cosmic rays and their anisotropy.

Cosmic rays up to at least 10^3 TeV, and perhaps as high as 10^6 TeV, are of galactic origin. Gamma rays up to 100 TeV will be observable by HAWC from individual point and extended sources as well as from the sea of cosmic rays interacting with matter in the Galactic plane. The highest energy observations are key to distinguishing gamma rays produced by electrons from those produced by hadrons. Electrons lose their energy more quickly than protons due to synchrotron emission and are therefore more difficult to accelerate to the highest energies. Also, the cross section for inverse Compton scattering decreases at higher energies, resulting in a break in the gamma-ray spectrum by at least 10–50 TeV. On the other hand, the spectra of the known TeV Galactic sources are hard with an average differential spectrum of index -2.3 as compared to the steeper Crab spectrum of index -2.6. HESS detects sources with 0.2 times the Crab flux above 200 GeV, but if the measured spectra continue to higher energies, then these sources would be as bright as the Crab above 100 TeV. HAWC would detect $\sim$20 gamma rays >100 TeV per year from such a source in its field of view.

Although γ-ray emission studies of galactic star formation regions (SFR) are few and controversial, Westerlund 2 (Wd2), W43 and Westerlund 1 (Wd1) are perhaps the most sampled ones (e.g., [1,4,5]). In SFRs it is believed that the γ-ray emission is produced by the interaction of energetic particles within the molecular gas. However it is not clear if the γ-ray emission from Wd2 comes from the SFR or from the PWN powered by PSR J1022–5746 [1]; moreover there is evidence that this does not occur in Wd1. In fact Luna et al. [4] based on ^{12}CO observations suggest that the source of γ-rays is a PWN powered by PSR J1648–4611 which is located behind Wd1 and in another spiral arm, instead of the dense gas surrounding the massive

stars in Wd1. Furthermore, the possible association of HESS J1848-018 to W43 seems controversial (see [5]). Considering this, it is possible that pulsars presented in galactic SFR, or in projection, can be the sources of γ-ray emission instead of the dense molecular gas or open clusters; or at least, pulsars could be the dominant one. More γ-ray and Multi Wavelength observations of these and similar regions are necessary to determine the source and to clarify the origin and nature of γ-ray emission. HAWC will be able to perform TeV observations of near degree size star formation regions in the range 50 GeV–100 TeV and hence, it will have a synergy (sensitivity/resolution) with Imaging Air Cerenkov Telescopes.

References

1. Abramowski, A., et al.: Revisiting the Westerlund 2 field with the HESS telescope array. Astronomy & Astrophysics. 525, A46–A53 (2011).
2. A.U. Abeysekara, et al.: On the sensitivity of the HAWC observatory to gamma-ray bursts. Astroparticle Physics. 35, 641–650 (2012).
3. Imram, Asif for the HAWC Collaboration: Study of HAWC Sensitivity to Active Galactic Nuclei. Proceedings of the 32nd International Cosmic Ray Conference (ICRC2011) OG2.3–2.4, 54–58 (2011).
4. Luna, A., et al.: The discovery of a molecular cavity in the norma near arm associated with H.E.S.S γ–ray source located in the direction of Westerlund 1. Astrophysical Journal Letters. 713, L45–L49 (2010).
5. Tibolla, Omar., et al.: New unidentified Galactic H.E.S.S. sources. In: Proceedings of the 2009 FERMI Symposium, Stanford, 1999, http://www.slac.stanford.edu/econf/C0911022/. [astro-ph.HE/0912.3811]

THE HAWC COLLABORATION (MEXICO–USA)

A. U. Abeysekara[1], A. Aguilar[2], J. A. Aguilar[2], S. Aguilar[3], R. Alfaro[3], E. Almaraz[3], C. Álvarez[4], J. de D. Álvarez-Romero[5], M. Álvarez[3], R. Arceo[4], J. C. Arteaga-Velázquez[5], C. Badillo[3], A. Barber[6], B. M. Baughman[7], N. Bautista-Elivar[8], E. Belmont[3], E. Benítez[10], S. Y. BenZvi[2], D. Berley[7], A. Bernal[10], E. Bonamente[11], J. Braun[7], R. Caballero-Lopez[12], I. Cabrera[3], A. Carramiñana[13], L. Carrasco[13], M. Castillo[14], L. Chambers[15], R. Conde[14], P. Condreay[15], U. Cotti[5], J. Cotzomi[14], J. C. D'Olivo[16], E. de la Fuente[17], C. De León[5], S. Delay[18], D. Delepine[19], T. DeYoung[15], L. Diaz[16], L. Diaz-Cruz[14], B. L. Dingus[20], M. A. Duvernois[2], D. Edmunds[1], R. W. Ellsworth[21], B. Fick[11], D. W. Fiorino[2], A. Flandes[12], N. I. Fraija[10], A. Galindo[13], J. L. García–Luna[17], G. García-Torales[17], F. Garfias[10], L. X. González[13], M. M. González[10], J. A. Goodman[7], V. Grabski[3], M. Gussert[22], C. Guzmán-Ceron[10], Z. Hampel-Arias[2], T. Harris[23], E. Hays[24], L. Hernandez-Cervantes[10], P. H. Hüntemeyer[11], A. Imran[20], A. Iriarte[10], J. J. Jimenez[4], P. Karn[18], N. Kelley-Hoskins[11], D. Kieda[6], R. Langarica[10], A. Lara[12], R. Lauer[25], W. H. Lee[10], E. C. Linares[5], J. T. Linnemann[1], M. Longo[22], R. Luna-García[26], H. Martínez[27], J. Martínez[3], L. A. Martínez[10], O. Martínez[14], J. Martínez-Castro[26], M. Martos[10], J. Matthews[25], J. E. McEnery[24], G. Medina-Tanco[16], J. E. Mendoza-Torres[13],

P. A. Miranda-Romagnoli[9], T. Montaruli[2], E. Moreno[14], M. Mostafa[22], M. Napsuciale[19], J. Nava[13], L. Nellen[16], M. Newbold[6], R. Noriega-Papaqui[9], T. Oceguera-Becerra[17], A. Olmos Tapia[13], V. Orozco[3], R. Pelayo–Ramos[14], V. Pérez[3], E. G. Pérez-Pérez[8], J. S. Perkins[24], J. Pretz[20], C. Ramirez[14], I. Ramírez[3], D. Rebello[23], A. Rentería[3], J. Reyes[13], D. Rosa-González[13], A. Rosado[14], J. M. Ryan[28], J. R. Sacahui[10], H. Salazar[14], F. Salesa[22], A. Sandoval[3], E. Santos[4], M. Schneider[29], A. Shoup[30], S. Silich[13], G. Sinnis[20], A. J. Smith[7], K. Sparks[15], W. Springer[6], F. Suárez[3], N. Suarez[13], I. Taboada[23], A. F. Tellez[14], G. Tenorio-Tagle[13], A. Tepe[23], P. A. Toale[31], K. Tollefson[1], I. Torres[13], T. N. Ukwatta[1], J. Valdes-Galicia[12], P. Vanegas[3], V. Vasileiou[24], O. Vázquez[3], X. Vázquez[3], L. Villaseñor[5], W. Wall[13], J. S. Walters[13], D. Warner[22], S. Westerhoff[2], I. G. Wisher[2], J. Wood[7], G. B. Yodh[18], D. Zaborov[15], A. Zepeda[27]

[1]Dept. of Physics & Astronomy, MSU, USA, [2]Dept. of Physics, UW–Madison, USA, [3]IFUNAM, México, [4]CEFYMAP, UNACH, México, [5] UMSNH, Morelia, México, [6]Dept. of Physics and Astronomy, UU, USA, [7]Dept. of Physics, UMD, College Park, USA, [8]IPP, Pachuca, México, [10]IAUNAM, México, [11]Dept. of Physics, MTU, Houghton, USA, [12]IGUNAM, México, [13]INAOE, Puebla, México, [14]FCFM, BUAP, Puebla, México, [15]Dept. of Physics, PSU, USA, [16]ICN–UNAM, México, [17]CUCEI, CUCEA, U de G, Guadalajara, México, [18]Dept. of Physics and Astronomy, UC–Irvine, USA, [19]Dept. of Physics, UG, Leon, México, [20]Phys. Division, LANL, USA, [21]Dept. of Physics and Astronomy, GMU, USA, [22]CSU, Ft. Collins, USA, [23]CRA, Georgia Tech, Atlanta, USA, [24]NASA–GSFC, USA, [25]Dept. of Physics and Astronomy, UNM, Albuquerque, USA, [26]CIC–IPN, México, [27]CINVESTAV–IPN. México, [9]UAEH, Pachuca, México, [28]Dept. of Physics, UNH, Durham, USA, [29]UCSC, USA, [30]OSU, Lima, USA, [31]Dept. of Physics and Astronomy, UA, Tuscaloosa, USA.